Laser-driven strong magnetic fields and high discharge currents : measurements and applications to charged particle transport

Mathieu Bailly-Grandvaux

▶ **To cite this version:**

Mathieu Bailly-Grandvaux. Laser-driven strong magnetic fields and high discharge currents : measurements and applications to charged particle transport. Plasmas. Université de Bordeaux, 2017. English. NNT : . tel-01653837v1

HAL Id: tel-01653837

https://theses.hal.science/tel-01653837v1

Submitted on 2 Dec 2017 (v1), last revised 8 Jun 2018 (v3)

HAL is a multi-disciplinary open access archive for the deposit and dissemination of scientific research documents, whether they are published or not. The documents may come from teaching and research institutions in France or abroad, or from public or private research centers.

L'archive ouverte pluridisciplinaire **HAL**, est destinée au dépôt et à la diffusion de documents scientifiques de niveau recherche, publiés ou non, émanant des établissements d'enseignement et de recherche français ou étrangers, des laboratoires publics ou privés.

université de BORDEAUX

N° d'ordre:

THÈSE

Présentée pour obtenir le grade de :

DOCTEUR EN SCIENCES DE
L'UNIVERSITÉ DE BORDEAUX

ÉCOLE DOCTORALE DES SCIENCES PHYSIQUES
ET DE l'INGÉNIEUR

Spécialité: Astrophysique, Plasmas, Nucléaire

par

Mathieu BAILLY-GRANDVAUX

Laser-driven strong magnetic fields and high discharge currents : measurements and applications to charged particle transport

Directeur de thèse :	M. João Jorge SANTOS	Maître de Conférences (Université de Bordeaux)
Co-directeur de thèse :	M. Dimitri BATANI	Professeur (Université de Bordeaux)

Soutenue le 20 Mars 2017 devant la Commission d'examen :

Président du jury :	François Amiranoff	Directeur de Recherche (Ecole Polytechnique UPMC - LULI)
Rapporteurs :	Marco Borghesi	Professeur (Queen's University of Belfast) *Royaume-Uni*
	John Moody	Directeur de Recherche (Lawrence Livermore National Laboratory) *États-Unis*
Examinateurs :	François Amiranoff	Directeur de Recherche (Ecole Polytechnique UPMC - LULI)
	Jean-Luc Miquel	Ingénieur (CEA)
Invités :	Philip Korneev	Maître de Conférences (MEPHI - Moscou) *Russie*
	José Javier Honrubia	Professeur (Universidad Politécnica de Madrid) *Espagne*

Thèse préparée au
Centres Lasers Intenses et Applications
CELIA (UMR 5107), Bât. C6
Université de Bordeaux
33400, Talence

Abstract

The problem of strong quasi-static magnetic field generation is a challenge in laser-plasma interaction physics. Proposed 30 years ago, the use of the laser-driven capacitor-coil scheme, which stands out for its compact design while not needing any additional pulsed power source besides the laser power, only recently demonstrated its potential.

This thesis work aims at characterizing the underlying physics and at developing this scheme. We demonstrated the generation of strong quasi-static magnetic fields by laser (500 J, 1 ns-duration and $\sim 10^{17}\,\mathrm{W/cm^2}$ intensity) of several hundreds of Teslas and duration of $2-3$ ns. The B-field space- and time-evolutions were characterized using three independent diagnostics: B-dot probes, Faraday rotation and proton-deflectometry). The characterization of the underlying physical processes involved also X-ray diagnostics of the laser-irradiated zone and optical shadowgraphy of the coil rod expansion.

A novel application of externally applied magnetic fields to guide relativistic electron beam in dense matter has been carried out and the obtained results set the ground for improved high-energy-density transport in matter. Indeed, allowing sufficient time for the dense target magnetization, a factor 5 improvement of the electron energy-density flux at 50 µm-depth was evidenced.

Besides, the generation of high discharge currents consecutive to short laser pulse irradiation (50 J, $<$ 1 ps-duration and $\sim 10^{19}\,\mathrm{W/cm^2}$ intensity) was also pointed out. Proton imaging of the discharge permitted to measure the propagation of an electromagnetic wave at a velocity close to the speed of light. This wave, of $\sim$ 40 ps-duration, was used as an electromagnetic lens to focalize and energy-select a narrow energy range within a multi-MeV proton beam (up to 12 MeV) passing through the coil.

All-above experimental measurements and application results were thoroughly compared to both computer simulations and analytic modeling.

The applications of this thesis work in a near future will concern:

- ◇ inertial confinement fusion, by guiding relativistic electron beams up to the dense core nuclear fuel, and by confining particles depositing their energy in it, or even those resulting from the fusion reactions;
- ◇ laboratory planetology and astrophysics, by generating secondary sources of energetic particles and radiation to reach the warm-dense-matter state or by magnetizing plasmas to reproduce astrophysical phenomena in scaled experiments;
- ◇ and finally, the control of charged particle beams in vacuum, useful in particular for the development of laser-driven sources for distant applications in science, industry or even medecine.

Keywords : Laser-driven magnetic fields, Inertial confinement fusion, Laser-driven fast electron transport, Fast Ignition, Magnetized plasmas, Magnetic guiding, Electromagnetic lens.

FORTS CHAMPS MAGNÉTIQUES ET DÉCHARGES DE COURANT INTENSES GÉNÉRÉS PAR LASER : MESURES ET APPLICATIONS AU TRANSPORT DE PARTICULES CHARGÉES

Résumé

La problématique de génération de champs magnétiques quasi-statiques intenses constitue un défi pour la physique de l'interaction laser-plasma. Proposé il y a 30 ans, l'utilisation de cibles "boucles" irradiées par laser se distinguent par leur design compact ne nécessitant aucune génération de courant pulsé en plus de la puissance laser et ont dévoilé récemment leur grand potentiel.

Ce travail de thèse s'attache à la caractérisation des phénomènes physiques et au développement de cette technique. On a ainsi montré la génération de forts champs magnétiques quasi-statiques par interaction laser-matière (500 J, durée laser de 1 ns et intensité $\sim 10^{17}\,\mathrm{W/cm^2}$) atteignant une amplitude de plusieurs centaines de Teslas pendant 2 à 3 ns. L'évolution temporelle et la distribution spatiale des champs magnétiques ont été mesurés par trois diagnostics indépendants : sondes B-dot, rotation de Faraday et défléctométrie de protons. La caractérisation des mécanismes physiques sous-jacents ont aussi fait appel à des diagnostics de rayonnements X de la région irradiée par laser ainsi qu'à des mesures d'ombroscopie optique du fil de la boucle en expansion.

Une application de ces champs au guidage magnétique d'électrons relativistes dans la matière dense a permis d'ouvrir de nouvelles perspectives au transport de hautes densités d'énergies dans la matière. En effet, en laissant suffisamment de temps pour que le champ magnétique pénètre dans la cible dense, une amélioration d'un facteur 5 de la densité d'énergie portée par les électrons après 50 µm de propagation a été mise en évidence.

En outre, des décharges de courants intenses consécutives à l'irradiation par impulsion laser courtes (50 J, durée laser < 1 ps et intensité $\sim 10^{19}\,\mathrm{W/cm^2}$) ont été observées. Une imagerie protonique de la décharge a permis de mesurer la propagation d'une onde électromagnétique à des vitesses proches de la vitesse de la lumière. Cette onde d'une durée de ~ 40 ps a été utilisée comme lentille électromagnétique pour focaliser et sélectionner sur une bande étroite d'énergie un faisceau de protons de plusieurs MeV (jusqu'à 12 MeV) passant dans la boucle.

Les résultats de ces différentes mesures et applications expérimentales ont été par ailleurs confrontées à des simulations et à des modèles analytiques.

Les applications de cette thèse se déploient sur des aspects comme :

- ◇ la fusion par confinement inertiel, en guidant des faisceaux d'électrons relativistes jusqu'au cœur de la capsule de combustible, tout en confinant les particules qui y déposent leur énergie ainsi que celles créées par les réactions de fusion nucléaire ;
- ◇ l'astrophysique et la planétologie de laboratoire, en générant des sources secondaires de particules énergétiques ou de rayonnement afin de porter la matière dense a de très hautes températures (matière tiède et dense), ou en magnétisant des plasmas pour reproduire des phénomènes astrophysiques à plus petite échelle au laboratoire ;
- ◇ et enfin le contrôle de faisceaux de particules chargées dans le vide pour le développement de sources laser dans le cadre d'applications s'effectuant à distance de la source notamment en science, dans l'industrie, ou même en médecine.

Mots-clés : Champs magnétiques générés par laser, Fusion par confinement inertiel, Transport d'éléctrons relativistes, Allumage rapide, Plasma magnétisés, Guidage magnétique, Lentille électromagnétique.

Acknowledgements

To acknowledge with precision all the people who contributed to this work or supported me by their affection during those three years is maybe the most difficult part of this manuscript. Therefore I will just try to be qualitative and not as rigorous as I intended to be in the following scientific part. This being said, and speaking about quality, my first acknowledgment is for my PhD supervisor Joao Santos. Qualities he has a lot, and one of them is that he is trustful! He trusted me from the beginning, giving me this opportunity to make a thesis in a field where I started completely from scratch (I did not even know what was a plasma). All along those three years he also handled my strong personality and found how to drive me as a better scientist and also a better man! He will stay as a friend and mentor in my future life after this PhD. Then I think to all other colleagues who participated or not in this work, and to name a few: Dimitri Batani, Vladimir Tikhonchuk, Michael Ehret, Alexandre Poyé, Lorenzo Giuffrida, Claudio Bellei, Michael Touati, Mokrane Hadj-Bachir, Alessio Morace, Pierre Forestier-Colleoni, ... (I realize here that if I wanted to be precise, this part would extend over a few pages). I want also to thanks all people of CELIA who gave me strength in coffee breaks, notably, and some people who made also my work easier: Sophie Heurtebise, Céline Oum, Sonia Senut and Emmanuelle Lesage, always here to solve my travel issues, among other administrative things! I also want to thanks my referees who are already, and rightly so, presented in the cover page. They worked a lot to read this long thesis and provide me exhaustive corrections and suggestions. They also appreciated my work and I found myself very proud of their nice comments and wish only that one day I could be a researcher as talented as they are. Then I want to finish this part giving a thanks to all my collaborators and people I met during conferences and experiments, I have a lot of good memories of travels and meetings with people always nice and welcoming! To resume, I had a lot of luck! Now I will switch to French to thanks my family and other friends who would certainly prefer to read me in my mother-tongue.

Je viens de finir en anglais en disant qu'il serait plus facile pour cette partie suivante de parler en Français (petite traduction pas forcément nécessaire pour le grand nombre d'entre-vous qui comprennent la langue de Shakespeare). Et j'ai parlé de langue maternelle. La transition est donc toute trouvée. En effet, je ne dois pas que ma langue à ma mère, je lui dois la vie bien entendu, mais surtout je lui doit CETTE vie! Je ressens une vive emotion à l'écriture de ces lignes mais je crois qu'il est important de le dire ici. Cet accomplissement, cette thèse, je sais que cela t'as rendu fière. Mais ce n'est rien au regard de l'amour d'une mère et bien que cela puisse être une petite preuve que tu ne t'es pas battue pour rien, que j'ai réussi, tu peux avant tout être fière de toi. Le courage et le dévouement que tu as eu avec nous (moi et ma soeur) est et restera le moteur le plus puissant qui m'anime. Merci! Je tiens également à remercier mon père qui m'a soutenu et a toujours été prêt à m'aider. Je sais que toi aussi tu t'es battu et pour autant je ne t'ai pas épargné, toi et Isabelle, je t'en remercie aujourd'hui et je vous aime. De l'amour j'en ai eu aussi pendant ces trois ans pour Léa, et je tiens à la remercier ici pour tout ce qu'elle m'a apporté. Je tiens enfin à parler de mes amis proches, qui se reconnaitront (c'est facile ce sont ceux qui sont toujours là, même si je suis pas très fort pour donner des nouvelles...). Eh bien je suis grand maintenant et j'espère que je vais m'améliorer et vous dire plus souvent que je pense à vous. Je dois quand même vous dire que je serai toujours là pour vous comme je sais que vous l'êtes pour moi: Fabien & Elsa (maintenant si beaux mariés), Julien, Cyrille, Boss, Mika,... Mes amis Gadzarts (je ne peux pas tous vous citer mais quel plaisir de passer des moments avec vous!). Ma famille enfin, mes grand-parents, mes oncles et tantes et cousins. J'ai une famille formidable et mon seul regret pour cette prochaine étape aux Etats-Unis en postdoc (UCSD), est d'être loin de vous et de ne pas pouvoir venir à toutes les réunions de famille. Je vous embrasse tous.

Bon voilà je vais finir ici ce "travail de thèse" sur moi-même et sur les gens qui comptent dans ma vie. C'est peut-être très émotif pour certains lecteurs mais c'était important pour moi aussi d'écrire cela. Après avoir écrit autant sur un sujet de sciences, il me paraissait normal de faire le même travail en plus petit sur moi même et cette section de la thèse me tendait les bras, ayant cet avantage qu'elle restera accessible.

Contents

List of physical units **15**

0 Introduction **17**

0.1 Magnetic fields in Nature . . . 17

0.2 Controlled nuclear fusion . . . 18

0.2.1 Focus on Inertial Confinement Fusion (ICF) . . . 23

0.3 State-of-the-art of strong magnetic field generation . . . 26

0.3.1 Conventional methods . . . 26

0.3.2 Laser-driven generators . . . 29

0.4 Goals and summary of the manuscript . . . 32

I An introduction to high intensity laser interaction with matter and acceleration of particles **33**

1 Introduction to the plasma state **34**

2 Motion of charged particles in electric and magnetic fields **38**

3 General concepts of intense laser interaction with overdense matter **44**

3.1 Fast electron generation . . . 45

3.1.1 Non-relativistic regime . . . 45

3.1.2 Relativistic regime . . . 50

3.1.3 Relevant mechanisms in our experimental conditions . . . 53

3.2 State-of-the-art of accelerated electron sources from over-dense targets . . . 53

3.2.1 Laser-to-electrons conversion efficiency . . . 53

3.2.2 Fast electron temperature . . . 55

3.2.3 Fast electron divergence . . . 57

3.3 Fast electron transport . . . 58

3.3.1 Collisional effects over transport . . . 58

3.3.2 Resistive effects over transport . . . 63

4 Laser-matter interaction in nanosecond regime ($\gtrsim 10^{16}\,\mathrm{W/cm^2}$) **71**

4.1 Self-generated fields . . . 72

4.1.1 Thermoelectric effect due to crossed gradients ($\vec{\nabla} n_e \wedge \vec{\nabla} T_e$) . . . 72

4.1.2 Influence of magnetic field over heat fluxes and transport coefficients . . . 73

4.2 Plasma expansion into vacuum . . . 74

5 Laser-matter interaction in picosecond and sub-picosecond regime ($\gtrsim 10^{18}\,\mathrm{W/cm^2}$) **77**

5.1 Self-generated fields . . . 77

5.2 Energetic ion beams . . . 80
5.2.1 Energetic ion beam acceleration . . . 80
5.2.2 Ion beam characterization . . . 84
5.2.3 Radiography and field measurements with laser-driven ions beams . . . 86

6 Mechanisms of target charging **87**
6.1 Return currents . . . 87
6.2 Transient target charging . . . 87
6.3 Transient target charging measurements . . . 90
6.3.1 EMP generation . . . 90
6.3.2 Proton imaging of the discharge . . . 93

II Novel platform for laser-driven strong magnetic field generation **95**

7 The challenge of measuring quasi-static laser-driven strong magnetic-fields **96**
7.1 Characteristics of the B-fields to measure . . . 97
7.2 Available diagnostics . . . 97
7.2.1 B-dot probe . . . 97
7.2.2 Proton Deflectometry . . . 100
7.2.3 Faraday rotation . . . 102
7.3 Conclusion on the presented diagnostics . . . 102

8 Characterization of magnetic field generation with different target materials and geometries **104**
8.1 Measurements of the B-field in LULI laser facility . . . 104
8.1.1 Experimental Setup . . . 105
8.1.2 B-dot probe results . . . 106
8.1.3 Faraday Rotation results . . . 113
8.1.4 Proton Deflectometry results . . . 115
8.1.5 Shielded proton deflectometry . . . 131
8.2 Extra physical information from complementary diagnostics . . . 134
8.2.1 Shadowgraphy results . . . 134
8.2.2 Streak Optical Pyrometry (SOP) . . . 135
8.2.3 X-ray spectrometry . . . 137
8.2.4 Bremsstrahlung Canon . . . 140
8.3 Conclusion . . . 141

9 Semi-analytical model of B-field generation in nanosecond regime **143**
9.1 A voltage-source model . . . 143
9.2 Improvement of the model . . . 146

9.3 Current-source approach : laser-pumped diode model . . . 150
9.3.1 Potential description (1D model) . . . 150
9.3.2 A 3D description of the potential and related issues of the 1D description . . . 153
9.3.3 Estimation of the maximum current of the diode in series with a resistance . . . 156
9.3.4 Model results . . . 158
9.4 Conclusions on the modeling . . . 161
9.5 Energetic qualifications . . . 162

III Application of imposed external B-field to guide charged particle beams in dense matter or in vacuum 165

10 Fast-Electron guiding by laser-driven strong external magnetic field in dense matter 166
10.1 Existing techniques to guide fast electron beams . . . 166
10.2 Experimental setup description . . . 167
10.3 Simulations of the magnetic-field diffusion over the transport targets . . . 169
10.4 Experimental results . . . 170
10.5 Fast electron transport simulations with external magnetic field in Particle In Cell (PIC) Hybrid - Code . . . 171
10.6 Calculation of CTR emission (post-processor) . . . 172
10.7 Simulations results and discussion . . . 172
10.8 Complementary information . . . 180
10.9 Conclusions . . . 182

11 High discharge current and application to proton beam tailoring in high laser intensity regime (picosecond interaction) 183
11.1 Experimental setup description . . . 183
11.1.1 Time-resolving proton radiography . . . 184
11.2 Previous results of electromagnetic lenses . . . 184
11.3 Experimental Results . . . 186
11.3.1 TNSA proton source characterization by Thompson Parabola . . . 186
11.3.2 Time-resolving proton radiography results . . . 187
11.4 Static simulations results . . . 191
11.4.1 Influence of an Electric Field only . . . 191
11.4.2 Influence of a combined Electric and Magnetic Field . . . 192
11.5 Dynamic simulation results . . . 193
11.6 2D PIC simulation results . . . 195
11.7 Conclusions . . . 197

IV Conclusions and perspectives 199

12 Highlights of the obtained results **200**

13 Discussion and perspectives **202**

13.1 Perspectives of ICF assisted by external magnetic fields . . . 202

13.2 Applying external B-field reduces the non-locality of electron heat fluxes . . . 205

13.3 Applications related to the control of laser-driven ion beams . . . 206

13.4 Highly magnetized plasmas . . . 207

13.5 Atomic physics under strong B-field . . . 207

V Appendix **211**

14 Intense laser beams as laboratory tools **212**

14.1 LULI 2000 Laser Chain . . . 215

15 Coil-target manufacturing **216**

16 B-dot probes **216**

16.1 Single strand loops . . . 216

16.2 Cylindrical loops . . . 218

16.3 Bandwidth of a B-dot probe . . . 220

16.4 Rise time and frequency limits . . . 220

16.5 Commercial B-dot probe Prodyn RB-230 . . . 220

16.6 Measurement system . . . 221

16.7 Calibration of B-dot probes . . . 222

16.7.1 Experimental setup description . . . 222

16.7.2 Experimental results compared to magnetostatic simulations . . . 224

16.8 Time synchronization of B-dot signals . . . 229

17 Magnetostatic code ©Radia **231**

18 Radiochromic Films (RCF) **233**

18.1 Stopping power determination . . . 233

18.2 Dose calibration . . . 235

18.3 Proton dose to spectrum . . . 240

19 Proton deflectometry analisis **241**

19.1 Analysis of grid deflections from the RCF imprint . . . 241

19.2 Particle ray-tracing simulations . . . 243

19.3 Simulation with one-step trajectory . . . 244

19.4 Parameter of the fits functions F and G . . . 246

20 Imaging Plate (IP) detectors **247**

21 Thompson Parabola **248**

22 X-ray diagnostics **251**

22.1 K-α emission 251

22.2 X-ray spectrometry 251

22.3 X-ray K-α imager 253

22.4 Hard X-ray spectrometry - "Bremsstrahlung Canons" 255

23 Coherent Transition Radiation (CTR) **257**

23.1 Focus on the CTR post-processor developed in this thesis work 258

23.2 Benchmarked simulations 259

23.3 Influence of the observation angle 261

List of publications and communications **263**

References **267**

List of physical units

Quantity	Symbol	Numerical value	Unit
speed of light in vacuum	c, c_0	299792458	$\mathrm{m\,s^{-1}}$
magnetic constant	μ_0	$4\pi \times 10^{-7}$	$\mathrm{N\,A^{-2}}$
electric constant $1/\mu_0 c^2$	ϵ_0	$8.854187187 \times 10^{-12}$	$\mathrm{F\,m^{-1}}$
Newtonian constant of gravitation	G	6.67408×10^{-34}	$\mathrm{m^3\,kg^{-1}\,s^{-2}}$
Reduced Planck constant $h/2\pi$	$\hbar$	$1.054571800 \times 10^{-34}$	$\mathrm{J\,s}$
elementary charge	e	$1.6021766208 \times 10^{-19}$	C
classical electron radius	r_e	$2.8179403267 \times 10^{-15}$	m
magnetic flux quantum $h/2e$	ϕ_0	$2.0767833831 \times 10^{-15}$	Wb
conductance quantum $2e^2/h$	G_0	$7.7480917310 \times 10^{-5}$	S
electron mass	m_e	$9.10938356 \times 10^{-31}$	kg
proton mass	m_p	$1.672621898 \times 10^{-27}$	kg
proton-electron mass ratio	m_p/m_e	1836.15267389	
fine-structure constant $e^2/4\pi\epsilon_0\hbar c$	α	$7.2973525664 \times 10^{-3}$	
inverse fine-structure constant	α^{-1}	137.035999139	
Rydberg constant $\alpha^2 m_e c/2h$	R_∞	10973731.568508	$\mathrm{m^{-1}}$
Avogadro constant	N_A	$6.022140857 \times 10^{23}$	$\mathrm{mol^{-1}}$
Faraday constant $N_A e$	F	96485.33289	$\mathrm{C\,mol^{-1}}$
molar gas constant	R	8.3144598	$\mathrm{J\,mol^{-1}\,K^{-1}}$
Boltzmann constant R/N_A	k_B	$1.38064852 \times 10^{-23}$	$\mathrm{J\,K^{-1}}$
Stefan-Boltzmann constant $(\pi^2/60)k^4/\hbar^3 c^2$	σ	5.670367×10^{-8}	$\mathrm{W\,m^{-2}\,K^{-4}}$
electron volt	eV	$1.6021766208 \times 10^{-19}$	J
Megaton of oil equivalent	$Mtoe$	4.187×10^{16}	J
(unified) atomic mass unit $\frac{1}{12}m(^{12}C)$	u	$1.660539040 \times 10^{-27}$	kg

0 Introduction

0.1 Magnetic fields in Nature

Magnetic-fields exist in the Universe on all scales from kilometers or less for tiny neutron stars to some millions of light years for clusters of galaxies which are the largest physical objects in Universe. As we saw before, most of cosmic matter is in plasma state, and plasma turbulence combined with rotation generates magnetic fields by dynamo effects. The extremely high electric conductivity of cosmic plasmas contributes to very long ohmic decay times. Magnetic fields play a very important role in astrophysics as they, first of all, together with gravity, are responsible for structure formation. Some beautiful examples are the radiation belts of the earth, the Parker spiral in the solar wind, sunspots and coronal loops. Also in protoplanetary and accretion disks, high magnetic fields mediate the angular momentum transport [10]. They also play an important role in the acceleration of particles to cosmic ray energies, as well as for the energy losses for high energy electrons and positrons by synchrotron radiation. Cosmic magnetic fields are usually weak compared with those relevant in laboratory physics, as one can see in Tab. 0.1. However, magnetic fields of degenerate objects such as white dwarfs, and in particular neutron stars, exceed by many orders of magnitude the laboratory magnetic fields achievable so far. In this following part, we will focus on these super strong magnetic fields.

The first observational proof for the existence of super strong magnetic fields came with the discovery of radio pulsars in 1968 [107]. It soon turned out to be spinning magnetized neutron stars converting rotational energy into relativistic particle beams and electromagnetic radiation. A relevant theoretical work was already made by Pacini in 1967, before pulsar were discovered [202]. In an attempt to explain the activity of Crab nebula, he proposed that the low frequency electromagnetic wave emitted by a rotating magnetic neutron star would energize the supernova remnant. For white dwarfs, the first qualitative evidence for strong magnetic fields was provided by the discovery in 1970 of circular polarization of white dwarf continuum emission in the optical and ultra-violet range [137]. Quantitative spectroscopic measurements of white dwarf magnetic fields are more complicated because in general the observed radiation originates from the whole stellar surface , showing a distribution of magnetic field strengths, and one is dealing with lines from highly magnetized ions. Measuring these fields became possible by observing the splitting of optical spectral lines in the range of validity of the linear and quadratic Zeeman effect ($B < 10^3$ T, [135]). In such compact stars, magnetic fields are very strong (see Tab. 0.1) and determine the star's structure and composition, as well as it's radiation properties [75]. The reason is that, at the atomic level, the electron cyclotron energy is comparable to, or larger than the Coulomb binding energy [155]. It is then expandable to the study of fundamental atomic physics processes in extreme fields [155, 108, 67]. In other astrophysical settings, expanding plasma outflows can generate turbulent B-fields through collisionless shocks and/or magnetic reconnection mechanisms, leading to the production of high-energy particles and radiation [258, 175].

Efforts in understanding these processes have up to now been restricted to a combination of modeling and observational analysis. In parallel, for many years, application of ultrahigh magnetic fields to plasmas has attracted and justified the development of technologies for operation

	Linear size (m)	Magnetic field (T)
Intergalactic space	10^{20}	10^{-12}
Interstellar Space	10^{16}	$\sim 10^{-10}$
Solar Wind	10^{11}	$\sim 10^{-7}$
Sun	10^{9}	$\sim 10^{-4}$
Sunspots	10^{5}	up to 1
White Dwarfs	10^{7}	up to 10^{4}
Neutron Stars	10^{4}	up to $> 10^{9}$

Table 0.1 – Magnetic fields of cosmic objects

at Megagauss field-levels ($1\,\mathrm{G} = 10^{-4}\,\mathrm{T}$). These applications have included the creation of high temperature sources of X-radiation and some schemes to attain controlled thermonuclear fusion. Opportunities derive from the ability to exert very high equivalent-pressures on small amounts of material and thereby achieve energy densities far in excess of those available at conventional levels of magnetic field and electromagnetic power.

Recently, the unique potential of powerful lasers to reproduce scalable physical conditions of high-energy astrophysics has been fully realized and started being explored:

- ◇ magnetic reconnection in plasmas [197, 161, 292, 304, 69],
- ◇ magnetically collimated plasma jets [51, 4],
- ◇ magnetized collisionless shocks [243];

thereby driving forward the relatively young field of laboratory astrophysics [225].

0.2 Controlled nuclear fusion

The *International Energy Outlook 2016* (IEO2016 [279]) reference case projects significant growth in worldwide energy demand over the 28-year period from 2012 to 2040. Total world consumption of marketed energy would increase by a 48 % from 2012 to 2040. The reference case assumes known technologies, technological and demographic trends, and generally reflects the effects of current policies.

To better understand the consequences of such increase in energy demand, a compilation of three graphs from IEA [118] are shown in Figure 0.1. For the reader, 1 ton of oil equivalent (1 toe) corresponds to:

- ◇ 41.87 GJ,
- ◇ approximately half of the energy released by the total fission of 1 g of U-235,
- ◇ 58 % of the energy consumed by an average automobile in the United States in 2000,
- ◇ approximately the average energy consumed for heating purposes per household in the U.S.A in 2000,
- ◇ approximately the kinetic energy acquired by a 2 km-height free fall of 2000 t of water.

It is worth mentioning first that the world energy consumption is unequally allocated. To illustrate this, the previous ton of oil equivalent also represents the average year electricity consumption of ≈ 20 people living in Africa.

The bottom graph of Figure 0.1 is showing the Total Primary Energy Supply (TPES) outlook for next decades. The demand of energy will be higher than what can be expected from actual resources, technology and policies. Moreover, fossil primary sources, which represents about 87 % of total world primary energy sources are limited resources, and even if new techniques of extraction (like for shale gas) are employed, the next century will know a quasi-complete depletion of fossil deposits.

An other issue is added by the numerous environmental constraints associated to fossil energies. The chemical pollution of new techniques of extraction and global warming by greenhouse gases emission are threatening the world ecosystem equilibrium. The middle graph of Figure 0.1 is showing the world CO_2 emissions from fuel combustion: CO_2 is the major contributor of greenhouse effect gases ($\sim$ 60 %). The world emissions of this gas have strongly increased in last decades due to fossil combustion. About one third of the total fossil primary sources are used to produce electricity, and it is more than the half for coal. The use of alternative greenhouse-free production of electricity could then reduce the part of fossil sources which represented about 67 % of the world electricity generation in 2013 (see top graph of Figure 0.1). A scenario based on policies needed to limit the global average to 2 °C is shown in the bottom graph of Figure 0.1 and is based on carbon pricing, sectoral agreements and national policies and measures in order to increase the part of poor contributors to CO_2 emissions in power generation, transport and industry together with building efficiency improvements.

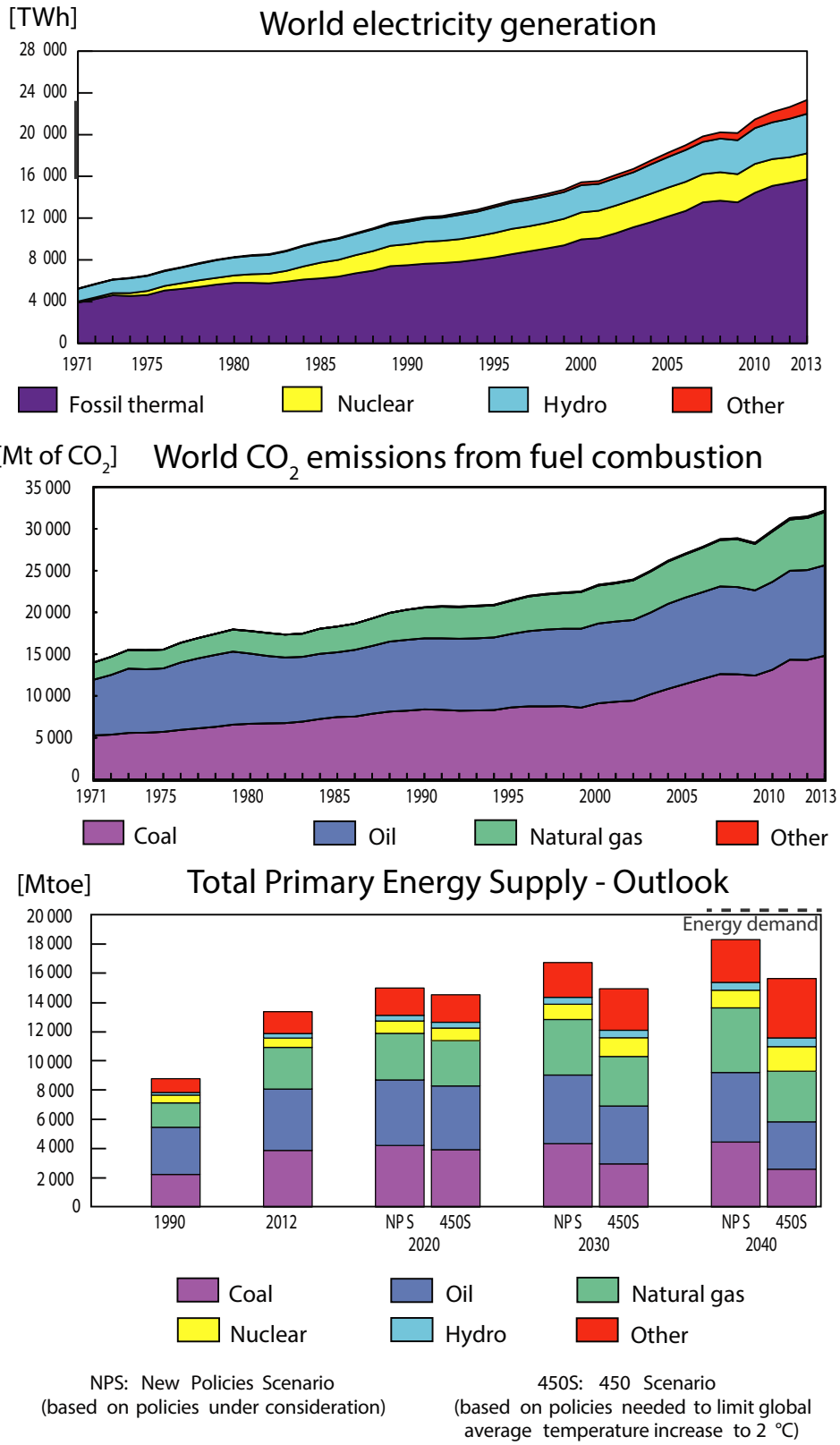

Figure 0.1 – Graphs extracted from [118]. The bottom graph outlook is obtained considering in both scenario (identified in legend) a slowing down of the worldwide growth rate. A gray dashed line has been added to the bottom graph, showing the IEO2016 reference case for energy demand expected in 2040, obtained without considering a slowing down of the worldwide growth rate ($\approx$ 20500 Mtoe).

The use of greenhouse-free supplies for electricity production could be even more extended than for this scenario if the use of electric cars are generalized. Indeed, more than half of the oil production is burned for transport. It drives greenhouse-free production of electricity as the only serious candidate to overcome the global warming effect and not deplete as fast fossil deposits.

Nonetheless, keeping the actual technologies for greenhouse-free production of electricity without slowing down of the worldwide growth rate would lead to not meet the energy demand in 2040. Indeed, the slowing down of the growth rate is included in the bottom graph outlook of Figure 0.1 in order to fulfill the energy demand in 2040. In the case of IEO2016 reference case, where no slowing down of the growth rate is considered, it will be even more difficult to fulfill the subsequent demand of $\approx$ 20500 Mtoe in 2040 (dashed line in bottom graph of Figure 0.1): an additional gap of $\approx$ 5000 Mtoe is missing from the two considered scenarii of the outlook. In conclusion, most of the greenhouse-free sources of energies, despite huge developments performed lastly, are hardly scalable to both replace the reduced part of fossils energies and fill this huge amount of energy lack if no slowing down of the worldwide growth rate occurs, which is quite unexpected.

Nuclear fission efficiency at large-scales led it to become a privileged path and was adopted by several developed countries (in France it represents 77 % of the total produced electricity). However, the increase of nuclear fission energy production is also impaired with limited uranium-235 deposits, very localized in the world map, and problems of radioactive wastes and nuclear plants safety. The nuclear accidents of *Three Mile Island* (1979), *Tchernobyl* (1986) and more recently *Fukishima* (2011) have worried the population and governments about nuclear impacts on environment. The new designs of 4^{th}-generation nuclear plants aims at reducing the risks of accidents and reducing nuclear wastes. Nevertheless, in order to really extend the nuclear fuel life significantly, the use of fast neutron generators, acting as breeder reactors, are needed to recycle most part of nuclear wastes in new usable nuclear fuel. Yet, the fast neutron reactors are coming with their own economic and safety problems. Concerning the safety, in Sodium-cooled Fast neutron Reactors (SFR) the sodium coolant is highly inflammable in presence of air and explode with water. It means that a vigilance on the installation obsolescence must be addressed and the risks are indubitably increased respect to the actual, better-known, conventional reactors.

Instead of using nuclear fission, an alternative would be to use nuclear fusion. This is potentially a huge source of energy which is cleaner, safer, and among all, almost inexhaustible. The nuclear fission reactions are produced in plasmas in the presence of light atoms (such as hydrogen isotopes) at very high temperatures (millions of °C). For instance, these reactions are typical reactions occurring in stars and are at the origin of heat and light which is emitting our sun.

The reactions that could be produced in earth could not be driven by the gravitational force of a star and concerns different hydrogen isotopes that those explored for fusion energy on earth. Indeed, in earth, other kind of plasma confinement forces and different fusion reactions have been examined. The above-mentioned fusion reactions are shown in Figure 0.2. The panel **b)** is showing the main proton-proton fusion chain reaction occurring in sun-like stars and lighter stars. The reaction of Deuterium-Tritium (panel **a)**) is the main fusion reaction able to produce an interesting amount of energy at conditions of plasmas reachable at present day on earth. Other candidates are Deuterium-Deuterium or Deuterium-^{3}Helium reactions. These exothermic reactions produce a tremendous amount of energy in form of kinetic energy which is transferred to the reaction products. With an adequate facility, this energy could be used in a thermal cycle to produce electricity. Otherwise, the helium-4 (α-particle) produced by the Deuterium-Tritium fusion reaction is not a greenhouse effect gas and does not trigger any chemical hazards.

To better understand the need of a confined plasma to trigger the reaction, one can introduce the evolution of the total probability of fusion reactions, also called *cross-sections* σ, which are represented in Figure 0.3 as a function of the incident particle energy for the three above-mentioned reactions (here the Deuterium is the incident particle, the other one being at rest). The number of fusion reactions per unit of time and volume, or reaction rate $< \sigma v >$, can be calculated with:

$$< \sigma v >= \int_0^\infty \sigma(v) f(\vec{v}) v \, d\vec{v} \tag{0.1}$$

where v is the relative velocity of the particle and $f(\vec{v})$ the velocity distribution of the particle in the plasma. The evolution of the reaction rate as a function of the temperature is also presented in Figure 0.3, assuming a plasma at thermal equilibrium and characterized by a Maxwellian distribution.

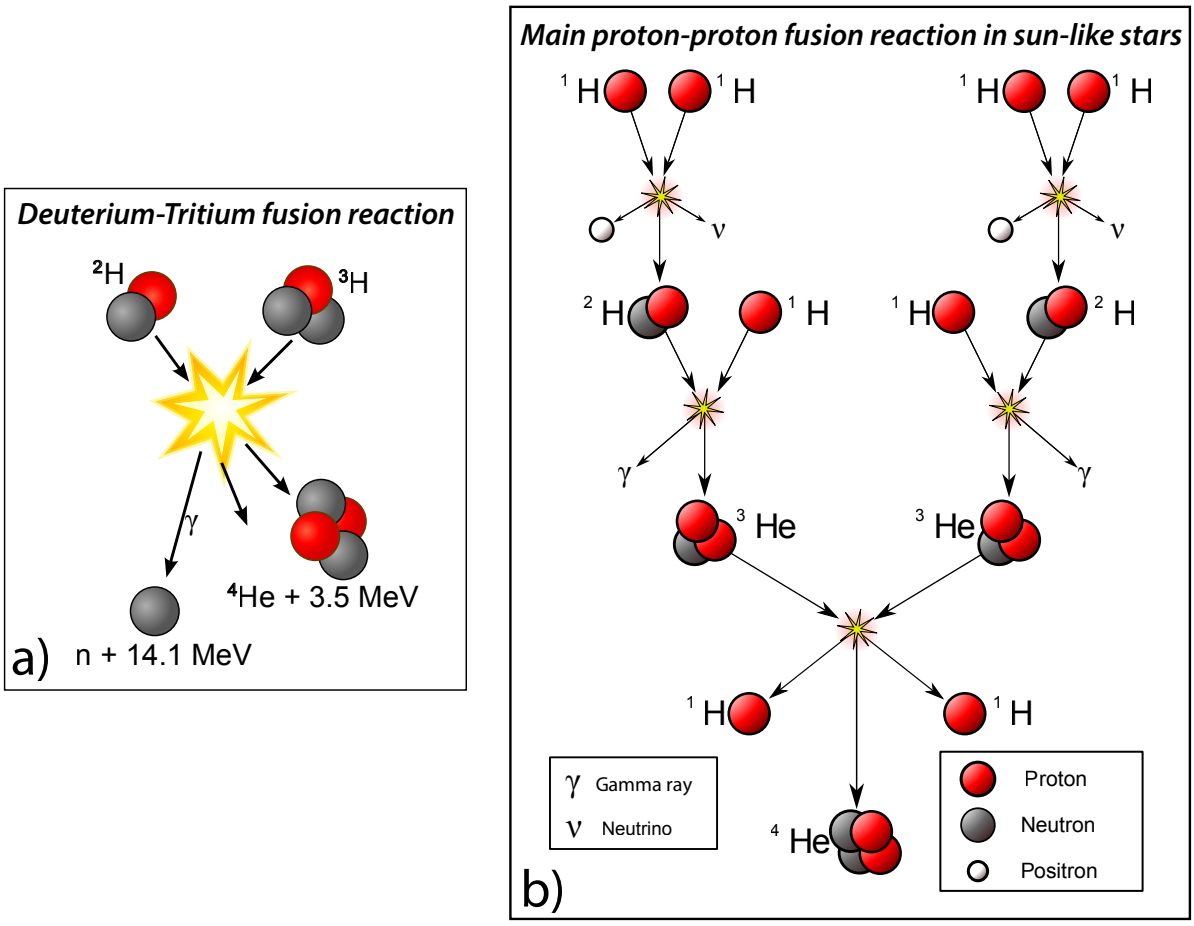

Figure 0.2 – Figure adapted from Wikimedia Commons repository files. It illustrates the fusion reactions of Deuterium and Tritium (**a)** and the main branch (PP1) of proton-proton chain predominant in sun-like stars or lighter.

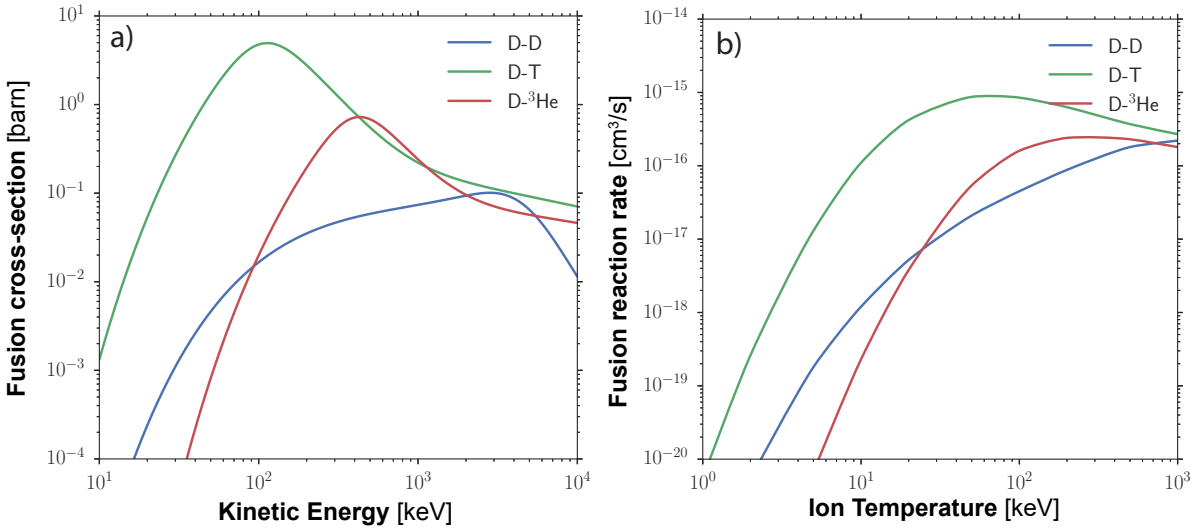

Figure 0.3 – a) Evolution of fusion reaction cross sections for D-D (blue), D-T(green) and D-^{3}He (red) as a function of Deuterium incident particle kinetic energy, the other ion of the pair being at rest. **b)** Evolution of the fusion reaction rate $< \sigma v >$ as a function of the ion temperature. All data are taken from [119].

It is clearly notable that D-T reaction yields the highest cross section for the lower range of temperature, of the order of tens of keV. As shown in Figure 0.2, the reaction releases 17.6 MeV of energy split in a neutron of 14.1 MeV and an alpha-particle of 3.5 MeV. The fast neutron is carrying the major part of the released energy. It causes technical issues since the neutron is a light and charge-neutral particle, then the energy collection have to be done outside the reactor. Also, the fast neutron activates the materials composing the chamber and radiation safety must be observed. The Tritium is also a radioactive element with 12.32 years half-life, but its activity is quite low. The activation that is induced by fast neutrons involves a radioactivity inventory and nuclear wastes management, nevertheless, the entire release of mobilizable radioactivity in fusion reactor would not require population evacuation because the activated materials remain immobilized in solid metal structures. D-D and D-^3He does not have activation drawbacks but the needed temperature to trigger reactions is almost 10 times higher and the ^3He is a very rare isotope on earth that could only be produced in enough quantity by fairly expensive nuclear reactions. For these reasons, the D-T reaction has consequently been selected as the best candidate for energy production purposes, despite important drawbacks. One can note that the maximum cross-section for the D-T reaction is almost 6 barns (1 barn $= 10^{-28}$ m^2) while the cross-section of the nuclear fission of ^{235}U with thermal neutrons is of ≈ 300 barns. It exemplifies well the difficulty to trigger fusion nuclear reactions respect to fission ones. Yet, the energy release of a complete fusion of 1 g of D-T is equivalent to the energy released by the fission of ≈ 4.2 g of ^{235}U, or the burn of ≈ 8 t of oil. Is is also worth mentioning that the fusion reaction does not involve chain reactions and consequently there is not any nuclear criticality safety issues. The reactivity excursions of the plasma are limited by inherent processes and the process stops by itself with low energy density and low afterheat.

Fusion fuel supply is available to all countries and is unlimited on the scale of human civilization. Tritium exists in nature only in small quantities but it can be produced by bombarding lithium with neutrons. This can be done inside the fusion reactor itself with a lithium blanket surrounding the reactor plasma, avoiding fuel transportation outside the plant. Therefore, the primary fuels in a fusion reactor are deuterium and lithium. The deuterium and lithium contained in sea water amounts to many of tonnes and would cover the full demand of fuel for electricity production for millions of years.

The fusion energy, as explained before, is not easily achievable since we need to confine a sufficient amount of hot plasma during a sufficient duration in order to recover more energy than what was injected to heat the plasma and trigger fusion reactions. This constraint was generalized in the concept of *Lawson criterion* which is obtained when the net balance between fusion energy power and losses by thermal conduction and radiation becomes positive. For the D-T reaction, the criterion writes for a plasma temperature of 1 keV:

$$n\tau_E \geq 10^{15}\,\mathrm{cm}^{-3}\mathrm{s} \tag{0.2}$$

with n the density of the considered plasma and τ_E the confinement time. Two approaches dealt with increasing at most one of the two operands of the criterion, either density of confinement time. Magnetic confinement fusion (MCF) has been studied since the end of the 1950s and is currently the most advanced approach. It consists in confining a low density plasma ($n \sim 10^{12} - 10^{14}\,\mathrm{cm}^{-3}$) during a fairly long duration ($\tau_E \sim 100$ s) by the use of intense magnetic fields. The most studied design for magnetic confinement is called *tokamak* and consists in confining the plasma in a toroidal chamber by a combination of both toroidal and poloidal magnetic fields, created by respectively magnetic induction into the plasma and by external magnets. The tokamak design is represented on the left panel of Figure 0.4.

An international project, the ITER tokamak, currently under construction in France, is an experimental facility which seek to obtain a net power gain of fusion energy power. The goal would be to recover a fusion power of 500 MW, 10 times higher than the injected 50 MW input power.

The other explored design is called *stellarator* and the bigger one is Wendelstein 7-X which construction was just finished in October 2015 (Germany), see right panel of Figure 0.4.
In the early 2016, a plasma of hydrogen was successfully confined. An upgrade is currently in process so as to achieve confinement time of the order of tens seconds. In a stellarator, the helically shaped magnetic field is produced by a coil system twisted in a rather complicated shape. It is difficult to build but the advantage is that it offers the best possibility for a continuous operation. Indeed, the disruptions, which are a big problem for tokamaks, arising from fast growing instabilities and release

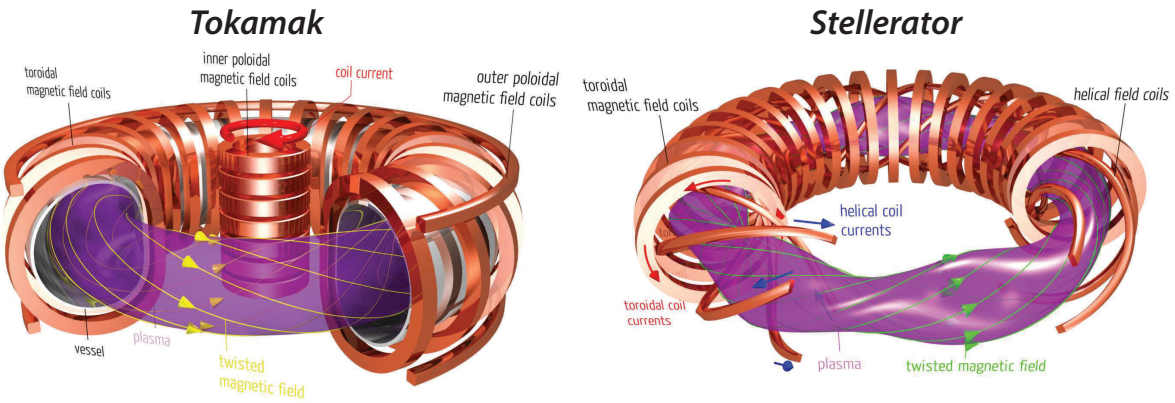

Figure 0.4 – (Left) Example of a tokamak fusion device. The helical magnetic field is generated by a combination of a toroidal field, created by external magnets, and by a poloidal field, created by magnetic induction of inner poloidal coils into the plasma. The outer poloidal field coils are only used for plasma positioning and shape control. (Right) Illustration of the magnet geometry and of the confined plasma in a stellarator device. Images taken from slides of Max-Planck-Gesellschaft Institute.

the plasma energy on target chamber walls, are almost absent in the stellarator design.

Coming back to the Lawson criterion, the other option to fulfill it would be to increase the density and afford lower confinement times. It is the strategy observed in Intertial Confinement Fusion (ICF), constituting an important field of interest for this thesis work. In ICF, the idea is to confine a millimeter scale D-T capsule, compressed ($\sim$ 1000 times) and heated ($5 - 10$ keV) by high-energy beams of laser light or X-rays. The compression is acting on the target during a few ns till obtaining the high density plasma ($n \sim 10^{26}$ cm^{-3}). The self-heating of the fuel is notably due to alpha particle heat release and widespread burning, increasing the temperature to the required levels ($60 - 110$ keV). A few tens of picoseconds later, the burn will rapidly extinguish, as the burn wave runs outward, toward the low density plasma that surrounds the dense core. However, the burn wave is entirely self-sufficient provided that dense fuel remains to be consumed. This latter process is called *ignition* and refers to the attainment of a situation in which thermonuclear burning is self-perpetuating. The *National Ignition Facility* (NIF) in United States was built in order to reach the so-called ignition (and also to test nuclear weapons simulations). In spite important efforts made on the last *National Ignition Campaign* (NIC), the neutron yield obtained was not sufficient. Yet, a shot in 2013 showed an output fission energy of a few kJ, greater than the energy deposited in the fuel [116], but still far under the 1.9 MJ of energy delivered by the laser beams. The reasons are still under investigation and are attributed to hydrodynamic instabilities during target compression [93]. A similar installation, the *Laser MégaJoule* (LMJ) in France, built also for nuclear weapons tests, will complementary seek for ignition in next years among other academic/civil experiments.

In the next subsection, we will give more details about inertial confinement fusion which framework is strongly linked with the work made in this thesis.

0.2.1 Focus on Inertial Confinement Fusion (ICF)

Inertial confinement fusion can itself be split in two different drive schemes called direct and indirect schemes. The classic schemes have also several alternatives, we will present some of them.

Direct and indirect drive schemes

These two ICF schemes are illustrated in Figure 0.5-a) and b). Historically, the first ICF scheme introduced was the *direct drive* scheme (a). In this scheme, the compression is directly performed by numerous laser pulses, irradiating the mm-scale D-T capsule during a few tens of nanoseconds. The external layer of the capsule, usually made of plastic, is heated and is rapidly ablated. As for

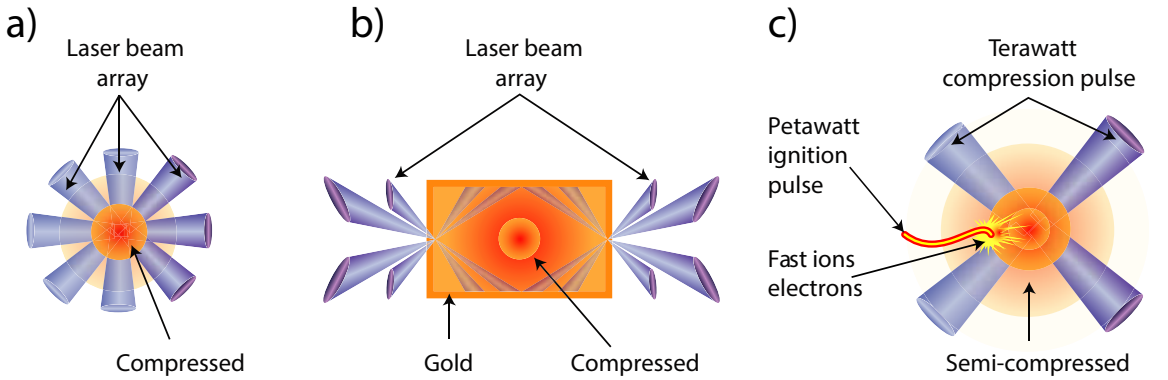

Figure 0.5 – a) Direct-drive laser fusion directly irradiates a millimeter-sized pellet with a spherically symmetric array of several hundred high-intensity laser beams. Ablation of the pellet surface compresses the core towards densities of around $300\,\mathrm{g/cm^3}$. The key to the success of this scheme is to ensure that the laser field enveloping the pellet is homogeneous and symmetric — a difficult prospect to achieve. **b)** The indirect-drive scheme — pursued by both NIF and the LMJ — works on same basic principle as direct drive, except that compression of the pellet is achieved by situating it inside a cylindrical container made of high-Z material. The inner walls of the container are irradiated by an array of lasers to produce an intense flux of X-rays around the pellet. **c)** Fast ignition proceeds by first compressing a pellet with an array of laser beams, and then rapidly heating a localized spot on the compressed plasma with a short petawatt-intensity laser pulse, to ignite a fusion reaction that will spread to the rest of the plasma. This scheme reduces the complexity and expense of the laser optics needed for the compression stage, and is predicted to reduce the total energy needed to achieve ignition. Images taken from [154]

a rocket-like blowoff, the coronal plasma expansion and momentum conservation of the D-T shell, initially in a cryogenic state, creates an inward acceleration and compresses the fuel. The material is compressed by its own inertial and at the end of compression, the imploding fuel is suddenly stopped by the high pressure: it forms at the center of the target dense core a *hot spot* which lasts during a *stagnation time* of $\approx 20\,\mathrm{ps}$. During the stagnation time, the pressure of the shell is balanced by the hot-spot pressure and the target assembly is isobaric. One can introduce the areal density of the hot-spot, being the product of its density ρ by its radius R. If the areal density is so that $\rho R > 0.3\,\mathrm{g/cm^2}$ and the ion temperature $T_i > 4\,\mathrm{keV}$, the alpha particles produced by the D-T nuclear fusion reactions are stopped in the hot-spot and deposit their energy inside. It increases the hot-spot temperature and the hot-spot begin to ignite, producing additional energy due to self-sustaining fusion reactions. As explained before, the nuclear burn wave propagates into the rest of the target, and providing that there is sufficiently fuel to be burn (high enough areal density $\rho R > 1\,\mathrm{g/cm^2}$), the release of energy becomes much more important than the amount of energy absorbed into the capsule.

The direct drive scheme requires a quasi-perfect uniformity of the laser irradiation. It is also necessary that the target surface roughness by itself does not induce non-uniformity of the laser irradiation. Indeed, the non-uniform shell acceleration leads to hydrodynamic instabilities growing over a few hundreds of ps and degrade strongly the compression of the ICF target. The two main hydrodynamic instabilities that are a source of preoccupation for physicists of direct drive ICF are the *Rayleigh-Taylor Instability* (RTI) and *Richmeyer-Meshkov Instability* (RMI). The first one is well-known in fluid mechanics and triggers at the interface between two fluids of different densities when the higher density fluid pressure accelerates towards the lower density fluid. It is responsible of the mix of the two fluids: exponentially growing spikes of the heavier fluid penetrates inside the lighter fluid. The RTI instability particularly affects the compression during the ablation phase, when the low density ablated plasma accelerates the higher density fuel inside the target. It can also affect the ignition at the end of the implosion when the dense fuel is suddenly slowed down by the high pressure hot spot, resulting in a mix between hot and cold fuels. The RMI instability appears when a shock is developing at a non-planar interface between two fluids of different densities. The shock induces a distortion of the interface which is accelerated with a non-uniform speed, causing the instability to grow. This

instability triggers at the initial stage of the target irradiation and is then further amplified by the RTI instability all along the compression.

A more recent scheme called *indirect drive* [Figure 0.5-b)] was inspired by the technique used in H-bombs to trigger the fusion reaction. Indeed, a reliable source of uniform radiation illumination is given by the X-rays produced during the explosion of a fission stage. The idea here, to get rid of the constraints associated with hydrodynamic instabilities, was to use similar irradiation for the target compression. This scheme, developed by Lindl in 1995 [163], consists in focusing the laser pulses on the inner walls of a cylindrical, or rugby-shaped, gold cavity, called *hohlraum* which contains the D-T capsule. The laser light is converted into a nearly black body emission of intense X-rays, at a temperature of $T_X \sim 300\,\text{eV}$, ablating the outer shell of the capsule and imploding it. The gold is an high-Z material and permits to have a strong X-ray conversion efficiency. The major drawback of such scheme is that it necessitates a more complex and expensive target design. Also, one could imagine that in operation, the release of high energy ions of gold debris on the chamber walls and on final optics will cause severe damage problems. Even if ignition is attained, for both schemes, the needed frequency of target supply needs to be around 10 Hz to get an interesting power generation. The target issues, together with intrinsic lower gains, makes the indirect drive scheme not very adequate for future prototypes of energy generation. Despite those drawbacks for future plants, in the goal of reaching ignition, indirect drive was the scheme adopted for the National Ignition Campaign on NIF and it will be also explored on LMJ. As mentioned before, the NIC did not succeed to create a proper ignition and future efforts on NIF are planned to maintain a significant control of the RTI on the ablation front while keeping a low adiabat implosion (high fuel compressibility).

Several alternative ignition schemes are also explored. In particular, we will introduce now the fast ignition scheme which is concerned by our research studies. We will show also in perspectives that our research do have also an impact on indirect drive by the use of magnetized holhraum.

Fast Ignition scheme (FI)

The *fast ignition* scheme was proposed to separate the compression and ignition phases of the capsule [270, 6], as illustrated in [Figure 0.5-c)]. The constraints on target and laser uniformities are not so significant here because the reduced implosion velocity also reduces strongly the RTI. The smaller compression is compensated by the use of a high energetic beam of particles in order to heat the dense core. With this alternative scheme, one expects a gain ~ 10 times higher compared to conventional schemes, while investing a significantly lower laser energy of about 350 kJ instead of 2 MJ, where only 250 kJ would be used to compress the target. For electron fast ignition, at the very end of the compression, during stagnation time, the remaining 100 kJ are used in a first intense laser pulse with $I_L > 10^{18}\,\text{W/cm}^2$ focused on the capsule to bore a channel through the ablated plasma and then a final intense laser pulse with $I_L > 10^{19}\,\text{W/cm}^2$ is focused into the channel and absorbed at the critical density surface: a population of fast electrons of adequate mean kinetic energy ($1 - 2\,\text{MeV}$) [113] are accelerated and deposit their energy in the dense core, creating thus the hot-spot to trigger the target ignition. However, the generation and transport of the fast electron beam in the bored channel is complex and still need to be characterized [232, 199]

The bored channel in the capsule can be avoided by using a re-entrant cone embedded into the spherical shell [144]. The idea is thought to keep directly a clear path for the ignitor laser pulse towards the inner cone tip and accelerate the electrons closer to the dense core. Also, in this latter design, more laser energy is let available to be converted to fast electrons. In 2001 [144], authors demonstrated an enhancement of D-D fusion neutron production by using a spherical target with a re-entrant gold cone, compressed by 9 laser beams of the Gekko laser facility (ILE, Osaka, Japan). The use of a 0.5 PW short pulse laser beam focused on the cone tip resulted in an enhancement of the neutron yield by a factor 10 compared to the case without any heating laser pulse. However, the introduction of a cone into a FI target raises some important issues. Indeed, the cone must survive the high pressure arising from the compression, and the asymmetric implosion of the target drives a strong shock in the cone walls. The shock is driving a plasma jet which moves the fast electron generation further away from the dense core. An adequate design for the cone to withstand the compression is not easy to make since the cone tip should be located as close as possible to the center of the shell in order to minimize the propagation distance between the tip and the DT dense core. Indeed, for an optimum cone-in-shell target design, the fast electron beam (FEB) source surface should be located to a minimum standoff

distance of about 100 µm [252].

Another possibility is to use ions instead of electrons to create the hot-spot [235]. The main advantages of ions are their typical peaked energy deposition (Bragg peak), allowing a fairly localized energy deposition and a weaker sensibility to nonlinear effects. The reader can refer to Sec. 5.2 for more details about energetic ion beams generation. The requirements are the same than for electrons and one have to deposit a minimum of 20 kJ of energy efficiently absorbed in the DT core of 1 g/cm^2 areal density and 20 µm-radius. For instance, a proton beam is generated away from the D-T capsule by focusing a high-intensity laser ($I_L > 10^{20}$ W/cm^2) in a foil, and transporting it ballisctically into the core. In the pioneering concept of ion fast ignition, the proton foil is encapsulated in the shell inserted cone. The generated protons by the TNSA mechanism (see Sec. 5.2) have a broad spectrum distribution but fortunately protons' stopping power increases significantly when increasing the plasma temperature, permitting to the important number of low energy protons to deposit their energy in the dense core previously heated by fast protons. Nevertheless, it is worth noting that a monoenergetic beam would do better the job, igniting the target with $\sim$ 25 % less energy requirement than with TNSA distributions [7]. New acceleration mechanisms, particularly Break-Out-Afterburner (BOA) (see Sec. 5.2) could be a suitable mechanism for the generation of a quasi-monoenergetic ion beam satisfying the ion fast ignition requirements. The required ion energy is yet available [125, 124] but the conversion efficiency is still an issue. The optimization of ions sources by the BOA mechanism is currently under study and one can refer to [79] to get more details about the current status of the ion fast ignition scheme.

In the next section we will detail the nowadays techniques in order to generate strong B-fields. These strong B-fields can potentially play a role in confinement fusion offering exciting perspectives. Prospects of magnetically-assisted inertial fusion will be further commented at the end of this thesis work in the *Conclusions and perspectives*, Sec. 13.1. More generally, the capability of generating such strong B-fields covers a wider range of applications and the third chapter of the manuscript (Part III) will present two of them, together with proof of concepts experiments carried out during this thesis.

0.3 State-of-the-art of strong magnetic field generation

0.3.1 Conventional methods

The magnetic field is a basic research tool in physics. The Physics Nobel Prize for the discovery of the quantum fluid in high magnetic fields by Laughlin, Störmer and Tsui is one of the recent highlights. Data concerning the field diffusion into conducting media, development of magneto hydrodynamic flows, the appearance of phase transitions in metals, and their pressures and temperatures have also been stimulated by the generation of more and more strong magnetic field. State-of-the-art magnets nowadays allow generation of B-fields in the $10 - 300$ T range, depending on their static/pulsed or destructive/non-destructive character [65]. Yet, conventional generation of strong magnetic field require special and very large magnet laboratory facilities.

Non-destructive magnets

Following the studies initiated in 1920s by Kapitza [130, 129] and Wall [284] in magnet technology, 33 T water-cooled magnets and a 45 T hybrid magnet have become available at the U.S National High Magnetic Field Laboratory (NHMFL) at Tallahasee and at the Nijmegen magnet laboratory now in operation in Netherlands. Several new laboratories with pulsed magnets have been established, and existing laboratories have been upgraded and modernized. The level of non-destructive "user" fields has been raised from 50 T to 70 T. In 2011, a record field close to 94.2 T has become available as the result of a European co-operative project at Dresden (HLD), adding a new dimension to pulsed field laboratories. This new dimension has been reached with the use of an incredible amount of 50 MJ (one of the world's largest capacitor bank) delivered over a pulse duration of $\approx$ 10 ms. However, fields at this record levels can only be obtained at the expense of a very short lifetime of the magnet, *i.e.* typically a few shots at the highest fields. The further development of the technology of non-destructive magnets is related to the development of more appropriate coil designs and the use of the strongest materials. Nevertheless, in spite of efforts of many laboratories, attempts to construct the magnets for multiple-use purposes with induction exceeding 100 T have failed. The maximum

field that can be generated without destruction of the coil is determined by the mechanical strength of the coil, which must contain the Maxwell stress generated by the strong currents. This stress increases proportional to the square of the magnetic field ($B_0^2/2\mu_0$) and is approximately 4 GPa at 100 T, which is beyond the yield strength of the strongest materials now available such as maraging steel, electrically non-conducting fiber composites, or well-conducting macro- and micro-composite wires.

Destructive magnets

Essentially, stronger-pulsed fields could be produced in destructive magnets and by using the method of magnetic cumulation. The first of the above approaches was developed in the late 1950s due to significant progress reached at that time in the development of powerful pulsed current generators, using small inductance high voltage condenser banks. In the pioneering work of Furth, Levin, and Waniek [88], field with induction of 160 T was attained. This work provided momentum to the numerous studies in which pulsed fields with small rise times were produced in single turn magnets with characteristic dimensions of the internal radius and length of the order of $\leq$ 1 cm. Several destructive single-turn coil installations have been built that provide fields up to 350 T [253, 148]. Nowadays, single-turn coil systems producing megagauss fields used for scientific materials research experiments are operated notably at the ISSP in Kashiwa (Japan) and at the LNCMI in Toulouse (France). For example, the LNCMI single-turn coil produce fields between 150 and 260 T for coil-diameter of respectively 15 and 8 mm, with a pulse duration of 6 µs. Its record field amounts to 331 T obtained in a single-turn coil of 3 mm inner diameter. It uses a 200 kJ modular capacitor bank that can be charged up to 60 kV.

The processes involved in the coil dynamics, comprising not only the mere expansion of the coil, but also processes in the coil (*e.g.* shock waves, phase changes, current density adjustment), is of utmost importance for the performance of this method and can be directly related to laser-driven generation of magnetic fields that will be presented further on, where coils and currents are similar. Although still higher fields can be obtained with flux compression techniques (presented just below), single-turn coils have the advantage that the coil destruction does not affect the experimentally useful volume: Samples, cyrostats and other equipment generally survive and experiments can therefore be performed reproducibly.

Magnetic-field compression

The strongest magnetic fields have presently been attained by the method of magnetic cumulation. This method, based upon the fast compression of the magnetic flux by the walls of the conductive cylinder. Fields up to 1000 T from explosive-driven flux compression have become available at Sarov (Russia) and Los Alamos (partner of NHMFL) and can be now routinely obtained [39]. The further development of this technology, based upon the comprehensive study of the physics of the process and due to further improvement of experimental techniques, allowed to obtain recently a record field with induction up 2800 T [33]. In these experiments, the conducting cylinder was compressed by explosion products. Another method, namely, the compression of the shell by electromagnetic forces, made possible to generate destructive 622 T reproducibly (at the University of Tokyo). Although flux compression methods are capable of generating the highest fields, their most inconvenient disadvantage is their fully destructive character, *i.e.* the generator and materials therein are destroyed completely. The equipment inside the generator will be in fact destroyed when hit by the arriving shock wave. We can include also on this section the technology of large-scale Z-pinch machines allowing to reach magnetic fields up to $\sim$ 10 kT [244, 94]. Likewise, the heavy technical and infrastructure constraints posed by high-performance pulsed magnets (exceeding 100 T), or by pinch machines, make them ill-suited to the compactness of laser experiments.

A review of different destructive and non-destructive generation techniques that are performed at University of Tokyo and at LNCMI can be found respectively in [181] and [65]. A summary of some magnetic field strengths is given in Box. 0.1.

Box. 0.1: Some magnetic field strengths

◇ In outer space the magnetic flux density is between 10^{-10} T and 10^{-8} T.

◇ Earth's magnetic field at latitude 50° is 5.8×10^{-5} T and at the equator (latitude of 10°), 3.1×10^{-5} T.

◇ The magnetic field of a horseshoe magnet is ≈ 0.1 T.

◇ In a sunspot, the field is 0.15 T

◇ The magnets in clinical medical MRI spectrometers operate around 4 T; high-resolution MRI operates at 9.4 T, and the highest field used for study of a living animal is 21.1 T

◇ Strongest NMR magnetic field in use: 23.5 T at 1 GHz (Lyon, France; 2009)

◇ Strongest continuous magnetic field yet produced in a laboratory:

- ⋆ 26.8 T with a single superconducting magnet (2007),
- ⋆ 35.4 T for any superconducting magnet (2011),
- ⋆ 36.2 T with a resistive magnet (2010),
- ⋆ 45.2 T with an hybrid magnet (2003).

◇ Strongest (pulsed) magnetic field yet obtained nondestructively in the laboratory: 100.75 T (2012) for ≈ 10 ms.

◇ Strongest (pulsed) magnetic field ever achieved (with explosives) in the laboratory: 2800 T (Sarov, Russia; 1998).

◇ The field on a neutron star is 10^6 T to 10^8 T.

◇ Maximum theoretical field strength for a neutron star, and therefore for any known phenomenon, is 10^{13} T.

Conventional B-field generators in laser-plasma experiments

The few laser experiments performed to date on externally magnetized samples have relied on capacitor-bank pulsed discharges in solenoids. In [213], an electromagnetic solenoid driven by a pulsed power system supplying 30 kJ was used. It achieved magnetic fields of 13 T in the gap between the two coils of the solenoid, letting a nearly open-area suitable for a laser-plasma experiment with external B-field. Indeed, a similar design [3] was effectively used to study the formation and collimation of a scaled protostellar jet, co-aligned with the external magnetic field [4]. Another similar device from University of Michigan (4.5 T) has also been used to study the interaction of high-velocity plasma flows in a background magnetic field [173]. A bank of capacitor delivering ≈ 20 kV to a device called MIFEDS [11] provides a seed magnetic field up to 8 T. This device has been used to study magnetic reconnection between colliding plumes of magnetized laser-produced plasma [80].

In the context of inertial confinement fusion, it has also been used to obtain a magnetic field of $2 - 4$ kT at maximum compression of an imploding dense target [95, 142, 109]. As we will see more in details in the perspectives of this thesis work (Sec. 13.1), a measure of the ion temperature and fusion yield showed an improvement by 15 % and 30 %, respectively, when the hot spot was magnetized [45].

The use of conventional B-field generators in laser-plasma experiment has contributed to move a step forward in the two fields of laboratory astrophysics and inertial fusion. But, in spite of assuring B-fields of interesting space- and time-scales, with cm-scale uniformity over of a few 100 µs, the needed additional electric pulse-power (of several tens of kV) limit their easy deployment in any laser facility. Besides, the rather closed geometry of the pulser coil(s) placed into the laser interaction chamber renders this technology cumbersome in experiments requiring wide access angles either for diagnostics or for the magnetisation and laser-driving of secondary samples. In this context, all-optical laser-driven generators could bring new solutions and perspectives.

0.3.2 Laser-driven generators

The idea of an all-optical generator of magnetic fields, without any pulsed power source, driven by laser pulses, arose from the already observed high currents and fields generated by laser interaction at high intensities (the interaction of intense laser pulses with matter is further described in the first chapter of this thesis). Indeed, laser-produced experiments, in particular, often require access to the target for multiple diagnostics and laser beams in a vacuum environment: an all optical generator is thus the key to provide magnetic fields in open geometry for numerous experiments that will benefit from the existing multipurpose features and diagnostics of laser facilities.

***First experiments by Korobkin** et al. **and Daido** et al.*

The first generation of a strong magnetic field by laser in external circuit was obtained in 1979 by Korobkin *et al.* [147]. The laser energy was limited to 1 J and a maximum B-field of 2 T was obtained at the center of the copper coil of this preliminary capacitor-coil target. In 1986, Daido *et al.* [58] followed the previous work using a more powerful laser and improved target design. A magnetic field of 60 T was generated at the center of a single-turn coil of 2 mm-diameter. The *capacitor-coil* target design consists of a coil, connected to a double-disk target, with one of the disk holed to let the laser pass and be focused on the other disk. In the experiment of Daido *et al.* , the two disks are 50 µm-thick and 2 mm-diameter and the front disk has a 1 mm-diameter hole. The entire target is made of copper and the coil is made of a rod of circular section of 80 µm-diameter. The laser driver is a CO_2 laser that delivers 100 J in 1 ns and is focused at an intensity of $1.3 \times 10^{14}\,\mathrm{W/cm^2}$. At this level of intensity, electrons are mostly accelerated by inverse Bremsstrahlung and the laser plasma temperature is not very high (estimated to be ~ 10 keV). The target and the measurement setup system are shown schematically in Figure 0.6. The bandwidth of the pick-up coil (or B-dot probe) used in this experiment was limited to 1 GHz.

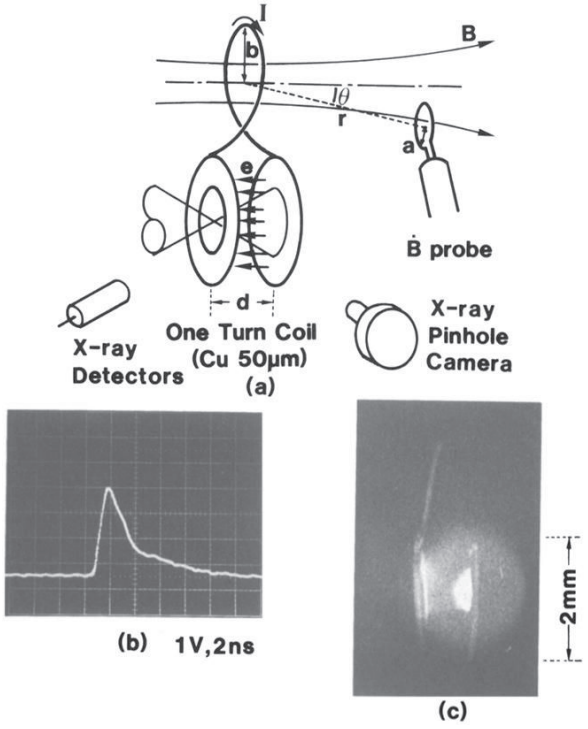

Figure 0.6 – (a) Schematic diagram of one-turn coil with the gap and the observation system. **(b)** Typical soft x-ray signal ($0.1 - 1.0$ keV) and **(c)** x-ray image (white regions) of the gap. The laser irradiates from the left. $a = 500\,\mu$m and $b = 1$ mm. Figure and caption taken from [58].

Several conclusions of importance emerged from this first study:

◇ If the laser pulse duration is longer than the characteristic time for the expanding plasma plume to fill the gap between the two disks, the generated magnetic field is then constrained by the distance between the two disks. The short-circuit time hence defines the B-field peak instant.

◇ When the gap between the disks is too large, the magnetic field is found to decrease. The explanation given by the authors for the physical mechanism for the drop in magnetic field when the gap is too large is based on the lateral spreading of the hot electrons propagating between the two disks, due to $\vec{E} \wedge \vec{B}$ drift, and preventing them to reach the front disk above a critical gap distance.

In this experiment, the hot electron energy is roughly estimated to be 10 % of the laser energy and the peak current and voltage for the best gap distance of 700 µm are respectively 100 kA and 220 kV.

Laser-driven Helmholtz coil (Courtois** et al. **)

A more recent experiment was performed by Courtois *et al.* in 2005 [53] with a different coil design. The target was a Helmholtz coil composed of two 2.5 mm-diameter loops connected to two plates separated by a fixed distance of 500 µm.
The all piece was obtained from a photoetched 50 µm-thick copper sheet. The results of this experiment differs from the previous work of Daido *et al.* also by the use of an higher laser intensity. Yet, on this respect, it almost did not differ from the previous experiment from Daido *et al.* : scaling to match the $I\lambda^2$ ensures that similar hot electron populations in terms of number and temperature are generated. Indeed, the B-field target was driven here by a Nd:glass laser at 1.053 µm (commonly used now in the majority of laser facilities around the world, in respect to CO_2 lasers) which can deliver 300 J in 1 ns-duration, yielding peak intensities of $4 \times 10^{16}\,\mathrm{W/cm^2}$. At this intensity level, an important fraction of the laser energy is resonantly absorbed and hot electrons with temperature exceeding 10 keV are expected to be generated by resonant absorption. The charging process is also attributed to hot electrons who preferentially stream down the electron density gradient ahead of the expanding plasma plume and impact the front plate. The arisen potential difference drives a reverse current through the wire loops. The B-field production was tested with different combinations of $E_L\tau_L$ (E_L is the laser energy and τ_L the laser pulse duration). The maximum amplitude of the magnetic field was observed to be ≈ 7 T at the center of the Helmholtz coil for the longest duration of $\tau_L = 1$ ns and maximum energy (see Figure 0.7), which was one order of magnitude larger than with the short 80 ps configuration.

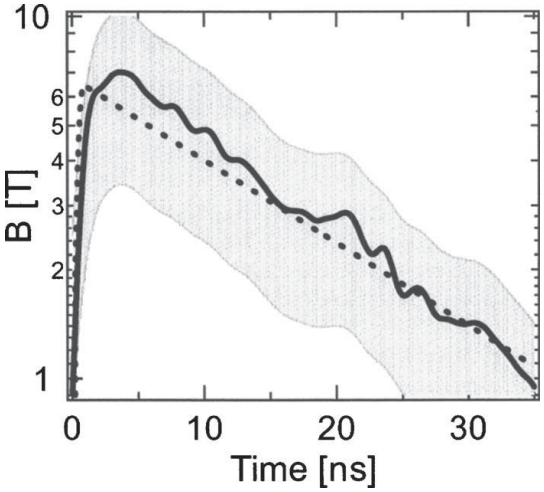

Figure 0.7 – Amplitude of the magnetic field at the center of the Helmhotz coil inferred from the experiment (solid line) and from the model (dotted line) as a function of time. The grey area indicates the experimental uncertainties. Figure and caption taken from [53].

Globally, the results show that the B-field increases with $E_L\tau_L$ in this regime of intensities. Also, at equivalent $E_L\tau_L$, there was no visible effect on the peak magnetic field for the long laser pulse configuration, changing the laser wavelength from 1 to 0.5 µm. The explanation outlined by the authors is that although $I\lambda^2$ was smaller for shorter wavelength, the short-circuit time was reached later. A

phenomenological model for the mechanism driving the B-field was proposed in the paper and is extensively described in Sec. 9.1, as an introduction to our own modeling.

A more recent experiment by Fujioka** et al. **at high laser irradiance

In 2012, Fujioka *et al.* [87] implemented the already known technique of laser-driven B-field production with capacitor-coil target, this time with a *kJ*-class laser. The capacitor was driven by two beams from the GEKKO-XII laser at 1 kJ (total), 1.3 ns-duration at either $\lambda = 0.53\,\mu m$ or $\lambda = 1\,\mu m$, yielding an intensity of $5 \times 10^{16}\,W/cm^2$. A magnetic induction of 1.5 kT was measured using Faraday effect 650 µm away from the coil.

According to an analytic extrapolation, the Faraday measurement at 0.65 mm of 1.5 kT leads to a magnetic field at the coil center bigger by one order of magnitude. This magnetic field is incredibly strong and would led to a total energy of the magnetic field of 15 kJ (integrating B^2/μ_0) much larger than the invested laser energy. The problem probably lies in the tabulated Verdet constants of the birefringent crystals that are of questionable validity in the presence of strong and rapidly changing B-fields, or maybe the crystal properties begin to be affected by x-rays and fast particles due to the close laser-target interaction.

An interesting fact also is that a measurement made by a B-dot probe at 0.85 mm far from the coil center, yields a magnetic field at the probe position of $\approx 33\,T$. According to the extrapolation curve, this would lead to a much more reasonable B-field at coil center of $\approx 520\,T$. The B-dot shot result was obtained with $\lambda = 0.526\,\mu m$, $E_L = 540\,J$ and a peak intensity of $8.2 \times 10^{14}\,W/cm^2$.

An interesting result is worth mentioning here, obtained by x-ray streak imaging of the plasma generated in the target capacitor. The imaging of the gap filling with plasma is of great interest to well understand the B-field generation mechanism by laser. The related image taken from [87] is shown in Figure 0.8.

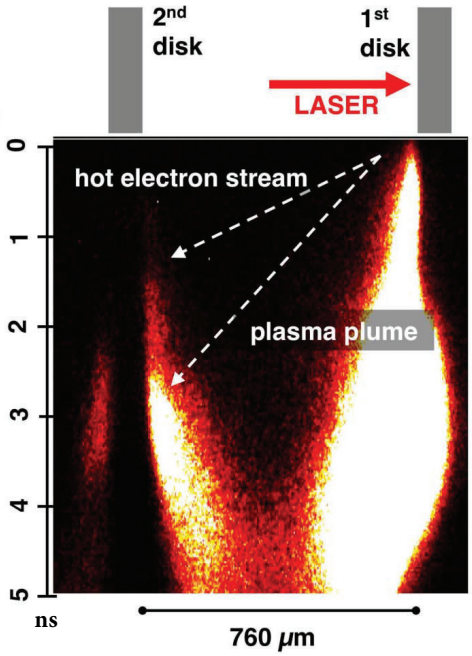

Figure 0.8 – An x-ray streak image of the plasma generated in the target capacitor. Image and caption taken in [87].

0.4 Goals and summary of the manuscript

The problem of strong magnetic field generation is one of challenging issues in the laser-plasma interaction physics. The use of capacitor-coil scheme allows to generate extremely strong magnetic fields exceeding MegaGauss level in a very compact design without any pulsed power source. Proposed a long time ago, it only recently demonstrated its potential.

Still, significant progress needs to be made on the experimental realization of this scheme and its theoretical comprehension. In this context, this thesis work aims at building a deeper understanding of magnetic fields generation with nanosecond and piscosecond laser pulses and their experimental validation using multiple diagnostics.

Application of externally applied magnetic fields to guide relativistic electron beam in dense matter has been studied so far in many simulation works but still needed to be explored experimentally. Besides, the generation of high discharge currents consecutive to picosecond interaction was pointed out and several designs of electromagnetic lenses were proposed in literature. Our recent results on target charging and on an alternative design of electromagnetic lens will be presented in this work.

The thesis manuscript is structured as follows:

Part I. An overview of high intensity laser interaction and particles acceleration is proposed in the first part. The herein concepts will serve as a theoretical background for magnetic field generation and some of its applications. In the latter case, insights will be given on the contributions that could provide an external magnetic field.

Part II. It details the experimental realization of the strong magnetic field generation platform and its characterization using multiple diagnostics. The magnetic field is measured for different target materials and geometries using three independent diagnostics (B-dot probe, Faraday Rotation and proton deflectometry). To better characterize underlying physical processes of magnetic field generation, X-ray diagnostics of the laser-irradiated area and optical shadowgraphy of the coil has also been performed. In the last section of this chapter, a semi-analytical model of B-field generation in coil-targets in nanosecond regime interaction is proposed.

Part III. This chapter presents a first experimental evidence of fast-electron guiding in dense matter using laser-driven strong external magnetic field. Thereafter, the high discharge current generated upon short-pulse irradiation is used to realize focusing and tailoring of a multi-MeV proton beam in vacuum.

Part VI. This last chapter provides a summary of the obtained experimental results and their interpretation in the framework of fast ignition studies and in the more general context of high-energy-density physics.

Part I

An introduction to high intensity laser interaction with matter and acceleration of particles

Summary

1 Introduction to the plasma state **34**

2 Motion of charged particles in electric and magnetic fields **38**

3 General concepts of intense laser interaction with overdense matter **44**
3.1 Fast electron generation . . . 45
3.1.1 Non-relativistic regime . . . 45
3.1.2 Relativistic regime . . . 50
3.1.3 Relevant mechanisms in our experimental conditions . . . 53
3.2 State-of-the-art of accelerated electron sources from over-dense targets . . . 53
3.2.1 Laser-to-electrons conversion efficiency . . . 53
3.2.2 Fast electron temperature . . . 55
3.2.3 Fast electron divergence . . . 57
3.3 Fast electron transport . . . 58
3.3.1 Collisional effects over transport . . . 58
3.3.2 Resistive effects over transport . . . 63

4 Laser-matter interaction in nanosecond regime ($\gtrsim 10^{16}\,\mathrm{W/cm^2}$) **71**
4.1 Self-generated fields . . . 72
4.1.1 Thermoelectric effect due to crossed gradients ($\vec{\nabla} n_e \wedge \vec{\nabla} T_e$) . . . 72
4.1.2 Influence of magnetic field over heat fluxes and transport coefficients 73
4.2 Plasma expansion into vacuum . . . 74

5 Laser-matter interaction in picosecond and sub-picosecond regime ($\gtrsim 10^{18}\,\mathrm{W/cm^2}$) **77**
5.1 Self-generated fields . . . 77
5.2 Energetic ion beams . . . 80
5.2.1 Energetic ion beam acceleration . . . 80
5.2.2 Ion beam characterization . . . 84
5.2.3 Radiography and field measurements with laser-driven ions beams . . 86

6 Mechanisms of target charging **87**
6.1 Return currents . . . 87
6.2 Transient target charging . . . 87
6.3 Transient target charging measurements . . . 90
6.3.1 EMP generation . . . 90
6.3.2 Proton imaging of the discharge . . . 93

1 Introduction to the plasma state

There are various ways of defining the plasma state, distinct from solid, liquid and gas. The definition of a plasma is a bit more complex than for other three state of matter where there are clear phases transitions. Indeed, in a phase-diagram (temperature *vs* pressure) of a given material, one can distinguish sharp transitions from solid to liquid (melting point) and from liquid to gas (boiling point). These transitions are realized by a given energy gain ΔE.

$$solid \underset{\Delta E}{\Rightarrow} liquid \underset{\Delta E}{\Rightarrow} gas \underset{\Delta E}{\Rightarrow} plasma \tag{1.1}$$

For the plasma, this transition is related to the fact that mostly all mater is ionized. It generally induces high electric conductivity. The mechanical properties are similar to a gaseous state. The complex part is summarized in the term "mostly" that can allow us to classify a metal or a semiconductor as a plasma, despite mechanical properties similar to a solid. Also, a very dense and high-temperature plasma can have properties similar for solids or liquid due to quantum effects by Fermi-Dirac degeneracy. An alternative definition can be that a plasma is a medium whose dielectric properties are determined only by free charges, without dipoles. In other words, a plasma contains charged particles, free electrons and ions, in sufficient proportion to be sensitive to electromagnetic forces. The collective behavior of a plasma is overly exemplified by assuming that a particle of the medium interacts with all others and not only the closest ones. This is due to the long range of Coulomb interactions in plasmas. If we write $V(r)$ the Coulomb potential in vacuum between two particles of charges q_1 and q_1.

$$V(r) = \frac{q_1 q_2}{4\pi\varepsilon_0 r} \tag{1.2}$$

where r is the distance between the two particles. If we calculate the interaction energy $\mathrm{d}W_{ee}$ of a given electron with a population of electrons located at a distance $r \pm \mathrm{d}r$ of homogeneous density n_e, we obtain:

$$\mathrm{d}W_{ee} \simeq \frac{e^2 n_e r}{\varepsilon_0}\mathrm{d}r \tag{1.3}$$

This quantity diverges when r tends to infinity, meaning that the interaction energy of an electron with all other electrons tends to infinity. In the case of quasi-neutrality, *i.e* $n_e = Z^* n_i$ (Z^* is the ion electric charge and respectively n_i and n_e the ion and electron density), the interaction term between electrons and ions $\mathrm{d}W_{ei}$ exactly compensates the one between electrons $\mathrm{d}W_{ee}$. Generally, a plasma is quasi-neutral at macroscopic scale and the overall interaction energy do not diverge. The quasi-neutrality is nonetheless not verified locally and, as charges move around, they can generate local concentrations of positive or negative charge, which give rise to electric fields. Motion of charges also generate currents and consequently magnetic fields. These fields affect the motion of other charged particles far away. It is this long-ranged Coulomb forces that make a plasma "collective" as motions not only depend on local conditions but on properties of the plasma in remote regions as well.

In a strongly ionized plasma of two species, electrons and ions, as the mass of a proton is 1837 times greater than the mass of an electron, we can consider on first approximation, for high frequency phenomena, that ions are quasi static and constitute a neutralization background. In a fluid model, the plasma is simplified as a medium composed by two perfect fluids and it is then characterized by macroscopic physical quantities. These quantities are, respectively for electron and ions : $n_{e,i}$ the density; $\vec{u_{e,i}}$ the mean velocity and $T_{e,i}$ the temperature. There are also four characteristic lengths for a plasma in this approach :

- ◇ $d_{e,i}$ the mean distance between particles (again i for ions and e for electrons)
- ◇ the Landau length r_0, which is the minimal closing distance for two particles.
- ◇ The Debye length which is representative of the electrostatic screening induced by a charge, λ_D
- ◇ The mean free path between two consecutive collisions, $\lambda_{e,i}$

There are also four characteristic angular frequencies for a plasma :

- ◇ The oscillation frequency of electrons or electronic plasma frequency, ω_{pe}

- ◇ The oscillation frequency of ions or ionic plasma frequency, ω_{pi}
- ◇ The rotation frequency of electrons and ions in magnetic field, or Larmor frequencies, $\omega_{ce,i}$
- ◇ The frequency between two consecutive collisions of particles $\nu_{e,i}$.

Landau length and plasma parameter

If one suppose that electrons and ions are uniformly spaced inside the plasma, we obtain a mesh where the mean distance between electrons (ions) is :

$$d_{e,i} = n_{e,i}^{-1/3} \tag{1.4}$$

The minimum distance between two particles (Landau length) is then defined when the mean kinetic energy of an electron equals the potential energy of interaction :

$$\frac{1}{2} m_e v_e^2 = k_B T_e = \frac{e^2}{4\pi\epsilon_0 r_0} \tag{1.5}$$

where v_e is the most probable velocity of an electron. We find out that the Landau length, r_0 is :

$$r_0 = \frac{e^2}{4\pi\epsilon_0 k_B T_e} \tag{1.6}$$

The last expression can be generalized to two arbitrary particles a and b of charge Z_a and Z_b and mass m_a and m_b, respectively. Their relative speed is given by $v_{rel} = \|\vec{v}_a - \vec{v}_b\|$ and the reduced mass of the system is $\mu = (m_a m_b)/(m_a + m_b)$, the generalized Landau length r_{ab} is given by :

$$r_{ab} = \frac{Z_a Z_b e^2}{4\pi\epsilon_0 \mu {v_{rel}}^2}. \tag{1.7}$$

The coupling parameter Ξ (or plasma parameter) is introduced, defined by the ratio between the density of electrostatic potential energy $\langle w_p \rangle$ and the mean density of kinetic energy $\langle w_k \rangle$:

$$\Xi \equiv \frac{\left|\langle w_p \rangle\right|}{\langle w_k \rangle} \approx \frac{n^{4/3} e^2 / 4\pi\varepsilon_0}{3nkT/2} \approx 10^{-5} \left[\frac{n}{10^{12}\,\mathrm{cm}^{-3}}\right]^{1/3} \left[\frac{T}{10^6\,\mathrm{K}}\right]^{-1} \tag{1.8}$$

This parameter permits to distinguish :

- ◇ $\Xi \ll 1$: Weakly coupled plasmas or *kinetic* plasmas, where disorder dominates.
- ◇ $\Xi \gg 1$: Strongly coupled plasmas, where the structure is similar to a fluid or even a solid.

By looking either at electrons (Ξ_e) or ions (Ξ_i) a factor $Z^{1/3}$ appears : $\Xi_e = Z^{1/3}\Xi_i$ ($n_e = Z n_i$, where Z is the ionization state).
For electrons, the plasma parameter is also directly related to Landau length :

$$\Xi_e = \frac{r_0}{d_e}. \tag{1.9}$$

Debye length - electrostatic screening

The name of Debye length comes from an effect discovered in 1923 by Peter Debye and Erich Hückel. This effect puts in evidence the screening of a charge in an ionized medium. If we take a plasma of electron density n_e and ion density n_i. Inside the plasma, $n_e = n_i = n_0$. Ions are considered heavy without any motion. In a very simplified situation, one can take a semi-infinite plasma for $x \leq 0$, at uniform temperature T, in which we suppose electrons exiting the $x = 0$ interface towards positive x. They feel the electric force coming from the potential made with ion interface and come back approximately after a distance noted λ. This length is thus the distance beyond which neutrality becomes valid. It is obtained for the case of a distribution of electrons by solving the Boltzmann-Poisson equation with suitable boundary conditions :

$$\begin{cases} \dfrac{d^2\phi}{dx^2} = -\dfrac{n_e(x) q_e + n_i(x) q_i}{\varepsilon_0}, \quad \phi(\pm\infty) = \dfrac{d\phi(\pm\infty)}{dx} = 0, \quad \phi(0) = \phi_0 \\ n_e q_e + n_i q_i = n_0 q_e \exp\left[\dfrac{-q_e\phi}{k_B T}\right] + n_0 q_i \exp\left[\dfrac{-q_i\phi}{k_B T}\right], \quad q_e = -q_i = -e \end{cases} \tag{1.10}$$

After some calculation, we obtain $\frac{e\phi}{2k_BT} \approx \frac{e\phi_0}{2k_BT} \exp\left(-\frac{|x|}{\lambda_D}\right)$, and :

$$\lambda_D = \sqrt{\frac{\varepsilon_0 k_B T}{n_0 e^2}} \rightarrow \lambda_D[\text{cm}] = 743\sqrt{\frac{T[\text{eV}]}{n[\text{cm}^{-3}]}} \tag{1.11}$$

It shows that the electric potential ϕ is screened by 63% at the distance of a Debye length λ_d.

It is important to note that the Debye screening effect can only be defined if there are enough electrons in what we call the sphere of Debye. This is simply a sphere of radius λ_D, containing a number of electrons $N_D \gg 1$, with:

$$N_D = \frac{4}{3}\pi n_e {\lambda_D}^3. \tag{1.12}$$

.

Collective oscillations : plasma frequency

The tendency of a plasma to be quasi-neutral can be explored through the study of the electronic response of an electric perturbation inside the plasma : rapid processes would be able to break the neutrality and induce a charge separation and slow processes would let the plasma reorganize itself and suppress the perturbation. To study this time scale, we take an unidimensional infinite plasma with the same approximations as before. We impose a displacement of all electrons in the plan $x = x_0$ towards the plan $x = x_0 + \xi(t)$ at time t, and release the system. The resulting electric field is the characteristic one of a charged parallel plate capacitor :

$$E = \frac{n_0 e \xi(t)}{\epsilon_0} \tag{1.13}$$

The mechanical dynamic of the electrode at $\xi(t)$ is given by Newton law :

$$m_e \frac{\partial^2 \xi}{\partial t^2} = -eE \Leftrightarrow \frac{\partial^2 \xi}{\partial t^2} + \frac{n_0 e^2}{\varepsilon_0 m_e}\xi = 0 \tag{1.14}$$

This is the typical equation of an harmonic oscillator whose angular frequency is :

$$w_p = \sqrt{\frac{n_0 e^2}{\varepsilon_0 m_e}} \rightarrow \frac{w_p[\text{Hz}]}{2\pi} = 8981\sqrt{n_0[\text{cm}^{-3}]} \tag{1.15}$$

The plasma frequency found above is also linked to the Debye length by the relation $\omega_p = v_{T_e}/\lambda_D$ where v_{T_e} is the electron thermal speed $v_{T_e} = \sqrt{k_B T_e/m_e}$. In the relativistic case, the previous calculation is still valid by considering the relativistic mass instead of the rest mass. It yields the relativistic plasma frequency $\omega_p' = \omega_p/\sqrt{\gamma}$ where γ is the Lorentz factor ($\gamma = 1/\sqrt{1 - v^2/c^2}$).

The mean free path and associated collision frequencies will be further detailed in the part describing a model for the thermal and electric resistivity of a plasma, Sec. 3.3.2.

PLASMA : THE PREDOMINANT STATE OF MATTER IN THE UNIVERSE

The so-called "fourth state of matter" is part of more than 99 % of the Universe matter. This rough estimate is obtained taking into account that stellar interiors and atmospheres, gaseous nebulae, and much of the interstellar hydrogen are plasmas. Interstellar magnetic fields are very weak, of the order of 5 nT (*i.e* a magnetic energy density of $\sim 1\,\text{eV cm}^{-3}$, 10 000 times weaker than earth's one!). In Earth, plasmas are present notably in : the flash of a lightning bolt, the soft glow of an Aurora Borealis, the conducting gas inside a fluorescent tube or neon sign, the fashion 80's plasma ball light, inside brand new televisions, or the slight amount of ionization in a rocket exhaust. We can thus explain that people know more about the 1 % of the universe in which plasmas do not occur naturally.

We can explain this plasma behavior looking at the Saha equation, which relates the amount of ionization that one can expect from a gas in thermal equilibrium :

$$\frac{n_i}{n_n} \approx 2.4 \times 10^{21} \frac{T^{3/2}}{n_i} e^{-U_i/k_B T} \tag{1.16}$$

where n_i and n_n are respectively the density of ionized and neutral atoms (in number per m^3), T is the gas temperature in °K, k_B is the Boltzmann's constant, and U_i is the ionization energy of the gas (that is the energy required to remove the outermost electron from an atom). Let's take an example of the ordinary air at room temperature. We may choose $n_n \approx 3 \times 10^{25}\,\mathrm{m}^{-3}$, $T \approx 300\,°\mathrm{K}$, and $U_i = 14.5\,\mathrm{eV}$ (for first ionization of nitrogen), where $1\,\mathrm{eV} \approx 1.6 \times 10^{-19}\,\mathrm{J}$. The fractional ionization $n_i/(n_n + n_i) \approx n_i/n_n$ calculated from Eq. 1.16 is ridiculously low :

$$\frac{n_i}{n_n} \approx 10^{-122} \tag{1.17}$$

The chance for an atom to suffer a collision and loose an electron falls exponentially with U_i/k_BT (Eq. 1.16). With increase of gas temperature, the degree of ionization remains low until k_BT is of the order of U_i. Then there is an abrupt increase of this ionization degree and the matter enters in plasma state. Further increase of temperature makes the ionization fraction to be close to one, in a state that we called *fully ionized*. In a cold gas, the number of fast atoms is so small that energetic collision and then ionization occurs very infrequently. Plasmas, which are very rare on Earth, conversely form the matter of astronomical bodies with temperatures of millions of degree.

After an atom is ionized, it remains charged until it meets an electron and very likely recombines to become neutral again. The rate of recombination is linked to the electron density that we can take equal to n_i. It emphasizes the term in n_i^{-1} in Eq. 1.16 that makes decreasing the ionization degree upon recombination processes. That is the reason why we can find very low density plasmas in Universe (with relatively low temperature), as for example in the interstellar medium where $n_i \approx 1\,\mathrm{cm}^{-3}$ and $T \approx 1\,\mathrm{eV}$ yielding $n_i/n_n \approx 10^{13}$.

Increasing the temperature is not the only way to generate a plasma, we can also provide this energy by electromagnetic fields (that creates electronic cascades) or by photons (photo-ionization). The last two methods are used to create *cold plasmas* in laboratories that are weakly ionized ($n_i/n_n \approx 10^{-5} - 10^{-1}$) and not in thermodynamic equilibrium ($T_i \approx T_n$ and $T_i/T_e \ll 1$). All other plasma that we will evoke in this thesis will belong to the other category of *hot plasmas*, at higher density and temperature and strongly ionized.

Figure 1.1 presents the temperature and densities of usual plasmas that can be found in the Universe. We can see the diversity of physical conditions of natural plasmas, and there is not an only tool that can reproduce and study all these kinds of plasmas. Nowadays, laser-matter interactions are a common tool to reach high density and temperature plasmas, that can be scaled with those of stellar interiors or coronas. The interaction of intense electromagnetic pulses, generated by high power lasers, with solid or gaseous targets, will be further detailed in this manuscript.

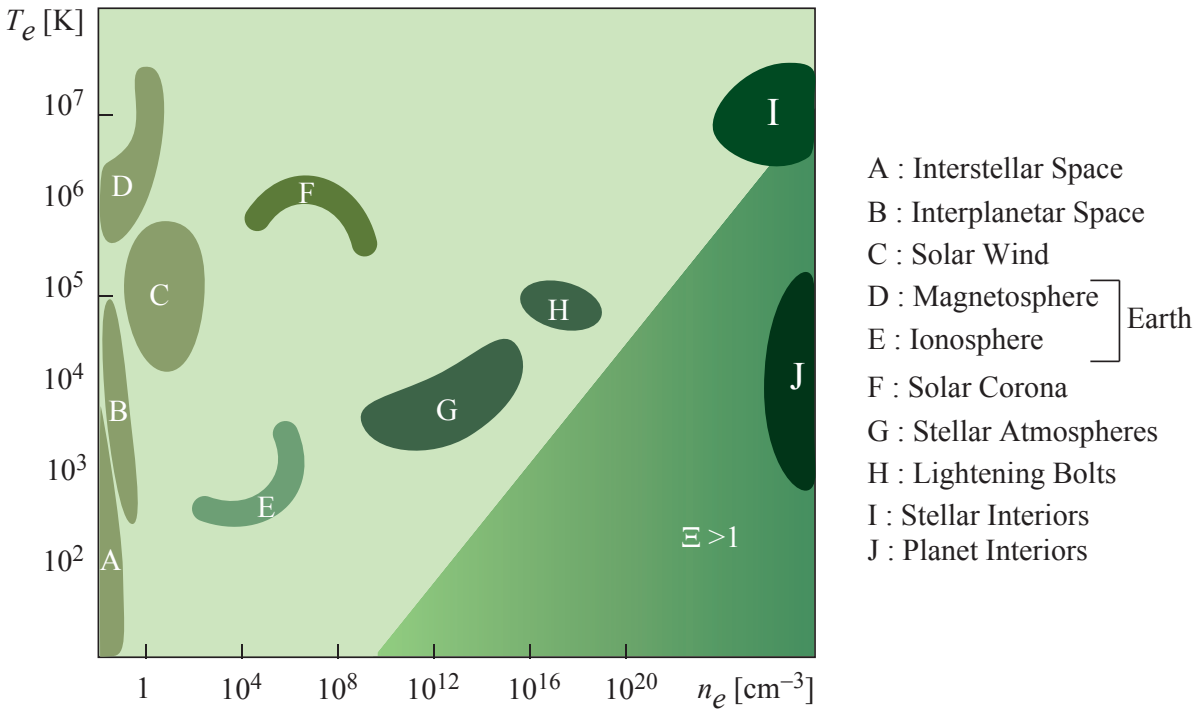

Figure 1.1 – Temperature and density of usual plasmas in Universe

2 Motion of charged particles in electric and magnetic fields

We have seen in the introduction that collective effects in a plasma came from the long-range of Coulomb forces between charged particles. Nevertheless, resolving the individual motion of plasma electrons and ions in presence of electromagnetic fields is a key to study the plasma and its applications. To begin with this study we will suppose that electric and magnetic fields preexist in the plasma and we will solve the motion of particles inside those fields. To obtain a self-consistent description, as particles themselves will produce electromagnetic fields by concentration of charge and current densities, we will need to process by iteration and recalculate the fields by Maxwell equations. For now, considering a plasma where only external fields are taken into account, the motion of a particle of mass m, velocity v and charge q in an electric field $\vec{E}$ and magnetic field $\vec{B}$ is ruled by the Lorentz force :

$$\vec{F_L} = q\left(\vec{E} + \vec{v} \wedge \vec{B}\right) \tag{2.1}$$

Considering non-relativistic particles, the third Newton law rise an acceleration of particles linearly linked with their velocity. However, the motion of particles can be rather difficult if the electromagnetic field is varying along the particle path. In the following, we will consider the approximation of uniform electric and magnetic field in both time and space.

In uniform and continuous magnetic field

By taking first the case of an uniform and continuous magnetic field, without electric field, the Eq. 2.1 reduces to :

$$\frac{d\vec{v}}{dt} = \frac{q}{m}\vec{v} \wedge \vec{B} = -\omega_c \vec{e}_B \wedge \vec{v} \tag{2.2}$$

and $\omega_c = qB/m$ is the Larmor frequency and $\vec{e}_B$ is the unit vector in direction of $\vec{B}$. If one decomposes the acceleration in the direction parallel ($\parallel$) and perpendicular ($\perp$) to $\vec{e}_B$:

$$\begin{cases} d\vec{v}_\parallel / dt = 0 \\ d\vec{v}_\perp / dt = -\omega_c \vec{e}_B \wedge \vec{v}_\perp \end{cases} \tag{2.3}$$

The charged particle has a rectilinear uniform motion along B-field lines with a circular rotation of angular frequency ω_c (called *cyclotron frequency*) in the plane perpendicular to the B-field lines. It

describes an helicoidal trajectory whose pitch depends on the parallel velocity $v_{\parallel}$ and the gyration radius on the perpendicular velocity $v_{\perp}$. An illustration of the trajectory of either a positive ion or an electron in an uniform B-field is shown in Figure 2.1-panel a). Taking a Cartesian representation with the axis $\vec{z}$ coincident with $\vec{e}_B$, $\vec{B} = B_0\vec{e}_B$, the motion is described by :

$$\begin{cases} x = \dfrac{v_{\perp}}{\omega_c}\sin(\omega_c t) + x_0 \\ y = -\dfrac{v_{\perp}}{\omega_c}\sin(\omega_c t) + y_0 \\ z = v_{\parallel} t + z_0 \end{cases} \tag{2.4}$$

We can introduce the gyration radius or Larmor radius defined by :

$$r_L = v_{\perp}/|\omega_c| = \frac{m v_{\perp}}{|q|B_0} \tag{2.5}$$

In the relativistic case, this formulation is still valid when mass correction is considered:

$$r_L = \frac{\gamma m v_{\perp}}{|q|B_0} \tag{2.6}$$

The transverse kinetic energy of a charged particle can be expressed in the non-relativistic regime by $W_{\perp} = \frac{1}{2} m {v_{\perp}}^2$. We can also write the Larmor radius as a function of this transverse kinetic energy:

$$r_L = \frac{\sqrt{2mW_{\perp}}}{|q|B_0} \tag{2.7}$$

In the general case of a distribution of particles, the previous parameters of motion are different for each particle.

The rotation of a particle forms a loop of current and there is a generated magnetic field characterized by the magnetic moment $\vec{\mu} = \frac{1}{2}\int \vec{r} \wedge \vec{j}\, d\vec{r}$ where $\vec{j}$ is the current density. This expression can often be simplified to:

$$\vec{\mu} = \frac{1}{2} q\vec{r} \wedge \vec{v} = \frac{1}{2} q r_L v_{\perp} \tag{2.8}$$

Using Eq. 2.7, we can write the magnetic moment as :

$$\vec{\mu} = -\frac{m {v_{\perp}}^2}{2B_0}\vec{e}_B \tag{2.9}$$

The resulting magnetic field, which is opposed to external magnetic field, evidences that free charged particles have a *diamagnetic* current. It is similar to the Lenz law for macroscopic induction currents which more generally states that effects are induced in order to counterbalance causes that have produced them. The configuration of the B-field is not uniform anymore and a diamagnetic force is directed along the B-field direction and is proportional to the magnetic moment μ and the gradient of the B-field ∇B. A population of particles will be considered as *magnetized* as soon as the frequency of collisions is small when compared to the cyclotron frequency. When a collision occurs, the helical trajectory is interrupted and the new particle momentum define a new helix with a different radius and pitch. It is worth noting that when the collision frequency is intermediate between electron and ion cyclotron frequencies, electrons are considered magnetized despite ions are not.

In uniform and stationary, crossed magnetic and electric field - electric drift

Introducing an additional stationary electric field to the previous situation, the general force exerted on a particle by the fields is given in Eq. 2.1. The component of the electric field $\vec{E}_{\parallel}$ parallel to $\vec{B}$ will produce an uniformly and rectilinear accelerated motion along the B-field direction. Electrons and ions move in opposite directions due to their opposite charge. The perpendicular component of the electric field $\vec{E}_{\perp}$ does not induce an acceleration but a drift velocity. To show this, one can suppose the simpler situation where $E_{\parallel} = 0$ and $v_{\parallel} = 0$:

$$\frac{d\vec{v}_{\perp}}{dt} = -\omega_c \vec{e}_B \wedge \vec{E}_{\perp} + \frac{q}{m}\vec{E}_{\perp} \tag{2.10}$$

The time derivative of this expression yields :

$$\frac{d^2\vec{v}_\perp}{dt^2} = -{\omega_c}^2\,\vec{v}_\perp - \frac{q}{m}\omega_c\vec{e}_B \wedge \vec{E}_\perp \tag{2.11}$$

Under the assumption $\vec{E}_\perp \ll c\vec{B}$, we can make a Lorentz transformation and introduce the velocity $\vec{v}_0 = \vec{v}_\perp - \vec{v}_E$, where $\vec{v}_E$ verifies $\vec{v}_E \wedge \vec{B} = -\vec{E}_\perp$. $\vec{v}_0$ is then ruled by $\frac{d\vec{v}_0}{dt} = -\omega_c\vec{e}_B \wedge \vec{v}_0$ and defines a new gyration velocity. This latter equation can be solved similarly than for the previous case without electric field (Eq. 2.2), and $\vec{v}_E$ writes:

$$\vec{v_E} = \frac{q}{m\omega_c}\vec{E} \wedge \vec{e}_B = \frac{\vec{E} \wedge \vec{B}}{B^2} \tag{2.12}$$

This velocity $\vec{v_E}$ is called *electric drift velocity*. It can be obtained more generally from the general motion equation with $E_\parallel \neq 0$ and $v_\parallel \neq 0$ as the first order of a Taylor series, considering the adiabatic hypothesis $\partial B/\partial t \ll |\omega_c|B$. The second order term is also found in literature and it is called the polarization drift velocity, $\vec{v_p} = \frac{1}{B\omega_c}\frac{d\vec{E}_\perp}{dt}$.

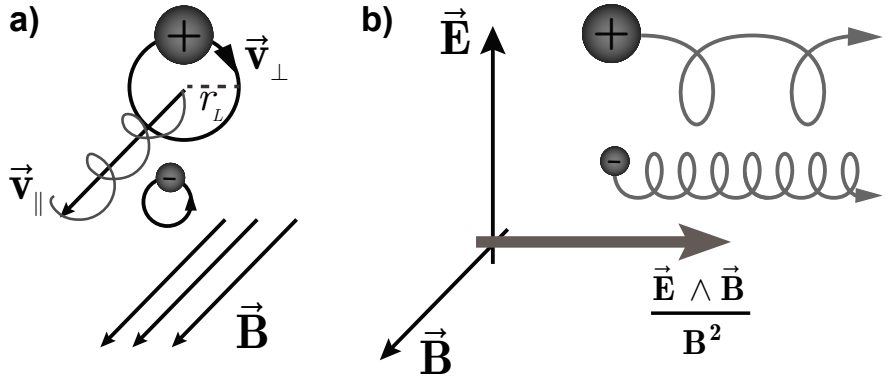

Figure 2.1 – Illustration of the trajectory of an electron or a positive ion in **a)** an uniform magnetic field ; **b)** uniform magnetic and electric field. It evidences here the electric drift due to cross fields.

The Figure 2.1-panel b) illustrates the orbits obtained for an electron and ion with zero initial velocities. The combination between a rotation and a translation is called a *cycloid*. One can note that the electrical drift velocity does not depend on the mass or the charge of the particle. In particular, because an electron is much lighter than an ion, the gyration radius will be much smaller whereas the frequency of rotation will be much larger.

Finally, the electrical drift velocity is the same for electrons and ions and, at first order (neglecting polarization velocity), crossed $\vec{E}$ and $\vec{B}$ do not produce charge separation.

Non uniform magnetic field - magnetic drift

In cases where magnetic fields are not uniform and/or are varying in time, the particles are not strictly following the field lines and the trajectories are more complex. One can make the approximation that the spatial and temporal variations of magnetic field are smooth. It is mathematically expressed introducing the gradient lengths of magnetic field in time and in space for perpendicular and parallel directions :

$$\tau_c = \left(\frac{1}{B}\left|\frac{\partial B}{\partial t}\right|\right)^{-1}, \qquad l_\perp = \left(\frac{|\vec{\nabla}_\perp B|}{B}\right)^{-1}, \qquad l_\parallel = \left(\frac{|\vec{\nabla}_\parallel B|}{B}\right)^{-1}. \tag{2.13}$$

The smooth variations are obtained making adiabatic approximations assuming that $\tau_c \gg 2\pi/\omega_c$, $l_\perp \gg r_L$ and $l_\parallel \gg 2\pi v_\parallel/\omega_c$. The trajectories are deformed helices, as shown further in Figure 2.2 for a particular non-uniform B-field configuration. The non uniformities of the magnetic field

are mathematically defined by the *divergence/convergence* and *gradient/curvature* of field lines. The diamagnetic behavior introduced before is raised from divergence/convergence inhomogeneities, as a consequence of the divergence-free character of the magnetic field. The gradient and curvature inhomogeneities contribute to drift and reflect particles. The reflections are yielded by an effect called *magnetic mirror* that will be studied in next paragraph. If one considers that the magnetic field is non-uniform, yet constant in time, the magnetic field lines (as shown in Figure 2.2) present a curvature and the velocity of a charged particle can then be written as:

$$\vec{v} = \vec{v_{\parallel}} + \vec{v_{\perp}} + \vec{v_B} \tag{2.14}$$

The first two terms, as before, represent the helical motion around the guide center. The guide center is here drift by $\vec{v_B}$, the *magnetic drift velocity*. This magnetic drift velocity can itself be decomposed as a sum of a *gradient drift velocity* and a *curvature drift velocity*. By means of the magnetic field gradient, under adiabatic approximations, the charged particle accelerates along the gradient direction. By integrating this acceleration over a cyclotronic rotation, we obtain ${v_{\perp}}^2/2l_c$ where $l_c = B/|\vec{\nabla}_{\perp} B_{\parallel}|$ is the local perpendicular magnetic field gradient length at the vicinity of the guide center. The gradient drift velocity is obtained for a random transverse gradient of magnetic field $\vec{\nabla}_{\perp} B$, identically than for electrical drift velocity, substituting the acceleration in Eq. 2.12. One can find:

$$\vec{v_g} = \frac{{v_{\perp}}^2}{2\omega_c} \frac{\vec{B} \wedge \vec{\nabla}_{\perp} B}{B^2} \tag{2.15}$$

The gradient drift velocity is perpendicular to both the magnetic field and its gradient direction. The sign of this gradient drift velocity is opposite for electrons and ions (contrary to electric drift velocity) and is proportional to the particle kinetic energy in the perpendicular plan. The curvature of magnetic field induces a centripetal acceleration directed along the unit vector $\vec{n} = \left(\vec{e}_b \cdot \vec{\nabla}\right) \vec{e}_B$ and whose norm is $v_{\parallel}^2/R_c$ where R_c is the curvature radius ($R_c = B/|\vec{\nabla}_{\parallel} B_{\perp}|$). Again, substituting the acceleration in Eq. 2.12, one finds:

$$\vec{v_c} = \frac{{v_{\parallel}}^2}{\omega_c} \frac{\vec{e}_B \wedge \vec{n}}{R_c} \tag{2.16}$$

This magnetic curvature drift velocity is perpendicular to both magnetic field direction and the local curvature radius direction. In this case it is proportional to the particle kinetic energy in the parallel plan.

It is worth noting that the sign of these two magnetic drift velocities depend on the charge of the particle. Consequently, there is a charge separation between electrons and ions, and they create currents that will self-generate magnetic fields. The magnetic fields here are not diamagnetic, neither paramagnetic, they just tend to smooth the gradients and curvature of the magnetic field. Those currents are small because most of the velocity is held by the cyclotron motion. A simplification of the magnetic drift velocities can be made under the assumption of an irrotational field ($\vec{\nabla} \wedge \vec{B} = \vec{0}$) yielding $\vec{e}_B \wedge \vec{\nabla} B/B = \vec{e}_B \wedge \vec{n}/R_c$. The sum of gradient and curvature drift velocities can then be written:

$$\vec{v_g} + \vec{v_c} = \frac{2v_{\parallel}^2 + v_{\perp}^2}{2\omega_c} \frac{\vec{B} \wedge \vec{\nabla}_{\perp} B}{B^2} = \left(v_{\parallel}^2 + \frac{v_{\perp}^2}{2}\right) \frac{\vec{e}_B \wedge \vec{n}}{R_c \omega_c} \tag{2.17}$$

Studying the drift velocities is of great interest for the confinement of thermonuclear plasmas. Indeed, the currents generated by drift velocities change the field configuration and the particles emit electromagnetic waves that can trigger instabilities.

This thesis is dealing with the transport of charged particle in a configuration of an applied external magnetic field. In that sense, we will finish this part by an example of magnetic mirror configuration, considering a magnetic field mostly directed along z, constant in time, and supposed to have an increasing gradient along z according to $B_z = B_0(1 + z/l)$, with the gradient length $l = \left(\frac{1}{B_0}\frac{\partial B_z}{\partial z}\right)^{-1}$. This field configuration is illustrated in Figure 2.2. As the magnetic field is divergence-free $\vec{\nabla} \cdot \vec{B} = 0$, it exists a radial component B_r that induce a force in the z direction. If

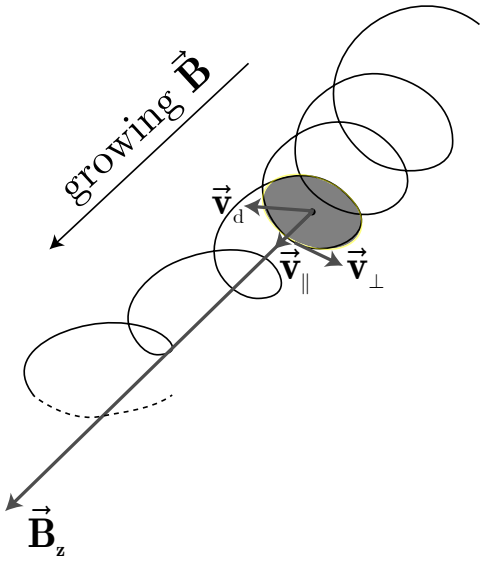

Figure 2.2 – Motion of a particle in a non-uniform magnetic field. Here the B-field is mostly directed along $\vec{z}$ and growing while z increases. The induction lines become more and more narrow with the increasing B-field. At a certain point, if the B-field gradient is too strong, the particle can be reflected back, as shown by the dashed trajectory line. This effect is called *magnetic mirror*

.

one writes the divergence of the magnetic field in cylindrical coordinates:

$$\frac{1}{r}\frac{\partial}{\partial r}(rB_r) + \frac{\partial B_z}{\partial z} = 0 \tag{2.18}$$

Assuming that the derivative of B_z does not depend on r, one finds that B_r writes :

$$B_r(r) = -\frac{r}{2}\frac{\partial B_z}{\partial z} = -B_0\frac{r}{2l} \tag{2.19}$$

Taking the radius of the electron trajectory equals to the Larmor radius $r = r_L$, we can deduce that the force is exerted on the electron along the z direction :

$$\vec{F} = -ev_\perp\vec{e}_\theta \wedge \vec{e}_r B_r = -\frac{m_e v_\perp^2}{2}\frac{1}{B_z}\frac{\partial B_z}{\partial z}\vec{e}_z \tag{2.20}$$

The sign of the acceleration is independent of the particle charge and both electrons and ions slow down along z (in this B-field configuration $\partial_z B_z > 0$).

The magnetic moment of a charged particle rotating in this magnetic field is :

$$\mu = m\frac{v_\perp^2}{2B_z} \tag{2.21}$$

We can rewrite the force as proportional to the magnetic moment and the gradient :

$$\vec{F} = -\mu\frac{\partial B_z}{\partial z}\vec{e}_z \tag{2.22}$$

It can be demonstrated that the magnetic moment is an adiabatic invariant, and particularly we have by the conservation of the kinetic energy $\frac{d\mu}{dz} = 0$ ($\vec{B}$ does not induce work). The force exerted on the electron is then directly proportional to the gradient. As the electron looses velocity along z ($v_\parallel$) it will gain velocity along perpendicular directions ($v_\perp$) and more the particle is decelerated (strong magnetic field gradient), more velocity will be transferred from parallel to perpendicular directions. In enough strong gradients, the particle can even be reflected back. That is why this configuration is called a *magnetic mirror*.

Box. 2.1: Conclusion of this section

In conclusion, the adiabatic motion of a single charged particle in an electromagnetic field is the combination of a cyclotronic motion, magnetic drifts of gradient and curvature, that are perpendicular to magnetic field lines, and a parallel motion along field lines, that can be accelerated or decelerated by the convergence or divergence of field lines and/or by electric drifts from crossed fields and polarization.

3 General concepts of intense laser interaction with overdense matter

This part is dedicated to provide a brief overview of the relevant phenomena occurring in laser-solid interactions. The plasma is considered overdense when the electron density n_e exceeds the critical density n_c. The critical density corresponds to a laser-light frequency ω (wavelength λ) equaling the plasma frequency $\omega = \omega_p$:

$$\omega = \sqrt{\frac{n_c e^2}{\epsilon_0 m_e}} \Rightarrow n_c = \frac{\epsilon_0 m_e \omega^2}{e^2} \rightarrow n_c[\mathrm{cm}^{-3}] \approx 1.1 \times 10^{21} (\lambda[\mu\mathrm{m}])^{-2} \tag{3.1}$$

Above critical density, the laser cannot propagate in the plasma, as shown in the dispersion relation of an electromagnetic wave propagating in a cold, collisionless plasma :

$$k^2 c^2 = \omega^2 - \omega_p^2 = \frac{e^2}{\epsilon_0 m_e}(n_e - n_c) \tag{3.2}$$

Indeed, if $n_e > n_c$, the refraction index $\eta = \sqrt{1 - n_e/n_c}$ yields imaginary values and the wave will be evanescent over the plasma skin depth δ_{sd} defined as :

$$\delta_{sd} = \frac{c}{\sqrt{\omega_p^2 - \omega^2}} \approx \frac{c}{\omega_p} \qquad \text{if} \quad \omega_p \gg \omega. \tag{3.3}$$

Thus, assuming a sharp boundary between vacuum and the target, the interaction between the laser fields and the target particles will happen only over the underdense region ($n_e < n_c$) or close to the critical density ($n_e = n_c$) in this thin layer of overdense matter. However, the relativistic effects change the critical density and the refraction index becomes $\eta' = \sqrt{1 - n_e/(\gamma n_c)}$. The relativistic regime is obtained when the Lorentz factor is bigger than 2. The Lorentz factor as a function of the normalized vector potential of the laser pulse a_0 writes $\gamma = \sqrt{1 + a_0^2/2}$ for a linearly polarized laser field and $\gamma = \sqrt{1 + a_0^2}$ for a circular polarization, where a_0 is defined by :

$$a_0 = \frac{eE}{m_e \omega c} \rightarrow a_0 \approx 0.85 \sqrt{\frac{I\lambda^2[\mu\mathrm{m}^2]}{10^{18}\,\mathrm{W/cm}^2}} \tag{3.4}$$

$\vec{E}$ is the laser electric field and I is the intensity of the laser beam $I = \epsilon_0 c \langle E^2 \rangle / 2$. The laser can propagate till the relativistically modified critical density, and this effect is known as *self-induced relativistic transparency*. The transparency, of course, only happens if the local laser beam intensity is over $10^{18}\,\mathrm{W/cm}^2$ in the region where $n_c < n_e < n_c'$, a region that is also affected by ponderomotive effects. This regime of intensity is very common nowadays after the advent of chirped pulse amplification technique [266, 189].

The ponderomotive force is nonlinear and arise from the spatial and temporal dependence of the laser intensity [191]. It describes the motion of the guide center of a charged particle in a non-uniform, alternative electric field, over a timescale longer than the oscillation period. The vector potential envelope is assumed to be sufficiently smooth in space and time [191]. Averaged over an oscillation period, the relativistic kinetic energy acquired by an electron oscillating in a quasi-monochromatic electromagnetic field writes (for a linear polarization):

$$W_h = m_e c^2 (\gamma - 1) = m_e c^2 \left(\sqrt{1 + {a_0}^2/2} - 1 \right) \tag{3.5}$$

The related ponderomotive force can be expressed as:

$$\vec{F}_p = -\vec{\nabla} W_h = -m_e c^2 \vec{\nabla} \left(\sqrt{1 + {a_0}^2/2} - 1 \right) \tag{3.6}$$

As the ponderomotive force is proportional to e^2 and m^{-1}, it acts both on electrons and ions and it is more effective on the lightest particles. It tends to push plasma electrons away from the laser pulse

envelope where $\langle E^2 \rangle$ is the highest. It can create very steep density gradients and charge separation and the corresponding electrostatic field can in turn, over a longer time-scale, accelerate ions [166]. Because of the ion movement, the ponderomotive effect is also directly involved in the hole boring mechanisms where the laser pulse is responsible of the inward movement of the target surface [290]. On the other hand, in the relativistic regime, electrons are not only radially ejected from the laser propagation axis, but they also acquire a longitudinal momentum due to the magnetic contribution of the Lorentz force. In underdense plasmas, where the laser pulse can propagate, the ponderomotive force created by charge displacements triggers longitudinal electrostatic waves that can be used to trap and accelerate electrons up to GeV energies [160]. In a multidimensional geometry, a laser pulse of finite width may produce a density depression around the propagation axis also because of the ponderomotive force pushing the electrons in the radial direction. Jointly with the relativistic effect and target expansion driven by electron heating, this mechanism may lead to a transition to transparency as soon as the electron density drops below the cutoff value [83].

Multi-dimensional geometry, relativistic and nonlinear effects, self-consistent plasma density profile modifications together with plasma thermal expansion make the laser-matter interaction a very challenging picture to be described. It is clear anyway that the laser cannot directly propagate in an overdense plasma and even in underdense plasma, the laser energy is absorbed along its propagation via different mechanisms. As shown before, there is a relativistic transition at $I\lambda^2 \sim 10^{18}\,\mathrm{Wcm^{-2}\mu m^2}$. In the experiments carried out in this thesis, the relativistic case was explored in picosecond and subpicosecond regime. A laser-matter interaction at intensities under the relativistic limit was furthermore experienced with the use of an energetic nanosecond laser-beam. More details about the mechanisms of fast electrons generation will be made in the next subsection (Sec. 3.1). The transport of the electron beam through dense matter will be described in Sec. 3.3. In the picosecond and sub-picosecond regime, as introduced before, one can also expect effective ion acceleration. The related mechanisms of acceleration are further described in Sec. 5.2.1.

3.1 Fast electron generation

Since the laser pulse cannot propagate into solid-density regions, the absorbed energy is transported to these regions mostly by energetic (commonly named *hot* or *fast*) electrons which may be generated during the interaction through several mechanisms. By *hot* electrons, one typically refers to electrons whose energy is of the order of the cycle-average oscillation energy in the electric field of the laser in vacuum (Eq. 3.5). Those electrons are accelerated by the laser-pulse at the front surface of the target and a fraction of them is able to cross the target bulk and are detected at the rear surface.

To further describe how those electrons are generated at the front surface, one can introduce the different possible absorption mechanisms. In this first part, we will describe mechanisms taking place in the non-relativistic regime. This regime is the one that will predominate for the high energy nanosecond regime studied in Sec. 4. Collisional absorption or inverse bremsstrahlung is dominant at laser irradiances $(I\lambda^2) \leq 10^{15}\,\mathrm{Wcm^{-2}\mu m^{-2}}$. When the laser intensity is not high and the coronal temperature is not high too, electron-ion collisions become dominant. Above intensities of $10^{14}\,\mathrm{W/cm^2}$, most of the absorption mechanisms depend on the laser wavelength (see the further presented absorption coefficients).

At higher intensities ($I\lambda^2 > 10^{18}\,\mathrm{Wcm^{-2}\mu m^{-2}}$), the electron motion becomes relativistic and absorption mechanisms belongs to the relativistic regime which will be detailed in the second part of this section. This regime of absorption is particularly relevant for the intense laser-interaction in the picosecond and sub-picosecond regime, further detailed in Sec. 5.

3.1.1 Non-relativistic regime

Inverse Bremsstrahlung

When a charged particle collide with another particle, the so-called bremsstrahlung (meaning in German "braking radiation") occurs. Inverse bremsstrahlung takes place when an electron absorbs a photon while colliding with an ion or with another electron. The inverse bremstrahlung theory can be derived from the Vlasov equation taking into account the distribution function of the electrons

and the positions of the ions. One can also consider a simple model of an infinite and homogeneous plasma with static heavy ions (single species). Since the laser electromagnetic waves have a phase velocity much higher than the thermal velocity of electrons, one can neglect the thermal force. The equation of motion for electrons is reduced to:

$$m_e \frac{d\vec{v}}{dt} = -e\left(\vec{E} + \vec{v} \wedge \vec{B}\right) - m_e \nu_{ei} \vec{v} \tag{3.7}$$

with $-e$, m_e and $\vec{v}$ respectively the electron charge, mass and velocity. $\nu_{e,i}$ is the electron-ion collision frequency. In the Spitzer regime of high temperatures, it writes:

$$\nu_{e,i} = \frac{(Z^*)^2 e^4 n_i \ln \Lambda_{e,i}}{3\epsilon_0^2 \sqrt{m_e} (2\pi k_B T_e)^{3/2}} \longrightarrow \nu_{e,i}[\mathrm{s}^{-1}] \approx 2.91 \times 10^{-6} Z^* n_e[\mathrm{cm}^{-3}] \left(T_e[\mathrm{eV}]\right)^{-3/2} \ln \Lambda_{e,i} \tag{3.8}$$

$$\text{with} \quad \ln \Lambda = \max\left[2, \frac{1}{2} \ln\left(1 + \frac{b_{\max}^2}{b_{\min}^2}\right)\right] \tag{3.9}$$

where Z^* is the number of free electrons per atom (see ionization state in Sec. 3.3.2), $b_{\max}$ and $b_{\min}$ are respectively the maximum and the minimum impact parameters (see Sec. 3.3.1). $\ln \Lambda$ is called the Coulomb logarithm (typically $10 < \ln \Lambda < 20$ in ideal plasmas, and in non-ideal plasmas, where close collisions are dominant, the Coulomb logarithm is close to its minimum value of 2). On the other hand, solving Maxwell equations for the electric field $\vec{E}$ of a monochromatic wave with a constant frequency ω propagating in a homogeneous plasma yields:

$$\Delta \vec{E} + \frac{\omega^2}{c^2} \epsilon(\omega) \vec{E} = 0. \tag{3.10}$$

$\epsilon(\omega)$ is the dielectric function. One generally introduces the electronic susceptibility $\chi_e(\omega)$:

$$\chi_e(\omega) = \frac{\omega_p^2}{\omega(\omega + i\nu_{e,i})} \tag{3.11}$$

and the dielectric function:

$$\epsilon(\omega) = 1 - \chi_e(\omega) \tag{3.12}$$

The dispersion relation for electromagnetic waves can always be written as:

$$k = \frac{\omega}{c} \sqrt{\epsilon(\omega)}. \tag{3.13}$$

In the corona, the collision frequency $\nu_{e,i}$ is generally far smaller than the plasma frequency $\omega_{p,e}$. The spatial damping rate of the laser energy by inverse bremsstrahlung κ_{IB} is given by twice the imaginary part of k:

$$\kappa_{IB} = 2\Im(k) = \frac{\nu_{e,i}}{c} \frac{\omega_p^2}{\omega^2} \left(1 - \frac{\omega_p^2}{\omega^2}\right)^{-1/2} \tag{3.14}$$

Using the definition of the critical density n_c together with Eq. 3.8, one obtains κ_{IB} at the critical density:

$$\kappa_{IB} = \frac{\nu_{e,i}(n_c)}{c} \left(\frac{n_e}{n_c}\right)^2 \left(1 - \frac{n_e}{n_c}\right)^{-1/2} \propto \frac{Z^* n_e^2}{T_e^{3/2}} \left(1 - \frac{n_e}{n_c}\right)^{-1/2} \tag{3.15}$$

To evaluate the absorption coefficient from Inverse Bremsstrahlung, let us consider a laser beam of intensity I passing through a slab of plasma in the z direction. Its attenuation is ruled by:

$$\frac{dI}{dz} = -\kappa_{IB} I \tag{3.16}$$

For a slab of plasma of length L, the absorption coefficient α_{IB} is given by:

$$\alpha_{IB} = 1 - \exp\left(-\int_0^L \kappa_{IB} dz\right) \tag{3.17}$$

For inhomogeneous plasma, the solution of Eq. 3.16 is more complicated since κ_{IB} is a function of n_e, T_e and $\ln\Lambda$ which may all depend on position and time. Solving Eq. 3.16 for a typical exponential profile $n_e = n_c \exp(-z/L)$ yields [150]:

$$\alpha_{IB} = 1 - \exp\left(-\frac{8}{3}\frac{\nu_{e,i}(n_c)L}{c}\right) \tag{3.18}$$

In [186], a model is given for planar and spherical expansion of the plasma, in order to evaluate the inverse bremsstrahlung absorption coefficient as a function of the laser intensity. The spherical model is adapted for experiments such as the product $c_s\tau_L$ (τ_L: laser pulse duration) is larger than L (intense long pulse interactions). For both models, a characteristic laser intensity I_0 is introduced and writes:

$$\text{planar}: \quad I_0 \approx 4.8\times10^{11}\,\mathrm{W/cm^2}(1.06\,\mu\mathrm{m}/\lambda_L)^5(2Z/A)^{5/4}\left[Z(\ln\Lambda/6)(\tau_L/100\,\mathrm{ps})\right]^{3/2} \tag{3.19}$$

$$\text{spherical}: \quad I_0 \approx 4.8\times10^{11}\,\mathrm{W/cm^2}(1.06\,\mu\mathrm{m}/\lambda_L)^4(2Z/A)^{1/2}Z^*(\ln\Lambda/6)(L/7.1\,\mu\mathrm{m}) \tag{3.20}$$

and the absorption coefficient is evaluated to:

$$\alpha_{IB} = 1 - \exp\left[-\left(\frac{\alpha_{IB}I_L}{I_0}\right)^{-2/3}\right] \tag{3.21}$$

The figure Figure 3.1 shows the evolution of α_{IB} with I_L/I_0: that is the laser intensity I_L normalized by the previously introduced characteristic laser intensity I_0 for a spherical expansion.

The dependence of κ_{IB} on n_e/n_c in Eq. 3.15 shows that a significant fraction of the inverse bremsstrahlung absorption appears in the region near the critical density ($n_e \sim n_c$).
Besides, it decreases strongly with laser intensity and is larger for short laser wavelengths. For intensities below $10^{15}\,\mathrm{W/cm^2}$, used in the conventional ICF schemes, Inverse Bremsstrahlung is the main absorption mechanism and it almost completely disappears for intensities $> 10^{18}\,\mathrm{W/cm^2}$, even more considering that high radiation pressure obtained at higher laser intensities make the density gradient steeper at the critical surface and thus L decreases. The Inverse Bremsstrahlung absorption produce an electronic distribution of the form [156]:

$$f_{IB} \propto \exp\left(-\frac{v^n}{v_0^n}\right) \tag{3.22}$$

where $2 < n < 5$ and v_0 is a time-increasing function. This distribution is called *super-Gaussian* and is relatively poor in particles of high energy.

If the laser incidence is not normal to target plane but instead forming an angle θ_0 with the normal, two cases have to be considered:

- ◇ The laser polarization is "s", meaning that the electric component of the laser EM wave is perpendicular to the density gradient and the wave vector $\vec{k}$.
- ◇ The laser polarization is "p", meaning that the electric component of the laser EM wave is in the plane of defined by the gradient density and the wave vector $\vec{k}$. The magnetic component is then perpendicular to this plane.

In the case of a "s" polarization, the laser wave is reflected at a density below the critical density $n_c(\theta_0) = n_c\cos^2\theta_0$, the absorption coefficient Eq. 3.18 can be rewritten:

$$\alpha_{IB-s} = 1 - \exp\left(-\frac{8}{3}\frac{\nu_{e,i}(n_c)L\cos^3\theta_0}{c}\right) \tag{3.23}$$

The angular dependence of the latter equation is plotted in Figure 3.1-**(b)** (blue curve). For a linear density profile instead of exponential, the angular dependence would be stronger ($\propto \cos^5\theta_0$).

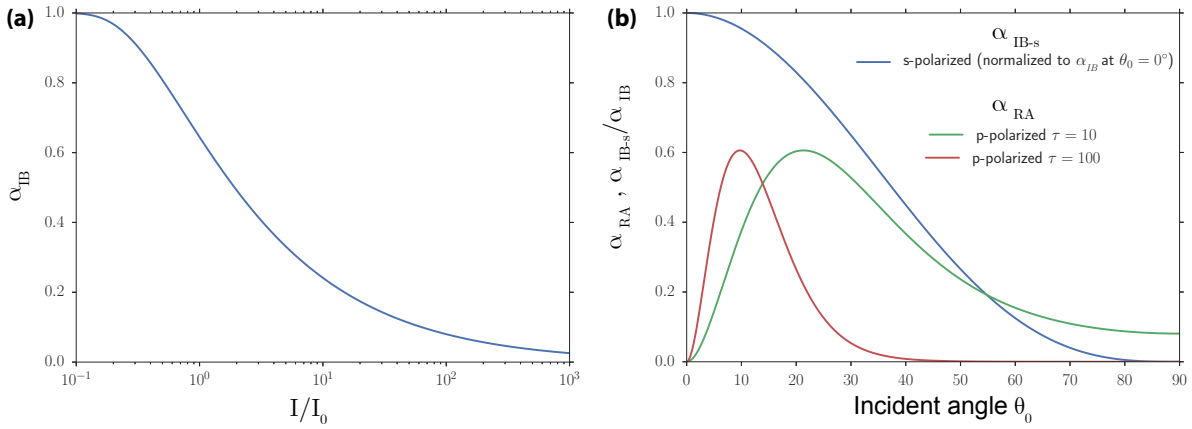

Figure 3.1 – (a) Evolution of the Inverse Bremsstrahlung (IB) absorption coefficient with normalized laser intensity I_L/I_0. I_0 is a characteristic intensity given in Eq. 3.20 for a spherical plasma expansion [186]. **(b)** is representing the incident angle dependency of the IB absorption coefficient with a s-polarized laser pulse (Eq. 3.23) and idem for Resonant Absorption (RA) with a p-polarized laser beam (Eq. 3.26). The latter puts in evidence that α_{RA} is peaking at $\approx 60\,\%$. In **(b)**, note that blue curve is normalized to the absorption coefficient α_{IB} that would be obtained at normal incidence ($\theta_0 = 0\,°$).

Others Collisional Absorptions

For small laser pulse duration, the laser-ionized plasma has no time to expand hydrodynamically. One can derive a linearized equation from Eq. 3.10 and couple it with the classical kinetic equation (see [237]). Each collisional absorption mechanism presented here is characterized by its skin-depth l_s and its associated absorption coefficient. For high electron temperatures and high laser frequencies, the accelerated electron mean free path can be shorter than the skin-depth: the laser pulse penetrates the solid over a skin-depth $l_{s,CA} \approx c/\omega_{p,e}$. The previous model for Inverse Bremsstrahlung is taken to be the limit where the penetration depth L is given by l_s (to be replaced in Eq. 3.18). This laser energy absorption mechanism is called *collisional absorption*. The absorption coefficient writes [237]:

$$\alpha_{CA} = \frac{2\nu_{e,i}}{\omega_{p,e}} \tag{3.24}$$

For lower laser frequencies and colder and/or denser solids, it happens that the electron-ion collision frequency can be higher than the laser frequency such as $\omega_L \ll \nu_{e,i} \ll \omega_{p,e}$ and the electron mean free path is still shorter than the skin-depth. In this regime, the dominant collisional absorption mechanism is called *normal skin effect*. The laser is absorbed in the skin-depth $l_{s,NSE} \simeq (c/\omega_{p,e})\sqrt{\nu_{e,i}/\omega_L}$. The absorption coefficient writes [237]:

$$\alpha_{NSE} = \frac{\omega_L}{\omega_{p,e}}\sqrt{\frac{8\nu_{e,i}}{\omega_L}} \tag{3.25}$$

Resonant Absorption

While increasing laser intensities and electron temperatures, "collisionless" absorption mechanisms become dominant. The mean free path of accelerated electrons can become larger than the skin depth. The absorption of the laser field consequently becomes non-local, the energy being transported deeper into the plasma.

In the case of a "p" polarization, when the laser is reflected at the critical density, the electric field has a component parallel to the density gradient: there is a violation of the condition $\vec{\nabla} \cdot \vec{E} = 0$ and a charge separation occurs according to the Poisson equation. This corresponds to an electrostatic behavior of the laser wave and the electron oscillates along the density gradient driving a plasma wave. Indeed, the electric field tends to diverge near the critical density when the plasma frequency converges to the laser frequency (where ϵ vanishes). This phenomenon is called *resonant absorption*.

A non-zero effective collision frequency limit the divergence. For a linear density profile and a p-polarized laser, the absorption coefficient has been calculated in [77, 210] and writes:

$$\alpha_{RA} = 36\tau^2 \frac{[Ai(\tau)]^3}{|Ai'(\tau)|} \tag{3.26}$$

where Ai and Ai' are respectively the Airy function and its derivative, and:

$$\tau = \left(\frac{\omega_L L}{c}\right)^{\frac{1}{3}} \sin\theta_0 = \left(\frac{2\pi L}{\lambda_L}\right)^{\frac{1}{3}} \sin\theta_0. \tag{3.27}$$

The graph in Figure 3.1-**(b)** shows the theoretical evolution of α_{RA} with the incident angle θ_0 for $\tau = 10$ (green curve) and $\tau = 100$ (red curve). If θ_0 is too large, then the evanescent electrostatic wave needs to tunnel too far and the plasma wave is not driven efficiently. On the other hand, if θ_0 is too small, the laser electric field along the density gradient is also small and the excitation of the plasma wave is limited. The maximum resonant absorption coefficient, as derived by the latter formula, is $\approx 60\,\%$ at an optimized incident angle θ_0 ruled by $\tau \approx 0.8$. An other condition required for resonance absorption to occur is that several optical cycles of the laser pulse must be able to penetrate into the underdense pre-plasma formed in front of the target. It is clear that this condition is not fulfilled if the amplitude of electrons oscillation becomes larger than L, in which case the excited plasma wave would be totally damped at each optical cycle.

It is crucial to mention that even with a light normally incident on the target surface ($\theta_0 = 0$), resonant absorption can still be significant if the plasma is weakly magnetized or if the critical density surface is rippled [59]. It is especially the case for long-pulses irradiation where density instabilites of the critical surface have time to develop. The main feature of the resonant absorption is the creation of hot electrons, since only a minority of the plasma electrons acquires most of the absorbed energy, in contrast to inverse bremsstrahlung which heats up all electrons. Numerical simulations performed by Forslund, Kindel and Lee (FKL) have shown that the energy distribution of accelerated fast electrons by resonnant absorption is close to a Maxwellian distribution characterized by an electron temperature given by [81, 76]:

$$T_{RA,FKL}[\mathrm{keV}] \approx 14 \left(I[10^{16}\,\mathrm{W/cm^2}]\lambda[\mu\mathrm{m}]T_e[\mathrm{keV}]\right)^{1/3} \tag{3.28}$$

T_e stands here for the plasma background temperature.

A similar analysis of hot electron spectra resulting from resonance absorption was made independently by Estabrook & Kruer [76] and the authors found an empirical formula for T_h varying I and T_e in their 2D PIC simulations:

$$T_{RA,EK}[\mathrm{keV}] \approx T_e[\mathrm{keV}] + 21 \left(I[10^{16}\,\mathrm{W/cm^2}]\right)^{0.42} (T_e[\mathrm{keV}])^{0.04} \tag{3.29}$$

The scaling with $I\lambda^2$ have been confirmed by experimental results, yet underestimating by a factor ≈ 2 the hot electron temperature compared with experiments [90].

This mechanism is the predominant mechanism for intense long-pulse lasers. By extension, it predominantly determines the fast electron temperature for the ns-pulse laser interaction used in our experiments. More details will be given in Sec. 3.2.2.

Other collisionless absorption mechanisms

In the case where the laser frequency is larger than the electron-ion collision frequency with the skin-depth still smaller than the mean distance traveled by electrons during one laser period ($\nu_{e,i} < \omega_L < \omega_{p,e} v_{T_h,e}/c$, $v_{T_h,e} = \sqrt{k_B T_e/m_e}$ is the electron thermal velocity). The absorption mechanism is called *anomalous skin effect* [286]. The laser is absorbed in the skin-depth $l_{s,ASE} = \left(\frac{2}{\pi}\right)^{1/6} \left(\frac{v_{T_h,e}}{\omega_L}\right)^{1/3} \left(\frac{c}{\omega_{p,e}}\right)^{2/3}$ and the absorption coefficients writes:

$$\alpha_{ASE} = \frac{8}{3\sqrt{3}} \left(\frac{2}{\pi}\right)^{1/6} \left(\frac{v_{T_h,e}}{c}\right)^{1/3} \left(\frac{\omega_L}{\omega_{p,e}}\right)^{2/3} \approx 1.43 \left(\frac{v_{T_h,e}}{c}\right)^{1/3} \left(\frac{\omega_L}{\omega_{p,e}}\right)^{2/3} \tag{3.30}$$

It is worth noting that the absorption coefficient does not depend anymore on the electron-ion collision frequency.

When considering a higher laser frequency, the skin-depth can be bigger than the mean distance traveled by electrons during one laser period ($\nu_{e_i} < \omega_{p,e} v_{T_h,e}/c < \omega_L$).
Here the absorption is mainly governed by the *sheath inverse bremsstrahlung* process [44, 295]. The associated skin-depth is the collisional one $l_{s,SIB} = c/\omega_{p,e}$ with the absorption coefficient:

$$\alpha_{SIB} = 8\sqrt{\frac{2}{\pi}} \left(\frac{v_{Th,e}}{c}\right)^3 \left(\frac{\omega_{p,e}}{\omega_L}\right)^2 \approx 6.4 \left(\frac{v_{Th,e}}{c}\right)^3 \left(\frac{\omega_{p,e}}{\omega_L}\right)^2 \tag{3.31}$$

The evaluation of these different absorption coefficients depends on various parameters. A self similar numerical solution for the temperature at the interaction interface is obtained assuming a square temporal laser pulse shape, thermodynamic equilibrium $T_i = T_e$, and that the absorption coefficient depends only on the electron temperature [90]:

$$T_i = T_e = 250 \left(\frac{n_i}{10^{23}\,\mathrm{cm}^{-3}}\right)^{-2/9} \left(\frac{\alpha_{abs} I_L}{10^{15}\,\mathrm{W/cm}^2}\right)^{4/9} \left(\frac{t}{100\,\mathrm{fs}}\right)^{2/9} \mathrm{eV} \tag{3.32}$$

where n_i is the atomic density. This expression is implicit since the absorption coefficient depends on the temperature.

One can inject the latter expression in the expressions of absorption coefficients presented before and therefore deduce explicit expressions for the different absorption mechanisms.

When the intensity is over $10^{18}\,\mathrm{W/cm}^2$, as for the used picosecond beam (short-pulse) of our experiments, the main absorption mechanisms are occurring in the relativistic regime. It is this regime that we will detail in the next subsection.

3.1.2 Relativistic regime

When exceeding laser intensities of $\sim 10^{16}\,\mathrm{W/cm}^2$, the amplitude of oscillation of electrons in the laser field v_{quiv}/ω_L, where the quiver velocity of the electrons in the electromagnetic field of the laser is $v_{quiv} = \dfrac{eE_L}{\gamma m_e \omega_L}$, can be higher than the collisional skin depth $c/\omega_{p,e}$. In this situation, non-linear absorption mechanisms must be taken into account.

Brunel Effect and Vacuum heating

Here, we consider an interaction of linearly polarized (p-polarized) laser pulse focused at very high intensities with a steep density gradient at an oblique incidence with the angle θ_0. Due to the steep gradient and higher laser intensities, the laser electric field is sufficiently intense to drag out into vacuum a fraction of electrons initially heated in the target skin depth, beyond the Debye screening length, during a half-period of the pulse. Unlike resonant absorption, the laser field do not drive any plasma wave. During the second half-period of the pulse, the electrons are recalled back to the target accelerated by the electric force created by charge separation. Then the adiabaticity of electron motion is broken at the moment when they are crossing the plasma skin layer and they acquire the kinetic energy gained from the electric force. This mechanism was proposed by Brunel [35] and is called *vacuum heating*. Vacuum heating is responsible for the acceleration of electrons up to energies close to the ponderomotive potential (see Eq. 3.5). By considering a capacitor model with the cathode composed of the electrons that are dragged out of the target surface at a distance Δx, the capacitor electric field is given by $E_{cap} = \sigma/\epsilon_0$ with $\sigma = n_e e \Delta x$. Considering that the accelerated electron mean kinetic energy is given by the ponderomotive potential and that all electrons propagate into the depth of the solid target after being re-injected, one can estimate the laser energy absorption [90]:

$$\alpha_{VH} \approx \frac{1}{\pi a_0} \beta \left(\sqrt{1 + (\beta a_0 \sin\theta_0)^2} - 1\right) \frac{\sin\theta_0}{\cos\theta_0} \tag{3.33}$$

where $\beta = 1 + \sqrt{1 - (4a_0 \sin^3\theta_0 / \pi \cos\theta_0)}$ and the fast electron temperature has been assumed:

$$T_h \approx \left(\sqrt{1 + \frac{v_{e,x}^2}{c}} - 1 \right) m_e c^2 \approx \left(\sqrt{1 + 4a_0^2} - 1 \right) m_e c^2. \tag{3.34}$$

The capacitor model used so far is not valid for high intensities since the contribution of the magnetic field was neglected and the electron orbits are then more complex than those predicted in the capacitor approximation. These magnetic fields saturate the absorption mechanisms due to deflection of electron orbits by the $\vec{v} \wedge \vec{B}$ force. Considering a more realistic case, Gibbon and Bell have shown [91], by performing numerical simulations, that the transition between resonance absorption and vacuum heating is more complex. The maximum laser absorption is obtained in those simulations for $\theta_0 \approx 45\,^\circ$ and the temperature scales with the laser intensity as $T_e \approx (I_L \lambda_L^2)^\alpha$ with α between $1/3$ and $1/2$ depending on the gradient scale-length. The maximum absorption of the Brunel mechanism peaks at $\sim 70\,\%$ at moderate intensities [$10^{16} - 10^{18}\,\mathrm{W/cm^2}$] and small density gradients ($L \sim 0.1\lambda$) and decreases down to $\sim 10\,\%$ at higher intensities. It is consequently not the main absorption mechanism for the short-pulse laser used in our experiments ($I_L \sim 10^{19}\,\mathrm{W/cm^2}$). Considering the magnetic field of the laser pulse, which cannot be neglected at very high intensities, a similar effect to similar vacuum heating on a steep density gradient can be also driven by the $\vec{v} \wedge \vec{B}$ component of the Lorentz force. This mechanism will be presented in the next subsection.

Hole boring and relativistic $\vec{j} \wedge \vec{B}$ heating

The so-called $\vec{j} \wedge \vec{B}$ heating was introduced in [149] and it is the main absorption mechanism at laser irradiances $I_L \lambda_L^2 \geq 10^{18}\,\mathrm{Wcm^{-2}\mu m^{-2}}$. First, by considering an incident laser pulse on a solid target, all charged particles, independently of their charge, are pushed away from the high intensity laser regions, both radially and inside the target. However, as seen before, the ponderomotive force is proportional to m^{-1} and the resulting effect is small on ions. Consequently, a charge separation occurs and an electric field drives ions at higher time scales, of the order of several ps. This effect is directly involved in the so-called *hole boring* process that has been demonstrated experimentally at laser intensity of $10^{18}\,\mathrm{W/cm^2}$ [126] and is responsible for the inward movement of the target surface [290]. This is due to the light pressure in the plasma which is higher than the thermal pressure and thus pushes the critical density surface.

In the relativistic regime, the $\vec{v} \wedge \vec{B}$ component of the Lorentz force creates an oscillating component of the ponderomotive force (Eq. 3.6) for a p-polarized laser pulse that can lead to laser energy absorption: during a quarter of the laser optical cycle, electrons from the plasma surface are ejected into vaccuum by this force, then a strong electrostatic field is generated due to the induced charge separation ; during the following quarter of the laser cycle, electrons are recalled back to the surface being accelerated by the electrostatic field. Bunches of electrons accelerated up to several MeV are then re-injected into the target at each half laser period. This effect is more efficient at normal incidence angle of the laser pulse, and with increasing laser intensity. This acceleration mechanism has been confirmed by kinetic simulations [290]. The authors find a good agreement between their numerical results and the estimate of the mean kinetic energy, often called "temperature" of the accelerated electrons, based on the ponderomotive potential scaling. The expression of T_h corresponds to the ponderomotive potential energy and has been given in Eq. 3.5.

Parametric instabilities

By considering long density gradients, generally caused by long underdense pre-plasma generated by the pulse pedestal, when laser contrast is not optimized, other nonlinear mechanisms can be responsible for the acceleration of hot electrons. This process can thus also occur with intense long-pulse lasers. The three-wave parametric instabilities consist in a decomposition of the laser wave at ω_0 into daughter waves of frequencies ω_1 and ω_2 where $\omega_1 > 0$ (Stokes configuration) or $\omega_1 < 0$ (anti-Stokes configuration). For different types of excited waves at the frequency ω_1: ion acoustic wave (IAW) ω_{ia}, electron plasma wave (EPW) $\omega_{p,e}$, electromagnetic wave (EMW) ω_{EMW}, an electron current is generating the electromagnetic fields at the frequency ω_2. It will be resonant if the phases match the electromagnetic dispersion relation :

$$\omega_0 = \omega_1 + \omega_2 \qquad \vec{k_0} = \vec{k_1} + \vec{k_2} \tag{3.35}$$

Depending on the location of the unstable zone, there are four distinct three-wave processes. They are summarized in Tab. 3.1.

Instability type	Daughter 1	Daughter 2	Unstable zone
Acoustic Decay	EPW: $\omega_1 \approx \omega_0$	IAW: $\omega_2 \ll \omega_0$	$n_e \approx n_c$
Stimulated Brillouin Scattering	EMW: $\omega_1 \approx \omega_0$	IAW: $\omega_2 \ll \omega_0$	$0 < n_e \leq n_c$
Two-Plasmon-Decay	EPW: $\omega_1 \approx \omega_0/2$	EPW: $\omega_2 \approx \omega_0/2$	$n_e = n_c/4$
Stimulated Raman Scattering	EMW: $\omega_1 \approx \omega_0/2$	EPW: $\omega_2 \approx \omega_0/2$	$0 < n_e \leq n_c/4$

Table 3.1 – Summary table of parametric instabilities

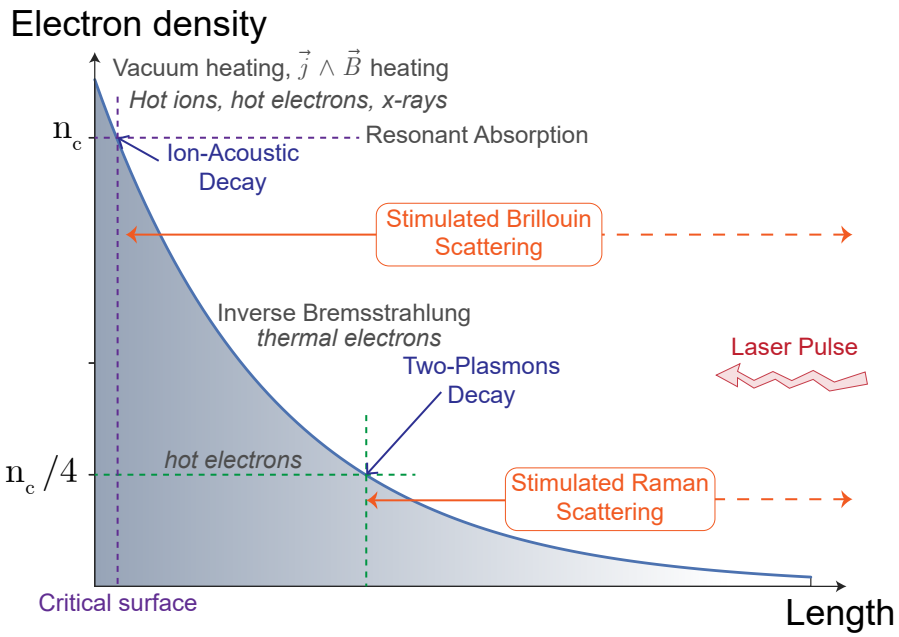

Figure 3.2 – Schematic of some of the main absorption mechanisms with their respective locations along the plasma density profile (in grey). An insight is also given for the location of unstable zones that could excite parametric instability waves. The reader can refer to Tab. 3.1 for a list of parametric instabilities parameters.

These non-linear processes are important because they can scatter the laser pulse and prevent it from reaching the absorption zone. In addition, part of the laser energy is transferred to electron plasma waves, which can then transfer part of their energy accelerating fast electrons. Also, the stimulated Brillouin scattering as well as the stimulated Raman scattering can lead to an energy transfer into a daughter electromagnetic wave propagating in the backward direction, which can destroy laser optics. In the case of short laser pulses in picosecond or subpicosecond regime, the motion of ions can be neglected so that stimulated Brillouin scattering and ion-acoustic decay can be neglected. Stimulated Raman scattering and two plasmon decay are for instance responsible for the

acceleration of fast electrons up to several MeV, until wave breaking. A summary of the instabilities creation zones are given in Figure 3.2.

3.1.3 Relevant mechanisms in our experimental conditions

For the short-pulse lasers we used in our experiments, of a duration of $\approx$ 1 ps focused at normal incidence at intensities of $\sim 10^{19}\,\mathrm{W/cm^2}$, the main absorption mechanism is the relativistic $\vec{j} \wedge \vec{B}$ heating which leads to fast electron temperatures of the order of the ponderomotive potential, *i.e.* of the order of MeV in our conditions.

For the long-pulse laser of a duration of $\approx$ 1 ns focused at normal incidence at intensities of $\sim 10^{17}\,\mathrm{W/cm^2}$, there are several mechanisms that contribute to the fast electron generation. The Inverse Bremsstrahlung is still efficient and creates an important amount of electrons in the range $1 - 10\,\mathrm{keV}$. Resonant absorption and parametric instabilities are responsible for the acceleration of electrons to higher energies.

3.2 State-of-the-art of accelerated electron sources from over-dense targets

The generation and transport processes of fast electron into a large panel of plasmas, of various densities and temperatures, have been significantly studied over the last 20 years, both theoretically and experimentally.

3.2.1 Laser-to-electrons conversion efficiency

Experiments measuring the radiation emitted by electrons when interacting with matter, have permitted to estimate the conversion efficiency from laser absorbed energy to electrons. The measured efficiency at a laser intensity of $3 \times 10^{19}\,\mathrm{W/cm^2}$, using the $K\alpha$ emission, was evaluated to 25 % [289, 195]. The Bremsstrahlung emission measurement coupled to numerical simulations have shown that the conversion can reach values of the order of $40 - 50$ % at higher laser intensity of $3 \times 10^{20}\,\mathrm{W/cm^2}$ [101]. The conversion efficiency seemed to follow a scaling with laser intensity and in this purpose, experimental measurements of the conversion efficiency were performed with varying laser intensities from $10^{18}\,\mathrm{W/cm^2}$ up to $3 \times 10^{20}\,\mathrm{W/cm^2}$. The conversion efficiency was seen to increase from 10 % to 50 % [296]. These early studies overestimated the conversion efficiency since they did not consider the fast electron refluxing at the target rear-side which amplifies the emission caused by electrons and consequently artificially increases the conversion efficiency. More recent experiments evaluated the conversion efficiency in the range of $30 - 40$ % at laser intensities $> 10^{19}\,\mathrm{W/cm^2}$ [196, 47, 282]. The conversion efficiency was seen to not be affected only by the laser intensity but also depends strongly on the hydrodynamic state of the plasma [272], laser contrast [240] and laser beam incidence angle [60]. In this latter paper, two experimental fits were proposed for the time integrated laser absorption coefficient η_{abs}.

$$\eta_{\mathrm{abs}}^{(1)} = \left(\frac{I_L \lambda_L^2}{3.37 \times 10^{20}\,\mathrm{W cm^{-2} \mu m^2}} \right)^{0.1958} \quad \text{or} \quad \eta_{\mathrm{abs}}^{(2)} = \left(\frac{I_L \lambda_L^2}{4.30 \times 10^{21}\,\mathrm{W cm^{-2} \mu m^2}} \right)^{0.2661} \tag{3.36}$$

Both expressions are valid for $I_L \lambda_L$ from $2 - 3 \times 10^{18}$ to $2 - 3 \times 10^{20}\,\mathrm{W cm^{-2} \mu m}$. The first fit $\eta^{(1)}$ is more adapted to moderate laser contrast ($10^{-6} - 10^{-8}$) while the second one $\eta^{(2)}$ works better for lower contrast ($10^{-3} - 10^{-4}$). Besides, the absorption is also known to be higher for a p-polarized laser in respect to a s-polarized laser [90].

The total conversion from laser energy to hot electrons has been measured in [138] and an estimation of η_h is proposed for laser intensities from $10^{18}\,\mathrm{W/cm^2}$ to $10^{20}\,\mathrm{W/cm^2}$:

$$\eta_h = 1.2 \times 10^{-15} \left(I_L[\mathrm{W/cm^2}] \right)^{0.74} \tag{3.37}$$

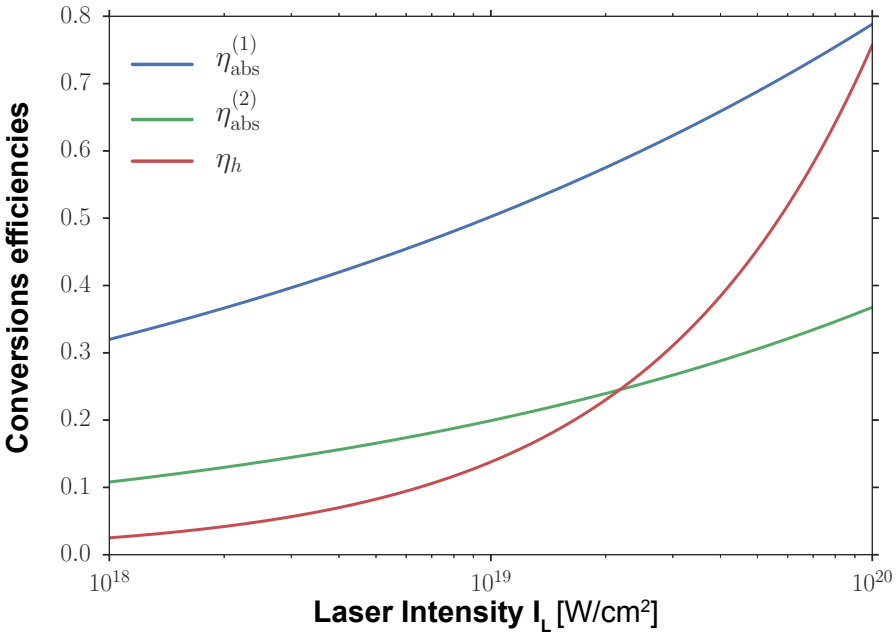

Figure 3.3 – Evaluation of the laser absorption coefficient from Eq. 3.36, (1) for good laser contrast and (2) for lower laser contrast, see comments in the text. The laser-to-electrons conversion efficiency η_h is calculated with Eq. 3.37. Results obtained for $\lambda_L = 1\,\mu\mathrm{m}$.

In Figure 3.3 we plot the expressions of $\eta^{(1)}_{\mathrm{abs}}$, $\eta^{(2)}_{\mathrm{abs}}$ together with the total conversion efficiency from laser to hot electrons η_h (Eq. 3.37). It is worth noting that η_h is denoted "total" conversion efficiency to hot electrons since it includes the proportion of absorbed energy $\eta^{(1)}_{\mathrm{abs}}$ and therefore $\eta_h < \eta^{(1)}_{\mathrm{abs}}$. The conversion efficiency could itself be decomposed for the different absorption mechanisms. The fitting laws are not extensively reflecting the complex picture of the absorption of laser energy and hot electron generation. Although it can be found in literature several experimental data for the conversion efficiency, there is presently no exhaustive and systematic study for it and it is actually quite a big concern for the fast ignition community.

3.2.2 Fast electron temperature

Short pulses

It has been said in Sec. 3 that the mean kinetic energy of accelerated electrons by intense laser pulses can be estimated by the ponderomotive potential scaling. The distribution of the relativistic electrons is commonly represented by a 3D relativistic Maxwell-Jüttner distribution:

$$f(\varepsilon) \propto \beta\gamma^2 \exp\left(-\frac{\varepsilon}{T_h}\right) \tag{3.38}$$

with T_h the *fast electron temperature*. It is important to clarify the term *temperature* which unit here is not in Kelvin. T_h in fact refers to the mean energy $< E > \approx \alpha T_h$ over the distribution and α varies from 1.5 for $T_h < m_e c^2$ to 3 in the relativistic limit. In the literature, distributions with two or even three temperatures can be found. It reflects the contribution of different acceleration mechanisms (see Sec. 3.1) on the fast electron population. The two temperature distribution corresponds to the weighted sum of a *colder* part at moderate energies ($\gtrsim 10$ keV) and an *hotter* part at higher energies ($\gtrsim 100$ keV). Recent results showed that the *colder* part of the electron distribution is better characterized by a power law of the form $f(E) \propto E^{-n}$ with $n > 0$ instead of an exponential law [226, 179]. This characteristic was also observed in the explored regime of this thesis work by experiments on the same laser beam facility [282, 281].

The ponderomotive scaling introduced in Sec. 3 estimates the fast electron temperature as [290]:

$$T_h^{\text{Wilks}}[\text{keV}] \approx 511\left(\sqrt{1 + 0.73 I_{18}\lambda_L^2[\mu\text{m}^2]} - 1\right) \tag{3.39}$$

with I_{18} the laser intensity in units of $10^{18}\,\text{W/cm}^2$. The above equation stands for a circular polarization of the laser. One has to divide by two the coefficient in front of I_{18} for a linearly polarized laser field (it means to have $1 + a_0^2/2$ instead of $1 + a_0^2$ in the square root, as in Eq. 3.5). A study over a wide range of laser intensities, using the Bremsstrahlung emission, has shown an empirical scaling with $I_L\lambda_L^2$ and Beg *et al.* [15] proposed the law:

$$T_h^{\text{Beg}}[\text{keV}] \approx 215(I_{18}\lambda_L^2[\mu\text{m}^2])^{1/3} \tag{3.40}$$

This law is valid till intensities of several $10^{18}\,\text{W/cm}^2$. For higher intensities, the ponderomotive scaling by Wilks yields more consistent evaluations of T_h.

Besides, the effect of preplasma tends to increase the mean kinetic energy of accelerated electrons [201]. A recent scaling law obtained by Kluge *et al.* [141] took into account the preplasma. It reads:

$$T_h^{\text{Kluge}}[\text{keV}] \approx 1000\left(\frac{2\pi}{\int_0^{2\pi}\gamma^{-1}(t)dt} - 1\right) \tag{3.41}$$

where $\gamma(t) = S^2/2 + 2/S^2 - 1$ and $S = \left(\sqrt{(3a_0\sin\omega_0 t)^2 + 8} + 3a_0\sin\omega_0 t\right)^{1/3}$. This law is represented by the purple line on Figure 3.4 and is in good agreement with the ponderomotive scaling for moderate intensities ($I < 10^{19}\,\text{W/cm}^2$) while correcting the overestimation of the ponderomotive scaling for higher intensities.

In reality, as we mentioned before, the fast electron distribution is composed by a *colder* and *hotter* parts. Obviously, the *colder* part tends to diminish the mean kinetic energy of the all fast electron distribution. For this reason, the formulation

$$T_h \approx \max\left[T_h^{\text{Wilks}}, T_h^{\text{Beg}}\right] \tag{3.42}$$

is adopted to estimate the temperature of the hot component of the fast electron distribution over a wide range of intensities. The Figure 3.4 is showing the above formulations of electron temperature for laser intensities varying in the range $10^{17} - 10^{21}\,\text{W/cm}^2$. Experimental points taken from [90] have been added to the graph and it is not surprising to see that measurements from electron spectrometer (blue dots) - collecting only electrons which are able to escape the rear target side potential - are fairly

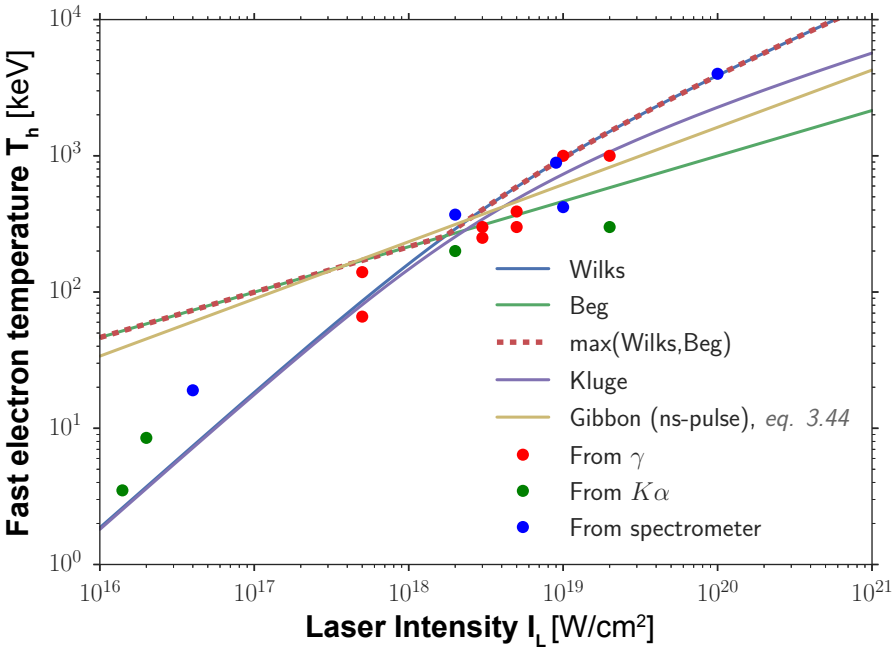

Figure 3.4 – Fast electron temperature T_h scaling laws obtained from Eq. 3.39 (blue), Eq. 3.40 (green), the maximum of both Eq. 3.42 (dashed red), and from Eq. 3.41 (purple), at $\lambda_L = 1\,\mu m$. One can note that the Wilks and Beg scaling laws intersect at $I_L \approx 10^{18}\,W/cm^2$, at the validity limit of Beg's law, justifying the Eq. 3.42 formulation. The experimental data points (dots) are taken from [90] making the distinction between measurements with Bremmstrahlung (red dots) and K_α (green dots, more sensitive to the colder electrons) and measurements with electron spectrometer (blue dots, more sensitive to the hotter electrons). The pale yellow curve corresponds to Eq. 3.46 obtained by P. Gibbon in [90] fitting numerous measurements made with ns-pulses.

closer to the ponderomotive scaling for $I > 10^{18}\,\mathrm{W/cm^2}$.

Long pulses

We saw that for intense long-pulse interactions, the fast electrons are mainly generated by resonant absorption and eventually parametric instabilities in the relativistic regime. The hot electron temperature scaling for resonant absorption was given in Eq. 3.28 and Eq. 3.29, Sec. 3.1). There are obtained ensuring a pressure balance, *i.e.* that the laser and plasma pressure are equal:

$$P_e = n_e k_B T_e = \frac{I_L}{c} \tag{3.43}$$

or equivalently, the electron density reads:

$$n_e = \frac{I_L}{c k_B T_e} \longrightarrow n_e \approx 200 \frac{I_L[10^{18}\,\mathrm{W/cm^2}]}{T_e[\mathrm{keV}]} n_c \tag{3.44}$$

and assuming that the absorbed laser flux is entirely carried away by a 1D Maxwellian population of free-streaming hot electrons with a temperature T_h, density n_h and velocity v_h, the following energy balance is obtained [90]:

$$\eta_{\mathrm{abs}} I_L = \sqrt{\frac{2}{\pi}} n_h v_h \frac{m v_h^2}{2} \tag{3.45}$$

P. Gibbon in [90] compared the two scaling laws for resonant absorption with measurements made with the Los Alamos nanosecond CO_2 laser [217] over a wide range of laser intensities. He observed a similar scaling, whereas noting that T_h was underestimated by the steady-state theories by $\approx 50\,\%$. A least-squares fit of experimental data was proposed by the author and yields:

$$T_h^{\mathrm{Gibbon}}[\mathrm{keV}] \approx 89 \left(I_L[10^{17}\,\mathrm{W/cm^2}] \lambda^2[\mu\mathrm{m}^2] \right)^{0.42 \pm 0.12} \tag{3.46}$$

The fitted function of Eq. 3.46 is plotted together with short-pulses scaling laws in Figure 3.4 (pale yellow curve). It is clear that for the same laser intensity, hot electron temperature is very similar to what is obtained for short laser pulses, in particular with Beg's scaling law.

3.2.3 Fast electron divergence

As already mentioned in the *Introduction*, the fast electron beam divergence is one of the major bottleneck issues encountered in fast ignition. It is then of primary importance to be correctly characterized. The divergence of the electron beam is mainly attributed to the development of the Weibel instability at the target surface, described further in the next section.

The dependence of the electron beam divergence on the intensity can be estimated by the following empirical scaling law (least-squares fit of [96] and references therein):

$$\theta_{1/2} \approx (17 \pm 3.8)^\circ + (13 \pm 2.5)^\circ \log \left(\frac{I_L}{10^{18}\,\mathrm{W/cm^2}} \right) \tag{3.47}$$

where $\theta_{1/2}$ is the half-angle of the diverging cone of electrons.

Moreover, the pre-plasma can strongly affect the electron divergence due to the deformation of the laser-plasma interaction region [64] and the divergence increases with the radial distance from laser-spot center. The resulting fast electron angular distribution can be corrected from the radial dependency using the following function:

$$f_\theta \propto \exp \left[- \left(\frac{\theta - \theta_0(r)}{\Delta\theta_0} \right)^2 \right] \tag{3.48}$$

where $\theta_0(r)$ is the mean propagation angle of electrons at the radial distance r and $\Delta\theta_0$ is the mean dispersion angle around the direction defined by $\theta_0(r)$.

The preplasma also affects the initial radius of the fast electron beam which is evaluated empirically to range between $3-4$ times the focal spot radius. This formulation is used to define the fast electron angular distribution in PIC Hybrid simulations performed in the framework of this thesis (see Sec. 10 for more details).

3.3 Fast electron transport

3.3.1 Collisional effects over transport

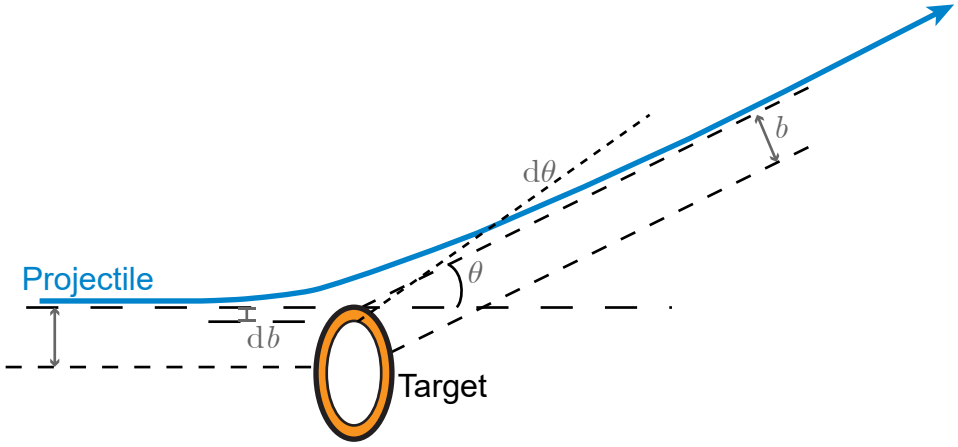

Figure 3.5 – Schematic view of a small angle binary collision.

Due to the fact the fast electron beam travel at relativistic velocities much greater than background electron or ion velocities, the principal effects of collisions are the beam electrons energy losses and their angular scattering. It is then important to introduce first a simple description of elastic collisions occurring when a fast electron "hits" an ion. The ions are considered in this theory as immobile and point-like particles (mass ratio of ≈ 1836). In a binary collision, the trajectory of the incident particle changes but the kinetic energy is considered to remain approximately unchanged. As represented in Figure 3.5, the fast electron of momentum p collide with the ion with an impact parameter between b ($b_{\min}$) and $b+db$ ($b_{\max}$). After the collision the projectile will be scattered and is exiting within a solid angle $d\Omega = 2\pi \sin\theta d\theta$, where θ is the deviation angle in the laboratory frame. The cross-section is defined here with $d\sigma(\theta) = (b/\sin\theta)(db/d\theta)$. The cross sections are describing the probability of a single collision. This is a simple uni-dimensional case with small-angle scattering approximation and without relativistic considerations.

For instance, more generally for an electron-ion binary collision, the minimum impact parameter, on the order of the distance of the closest approach, is given by:

$$b_{i,\min} = \frac{\hbar}{2p}. \tag{3.49}$$

The maximum impact parameter is given by:

$$b_{i,\max} = D \tag{3.50}$$

D is the effective Debye length given by $D = \max(\lambda_D, r_i)$ where r_i is the inter-atomic distance $r_i = \sqrt[3]{3/(4\pi n_i)}$.

The quantum relativistic differential cross section (cross section : σ, solid angle vector: $\vec{\Omega}$) of such a binary collision for the scattering angle θ has been obtained in [194] under the first Born approximation which considers a small angle deviation and a moderate Z target. It reads:

$$\left(\frac{d\sigma}{d\vec{\Omega}}\right)_i = 4r_e^2 \frac{Z^2}{\beta^4\gamma^2}\left(\frac{1}{4\sin^2(\theta/2)+\theta_0^2}\right)^2 \tag{3.51}$$

Where θ_0 is the screening angle and $\theta_0 = \alpha Z^{1/3} c/(0.995\gamma\beta)$, with $\alpha = e^2/(4\pi\epsilon_0\hbar c)$ the fine structure constant (see List of physical units at the beginning of this manuscript). The first term ($\theta_0 \to 0$) is the relativistic generalization of the Rutherford differential cross section and the second term corrects for the electronic screening of the nucleus.

Elastic electron-ion clollisions are responsible for the angular scattering of the beam and its subsequent isotropisation. Yet, the fast electron divergence is in fact mainly determined by the laser-plasma interaction, and fairly less by elastic electron-ion collisions along its transport in the target depth [64]. The dispersion angle of the REB (for energies $\gtrsim$ 500 keV) is mainly conditioned by its scattering in magnetic fields driven by the so-called Weibel instability, described further in Sec. 5.1.

Collisional stopping power

The general definition of a collisional stopping power is the energy loss dE per unit of path length ds experienced by a particle due to collisions with other particles of the medium. We have seen before that the collisions with ions are elastic collisions and do not contribute to the slowing down of the electron. The collisions of the fast electron with other electrons are therefore the candidate for the collisional losses of energy of fast electrons. The electron collisional stopping power with background electrons is then introduced and reads:

$$\frac{dE}{ds} = -Z(\gamma-1)m_e c^2 n_i \int_0^{1/2} \epsilon \frac{d\sigma}{d\epsilon} d\epsilon \tag{3.52}$$

with n_i the density of atoms, $E = (\gamma-1)m_e c^2$ the kinetic energy of the incident electron and $\epsilon = \Delta E/E$.

One may then separate this integral evaluating the contributions of the collisions with free electrons ($\epsilon > \epsilon_c$) from those with bound electrons and/or with screened free electrons ($\epsilon < \epsilon_c$) by introducing:

$$\epsilon_c \approx \left(\frac{b_{e,\min}}{b_{e,\max}}\right)^2 = \left(\frac{\max(r_0, \lambda\!\!\!^{-})}{D}\right)^2 \tag{3.53}$$

with r_0 the Landau length (Eq. 1.6) and $\lambda\!\!\!^{-}$ the De Broglie length calculated in the center mass frame [256]:

$$\lambda\!\!\!^{-} = \frac{\hbar}{m_e c\sqrt{2(\gamma-1)}} \tag{3.54}$$

It is worth noting that $\lambda\!\!\!^{-}$ and D are considered as respectively the minimum ($b_{e,\min}$) and maximum ($b_{e,\max}$) impact parameters: the integration of $d\epsilon$ from 0 to ϵ_c in Eq. 3.52 would be equivalently obtained by integrating an alternative formula written with the impact parameter, integrating db from $b_{e,\min}$ to $b_{e,\max}$ ("binary part"). Note also that $b_{e,\min}$ is much smaller than $b_{i,\min}$ for ultra relativistic electron projectiles, while $b_{e,\max} = b_{i,\max}$.

The integration of Eq. 3.52 gives for a cold plasma approximation, considering only the binary collisions (see Eq. 3.51):

$$\left(\frac{dE}{ds}\right)_{\text{free}}^{\text{cold}} = -En_i\sigma_e Z\left[\ln\frac{1}{4\epsilon_c} + 1 - \frac{2\gamma-1}{\gamma^2}\ln 2 + \frac{1}{8}\left(\frac{\gamma-1}{\gamma}\right)^2\right]. \tag{3.55}$$

In case of hotter plasma, the contribution of collision with background free electrons can be obtained [188] by replacing in the previous equation Z by Z^*:

$$\left(\frac{dE}{ds}\right)_{\text{free}}^{\text{hot}} = -En_i\sigma_e Z^*\left[\ln\frac{1}{4\epsilon_c} + 1 - \frac{2\gamma-1}{\gamma^2}\ln 2 + \frac{1}{8}\left(\frac{\gamma-1}{\gamma}\right)^2\right] \tag{3.56}$$

The first term in the square brackets corresponds to the well-known Coulomb logarithm from the non-relativistic theory by taking the limit $\gamma \to 1$. That is the reason why the cut energy ϵ_c may be estimated by $(b_{e,\min}/b_{e,\max})^2$. The other terms account for the quantum relativistic effects.

On the other hand, fast electrons collisions with bound electrons in a cold plasma approximation has been calculated in [24], considering that the energy is transferred in form of atomic excitation by

the electric field, the incident electron moving at constant velocity. It reads:

$$\left(\frac{dE}{ds}\right)^{\text{cold}}_{\text{bound}} = -En_i\sigma_e Z\left[\ln\left(\frac{2\epsilon_c(m_ec^2)^2(\gamma^2-1)(\gamma-1)}{I_0^2}\right)-\beta^2\right] \tag{3.57}$$

I_0 stands for the mean ionization potential defined as:

$$\ln I_0 = \sum_n f_n \ln E_n \tag{3.58}$$

where E_n is the excitation energy and f_n the excitation transition probability. For $Z \geq 13$, a semi-empirical formula reproducing experimental results in the cold plasma approximation is given in [264]:

$$I_0[\text{eV}]^{\text{cold}} \approx 9.76Z + 58.6Z^{-0.19} \tag{3.59}$$

Using a Thomas-Fermi model [114] a formula for the ionization potential can be derived for hot plasma at any charge state:

$$I_0[\text{eV}]^{\text{hot}} \approx 10Z\frac{\exp\left[1.29(Z^*/Z)^{(0.72-0.18(Z^*/Z)}\right]}{\sqrt{1-(Z^*/Z)}} \tag{3.60}$$

Similarly, in ionized case (hot plasma), the formula Eq. 3.57 can be extended replacing Z by $(Z-Z^*)$:

$$\left(\frac{dE}{ds}\right)^{\text{hot}}_{\text{bound}} = -En_i\sigma_e(Z-Z^*)\left[\ln\left(\frac{2\epsilon_c(m_ec^2)^2(\gamma^2-1)(\gamma-1)}{I_0^2}\right)-\beta^2\right] \tag{3.61}$$

The total collisional stopping power in a cold matter is finally given by the sum of the bound and free cold stopping powers:

$$\left(\frac{dE}{ds}\right)^{\text{cold}}_{\text{total}} = -En_i\sigma_e Z\left[\ln\left(\frac{(m_ec^2)^2(\gamma^2-1)(\gamma-1)}{2I_0^2}\right)\right.$$
$$\left.+1-\beta^2-\frac{2\gamma-1}{\gamma^2}\ln 2+\frac{1}{8}\left(\frac{\gamma-1}{\gamma}\right)^2-\delta\right]. \tag{3.62}$$

To account for the polarization electric field which screens the incident electron field at the position of the projectile, an additional parameter δ has been introduced. It is called *density effect* and was derived by Fermi [78] in the limit of an ultra-relativistic electron projectile:

$$\delta = 2\ln\left(\frac{\gamma\hbar\omega_{p,e}}{I_0}\right)-\beta^2 \tag{3.63}$$

The *density effect* leads to a decrease of the electron stopping power, especially for high energy electrons propagating at the same speed as the polarization wave $c/\sqrt{\epsilon_r\epsilon_0}$, with ϵ_r the relative dielectric permeability of the medium.

An approximate analytic formula for the parameter δ was further derived for a relativistic electron [265] in the case of bound electrons:

$$\delta = \begin{cases} 0 & \text{if } X \leq X_0 \\ 4.606X + C + a(X_1-X)^m & \text{if } X_0 < X < X_1 \\ 4.606X + C & \text{if } X \geq X_1 \end{cases} \tag{3.64}$$

with the parameters: $X = \log\gamma\beta$, $C = -2\ln I_0/(\hbar\omega_{p,e}) - 1$, $a = -(C+4.606X_0)/(X_1-X_0)^3$ and:

$$X_{0|I_0<100[\text{eV}]} = \begin{cases} 0.2 & \text{if } -C < 3.691 \\ -0.326C-1 & \text{if } -C \geq 3.681 \end{cases} \tag{3.65}$$

$$X_{0|I_0>100[\text{eV}]} = \begin{cases} 0.2 & \text{if } -C < 5.215 \\ -0.326C-1.5 & \text{if } -C \geq 5.215 \end{cases} \tag{3.66}$$

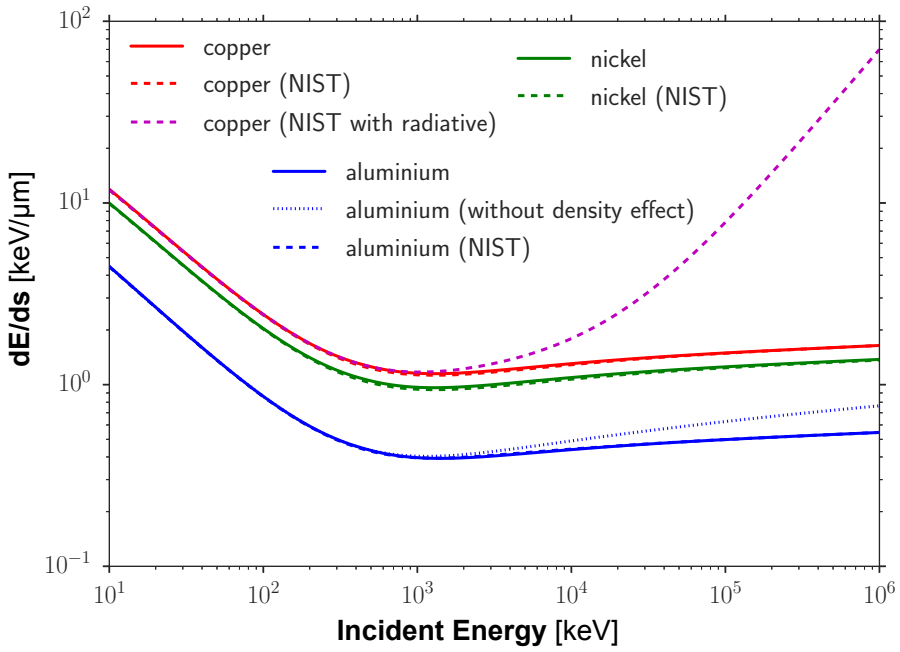

Figure 3.6 – Total stopping power at solid densities for cold Copper (red), Aluminium (blue) and Nickel (green). The results are compared with the NIST-Estar database. The dashed magenta line corresponds to Copper in the NIST database, including effects of radiative stopping power. The dotted blue line stands for an Aluminium case where the *density effects* are not taken into account.

$$X_1 = \begin{cases} 2 & \text{if } I_0 < 100[\text{eV}] \\ 3 & \text{if } I_0 > 100[\text{eV}] \end{cases} \tag{3.67}$$

Figure 3.6 represents the total stopping power obtained in the cold approximation for Copper, Nickel and Aluminium targets at solid densities. The results are compared with the NIST-Estar database (http://physics.nist.gov/PhysRefData/Star/Text/ESTAR.html) represented by the dashed curves for the three materials. In the curves of Figure 3.6 we used the latter model to calculate the δ parameter, except for the dotted blue line for Aluminium calculated without density effect.

The contribution of electron-driven plasma waves (*plasmons*) was obtained in [211]. The corresponding contribution to the stopping power in ionized matter writes:

$$\left(\frac{dE}{ds}\right)^{\text{hot}}_{plasmon} = -En_i\sigma_e Z^* \ln\left[\frac{c\sqrt{\gamma^2-1}}{\gamma\omega_{p,e}D}\right]. \tag{3.68}$$

A relativistic electron is also experiencing energy losses by bremsstrahlung. This contribution is usually small as radiative losses become predominant only for relativistic electron energies greater than $800\,\text{MeV}/(Z+1.2)$ [23].
The corresponding contribution to the electron stopping power of such high energetic electrons is thus beyond the scope of this thesis. One can see it for instance in Figure 3.6: the magenta dashed curve is obtained for Copper in the NIST database, accounting for radiative losses. A discrepancy with only collisional stopping power appears nonetheless for energies $\gtrsim 5\,\text{MeV}$ (for high Z materials such as Cu).

The total collisional stopping power in hot matter finally writes as a sum of the three contributions:

$$\left(\frac{dE}{ds}\right)^{\text{hot}}_{\text{total}} = \left(\frac{dE}{ds}\right)^{\text{hot}}_{\text{bound}} + \left(\frac{dE}{ds}\right)^{\text{hot}}_{\text{free}} + \left(\frac{dE}{ds}\right)^{\text{hot}}_{plasmon} \tag{3.69}$$

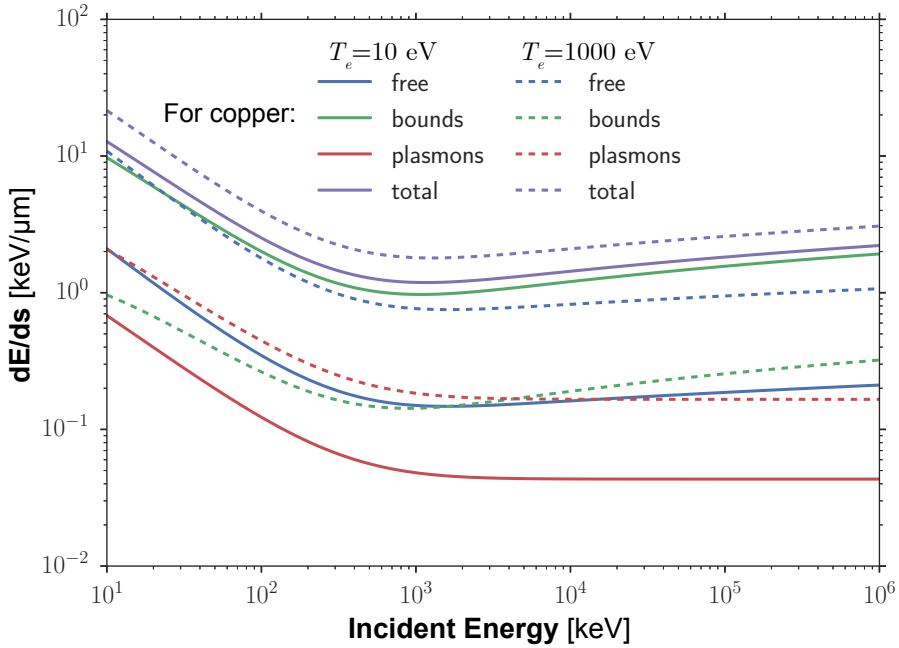

Figure 3.7 – Different contributions of the total stopping power in ionized copper at solid density. The solid lines correspond to $T_i = T_e = 10\,\text{eV}$ while the dashed lines correspond to $T_i = T_e = 1000\,\text{eV}$.

Figure 3.7 represents these three contributions and the total for a copper plasma at $T_e = T_i = 10\,\text{eV}$ (solid lines) and $T_e = T_i = 1000\,\text{eV}$ (dashed lines), at solid density. The contribution of bounded electrons is seen to vanish when reaching background temperature in excess of $\sim 1\,\text{keV}$.

3.3.2 Resistive effects over transport

The resistive effects arise when considering the propagation of a current of fast electrons in the dense matter. Indeed, in addition to the individual collisions of the fast electrons with the background that we studied in the last section, the fast electron beam will heat the surrounding plasma and self-generated electric and magnetic fields will strongly impact its propagation. This section dedicates to the electrical resistive behavior of the propagation of the fast electron beam current in dense plasma. The reader can refer to the dedicated parts for the description of self-generated magnetic fields in Sec. 4.1 for the nanosecond regime and in Sec. 5.1 for the picosecond and subpicosecond regime.

Neutralization of a monoenergetic relativistic electron beam

A relativistic electron beam which is propagating in a dense plasma will generate an electric field due to the charge accumulation that will expel radially a small part of the background electrons out of the beam volume. Those accelerated free electrons will induce a return current $\vec{j_e}$ which tends to exactly compensate the beam current density $\vec{j_e} \approx -\vec{j_b}$. The return current creation process is performed in time-scales of $\tau_{\text{neut}} \sim \max[1/\nu_{e,i}, 1/\omega_{p,e}]$, with $\nu_{e,i}$ the electron ion collision frequency and $\omega_{p,e}$ the plasma frequency. This time-scale results in few femtoseconds and can be considered as instantaneous in our experimental conditions, where the electron beam duration is much larger ($\sim$ ps). When dealing with very strong currents, Alfvén showed that the self-generated magnetic fields could deviate the fast electron beam towards the reverse direction, limiting the beam propagation. The so-called Alfvén limit is obtained by equaling the Larmor radius to the electron beam radius. The maximum beam current [99] is given by:

$$I_A[\text{kA}] = \frac{4\pi m_e c}{e\,\mu_0}\gamma_b\beta_b \approx 17\gamma_b\beta_b \tag{3.70}$$

In reality this limit that would prevent the propagation MeV-energies of a relativistic electron beam with MA-currents (yet observed in picosecond regime interaction with dense matter, see Sec. 10) is evaluated without considering the already mentioned neutralization current. The net total current density ($\vec{j} = \vec{j_b} + \vec{j_e}$) is then decreasing fast to lower values due to the beam neutralization. A perfect neutralization of the beam is however never reached completely and its efficiency depends on the ratio between the radius of the beam and the skin depth r_b/λ_e ($\lambda_e = c/\omega_{p,e}$). When this ratio is < 1 the return current is able to counter the beam current within the magnetic field region and the neutralization is efficient. In our experiments, this can be considered as always fulfilled, except for the very beginning of the injection.

After the neutralization begins, its duration will be given by the magnetic diffusion time:

$$\tau_D = \frac{\mu_0 r_b^2}{\eta} \tag{3.71}$$

where η is the resistivity of the background plasma, detailed in the next subsection. In our experimental conditions, $\tau_D \sim 30$ ps, which is longer than the beam duration: the neutralization is thus considered as fairly efficient. For our long laser pulse conditions, the neutralization is also efficient during sufficient time to allow a fast electron beam to propagate deep in the target.

The propagation of a fast electron beam in a dense plasma is strongly dependent on its background temperature. The resistivity, or inversely, the conductivity of the plasma in which the fast electron beam propagates is at the basis of the evaluation of resistive effects that will affect the fast electron transport. To begin, we will introduce a model that will compute the ionization state of the plasma Z^* that has been already used in the evaluation of the collisional stopping power in plasmas and will be used again for the evaluation of the plasma resistivity.

Ionization state

The ionization state Z^* of the material defines the ratio of free and bound electrons in the material. Based on the Thomas-Fermi model, More [188] proposed a useful formula for the ionization state as a function of the density $\rho = n_i m_i$ and the electron temperature T_e of the material (itself defined by the atomic number Z and mass number A). It reads:

$$Z^* = Z^*_{TF}\left(\frac{T_e}{Z^{4/3}}, \frac{\rho}{AZ}\right) = \frac{ZX_Z}{1 + X_Z + \sqrt{1 + 2X_Z}} \tag{3.72}$$

The two input parameters are $T_0 = T_e[\text{eV}]/(Z^{4/3})$ and $R = \rho/(ZA)$ with ρ in units of gcm^{-3}, and we have:

$$\begin{aligned}
T_f &= \frac{T_0}{1 + T_0} \\
A_Z &= 0.003323 T_0^{0.971832} + 9.26148 \times 10^{-5} T_0^{3.10165} \\
B_Z &= \exp\left(-1.7630 + 1.43175 T_f + 0.315463 T_f^7\right) \\
C_Z &= -0.366667 T_f + 0.983333 \\
Q_1 &= A_Z R^{B_Z} \\
Q &= \left(R^{C_Z} + Q_1^{C_Z}\right)^{1/C_Z} \\
X_z &= 14.3139 Q^{0.6624}.
\end{aligned}$$

This formula is valid for materials with $Z \geq 10$ that are used in our experiments and for sufficient background temperature: $k_B T_e \gtrsim E_F$, where $E_F = \hbar^2 (3\pi^2 n_e)^{2/3}/(2m_e)$ is the Fermi energy. For instance, the Thomas-Fermi model is inadequate for describing the metal-insulator transition since it neglects atomic structure effects on the ionization equilibrium.

To get an appropriate estimation of the ionization state at lower temperature, we modified the above model by interpolating it with known values of atomic structure at solid state. Indeed, we know that the number of electrons per atom in the conduction band (s-band) is for example $Z^* = Z_c = 1$ for copper, whereas the More model yields $Z^* = 4.39$. To exemplify the error, one can calculate for example the Fermi energy at room temperature using the More model, it yields for the copper $E_F \approx 18.9\,\text{eV}$ which is completely overestimated! The Fermi energy for copper found in literature is 7 eV and it is exactly the value obtained when considering $Z^* = 1$. To interpolate the real value of $Z^* = Z_c$ in the solid metal with the More model at energies above E_f, a weight function f was built:

$$f = 1 - \left[\exp\left(-\frac{k_B T_e}{E_F}\right)\right]^{\alpha} \tag{3.73}$$

And the corrected ionization state Z^*_{cor} writes:

$$Z^*_{cor} = (1 - f) Z_c + f Z^*_M, \tag{3.74}$$

being Z^*_M the ionization state calculated with the model of More. The α constant ranges between 1 and 2, depending on materials.

In Figure 3.8, we compared the ionization state obtained with the modified model and the ionization state obtained with the More model. The results are plotted for copper, aluminum and nickel.

Electric resistivity

The electric resistivity can be described by the Drude model where valence electrons are considered as free to move into the material, colliding with fixed ions. The resistivity writes:

$$\eta = \frac{m_e \nu_e}{e^2 n_e} \tag{3.75}$$

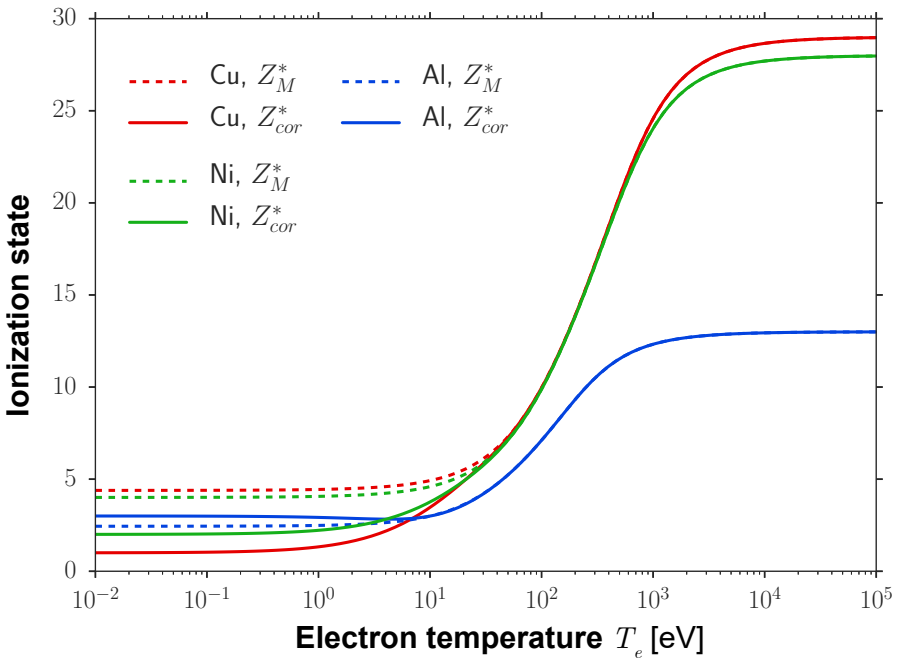

Figure 3.8 – Ionization state calculated for Copper (red), Aluminium (blue) and Nickel (green), evaluated with the model of More Z^*_M in dashed lines and with the modified model Z^*_{cor} (Eq. 3.74) in solid lines. One can note that the number of electrons in the conduction band at solid state is correctly inferred from the corrected model: $Z_c = 1$ for copper, $Z_c = 3$ for aluminium and $Z_c = 2$ for nickel.

where ν_e is the background electron relaxation rate. This is a key parameter to be evaluated in order to know the electrical resistivity on a wide range of background electron temperatures. For low temperatures, it is mostly determined by the electron-phonon collision rate ; at moderate temperatures, it is mostly determined by the electron-electron collision rate; and at high temperatures, the Spitzer regime is reached and this rate is function of the background temperature at the power of $-3/2$. We will now detail these regimes.

At a very low electron temperature, well below the Fermi temperature $T_F = E_F/k_B$, the electron-phonon collisions are predominant and the associated collision rate writes [294]:

$$\nu_{e,ph} \approx \frac{k_s e^2 k_B T_i}{2\pi\epsilon_0 \hbar^2 v_F} \tag{3.76}$$

with T_i the ion temperature ($T_i = T_e$ here), $v_F = \sqrt{2E_F/m_e}$ is the Fermi velocity and k_s is a tabulated constant depending on the considered material which permits to match the calculated resistivities with experimental data measurements available for cold metals.
For copper, for example, one finds $k_s \approx 0.37$. It is worth mentioning that the value of k_s depends on the ionization state calculated at low temperatures. The k_s gave as an example here and all the following resistivity results are obviously calculated with the corrected ionization state Z^*_{cor} (see Eq. 3.74).

At moderate temperatures $0.1T_F < T_e < T_F$, the material is ionized and the electron-electron collisions become the dominant process :

$$\nu_{e,e} = A_\nu \frac{k_B T_e^2}{\hbar T_F} \tag{3.77}$$

with A_ν a fitting parameter ranging from 1 to 1000. For copper, $A_\nu = 10$ [48].

At high temperatures, the collision frequency is described by the Spitzer model, considering a Maxwellian background electron distribution [259]:

$$\nu_{sp} = \frac{4}{3}\sqrt{2\pi} k_{sp} \frac{Z^* e^4 m_e n_e}{(4\pi\epsilon_0)^2 (m_e k_B T_e)^{3/2}} \ln\Lambda \tag{3.78}$$

with k_{sp} a dimensionless parameter equal to $3\pi/32$ and $\ln\Lambda$ the Coulomb logarithm.

In order to connect the regime below the Fermi temperature (scaling as T_e^2) and the Spitzer regime where all degeneracy effects are ignored (scaling as $T_e^{-3/2}$), one can calculate a maximum value of ν_e in the intermediate range. By considering that the mean electron free path λ_e cannot be smaller than the atomic inter-distance r_i, at a characteristic electron velocity chosen as the geometric mean between the Fermi velocity and the electron thermal speed $v_{ch} = \sqrt{v_F^2 + v_{T_e}^2}$. The corresponding maximum collision rate introduced by Eidmann *et al.* [73], writes:

$$\nu_c = \frac{v_{ch}}{r_i} \tag{3.79}$$

In [48], a weighted average of the electron relaxation rate at different temperature regimes is proposed and reads:

$$\nu_e^{-2} = (\nu_{e,ph} + \nu e, e)^{-2} + \nu_c^{-2} + \nu_{sp}^{-2} \tag{3.80}$$

The advantage of the latter Eidmann-Chimier model, in respect to other models found in the literature (*e.g.* Lee-More [159] or Hubbard-Spitzer [115]), is that it permits to take different ion/lattice temperature T_i and conducting electron temperature T_e into account.

The dependence of the total collision rate and its separated contributions with the background electron temperature are represented in the top graph of Figure 3.9 for copper, fixing $T_i = 0.03\,\text{eV}$. The bottom graph shows the corresponding resistivities as calculated by Eq. 3.75 for Copper (red), Aluminium (blue) and Nickel (green). The resistivity with the Spitzer model is also plotted for copper in dashed red line.

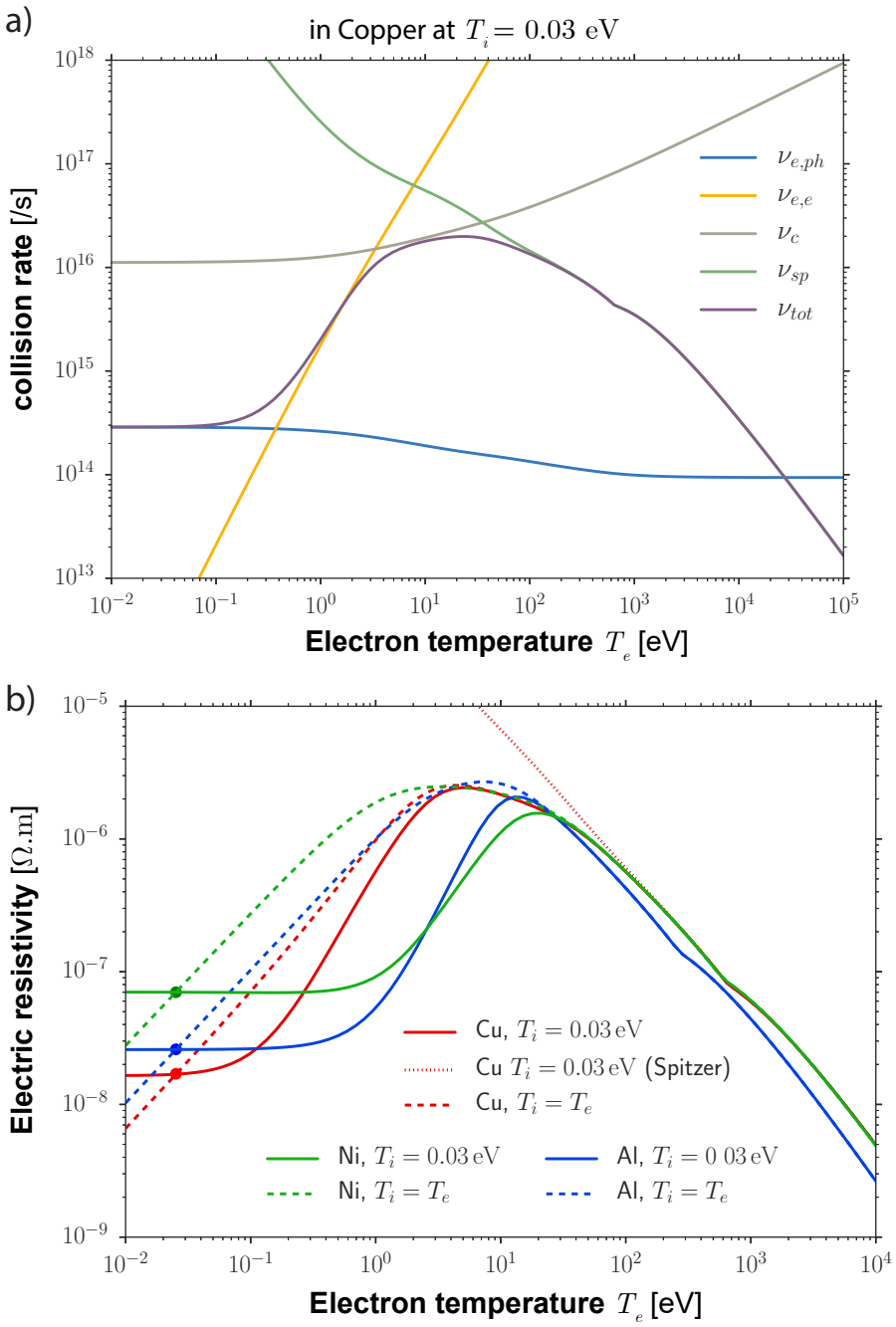

Figure 3.9 – a) Collision frequency $\nu_e = \nu_{tot}$ and its different components (see Eq. 3.80) for Copper as a function of the background electron temperature and considering an ion temperature $T_i = 0.03\,\text{eV}$. **b)** Electric resistivities obtained by the Eidmann-Chimier model for Copper (red), Aluminium (blue) and Nickel (green) at $T_i = 0.03\,\text{eV}$ in solid lines, and at $T_i = T_e$ in dashed lines. The copper resistivity obtained with Eidmann-Chimier model is compared with the resistivity obtained with Spitzer model (dotted red curve). The dots are measurements of the electric resistivities at 20 °C which evidence a good choice of the fitting parameter k_s for solids.

Electron thermal capacity

From the ionization state, one can deduce the electron thermal capacity in the hot plasma temperatures, at constant volume. Considering a perfect electron gas, it follows:

$$C_{V,e}^{hot} = \frac{3}{2} Z^* n_i k_B = \frac{3}{2} k_B n_e \tag{3.81}$$

However, even if we build a corrected model for the ionization state at solid temperatures, it is known from experiments that, at temperature below the Fermi temperature, the electron heat capacity of metals has to be written instead:

$$C_{V,e}^{cold} = \gamma_{exp} T_e \tag{3.82}$$

where γ_{exp} is the Sommerfeld parameter. It can be estimated theoretically assuming a constant Density of States (DOS) for a free electron gas at Fermi Energy:

$$\gamma_{exp} \approx \gamma_{th} \quad \text{with} \quad \gamma_{th} = \frac{\pi^2}{2} \frac{n_e k_B}{E_F} \tag{3.83}$$

In order to model the electron thermal capacity starting from the ambient temperature $T_e \approx 300\,\mathrm{K}$ to $k_B T_e \approx 10\,\mathrm{keV}$, we used tabulated data for $T_e < 5\,\mathrm{eV}$, instead of the theoretical Sommerfeld parameter that differs quite significantly from measured values. Indeed, the constant DOS is a too much strong assumption. The tabulated data is obtained based on electronic structure calculations for the DOS by Lin *et al.* (see [162] and the website http://www.faculty.virginia.edu/CompMat/electron-phonon-coupling/). An interpolation is performed between the tabulated data and Eq. 3.81 for $T_e > 100\,\mathrm{eV}$. The figure Figure 3.10 is showing the result for copper at solid density. It is worth noting that at low temperature, the perfect electron gas formula (red dashed line) is yielding very inaccurate results. The interpolation is also compared with a piecewise function (purple line), as used in [281], defined by:

$$C_{V,e}^{pw} = \begin{cases} \frac{3}{2} k_B n_e \frac{T_e}{T_F} & \text{if} \quad T_e \leq T_F \\ \frac{3}{2} k_B n_e & \text{if} \quad T_e > T_F \end{cases} \tag{3.84}$$

For the modeling in this thesis, we used instead the built-in interpolation function (green solid line).

Concerning the ion thermal capacity, similarly to electrons, assuming an ideal gas, we have:

$$C_{V,i}^{hot} = \frac{3}{2} n_i k_B \tag{3.85}$$

This expression is valid for $T_i \gg \hbar\omega_E$ where ω_E is the phonon frequency assuming the Einstein phonon DOS. The values of $\hbar\omega_E$ are very low ($\sim 200 - 300\,\mathrm{K}$), that is the reason why one can assume that $C_{V,i} \approx C_{V,i}^{hot}$ for our experimental conditions.

Resistive heating

The heating of the target by collisions will induce a resistive process which is also contributing to the electron energy losses. The already mentioned return current is responsible for the target heating by the collisions of thermal electrons that constitute it. If the electron beam current is high enough ($j_b \geq 10^{10} - 10^{11}\,\mathrm{Acm}^{-2}$), the counter return current will be also high enough to heat significantly the target and the resistive losses become non negligible and can even exceed the collisional losses.

One assumes for simplicity that the electron beam is rigid *i.e.* that the electric response is a fixed value, implying a fixed beam current density. The collective stopping power can be calculated using as simple model developed by Lovelace and Sudan [165] and modified by Gremillet [97]. This model is based on the solution of the energy conservation equation by separating the contribution of the magnetic field of the beam itself ($\vec{B}_b$) and the contribution of the plasma magnetic field ($\vec{B}_p$). The two contributions are linked by $\vec{B}_b = -f\vec{B}_p$ with f the neutralization rate. The energy conservation equation, given by the Poynting theorem writes:

$$\frac{\partial \varepsilon_{b,p}}{\partial s \partial t} = \int \vec{j}_{b,p} \cdot \vec{E} dS \tag{3.86}$$

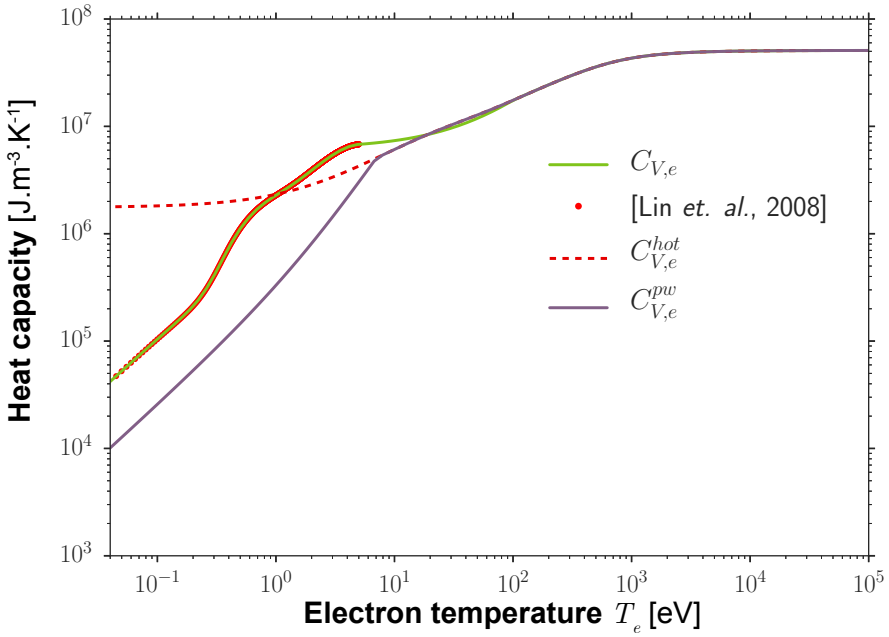

Figure 3.10 – Thermal capacity of copper, at constant volume, obtained for: (purple) from Eq. 3.84, (red points) the tabulated data of [162], (dashed red) from Eq. 3.81, (solid red) interpolation between the two latter.

The rigid beam is assumed to be collimated and its spatial distribution is characterized by a Gaussian shape (in the transverse plan). After integration over time, the amount of energy per unit of length lost in the electromotive field writes:

$$\frac{d\varepsilon_b}{ds}(t) = \frac{I_b^2}{4\pi\epsilon_0 c^2} \ln\left(1 + 2\frac{t}{t_D}\right) \tag{3.87}$$

with $I_b = e\pi r_b^2 n_b \beta_b c$ the fast electron current and τ_D the magnetic diffusion time (Eq. 3.71). It is worth noting that for simplicity, the electron beam was considered as monoenergetic, propagating at the speed $\beta_b c$.

Similarly, we obtain the contribution of the losses by Joule effect:

$$\frac{d\varepsilon_p}{ds}(t) = \frac{1}{2}\frac{I_b^2}{4\pi\epsilon_0 c^2} \ln\left(1 + 4\frac{t}{t_D}\right) \tag{3.88}$$

Using the previous equation, one can deduce the plasma temperature, by using a model of free electron gas for the electrons of the beam:

$$\frac{3}{2} n_p k_B T_e \pi r_b^2 = \frac{d\varepsilon_p}{ds} \tag{3.89}$$

The temperature of the target, in practical units, is then given by:

$$T[\text{eV}] \approx 400\beta_b^2 \left(\frac{Z^* n_i}{6\times 10^{22}\,\text{cm}^{-3}}\right)^{-1} \left(\frac{n_b}{10^{20}\,\text{cm}^{-3}}\right)^{2} \left(\frac{\eta}{10^{-6}\,\Omega\text{m}}\right) \left(\frac{\Delta t}{500\,\text{fs}}\right). \tag{3.90}$$

The resistive heating can be obtained in the approximation of perfect neutralization $\vec{j}_b = -\vec{j}_r$ and by neglecting both thermal conduction and ionization [61]. The heat equation, by energy conservation, then writes:

$$C_{V,e}\frac{\partial T_e}{\partial t}\bigg|_{\text{res}} = -n_b v_b \left(\frac{dE}{ds}\right)_{\text{res}} = \eta j_b^2 \tag{3.91}$$

with the thermal capacity at constant volume $C_{V,e}$, taken as constant. n_b and v_b are respectively the electron beam density and velocity.

Now, we will compare the contribution of the resistive heating by the electron beam, by comparing it with the collisional energy losses. The collisional stopping power in cold matter is taken from the Bethe formula (Eq. 3.62) keeping only the contribution of the logarithmic term. For the electron beam, the energy conservation considering collisional stopping power losses writes:

$$C_e \frac{\partial T_e}{\partial t}\bigg|_{\text{col}} = n_b v_b \left(\frac{dE}{ds}\right)_{\text{col}} = \frac{2\pi r_e^2 Z m_e c^2 v_b n_i n_b}{\beta_b^2(\gamma_b - 1)} \ln\left(\frac{(m_e c^2)^2(\gamma^2 - 1)(\gamma - 1)}{2I_0^2}\right) \tag{3.92}$$

It is worth noting that the collisional heating scales as j_b whereas resistive heating scale as j_b^2. For high current densities, the contribution of resistive heating will become clearly dominant. The absorption and scattering of the electrons of the beam will then decrease the current density and this trend may be inverted. One can build a ratio between collisional and resistive losses:

$$R_{\text{col/res}} = \frac{\partial_t T_e|_{\text{col}}}{\partial_t T_e|_{\text{res}}} = \frac{2\pi r_e^2 Z m_e c^2 n_i}{\beta_b^2(\gamma_b - 1) e\eta j_b} \ln\left(\frac{(m_e c^2)^2(\gamma_b^2 - 1)(\gamma - 1)}{2I_0^2}\right) \tag{3.93}$$

The ratio $R_{\text{col/res}}$ is plotted in Figure 3.11 as a function of fast electron current density, for copper at solid density and $T_i = 0.03\,\text{eV}$. The resistivity is computed using Eidmann-Chimier model, for $T_e = 10\,\text{eV}$ (solid lines) and for $T_e = 100\,\text{eV}$ (dashed lines). The electron beam temperature has been set to $T_b = 100\,\text{keV}$ (light red curves) and $T_b = 1000\,\text{keV}$ (dark red curves). Globally the resistive heating become preponderant at current density in excess of $\sim 10^{11} - 10^{12}\,\text{W/cm}^2$.

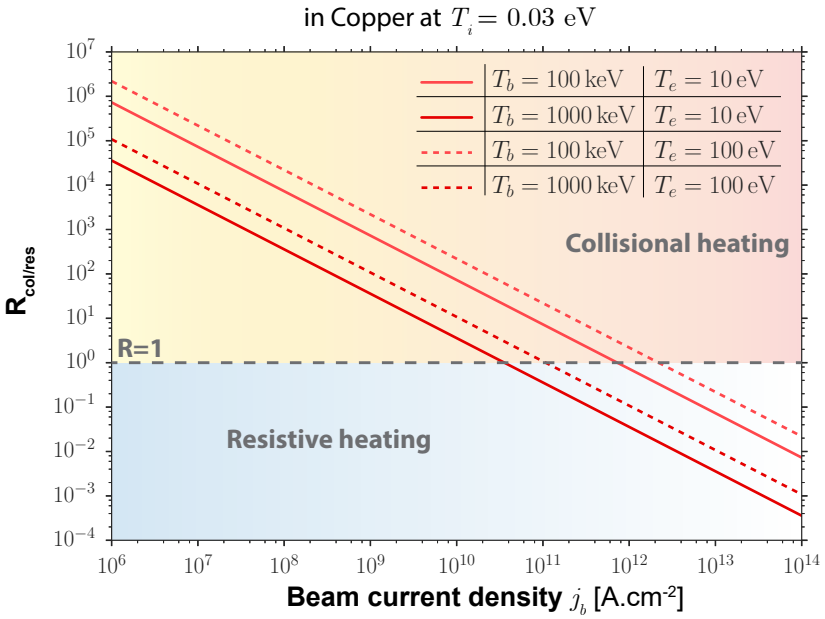

Figure 3.11 – Ratio between collisional and resistive losses as a function of the beam current density. The ratio is represented for different couples of values for the beam temperature T_b and the background electron temperature T_e, as listed in the legend table inserted in the graph. The resistivity is computed using Eidmann-Chimier model at $T_i = 0.03\,\text{eV}$

4 Laser-matter interaction in nanosecond regime ($\gtrsim 10^{16}\,\mathrm{W/cm^2}$)

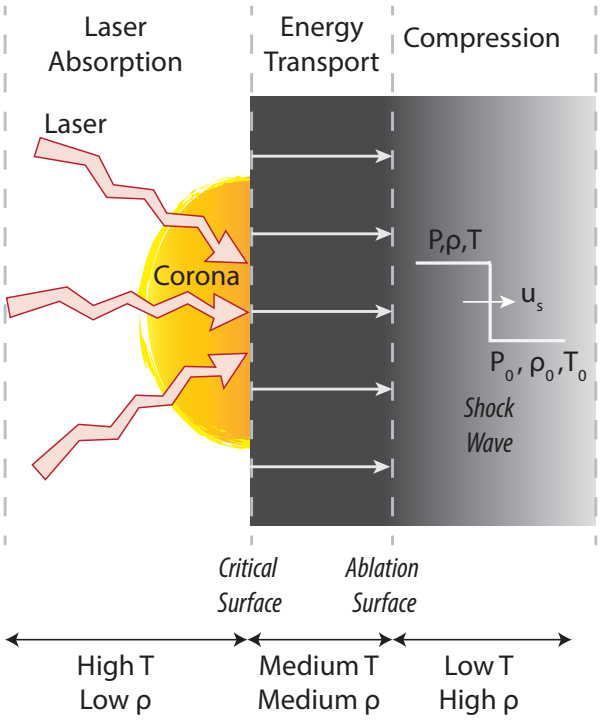

Figure 4.1 – A schematic description of laser-plasma interaction in nanosecond regime

When a high power laser hits a solid or gaseous target, a high temperature plasma is created at its interaction surface. It is due to extremely rapid ionization by direct photoeffect or, depending on wavelength of the laser and target material, by multiphoton processes. The formation of the plasma is followed by its dynamic expansion in vacuum or in surrounding gas, forming a corona in which the density decreases from the dense zone to ambient density of vacuum or surrounding gas. The corona corresponds then to the region where $n_e < n_c$. The high pressure created in this corona can compress the dense zone and push it towards the inside of targets. Afterwards, the electrons in the corona absorb the laser energy which is then transported from the critical density to the area where the plasma was created, defined as the ablation surface. The laser-plasma system is described schematically in Figure 4.1.

In the absorption domain, the density is $< 0.01\,\mathrm{g/cm^3}$, the temperature is $\sim 1000\,\mathrm{eV}$; in the transport domain, the density is between $\sim 0.01\,\mathrm{g/cm^3}$ and the solid density ρ_0 ($1 - 10\,\mathrm{g/cm^3}$), with temperature scaling from $\sim 30\,\mathrm{eV}$ to $\sim 1000\,\mathrm{eV}$; and finally, in the compression domain the density grows from $\sim \rho_0$ up to $\sim 10\rho_0$ and temperature from $\sim 1\,\mathrm{eV}$ to $\sim 30\,\mathrm{eV}$. The blow-off velocity of the plasma (towards the laser) is nearly equal to the sound speed c_s (at constant temperature) at the critical density :

$$c_s = \sqrt{\frac{Z^* k_B T_e}{m_i}} \rightarrow c_s[\mathrm{cm/s}] \approx 3.1 \times 10^7 \sqrt{\frac{Z^*}{A}} \sqrt{T_e[\mathrm{keV}]}. \tag{4.1}$$

Because of the ion ablation, exponential density profile is formed in the corona and its size is about a few times $c_s \tau_L$:

$$L \sim c_s \tau_L \rightarrow L[\mu\mathrm{m}] \approx 311 \sqrt{T_e[\mathrm{keV}]} \sqrt{\frac{Z^*}{A}} \tau_L[ns] \tag{4.2}$$

For sufficiently high laser irradiance $I_L \lambda_L^2 > 10^{14}\,\mathrm{W/cm^2}$, two (or more) types of electrons are produced : the *thermal* electrons, with a temperature T_e of the order of $\sim$ keV, and the *hot* electrons with a typical temperature $T_h \gtrsim 10\,\mathrm{keV}$. The *thermal* electrons carry energy away from the point of absorption by diffusion processes (thermal conduction). The *hot* electrons deposit their energy ahead of the thermal conduction front induced by the *thermal* electrons, causing *hot* electron preheating. Those electrons induce pressures in the plasma together with the ablation pressure associated with the flow of heated plasma from the solid target.

4.1 Self-generated fields

During the plasma expansion of the corona, self-generated magnetic fields appears mainly due to the non-colinearity between density and temperature gradients creating thermoelectric currents, as observed experimentally for the first time in 1971 [261]. The self-generated magnetic fields can be quite strong, of the order of several 100s of T at most [293]. The self-generated fields are particularly strong with interactions at laser intensities $> 10^{15}\,\mathrm{W/cm^2}$, where a significant population of fast electrons are produced together with strong heat fluxes. The hot electron can generate magnetic field through the Nernst effect away from the focal region in the overdense region of the plasma.

The self generated magnetic field can be calculated by combining Faraday and Ohm laws of Maxwell equations:

$$\frac{\partial B}{\partial t} = -\vec{\nabla} \wedge \vec{E} \tag{4.3}$$

$$\vec{E} = -\left(\vec{v} \wedge \vec{B} - \frac{\vec{J} \wedge \vec{B}}{e\, n_e} + \frac{2\,\vec{q}_e \wedge \vec{B}}{5 n_e T_e} + \frac{\vec{\nabla} P_e}{e\, n_e} + \beta \frac{c \vec{\nabla} T_e}{e\, n_e} - \eta \vec{J} - \frac{m_e}{e^2\, n_e} \frac{\partial \vec{J}}{\partial t} \right) \tag{4.4}$$

where $\vec{v}$ is the electron velocity, $\vec{J}$ is the plasma current density, $\vec{\nabla} P_e$ is the pressure gradient with the electron pressure ($P_e = n_e T_e$), n_e is the electron density, T_e the electron temperature, e the charge of the electron, $\vec{q}_e$ the electron heat flux (where the speed associated to the heat flux is $\vec{v}_T = 2\vec{q}_e/(5 n_e T_e)$) and η is the plasma resistivity. β refers to the Braginskii coefficient [34]. Note that the Nernst effect corresponds to third term of Eq. 4.4. Considering only the major source terms, then we get,

$$\frac{\partial \vec{B}}{\partial t} = \vec{\nabla} \wedge \left[(\vec{v} + \vec{v}_T) \wedge \vec{B} \right] + \frac{1}{e\, n_e} \vec{\nabla} T_e \wedge \vec{\nabla} n_e - \vec{\nabla} \wedge \left(\vec{J} \wedge \frac{\vec{B}}{e\, n_e} \right) - \vec{\nabla} \wedge (\eta \vec{J}) \tag{4.5}$$

The first term of the equation is the convection term due to i) the ion motion and ii) Nernst effect (by $\vec{v}_T$). The first part of this convection term is sometimes called *dynamo effect*. The second term is the thermoelectric source. Following terms are loss due to Hall effect and electrons return current. In the following, we will detail more the effects that are preponderant in the nanosecond regime, where the current of hot electrons is not as high as in picosecond regime.

When the magnetic field is low, the Nernst effect will be reduced because of a reduced heat flux. With self-generated fields of the order of 100s T (or more generally if the hall parameter $\omega_e \tau_e$ is between 1 and 10), the Nernst velocity cannot be neglected.

4.1.1 Thermoelectric effect due to crossed gradients ($\vec{\nabla} n_e \wedge \vec{\nabla} T_e$)

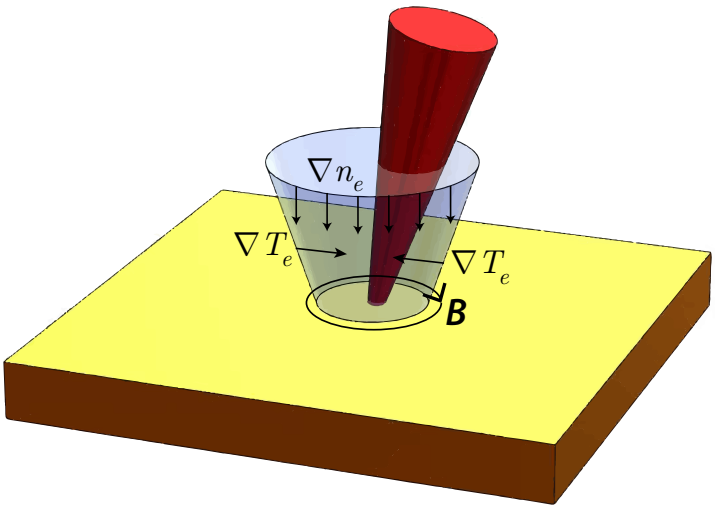

Figure 4.2 – Sketch representation of the magnetic field generation by crossed temperature-density crossed gradients (thermoelectric effect).

The electronic pressure gradient in the plasma $\vec{\nabla} P_e$ give rise to charge separation and thus to the development of an electric field. The growth-duration of this development will depend on the screening velocity of the considered plasma. Anyway, as soon as it exists an electronic pressure gradient, there will be an electric field ($e\, n_e \vec{E} = -\vec{\nabla} P_e$).

Strong density gradients can also appear near composition jumps or shock waves and produce $\vec{\nabla} n_e \wedge \vec{\nabla} T_e$ magnetic fields.

Experimental observations of magnetic fields due to this thermoelectric mechanism are reported in [224, 18, 15]. Assuming that the density gradient $\vec{\nabla} n_e$ is directed along the target normal, the magnitude of this field can be estimated as follows [18]:

$$B[\mathrm{kT}] \sim 2 \left(\frac{\tau_L}{1\,\mathrm{ps}}\right) \left(\frac{T_e}{1\,\mathrm{keV}}\right) \left(\frac{L_T}{1\,\mu\mathrm{m}}\right)^{-1} \left(\frac{L_n}{1\,\mu\mathrm{m}}\right)^{-1}, \tag{4.6}$$

where L_T and L_n are the transverse temperature and longitudinal density gradient scale-lengths, respectively. The magnetic field generated by the temperature-density crossed gradients can modify the electron transport on a time scale of a few ps [193] or bigger, but on shorter time-scales it can be neglected. This is why it is an important mechanism for intense ns-pulses.

In the expanding plasma, created by a finite focal spot, the density gradient is directed towards direction of propagation of the laser field at the point of interaction (target normal) and the temperature gradient is in the radial direction (Figure 4.2). The resulting self-generated magnetic field is developed by the non-colinearity between density and temperature gradients. Since the intensity distribution at the center of the focal spot is uniform compared to the edges, the magnetic field will preferentially be strong on the laser beam edges where temperature gradients are larger. This magnetic field can be up to several 100s of T for intense ns-pulses.

Otherwise, thermal instabilities found on the electron thermal conductivity can generate steady-state magnetic fields [274]. The perturbation in the plasma temperature varies across the density gradient and creates small scale magnetic field due to $\vec{\nabla} n_e \wedge \vec{\nabla} T_e$ mechanism. The dependence of the B-field on electron thermal conductivity produces heat flow such that the original temperature perturbation is enhanced and this acts as a feedback mechanism for instability. However, this effect requires larger instability wavelength compared to the collisional mean electron free path. The wavelength of magnetic perturbations yielding the maximum growth (with target whose $Z \gg 1$) is given by:

$$\lambda_{max} \approx 4 \sqrt{\frac{c L_n L_T}{\omega_{p,e} \lambda_e}} \tag{4.7}$$

where λ_e is the electron mean free path length. The thermal instability mechanism is only significant for high Z plasmas.

4.1.2 Influence of magnetic field over heat fluxes and transport coefficients

Before introducing the self generated fields contribution over heat transport, a look to the previously introduced magnetic induction equation Eq. 4.5 clearly evidences that distributions of electron current, pressure and temperature play important roles in the heat transport. It is then necessary to describe them accurately. The modeling of the interaction and heat fluxes uses in general the classical model of Spitzer and Harm. It takes a local form where it is described by the Fourier law $Q_{SH} = -\kappa_{SH} \nabla T_e$, where the thermal conductivity k_{SH} only depends on local properties of the plasma [260]. Meanwhile, in inertial confinement fusion context, electron temperatures are important and the mean free path of electrons can be larger than the steep temperature gradients: in that case the local theory is invalidated. Bell [17] evaluates this limit to $\lambda_e / L_T \gg 2 \times 10^{-3}$ where λ_e is the mean free path of the electron and $L_T = T_e / \nabla T_e$ is the temperature gradient length. Above this limit, the heat fluxes observed experimentally near the critical surface are frequently weaker than the predicted values by Spitzer and Harm theory [297]. To describe the observations, a *flux limiter* has been introduced empirically [172]. But the applicability range of this flux limiter has been shown to be restricted since it does

not describe correctly the hot electron heat transport outside the interaction zone: an added kinetic description of the plasma in hydrocodes [248, 297] is then needed.

Concerning self-generated magnetic fields, they also affect the electron heat fluxes by modifying their transport. Indeed, we saw in Sec. 2 that the motion of electron in a magnetic field is characterized by a gyration motion at the characteristic Larmor radius $r_L = m_e v_\perp / eB$. If the Larmor radius is sufficiently small compare to temperature gradient length, the electron will be confined and therefore localized. This condition $r_L < L_T$ writes:

$$B > \frac{m\, v_\perp \nabla T_e}{e T_e} \tag{4.8}$$

It means that under strong magnetic fields, the Spitzer-Harm theory of transport is valid again by mitigating the non-local transport effects [82]. Still the non locality can occur again if the plasma evolution induces a cavitation of the magnetic field [228].

4.2 Plasma expansion into vacuum

In this section, we will focus on the plasma created by laser when it expands through vacuum from target surface. This expansion can be obtained by a simple approach using a 1D fluid description for a semi-infinite plasma in a self-consistent model [184]. The initial conditions of this model have to be precised : at t_0, ions are assumed to be cold, fill the region of $x < 0$ with a density $n_i = n_{i,0}$ for $x < 0$ and $n_i = 0$ for $x > 0$; electrons have a density $n_e(x)$ and a temperature T_e and are in equilibrium as described by a 1D Boltzmann relation for the electrostatic potential,

$$n_e = n_{e,0} \exp\left(e\phi / k_B T_e\right) \tag{4.9}$$

The boundary conditions are that the electron density should remain equal to the background value well inside the plasma, so $n_e(x) \to 0$ for $x \to -\infty$, and should vanish in vacuum far from the surface $n_e(x) \to 0$ for $x \to +\infty$. The plasma is quasi-neutral and $n_{e,0} = Z n_{i,0}$, with Z the atomic charge of the considered ion species. The electrostatic potential is given by the Poisson equation:

$$\epsilon_0 \frac{\partial^2 \phi}{\partial x^2} = e(n_e - Z n_i) \tag{4.10}$$

The electron density is vanishing fast from the plasma border over a characteristic distance of the order of the Debye length written here for the unperturbed plasma $\lambda_{D,0} = \sqrt{\epsilon_0 k_B T_e / n_{e,0} e^2}$. The electric field $E = -\partial\phi/\partial x$ triggers the ion expansion, ruled by the following set of equations for a cold fluid description, neglecting relativistic effects:

$$\begin{cases} \dfrac{\partial n_i}{\partial t} + u_i \dfrac{\partial n_i}{\partial x} &= -n_i \dfrac{\partial u_i}{\partial x} \\ \dfrac{\partial u_i}{\partial t} + u_i \dfrac{\partial u_i}{\partial x} &= -\dfrac{Ze}{m_i} \dfrac{\partial \phi}{\partial x} \end{cases} \tag{4.11}$$

In the quasi-neutral limit $n_e \approx Z n_i$, the motion equation writes:

$$\frac{\partial u_i}{\partial t} + u_i \frac{\partial u_i}{\partial x} = -c_s^2 \frac{1}{n_i} \frac{\partial n_i}{\partial x} \tag{4.12}$$

One can find a self-similar solution where physical quantities only depend on time and space through the self-similar variable $\xi = x/t$. The set of equation Eq. 4.11 are now:

$$\begin{cases} (u_i - \xi) \dfrac{dn_i}{d\xi} &= -n_i \dfrac{du_i}{d\xi} \\ (u_i - \xi) \dfrac{du_i}{d\xi} &= -c_s^2 \dfrac{1}{n_i} \dfrac{dn_i}{d\xi} \end{cases} \tag{4.13}$$

and the solution verify $u_i - \xi = \pm c_s$. Only the positive solution is in agreement with the initial condition where the plasma is filling the $x < 0$ region at $t = 0$. The ion density can be expressed then as:

$$n_i = n_{i,0} \exp\left(-\xi/c_s + 1\right) \tag{4.14}$$

The self-similar electric field is given by:

$$E_{ss} = \frac{k_B T_e}{e\, c_s t} = \frac{E_0}{\omega_{pi} t} \tag{4.15}$$

and $E_0 = \sqrt{n_{e,0} k_B T_e / \epsilon_0}$. This is the typical electric field of a capacitor with a cathode situated where the rarefaction wave is emerging, at $x = -c_s t$, and holds a surface charge density of $\sigma = \epsilon_0 E_{ss}$, while the anode holds the opposite charge and is situated at the border of the plasma. The anode is approximately located where $\lambda_D = c_s t$. Here the local Debye length is predicted by the self-similar model and writes:

$$\lambda_D = \lambda_{D,0} \sqrt{\frac{n_{e,0}}{n_e}} = \lambda_{D,0} \exp\left[\frac{1}{2}\left(1 + \frac{x}{c_s t}\right)\right] \tag{4.16}$$

We obtain the anode position $x_f = c_s t \left[2 \ln\left(\omega_{pi} t\right) - 1\right)\right]$. In this anode position, the self-similar solution predicts a velocity of the front of $u_f = 2 c_s \ln\left(\omega_{pi} t\right)$, which corresponds to an electric field at the border of the plasma equal to twice the self-similar one calculated in Eq. 4.15,

$$E_f \approx 2 E_{ss} = 2 E_0 / \omega_{pi} t. \tag{4.17}$$

The self-similar electric field governed the quasi-neutral region $-c_s t \leq x < x_f$. One can note that there is a discontinuity of the electric field at the front position x_f.

In reality, one cannot ignore totally the effects of charge separation which are dominant in the early phase of the expansion $\omega_{pi} t \lesssim 1$ and are necessary to calculate the structure of the anode and cathode charge densities together with the exact position of the anode. The result of the resolution of Eq. 4.9 - Eq. 4.11 is shown in figure Figure 4.3 for the ion and electron separation charge and the resulting electric field, obtained at $\omega_{pi} t = 50$.

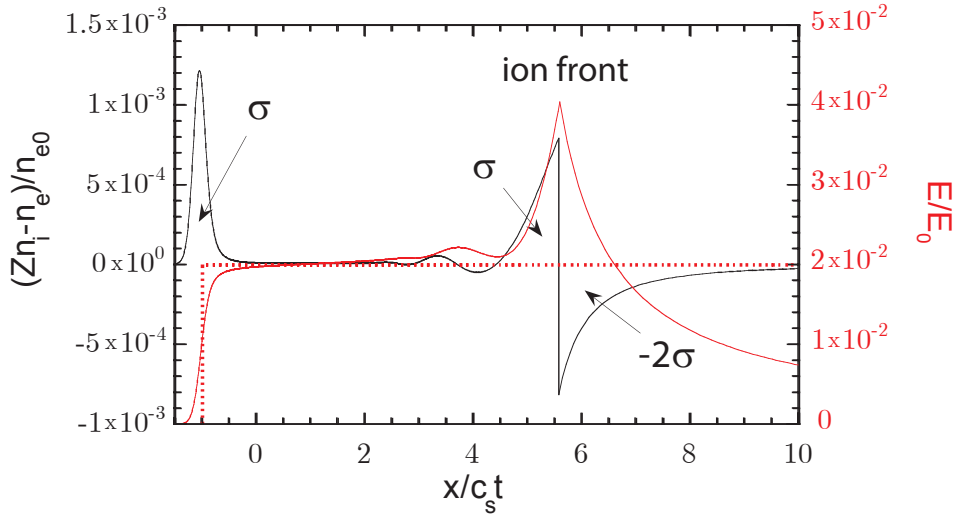

Figure 4.3 – Charge separation (black solid line, left ordinates) and electric field (red solid line, right ordinates) at time $\omega_{pi} t = 50$. The ion front stands at $x/c_s t \approx 5.59$ where the electric field peaks. The dotted red line (right ordinates) corresponds to the usual self-similar solution, Eq. 4.15. Note that the electric field at the ion front is approximately twice the self-similar field, as predicted by Eq. 4.17. Results and curves from [184].

After resolution, the electric field at the front position is given more generally by:

$$E_f \approx \frac{2 E_0}{\sqrt{2e + \omega_{pi}^2 t^2}} \tag{4.18}$$

which consistently reduces to the Eq. 4.17 for $\omega_{pi}t \gg 1$. e ≈ 2.71828 is Euler's number.

The velocity of the ionic front writes:

$$u_f \approx 2c_s \ln\left(\tau + \sqrt{\tau^2 + 1}\right) \tag{4.19}$$

where $\tau = \omega_{pi}t/\sqrt{2\mathrm{e}}$ and this permits to calculate the maximum energy of the ions accelerated in the expansion process:

$$E_{max} \approx 2Zk_BT_e \left[\ln\left(\tau + \sqrt{\tau^2 + 1}\right]^2\right. \tag{4.20}$$

The major drawback of Eq. 4.19 is that the maximum velocity of ions, and hence the cut-off energy, diverges logarithmically with time. This is not surprising, being an unavoidable consequence of the isothermal assumption and the chosen boundary conditions.
The system has an infinite energy reservoir in the electron fluid and thus it is able to accelerate ions indefinitely.

Nevertheless, even if the simplicity of Eq. 4.19 make it attractive, it has been then suggested inserting a phenomenological "maximum acceleration time" t_{acc} at which the acceleration should stop. Heuristically, $t_{acc} \sim 1.3\tau_L$, according to [84], in attempts to fit experimental data. The electron temperature decays in time due to the plasma expansion and to collisional and radiative losses. The electron cooling cooperates with the effects of finite acceleration length and maximum electron energy in the determination of a finite value for the maximum energy gain. The electron loss is a reasonable result if a realistic warm 3D plasma is considered, because the energy required to escape from 3D charge distribution has a finite value. In any case, the assumption of a planar 1D model is valid only over $\sim 2r_s$, where r_s is the plasma sheath size (see Eq. 5.17).

The expansion of plasma slabs of finite thickness, and hence of finite energy, has been considered analytically and numerically. In these models the electron temperature is taken as a function of time $T_h = T_h(t)$ determined either by the energy conservation equation [26, 185] or with had-hoc modeling of $T_h(t)$ [38].

5 Laser-matter interaction in picosecond and sub-picosecond regime ($\gtrsim 10^{18}\,\mathrm{W/cm^2}$)

From 1976, generation of short laser pulse has been made possible by the development of the mode locking technique (see *Appendix*, Sec. 14). The achievable intensity was however yet small due to the limitation of the laser pulse energy to a few mJ. The novel amplification technique called Chirped Pulse Amplification (CPA) - also described in Sec. 14 - allows presently the generation of PW laser pulses, with peak intensities up to $10^{21}\,\mathrm{W/cm^2}$, largely enough to accelerate numerous fast electrons (MA-currents) at relativistic velocities (see Sec. 3.1). In the next section, we will introduce the key features of the fields self-generated by such high currents of fast electrons. Afterwards, we will describe how they can accelerate energetic ion beams out of the target. The charaterization and some applications of laser-accelerated energetic proton beams will be also given.

5.1 Self-generated fields

The propagation of a MA-current electron beam in dense plasma will induce intense electromagnetic fields which can greatly affect the beam propagation. We already saw in Sec. 3.3.2 that this current is responsible of resistive heating and result in a collective stopping power for electrons. The nature of self-generated fields effects over the transport of a fast electron beam is a complex picture to draw as it affect the electron beam both positively (it can compensate the divergence of the beam and self-focalize it) and negatively (divergence or instabilities and filamentation). To study the effects of self-generated fields over fast electron transport, we will introduce again the magnetic induction equation (see Sec. 4.1) keeping the terms that are preponderant in respect to fast electron generation in the picosecond and subpicosecond regime:

$$\vec{E} = -\eta \vec{j_b} + \frac{\eta}{\mu_0}\vec{\nabla}\wedge\vec{B} + \frac{1}{e\,n_e}\vec{\nabla}(n_e T_e) \tag{5.1}$$

$$\frac{1}{c}\frac{\partial \vec{B}}{\partial t} = -\vec{\nabla}\wedge\vec{E} \tag{5.2}$$

This equation remains valid under the assumption of a fast electron beam duration longer than the charge neutralization time, and shorter than the magnetic diffusion time. After combining the two equations of Eq. 5.2, one gets:

$$\frac{\partial \vec{B}}{\partial t} + \frac{\partial}{\partial \vec{r}}\wedge\left[\frac{\eta}{\mu_0}\vec{\nabla}\wedge\vec{B}\right] = \underbrace{\eta\vec{\nabla}\wedge\vec{j_b}}_{\text{shear current}} + \underbrace{\vec{\nabla}(\eta)\wedge\vec{j_b}}_{\text{resistivity gradients}} + \underbrace{\frac{1}{n_e e}\vec{\nabla}(n_e)\wedge\vec{\nabla}(T_e)}_{\text{crossed gradients}} \tag{5.3}$$

In Eq. 5.3, one can distinguish three main effects that are producing self-generated magnetic fields. The first term, labeled *shear current* is causing self-collimation of the fast electron beam. The second term, labeled *resistivity gradients* stands for the generation of magnetic field by resistivity gradients, which can be produced due to inhomogeneous compression or specific target designs and/or heating of the medium. The resistivity gradients can collimate or deflect the electron beam depending on the sign of the resistivity gradients. The collimation by resistivity gradients is one of the major option that has been studied to counterbalance the intrinsic divergence of fast electron beams (see Sec. 10.1). The desired effects are qualitatively similar to those obtained when applying an external magnetic field, as studied in this thesis work. Yet, as we will show, the imposed B-field significantly improves the energy-density flux compared to the method of resistivity gradients. Finally, the third term, labeled *crossed gradients* is the thermoelectric effect already discussed in Sec. 4.1.1.

Keeping only the first two terms of Eq. 5.3 (fast electron current), the maximum electric and magnetic field amplitudes induced by the fast electron beam propagation can be estimated in function of the laser intensity I_L, pulse duration τ_L and plasma resitivity η [62].

Assuming a Gaussian laser pulse of wavelength λ_L for both time and space distributions, r_b the fast electron beam radius and η_h the laser-to-fast-electrons conversion efficiency, one reads:

$$E_{\max}[\mathrm{Vm^{-1}}] \approx 6\times 10^{9}\left(\frac{\eta}{2\times 10^{-6}\,\Omega\mathrm{m}}\right)\left(\frac{\eta_h}{0.3}\right)\left(\frac{I_L}{10^{17}\,\mathrm{W/cm^2}}\right)\left(\frac{1\,\mu\mathrm{m}}{\lambda_L}\right)^{2/3} \tag{5.4}$$

$$B_{\max}[\mathrm{T}] \approx 3.83\times 10^{-8} E_{\max}[\mathrm{Vm^{-1}}]\left(\frac{2\tau_L}{1\,\mathrm{ps}}\right)\left(\frac{10\,\mu\mathrm{m}}{r_b}\right) \tag{5.5}$$

According to these equations, for fast electrons of energies $\gtrsim$ 40 keV, expected for laser intensities $I_L \geq 10^{18}-10^{19}\,\mathrm{W/cm^2}$, their transport is dominated by the fields that they generate [62]. This is the case for the short-pulse laser intensity used in our experiments: it can be seen in the energy balance made on PIC-Hybrid simulations of Part III (Sec. 10.7 - Figure 10.12).

In the following, we will make a non exhaustive list of the contributions to self-generated fields resulting from large-scale and small-scale instabilities.

Non uniformities of the ponderomotive force

The ponderomotive force was introduced in Sec. 3. Theoretical work of Sudan [269] has shown that the spatial and temporal variation of the incident laser pulse could generate large-scale magnetic fields of several 10s of kT when an ultra-intense short-pulse interacts with solid density plasma. This field arise from the DC current generated by the temporal and spatial non-uniformities of the ponderomotive force exerted by the laser pulse on the plasma electrons. Magnetic field generated due to this mechanism is comparable to the oscillating laser magnetic field. Also, the duration of the magnetic field is the same as the duration of the laser pulse. The detailed analytical solution given in [269] shows that the average DC magnetic field generation is a function of the resultant amplitude of the incident and reflected laser pulses. By construction, the direction of the B-field is azimuthal and can be determined by the electron flow in the propagation direction. The maximum is reached at the interface and fall off rapidly.

Magnetic fields of $\sim$ kT at target surfaces were measured by proton imaging at a laser intensity of $\sim 10^{19}\,\mathrm{W/cm^2}$ [242]. The previously introduced model predicts magnetic fields $10\times$ higher (100 kT) for laser intensities of the order of $10^{20}\,\mathrm{W/cm^2}$. However, not any experimental proof has confirmed so far this prediction at such high laser intensity.

Apart from large scale DC magnetic fields, there are also small scale intense magnetic fields, as presented in the following.

B-fields due to resonance absorption

Theoretical and computational studies (for example in [273]) have suggested the generation of 100s of Tesla magnetic fields due to resonance absorption of incident laser light (this absorption mechanism was described in Sec. 3.1.1). The electric field can be written as:

$$\vec{E} = -\frac{1}{e\,n_e}\vec{\nabla}\cdot\overline{\overline{P}}_r \tag{5.6}$$

where $\overline{\overline{P}}_r$ is the electromagnetic stress tensor [27]. The growth of magnetic field can be written as:

$$\frac{\partial\vec{B}}{\partial t} = -\vec{\nabla}\wedge\vec{E} = \vec{\nabla}\wedge\frac{1}{e\,n_e}\vec{\nabla}\cdot\overline{\overline{P}}_r \tag{5.7}$$

In the presence of absorption, $\vec{\nabla}\wedge(\vec{\nabla}\cdot\overline{\overline{P}}_r)$ does not vanish and can give rise to steady-state B-field. The field is localized near the critical density surface over a fraction of the laser wavelength. Hence, it does not play a major role in inhibiting the heat flow towards higher densities.

B-fields due to Weibel instabilities

The so-called Weibel instabilities are triggered by perturbations of beam current density in the transverse direction - in respect to the beam propagation direction - by incident hot electrons and

neutralizing thermal electrons and produce small scale magnetic fields in the plasma [287]. Low-frequency electromagnetic modes become unstable and the fields generated by this mechanism are oscillating, unless the electron transit time is less than the oscillation period. In that latter case, the generated B-field is considered as quasi-static. The magnitude of magnetic perturbation by Weibel instabilities is calculated in detail in [222] and reads:

$$B[\mathrm{T}] \approx 200 \left(\frac{n_e}{10^{21}\,\mathrm{cm}^{-3}}\right)^{1/4} \left(\frac{T_e}{1\,\mathrm{keV}}\right)^{1/2} \left(\frac{L_n}{1\,\mu\mathrm{m}}\right)^{-1/2} \tag{5.8}$$

The instability occurs if the instability wavelength λ_W satisfy $\lambda_W < \lambda_e < L_n$. Considering the Weibel-unstable distribution function generated by two counter-propagating electron beams, such as the incident and the return current, the Weibel instability is responsible for the creation of strong opposite micro-currents separated by the skin-depth $c/\omega_{p,e}$ that deteriorates the current neutrality. As the instability grows, these magnetic filaments merge into larger filaments. The Weibel instability strongly affects the beam propagation in the target and plays an important role on the initial divergence of the electron beam [1, 64]. A purely transverse instability is called *filamentation instability*. It is extended to the denomination of *resistive filamentation* in the case of a predominant resistive regime (see Sec. 3.3.2).

The Weibel instabilities are capable of generating magnetic fields of the order of several hundreds of T or more with nowadays high power lasers. The filamentation in unmagnetized transport conditions evidences strong effects on the fast electron transport, playing an important role in reducing the efficiency of energy-density propagation through the target depth by the electron beam. Simulation of the transport of a relativistic electron beam in dense matter performed in this thesis work (see Sec. 10) shows that this instability is strongly mitigated when a strong external B-field is applied.

Two stream instability

In collisionless plasmas, when the fast electron beam density n_b is far bigger than the plasma electron density n_p, or more precisely [97], when:

$$n_b > \min\left[n_p, \frac{16 n_p \gamma_b^3}{3^{3/2}(\omega_{p,e}/\nu_{e,i})^3}\right] \tag{5.9}$$

an instability called *two stream instability* [37] arise from the longitudinal density perturbations and resultant longitudinal electrostatic waves due to the counter-propagating electron beams. In our experimental conditions, we always have $n_b \ll n_p$ and this instability can be neglected.

5.2 Energetic ion beams

5.2.1 Energetic ion beam acceleration

The direct acceleration of ions in the laser field is very inefficient, since $\frac{v_i}{c} \approx \frac{eE_L}{m_i \omega c} = \frac{m_i}{m_e} a_0 \leq \frac{a_0}{1836}$. In order to get MeV ion energies with laser field acceleration, one would need $a_0 \sim 2000$ or $I\lambda_L^2 \geq 5 \times 10^{24}\,\mathrm{W\,cm^{-2}\,\mu m^{-2}}$, that is totally unrealistic with our current laser technology. Instead, ion acceleration is consequent to strong electric fields generated by a collective displacement of large number of electrons, and such electric fields accelerate ions until charge neutrality is restored. As a result, ions move together with electrons in a ballistic way. Proton emission from metallic target is possible because of the presence of hydrogen-containing impurities on the target surface, due for example to the residual moisture in the interaction chamber.

Ions having energies up to several MeVs had been observed in several high-intensity laser-matter interaction experiments for different targets, including relatively thick - $\approx 40\mu m$ - solid targets ([15] and references therein), sub-micrometric clusters ([68], and references therein) and ponderomotive channeling in gas jets ([151] and references therein). Common to these experiments was the rather isotropic ion emission and the resulting low brilliance, making these configurations not attractive as ion accelerators for applications. More recently, some experiments [52, 171, 255] independently reported the observation of an intense emission of multi-MeV protons from thinner solid targets, either metallic or plastic (CH), of a few microns thickness irradiated by high intensity laser pulses. The further increase in laser contrast permitted even to explore new mechanisms of acceleration with even thinner targets. The inherent mechanisms are collisionless shock formation by hole boring, or the *light-sail* mechanism with high radiation pressure on mass-limited targets. We will focus first on the electrostatic sheath mechanism by hot electron cloud, called *Target Normal Sheath Acceleration* (TNSA) as it is the major ion acceleration regime involved in this thesis, given the used laser intensity and target thickness (10 µm).

TNSA mechanism and derived

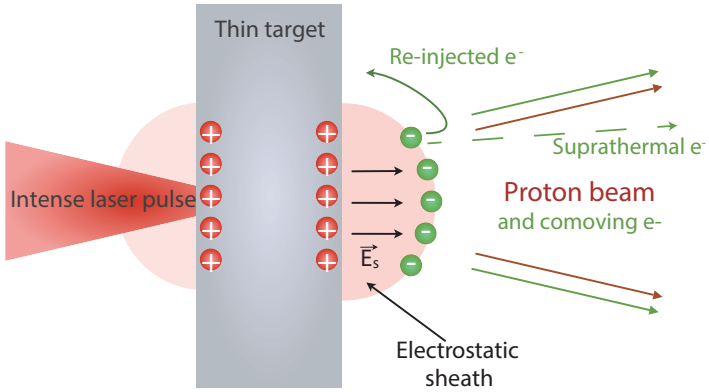

Figure 5.1 – Illustration of the TNSA mechanism. Suprathermal electrons leaving the target at the rear-side (with steep density gradient) create an intense charge separation field accelerating protons from rear surface impurities. Electrons of lower energy are re-injected back in the target and form an electron cloud. The proton beam will pull part of this electron cloud which will travel in co-motion with protons. The subsequent neutral TNSA beam will then propagate in vacuum with a certain divergence.

Historically, a debate arose on the actual location of the region where the protons were accelerated and, consistently, on the mechanism driving acceleration. In references [52] and [171] authors suggested that protons were accelerated at the front side of the target, crossing the latter and being detected on the opposite rear side. In contrast, in [255], the author provide evidence that protons were accelerated at the rear side (see also [101]). To support the interpretation of these latter experiments (performed at the Petawatt facility of Lawrence Livermore National Laboratory, USA), the so-called TNSA model was introduced by Wilks *et al.* in 2001 [291]. TNSA mechanism is schematically shown in Figure 5.1.

The hot electrons generated by laser interaction with the solid target propagate through the plasma bulk, reaching finally the rear side of the target and escaping from its surface. Consequently a negative charged sheath and an electrostatic field normal to the target surface are produced and can thus accelerate ions. Protons which are situated on the target surface are the main accelerated population because of their relatively high charge to mass ratio respect to heavier ions, such as C. As the electrostatic field is very oriented and the proton acceleration needs a very short time to develop (on the order of the laser pulse duration, *i.e.* $\sim$ ps), the proton beam is thus emitted rather collimated. At this stage, if the proton density is not too high to modify the sheath field, one can draw a static model to calculate the acceleration of protons. Under this consideration, the sheath electric field at the rear surface of the target - for an hot electron temperature T_h - can be easily estimated as follows:

$$E_{s,rear} \sim \frac{T_h}{e\,L_s} = \frac{T_h}{e\,\lambda_{D,h}} \tag{5.10}$$

L_s is the extent of the charge sheath, assumed for a steep interface to be equal to the Debye length for hot electrons.

Another important parameter is the conversion efficiency η_h of the laser energy E_L into hot electrons. The evolution of η_h was previously plotted in Sec. 3 - Figure 3.3. Taking a laser irradiance $I_L\lambda^2 = 2\times10^{19}\,\mathrm{Wcm^{-2}\mu m^2}$, it yields $\eta_h = 25\,\%$ of laser absorption to hot electrons (Sec. 3 - Eq. 3.37). The hot electron temperature is then found to be $T_h \approx 1\,\mathrm{MeV}$ according to ponderomotive scaling law, by balancing the absorbed laser intensity by hot electrons $I_L\eta_h$ with their transported energy flux at critical density $\sim n_c T_h c$. It follows $E_{s,rear} \sim 42\,\mathrm{GV/cm}$. In place of taking the critical density n_c, the number N_h and density n_h of hot electrons in the sheath could have been more precisely estimated as follows:

$$N_h = \frac{\eta_h E_L}{T_h}, \qquad n_h = \frac{N_h}{c\tau_L \pi r_s} \tag{5.11}$$

r_s is the plasma sheath radius at the target rear, further estimated in Eq. 5.17.

This huge field will hold back most of the escaping electrons, ionize atoms at the rear surface and start to accelerate ions. Considering a test ion crossing such field, it would acquire the energy $\varepsilon_i \sim \alpha Ze E_{s,rear}\lambda_{D,h} = \alpha Z T_h$ resulting in MeV energies and scaling as T_h. The parameter α includes effects related to the target thickness. According to [251], $\alpha = L_L/(2L)$ being L_L the laser pulse length and L the target thickness. In thin targets, re-circulation effects have been proven to enhance the maximum proton energy by almost three times with respect to a thicker target [178]. Although re circulation efficiency is hampered by the angular spread of the forward-propagating hot electron beam, reflection of these electrons at the edges of the target contributes to maintain the charged-sheath hotter, denser and more homogeneous, increasing the maximum energy in the TNSA proton beam and containing its divergence [36]. One can note in Eq. 5.10 that $E_{s,rear}$ decreases if $L_s \gg \lambda_D$, meaning that a preplasma at the rear surface of the target would damp the ion acceleration. For this reason, the TNSA mechanism is always much more effective at the rear surface of the target where density gradients are steep, while at the front surface they are likely smoothed by prepulses.
In [167] authors reported consistently with Eq. 5.10, experimental observations of the interaction of ultraintense laser pulses using targets with and without preformed plasmas on the rear surface of the foil. The peak and mean energies of the proton beam were found to depend strongly on the plasma scalelength L_s at the rear of the target. No evidence of high energy protons was recorded when a large local scalelength in the ion density at the rear surface was induced.

There are two main categories of models which describe TNSA, namely "static" and "dynamic" models which, depending on the starting assumptions, allow to provide simplified analytic descriptions to be used to interpret experimental data. The acceleration of heavier ions populations on a longer time scale has been observed if the proton number is not high enough to balance the charge of the escaping hot electrons, and especially if impurity protons are removed before the interaction, for example by pre-heating the target [104, 102]. As seen before, a "static" model successfully describes light ions' acceleration in the early formation of the sheath, which is assumed to be stationary and unperturbed, effects of light ions on the electrostatic potential are usually neglected, while the heavy ion population remains immobile. Later, 'dynamic' models can account for the sheath temporal evolution. Ions can acquire kinetic energy and propagate with electrons in a quasi-neutral expanding plasma. Both models rely on an electrostatic, non-relativistic 1D fluid description of the ion dynamics, which is consistent with the highest proton energy experimentally found so far ($< 100\,\mathrm{MeV}$).

The 'dynamic' model approach is linked to the classic problem of plasma expansion in vacuum previously described for the nanosecond interaction regime in Sec. 4.2.

In the static assumption limit described before, solving Poisson equation for hot electrons one-temperature Boltzmann distribution and a single species of immobile heavy ions filling the $x < 0$ region with uniform density, gives:

$$\frac{\partial^2 \phi}{\partial x^2} = \frac{e\, n_0}{\epsilon_0} \left[\exp\left(\frac{e\phi}{T_h}\right) - \Theta(-x) \right]. \tag{5.12}$$

Θ is the usual Heaviside step function. The corresponding electron density, electric field, and energies of test ions moving in this potential can be calculated. The simplest self-consistent approach to solve Eq. 5.12 in the semi-infinite region $x > 0$ is given in [57]:

$$\phi(x) = -\frac{2T_h}{e} \left[\ln\left(1 + \frac{x}{\sqrt{2\mathrm{e}}\lambda_h}\right) - 1 \right]. \tag{5.13}$$

The electric field reaches its maximum at the surface and is given by (it corresponds to Eq. 4.18 for $t \to 0$):

$$E(0) = \sqrt{\frac{2}{\mathrm{e}}} E_0, \qquad E_0 = \frac{T_h}{e\lambda_D}, \tag{5.14}$$

which justifies the simple estimates made in Eq. 5.10. One can solve the consequent electric field from Eq. 5.13 for $x \geq 0$:

$$E(x) = \frac{T_h}{e\,\lambda_D} \frac{2}{\sqrt{2\mathrm{e}} + x/\lambda_D} = E_0 \frac{2}{\sqrt{2\mathrm{e}} + x/\lambda_D} \tag{5.15}$$

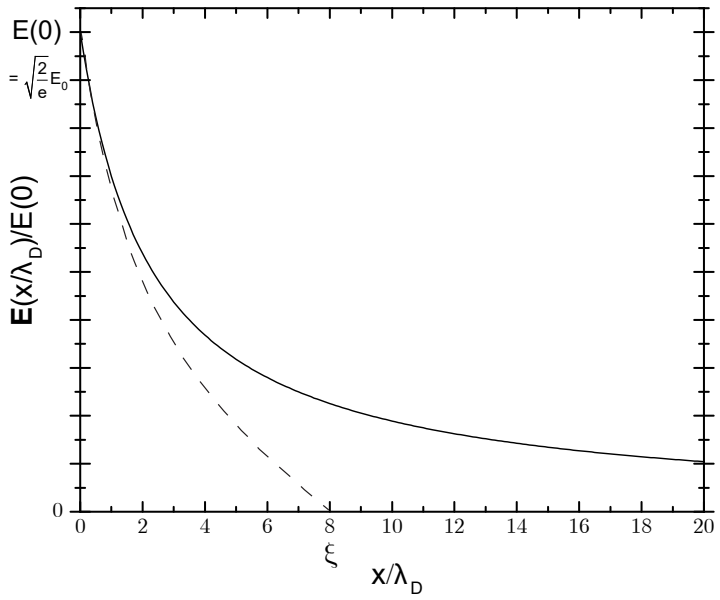

Figure 5.2 – Electric field in the vacuum region ahead of the surface, as obtained from formula Eq. 5.15 (solid line) and assuming a truncated electron distribution (dashed line) so that the electric field vanishes at a certain point (here at $x/\lambda_D = \xi = 8$).

The electric field obtained from this formula is plotted in figure Figure 5.2. One can note in Eq. 5.13, that the potential diverges at large distances (mathematically, $\phi \to -\infty$ if $x \to +\infty$). Therefore, a test ion would be able to acquire an infinite acceleration and it would then imply the existence of particles with infinite kinetic energy, which is not physically meaningful. This serious issue is related to the choice of a 1D Boltzmann relation ($n_h = n_0 \exp(e\phi/T_h)$): one would need an infinite electrostatic potential at large distances in order to not have an ion density converging to zero. To deal with this issue, different approaches keeping the uni-dimensional approach of the Boltzmann relation have been developed either by assuming an upper energy cut-off in the electron distribution function [164, 204], or by assuming that the hot electron population occupies only a finite region of a

certain width [203]. Both rely finally on breaking the indeterminate status of infinite distance or infinite energies. The latter model from [203] is also called "strong charge-separation field" (SCSF) model and more precisely describes the acceleration of a few light ions which are treated as test particles; this is in contrast to the TNSA model, which treats the accelerating ions as dominant species affecting the electron distribution. In this model, the energy gained by the light ion at position x_i along the target normal is:

$$\varepsilon_i = 2Z_i T_e \ln\left[\frac{C_I + x_i/\lambda_{D,0}}{\sqrt{2}}\right] \tag{5.16}$$

C_I is a constant approximately equal to 2.

Another possibility to overcome the infinite energy issue is to extend the dimensions of the Boltzmann equation, as explored in [246], assuming that the hot electrons' expansion in vacuum creates a cylindrical quasi-static cloud, behind the target, and a circular positive charge on the rear surface. The generated electrostatic potential is evaluated on the symmetry axis, along which the most energetic ions are accelerated. The total surface charge and the radius of the distribution are model parameters estimated from experiments. Especially, the plasma sheath radius r_s at the target rear surface is calculated assuming the ballistic propagation of the electrons from the front surface through the target of thickness l [239, 85, 127]:

$$r_s = r_0 + l\tan\theta \tag{5.17}$$

r_0 stands for the laser focal spot radius and θ is the half-divergence angle of the electron beam inside the target. The half-divergence angle is of the order of several to a few tens of degrees ($\theta = 8\,°$ [127], $\theta = 25\,°$ [85]). We proposed a fitted scaling law with laser intensity for θ in Eq. 3.47 - Sec. 3.2.2. Alternatively, in order to consistently overcome the previously discussed limits, Lontano *et al.* in [164] proposed to solve the Poisson equation by assuming that a quasi-stationary state is established where only *trapped electrons* with negative total energy $\varepsilon_h = mc^2(\gamma - 1) - e\phi$ are retained, while those with positive total energy are lost from the system. The corresponding trapped electron density, given by $n_h = \int_{\varepsilon<0} f_h(x,p)dp$, is included in the Poisson equation and the corresponding analytical solutions determined. As a general feature, which can be also encountered in our laser-pumped diode model in Sec. 9.3, the potential reaches a minimum value at a finite position x_f of the order of several λ_D. In this case, the potential, the electrostatic field and the electron density distributions go to zero at x_f. To conclude, the 'static' and 'quasi-static' approach allows to draw several general properties of the accelerating TNSA field. The spatial profile is characterized by very steep gradients, with the field peaking at the target surface and decaying typically over a few µm distance. The most energetic ions, accelerated in the region of maximum field, cross the sheath in a time shorter that the typical timescale for plasma expansion, electron cooling and sheath evolution. As a consequence, the static approximation will be more accurate for the faster ions produced by intense laser drivers of short duration, typically in the picosecond and subpicosecond regime. A description of ion acceleration over long times - and/or in conditions such that the "quasi-static" modeling introduced here is not valid anymore - demands for the inclusion of the ion dynamics. The description may be based either on a fluid modeling or on a kinetic one.

New acceleration mechanisms

With laser intensities higher than $5 \times 10^{19}\,\mathrm{W/cm^2}$, a very good laser contrast and very thin targets, a transparency acceleration regime can be reached. The main advantage of all the hereinafter presented mechanisms is the potentially more efficient conversion energy from laser to accelerated ions and higher energy for accelerated ion. While with a TNSA-like mechanism, only ions from the surface are accelerated, here, the acceleration is effective in the target's volume. It is particularly interesting for applications using ions of high energy with $Z > 1$. The accelerated species depend on the target chemical composition. Some theoretical studies have shown that with a target containing both protons and carbon ions, quasi-monoenergetic beams of protons and carbon ions can be accelerated. Yet, the corresponding dynamics with various species in the target has not been explored in detail. By pre-heating the target to remove protons of the target, a recent experiment shown that it optimized the acceleration of heavier ions (like it was the case in TNSA).

In 2009, Henig *et al.* [106] using a 30 nm-thick diamondlike carbon foil obtained C^{6+} accelerated ions up to 185 MeV (15 MeV/u). The invoked accelerating mechanism, called *BreakOut Afterburner*

(BOA) is induced by a relativistic transparency that permits the laser passing through the overdense plasma: a strong heating in the volume of the target is produced. The main acceleration of the ions occurs between a time t_1, when the target becomes relativistically transparent to the laser propagation ($n_e/\gamma_e n_{cr} \sim 1$, n_{cr} stands for the critical density) and a time t_2, when the target becomes classically underdense ($n_e \lesssim n_{cr}$). For the BOA mechanism, there is an optimized thickness to accelerate ions to higher energies when the laser pulse peak occurs between time t_1 and t_2. To trigger relativistic transparency and strong volume heating, the needed target thicknesses are typically < 700 nm. The highest ion energy is obtained along the perpendicular direction of the laser polarization. In 2013, two experiments put a milestone in C^{6+} ion acceleration by the BOA mechanism: in [125] they measured with a 200 nm-thick target 5×10^{11} C^{6+} ions between 33 MeV and 700 MeV-maximum energy (60 MeV/u), a conversion efficiency of 6 % and a half-angle divergence of $\approx 22.5°$; in [124], by a pre-heating of the target, they could accelerate C^{6+} ions to energies above 1 GeV (83 MeV/u). Effective proton acceleration was also performed in [103], $10^7 - 10^8$ protons with a maximum energy of 160 MeV were accelerated. The BOA mechanism has been confirmed by PIC 1D and 2D simulations and by an analytic model as discussed in the previously cited articles, and the experimental data are so far consistent with the simulations and models. It has been proved then that the BOA mechanism is able to increase significantly the accelerated ion energy and the conversion efficiency. The simulation showed for instance a reachable 250 MeV maximum proton energy using a laser intensity of 5×10^{21} W/cm^2.

Other mechanisms like Radiation Pressure Acceleration (RPA), Phase-Stable Acceleration (PSA) or Soliton-Driven Ion Acceleration appears to be dominant when the laser intensities are in excess of 10^{22} W/cm^2. For now, they have been reached only partially in experiments (at lower intensities) and do not compete yet with BOA mechanism or even TNSA. However, an acceleration of protons or ions based on these mechanisms could produce a peaked energy higher than BOA at the same laser intensity, as soon as the required laser intensities will be available. With actual laser intensities, experimental RPA with tick targets (hole boring) has shown an interest for applications requiring large numbers of ions at energy of only a few MeV.

5.2.2 Ion beam characterization

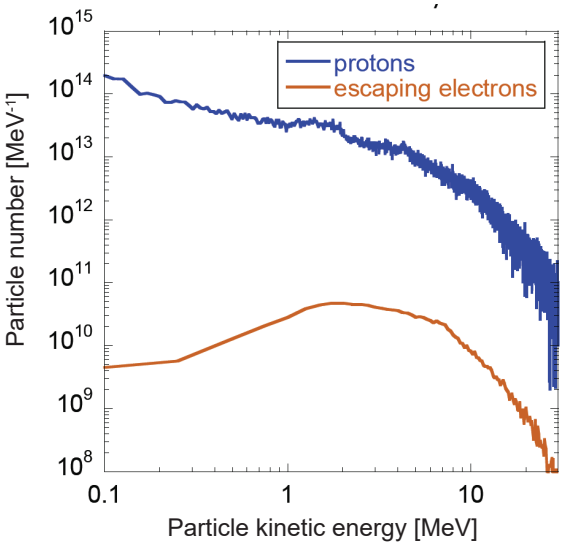

Figure 5.3 – Simulated energy spectrum for accelerated protons and electrons by TNSA mechanism at the rear-side of a 10 µm-thick gold foil, with LULI pico2000 laser parameters (50 J, $\sim 10^{19}$ W/cm^2). This is the typical spectrum of the proton source used in this thesis work. It was obtained by a PIC simulation performed by A. Morace (ILE, Osaka, Japan).

The energy spectrum of laser-driven TNSA ion sources have been measured in numerous experiments (*e.g.* in our experiment: Part III - Figure 11.5 using a Thompson Parabola spectrometer). The spectrum is typically broadband, high flux, significantly divergent, up to a cut-off energy. The particle number per MeV can be roughly approximated by a quasi-thermal distribution with a sharp

cut-off at a maximum energy (see [86, 127] for reference), which scales with the laser parameters. A typical energy spectrum - obtained from a PIC simulation performed by A. Morace (ILE, Osaka, Japan) - is also given here in Figure 5.3 and corresponds to the short-pulse laser parameters used in our experiments in LULI.

Experiments have reported spectral observations for a wide range of laser and target parameters, and partial surveys have been provided in a number of publications [84, 300]. Experimental studies have also been devoted to the investigation of the spatial and angular characteristics of the emitted beams. These latter are closely dependent on the electron sheath spatial distribution, and consequently on the target properties (resistivity, surface roughness, etc.) affecting the electron propagation.
The beams are produced at the rear target surface with a source diameter many times larger than that of the laser irradiation area, up to a few tens of even hundreds of µm. The beam is diverging, and it appears that it comes from a spot with a typical diameter of less than 10 µm called virtual source and located behind the real larger source of target's surface. The higher energy component is situated closer to the beam axis [255]. In [236] and [200], the authors have shown the comparison of experimental results obtained at several relatively high-energy laser installations : the particle energy gradually decreases as the radial distance from the beam axis increases; in other words, the proton beam divergence decreases at higher particle energies. Similar properties of the proton beam can be found in experiments using smaller energy and lower intensity lasers [198].

The most significant feature of the laser-driven ion beam is its ultra-high peak power in a short time period. Another feature is that the acceleration length is extremely short, leading to a potentially very compact source. Further, in contrast to the conventional (RF-based) ion sources, due to the charge neutralization by co-moving electrons [55], the space charge effect does not limit the current density. Therefore, a low voltage and high current density ion source can be implemented. For example, a picosecond proton beam which contains $> 10^{10}$ protons was demonstrated [56]. Such a beam has never been achieved by any other type of accelerator.

Nevertheless, the stability of the laser-driven ion sources remains an issue. For practical applications, fluctuations in the ion energy spectrum, position of the virtual source, its size, angular beam profile and other properties of the source and possibly beam transport system should be characterized precisely shot by shot and reduced to the required level. It is important to note however that most of these fluctuations are directly correlated with laser spot fluctuations. A more characterized laser spot would certainly lead to more controlled properties of the laser-driven ion source.

The beam power and intensity of laser-driven ion sources, and their dependence on the distance from the target, can be estimated. It is a key issue for many applications. For example, the beam power formula relevant to fast ignition by the ion beam can be found in [110]. Considering a diverging beam from a point-like source, which is the ordinary case of laser-driven beams, a formula for current intensity and density should incorporate the beam divergence effect. In the simplest case of a quasi-monoenergetic beam, the divergence is approximately constant, in which case the maximum beam current intensity I_{max} is given at the distance d by:

$$I_{max} \approx 4\sqrt{\frac{\ln 4}{\pi}}\frac{W}{d\Delta_0}\sqrt{\frac{\epsilon_0^3}{m_i}}\frac{1}{2\pi d^2(1-\cos\theta)} \tag{5.18}$$

where ε_0 and W are respectively the mean and total kinetic ion energies, Δ_0 is the energy spread (FWHM) and θ is the half-divergence angle (under approximation that $\theta \ll 1$). One can note that the beam intensity decreases as $1/d^3$ and is globally divided by $\approx \theta^2$ due to the beam divergence.

To finish, the laser-driven ion sources are strongly impaired with the electron transport behavior in the target. It was observed relatively early on that the use of conducting targets leads to smooth proton beam profiles with a sharp boundary while using dielectric targets creates inhomogeneities in the proton density across the beam section. In the dielectric case, the transport of the electron current is prone to electromagnetic instabilities, which break the hot electron flux into filaments. The close correlation between proton beam properties and electron beam transport characteristics has indeed been exploited in a number of experiments, which have used the proton beam as a diagnostic for the electron beam behavior inside the target, revealing, beside the aforementioned differences related to the target conductivity [85], effects on magnetic collimation on the beam transport [92, 298] or the role of lattice structure in dielectric targets [177]. The surface roughness was studied in [234] as well as intensity modulations in focal spot in [85].

5.2.3 Radiography and field measurements with laser-driven ions beams

The use of ion beams, and particularly proton beams, for radiographic applications was first proposed in 1960s [145]. Quasi-monochromatic beams of ions from conventional accelerators have been used for detecting areal density variations in samples via modifications of the proton beam density cross-section, caused by differential stopping of the ions, or by scattering. Radiography with very high energy protons ($\sim 1-10\,\mathrm{GeV}$) is being developed as a tool for weapon testing [139]. The use in laser-plasma experiments of ion beams produced with standard accelerators is limited by the relative long duration of the produced ion pulses and the difficulties and high cost involved in coupling externally produced particle beams of sufficiently high energy to laser-plasma experiments. The unique properties of protons from high intensity laser-matter interactions, particularly in terms of spatial quality and temporal duration, have opened up a totally new area of application of proton probing or radiography with laser-driven ion beams. As seen in Sec. 5.2.1, the protons emitted from a laser-irradiated foil by TNSA can be described as emitted from a virtual, point-like source located in front of the target [32]. A point-projection magnifying imaging scheme is therefore automatically achieved and set by the geometrical distances at play. The proton beam as a backlighter yields a spatial resolution of a few µm. Moreover, a special arrangement of a multilayer detector, employing RCFs (Sec. 18) for example, offer the possibility of energy-resolved measurements, despite the broad spectrum, by energy discrimination consequent to the localized energy deposition (Bragg peak) characteristics of the ions in matter (Sec. 18.1). More precisely, as the detector performs spectral selection, each RCF layer contains, in a first approximation, information pertaining to a particular time, so that a "movie" of the interaction made up of discrete frames can be taken in a single shot (as shown in Sec. 11.1.1). Depending on the experimental conditions, 2D proton deflection map frames spanning up to 100 ps can be obtained. The ultimate limit of the temporal resolution is given by the duration of the proton burst at the source, which is of the order of the laser pulse duration. Proton radiography, as a density diagnostic, has been successfully used to study the various stages of the compression of empty CH shells under multi-beam isotropic irradiation at the moderate intensity of $10^{13}\,\mathrm{W/cm^2}$ [168]. Also, radiographs of cylindrically compressed matter [283] and of shock wave propagation [223] have been carried out.

Alternatively, very successful applications of proton probing related to the detection of electric and magnetic fields in plasmas [31, 169], or in vacuum (as investigated in this thesis work), have been performed. Proton probing with laser-accelerated protons has provided in this way novel and unique information on a broad range of plasma phenomena and discharge currents induced by lasers. The high temporal resolution is here fundamental in allowing the detection of highly transient fields following short pulse interaction. Two main techniques have been explored: *proton imaging* (*i.e* simple backlighting projection of the sample where deflections cause local modulations in the proton density n_p across the proton beam cross section) or *proton deflectometry* (thin meshes are inserted in the beam between the proton source and the object as "markers" of the different parts of the proton beam cross sections). These techniques have been used in our experiments and more details are given for laser-driven fields measurements in Sec. 7.2.2 and Sec. 11.1.1.

6 Mechanisms of target charging

6.1 Return currents

Let us consider for now an irradiated foil at laser intensities $> 10^{17}\,\mathrm{W/cm^2}$. Numerous hot electrons are generated in intense laser-solid interactions and lead to the production of significative return currents in the plasma. One can distinguish two types of return currents. The first one appear when the fast electron beam crosses the target bulk. It is the neutralization process already discussed in Sec. 3.3.2, that appears inside the target and in the plasma plume expanding in vacuum. The second one, which is of interest here, is due to the loss of some hot electrons which have enough kinetic energy to escape from the target sheath potential, leaving a net positive charge on the target [16]. An intense electric field $E_s \sim k_B T_b / e\lambda_D$ of the order of several MV/µm is created in the charge separation layer over a distance comparable to the Debye length λ_D. This electric field is responsible for the creation of a force which tends to re-inject electrons into the target. It explains that only a fraction of electrons which have a sufficient energy $\gtrsim E_s\lambda_D$ are able to escape the intense charge separation field and propagate into vacuum [275]. If the return current can respond quickly to the charge imbalance, more hot electrons can consequently be emitted from the plasma and the target keep on charging, as long as the laser pulse is able to produce new hot electrons. The return currents are composed of electrons from the conduction band in metals or by thermal electrons issuing from field or collisional ionization in insulators. It is worth noting that in the case of very intense laser pulse and thin targets, the ejection occurs both on front and rear side of the targets.

6.2 Transient target charging

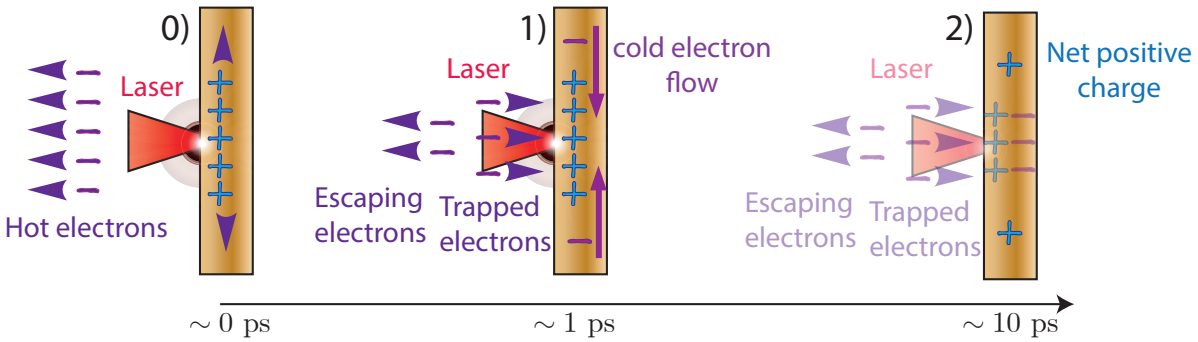

Figure 6.1 – Illustration of the transient charging at the front side of a metallic foil irradiated at high laser intensities. For a thin target, the process also takes place at the target rear side. If the laser pulse duration is longer than the transient time scale represented here, the process will be iterated as long as the laser pulse accelerates new electrons. A steady-state regime is reached for long laser pulses.

The transient target charging process is illustrated in Figure 6.1.

0) & 1) : As a consequence of the electron cloud expanding in vacuum, an uniformly positively charged disk expands radially on the target surface. The net positive charge recalls a return current from the regions around the laser-irradiated area, and whose rise time, which depends on the target inductance, has been estimated to tens of ps [16]. Simultaneously, the motion of hot electrons within the target, due to the target resistivity, gives rise to an electric field which damps the net positive charge expansion. As a consequence, the net positive charge expansion velocity is less than speed of light and has been measured to be $0.75c$ in metallic foils [176]. When electrons reach the target edges, where the return current can no longer be supported, a net negative charge is building up. A flow of cold electrons is then driven inward the target.

2) : After charge redistribution process, a net positive charge is left at several mm far from the laser-irradiated area. The net positive charge can then eventually be neutralized by electrons provided by the target mount connected to the ground.

We denote here as transient, in opposition to steady-state, a regime where the hot electrons are heated quasi-instantaneously in respect to the characteristic time of the target charge balancing. It is valid for pulse durations of ps or shorter. For longer pulse durations, the laser continuously heats new electrons while the charge balancing is operating, the transient regime is looped and a steady-state regime is obtained.

A modeling for the estimated charge left on the target during this transient process has been performed by Poyé *et al.* [70, 216, 215] at the CELIA laboratory, also based on experimental measurements. A general description sketch of the model parameters is given in Figure 6.2.

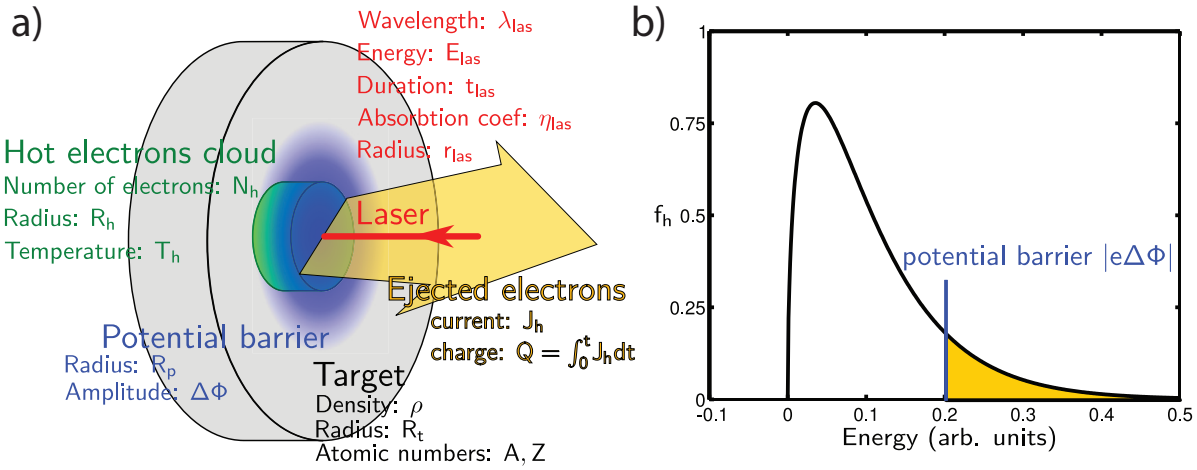

Figure 6.2 – a) Scheme of target charging by laser and the key interaction parameters. **b)** Hot-electron distribution function and the potential barrier ϕ. *Figures taken from [215].*

The laser heating accelerates hot electrons, and assuming a linear production of hot electrons within the time duration of the laser t_{las}, the total number of hot electrons N_{tot} reads:

$$N_{tot,0} = \frac{\eta_{abs} E_L}{\varepsilon_m} \tag{6.1}$$

where η_{abs} is the absorption efficiency of laser energy to electrons and ε_m is the average initial hot electron energy, defined as $\varepsilon_m = \int_0^\infty \varepsilon f(T_0) d\varepsilon$ with T_0 the initial hot electron temperature and f their energy distribution function, normalized to 1. E_L is the total laser energy deposited on target.

The hot electron production rate is estimated as:

$$\frac{\partial N_h}{\partial t} = \frac{N_{tot,0}}{t_{las}} \tag{6.2}$$

We assume that the hot electron average energy and temperature are constant during the injection period. The collisions between hot and cold electrons in the plasma bulk induce energy transfer from the former to the latter.

The number of hot electrons N_h decreases according to:

$$\frac{\partial N_h}{\partial t} = -N_h / t_{life} \tag{6.3}$$

and t_{life} is equal to the mean free flight time (t_{ee}) plus a cooling time (t_{cool}). The cooling time is defined as the time needed through collisions for an electron of temperature T_0 to slow down till $0.01 T_0$. After the end of the laser pulse, the laser does not maintain anymore the temperature of new hot electrons: there is a cooling of the initial hot electron temperature and one has to take into account this decrease. We consider that:

$$\frac{\partial T_h}{\partial t} \approx -T_h / t_{ee} \quad \text{if} \quad t > t_{las}, \tag{6.4}$$

The ejection current is also responsible for the reduction of the number of hot electrons in the cloud by the term $-J_h/e$. For the rest, the coupling existing between N_h and N_{tot} strongly depends on the ratio t_{life}/t_{las}.

Summarizing the full set of equations describing the evolution of the hot electron cloud, we have:

$$\frac{\partial N_h}{\partial t} = \frac{N_{tot}}{t_{las}} - \frac{N_h}{t_{life}} - \frac{J_h}{e} \quad \text{if} \quad t \leq t_{las} \tag{6.5}$$

$$\frac{\partial N_h}{\partial t} = -\frac{N_h}{t_{life}} - \frac{J_h}{e} \quad \text{if} \quad t_{las} < t \leq t_{las} + t_{life} \tag{6.6}$$

$$\frac{\partial N_h}{\partial t} = -\frac{J_h}{e} \quad \text{if} \quad t > t_{las} + t_{life} \tag{6.7}$$

The general case is given above but we can consider two asymptotic regimes:

- ◇ When $t_{las} \ll t_{life}$, we are in a *full ejection regime*, where the electron average energy is higher than the potential barrier and $N_h \approx N_{tot,0}$. Obviously it concerns very short laser pulses, delivering logically less laser energy for the same laser intensity. Consequently, even if all electrons are able to escape and are contributing to the ejection current, their number is reduced.
- ◇ When $t_{las} \gg t_{life}$, we are in a *steady-stage regime* where an equilibrium is reached. The laser energy is rather large and the ejection charge is very small compared to the total charge. This equilibrium is then close to the one obtained neglecting the ejection current in the above equations, and in this case $N_h \approx N_{tot,0} t_{life}/t_{las}$. Also, as the temperature is constant and the cloud is sustained, the thermal potential can thus be considered as constant.

The ejection current is emitted over a surface of πR_h^2 with R_h the electron cloud radius:

$$i_h = e\,\eta_{ej}\,\underbrace{\frac{N_h}{\pi R_h^2 (R_h - r_{las})}}_{n_h}\,\underbrace{\pi R_h^2}_{S_h}\,\underbrace{\int_{e\phi(n_h,T_h,R_h)}^{\infty} f(T_h) v_h d\epsilon}_{<v>_h} \tag{6.8}$$

with η_{ej} the proportion of hot electrons in the cloud (N_h) having sufficient energy to escape the potential barrier. This factor is calculated by calculating the ratio of moments over the Maxwell-Jüttner distribution of hot electrons. The volume of the electron cloud is considered here as a cylinder of section S_h having a height $R_h - r_{las}$. The height formulation is taken so as to be zero at $t = 0$ (where we initialized $R_h = r_{las}$). An important parameter here is the rise of the target potential barrier $\phi = \phi_{th} + \phi_{el}$ from the contribution of a thermal potential (ϕ_{th}) and an electrostatic potential (ϕ_{el}). Both are extensively described in [215] and correspond respectively to the potential created by charge separation at the target surface and the one created by the positive charge at the surface of the target, left by the current of ejected hot electrons. The model take into account the time evolution of those two potentials to calculate consistently the dynamic of the transient charging process.

An adaptation of this model to longer laser pulses and in the particular case of capacitor-coil targets will be given in Sec. 9.3.

An heat map is given in Figure 6.3 to calculate the order of magnitude of the total ejected charge for different set of laser energy and durations.

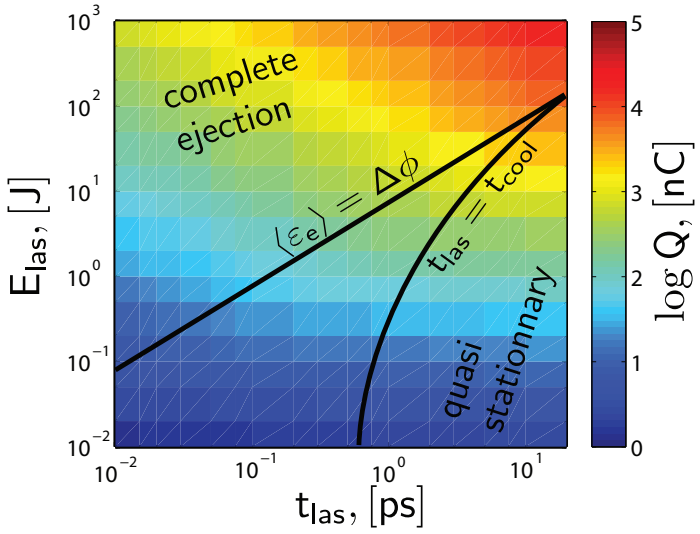

Figure 6.3 – Expected total target charge in logarithmic scale calculated from the model of Poyé *et al.* , in function of the laser energy and pulse duration for $r_{las} = 6\,\mu m$, $\eta_{abs} = 0.4$ and $\lambda_{las} = 0.8\,\mu m$. *Figure from [216]*

6.3 Transient target charging measurements

6.3.1 EMP generation

The return current from the target holder is able to generate strong EMP in short-pulse laser experiments. During the electron ejection, the cloud of hot electrons and the positive charge induced on the target surface by the electrons act as a time-varying electric dipole. Then, the return current from the target-holder forms a new dipole with its mirror charge on the opposite side of the ground plate. The dipole configuration is responsible in both cases of an EMP generation with the system viewed as an antenna. It is important to mention that the EMP can reach very high values when considering large PetaWatt lasers, exceeding 1 MV/m, which could be very destructive for any electronic device in the target chamber. The dipole built on during the laser irradiation yields THz radiation, which is out of the scope of the experiment diagnostics and not critical for electronic devices.

To validate the previously introduced model of transient target charging, experiments were carried out at CELIA laboratory in the Eclipse laser chain. The laser is a Ti:Sapphire with a central wavelength of 807 nm which was focused to a Gaussian focal spot of 12 µm-FWHM at normal incidence on the flat surface of a cylindrical (10 mm-diameter, 3 mm-thick) target of either Copper, Aluminum or Tantalum. Both the energy on target [20 mJ $\leftrightarrow$ 80 mJ] and the pulse duration [30 fs $\leftrightarrow$ 5 ps] were varied on each type of target.

The experimental setup, shown in the left panel of Figure 6.4, was composed of the above-described target supported by a brass wire of 1 mm-diameter fixed to a connector located in the middle of a large metallic ground plane of 20 cm $\times$ 20 cm. With such a system, we could directly connect the brass wire to the core of a coaxial cable and fix the distance between the target side and the ground plate to $l = 4.5$ cm. The coaxial cable is then connected with a 60 dB attenuation to a 6 GHz bandwidth oscilloscope to measure the charge current I circulating in the target. The integration of this current provides the charge of the target generated by the laser pulse interaction. To measure the antenna radiation, a magnetic probe (B-dot probe) was set behind the target at a distance of 225 mm from the target center (46 mm top and 90 mm right with respect to the laser axis).

In the right panel of Figure 6.4, one can see the FFT of the raw current signal (a) and of the raw B-dot signal (b). Despite the various laser parameters and target materials used, all electric current and magnetic field spectra present the same main frequency $f_{exp} = 1.0 \pm 0.1$ GHz. This can be explained by considering the target-holder system as a dipole antenna where the ground plate plays the role of

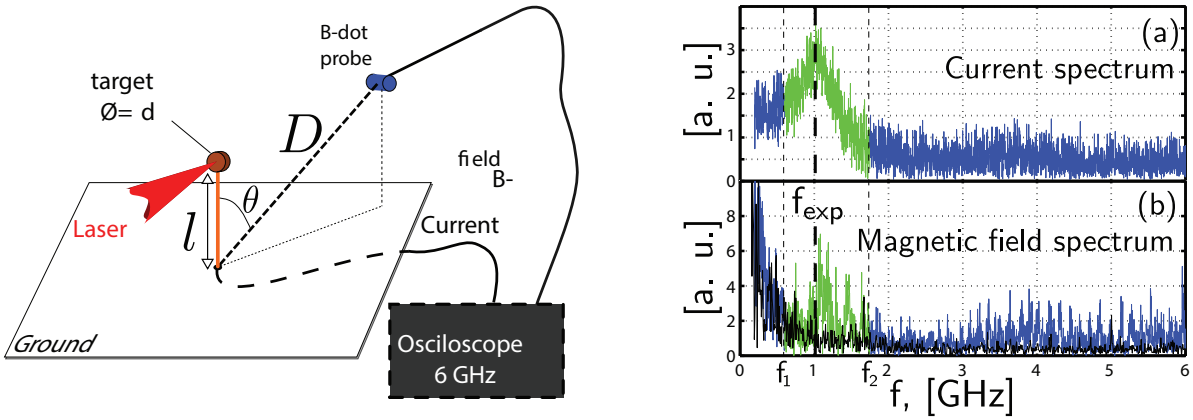

Figure 6.4 – Left: sketch of the experimental set-up ; **Right:** Typical signal spectra for (a) the current and (b) the magnetic field, $f_{exp} = 1.0 \pm 0.1\,\mathrm{GHz}$, $f_1 = 0.6\,\mathrm{GHz}$ and $f_2 = 1.7\,\mathrm{GHz}$ for all experimental points. The black signal is the integration noise. *Figures taken from [216]*

charge mirror. In that case, the emission frequency is given by:

$$f_a \approx \frac{c}{4(l + \pi d/2)} = 1.2\,\mathrm{GHz} \tag{6.9}$$

The target-holder system is assimilated to a stalk of a length which equals the holder length plus half the target perimeter. This estimate corresponds fairly well to the measured frequency considering the antenna volume simplification made in this calculation.

The relation obtained between the experimental charge and magnetic field measurements is illustrated in Figure 6.5-c). The B-dot signal was filtered out from electromagnetic coupling with the target chamber by applying a bandpass filter around the characteristic antenna frequency (see frequency limits f_1 and f_2 in Figure 6.4). The filtered signal is then time-integrated and its maximum value is retained. Results with and without filtering are shown in Figure 6.5-c), respectively labeled "Copper, filtered signal" and "Copper". The closer agreement with the solid line from far field theory confirms that the system is well behaving like an antenna and is the energy source of the EMP generation.

A comparison of the transient charging model with the measured charge is shown in Figure 6.5-a) varying the laser energy and b) varying the laser pulse duration.

Based on the fair comparison obtained with experiments, model predictions were performed to estimate the order of magnitude of the emitted EMP on large PetaWatt lasers. The predictions are shown in Figure 6.6. The EMP magnitude would be particularly strong on Petal Laser and could deteriorate close electronic devices.

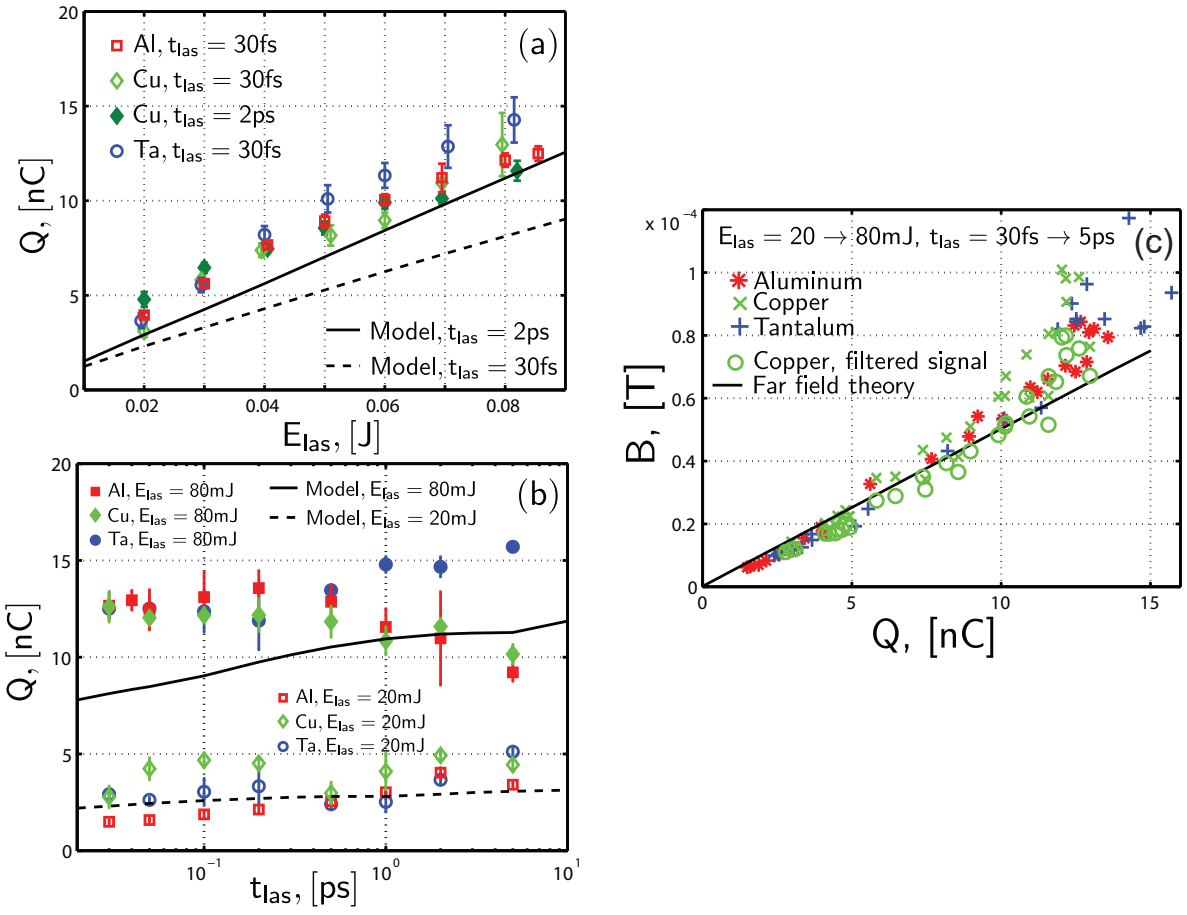

Figure 6.5 – Target charge in nC measured experimentally (dots) and calculated with the model (lines) as a function of laser energy E_{las} **(a)** and pulse duration t_{las} **(b)**, for different target materials. The points are averaged over 5 shots. The error bars are the standard deviation on these points. **(c)** is the maximum emitted magnetic field versus associated target charge for several laser parameters and different target materials. The experimental points are also the average over 5 shots. The points labeled "Copper, filtered signal" are obtained after isolating the antenna component signal (details in the text). *Figures taken from [216]*

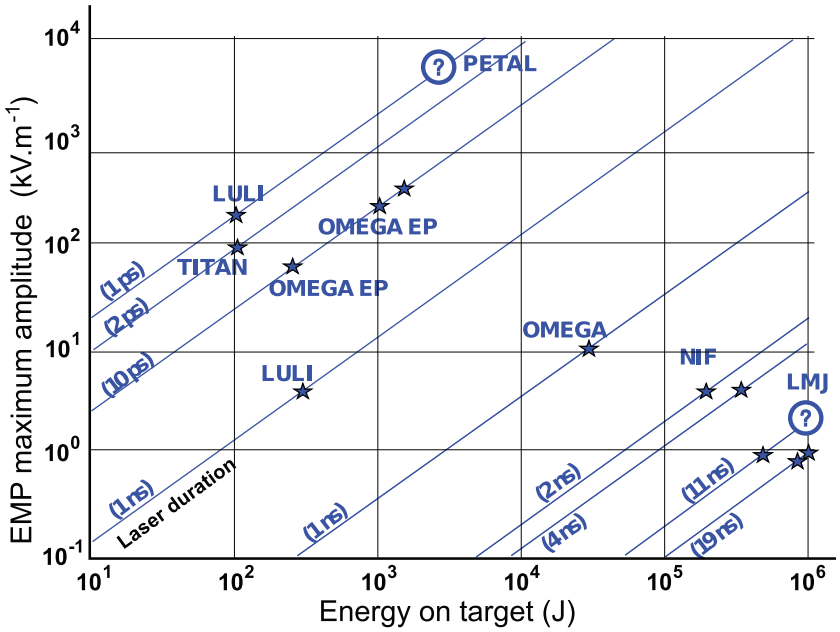

Figure 6.6 – EMP magnitude predicted by the transient charging model. The huge EMP on Petal would be prejudicial for the surrounding electronic devices. *Courtesy of A. Poyé.*

6.3.2 Proton imaging of the discharge

Transient charging of laser-irradiated targets has been investigated and reported during the past few years, firstly as an application of the laser-driven proton radiography technique. Briefly, the diagnostic employs the proton beam generated by the TNSA mechanism (see Sec. 5.2.1). The radiography technique uses it as a point-projection imaging scheme to detect electromagnetic fields in laser-plasma experiments. The charging of a laser-irradiated metallic wire was measured this way by Borghesi *et al.* [31], with the extra help of numeric simulations. The amount of charge was found to be $Q \sim 10\,\mathrm{nC}$, related to $\sim 10^{11}$ electrons escaped from the target. The rise time of the wire charging, $\sim 10\,\mathrm{ps}$, was explained with the early generation of escaping hot electrons by the prepulse preceding the arrival of the laser pulse peak.

Using the proton radiography technique with a time-resolving detector arrangement [219] (similarly used in our experiment Sec. 11.1.1), Quinn *et al.* [218, 220] diagnosed the propagation of the fields responsible for the wire charging and discharging, away from the laser interaction point. Using the same technique, they measured a front field velocity of $(0.95 \pm 0.05)c$. The electric field inferred by analyzing the experimental data allowed to obtain the net number of electrons flowing to the laser interaction point in order to restore the target charge neutrality. For instance, this estimation was found to be consistent with the estimated number of hot electrons escaped to vacuum from the potential barrier of the target, under the assumption of a charged emitting sphere. This simple model will be introduced here. If N_{ej} is the number of electrons which have already escaped from a charged sphere of radius R and charge $Q = eN_{ej}$, the minimum energy required for a new electron in order to escape the charged sphere is given by:

$$U_{ej} = e\frac{Q}{R} = \frac{e^2}{R}\frac{1}{T_h}\int_{U_j}^{\infty} N_0 \exp\left(-\frac{U}{T_h}\right) dU = \frac{e^2}{R} N_0 \exp\left(-\frac{U_j}{T_h}\right) \tag{6.10}$$

where T_h is the characteristic temperature of the assumed Boltzmann distribution for hot electrons. N_0 is the total number of electrons in the plasma ($N_0 = 4\pi R^3 n_0/3$). If the ratio of escaped electrons writes $\xi = N_{ej}/N_0$, it is found that:

$$\frac{\ln \xi}{\xi} = -\frac{1}{3}\left(\frac{R}{\lambda_D}\right)^2. \tag{6.11}$$

One has to additionally model the time-varying temperature $T_h(t)$, whose value decays after the end of the laser pulse.

The setup used in the wire charging experiment [220] is shown in Figure 6.7. The laser intensity is of $3 \times 10^{19}\,\mathrm{W/cm^2}$ and the wire has a thickness of 125 µm. Over a time window of ~ 20 ps, the wire is observed to charge and discharge, as it is visible from the deflections recorded on the RCF layers in Figure 6.7. A setup disposition with a tilted wire by 30 ° permitted to capture a larger time of the process and the field front velocity was estimated to be $(0.95 \pm 0.05)c$. Details about the resolution of such time-resolving proton radiography measurements will be given further in the thesis, in Sec. 11.1.1. Consistent PIC simulations in [220] also concluded that the current density is propagating within the skin-depth of the conductor, which is not surprising at those levels of excitation frequencies. In [276], the underlying physical process of the finite pulse propagation along the wire was further investigated and authors describe it as a Sommerfeld Wave, exhibiting a transverse mode propagation where the radial $\vec{E}$ and azimuthal $\vec{B}$ are the most important component. The wave behavior was further confirmed noting its reflection at the end of the wire. Finally, in [2], a dedicated setup to observe the pulse propagation over cm scale was used and confirmed that the wave stands over a long wire of a few cm, which is an important feature at the time of using the pulse for controlling and optimizing charged particle beams. On this basis, the use of such high discharge has been exploited to focus and transport charged particle beams. This technique has been explored in this thesis and our first results are detailed in Sec. 11.

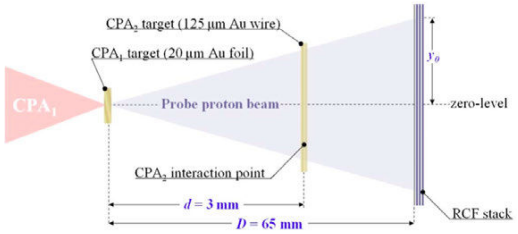

(a) Setup A, wire placed vertically. CPA 2 pulse strikes into the page.

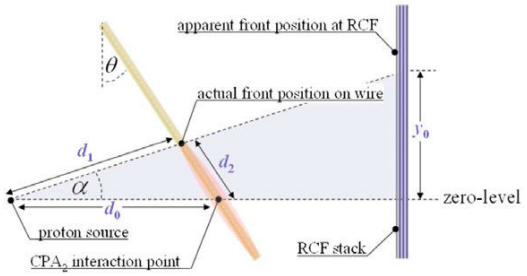

(b) Setup B, wire tilted by 30° to the vertical. CPA 2 strikes into the page.

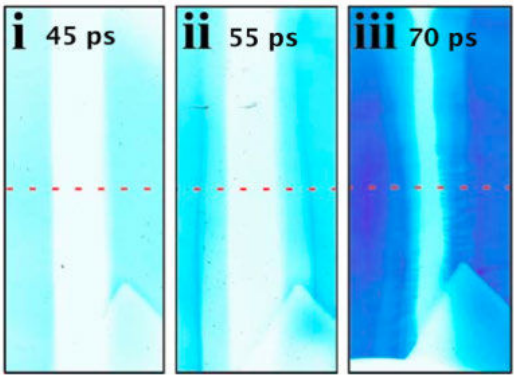

(c) RCF layers acquired with setup A. Probing times are also indicated.

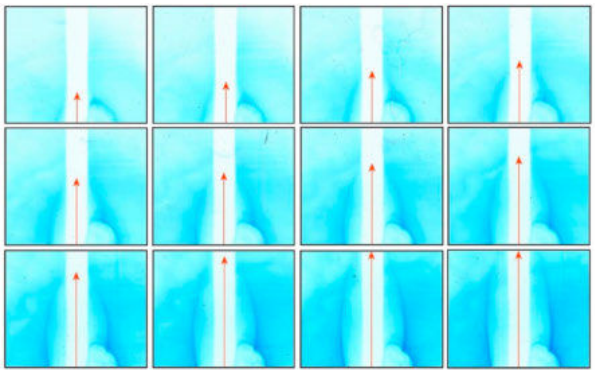

(d) Chronologically ordered RCF layers acquired with setup B. The red arrow highlights the front motion.

Figure 6.7 – Charging and discharging of the wire is observed in **(c)** with the experimental setup A sketch in **(c)**. There is an accumulation of the deflected protons on both sides of the wire at the probing time of 55 ps which evidences the charging of the wire. At latter times, these deflections are closer to the wire surface, meaning that the wire has discharged. With setup B, clear field front propagation is diagnosed. The bubble in the right bottom corner correspond to the CPA_2 interaction point. *Figures taken from [220].*

Part II

Novel platform for laser-driven strong magnetic field generation

Summary

7 The challenge of measuring quasi-static laser-driven strong magnetic-fields 96

7.1 Characteristics of the B-fields to measure . . . 97
7.2 Available diagnostics . . . 97
7.2.1 B-dot probe . . . 97
7.2.2 Proton Deflectometry . . . 100
7.2.3 Faraday rotation . . . 102
7.3 Conclusion on the presented diagnostics . . . 102

8 Characterization of magnetic field generation with different target materials and geometries 104

8.1 Measurements of the B-field in LULI laser facility . . . 104
8.1.1 Experimental Setup . . . 105
8.1.2 B-dot probe results . . . 106
8.1.3 Faraday Rotation results . . . 113
8.1.4 Proton Deflectometry results . . . 115
8.1.5 Shielded proton deflectometry . . . 131
8.2 Extra physical information from complementary diagnostics . . . 134
8.2.1 Shadowgraphy results . . . 134
8.2.2 Streak Optical Pyrometry (SOP) . . . 135
8.2.3 X-ray spectrometry . . . 137
8.2.4 Bremsstrahlung Canon . . . 140
8.3 Conclusion . . . 141

9 Semi-analytical model of B-field generation in nanosecond regime 143

9.1 A voltage-source model . . . 143
9.2 Improvement of the model . . . 146
9.3 Current-source approach : laser-pumped diode model . . . 150
9.3.1 Potential description (1D model) . . . 150
9.3.2 A 3D description of the potential and related issues of the 1D description . . . 153
9.3.3 Estimation of the maximum current of the diode in series with a resistance . . . 156
9.3.4 Model results . . . 158
9.4 Conclusions on the modeling . . . 161
9.5 Energetic qualifications . . . 162

State-of-the-art magnets nowadays allow generation of B-fields in the $10 - 300\,\mathrm{T}$ range, depending on their static/pulsed or destructive/non-destructive character. However, reaching, or exceeding the 1 kT level, as required for some high-energy-density or atomic physics applications, is much more challenging, unless resorting to large-scale Z-pinch machines or explosive experiments. Likewise, the heavy technical and infrastructure constraints posed by high-performance pulsed magnets (exceeding 100 T) make them ill-suited to the compactness of laser experiments. This motivates the development of portable, all-optical magnetic generators that may be easily implemented in any high-energy and/or high-power laser facility. Relativistic laser interaction with dense targets and the issuing intense currents over the target surface or into the target bulk can generate super-strong B-fields [208, 146], on the range of 10 kT for current short-pulse laser parameters, but these are rather transient (time scale of $\sim 10\,\mathrm{ps}$) and not located in a vacuum open space. Quasi-static magnetic-field production coupled to laser facilities has been explored so far by the development of capacitor-bank pulse discharges in solenoids (magnetic pulsers) [213, 82], but the specific physical limitations restrain the maximum generated fields to the range of $\sim 40\,\mathrm{T}$ (lowered to a more safe level of $\sim 20\,\mathrm{T}$ in usual operation). Moreover, this last technique still needs cabling, cryostat, and rather important dedicated space in the target chamber.

Instead, the use of powerful lasers interacting with so-called capacitor coil targets - first proposed by Korobkin *et al.* and Daido *et al.* back in the 1980s [147, 58], extended by Courtois *et al.* in 2005 [53], and recently explored to higher levels by Fujioka *et al.* [87] - give unprecedented quasi-static (time-scale of a few ns, longer than the laser pulse duration) high B-field amplitude for such a compact system (mm) and an energy laser pulse driver of 1 kJ. More information about previous studies of laser-driven magnetic field generation is given in Sec. 0.3.

Besides reaching high B-field strengths, advantages of laser-driven coil-targets is that they can be of relatively low cost if mass-produced and are adaptable to laser sources with higher repetition rate. More importantly, these coils have an open geometry providing easy access for several diagnostic views and to magnetize secondary samples eventually driven by secondary laser or particle beams. In this thesis part, we present an accurate characterization of the B-field produced by laser-driven capacitor -coil targets using three independent diagnostics, detailed in Sec. 7.2. This combination of diagnostics confirms that high power laser facilities may be used for B-field production in the range of several hundred Tesla with a controlled and reproducible rise time, peak value and spatial distribution. Before presenting the results of the different B-field characterization campaigns, we will introduce in the first section of this chapter, how the physicist can measure such strong B-fields that are localized in a small cubic mm, and surrounded by hardened X-ray radiation.

7 The challenge of measuring quasi-static laser-driven strong magnetic-fields

The use of high-power lasers generates X-rays and Electro-Magnetic-Pulses (EMP) that prevent us from using standard methods for probing the B-field. For instance, a standard pickup coil would hardly be perturbed or either blown up by the ionization from X-ray radiation. A Faraday rotator or all other kind of optical methods needing an optically transparent media are also very sensitive to hardened radiation under which they become opaque very fast. The EMP that can be generated by the target holder, acting as an antenna, or the EMP radiation of the laser irradiated area itself, are also issues for B-dot probe measurements.

Apart from this radiation environment - that we will evoke again in Sec. 7.2 - the characteristics of the B-field to measure, make by themselves, the probing procedure a challenging topic. Hereinafter, we will present the available diagnostics and we will conclude with their advantages and drawbacks.

7.1 Characteristics of the B-fields to measure

Here we will expose, on the basis of previous experiments results with laser-driven targets, the characteristics of the B-field produced by capacitor-coil targets or other kind of laser-driven loops' targets. We will focus on laser driver beams of several hundreds Joules energy at intensities higher than $10^{16}\,\mathrm{W/cm^2}$.

The B-field to measure in this context are called strong, but there are in fact very strong respect to standard methods of B-field production: we speak here about hundreds of Tesla. Such strong B-fields are obtained from several hundreds Joules of laser energy focused in a small metallic target, with pulse duration in the ns-scale. The dynamic of target heating and plasma expansion are playing a non negligible role in this regime. Hardened radiation and emission of fast particles are also produced consequent to the long-pulse (LP) interaction in this relatively high intensity regime. Additional electric field created by the space charge of the traveling charged particles is thus expected.

Although, the produced quasi-static B-field in loop targets will be dipolar-like and vanish very fast (typically as $1/r^n$ with n between 2 and 3) from the size of $\sim 1\,\mathrm{mm^3}$ where the magnetic field will be on the previously mentioned magnitudes. It means that the diagnostic will need to be sensitive and close enough to probe and yield a valuable signature of the B-field.

7.2 Available diagnostics

The precise and reliable measurement of the magnetic field is an important prerequisite for all applications. In the following part, we will focus on diagnostics that can be used to measure the magnetic field in our experiments, in the conditions we introduced just before.

7.2.1 B-dot probe

Field measurements

The most common method is to measure the voltage induced in a compensated pick-up coil. Such a pick-up coil is simply made of one or more turns of thin wire to form a definite area of the order of a fraction of $\mathrm{mm^2}$ to a few $\mathrm{mm^2}$. It has typically a very low inductance, and its response in the probe system is exactly described by the considerations found in *Appendix*, Sec. 16. The induced voltage is proportional to the time derivative of the enclosed B-field for B-field frequencies lower than the B-dot cut-off frequency (bandwidth). As seen in previous experiments, the produced B-field duration is of the order of the laser pulse duration and therefore the required bandwidth for the B-dot should be at least $> 1\,\mathrm{GHz}$ for a ns duration laser pulse driver.

In order to measure the signal of the field pick-up coil, several possibilities exist with regard to signal transmission (long or short cable, with or without matched termination) and in which form the signal should be digitized (directly or integrated). When devising such a system, one should keep in mind that due to the high field sweep rates, the induced voltage in typical high frequency B-dot probe can amount to values of several kV. Thus, termination with the cable impedance, which is in the order of $10^2\,\Omega$ ($50\,\Omega$ for a standard RG58 coaxial cable) may cause enormous currents. This is especially critical due to the high current load of the thin probe's wires and the subsequent high forces acting on the pick-up coil. Pick-up coils with much smaller area, which would reduce voltage and current, are also used for probing higher frequency fields. However, they experience the drawback that the uncertainty of the measurement increases due to the finite diameter of the wire in respect to the coil diameter, while reducing the coil area. It is worth noting that if the cable would be electrically short, *i.e.* if it is physically shorter than a quarter wavelength of the transmitted signals, matched termination may have been omitted and all the resulting problems can be avoided. Yet, such situation

is not practically feasible and one has to build or use an impedance matched circuit to avoid inaccuracy of measurements.

The second consideration concerns the actual measurement of the signal with an oscilloscope, by doing it directly using a voltage divider or after passing an integrator. In particular, the impact of high frequency components will be different. An ideal voltage divider matching the scope impedance does not change the distribution of the power spectral density. The output is thus attenuated by a frequency-independent factor. However, enormous voltage peaks may arise in the output if large slopes are present in the time derivative of the input signal. They can interfere with the scope and cause an overload. Strong, disturbing high frequency signals are often produced in laser-driven experiments, by resultant EMP generation by the target coupled to its target holder, acting as an antenna. They may easily exceed the intended B-field signature to measure and thus limit the resolution of the field measurement.

The use of an integrator could avoid some of these problems. The transfer function of an ideal integrator has a slope of $-6\,\mathrm{dB/octave}$ (or $-20\,\mathrm{dB/decade}$) and a constant phase of $-90\,^\circ$. Higher frequencies are thus damped in the output. Hence, the resolution can be improved by using an integrator. Nevertheless, problems may also originate from the non-ideal behavior of its internal parts in the high-frequency limit, so that the circuit no longer operates in this range as an integrator. Errors related to an RC integrator, which are caused by its finite time constant $\tau = RC$ make the integrator a part difficult to use for signal of frequency higher than 100 MHz. In our experiments, the measurement bandwidth was expected to be extended to 2.5 GHz and an integrator is not easily adapted in the measurement system at such high frequencies. The drawback of an integrator is also that no filtering is made for low-frequency and the integration will create a trend on the baseline. For these reasons, we made the choice to directly measure the B-dot signal after voltage division.

On behalf of this choice, high-frequency were limiting our signal-over-noise ratio. It was mostly the case when either an EMP was emitted by the target in the chamber, or when the selected sweep frequency and bandwidth of the scope were too high. Even though we loose the benefit of blocking high-frequency and use the full sensitivity for the scope, the filtering and integration was made afterwards numerically with the benefit in return of being able to do tests and trials.

Shielding of the Measurement System

When devising a complete measurement system, two strategies may be pursued to achieve a good signal-to-noise ratio and to obtain sensitive measurements. The first one is to construct the field generator and shield it in such a way that any possible or unwanted signal would interfere with the measurement system. The second one consists in shielding the measurement system in such a way that it becomes insusceptible to any unwanted external interference. While the first method has been implemented for instance for a single-turn coil system [190] or other pulse power systems by placing these systems completely in a large Faraday cage, it is only useful for equipment not located inside the Faraday cage. If there are any electrical probes inside the cage, the problem of suppressing unwanted interferences requires different approaches. In general four main mechanisms of interference to the measurement system can be distinguished:

- ◇ galvanic coupling (wiring),
- ◇ capacitive coupling (E-field),
- ◇ magnetic coupling (B-field),
- ◇ radiation coupling (E/B-field).

By means of operating the measurement system freely floating (or by connecting all the grounds together in a fine mesh), galvanic coupling can be safely avoided. The strength of the latter three mechanisms depends strongly on actual conditions. Owing to the operating conditions of the driver, for instance if the intensity of the laser beam driver is high, it is likely that capacitive and mostly radiation coupling may occur. If we are in presence of high currents, magnetic coupling can also play a major role. In order to reduce external disturbance, it is desirable to diminish the strength of all of these couplings. At the same time, the magnetic coupling is essential inside the field coil: it provides the magnetic field to the probe and should therefore not be reduced. This is the problem

that has to be solved for electromagnetic shielding in high strength and high frequency B-fields. It means that when the probe is close to the coil producing high B and high dB/dt, one has to provide an adequate reduction of capacitive and radiation coupling in the vicinity of the coil without diminishing the magnetic coupling. The magnetic coupling vanishes fast distant to the coil and in far-field, only radiation coupling (EMP) is present. Full shielding in both high B and high dB/dt can only be obtained by enclosing all parts of the system, including the pick-up coil and would need shielding techniques such as:

- ◇ thin-walled cylinders,
- ◇ slit cylinders,
- ◇ wire metals / wire conductors.

Measurement very close to the source, even with a perfect shielding is anyway not suitable in our experiments since the too high B would create harmful voltages in the B-dot probe. In our case, the B-dot probe was not probing very close to the coil and the magnetic field was measured instead at several tens of mm far from the coil, where the magnetic field drops to values in the range of a $\sim 100's$ µT to $\sim$ mT, which is still enough, for not too high dB/dt, to induce a magnetic coupling predominant over radiation and capacitive coupling. One has then to mainly solve the issue of galvanic coupling in this situation. We dealt with this issue by doing fine meshing of the grounds at various points of the measurement system and connecting all of them to a common ground of the chamber (to avoid ground loops of current within the measurement system). Moreover, the commercial B-dot probe Prodyn RB-230 has its cylinder head cast into an epoxy resin that prevent X-rays and Eddy currents in the conductive part. In high dB/dt cases, experienced when probing B-fields generated by very intense laser drivers of very short duration (picosecond or subpicosecond durations), additional aluminium shielding was used on cables and connections. The goal was to reflect external interferences and avoid them to penetrate the inner conductor of the coaxial transmission line to keep only the signal measured by the B-dot probe.

Concerning the data acquisition part, in order to suppress unwanted interference, the whole acquisition system was enclosed in a Faraday cage. To avoid any (unfiltered) electrical connections through the Faraday cage, optical signal transmissions via glass fibers should be preferred to trigger the scope. Also if possible, the Faraday cage should have a stabilized and filtered power supply, in this same philosophy of noise reduction.

7.2.2 Proton Deflectometry

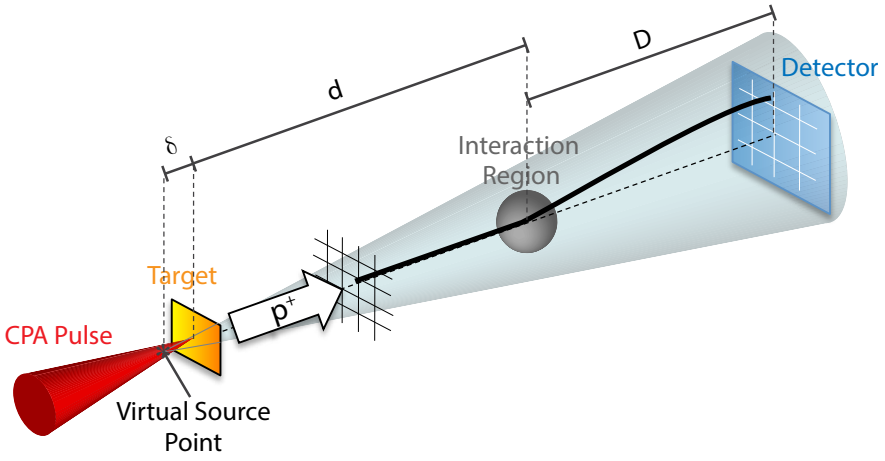

Figure 7.1 – Scheme of the typical experimental setup for proton radiography/deflectometry

.

The typical proton deflectometry experimental setup is shown in Figure 7.1. The short, ultra-intense laser pulse is focused on a metal foil; protons, produced at rear surface of the foil, via the TNSA mechanism (see Sec. 5.2), propagate in vacuum, in a diverging cone, towards the interaction region. Here, they are deflected either by electromagnetic fields or density gradients. After coming out from the interaction region, they ballistically proceed to the transverse detector. The detector was in our case composed of several Radiochromic films (RCF). This type of detector is described in Sec. 18 (*Appendix*).

The proton beam is emitted quasi-laminarly, with both transverse and longitudinal emittance between two and four orders of magnitude below what is obtained with conventional accelerators. Low longitudinal emittance is well explained by the fact that the bunch duration is comparable with the accelerating time in the target, which is on the same order of the laser pulse duration ($\sim$ 1 ps). Regarding the transverse emittance, its low value is due to the fact that once the protons propagate out of the metal foil, they are surrounded by the cloud of co-moving hot electrons, which contains the proton transverse motion. The protons are emitted by a virtual source which lies either ahead of the front surface or behind the rear surface of the metal foil, depending on the target geometry and laser parameters. For intensity regimes $\leq 10^{20}$ W/cm^2, the virtual source is usually located at $\sim$ 100 µm ahead of the front surface of the metal foil. Its dimensions can be estimated to be $\sim$ 10 µm in radius, so that the real source size at the rear surface of the foil has a radius between 10 and 100 µm (depending on the measured divergence of the proton beam) [32, 200]. In this way, the intrinsic spatial resolution of the proton beam is of the order of $\sim$ µm. Later on, it will be shown that this is not the only limit to the spatial resolution of the technique, as it has also to be compared with the detector resolution. For deflectometry, the field measurement spatial resolution is mostly limited by the minimum grid spacing to not experience blurring effect on the RCF imprint.

The divergence of the proton beam can be related to the spatial and angular properties of the accelerated hot-electron cloud, which in turn depends on the laser parameters, and more importantly, on the target characteristics. As protons are accelerated by an electric field perpendicular to the surfaces where the hot-electron density is more or less constant, then if these surfaces are bent (the bell-shaped profile of the sheath make an observable imprint on the proton radiographs themselves), protons will be emitted with a given angle. This latter depends also on proton energy since the electric field orientation changes with time and accelerate differently more energetic protons and slower ones [236].

The magnification imposed by the positions of the virtual source, real source, and detector is described by the following formula:

$$M = \frac{D + d + \delta}{d + \delta} \approx \frac{D + d}{d} \tag{7.1}$$

where, referring to Figure 7.1, d is the distance between metal foil and interaction region, D between interaction region and detector, and δ between virtual source and metal foil (it can be either positive or negative depending on the virtual source position with respect to the foil). In a typical experiment configuration, δ is much smaller than the other distances ($\sim$ µm against mm), the virtual position can be assumed to be on the rear surface of the metal foil, as it is approximated in the second expression in Eq. 7.1.

After being generated at the source, the divergent, laminar proton beam reaches the *interaction region*. Several mechanisms can affect the proton beam in this region: the protons can be deflected by electromagnetic fields, either generated by laser-plasma interaction [218, 219] or due to the mean electronic density of the media probed by the protons. When probing solid objects or overdense plasmas, scattering sets a limit to the spatial resolution attainable in the radiography. This is due to the mixing of scattered proton trajectories, which will produce a *blurred* image on the detector [168]. The spatial resolution can be improved by using more energetic protons, which result in a smaller scattering angle. In our case, there is just interest in detecting proton deflections outside solid objects, then this limitation is not anymore an issue. It would however raise an issue in an attempt of reducing strongly the mesh grid spacing, but it was not necessary either. Therefore, the trajectories of protons are modified only by electromagnetic forces created by currents and free charges and their motion is ruled by the Lorentz force:

$$m_p \frac{d\vec{v}_p}{dt} = e\left(\vec{E} + \vec{v}_p \wedge \vec{B}\right) \tag{7.2}$$

where m_p and $\vec{v}_p$ are proton mass and velocity and $\vec{E}$ and $\vec{B}$ are time-varying functions of the electromagnetic fields to be probed.

The detector we used in experiment, RCFs, are described extensively in Sec. 18 and especially the analysis procedure for proton-deflectometry measurements is given in Sec. 19. The RCFs are disposed in a stack to get information from different proton energies of the characteristic broadband spectrum of the beam. The energy spectrum is typically exponential-like with a maximum energy called cut-off (see Sec. 5.2.1). Due to the localized energy deposition of protons in matter (Sec. 18.1), a stack of RCF can be used to deconvolve the proton spectrum by the information contained in their dose profile (Sec. 18.3). The B-field to probe in our experiments has a duration > 1 ns, this is a lot longer than the proton beam bunch duration of ~ 1 ps and longer than the overall time-of-flight range of ~ 100 ps. In these conditions, consecutive layers of the RCF stack are probing the B-field in a time-range short enough to have low variations on the B-field magnitude. The benefit of the time-of-flight arrangement of RCF has been used in Sec. 11.1.1, where the electromagnetic fields are evolving at lower timescale. Since RCFs are actually sensitive to different types of ionizing radiation, optical density signal rising from electrons, X-rays and heavy ions is expected to be present too. However, electrons and X-rays stopping power is low compared to protons, and also their signal can be recognized in deeper layer of the stack, where no proton contribution is expected. When performing analysis which employs relative dose measurements, this constant background signal is immediately removed. As far as heavy ions are concerned, the RCF stack is usually wrapped with kitchen aluminium (~ 11 µm-thick) and sometimes an additional filter is put in front of the first layer, which is thick enough to prevent them from penetrating the stack and saturating the first RCF layer. The front filters also protects the RCF stack from target debris.

7.2.3 Faraday rotation

The Faraday rotation is the name given to the effect that rotates the polarization angle of an electromagnetic wave if this wave is propagating along a magnetic field. This effect occurs equally in any propagation media, and in solids it is characterized by the formula:

$$\alpha = VLB \tag{7.3}$$

where V is the Verdet constant (whose value is 11.35 °/T/m for Terbium Gallium Garnet (TGG) crystals, 38 times higher than that of SiO_2), L the length of light travel in the solid and B the magnetic field strength. More precisely, one has to point out here that the product LB is in fact a simplification for uniform B-field strength and more generally one has to use the B-field integral $\int \vec{B}\vec{dl}$ instead. Moreover, the Verdet constant is not a constant anymore when time varying B-fields are involved and significant temperature variation of the propagating medium occurs.

Apart from being a tool to measure magnetic field, the Faraday rotation is at the basis of optic isolation devices composed of a Faraday rotator coupled with a polarizer, used to allow light propagation in one direction only [278]. This is an important piece in laser chain to avoid any travel back of the laser light which would damage seriously the upstream laser chain. The Faraday rotation is also a well-known effect in magnetic fusion [153] and astrophysics [299]. The formulation in plasmas, assuming immobile ions [117], is:

$$\alpha = \frac{1}{2}\int XY\cos\theta\frac{\omega}{c}dl \tag{7.4}$$

with $X = n_e/n_c$, $Y = \omega_{ce}/\omega_L$ and ω_{ce} is the electronic cyclotron frequency, θ the angle formed between wave propagation and B-field direction and ω the wave frequency of the propagating wave.

7.3 Conclusion on the presented diagnostics

To conclude this section, we will recapitulate the features of the three main diagnostics to measure the B-field in our experiments. We began to describe the B-dot probe, also detailed technically in *Appendix*, Sec. 16. This diagnostic has the great advantage of being almost insensitive to electric field by construction and being sensitive enough to measure very low B-field of several hundreds of µT with high temporal and spectral accuracy. Of course this high resolution needs to be supported by a high frequency bandwidth measurement system (cables, oscilloscope, connectors). The hardened version we used is also very interesting to measure the B-field without being much affected by particle and radiation emission from the interaction. The major drawback of this diagnostic, in our case, is the probe size in respect to the size of the magnetic field source ($\sim$ 700$\times$ bigger in volume). Indeed, the induction of $\vec{B}$ on the probe axis is sensitive to both the spatial gradient of $\vec{B}$ and the varying orientation of $\vec{B}$ along the B-dot. Consequently, one may encounter significant B-field variations over the B-dot volume, inducing strong spatial uncertainties in the measurement. If the measure is made in far-field, $\vec{B}$ is more uniform and the probe size is not an issue anymore, however the dipole B-field strength rapidly decreases to similar level than parasitic EMP noise (one needs $B > 10^{-4}T$). A trade-off location has been found in our experiments at several cm far from coil center, yielding B-field values at B-dot position on the order of mT and relative errors of the order of 10 %. Another obvious drawback of this diagnostic is that it measures the B-field in only one distant point and rely then entirely on the accuracy of the related B-field distribution in order to extrapolate this value to another point, particularly to coil center position. The B-dot probe raw signals have also to be filtered and integrated. This process is sometimes difficult to handle due to the numerous origins of interference (as described in Sec. 7.2.1).

Concerning the Faraday rotation, the main advantage is that this diagnostic is totally insensitive to electric field, in a even more reliable way than B-dot probe. It is a versatile mechanism that can be also used to probe the magnetic field in underdense plasmas. The crystals can be cut in small pieces and it is then easier to position them near the source with less gradient issues than those arising for B-dot probing. Unfortunately, for our kind of B-field distribution to be probed, it is difficult to benefit from the small size of the Faraday rotator since it needs to be located very close to the source to have a measurable change in the polarization. In other words, even with good Verdet constant materials, small Faraday rotators are only sensitive to high B-fields (see Eq. 7.3). When getting closer

to the source, the uncertainties due to B-field gradients are becoming important, and besides that, another limitation is also emerging. This limitation raise from the fact that the Faraday rotator is not hardened like the B-dot probe from surrounding particles and radiation. The crystal turns opaque rapidly, notably under hard X-ray radiation produced by the energetic long-pulse interaction. This effect is hard to mitigate in experiments: even using coated tantalum shields to prevent direct exposure of the crystals from interaction point, the crystal was still darkening $\sim 0.4\,\text{ns}$ after laser interaction instant (the "blackout" is seen in the results Sec. 8.1.3).

The third presented diagnostic, Proton Deflectometry, is the only one that is able to probe directly the magnetic field without need of extrapolation from a far measure point. It also gives spatial field distribution around the source by the use of a mesh imprint. By using a stack configuration for the detector, one can extract a time-variation of the probed fields in a time-window of $\sim 100\,\text{ps}$ (for our TNSA probe beam characteristics). The use of a ballistic code coupled to magnetostatic computations in order to match the RCF imprint is for instance the more precise and reliable way to probe the strong B-fields created by small current-carrying targets. In return, it needs an extra intense laser source to generate the proton beam. Moreover, we will see also in the following that this diagnostic - intrinsically sensitive to both B-field and E-field (Lorentz force) - can be strongly perturbed by plasma effects occurring from energetic long pulse interactions.

In summary, there is not an ideal diagnostic. One can consider instead that the B-field diagnostics presented so far are complementary. The problematic of measuring strong localized laser-driven B-fields would consequently benefit from consistent measurements by those three different diagnostics. It is the intended purpose of the work presented in the next section.

8 Characterization of magnetic field generation with different target materials and geometries

8.1 Measurements of the B-field in LULI laser facility

The following experiments were performed at the pico2000 laser facility (LULI, France). This laser system offers the combination of a long-puslse (LP) beam and a short-pulse (SP) beam. The SP beam has a wavelength of $\lambda_L = 1.06\,\mu m$, a duration of 1 ps-FWHM and deliver $\approx 50\,J$ on target in a $\sim 12 \pm 2\,\mu m$-FWHM focal spot containing $\sim 40\,\%$ of the pulse energy, yielding a peak intensity of $\sim 1.5 - 3 \times 10^{19}\,W/cm^2$. The SP beam was used to accelerate protons by TNSA mechanism for proton deflectometry probing of the generated B-fields. The LP beam has the same wavelength ($1\omega_0$), 1 ns flat-top duration ($\approx 100\,ps$ rise-time), and delivers $500 \pm 30\,J$ in a focal spot of $\sim 12 \pm 2\,\mu m$-FWHM containing $\sim 30\,\%$ of the pulse energy, focused at peak intensity of $\sim 1 - 2 \times 10^{17}\,W/cm^2$. The LP beam is used as the driver for the B-field generation. The architecture of the LULI 2000 laser chain will be detailed in *Appendix* Sec. 14.1. In the herein section we will group together all the characterization of the generated B-field from the three experimental campaigns conducted at the LULI 2000 facility.

Box. 8.1: Laser parameters

In this box we will present the measured laser spot characteristics for both LP and SP beams. To measure the focal spot size, an imaging system is looking at focal point and a capture of the spot is made at lower energy into a CCD unit. The imaging system consists of a magnifying telescope system built with lenses. The magnification of the imaging system is previously calibrated with glass targets - such as µ-balloons or small tips - that are moved in the focal plane by known distances. First, the focal spot image is corrected from background noise. Afterward, a 2D Gaussian fit of the spot gives an estimate of its mean FWHM and the energy fraction that is encircled inside FWHM. Typical focal spots are shown in the following figure: panel **a)** for the LP laser beam and panel **b)** for the SP laser beam. By assuming a Gaussian 1D laser pulse shape of total energy E_l with HWHM spot radius r_0 and FWHM duration τ_0, the peak irradiance I_0 writes:

$$I_0 = 2\left(\frac{\ln 2}{\pi}\right)^{3/2} \frac{\eta E_l}{r_0^2 \tau_0} \approx 0.65 \frac{\eta E_l}{\pi r_0^2 \tau_0} \tag{8.1}$$

with η the ratio of experimental encircled energy inside FWHM divided by the ratio of encircled energy inside FWHM in a perfect Gaussian case (0.5). By applying Eq. 8.1 for focal spots of the bottom figure, one find peak intensities (or irradiance) of $1.4 \times 10^{17}\,W/cm^2$ for the LP laser pulse and $2.2 \times 10^{19}\,W/cm^2$ for the SP laser pulse.

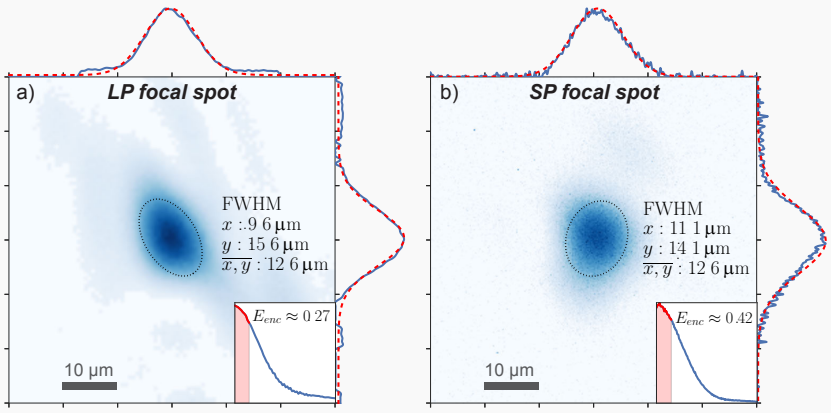

Figure 8.1 – Typical focal spot of **a)** LP laser beam and **b)** SP laser beam. The annotations of FWHM are obtained by a 2D gaussian fit. The insert is showing the azimuthally averaged radial profile with a 1D evaluation of the ratio of encircled energy over mean FWHM.

8.1.1 Experimental Setup

The B-field production targets were made of two parallel disks (3500 µm diameter, 50 µm thickness, with a hole in the front disk enabling the focus of the laser pulse into the rear disk's surface), connected by a coil-shaped wire (coil radius $a = 250\,\mu m$, squared rod section of $50\,\mu m \times 50\,\mu m$): see Figure 8.2. More dehapedtails on the manufacturing of these so-called capacitor-coil targets are given in *Appendix* - Sec. 15.

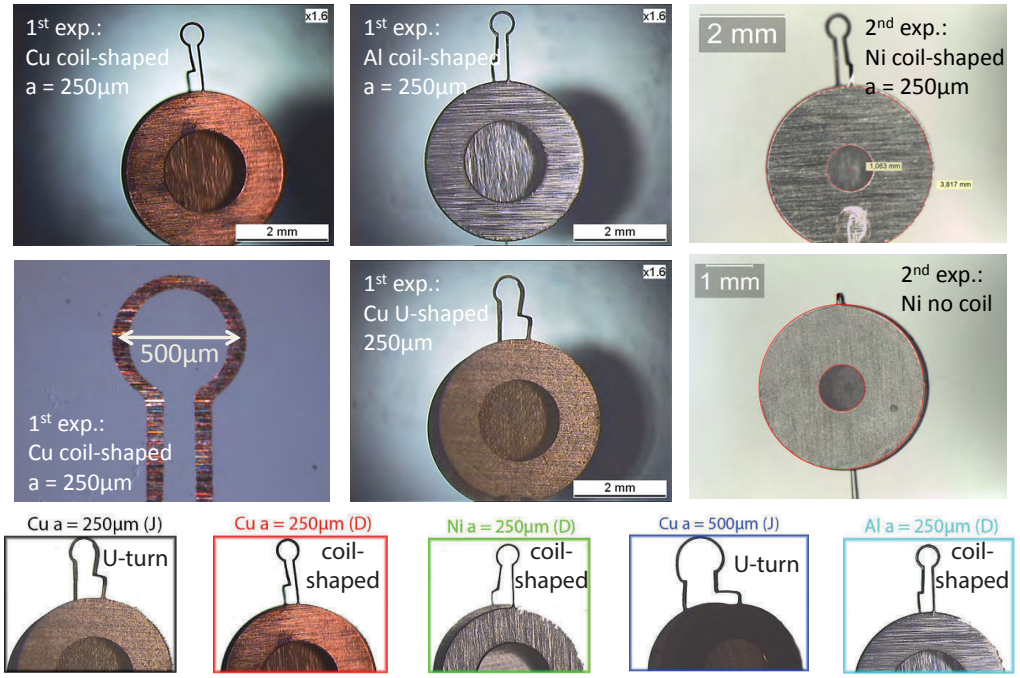

Figure 8.2 – Photographs of capacitor-coil target samples.

The B-field production targets were made of Cu, Ni or Al (1^{st} experiment, with a 1750 µm-diameter hole in the front disk), or exclusively of Ni (2^{nd} and 3^{rd} experiment, with a 1000 µm-diameter hole). The choice of Ni targets for 2^{nd} and 3^{rd} experiments was to avoid interference with K_α-fluorescence from a Cu tracer inserted in secondary targets (results presented in the next thesis chapter). The target parameters were reproducible within a $\pm 1\,\mu m$ precision thanks to accurate laser cutting of an initial 2D metallic sheet, the only effectively variable parameter being the distance between the disks, $d_0 = 900 \pm 200\,\mu m$, as a consequence of the manual target folding.

The laser pulse irradiates the rear disk passing trough the hole of the front disk and creates suprathermal electrons that can escape the potential barrier [70, 216]. A fraction of them may be captured by the opposite disk. The target reacts like an RL-circuit to the potential difference between the disks and the subsequent discharge current flows through the coil-shaped wire. The RL parameter of the external RL circuit are developed in the modeling section, Sec. 9.The laser-driven target charging and the discharge current process simultaneously (steady-state regime), during the laser-pulse irradiation, establishing a quasi-static current I looping in the space between the disks and in the connecting wire.

The coil, of radius a, concentrates the magnetic flux yielding a quasi-static, dipole-like B-field over a time-scale of a few ns. The amplitude of the B-field near the coil center scales like:

$$B_0 \approx \frac{\mu_0 I}{2a}, \tag{8.2}$$

where μ_0 is the vacuum permeability. The target geometry, namely the distance between the disks and ion dynamics from one disk to another, define the short-circuiting time of the system which is of the order of $1 - 2\,ns$. It happens when the plasma plume ejected from the irradiated disk reaches the opposite disk (the gap distance between the two disks is likely reduced by the front disk thermal expansion induced by x-ray irradiation emitted from the rear disk plasma). The short-circuit can also

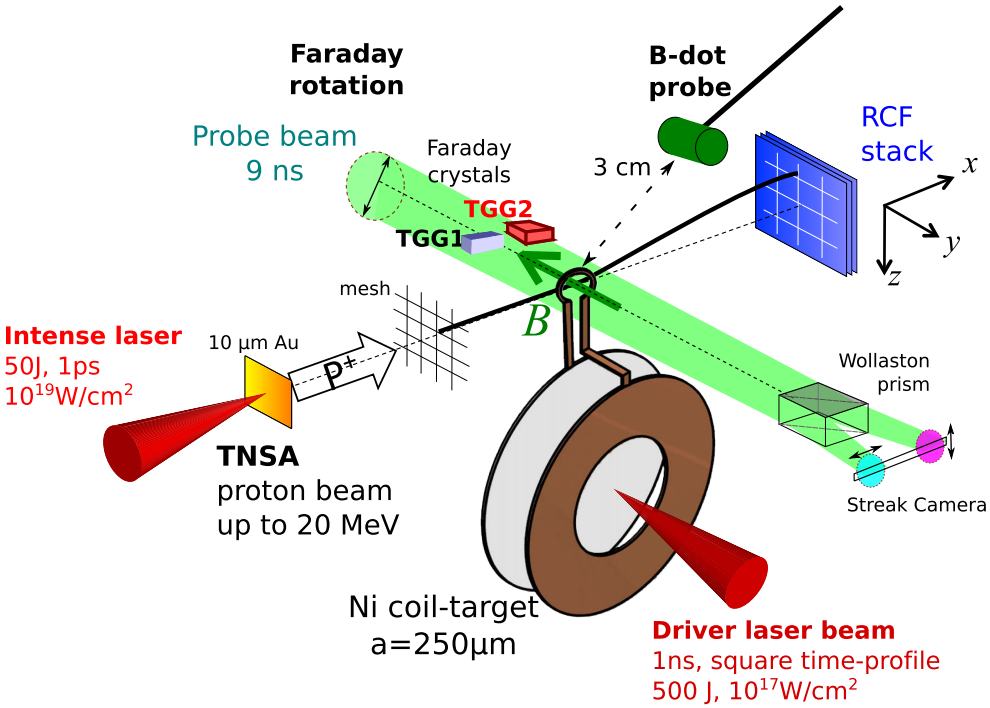

Figure 8.3 – Sketch of the experimental setup.

occur when thermally expanding conducting wires below the coil start to overlap. After this time, the potential difference between the disks drop to zero and the external circuit is freely discharging with RL characteristic time. If the system is still charging, the current will then preferentially circulate through the conductive plasma channel between the two disks. The experimental setup is sketched in Figure 8.3.

8.1.2 B-dot probe results

The B-dot probe axis was positioned parallel to the target's coil axis, either in the plane of the coil at 30 ± 0.5 mm distance from the coil center and at a 33 ° angle above equator (1^{st} experiment), or approximately along the coil axis at 70 ± 1 mm (2^{nd} experiment) and 60 ± 1 mm (3^{rd} experiment) distance from the coil center, with 10 ± 0.5 mm horizontal offset to clear the path for the probe beam used for Faraday rotation and shadowgraphy. The B-dot probe (and associated electronics) has a 2.5 GHz acquisition bandwidth, limited by cable connection adapters, and the chosen sampling frequency yielded signals with time resolution of 50, 6.25 ps and 25 ps respectively in the 1^{st}, 2^{nd} and 3^{rd} experiments. The measurement system is described in *Appendix* - Sec. 16.6.

Figure 8.4 details the analysis of a signal obtained in the 1^{st} experiment with a Cu capacitor coil-target of radius $a = 250\,\mu$m : **a)** a raw detected signal (attenuators excluded), proportional to the time-derivative of the B-field at the probe position (see Sec. 16.1), **b)** the signal corresponding power spectrum, calculated by the fast-Fourier-transform (FFT) of the signal (thick red curve; the thin black curve is the power FFT of the signal for $t < -50$ ps, that is the noise spectrum). Figure 8.4 **c)** and **d)** show the temporal evolution of the B-field, on the level of a few mT. This was obtained by integration of the signal in panel **a)** for different configurations of bandpass filtering: the optimized result, represented by the thicker red curves, was obtained with the minimum frequency of $f_{min} = 1$ MHz to cut the DC component and low-frequency $1/f$ noise, and a maximum frequency of $f_{max} = 1$ GHz to cut the high frequency parasitic EMP emission from higher frequency ground discharges current, still present in spite of using capillary insulator target-stalks ([70, 216]).

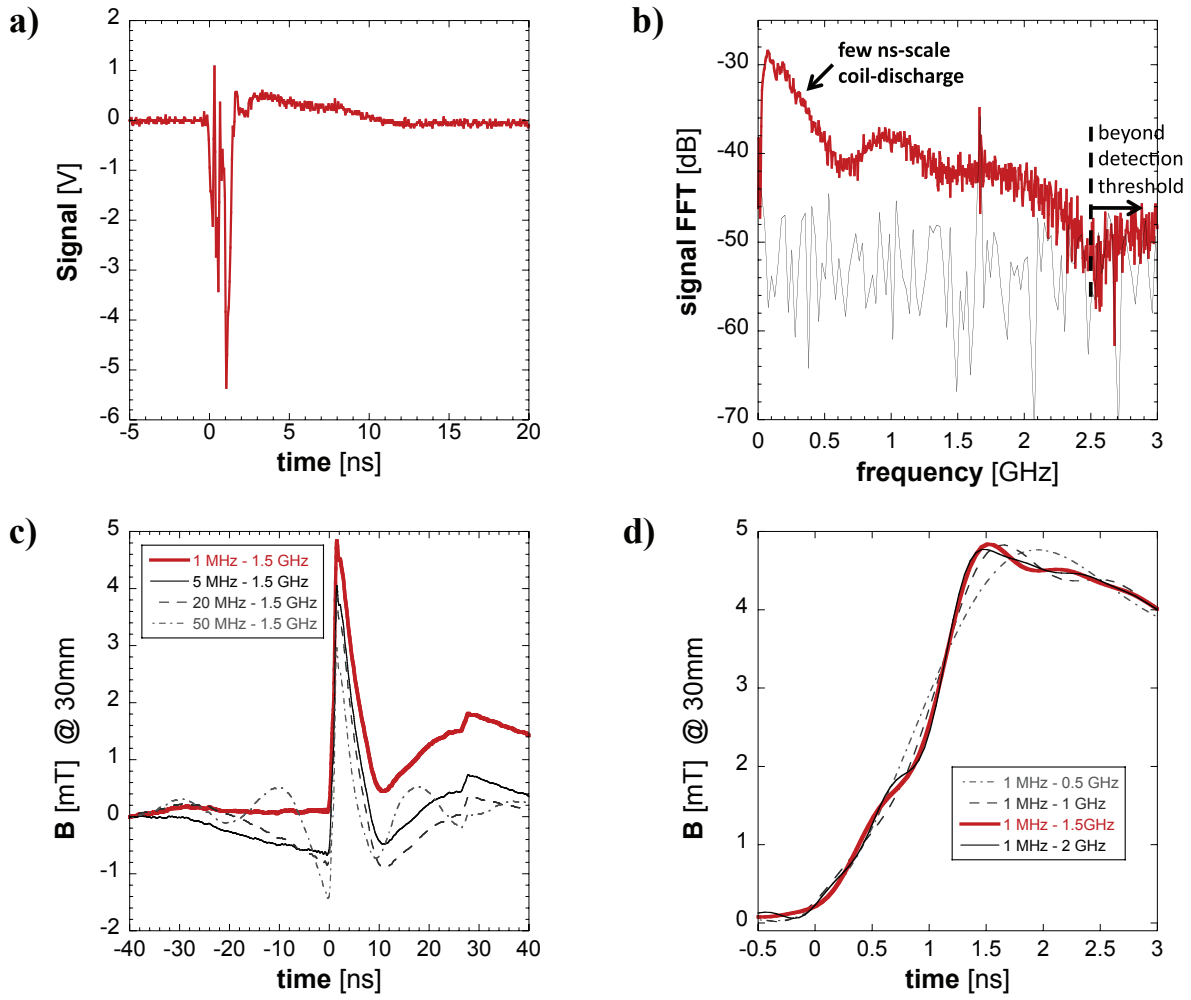

Figure 8.4 – Sample B-dot signal and analysis obtained on the 1^{st} experiment, for a Cu capacitor-coil target ($a = 250\,\mu m$), with the probe at 30 mm from the coil-center. **a)** Raw signal measured by the 2.5 GHz bandwidth detection system. **b)** Power FFT of the raw signal (thicker red curve). The thin black curve is the noise spectrum evaluated from the signal FFT for $t < -50$ ps. **c),d)** B-field signal after integration of the B-dot raw signal and corrected from attenuation (see Sec. 16.6). Thicker red curves are for the chosen frequency bandpass from $f_{min} = 1$ MHz to $f_{max} = 1.5$ GHz, thinner black curves for test variations on **c)** f_{min} and **d)** f_{max}.

The chosen high frequency limit permits also to exclude some white noise identified on the raw signal (discussed later with a spectrogram trace). Thinner curves correspond to variations either on f_{min} (panel **c)**) or on f_{max} (panel **d)**) testing the result sensibility to these parameters. Raising of f_{min} yields an offset of the B-field at $t = 0$ and one has to check also if the integrated signal after filtering has a zero baseline trend over integration domain, yet the amplitude of the signal is consistent for f_{min} up to 20 MHz. For fixed $f_{min} = 1$ MHz, the B-field rise-time and maximum yield do not significantly change for f_{max} down to 1 GHz. Therefore, the large spectral peak at a few hundreds MHz in panel **b)** corresponds to the main B-field signal due to the target discharge through the coil-shaped wire, the second large peak around 1 GHz determines the second B-field peak at $t \gtrsim 2$ ns. The spectral analysis is extensively characterized by a spectrogram plot, shown in Figure 8.5. The spectrogram shows the main frequencies of the coil discharge beginning at $t = 0$. The second peak around 1 GHz is also identified few ns after. It is interesting to note that the peak seen in Figure 8.4-c) at ≈ 1.7 GHz covers in the spectrogram the entire time window and then cannot be attributed to a laser-driven phenomenon. It may result instead of a digitizing noise from the scope.

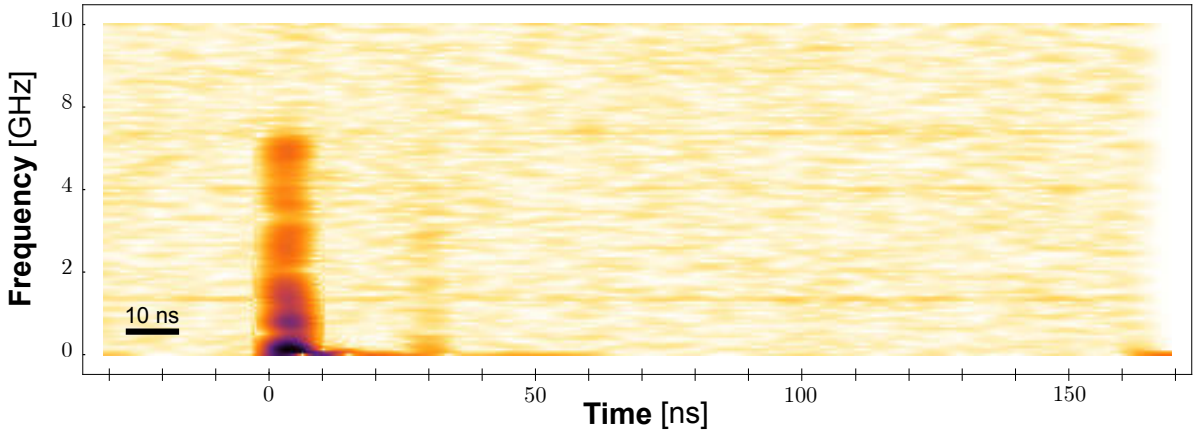

Figure 8.5 – Spectrogram of the raw signal presented in Figure 8.4.

The 3D magnetostatic code ©Radia (see Sec. 17) was used to simulate the spatial distribution of the B-field taking into account the target and coil geometry, and their connection wires. We used the current I as a free parameter, varying it to obtain an equality between the measured and simulated B-field values at the B-dot spatial positions. The boundary condition consisted in imposing a closed-circuit with the same current everywhere. To properly close the circuit, the current is also imposed in a wire connecting the two plates to mimic the plasma current flowing between them. The calculated field is then the superposed contribution at the probe position of the current in the coil, wires, disks (supposed to be vertical), and between the disks.

Box. 8.2: Low-bandwidth B-dot

Our extrapolation of the B-field takes also into account a comparison performed in the 2^{nd} experiment between the results of the high bandwidth B-dot probe and those of a 3-axis low-bandwidth (100 MHz) B-dot probe located at 25 mm from the coil center, at $\approx 45°$ above equator. To do this comparison, we imposed a maximum cutoff frequency of 100 MHz to the time-integration of the high-bandwidth probe signals, artificially reducing its bandwidth to values comparable to the signals obtained with the low-bandwidth probe (shown in figure below). One can notice that the transverse component of the B-field at the low-bandwidth B-dot position (along $\vec{x}$) extrapolates to a strongly overestimated B-field at the coil center. The reason is that this component is rather low in respect to the two others and is thus sensitive to the uncertainty on the probe position or to the 3D modeling approximations. It cannot be considered as an accurate measurement. Yet, the two main components, namely B_y and B_z, are yielding a magnetic field at coil center (B_0) consistent with the value extrapolated from the high-bandwidth probe (Figure 8.8).
These measures together with the calibration campaign carried out at CEA-CESTA and presented in previous section permitted to validate our 3D magnetostatic extrapolation protocol.

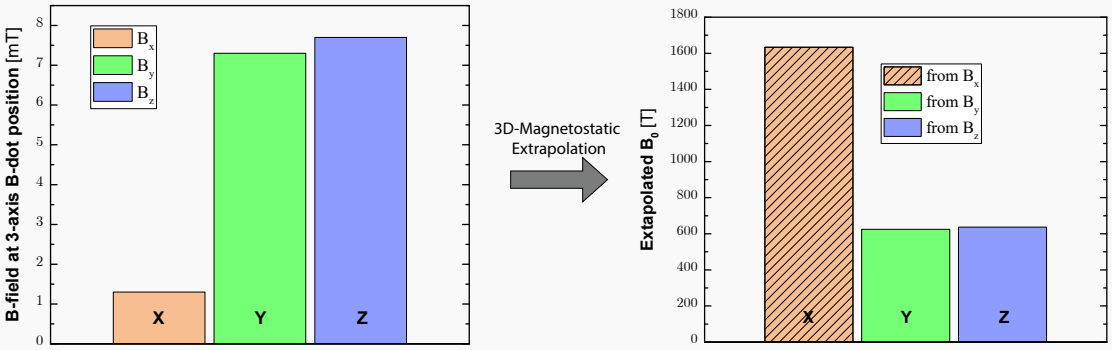

Figure 8.6 – 3-axis low-bandwidth B-field probe measurement at the probe position extrapolated to the B-field at coil center by 3D-Magnetostatic code. The fair comparison (except for the very sensitive low component B_x) to results obtained with an higher bandwidth probe shown in Figure 8.8 permitted to validate our 3D-magnetostatic geometry from consistent measurements at different probe positions.

Figure 8.7-a) represents two perpendicular planar sections of the B-field map obtained with Radia, one horizontal containing the coil axis, $z = 0$ (left), the other vertical corresponding to the coil plane, $y = 0$ (right) (see Figure 8.3 for the axis orientation: the y-axis is the coil axis and the origin is located at the coil center). The field was calculated with an injected current $I = 340$ kA and a coil radius $a = 250$ µm, yielding the measured B-field peak value for the Cu target in the 1^{st} experiment. Given the small (≈ 10 µm/ns) coil rod expansion velocity [measured by time-resolved optical shadowgraphy (see Sec. 8.2)], no rod expansion was considered in the magnetostatic calculations. The B-field norm is on color scale, the arrows represent the B-field vector projections on the two planes. The spatial distribution on the "$z = 0$"-plane clearly evidences, as expected, a dipole-like B-field. One can also see on the "$y = 0$"-plane that the B-field norm is quite homogeneous over the space inside the coil. Poloidal fields around the coil rod and straight parts of the wire are quite strong, and they mostly determine the B-field distribution below the coil region.

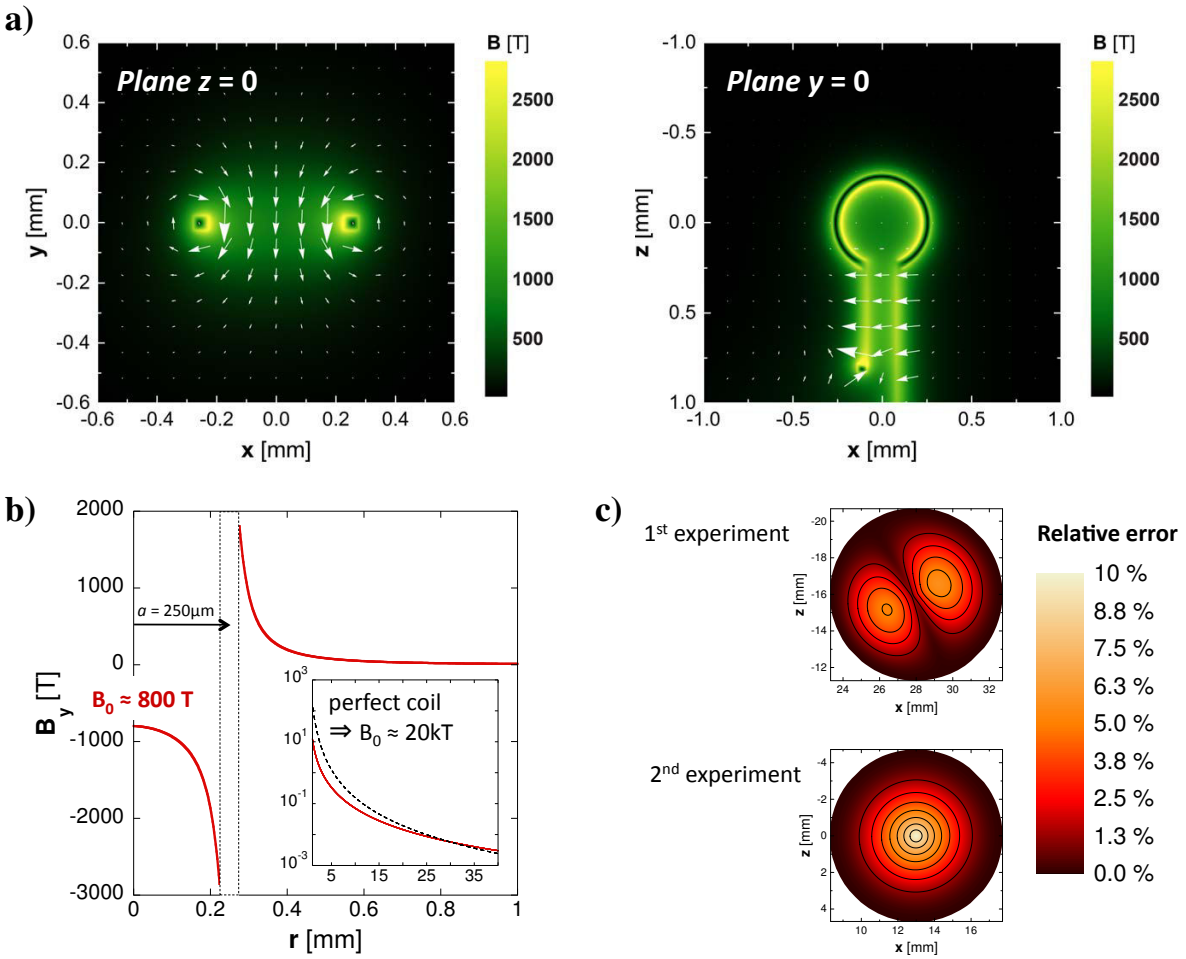

Figure 8.7 – Figure 3. **a)** 2D projections of the 3D Radia magnetostatic code extrapolation of the B-field produced by a $a = 250\,\mu m$ capacitor-coil target for a circulating current $I = 340\,kA$: plane $z = 0$ on the left, plane $y = 0$ on the right (the coil center is at the frame origin). **b)** Corresponding axial component of the B-field against distance from the coil center, along the line between coil center and the B-dot probe position for the 1^{st} experiment, for a capacitor-coil target (solid red curve) and for a perfect coil of the same radius a (dashed black curve), for the same current. (c) Relative uncertainty of the B-field measurements by the B-dot probes at their positions, respectively in the 1^{st} (top) and the 2^{nd}&3^{rd} (bottom) experiments.

For the same calculation, Figure 8.7-b) shows the amplitude of the B-field component parallel to the coil-axis as a function of the perpendicular distance, along the line connecting the coil and the B-dot probe centers, respectively at $r = 0$ and $r = 30$ mm (solid red curve) for the 1^{st} experiment. The vertical dashed lines delimit the 50 µm-thick coil rod position. For a measured 5 mT at $r = 30$ mm, the extrapolated value at the coil center is $B_0 = 800$ T for the capacitor-coil target. The uncertainty range is of $[795, 825]$ T accounting for target-to-target variations of ± 2 µm on the separation between the two connection points of the wire circular part with the vertical rods. Our target production and characterization are sufficiently precise to have only a very small contribution to the result uncertainty. An over-estimated extrapolation B-field value of $B_0 = 20$ kT (for a $I = 8.5$ MA current) is obtained when simulating a perfect circular coil of the same radius without straight parts (dashed black curve in the insert). Such unrealistic value (magnetic energy would be higher than invested laser energy) illustrates the importance of using an accurate modeling of the 3D target geometry.

As for the uncertainty on the B-dot probes distance with respect to the coil, Figure 8.7c) shows the calculated relative uncertainties of the B-field measurements at the probe positions: the values are plotted over the probes circular section and account for the 3D B-field gradients over the probes cylindrical volume. The estimated B-field errors, which remain under the 6 % and the 10 % respectively for the 1^{st} and $2^{nd}/3^{rd}$ experiments (due to two different probe orientations and distances relative to the coil), are mainly determined by the gradients along x and z in the first case (top), and along y for the second case (bottom), as expected from the setup geometry.

The typical final results for the produced B-field, as a function of time are summarized in Figure 8.8. The solid curves are the B-dot results obtained with capacitor-coil targets for the B-field at the probe positions (left-hand side ordinates) and the corresponding B_0 values at the coil's center (right-hand side ordinates, as extrapolated from the Radia magnetostatic calculations). In the 1^{st} experiment, panel **a)**, the peak values of the B-field for the best set of parameters, depending on the target material, yield $B_0 \approx 800$, ≈ 600 and ≈ 150 T (± 6 %), respectively for Cu (red), Ni (green) and Al targets (cyan). The two curves of panel **b)** are obtained for a Cu U-shaped target with $a = 250$ µm (black) and $a = 500$ µm (blue). The measured B-field at B-dot position is higher for the bigger coil, but as the B-field distribution is more extended for bigger coils, the extrapolation gives in fact a B-field at the coil center $\approx 2.6 \pm 0.2$ times lower with a target of twice radius. The uncertainty (± 0.2) is due to the worst shape repeatability of the tested U-turn targets with $a = 500$ µm. Yet, the B_0 indicates a current slightly smaller for the bigger coil than it would be expected by only geometric consideration (the B_0 would be reduced by a factor 2.1 according to Radia, modeling the full geometry): the remaining ≈ 23 % drop in B_0 should be due to an additional current loss by Joule effect. The additional current loss is consistent with ≈ 30 % longer wire total length between the two target geometries, increasing in approximately the same proportion the total wire resistance and Joule effect losses.

In the 2^{nd} experiment, Figure 8.8-panel c), the B-dot probe measurements are showing a shot-to-shot reproducible charging using Ni targets: the B-field production is synchronous with the beginning of the laser irradiation (at $t = 0$, within a ± 200 ps calibration uncertainty: see Sec. 16.8 in *Appendix*) and the rise time of ≈ 1 ns seems to be consistent with the duration of the laser pulse (that is the system charging time). The reproducible measurement of a peak B-field of 1 mT are extrapolated to the coil center, peaking then at $B_0 \approx 600$ T (± 10 %). For information, the laser operated with an improved and more stable laser focalization and energy in the 2^{nd} experiment. The results obtained are in very good agreement with the best result obtained with the Ni target in the 1^{st} experiment, which was measured with the B-dot probe at a different position relative to the coil.

The targets used in the 2^{nd} and 3^{rd} experiment had a reduced front disk hole (diameter of 1 mm instead of 1.75 mm for the 1^{st} experiment), seeking to capture more supra-thermal electrons. However, a comparison of the results leads to the conclusion that the hole size is not a key parameter for the peak B-field strength. Yet, the second B-field peak oscillation occurring at $t \gtrsim 2$ ns is more pronounced in the latter case. The typical duration of the pulsed B-field is of a few ns, with fluctuations mostly due to the varying distance d_0, inherent to foil folding at the target production process. All signals present slow amplitude variations at later times (non-represented), probably corresponding to electromagnetic coupling with objects around the target (secondary targets, diagnostics, chamber walls). Yet, the signals are converging back to zero after ~ 150 ns, sign of a good integration and filtering.

The laser interaction produces strong short-lived magnetic fields due to electron density and temperature gradients within the ablating plasma. Since these spontaneous magnetic fields have a

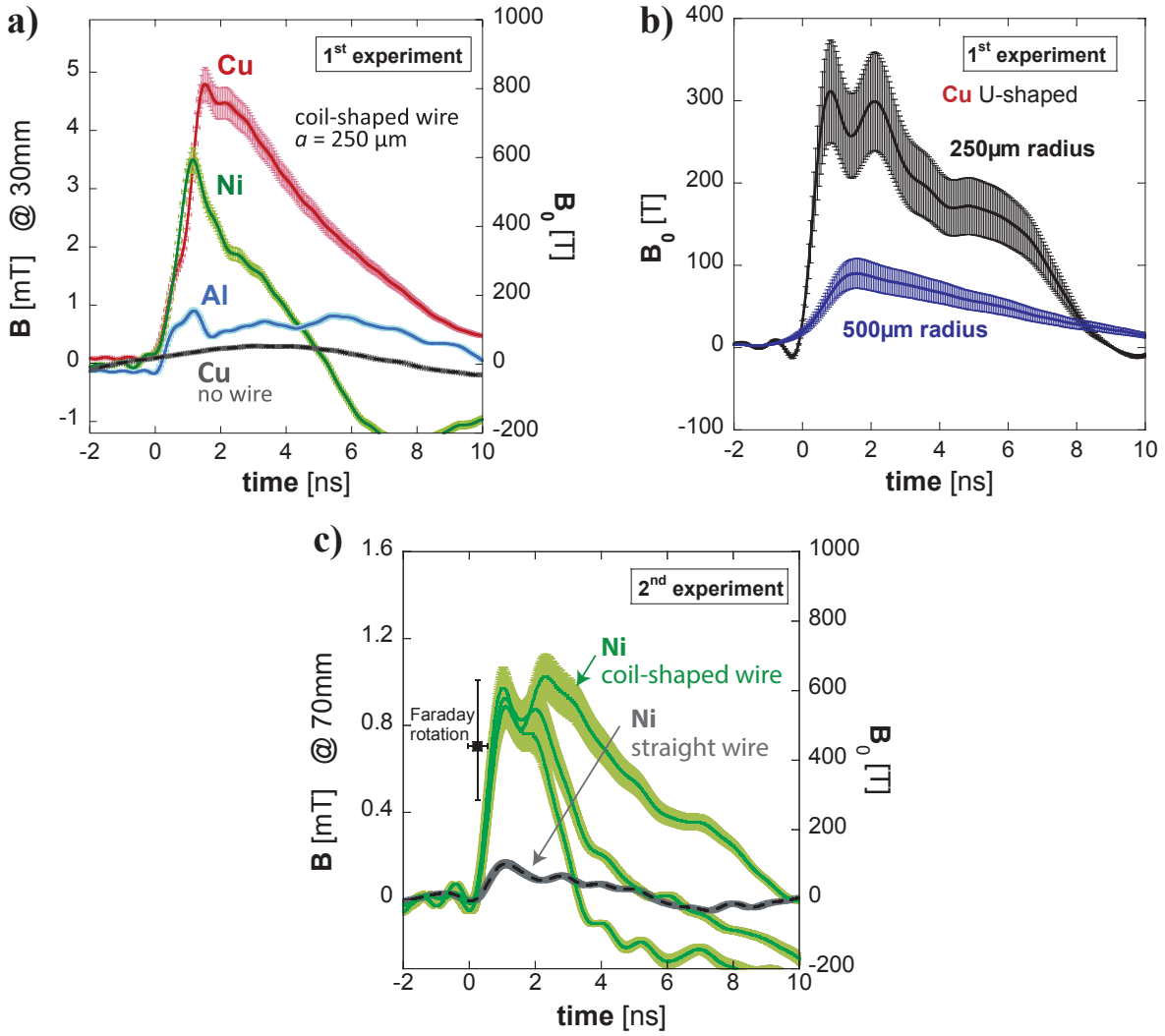

Figure 8.8 – Capacitor-coil target results of B-field against time measured by the B-dot probes (solid curves), for the B-field at the probe positions (left-hand side ordinates) and the corresponding B_0 values at the coil's centre (right-hand side ordinates): **a)** for 1st experiment targets of different materials, **b)** for two U-shaped targets with different radius and **c)** for 2nd experiment Ni targets. The grey dashed curves correspond respectively to a shot on the rear disk holding the two Cu disks parallel at the distance $d_0 = 900\,\mu\text{m}$ but without any connecting wire, and to a Ni target with a straight wire between the disks (no coil): their values refer exclusively to the B-field at the probe position (left-hand side ordinates). The symbols refer exclusively to the B-field at the coil centre, B_0 (right-hand side ordinates), and are the measurements obtained for Ni capacitor-coil targets by Faraday rotation (square, at $t = 0.2\,\text{ns}$) and by proton-deflectometry (red circle, at $t = 0.35\,\text{ns}$). The smaller orange circles represent B-field estimates from proton-deflectometry images obtained at later times: the discrepancy with B-dot probe results is explained in the text by electrostatic effects due to electron trapping near the coil.

poloidal geometry centered on the laser focal spot, they can contribute to the signal recorded by the B-dot probe. The efficiency of the coils and interaction noise level was tested by B-dot measurements in two *blank* shots: grey dashed curves in Figure 8.8 **a)** and **c)**, corresponding respectively to two Cu disks without any connecting wire (held separately), and to a Ni target with a straight wire between the disks (no coil). The dashed curves' values correspond exclusively to the measurements at the probe positions (left-hand side ordinates). One concludes that i) the irradiated disk charging by laser-target interaction and current of escaping electrons have a negligible contribution to the integrated signals (as well as any neutralizing current from the ground through the disk stalk) unless there is a physical connection between the disks, and ii) the magnetic field contribution from currents flowing through other target segments besides the coil (in particular the straight parts of the connecting wire) are sufficiently weak if compared to the results obtained with coil-shaped wires: the coil is the dominant source of the magnetic flux and plays fully its role of magnetic flux concentrator.

The B-dot results for $t \lesssim 0.4\,\text{ns}$ were confirmed in the 2^{nd} experiment by measurements of the Faraday rotation of the polarization direction of a linearly-polarized probe laser beam, and of the laser-accelerated proton deflections: respectively full square and circular-symbols in Figure 8.8 **c)**. The B- field peak values could not be measured by these two diagnostics due to laser-plasma effects, as described in the next sections.

8.1.3 Faraday Rotation results

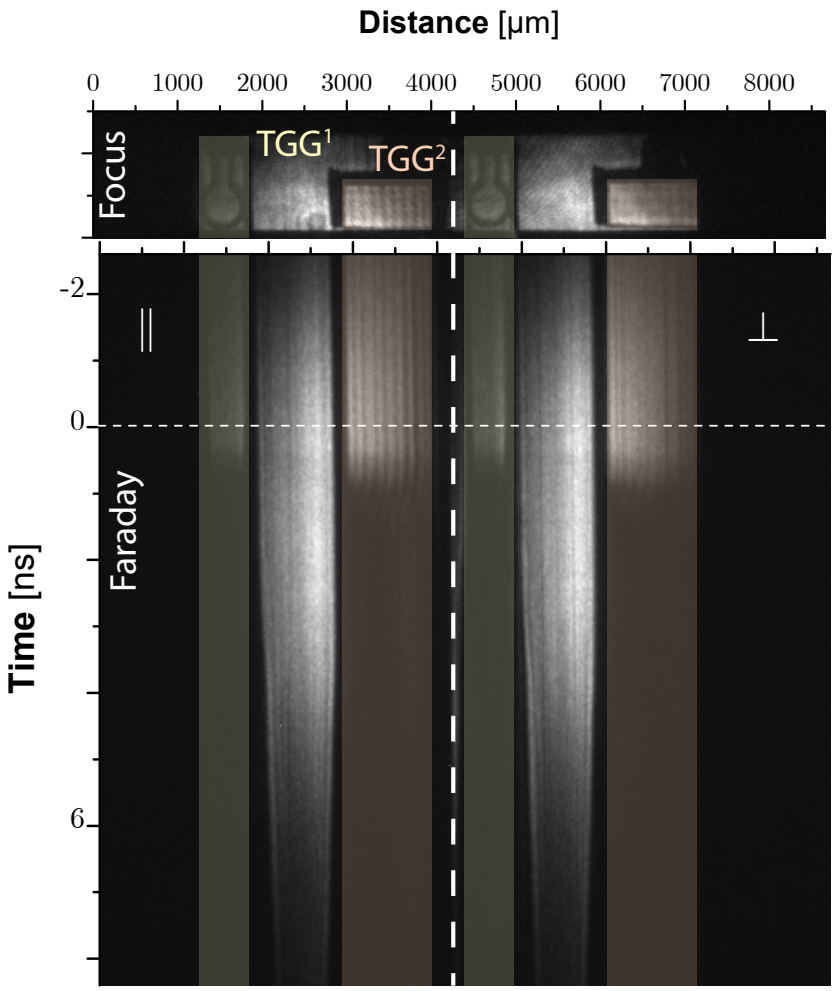

Figure 8.9 – Time-resolved polarimeter result for the shot analyzed in the text. It is composed of images of the two TGG crystals by probe beam, split in parallel (left) and perpendicular (right) polarization direction by a Wollaston prism. The streak camera is in focus mode on top image which was taken before shot and in streak mode for the shot in bottom image.

The Faraday rotation measurements, using a 9 ns duration probe laser at $\lambda = 533$ nm incident along the coil-axis, were performed with two 500 µm-thick birefringent terbium gallium garnet (TGG) crystals with their center place at 3.5 mm from the coil plane: TGG^1 (0.5 mm-wide) was centered on the coil axis and TGG^2 (1 mm-wide) at a 1.9 mm perpendicular offset (see Figure 8.9-top). As introduced in Sec. 7.2.3, the Verdet constant for the TGG crystals we used, 11.35 °T^{-1}mm^{-1}, is 38 times higher than that of SiO_2 used in the earlier work by Fujioka *et al.* [87], allowing to be sensitive to weaker B-field strengths. No Faraday rotation measurements were successful with crystals located closer to the coil, because of the signal blackout quasi-synchronous with the laser irradiation of the target - due to very rapid crystal ionization by the hard x-rays and fast particles issuing from the interaction region - nor further away from the coil where the local B-field is too weak. The Faraday effect was measured by using a time-resolved polarimeter, constituted of a Wollaston prism to separate the two perpendicular components of the probe beam field, and a streak camera (the setup is shown in Figure 8.3 and a streak image is shown in Figure 8.9-bottom). The time resolution of ≈ 300 ps was limited by the camera time-resolution and by the laser jitter.

The quantification of the rotation angle was previously calibrated, without B-field, by quantifying the polarization ratio of the two transmitted perpendicular polarization signals, defined as $R = E_{\parallel}^2/(E_{\parallel}^2 + E_{\perp}^2)$, as a function of the orientation of the incident light polarization. The obtained linear fit of the experimental data was consistent with the Malus law by an average $\chi^2 \approx 0.002$ adjustment. For the shots with the B-field, the incident polarization was set-up at $-45\,°$ and $+45\,°$ relative to $E_{\parallel}$ and $E_{\perp}$ respectively, yielding a ratio $R = 0.50 \pm 0.01$ for the situation without B-field.

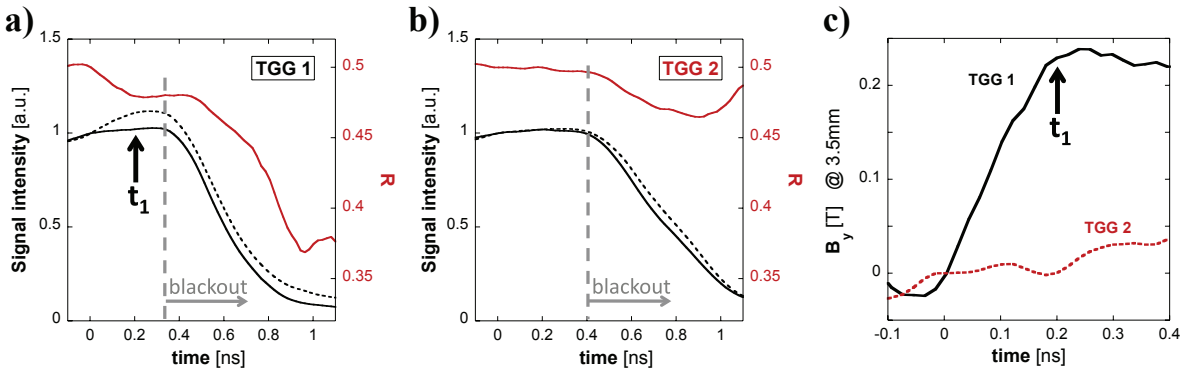

Figure 8.10 – Faraday rotation effect on probe laser light over two TGG crystals, placed at 3.5 mm from the coil plane, TGG^1 centered on the coil axis and TGG^2 at a 1.9 mm perpendicular offset, evaluated from a time-resolved polarimeter: **a)** detected signals of perpendicular polarizations : $E_{\parallel}^2$ (solid black) and $E_{\perp}^2$ (dashed black), and the corresponding polarization ratio R (red), for TGG^1. **b)** Idem, for TGG^2. **c)** Axial component of the B-field averaged over the crystals 500 µm-thickness: solid black for TGG^1, dashed red for TGG^2

Figure 8.10 shows the analysis of a successful shot for the Faraday rotation effect measurement, as a function of time: transmitted $E_{\parallel}^2$ (solid black) and $E_{\perp}^2$ (dashed black); and corresponding R (solid red) are plotted for **a)** TGG^1 and **b)** TGG^2 (the plotted values correspond to averages over the respective crystals' width). The crystals' blackout times are indicated by the light grey dashed vertical lines. Panel **c)** plots the corresponding local axial component of the B-field averaged over the crystals thickness and width, solid black for TGG^1, dashed red for TGG^2, obtained assuming that the TGG Verdet constant does not change with time due to the increase in crystal temperature. We see that the B-field inferred from the TGG^2 measurements is too weak and remains at the signal noise level of ± 0.03 T. As for the TGG^1 measurements, the B-field clearly rises up till the blackout time. To compare with B-dot probe measurements, we selected the time $t_1 \approx 0.2$ ns, indicated in both panels **a)** and **c)**, where averaged B-field is evaluated to $\approx 0.22 \pm 0.05$ T along the coil axis at a 3.5 ± 0.25 mm distance from its centre. The black square symbol in Figure 8.8 **c)** corresponds to the B_0 strength (right-hand side ordinate axis) extrapolated from that measurement, using the same magnetostatic code Radia [50] and a similar protocol as for the B-dot data extrapolation. In spite of the diagnostic uncertainties - related to the crystal thickness, accessible width and equivalent height of the streak slit

on the crystal plane, and the B-field gradients over such crystal volume - the obtained value for the order of magnitude of the extrapolated B_0 is fairly consistent with the B-dot probe measurement.

8.1.4 Proton Deflectometry results

The proton-deflectometry technique has been introduced in Sec. 7.2.2 and it allows to measure the B-field directly in the coil region. In the experiments, the proton beam was created using a short laser pulse (50 J on target, 1 ps FWHM at $1\omega_0$) focused onto 10 µm-thick Au foils at $\approx 10^{19}$ W/cm^2 intensity. Proton beams of $\sim$ 20 MeV cutoff energy were generated by the TNSA mechanism at the rear sides of the foils (see Sec. 5.2). The foils were located at a distance of 5 mm from the target coil. The proton beam propagation axis was perpendicular to the coil axis, and it was detected 45 mm away from the coil by a stack arrangement of radiochromic films (RCF). The proton deflections due to the B-field were quantified with the help of a 42 µm-pitch mesh, positioned 3 mm before the coil. One can refer to Figure 8.3 to see the diagnostic implementation. Applying Eq. 7.1, one estimates a magnification of 10 at the coil plane and of 25 for the mesh plane. The stopping power of protons in a typical RCF stack used in the experiment is shown in Sec. 18.1 and one can see in the deposited energy of the first RCF (Figure 18.2) that the front layer of 195 µm-Al filter protection put before the RCF stack limited the detection to protons of energy $\epsilon_p \geq 5$ MeV. The goal of such filter is to have a non-saturated dosis on the first RCF due to the high number of low energy electrons, as seen in the typical spectrum of TNSA accelerated particles Figure 5.3. Calculations of electron stopping power in Al show also that the protection blocks electrons of energies $\epsilon_e \lessapprox 260$ keV. Accounting for the time-of-flight (TOF) between proton source and the coil, each shot, with a chosen delay $\Delta\tau$ between the main and proton-driving lasers, scanned the effects of the B-field on the proton-trajectories over the time range of $t = \Delta\tau + \text{TOF}$ with TOF ranging between 80 and 160 ps. It was the first time that an experiment employed this diagnostic to measure the B-field of a laser-driven coil target.

Qualitative result: a dipolar-like B-field

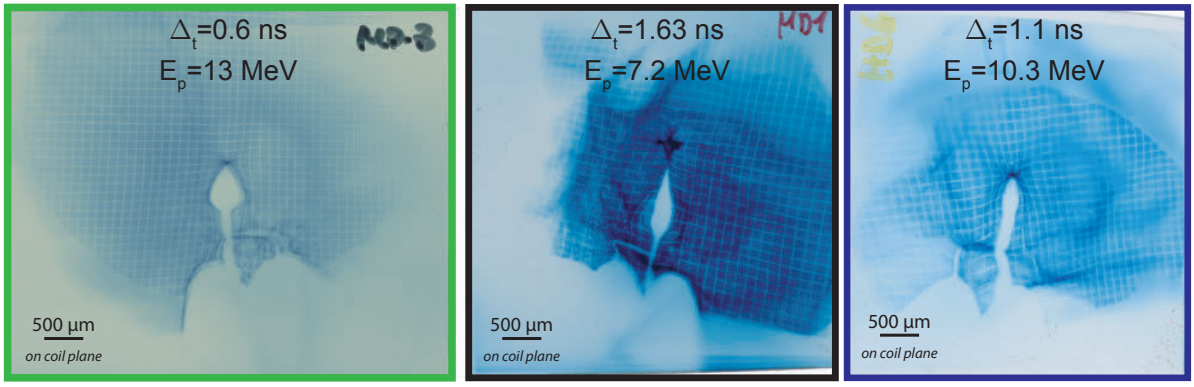

Figure 8.11 – Three RCF layers for different coil targets. The frame colors identify the target type and are referenced in Figure 8.2.

The 2D grid deflections, as calculated by the methodology presented in Sec. 19, are shown for three sample RCF layers (Figure 8.11) from shots obtained with different coil-shaped targets in Figure 8.12 ($a = 250$ µm) and U-turn targets in Figure 8.13 ($a = 500$ µm). The deflections obtained for the grid are compared with a B-field integral computation made with the magnetostatic code Radia, for an arbitrary current of $I = 100$ kA. The given spatial scale corresponds to the plane of the coil center, perpendicular to the proton beam axis, where the unperturbed mesh shadow has a pitch of 105 µm. The result fairly corresponds to a dipole-like B-field spatial distribution. The consistency of the experimental image with Radia calculation is actually the first experimental direct evidence that the current was actually circulating through the coil.

The spatial distribution discrepancy with the B-field integral computation can be attributed mostly to plasma effects in the coil vicinity. However, the B-field distribution tends to converge to a dipolar one at larger distance and the geometric differences are then becoming less important.

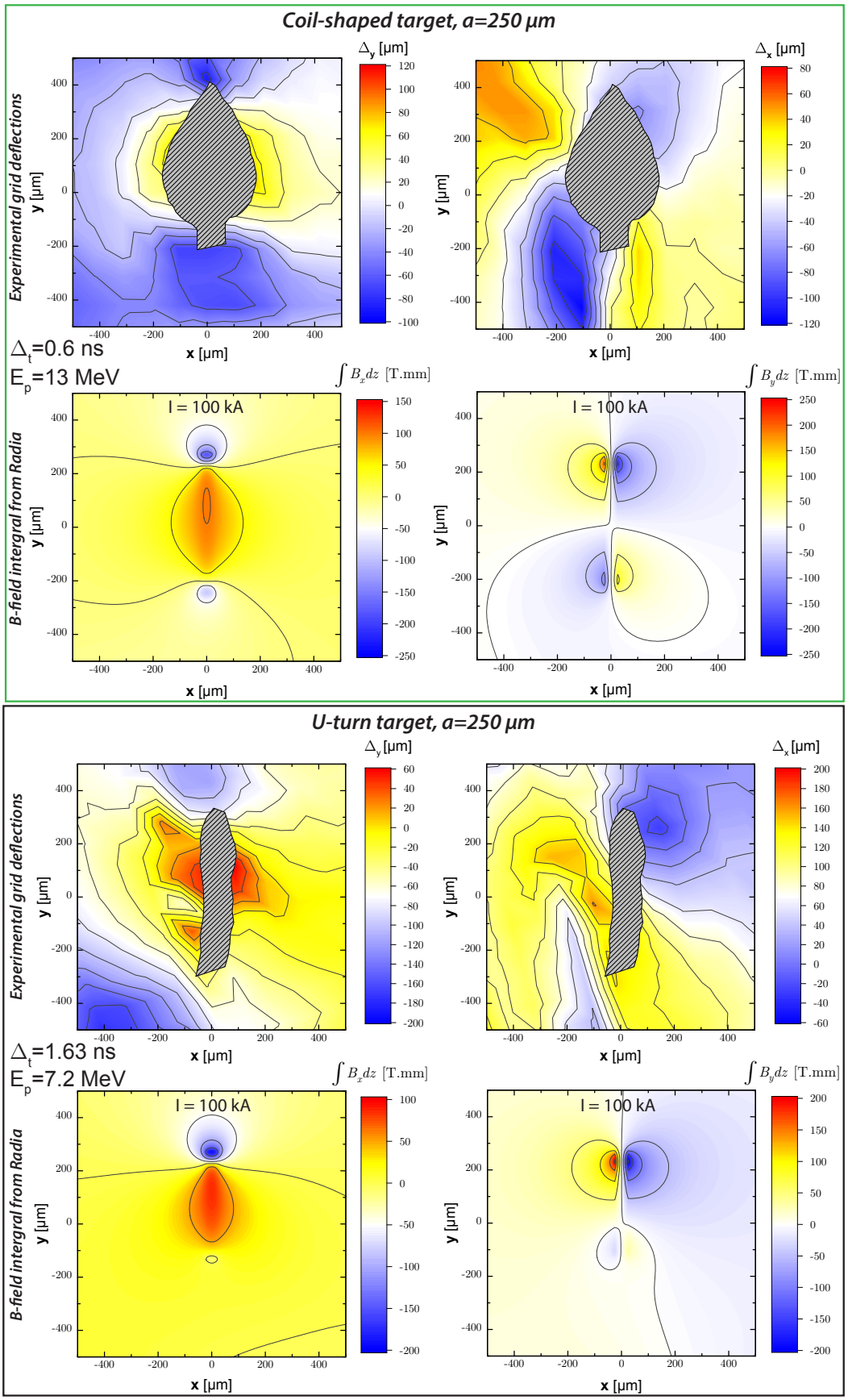

Figure 8.12 – Map of the mesh shadow deformation at coil plane for $a = 250\,\mu m$ coil radius targets and comparison with the B-field integral computed from the magnetostatic code Radia with $I = 100\,kA$ as a reference. The frame colors for the two sets of data are representative of the target type and can be identified in Figure 8.2: coil-shaped target (top) and U-turn target (bottom).

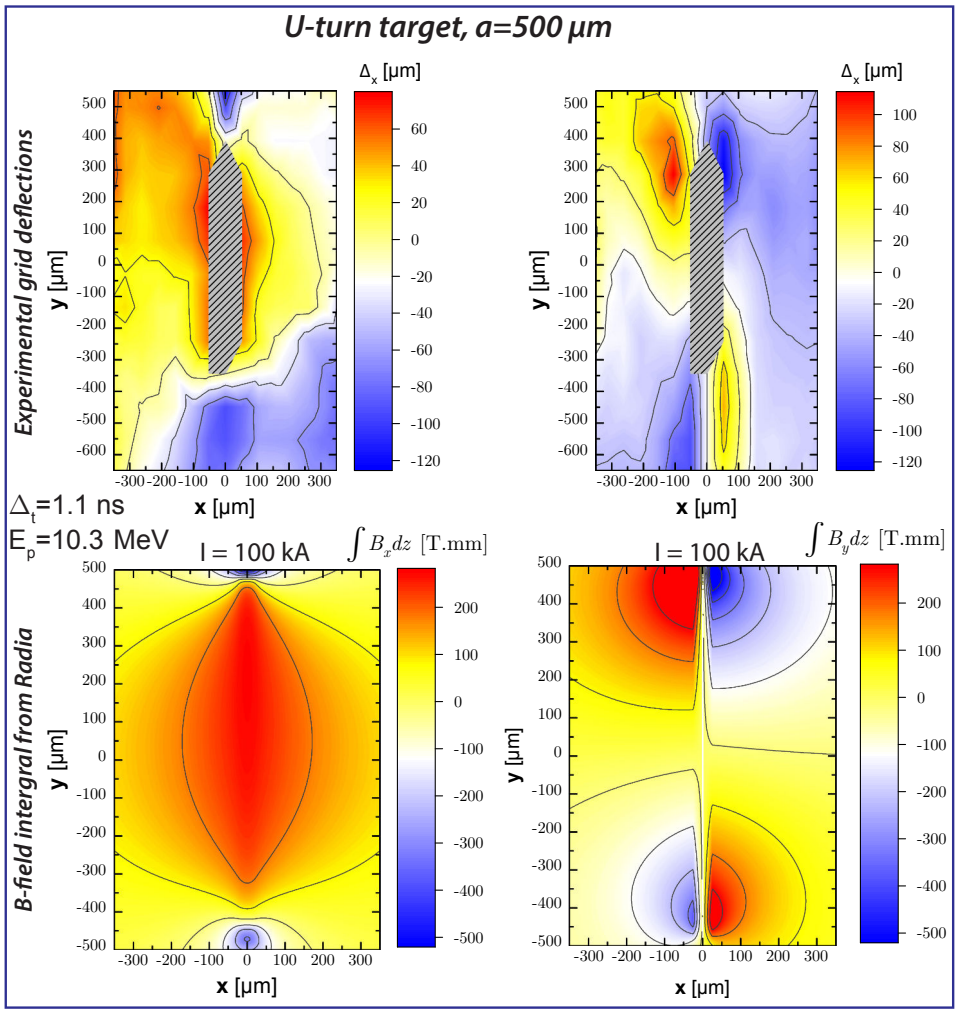

Figure 8.13 – Map of the mesh shadow deformation at coil plane for $a = 500\,\mu m$ coil radius targets and comparison with the B-field integral computed from the magnetostatic code Radia with $I = 100\,kA$ as a reference. The frame colors for the two sets of data are representative of the target type and can be identified in Figure 8.2.

Quantitative results: Extract the coil current from an RCF imprint

At this point, no qualitative discussion of the B-field strength was addressed. One can in a first approximation relate roughly the B-field integral values to deflections and compare the quantities obtained with experimental deflections. The relations allowing to obtain the deflections Δ_y and Δ_z (see frame orientation in Figure 8.3) in the coil plane are:

$$\arctan\left(\frac{M\Delta_z}{D}\right) = \frac{e}{\sqrt{2m_pE_p}}\int B_y dx \tag{8.3}$$

$$\arctan\left(\frac{M\Delta_y}{D}\right) = \frac{-e}{\sqrt{2m_pE_p}}\int B_z dx \tag{8.4}$$

with M the system magnification (in our experiments $M = 10$) and D the distance from coil plane to detector plane (in our experiments $D = 45\,\text{mm}$).

The conversion factor from B-field integral to deflection in the coil plane are $9\,\mu\text{m/T/mm}$ and $12\,\mu\text{m/T/mm}$ respectively for coil-shaped target and U-turn target with $a = 250\,\mu\text{m}$ (Figure 8.12), and $10\,\mu\text{m/T/mm}$ for the U-turn target with $a = 500\,\mu\text{m}$ (Figure 8.13). It leads to $B_0 < 250\,\text{T}$ for the three cases.

In particular for the reference case of coil-shaped target with $a = 250\,\mu\text{m}$, Figure 8.14 shows a quantitative analysis of an RCF imprint by different methods. Identically as for the previous figures, the map of vertical deformations of the mesh shadow is seen in **c)**. From those vertical deformations, a corresponding horizontal lineout at the coil center vertical position $z = 0 \pm 105\,\mu\text{m}$ has been extracted and compared with B-field integrals from the magnetostatic code Radia, converted in deformation values, using again Eq. 8.4. The deformations are computed for different strengths of the B-field (curves), the matching with experimental data (circles) leads to the evaluation of $B_0 = 95 \pm 20\,\text{T}$ at the corresponding probing time, $t \approx 0.35\,\text{ns}$.

In addition to the mesh imprint deformations, a more outstanding feature that can be noticed in Figure 8.14-**a)** is the centered bulb region void of any proton imprint due to the very strong B-field in the vicinity of the coil. The void zone size is actually a much more relevant signature of the B-field created by the coil and the access to this information is particularly valuable since it concerns the region where we ideally aim at measuring the B-field. For these reasons, the quantitative analysis of the RCF imprints will be more accurately performed using the void size.

Figure 8.14-**b)** shows the result of a ballistic simulation of the trajectories of randomly injected protons within the energy range of the experimental imprint in **a)**. For more information about the simulation technique, the reader can refer to Sec. 19.2. The void zone (bulb) size inferred from the ballistic simulation compares very well with the experimental image for a current $I = 40\,\text{kA}$, corresponding to $B_0 = 95\,\text{T}$, and consistently agrees with the mesh-shadow deformation analysis. The measure of the bulb size from experimental data is very fast and accurate, while the estimation from the barely readable mesh-shadow imprint is rather tedious. An analytic estimate of the bulb size can also be made, it is what is discussed in Box. 8.3.

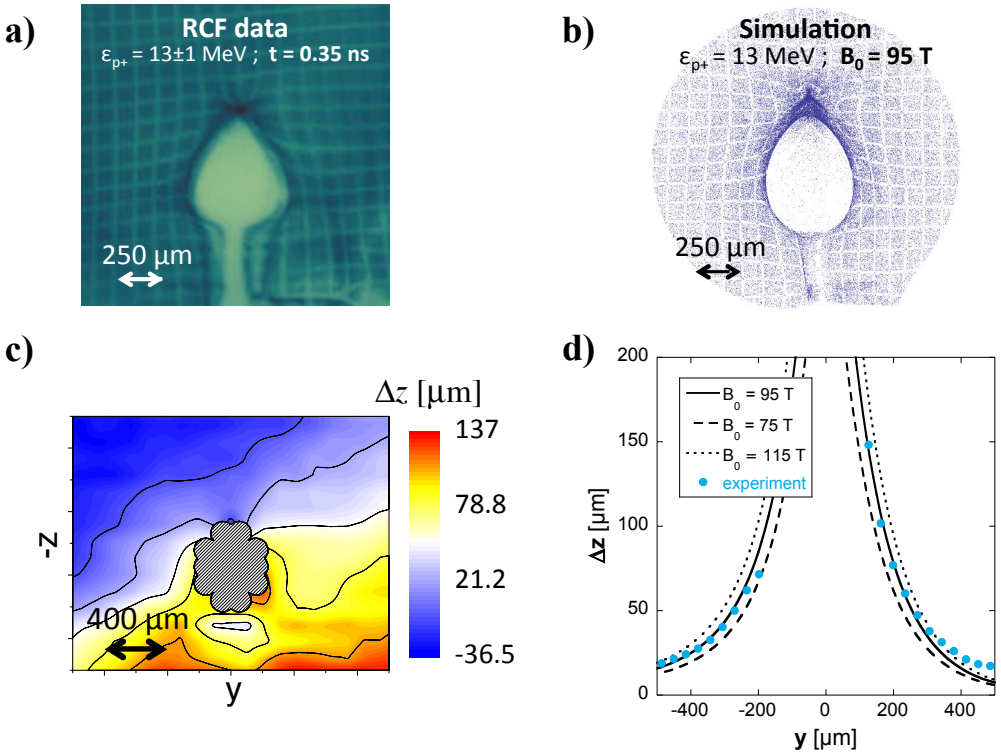

Figure 8.14 – a) Sample RCF image of proton-deflectometry measurement in an early probing time $\Delta\tau = 0.35\,\text{ns}$ after ns-laser light starts to irradiate the B-loop target's rear disk. The RCF position corresponds to the imprint of $13 \pm 1\,\text{MeV}$ protons. **b)** $13 \pm 1\,\text{MeV}$ proton imprint on detector plane given by a ballistic simulation of their trajectories over a 3D B-field map with $B_0 = 95\,\text{T}$ (previously calculated by the magnetostatic code). **c)** Map of experimental vertical deformations of the mesh shadow. The spatial scale on each image corresponds to the plane of the coil. **c)** Corresponding horizontal lineouts of the experimental (circles) and synthetic (curves, for different B-field strengths) vertical deformations of the mesh imprint.

Box. 8.3: Analytic estimation of the bulb size

First we will introduce a rough analytic estimation of the void zone as a function of the current in the coil and the kinetic energy of protons making the imprint.
The following analytical estimate, developed in [89], is based on a basic paraxial mapping between a proton ray at the object plane and the same ray at the detector plane after deflection by electromagnetic fields [152]. By assuming a first-order estimate of the B-field from a straight wire:

$$|B(r)| = \frac{\mu_0 I}{2\pi r} \quad (r \geq R), \tag{8.5}$$

with R the wire radius of the coil and r the distance from the proton ray to the current, which equals to $\sqrt{y^2+z^2}$ in our setup frame (see Figure 8.3) where $\vec{x}$ is the proton propagation axis. The horizontal and vertical components of the B-field perpendicular to the proton beam axis write, in the case of a straight wire parallel to the x-axis:

$$B_y(r) = B(r)\frac{z}{r} = \frac{\mu_0 I}{2\pi}\frac{z}{r^2} \quad (r \geq R), \tag{8.6}$$

$$B_z(r) = B(r)\frac{y}{r} = \frac{\mu_0 I}{2\pi}\frac{y}{r^2} \quad (r \geq R), \tag{8.7}$$

The system has a cylindrical symmetry and proton deflection depends only on r. The mapping relation can then be generally written depending only on r between the object plane (r,z) and the image plane (r_i,z_i) and:

$$r_i = Mr + \frac{\mu_0 I}{2\pi r}\frac{e\Delta_x D}{\sqrt{2m_p E_p}} \tag{8.8}$$

where Δ_x is the characteristic length of the field for a given proton path.
According to [152], a *caustic* is formed, creating a sharp pile-up of protons in the image intensity when $dr_i/dr = 0$. The radial position of the caustic corresponds to the edge of the proton void and will determine its size. One obtain a proton void width on the image plane given by:

$$w = 4\left(\frac{e\mu_0 I\Delta_x DM}{2\pi}\right)^{\frac{1}{2}}\left(2m_p E_p\right)^{-\frac{1}{4}} \tag{8.9}$$

It is worth mentioning that the bulb horizontal size is determined under this approximation by the poloidal field of the wires of the bottom part of the coil. Indeed, due to our current orientation in the coil in respect to proton propagation direction (see Figure 8.17), the horizontal force is exerted outward for the coil bottom part while it is exerted inward for the coil top part. It explains the "pear" shape of the bulb observed in experimental RCF imprints. The equation Eq. 8.9 yields for 13.2 MeV-protons a void width of respectively 3.3 mm and 4.7 mm for a current $I = 20$ kA and $I = 40$ kA (with $\Delta_x = 200$ µm representing the effective length along $\vec{x}$ of the coil bottom wires, accounting for the open angle gap located in this part). This is consistent with the further presented fitting laws obtained from ballistic simulations yielding 3.4 mm and 4.9 mm respectively. However, this estimate is strongly dependent on the choice of the parameter Δ_x which depends itself on the coil geometry. Moreover, the estimate rely on the questionable paraxial approximations and one-step integration of the proton trajectory. Yet, it can give a rather correct estimation for small deflection angles.

A Monte-Carlo technique (or similar) to evaluate the B-field integral along the proton path for the 3D fields can be used to drastically improve the above estimate and construct synthetic imprints in the paraxial limit. This method is presented in Sec. 19.3 and is a powerful alternative for low deflection angles to the ballistic method presented in Sec. 19.2 which, in contrast, do not rely on paraxial approximations. Later on we will see that ballistic simulation matching the proton imprint - and this void zone size in particular - is the more reliable tool to measure the B-field from proton imprints.

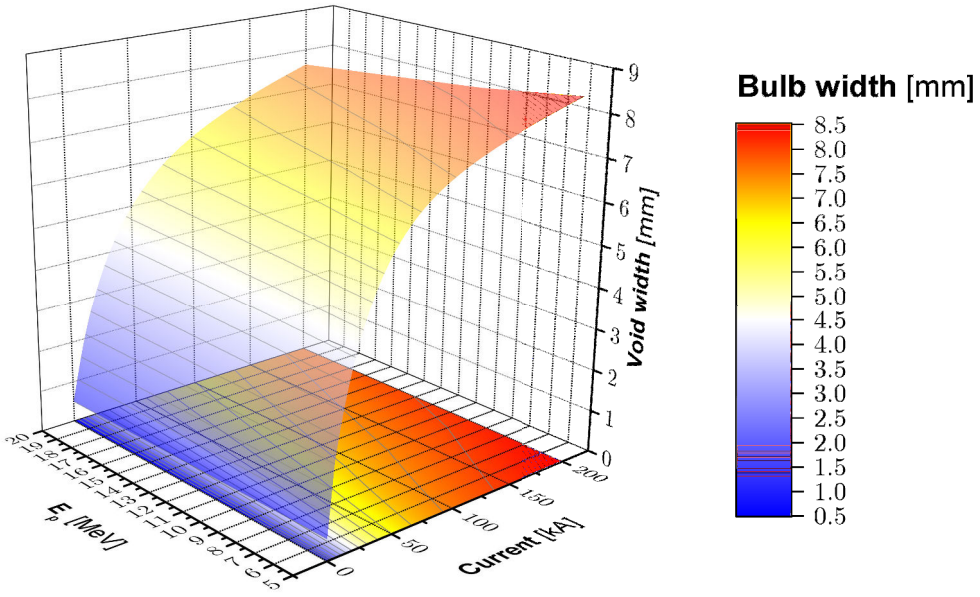

Figure 8.15 – Bulb horizontal size on detector plane at a distance $D = 45\,\text{mm}$ from coil plane, obtained from a set of ballistic simulations varying the current in the coil and the kinetic energy of the probing protons. These simulations were made with the geometry of the coil-shaped target with $a = 250\,\mu\text{m}$.

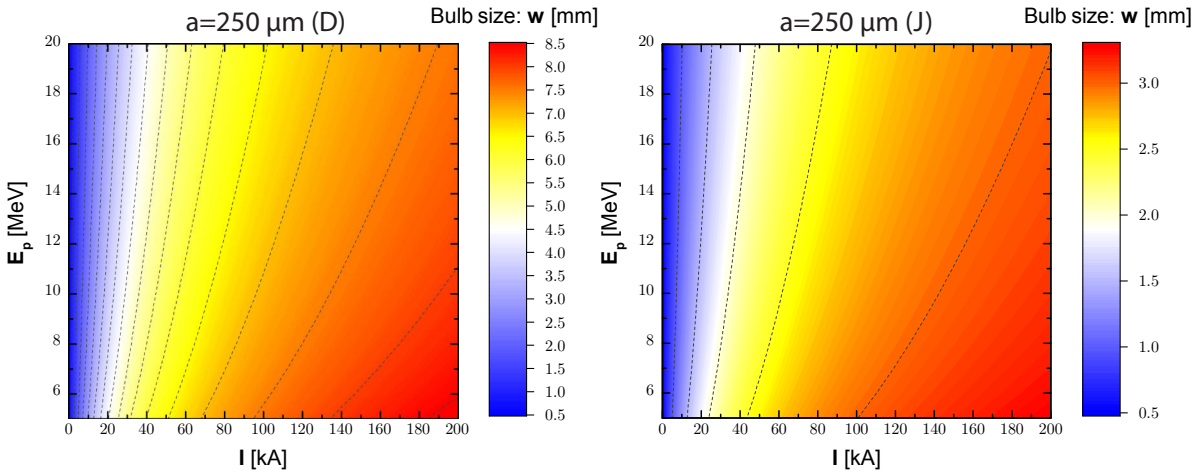

Figure 8.16 – Fitted functions for the bulb horizontal size respectively from Eq. 8.10 and Eq. 8.11 for the coil-shaped target with $a = 250\,\mu\text{m}$ and U-turn target with $a = 250\,\mu\text{m}$.

In Figure 8.15, we show the compilation of a set of ballistic simulations at different proton kinetic energy and current strengths in a coil-shaped target with $a = 250\,\mu\text{m}$. The results are fitted to a law that will be used to systematically estimate the current from the measured bulb size in experimental RCF imprints.

A fit of the two parameters function of bulb width is proposed and writes:

$$w_{D-250}\left[I[\text{kA}], E_p[\text{MeV}]\right] = 0.5 + 4.7\left(1 - \exp\frac{-0.105I}{Ep^{0.5}}\right) + 0.36\frac{I^{0.5}}{E_p^{0.25}}[\text{mm}] \tag{8.10}$$

This function is plotted in the left panel of Figure 8.16.

An equivalent fitting function has been made for the U-turn target geometry with $a = 250\,\mu m$:

$$w_{J-250}\left[I[\mathrm{kA}], E_p[\mathrm{MeV}]\right] = 0.5 + 1.895\left(1 - \exp\frac{-0.0925I}{Ep^{0.5}}\right) + 0.0945\frac{I^{0.5}}{E_p^{0.25}}[\mathrm{mm}] \tag{8.11}$$

This function is plotted in the right panel of Figure 8.16. In both cases the coefficient of determination for the fits is $R^2 > 0.999$.

It is worth pointing out here that the power coefficients for the current and proton kinetic energy in the fit formulas exhibit the same tendency with $I^{0.5}$ and $E_p^{-0.25}$ than for the analytical estimate of the void bulb size shown in Box. 8.3. Yet, the tendency is quite different from this analytic estimate for low currents or high kinetic proton energy. Indeed, in those cases, the proton is not kicked out by the poloidal field of the wires and the B-field "seen" by the proton is thus more complex.

Influence of the target geometry

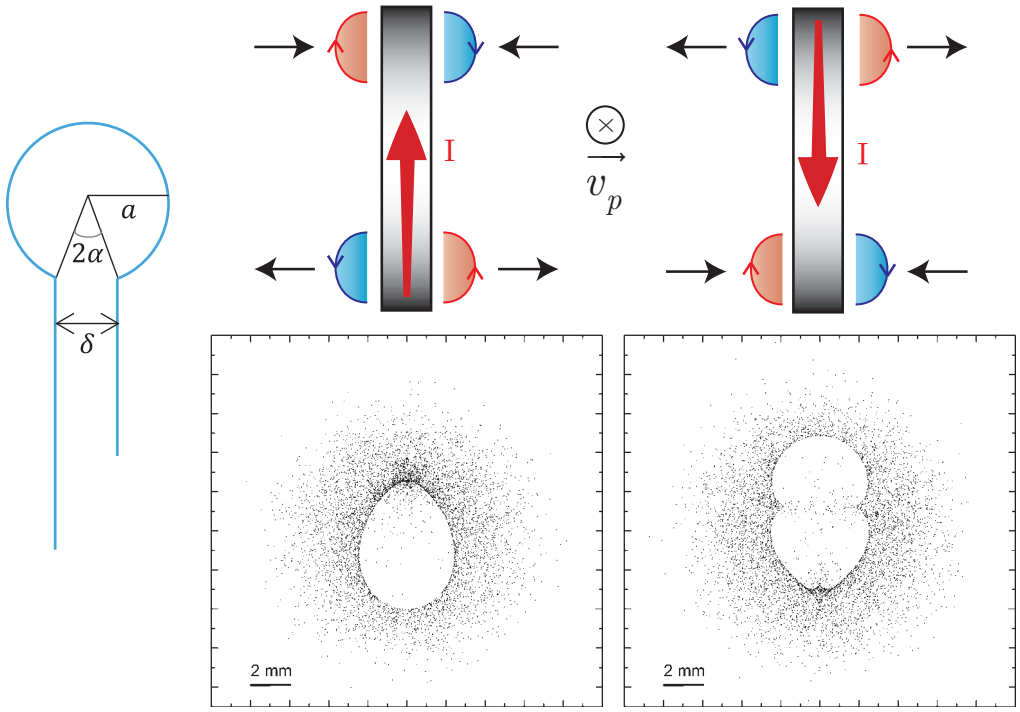

Figure 8.17 – Left: Geometrical parameters of the coil. **Right:** Bulb shape influence on the current orientation with the associated synthetic proton imprints on detector for both case. The top and bottom part of the coil's wires poloidal B-field is either creating an inward or outward force on protons. This contribution is reversed while reversing the current orientation, schematized by the B-field in blue (negative) and red (positive) arrows and the resulting force in black arrows.

Here we will show how the target geometry influences the bulb shape and size. The most important geometric parameter is δ, defining the gap distance between the two stands wire below the coil (see Figure 8.17). Since the 2^{nd} experiment, for the coil-shaped targets with $a = 250\,\mu m$, the uncertainty remains under $20\,\mu m$ ($\delta = 200 \pm 10\,\mu m$). The related open angle $\alpha = \frac{1}{2}\arccos\left(1 - \frac{\delta^2}{2a^2}\right)$ is then equal to $23.6 \pm 1.3\,°$ and the variation is small enough to not induce important variation on bulb horizontal size, which remains under 3 %.

Yet, the bulb horizontal size is seen to be much less dependent on the gap size δ (Figure 8.19) when either driving the current in opposite direction or reversing the proton probing axis, with respect to the orientation of our experiments (Figure 8.18). The reason is that the upper part of the coil is obviously almost not influenced by the gap size. Another purpose to change the orientation is linked to what we will present further on added electrostatic effects from LP interaction since the top part of the coil

is located further from LP interaction region. It is then definitively something that can be considered in order to improve the proton-deflectometry accuracy. Nonetheless, the orientation may be imposed by the chamber geometry and in our experiments the relative angle between LP and SP laser pulses were fixed.

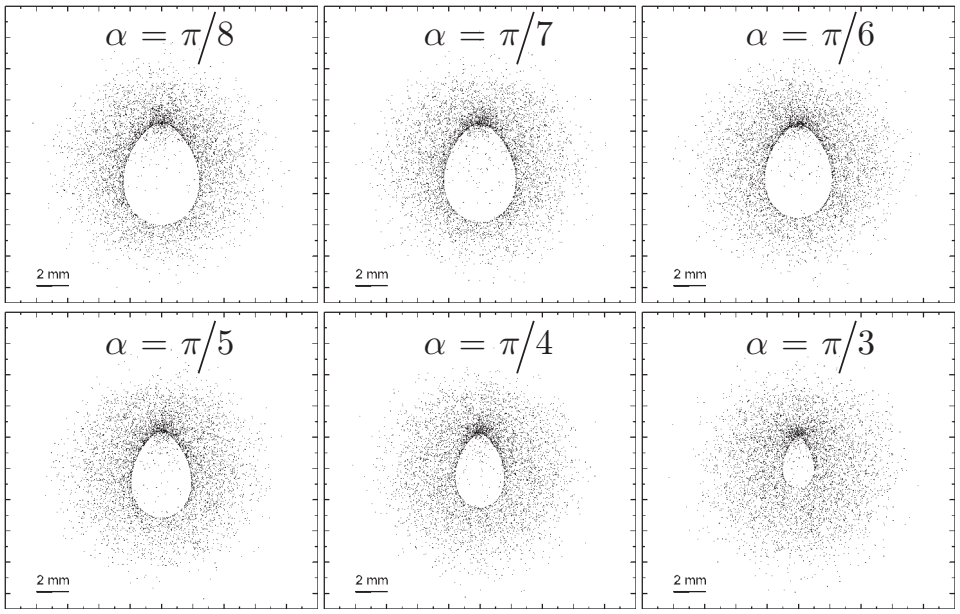

Figure 8.18 – Influence of the open angle α (see geometry in Figure 8.17) on the bulb horizontal size. Synthetic proton imprints on detector plane are obtained with a fixed current $I = 40\,\mathrm{kA}$ (see orientation in Figure 8.17) and proton kinetic energy $E_p = 13.2\,\mathrm{MeV}$.

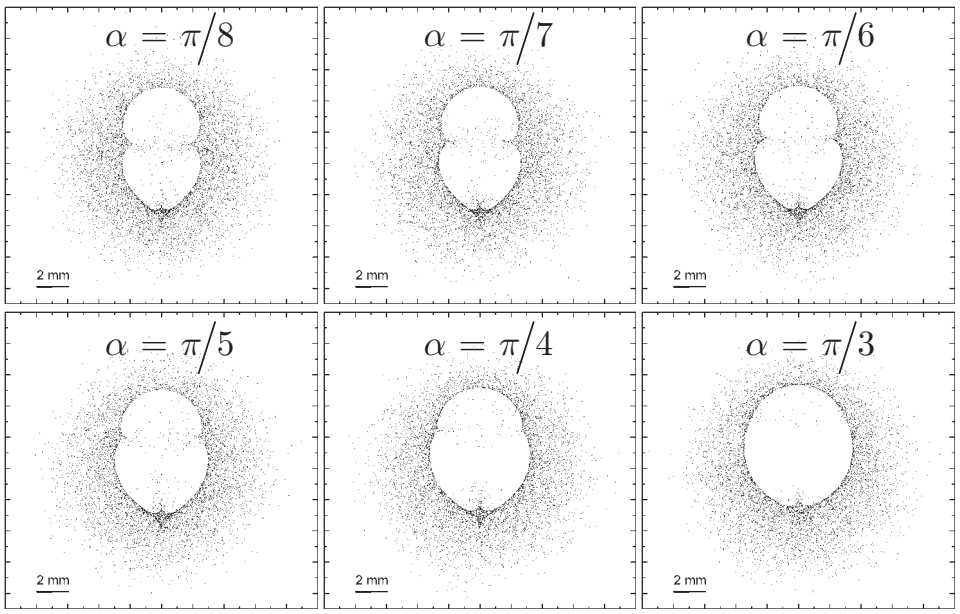

Figure 8.19 – Same as Figure 8.18 but with reversed current orientation.

Systematic bulb-size analysis: results

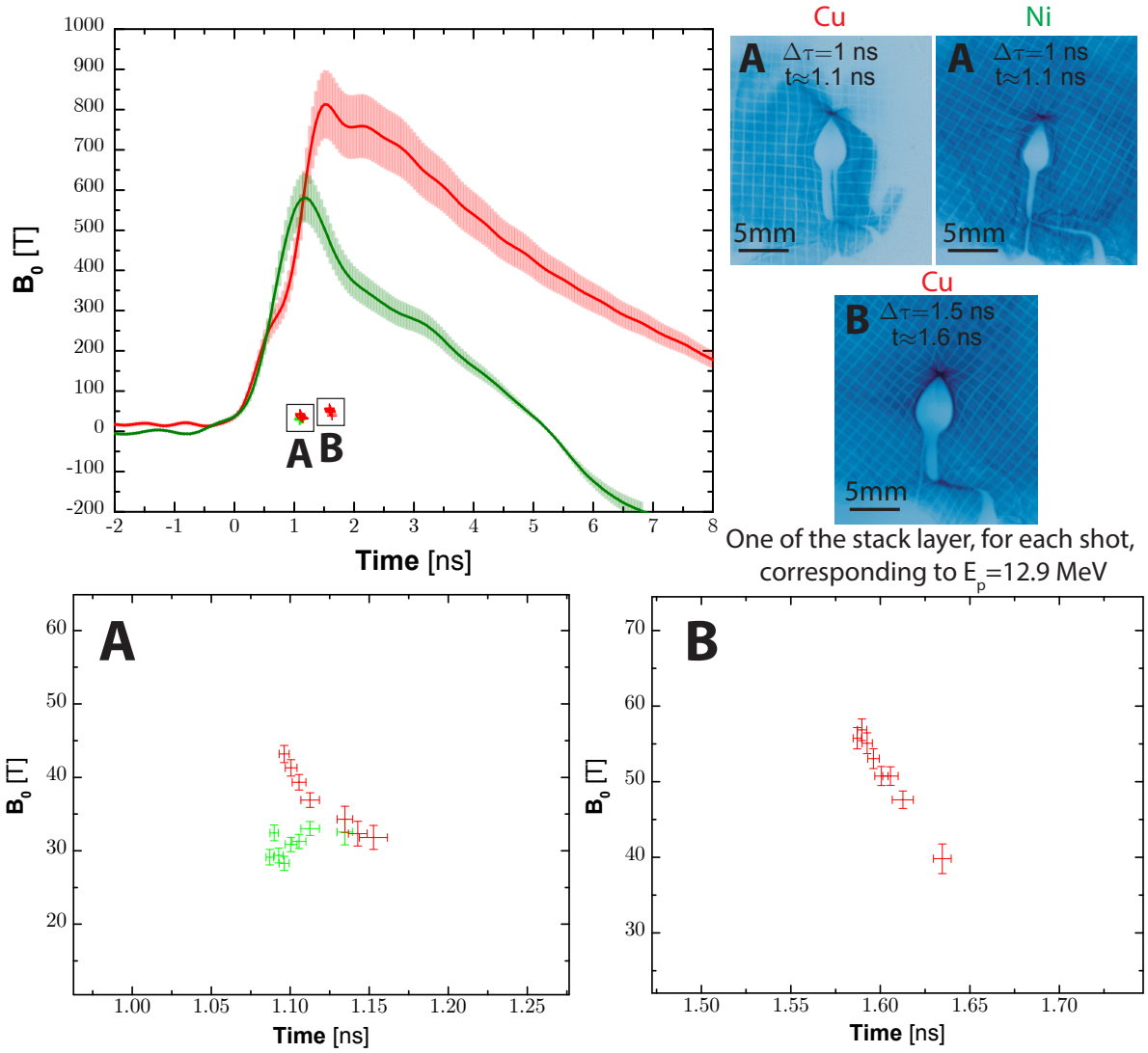

Figure 8.20 – 1^{st} experiment with $a = 250\,\mu m$ (**D**) coils: results of proton deflectometry measurements compared with B-dot measurements. The proton deflectometry B-field were evaluated on the different readable layers of the RCF stack and zooms over the corresponding probing time window are given for the two delays in **A** and **B**. The discrepancy between the two diagnostics is discussed in the text.

In this last part, the results obtained from a systematic measure of the bulb width size in experimental proton imprints will be given. The related current in the coil is obtained using the fitting laws introduced in Eq. 8.10 or Eq. 8.11, depending on the concerned target geometry. In Figure 8.20 the proton deflectometry shots were made at two different probing times, respectively $\tau = 1.12\,ns$ and $\tau = 1.61\,ns$ taking into account the mean TOF of protons. Due to the stack configuration, the probing time window around τ was of $\approx 80\,ps$ and $\approx 60\,ps$ respectively. The results for $\tau = 1.12\,ns$ are shown and compared to B-dot probe results for the Cu (red) and Ni (green) coil-shaped targets with $a = 250\,\mu m$. The measured B-field strength from proton deflectometry is about one order of magnitude lower than the B-dot probe results.

Other peculiar behavior is the trend observed in graphs **A** and **B** zoomed over proton deflectometry points and showing for both cases decreasing B-field strength versus time, while values of **B** (latter in time) are weaker than those of **A**.
If one suggest that the B-field is reaching its maximum before $\tau = 1.12\,ns$ (**A**), it would then also mean that a second maximum exists between $\tau = 1.12\,ns$ and $\tau = 1.61\,ns$ and then the B-field decreases again. Besides that, looking at the Ni results, one see that proton deflectometry points

around $\tau = 1.12\,\text{ns}$ exhibit a quasi-constant B-field which is consistent with the B-field trend seen in B-dot results at the same probing time (near the maximum). Although, one can rely on the B-dot probe evolution with time yielding a maximum at times close to the end of the laser pulse duration. There is not any particular reason that the B-field would decrease during the charging time when the laser is still feeding the electron current.

At this point, both trend and measured B-field strength of proton deflectometry would rather suggest there is a screening effect which is growing during the charging time and affecting the proton results. It is worth mentioning again that proton deflectometry diagnostic is sensitive to both B-field and E-field. Therefore, an added electrostatic charge accumulating in the vicinity of the coil would be a good candidate to explain proton deflectometry results discrepancy. One expect that the proportion of plasma electrons trapped in the region of strong B-field (coil-vicinity) is a monotonously increasing function over the ns time scale of the main laser irradiation. The main-laser interaction with the target rear disk creates plasma 3 mm below the coil. As determined by X-ray spectrometry along with a comparison with calculated atomic spectra, the plasma bulk temperature is estimated to be $T_b \approx 1200\,\text{eV}$ (see X-ray spectroscopy results in Sec. 22.2. High-energy electrons are characterized by a two-exponential law and the first cooler exponential corresponds to the temperature $T_h \approx 45 \pm 5\,\text{keV}$ (see Sec. 8.2.4). The hotter electrons can stream upward and reach the coil region in less than 30 ps, where they can be magnetized: their Larmor radius is $< 10\,\mu\text{m}$ after $\approx 300\,\text{ps}$ ($B_0 \approx 100\,\text{T}$) which is much smaller than the typical size of the strong B-field region, $\sim 2a = 500\,\mu\text{m}$. Colder electrons need $\approx 150\,\text{ps}$ to stream up to coil vicinity and are even more easily magnetized: their Larmor radius is $< 10\,\mu\text{m}$ for $B_0 > 10\,\text{T}$. The progressively increasing charge of magnetized electrons at the coil vicinity can produce an electrostatic effect sufficiently important to influence the deflection trajectories of the probing particles, with increasing *focusing* of the TNSA probing protons. Other plasma effects can influence proton-deflectometry measurements, but their effect is expected to be negligible compared to the electrostatic one: i) the pressure of the magnetized electrons in the coil region $p_e = n_e^{mag} T_e \lesssim 10^7$ Pa, which remains much smaller than the density of magnetic energy $p_B = B_0^2/2\mu_0 \sim 4 \times 10^9$ Pa, for $B_0 = 100\,\text{T}$. ii) Diamagnetic currents of the trapped electrons $j_D \sum e n_e^{mag} v_e$, yielding a magnetic field over the characteristic length a of $B_D \sim \mu_0 j_D a \lesssim 10\,\text{T}$, eventually opposed but much smaller than the B_0 inferred by the other diagnostics.

In the 2^{nd} experiment, we made proton deflectometry measurements at four different probing times (Figure 8.21) which are in chronological order $\tau = 0.36\,\text{ns}$ (**A**), $\tau = 0.62\,\text{ns}$ (**B**), $\tau = 1.12\,\text{ns}$ (**C**) and $\tau = 2.12\,\text{ns}$ (**D**) with a TOF window around τ of $\approx 60\,\text{ps}$. Surprisingly, the bulb size and the overall mesh imprint deformations decrease with time: protons of the same energy undergo smaller deflections if injected at later times. The B_0 decreasing behavior as a function of time is in contradiction with the B-dot probe measurements, and does not agree with the laser-charging process up to $t \approx 1\,\text{ns}$.

Although, we have i) at the earlier probing time ($\tau = 0.36\,\text{ns}$), the proton deflectometry values are resulting to be consistent with B-dot probing and ii) the trend observed in **C** and **D** in respect to B-dot probe suggests that the screening effect converges to a stable value which does not affect anymore the relative time evolution of proton deflectometry measurements. It supports the hypothesis of an added electrostatic charge that would be progressively accumulated (trapped) in the coil vicinity whilst the total charge is converging to a stable value.

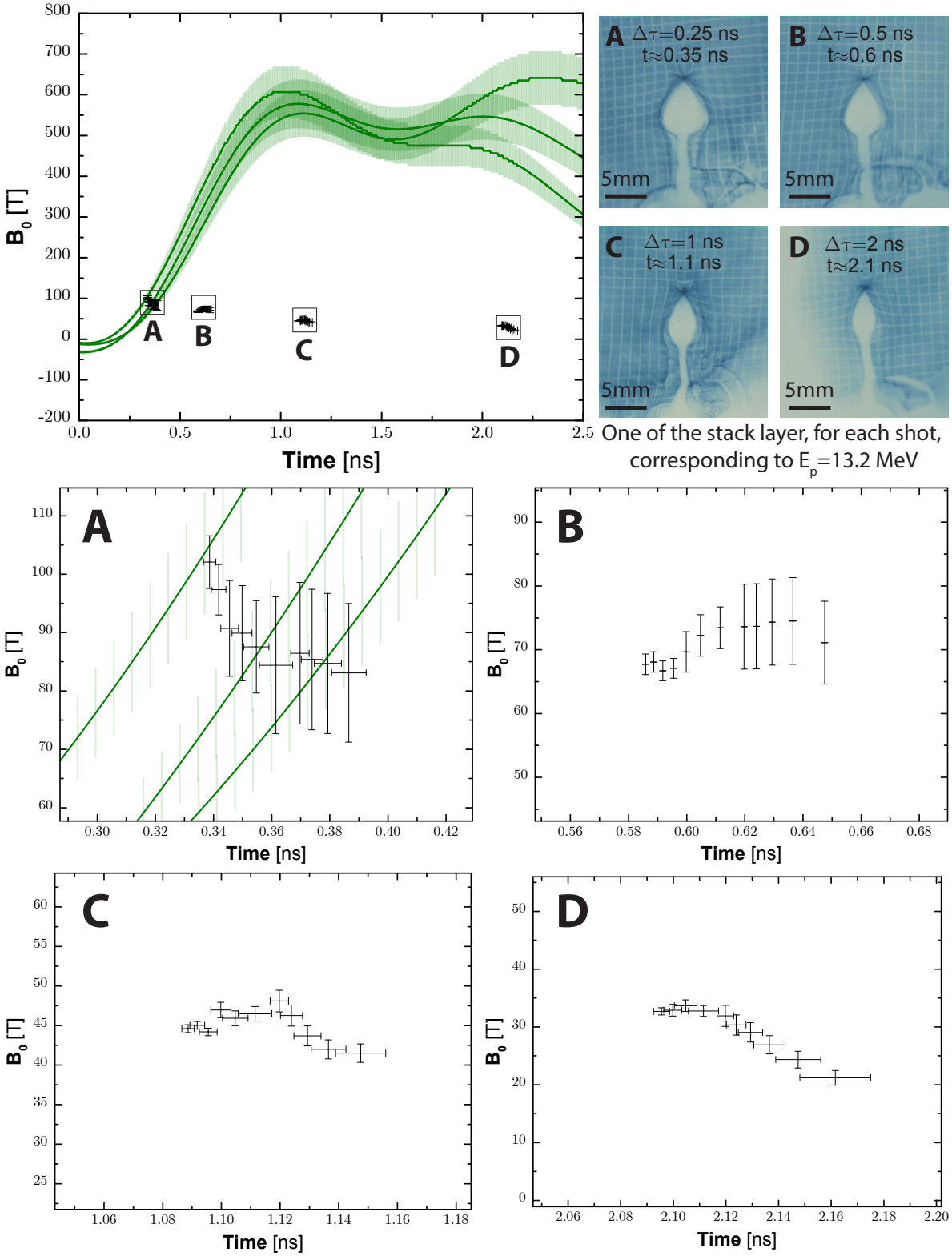

Figure 8.21 – Same as Figure 8.20 for the 2^{nd} experiment.

Box. 8.4: Electrostatic contribution (analytic estimate)

To analyze deeper the contribution of an added electrostatic charge, we can modified the previous analytic estimate of bulb width in order to include an electrostatic effect. The mapping relation for B-field only (Eq. 8.8) writes now:

$$r_i = Mr + \frac{\mu_B \Delta_x D}{r} - \frac{\mu_E \Delta_x D}{r} \tag{8.12}$$

where $\mu_B = \dfrac{e\mu_0 I}{2\pi\sqrt{2m_p E_p}}$ as it can be identified in Eq. 8.8, and the added electrostatic effect with $\mu_E = \dfrac{e}{2E_p}\dfrac{Q}{2\pi\epsilon_0\Delta_x}$. The added electrostatic effect is here caused by the charge Q distributed over a cylinder of length Δ_x (the related electric field formulation $E = \dfrac{Q}{2\pi\epsilon_0 r\Delta_x}$ is a good approximation for the field close to a long conducting cylinder).
After solving the *caustic* location $dr_i/r = 0$ and replacing it in Eq. 8.12 yields the bulb width on detector plane:

$$w = 4\sqrt{DM\Delta_x(\mu_B - \mu_E)} \tag{8.13}$$

The charged cylinder formulation for the electric field is yielding a simple formula for the bulb width. For information, a more complex formula would be obtained taking a charged sphere, but the numerical application is giving similar results. The charge is also located here at the bottom part of the coil and both magnetic and electrostatic cylinders are directed along $\vec{x}$.

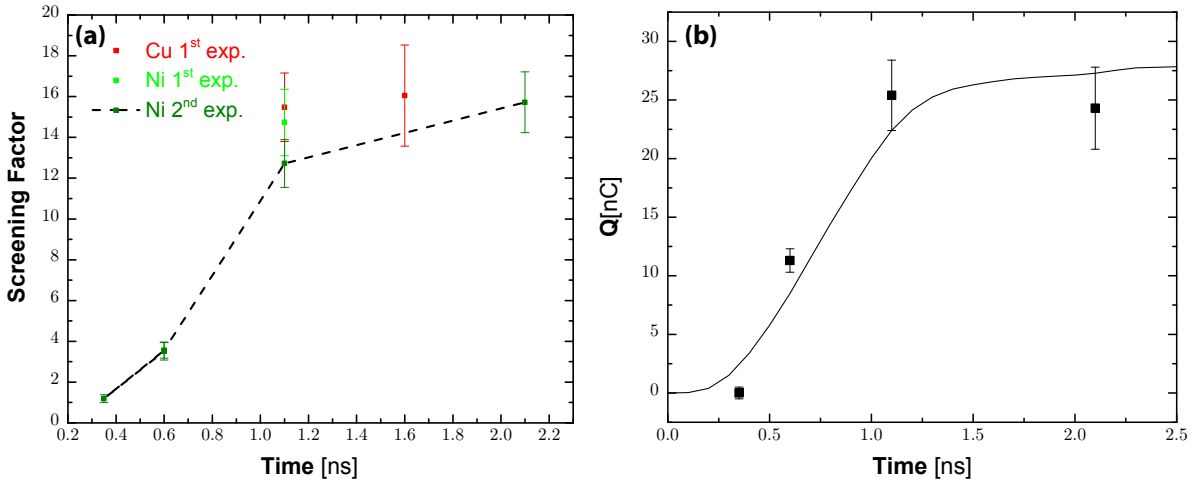

Figure 8.22 – (a) Screening factor (ratio between inferred B-field from B-dot measurements and proton deflectometry measurements) for the different results of coil-shaped targets with $a = 250\,\mu m$. The associated discrepancy is repeatable between the two experiments and is similar for Cu and Ni targets. Yet, the screening factor for Cu is a bit higher, which could correspond to more trapped electron since the B-field strength is higher. Explanations of the electrostatic screening hypothesis are given in the text. **(b)** Total charge Q needed to match the experimental bulb width of Ni target in the 2^{nd} experiment, taking the coil current inferred from B-dot measurements. The solid line results of a fraction of the electrons populating the plasma plume, estimated by an ablation model described in text.

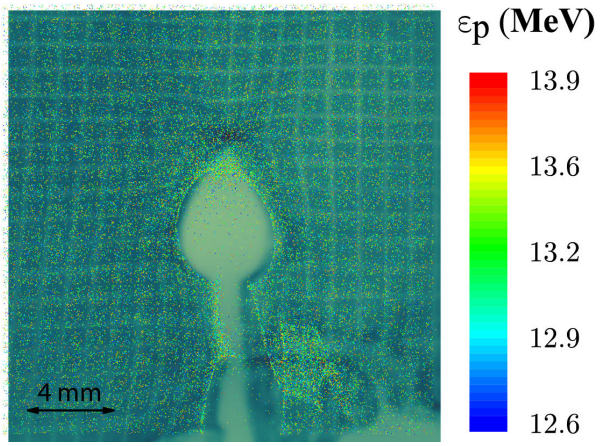

Figure 8.23 – Overlapped experimental and synthetic RCF imprints at $t = 0.6\,\text{ns}$ for protons of $\epsilon_p = 13.2 \pm 0.7\,\text{MeV}$. The synthetic RCF imprint is obtained for a ballistic simulation with a coil current of $I = 130\,\text{kA}$ and an added charged sphere containing 12 nC located below the coil. The bulb width and added electrostatic charge is consistent with the point at $t = 0.6\,\text{ns}$ obtained under analytic estimations in Figure 8.22-**(b)**.

Using Eq. 8.13, one can estimate the total charge Q that would be trapped near the bottom part of the coil so as to match with the experimental bulb width while considering the related current from B-dot measurements. It has been done for the Ni coil target results of the 2^{nd} experiment, Figure 8.21. The results for Q are shown together with the so-called *screening factor*, representing the ratio between the B-field strength inferred from B-dot measurements and proton deflectometry measurements in Figure 8.22-**(a)**. In the right graph **(b)** of this figure, a continuous estimation of the accumulated charge is obtained taking a fraction of the electronic population of the plasma plume generated by the laser heating. To do so, we estimated the electron generation rate from the ablation model proposed by Atzeni *et al.* in [8]. It writes:

$$\frac{dN_e}{dt} = n_c c_s A_L \tag{8.14}$$

where n_c is the critical density, c_s the ion acoustic sound speed and A_L the laser ablation spot area. Taking the Ni estimated maximum temperature of the plasma plume $T_b = 1200\,\text{eV}$ and the laser parameters found in Box. 8.1, it yields $dN_e/dt \approx 3.1 \times 10^{23} s^{-1}$. By multiplying this value by the normalized intensity trace of the laser and then integrating, one obtains the evolution of the solid curve in Figure 8.22-**(b)**. The total charge reported on the left hand ordinates of the graph represents actually 1/200 times the estimated total charge of electrons in the plume N_e, meaning that this tiny part of the electron created from LP interaction is enough to induce the previously quantified electrostatic effect.

The analytic estimate introduced in Box. 8.4 has been compared to ballistic simulations. As an example, to compare with the point at $t = 0.6\,\text{ns}$ in Figure 8.22-**(b)**, a ballistic simulation for a coil current of $I = 130\,\text{kA}$ and an added charged sphere located below the coil containing 12 nC is given in Figure 8.23. The obtained bulb width is seen to be consistent with the overlapped experimental RCF imprint for the same proton energies of $13.2 \pm 0.7\,\text{MeV}$. The added charge of 12 nC at $t = 0.6\,\text{ns}$ is therefore confirmed by the ballistic simulation.

Relativistic electrons signature

Here we will present some features observed from RCF imprints deep in the RCF stack, corresponding to either protons of high energy or relativistic electrons.

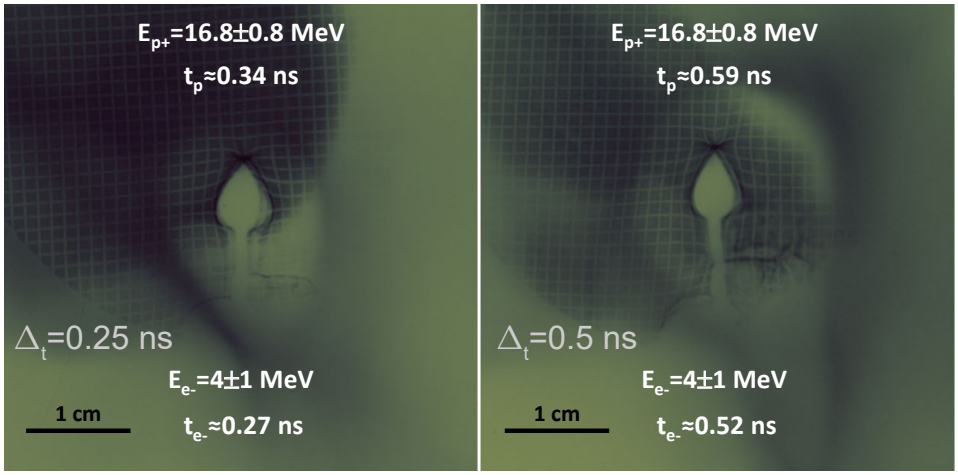

Figure 8.24 – Sample RCF data for a deep layer of the stack from different shots with delays of $\Delta\tau = 0.25\,\text{ns}$ and $\Delta\tau = 0.5\,\text{ns}$. The spatial scale corresponds to the plane of the coil center.

In Figure 8.24 are shown images from RCF layers corresponding to $E_p = 16.8 \pm 0.8\,\text{MeV}$ protons, for delays of $\Delta\tau = 0.25\,\text{ns}$ and $\Delta\tau = 0.5\,\text{ns}$: for each delay, the usual mesh imprint and void-bulb proton signatures are smaller respect to the same shot image labeled **B** in Figure 8.21 ($E_p = 12.9\,\text{MeV}$), consistently with the higher proton energy. Yet, we detect a second particle species producing a large halo on both images which is increasing in size with probing time, superposed to the proton signature which is reversely decreasing in size with probing time. For each shot, such a halo is clearly visible with the same size and shape over the successive last six layers of the RCF stack till the cutoff proton energy $E_p \approx 20\,\text{MeV}$. This halo signature should be the signature of relativistic electrons, accelerated at the Au-foil surface by the short laser pulse, and relatively homogeneously deposing their energy over the successive RCF layers. Accounting for their spectrum (inferred from particle-in-cell simulations of the short pulse laser interaction and presented in Figure 5.3), the foil potential barrier and the integrated electron stopping power in the RCF stack over the first layers, the halo signal would then correspond to electrons with energy between 3 to 5 MeV.

In Figure 8.25-**a)** and **b)** we present two supplementary sample RCF images at a delay between laser pulses of $\Delta\tau = 0.5\,\text{ns}$, for higher proton energies (shorter TOF, slightly earlier probing times). To further study this signature origin, new calculations of particle propagation over simulated 3D B-field maps were performed: the RCF imprint results are presented in Figure 8.25 for **c)** $20 \pm 1\,\text{MeV}$ protons propagating over a B-field map with $B_0 = 290\,\text{T}$ (assuming no screening effect at $t = 0.58\,\text{ns}$) and for **d)** $3 - 5\,\text{MeV}$ electrons propagating over a "screened" weaker B-field map, with $B_0 = 23\,\text{T}$. On the contrary, while the shape of the simulation result obtained for the 20 MeV protons is qualitatively very similar to the experimental ring imprint, the dimensions of the former are significantly smaller, and this assuming no B-field amplitude screening by plasma magnetization: this rules out protons from being responsible for the detected ring pattern. On the other hand, the simulation result for the relativistic electrons presents a halo size fairly comparable to the experimental one, whilst having a slight different shape. It is worth mentioning that this matching is obtained assuming a B-field strength that is a factor ≈ 10 times weaker than the B-field expected from the B-dot measurement at $t \approx 0.52\,\text{ns}$ (the average time, for this shot, at which the considered relativistic electrons probe the B-field).
Nonetheless, by considering an electrostatic screening effect by trapped electrons, the electrons would be reversly more deflected and would exhibit a very big halo size. At the present time, this signature observed in the last RCF layers remains thus unclear.

Other imprint signatures at low energies

In Figure 8.26, we present sample images at different delays, as labeled in the figure, and

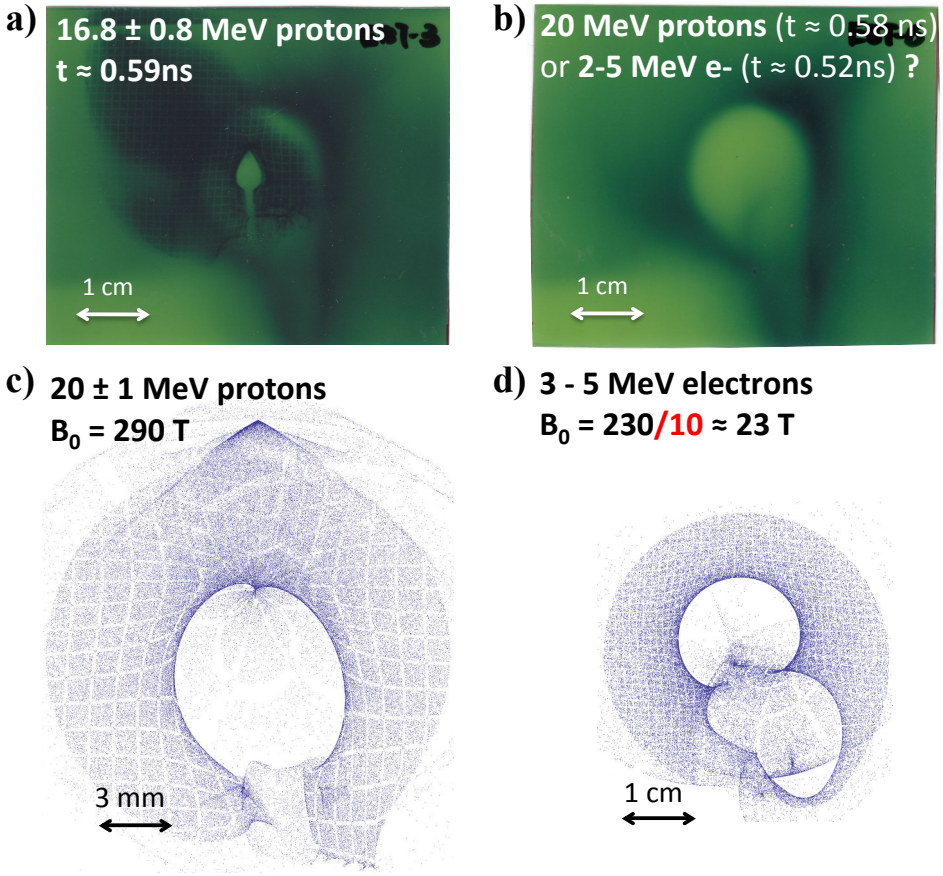

Figure 8.25 – a) and **b)**: Supplementary experimental images of proton-deflectometry for $\Delta\tau = 0.5\,\text{ns}$ delay between the laser pulses, and corresponding to different proton energies (as labeled). **c)** $20 \pm 1\,\text{MeV}$ proton imprint on detector plane given by simulation of their trajectories over a simulated 3D B-field map with $B_0 = 290\,\text{T}$ (assuming no screening effect at $t = 0.58\,\text{ns}$) and **d)** idem for $3 - 5\,\text{MeV}$ electrons propagating over a B-field map with $B_0 = 23\,\text{T}$ (assuming a 10 times screening effect at $t = 0.52\,\text{ns}$). The spatial scales correspond always to the plan of the detector.

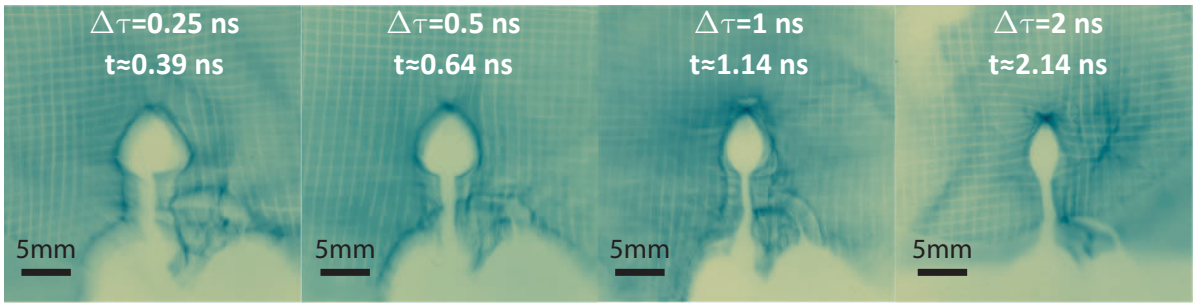

Figure 8.26 – Sample RCF data for a one of the first layer of the stack, from different shots with delays of $\Delta\tau = 0.25\,\text{ns}$, $\Delta\tau = 0.5\,\text{ns}$, $\Delta\tau = 1\,\text{ns}$ and $\Delta\tau = 2\,\text{ns}$. The spatial scale corresponds to the plane of the coil center.

corresponding all to $E_p = 7 \pm 0.6\,\text{MeV}$. One can see that for this range of protons, superposed to the void-bulb, there is a pile-up caustic which forms a similar pattern, bigger in size. This signature is also decreasing significantly with the probing time and should then correspond to a proton signature. Interestingly it almost disappear for the last delay at $\Delta\tau = 2\,\text{ns}$. Yet, a ring-pattern can be seen at this late delay and would correspond to hydrodynamic effects of the plasma, filling the vicinity of the coil and affecting low energy proton propagation and trajectories. The pattern seen at earlier delay is caused by a defocusing effect on protons of low energies summed up by the already characterized B-field effect. The defocusing could be due to a neutralizing positive charge circulating along the conducting wires of the target and lasting all along the laser duration of $\sim 1\,\text{ns}$. A similar effect has been observed when irradiating shaped target with a short laser pulse. It has been associated for this regime of irradiation to an electromagnetic wave of positive charge displacement. These features will be detailed for short pulse laser-driven coil targets, based on previous studies and an experiment we realized at GSI, Darmstadt, in Sec. 11. The pattern observed here has characteristics of an electrostatic cusp, signature of a force pushing away the protons from current-carrying elements of the circuit, similarly to what we observed in the above mentioned experiment.

8.1.5 Shielded proton deflectometry

Based on the observed discrepancy of proton deflectometry measurements in respect to B-dot, an experiment led by our collaborators from Japan used a shielded proton deflectometry setup in order to avoid electrons from LP interaction to stream up to the coil vicinity.

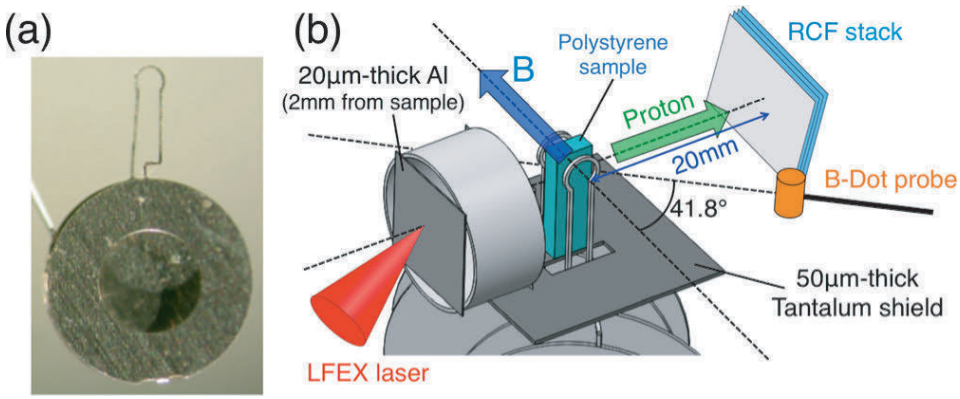

Figure 8.27 – (a) Photography of a capacitor-coil target used in this experiment. (b) Experimental setup of magnetic field generation with two laser-driven capacitor-coil targets. In this experiment, B-dot probe and proton deflectometry were used to measure the produced magnetic field amplitude. The magnetic field was generated using GEKKO-XII laser beams, and the proton beam was accelerated using LFEX laser. The proton beam propagates (green arrow) perpendicular to the magnetic field direction (blue arrow) and the proton pattern was recorded on a RCF stack. Between the two coils, a 250 µm-thick polystyrene foil was placed to investigate magnetic field diffusion in the plastic medium.

A 50 µm-thick tantalum (Ta) shield was placed between the capacitor plates and the coil-wire in order to keep the volume surrounding the coil center clear of the plasma. The setup is shown in Figure 8.27. The experiment was conducted on the GEKKO-LFEX laser facility. Two capacitor-coil targets were aligned in Helmholtz geometry to generate a B-field with relatively uniform spatial distribution between the coils. A 50 µm-thick Ta plate was placed between the coil and capacitor plates to block the plasma streaming from the capacitor part. A 250 µm-thick plastic foil was placed between the two coils to study magnetic field diffusion in the dielectric media and acts also as an additional protection against plasma accumulation in the coil gap. The disk plate of each capacitor was driven by one GEKKO XII laser beam, propagating through the 1800 µm-diameter hole of the front ring-shaped plate, with wavelength, energy, pulse duration and intensity of respectively 1053 nm, $540 \pm 100\,\text{J}$, 1.3 ns, and $(2.1 \pm 0.4) \times 10^{16}\,\text{W/cm}^2$. For the proton deflectometry shot, the laser beam energy was $880 \pm 50\,\text{J}$, corresponding to intensity of $(3.4 \pm 0.2) \times 10^{16}\,\text{W/cm}^2$, which is 1.63 times of that being used during B-dot probe measurement. The coil diameter was 500 µm, with half open angle

of 36.9 ° for wire connection to the capacitor plates. The two capacitor-coils were aligned coaxially at 500 µm distance to each other. The midpoint between the coils was at the target chamber center (TCC).

In this experiment, our B-dot probe was used to measure the temporal evolution of the field amplitude, placed at 100 mm from TCC on the equatorial plane and aligned at 41.8 ° from the common coil axis. The B-dot probe and oscilloscope had 4 GHz maximum bandwidth with sampling time interval of 50 ps. Similarly to what we made for the experiments in LULI, the B-dot raw signals were filtered by a band-pass filter from 2 MHz to 4 GHz to reduce direct current background and unphysical fluctuations above the detection threshold. Then the signal is corrected from attenuations which was of 13 dB in the given measurement with 9 dB of additional attenuation (8 dB from the balun and 1 dB from cables and connectors). To extrapolate the values to the coil center, the 3D spatial distribution of magnetic field amplitude was calculated with the magnetostatic code Radia for the given geometry of the B-field targets. Figure 8.29-a) shows the calculated profile of the magnetic field amplitude along the coil axis.

The proton deflectometry measurement was performed with the setup shown in Figure 8.27. The proton TNSA target was a 20 µm-thick aluminium foil attached to an Al_2O_3 cylinder having 2000 µm of outer surface diameter and 500 µm of wall-thickness. The cylinder is mounted over the tantalum shield. Assuming that energy conversion efficiency from laser to magnetic field is constant with laser energy, the laser intensity is 1.63 times larger for the proton deflectometry shot in respect to the B-dot probe shot. It would correspond to a probed magnetic field $\sqrt{1.63} \approx 1.28$ times larger for the proton deflectometry shot, based on the relation of magnetic energy density ($W_B = B^2/\mu_0$). The LFEX laser beam, with wavelength, pulse duration, energy, and intensity on target being, respectively 1053 nm, 1.5 ps, 1060 ± 90 J, $(1.1 \pm 0.1) \times 10^{19}$ W/cm^2, was focused onto the aluminium backlighter foil with an incident angle of 41.8 °, at 1.5 ± 0.15 ns after the peak of the driving GEKKO XII laser beam. The TNSA proton beam of maximum energy of 35 MeV was directed to TCC perpendicularly to the common coil axis. Proton generation was 2 mm away from TCC, and a 35-layer RCF stack was placed at 20 mm from TCC to record proton beam pattern after traveling through the magnetic field.

The results from proton delfectometry measurements with magnetic field are shown in Figure 8.28-(h) on a RCF layer corresponding to proton energy of 23 ± 0.9 MeV. Time of flight of protons between the proton backlighter and the coil region (30 ps) is negligibly small in this case: the timing of the proton delfectometry measurement is thus determined dominantly by the temporal delay between GEKKO and LEFEX laser beams. In this experiment, the delay was fixed to 1.5 ± 0.15 ns. To unfold the results of the RCF imprint, a Monte-Carlo simulation, combined with the magnetostatic code was run to simulate the proton distribution on RCF. The current in the coil was varied from 100 kA to 300 kA, corresponding, respectively to maximum magnetic fields of 240 T and 730 T. Electric field is neglected in this analysis.
We obtained umbrella-like patterns in the simulated images, in fair comparison with the experimental RCF imprint. The synthetic results are shown in Figure 8.28 for (b) 240 T, (c) 490 T, (d) 610 T, and (e) 730 T of the field amplitude at the coil center. The best match for the umbrella-like shape pattern, particularly the separation distance between the two peak density points, is obtained for a current of 250 kA (610 T at coil center) and shown with the experimental RCF imprint in Figure 8.28-(h). A deeper analysis of the proton signal distribution along the line connecting two sideway spots (indicated with dotted lines), with integration width of 0.1 mm, is plotted in Figure 8.28-(g), together with same line plot of the experimental data. Again the best match is obtained with the current of 250 kA.

Proton deflectometry probed the field amplitude $\approx$ 1.5 ns after the peak timing, as shown in Figure 8.29. At the proton probing time, the scaled amplitude of B-dot measurement, after multiplying by the energy scaling factor of 1.28, is $410 - 670$ T. It consistently agrees with the result of 610 ± 30 T obtained from proton deflectometry. In conclusion, this experiment shows a fair comparison at high field amplitudes between proton deflection and B-dot probe measurement, when shielding the coil region against plasma expansion from the capacitor plates. This strengthen the evidence that the laser-driven plasma between the disks was indeed the source of the electrostatic perturbation seen on proton deflectometry measurements in previous experiments in LULI.

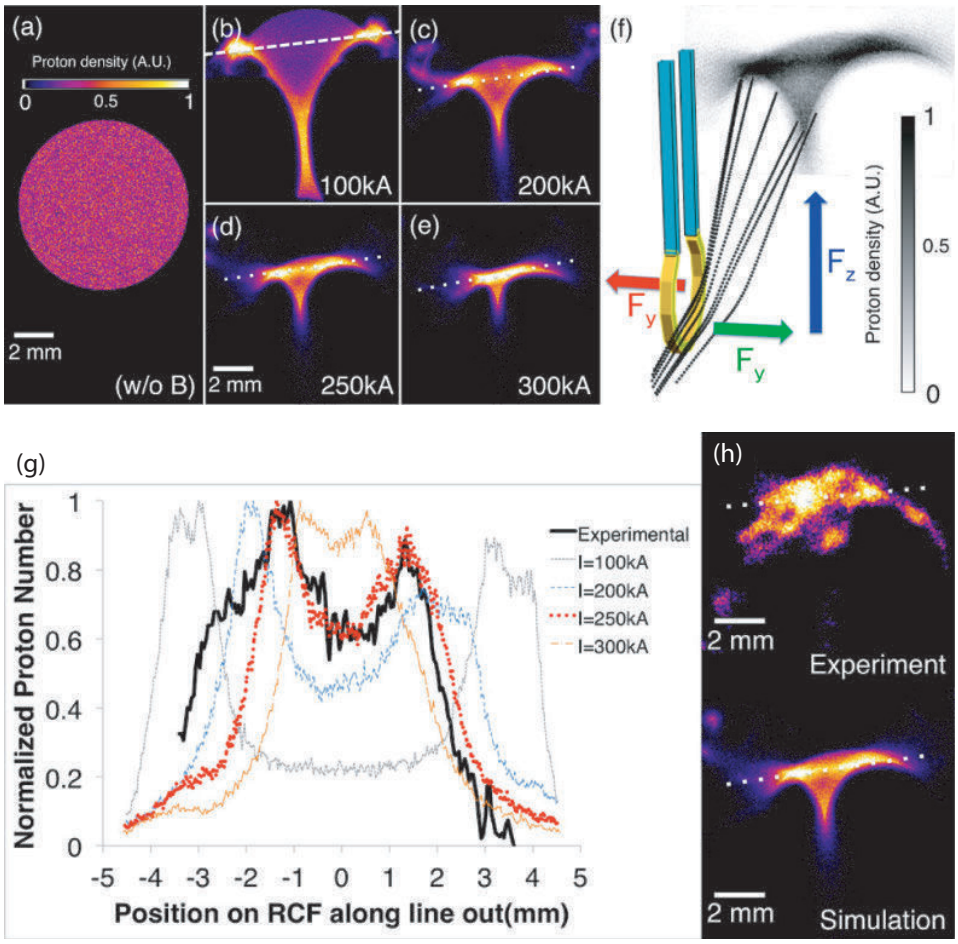

Figure 8.28 – (a)-(e) Synthetic proton deflection patterns, respectively for (a) without magnetic field, (b) 240 T, (c) 490 T, (d) 610 T and (e) 730 T at the coil center. (f) Simulated proton trajectories, here y and z are, respectively, the coil axis and the vertical directions in the proton patterns. All protons are deflected by the Lorentz force, along the z-direction (blue arrow), and depending on the proton position in z, along the y-direction (red and green arrow), due to the fringing field around the coil wire. This produces the umbrella-like proton pattern. (g) Line profiles drawn along the white dotted lines in (b)-(e). The line profile for 250 kA (610 T of field amplitude at the coil center, red dotted line) shows the best agreement with the experimental result (black solid line). (h) Proton patterns obtained from experiment (top) and from simulation corresponding to (d) (610 T) and showing the best matching.

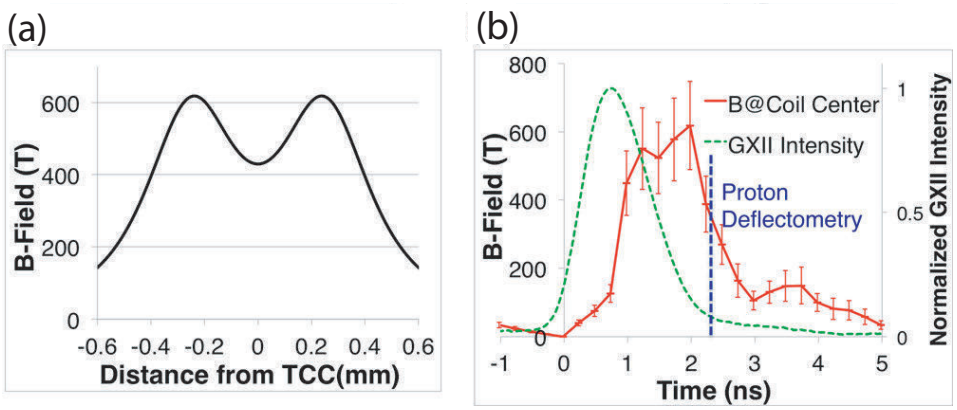

Figure 8.29 – (a) Spatial distribution of magnetic field amplitude between the two coils, along their common axis, as calculated with the 3D magnetostatic code RADIA. (b) Temporal evolution inferred magnetic field amplitude at coil center from B-dot probe measurement (red solid line) and GEKKO XII laser pulse profile (green dotted line). Peak amplitude of the magnetic field generated by the pair of capacitor coils was estimated to be 620 ± 130 T with $1.5 pm 0.3$ ns full-width half-maximum (FWHM) pulse duration, ranging from 0.2 to $1.7 (pm 0.15)$ ns after the peak of the drive laser pulse. Vertical dotted line indicates the timing of the proton deflectometry measurement.

8.2 Extra physical information from complementary diagnostics

8.2.1 Shadowgraphy results

In the setup presented in Figure 8.3, when removing the TGG crystals for Faraday rotation, we could obtain shadowgraphic images of the coil onto both a Gated Optical Imaging (GOI) system and a Streak camera (at the incident probe polarization). Figure 8.30-a) and b) show typical images obtained with respectively these two detectors from Cu $a = 250\,\mu$m targets. We can clearly observe the coil-rod expansion perpendicularly to the coil axis, as a function of time. The rod expansion speed of $v_{\text{exp}} = 11 \pm 3\,\mu$m/ns was estimated from a series of consistent Streak images [cf. slope of the dashed orange line in Figure 8.30-b)]. Noteworthly, a space of several hundreds of microns remains accessible inside the coil for several nanoseconds, assuring the possibility of magnetizing secondary targets placed at the coil vicinity, or let pass through the coil center a bunch of charged particles without collisions with a dense plasma. This feature is important for applying the produced B-field externally to a secondary target or to guide charged particles in vacuum. These applications will be explored in the next chapter Part III.

Besides, the information of the coil-rod expansion of $\sim 10\,\mu$m/ns would correspond without magnetic field to a thermal expansion by electron thermal pressure $p_{th} = n_e k_B T$ with $T \sim 10$ eV. This would constrain the modeling of the heating of the wire rod by Joule effect and gives an important feedback for the estimated magnitude of the current flowing through the coil. The modeling will be detailed in Sec. 9 and will include a discussion about coil-rod expansion, while considering the additional magnetic pressure induced by the high current flowing through the coil.

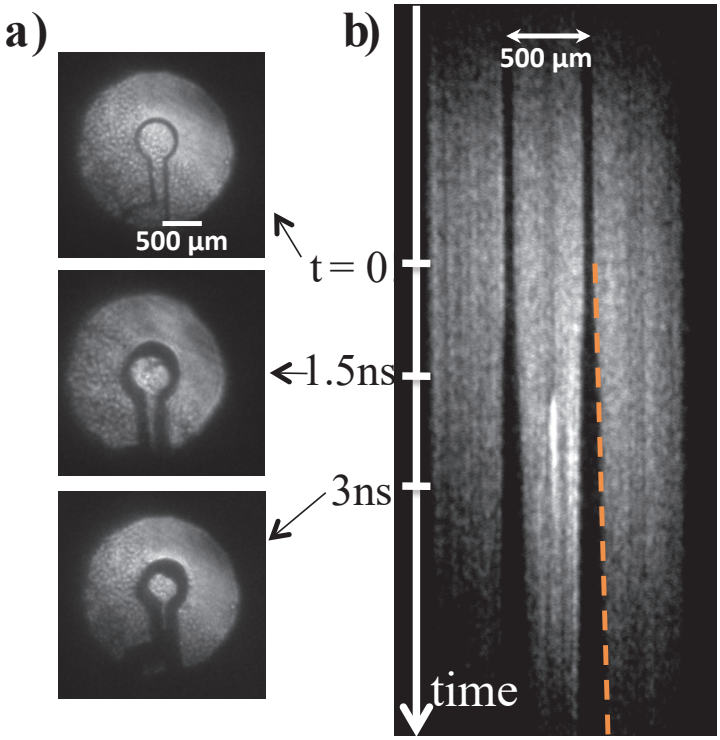

Figure 8.30 – Coil expansion inspected by optical shadowgraphy at $\lambda = 532\,\text{nm}$: **a)** optical gated images (0.65 ns window) from different shots and **b)** one shot streaked image (10 ns sweep window).

8.2.2 Streak Optical Pyrometry (SOP)

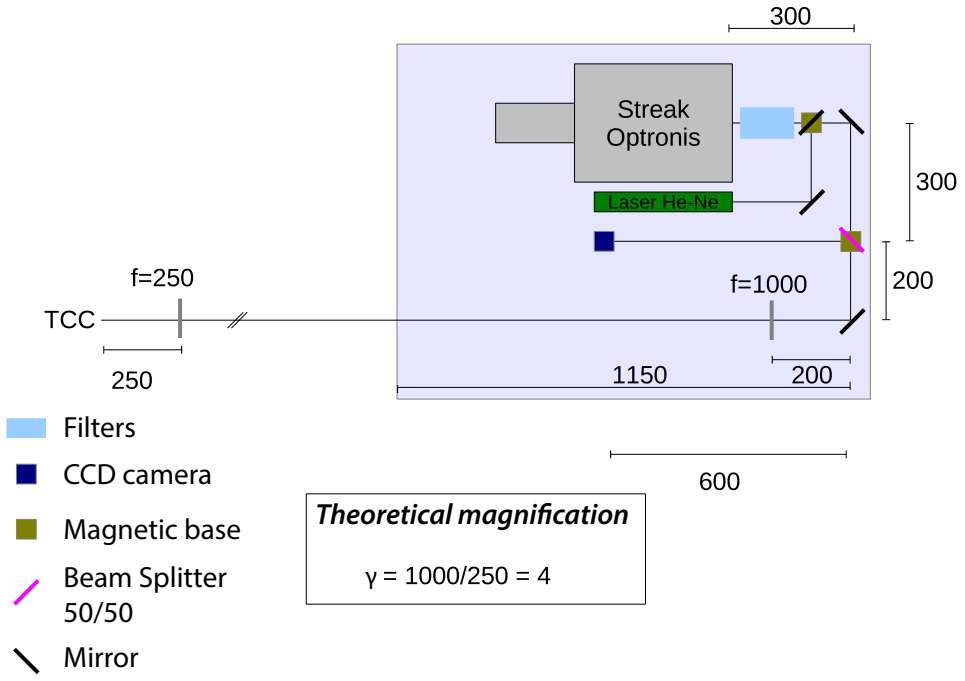

Figure 8.31 – Setup of the Streak Optical Pyrometry (SOP) table

The SOP setup is presented in Figure 8.31. The thermal emission at the rear side of the capacitor-coil irradiated disk is first collected by a $f = 150\,\text{mm}$ lens. A beam splitter separates the incoming signal into the SOP and a CCD used to make the characterization of the LP focal spot and alignment. A $f = 1000\,\text{mm}$ lens images the emission to the slit of an Optronis streak camera slit. Optical densities,

a notch-space filter at 532 nm - blocking any $2\omega_0$ laser light noise - and color filters (OG530 and KG3) - preventing direct exposure to laser light at $1\omega_0$ - are disposed in the filter's area, located in front of the entering of the camera. Hence, the thermal emission is observed avoiding any polluted light from the laser and its reflections which would have otherwise strongly saturated the image.

An example of SOP streaked image is shown in Figure 8.32-a). The spatially-averaged emission of the center zone is plotted in solid red line over the time window of 5 ns-duration in b).

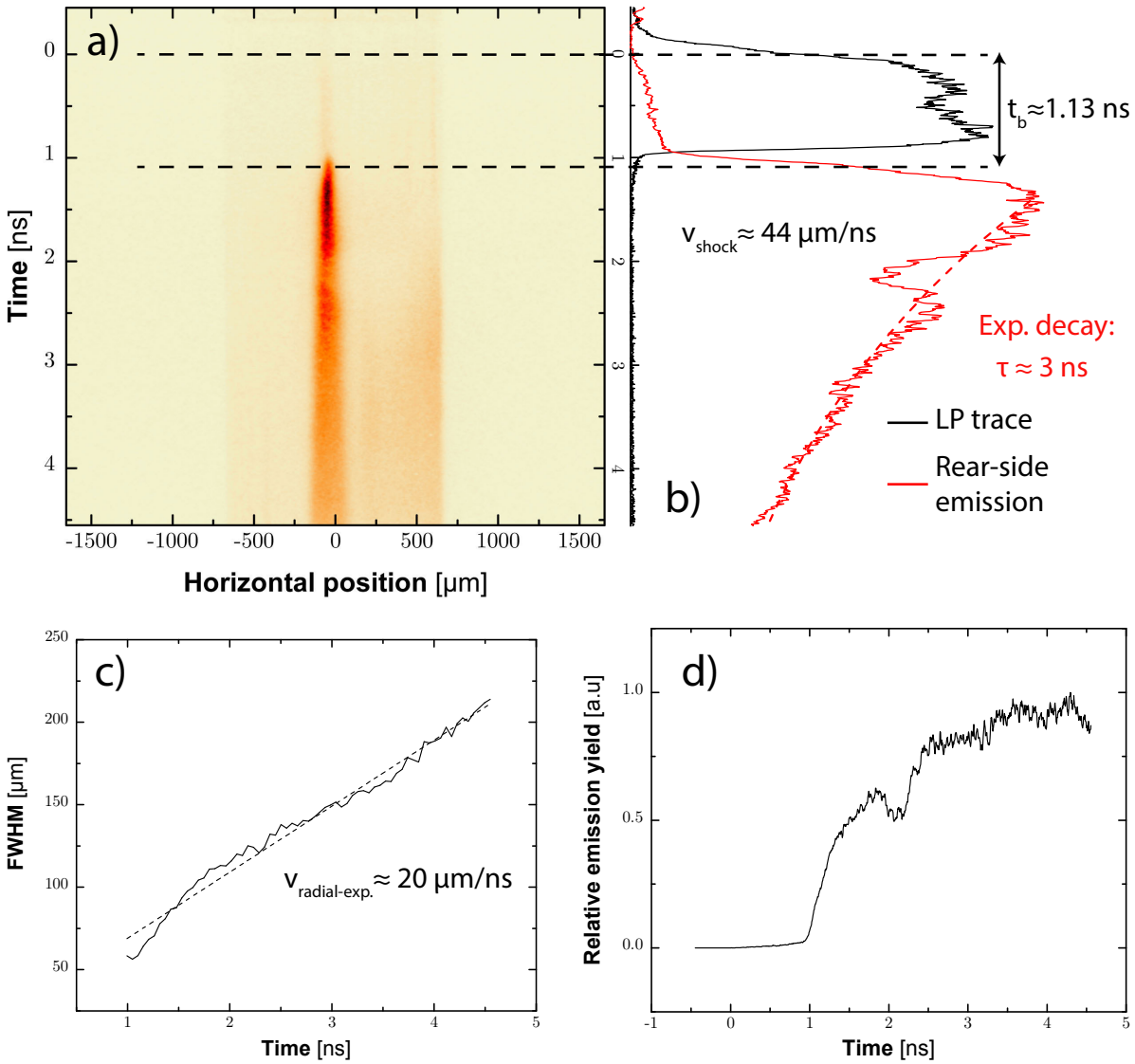

Figure 8.32 – a) Streaked image of the thermal emission of the irradiated disk's rear side of capacitor-coil target, obtained by SOP measurement (see setup in Figure 8.31). b) Averaged profile over streak time for the rear-side emission (red solid line) and from LP laser pulse (black solid line). Labeled information of the breakout time of the rear-side emission ($t_b \approx$ 1.13 ns) and of an exponential fit of the emission decay ($\tau \approx 3$ ns) are presented. c) Result of the FWHM of the transverse emission over time, yielding a radial expansion velocity of the emission of $v_{\text{radial}-\text{exp.}} \approx 20\,\mu\text{m/ns}$. d) Relative emission yield as obtained after multiplying the rear-side emission [panel b)] by its size [panel c)].

The emission decay with time is fitted by a decreasing exponential function. In the same graph, the direct imaging of the LP laser beam spot (at lower power) obtained for the same streak timing is shown in black solid line. The delay between half-maximum rise time of both signatures allows us to identify that the rear side emission occurs $\approx$ 1.13 ns after LP interaction. This delay can be related to a shock velocity over the 50 µm-thick target of $\approx$ 44 µm/ns. A strong density jump/discontinuity is

created at the interface between the laser-heated area and the colder solid target located behind, and when this expanding interface is moving at a velocity far exceeding the sound speed velocity c_s, a shock wave is launched.

Here, the high laser intensity suggests in addition a major role of fast electrons which affect strongly the transport conditions of the shock in target-depth. However, it is clear that the imaged emission at target rear side does not correspond to the thermal emission of hot electrons breaking-out at the target rear side. Indeed, electrons would have in the latter case kinetic energies of maximum $\approx 6\,\mathrm{keV}$ to match the measured break-out time and would be thus stopped by collisional drag before reaching the target rear side. This rather large shock velocity conveys instead the idea that prior fast electrons deposition in target depth has created an heated channel, boosting the shock propagation. The simulations of the hydrodynamic properties of the target to match experimental breakout time would thus necessitates beforehand a treatment of fast electron energy deposition.

The SOP measurement can also provide other parameters that could be compared to hydrodynamic simulations: i) when reaching the target rear-side - after a rapid rise-time (typical of a shock breakout) - the emission is decaying and corresponds here to an exponential decay of characteristic time $\tau \approx 3\,\mathrm{ns}$ [see Figure 8.32-b)]; ii) the radial spread of the emission can be characterized doing a Gaussian fit of a transverse profile of the emission over time and a radial velocity of $v_{\mathrm{radial-exp}} \approx 20\,\mu\mathrm{m/ns}$ is found [see Figure 8.32-c)]. These two parameters are obviously coupled since the radial spread of the emission is contributing the decay of the emission rate. Yet, the combination of both information (multiplying the emission decay by its size), led to an estimation of a time-variation of the relative spatially-integrated emission, shown in Figure 8.32-d).

8.2.3 X-ray spectrometry

The complementary diagnostics whose results are presented in the following are described in detail in *Appendix*. Namely the tronconic spectrometer, K_α emission imaging, and Bremsstrahlung cannons spectrometers are respectively detailed in Sec. 22.2, Sec. 22.3 and Sec. 22.4.

Tronconic spectrometer

The Tronconic spectrometer used in our experiments was set up to register the emission lines in the range $1.4\,\mathrm{keV} - 1.7\,\mathrm{keV}$. The crystal setup is detailed in *Appendix* - Sec. 22.2 and the center Bragg's angle value was $\theta_{\mathrm{Bragg}} = 17.52\,^\circ$, corresponding to a photon energy averaged between Cu-K_α at the diffraction order $n = 5$ and Al-K_α at the diffraction order $n = 1$. One can see in Figure 8.33 that the $\sim 2\,\mathrm{eV}$ resolution of the spectrometer permitted to distinguish between Cu-$K_{\alpha,1}$ and Cu-$K_{\alpha,2}$ of Cu at $n = 5$. This acquisition is also used to characterize the photon energy scaling of the scanned imaging plate (IP), thus giving the conversion factor from px to eV on the image. The K-shell emission of Cu was induced in a secondary target at the coil vicinity which contained a layer of Cu, used for the shots devoted to study relativistic electron transport.

The emission lines from the LP interaction on the rear-disk are given for a Ni coil-shaped target with $a = 250\,\mu\mathrm{m}$ in Figure 8.34. The coil was situated above the rear disk of the capacitor-coil target in the 2^{nd} experiment and above the front disk in the 3^{rd} experiment. It is the reason why the emission lines of LP interaction are shifted vertically either by 2.1 mm or 2.5 mm from the coil position, respectively. Indeed, the tronconic view was inclined above equatorial plane and invariably located on the side of the front disk for both experiments: the shifted positions on the tronconic detector are then geometrically consistent with the LP interaction point's location.

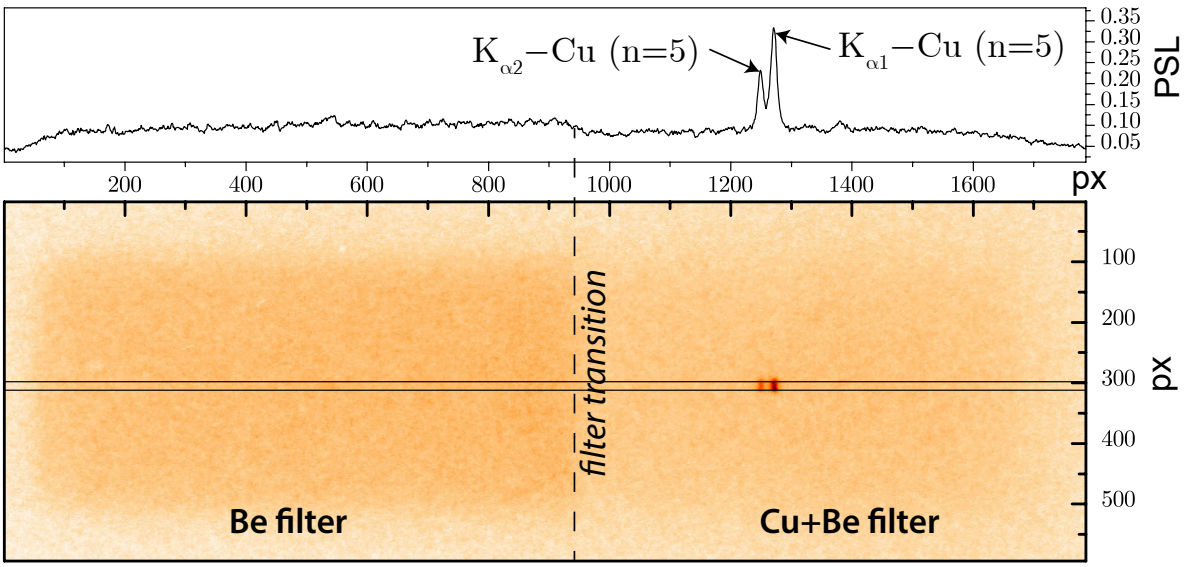

Figure 8.33 – Scanned IP of the Tronconic Spectrometer where it can be identified the $K_{\alpha,1}$ and $K_{\alpha,2}$ emission of Cu at the order $n = 5$, at respectively 1609.6 and 1605.6 eV.

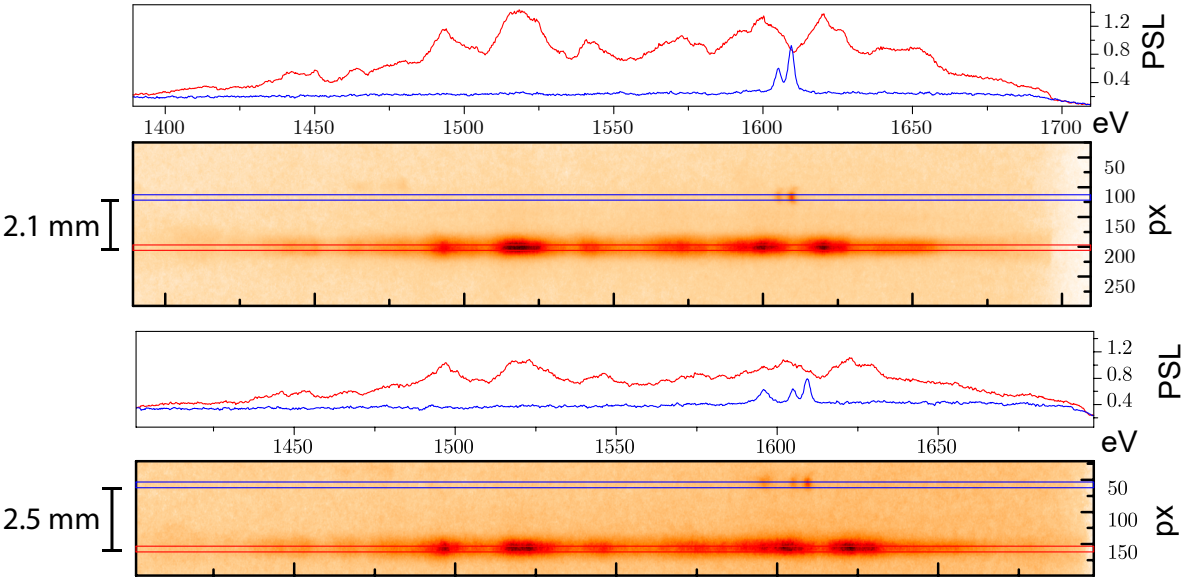

Figure 8.34 – top: Spectral emission of a Ni-coil target of the 3rd experiment, with a secondary target at the coil vicinity containing a Cu-layer. **bottom**: Idem, but for a Ni-coil target of the 2nd experiment. The combination of both images allows us to identify clearly the localization of the two observed emission lines of each image: more details are given in the text.

The X-ray spectra of the ns-plasma, after correcting from filtering (see Box. 22.1 in Sec. 22.2), is then compared to atomic line emission calculations for a plasma at critical density and at different temperatures. It is assumed in the atomic model that the global thermodynamic equilibrium is reached and $T_i = T_e = T$. The model used is called SCKIM (SuperConfiguration Kinetics Model) and the calculations were performed by O. Peyrusse. In Figure 8.35, the experimental X-ray spectrum from tronconic spectrometer is compared with the calculated atomic emission lines (dashed lines) for three temperatures $T = 1000\,\text{eV}$ (blue), $T = 1200\,\text{eV}$ (purple) and $T = 1500\,\text{eV}$ (dark red). The atomic emission lines (in arbitrary units) match fairly well with the experimental spectrum. Based on the uncertainties of the plasma density and linearity approximation of the crystal response (especially in the range from 1400 eV to 1480 eV at the crystal border), the value of $T = 1200 \pm 300\,\text{eV}$ seems to be a reasonable estimation for the background thermal plasma temperature. Obviously the experimental spectrum is time-integrated and the estimated value of T is consequently time-averaged.

A similar comparison is made for Cu coil target in Figure 8.36. The emission lines structure is not well reproduced in this case. Yet, based on the relative peak emissions values, an similar estimation of T of about $1200 \pm 300\,\text{eV}$ seems reasonable. Although, it is worth to note that a variation of 300 eV around 1200 eV induces a variation of $\pm 15\,\%$ for ion acoustic speed. Therefore, for the modeling of the plasma expansion, this level of accuracy is satisfactory.

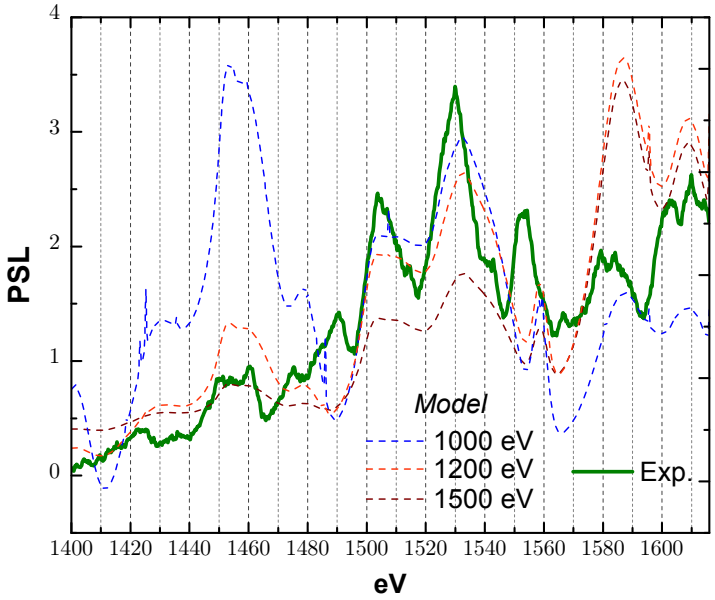

Figure 8.35 – X-ray spectrum of Ni coil target obtained from tronconic spectrometer (solid line) and compared with the emission lines of the code SCKIM in dashed lines. The calculations on this code are a courtesy of O. Peyrusse. The density of the emitting plasma is taken to be the critical density n_c. The plasma bulk temperature can be estimated to be $T = 1200 \pm 300\,\text{eV}$.

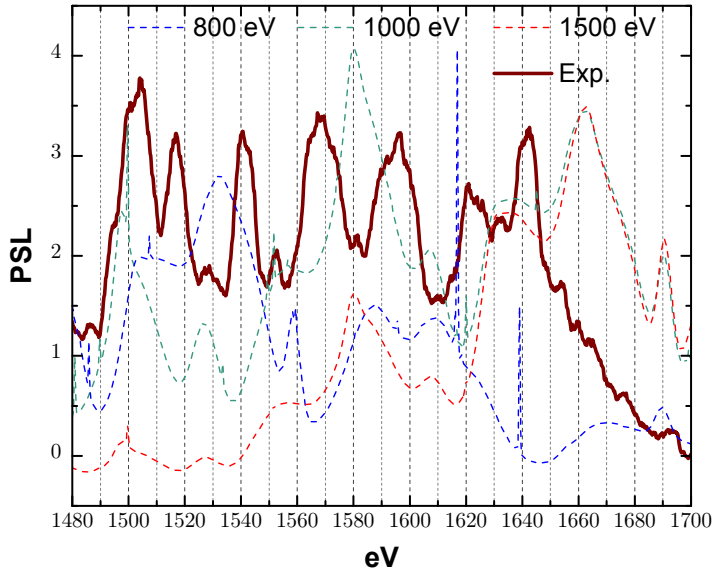

Figure 8.36 – Same as Figure 8.35 for a Cu coil target. The dashed curves are obtained from SCKIM at critical density and for the labeled bulk temperatures: 800 eV (blue), 1000 eV (purple) and 1500 eV (dark red). For an unknown reason, the comparison is not as fair as for Ni. Yet, the related peak emission values in the given energy range would suggest a temperature around 1000 eV.

8.2.4 Bremsstrahlung Canon

In this subsection we will present the results of hard X-ray spectrometry. Some details on the used spectrometer - so-called *Bremsstrahlung Canon* - and deconvolution methods are given in *Appendix*, Sec. 22.4.

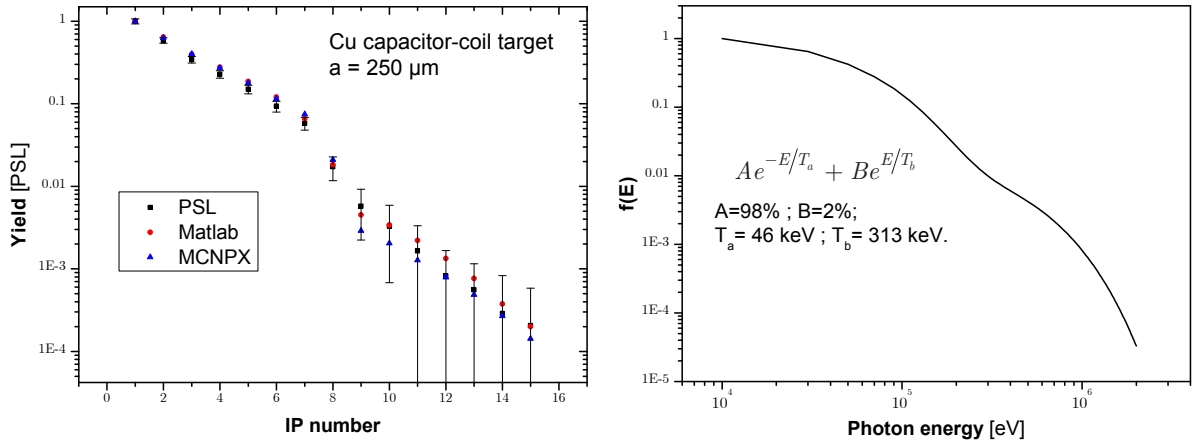

Figure 8.37 – Left: Typical signal on the IP-stack of Bremsstrahlung Canon (black squares) compared with corresponding points computed by: (red dots) a Matlab script, solving the matrix system with tabulated filter transmission ; an MCNPX calculation (blue triangles). **Right:** Inferred photon spectrum to reproduce the PSL signal over the IP-stack (left panel), used as an input for the two presented computation methods Matlab and MCNPX.

In Figure 8.37, we present a typical deconvoluted spectrum of the bremsstrahlung-emitting photons, infered from a calculation from both MCNPX and a simpler Matlab script solving the matrix system with tabulated transmission values. The corresponding synthetic photon signals in PSL on the IP-stack are given in comparison with experimental values in the left panel of Figure 8.37.

A similar analysis performed on several shots of the 1^{st}-experiment in LULI concluded in a

photon spectrum (with photon energy E_{ph}) characterized by the sum of two exponentials:

$$Ae^{-E_{ph}/T_a} + Be^{-E_{ph}/T_b} \tag{8.15}$$

with $A = (96.8 \pm 2.1)\,\%$, $T_a = (46.5 \pm 5)\,\text{keV}$; $B = (3.2 \pm 2.1)\,\%$, $T_b = (280 \pm 27)\,\text{keV}$. On another note, MCNPX calculations agrees with a total number of emitted photons per steradian of $N_{ph} = (2.4 \pm 0.4) \times 10^6\,\text{sr}^{-1}$.

The mean energy of the double exponential expression of Eq. 8.15 is:

$$\overline{T_h} = \frac{AT_a^2 + BT_b^2}{AT_a + BT_b} \tag{8.16}$$

It yields $\overline{T_h} \approx 85.3\,\text{keV}$ for the previous parameters.

As mentionned in Sec. 22.4, the bremsstrahlung spectrum emitted by fast electrons has an intensity-dependance with the kinetic energy of electrons who produced it and therefore one can relate the emitted photon spectrum with the fast electron distribution. As we normalized the photon spectrum, the photon energy in X-axis can be directly interchanged with fast electron energy, and in particular Eq. 8.15 describes accurately the fast electron distribution.

8.3 Conclusion

In conclusion, our experimental results were obtained in a common setup using three independent diagnostics (dedicated shots) and show a reproducible quasi-static B-field generation by laser interaction with capacitor-coil targets, typically with a few ns duration and a mm^3-volume, yielding peak strengths of several hundreds Tesla, depending on the target material: the coil dipole-like magnetic field total energy is of the order of $8.3 \pm 1.5\,\%$, $4.5 \pm 0.8\,\%$ and $0.35 \pm 0.05\,\%$ of the mean invested laser pulse energy (500 J), respectively for Cu, Ni and Al targets.
Including the support leads, the magnetic field energy amounts to $\approx 3.2\times$ the previous values and is distributed over a volume of $\sim 5\,\text{mm}^3$ as shown for Ni in Figure 8.38.

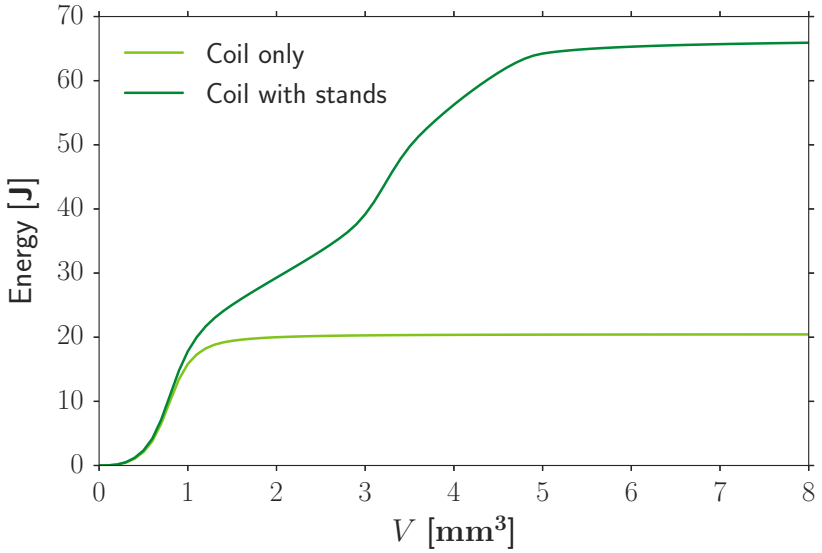

Figure 8.38 – Integrated magnetic energy $W_m = \frac{1}{2}LI^2$ for a Ni target ($a = 250\,\mu\text{m}$ (**D**) peaking at 600 T (*i.e.* $I = 250\,\text{kA}$), as a function of the integrated volume V in mm^3. The computation is made for the dipole-like magnetic field of the coil (green) and for the complete circuit including the wire stands (dark green).

The observed differences with the different target materials may be attributed to (i) the different resistivity values at low temperature, though the current rise time and consequent wire heating is

identically rapid erasing resistivity differences for the three materials, and, probably more important, to (ii) the plasma temperature and hydrodynamics yielding different short-circuiting times: this will be object of further investigations in the modelling part in the following section. The modeling of these aspects will also give more detailed conclusions on the dependence of the laser and target parameters.

The extrapolation of the B field amplitude at the center of the coils from distant measurements (at a few mm for Faraday rotation, and at a few cm for the pick-up coil probes) is performed by modeling the 3D target geometry in magnetostatic computations. Results from Faraday rotation and proton-deflectometry are consistent with the B-dot probe measurements at the early stages of the target charging, up to $t \approx 0.35$ ns, and then are disturbed by radiation and plasma effects, respectively the blackout of the birefringent crystal and, as we concluded, a negative electrostatic potential. The latter is formed due to electron magnetization around the coil region, summing up to the main B-field effect and explaining the decreasing proton deflections for $t > 0.35$ ns. This hypothesis, arisen from the results obtained at the LULI experiments, has been reinforced by an experiment that followed in Japan using a shielded proton deflectometry setup (Sec. 8.1.5).
It confirmed the ability to measure consistently the B-field by B-dot probe measurements and protons deflectometry at the peak B-field amplitude of ≈ 600 T when correctly shielding the coil region.

While the typical mm^3-volume and ns-duration of the produced B-field pulses are small compared to the parameters achieved with the state-of-the-art magnets mentioned in the introduction, they are characterized by an unprecedentedly high magnitude of magnetic field. Moreover, the presented laser-driven B-field platform presents an open geometry providing easy access for several diagnostic views and incoming secondary laser pulses or particle beams. Consequently, the all-optical technique lends itself to the magnetization and accurate probing of high-energy-density samples driven by secondary powerful laser or particle beams. As a matter of fact, given the $\approx 10\,\mu m/ns$ expansion velocity of the coil rod, the strong B-field region remains accessible for several ns, leaving time to magnetize secondary samples and study magneto-hydrodynamic processes occuring in this time-scale.

9 Semi-analytical model of B-field generation in nanosecond regime

9.1 A voltage-source model

This model tends to calculate the expected magnitude of the magnetic field created by a laser-driven capacitor-coil target treating the coil as a RL electrical circuit and the capacitor part as a capacitance $C = \epsilon_0 S/d$ (S is the mean section of the plates, ϵ_0 the dielectric permitivity of free space and d is the distance between the plates). The associated differential equation for the current $I(t)$ flowing through the coil writes:

$$L\frac{dI(t)}{dt} + RI(t) = V_0(t) \tag{9.1}$$

Voltage source definition

The circuit tension $V_0(t)$ arises from the hot electron current emitted from the laser-irradiated plate I_h, which charges the capacitor. In this model, the two currents I and I_h are calculated independently (in particular we have $I \neq i_h$). The voltage source is defined by:

$$V_0(t) = \frac{1}{C}\int_0^t I_h(t) \tag{9.2}$$

with L and R respectively the inductance and the resistance of the coil. Assuming that the hot electrons distribution is a Maxwellian distribution $f(u) = \left(\frac{m_e}{2\pi k_B T_h}\right)^{3/2} 4\pi u^2 e^{-\frac{m_e u^2}{2k_B T_h}}$ with the hot-electron temperature T_h. The absorbed laser flux writes:

$$I_{abs} = \frac{1}{2} n_e m_e \int_0^\infty u^3 f(u) du \tag{9.3}$$

The net balance between the absorbed laser flux with the hot electron flux yields [22]:

$$I_h(t) = \frac{2ehP_{laser}}{m_e}\frac{\int_{u_1}^\infty u f(u) du}{\int_0^\infty u^3 f(u) du} \tag{9.4}$$

where e and m_e are the electron charge and mass, respectively. P is the laser power, $\eta_{\text{laser}\to\text{e}^-}$ is the fraction of laser energy absorbed by the hot electrons and u_1 is the minimum velocity for an electron to escape the potential $u_1 = \sqrt{2eV_0/m_e}$.

Injecting the expression of $f(u)$ in Eq. 9.4, we obtain:

$$I_h(t) \approx \frac{e\eta_{\text{laser}\to\text{e}^-} P_{laser}}{2}\frac{k_B T_h + eV_0(t)}{(k_B T_h)^2}\exp\left(-eV_0/k_B T_h\right) \tag{9.5}$$

This equation evidences that the hot electron current maintains the potential difference, and as a consequence of the voltage source formulation, we have $I_h \ll I$.

The model is also based on a simple estimation of the plasma dynamics between the two plates of the capacitor-coil target. It is assumed that the fast ion expansion speed is at the sound speed $c_s = \sqrt{Z^* k_B T_b/m_i}$ with T_b the plasma bulk temperature. One can then estimate the short-circuit time $t_{cc} = d/c_s$. After the short-circuit instant, one has $V_0(t \geq t_{cc}) = 0$.

For $t < t_{cc}$, the differential equation is integrated assuming that I_h is only a function of the laser power P_{laser}, and $eV_0 \gg k_B T_h$. Under these assumptions, the potential difference writes:

$$V_0(t < t_{cc}) = \frac{k_B T_h}{e}\ln\left[\frac{\eta_{\text{laser}\to\text{e}^-} e^2 \int_0^t P(t)dt}{2}\frac{d(t)}{\epsilon_0 S}\frac{1}{(k_B T_h)^2}\right]. \tag{9.6}$$

The term $\int_0^t P_{laser}(t)dt$ is the total laser energy deposited at the instant t. For a constant laser power, the deposited laser energy $E_{las}(t)$ rises linearly, as assumed in the original paper by Courtois *et al.* [53].

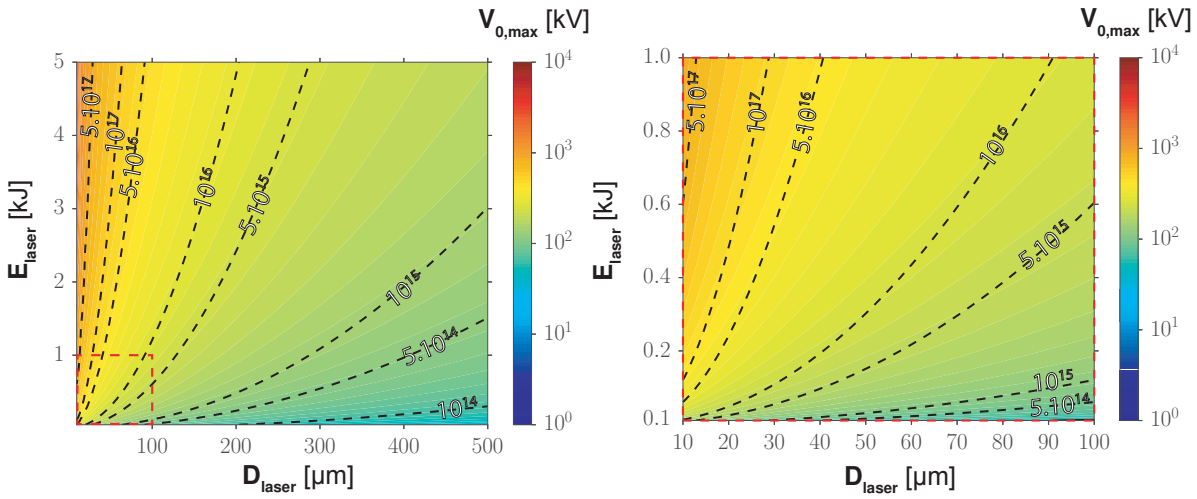

Figure 9.1 – Estimation of the peak gap voltage V_0 as a function of the laser energy and focal spot diameter, from Eq. 9.7. It was calculated for $C = 0.1\,\text{pF}$, $\tau_L = 1\,\text{ns}$ and T_h is calculated from Eq. 3.42 (Sec. 3.2). An estimation of the maximum current can be made by calculating $\max\left(V_{\max}/R, V_{\max}\tau_L/L\right)$.

The formulation is nonetheless written here to include directly the time-evolution of $E_{las}(t)$ which will determine the evolution of $V_0(t)$.

The evolution of $V_0(t)$ will be also constrained by the time-varying capacitance $C(t)$. The expanding plasma plume reduces the cathode-anode distance $d(t)$. Besides, hot electrons propagating at several tenths of the speed of light, reach the plate edges in $\sim 10\,\text{ps}$, which can be assumed to be instantaneous in respect to the time-variation of the B-field. Consequently, we have $C(t) = \epsilon S/d(t)$ and $V_0(t) \propto 1/C(t) \propto d(t)$, since the time variation of S is neglected. The continuity of the potential is ensured at short-circuit time t_{cc}: the anode-cathode distance d tends to 0 and thus V_0 tends to 0 equally.

With this model description, the current is maximum at t_{cc}. In experiments, the peak instant is measured by the B-dot probe in the range of $1-2\,\text{ns}$. Four our targets we have $d_0 \approx 850\,\mu\text{m}$. Taking the short-circuit time from an expansion at sound speed, it would correspond to a plasma bulk temperature of $\sim 4-16\,\text{keV}$, which is strongly overestimated according to X-ray measurements (see Sec. 8.2). With a more reasonable value of the plasma temperature of 1 keV one obtains a short-circuit time of $\sim 4\,\text{ns}$. Taking a self-similar description of the front ion velocity, the velocity is $\approx \sqrt{3}c_s$. For a plasma plume temperature of 1 keV, the short-circuit time is of $\sim 2\,\text{ns}$. It is closer to what is observed experimentally. Nevertheless, more detailed description of the ion dynamic and its sheath potential is missing in this model: the peak magnetic field time and short-circuit is not satisfactory reproduced. This statement was also made by the authors in the original paper [53] : they measured B-field peaks at $\approx 3.5\,\text{ns}$ while the short-circuit time is evaluated to occur at $t_{cc} \lesssim 0.9\,\text{ns}$ ($T_h \sim 10\,\text{keV}$).

Furthermore, we can adapt the model to include an additional thermal potential (it is a small correction of the order of $\sim 10\,\%$ of the total potential). The thermal potential at the ion front can be estimated from a self-similar description [184] and writes $U_{th} \approx \sqrt{2}k_B T_h$. The minimum velocity for an electron to escape the sheath potential is thus replaced by $\sqrt{2e(V_0 + U_{th})/m_e}$ and Eq. 9.6 rewrites:

$$V(t < t_{cc}) = \frac{k_B T_h}{e} \ln\left[\frac{\eta_{\text{laser}\to\text{e}^-} e^2 \int_0^t P(t)dt}{2} \frac{d(t)}{\epsilon_0 S} \frac{1}{(k_B T_h)^2}\right] - \sqrt{2}k_B T_h. \tag{9.7}$$

Inductance

The circuit element L could be expressed following a simplified formula for a perfect circular coil:

$$L = a\left[\mu_0\left(\ln\left(\frac{8a}{b}\right) - 2\right) + \frac{\mu}{4}\right] \tag{9.8}$$

with a the coil radius and b its wire radius. $\mu = \mu_r \mu_0$ being μ_0 the magnetic permeability of vacuum and μ_r the relative magnetic permeability of the considered material for the coil. However, as the coil is not perfectly circular and is instead connected by straight wires to the two parallel disks, this formula is not yielding a good estimation of the total inductance. The global procedure to calculate the total inductance is to drive a known current I in the complete 3D geometry and calculate by magnetostatic code the integrated magnetic energy $W_m = \int_0^\infty B^2/(2\mu_0) dV$. The inductance is then simply calculated as $L = 2W_m/I^2$.

Resistance

The coil resistance R is given by:

$$R = \eta l / s \tag{9.9}$$

with η the resistivity of the coil material and l the total length of the coil's wire (including the leads). In this model by Courtois *et al.* , the resistivity is taken as a constant over time and thus do not include an heat equation for the coil's material. The following estimations are made with a capacitor-coil target whose coil radius is $a = 250\,\mu\text{m}$ and at ambiant temperature.

Cold parameters of the RL circuit

Taking the cold resistivity at ambient temperature and no wire thermal expansion, it yields the following parameters for the coil RL circuit:

Material	Coil resistance (R)	Coil inductance (L)	Time constant ($\tau = L/R$)
Copper	28 mΩ	2 nH	71.3 ns
Nickel	116.4 mΩ	9.2 nH	79 ns
Aluminum	43.1 mΩ	2 nH	46.4 ns

Table 9.1 – Coil RL circuit parameters at 300 K.

It is worth noting here that the coil inductance at ambient temperature for the Ni is almost five times higher than for the two other materials. This is due to the initial magnetic permeability of this ferromagnetic material. However, all ferromagnets have a maximum temperature where the ferromagnetic property disappears as a result of thermal agitation. This temperature is called the Curie temperature and is equal to 627 K for Ni, a temperature which is reached fast: the ferromagnetic property of Ni while taking into account reallistic temperature rise in the wire will be seen to not play any significant role.

Model results

The temporal results of the model are given in Figure 9.2. On the left panel, the potential difference is represented, assuming a fraction of laser energy (500 J) absorbed by the hot electrons of $\eta_{\text{laser}\to e^-} = 4\,\%$ (40 % of laser absorption and 10 % of conversion efficiency to hot electrons). The evolution of the laser deposited energy with time was inferred integrating typical power trace measurements of the LULI2000 ns-pulse. The hot electron temperature is calculated from Eq. 3.42 of the scaling laws introduced in Sec. 3.2. The mean surface of the capacitor is $S \approx 8.42\,\text{mm}^2$ and $d_0 = 850\,\mu\text{m}$ yielding $C(0) \approx 0.1 pF$. The model is evaluated at 300 K and at 10 eV to show the strong material resistivity dependence with temperature. One can refer to Sec. 3.3.2 to see how the resistivity is computed from solid to plasma state.

One can conclude here that the model introduced by Courtois *et al.* is giving a quite correct order of magnitude for the produced B-field of several hundreds of Tesla. Yet, the temporal dependence of the wire heating by Joule effect is clearly missing in this firt model, as it is seen to play a big role on the current estimation. On the following, we will introduce a complementary set of equations to describe the circuit resistance variation with temperature growth.

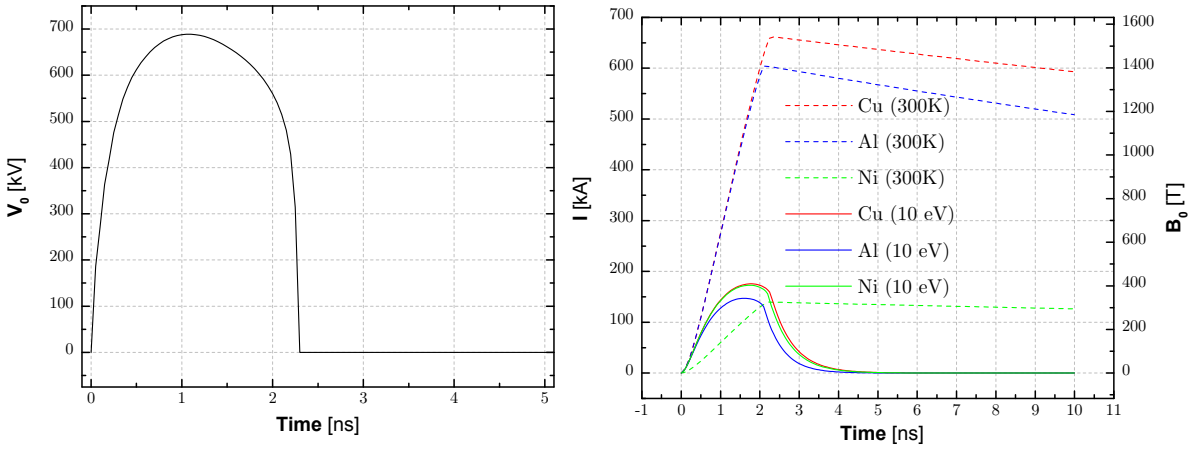

Figure 9.2 – Left: Potential difference obtained from Eq. 9.6. **Right:** Estimated current (left ordinates) and B-field at the coil center of our coil target (right ordinates), evaluating the material resistivity at 300 K (dashed lines) and at 10 eV (solid lines). It is worth noting also that the inductance is bigger for Ni at ambient temperature due to its magnetic permeability. This difference disappears at temperatures over 627 K (the Curie temperature of Ni). More importantly, the huge difference between the two temperature sets suggests that the resistivity evolution with time is mandatory to be modeled.

9.2 Improvement of the model

In this part, we will detail the addition made to the previous model, notably concerning the time evolution of the wire heating and its consequence on material resistivity.

First, one second order parameter that was chosen to not be calculated directly in the model is the wire expansion. The expansion would depend both on the wire thermal and magnetic pressures. For sake of simplicity and numerical stability, the equivalent pressure equation was not included to the system of equations already very coupled. Moreover, a modification of a factor 2 for the expansion velocity induces a variation on the maximum current of less than 10 %. Nevertheless, it is important to be taken into account for the role it plays in the estimation of the wire temperature and the resistance evolution along the discharge.

In the purpose of comparing the model with experimental measurements, we choose then to take the following expression of the wire's edge length (the wire have squared shape):

$$b(t) = b_0 + 2v_{exp}t \tag{9.10}$$

with v_{exp} fixed to 11 µm/ns, as it was measured experimentally (see Sec. 8.2.1). Also, the density of the conducting material decreases with the wire expansion such as:

$$\rho(t) = \rho_0 \frac{b^2(0)}{b^2(t)} \tag{9.11}$$

Now we will list the physical features and their associated equations which have been included in the model:

◇ **Skin depth:** At high frequency, effective conductor area is decreased by skin effect. The skin depth is defined as the effective conducted current penetration's depth. For a pulsed current of duration equals to the laser pulse duration τ_L, the skin depth δ writes:

$$\delta(t) = \min\left[\sqrt{2\tau_L \eta(t)/\mu}, b(t)/2\right] \tag{9.12}$$

The section over the square wire in which the current is propagating is then defined as:

$$s_{skin}(t) = b(t)^2 - (b(t) - 2\delta(t))^2 \tag{9.13}$$

◇ **Resistivity and resistance:** The resistivity of the wire is calculated from solid to plasma state, using the model described in Sec. 3.3.2, in particular the reader can refer to Figure 3.9. Local thermodynamic equilibrium is assumed ($T_i = T_e$) and the resistivity is computed following the time evolution of the wire temperature T_{wire} for a given material (Z,A,ρ). We have then the wire resistance:

$$R(t) = \eta(t)\frac{l}{s_{skin}(t)} \tag{9.14}$$

with l the total wire length, equals to $\approx 4.2\,\text{mm}$ in the case of the standard capacitor-coil target used in our experiments [$a = 250\,\mu\text{m}$ (D), see Figure 8.2]. Due to the resisitivity increase with the wire heating, the skin depth becomes larger than the conductor radius and δ is thus converging rapidly to $b(t)/2$: for pulses duration of 1 ns and beyond, the skin depth effect can be neglected.

◇ **Inductance:** It is calculated by evaluating the magnetic energy W_m in magnetostatic code, for the 3D geometry of the coil, and $L = 2I^2/W_m$. The effect of magnetic permeability at temperatures below Curie temperature is neglected, since this temperature is reached very fast. We have then, independently of the material, for the same standard capacitor-coil target as before, an inductance $L \approx 2\,\text{nH}$.

◇ **Heat equation:** The differential algebraic equation (DAE) associated to the wire heating is expressed as follow:

$$C_e[T_{wire}(t)]\frac{dT_{wire}(t)}{dt} = R(t)\frac{I^2}{lb^2(t)} \tag{9.15}$$

with $C_e[T_{wire}(t)]$ is the heat capacity of the wire at the temperature $T_{wire}(t)$ and is computed using the model described in Sec. 3.3.2, in particular the reader can refer to the example given for Cu in Figure 3.10.

The DAE for the RL circuit does now include the resistance evolution over time:

$$L\frac{dI(t)}{dt} + R(t)I(t) = V_0(t) \tag{9.16}$$

The gap potential $V_0(t)$ is still defined with Eq. 9.6.

The system of the two DAE is solved numerically and the results are given for the three materials used in our experiments in Figure 9.3.

The magnetic field magnitudes and evolution are fairly reproduced for the best cases of Cu and Ni targets (slightly overestimating the current, as expected from the modeling). Yet, the material dependency is not reproduced. The conclusion to be drawn here is that resistivity seems not a key parameter to reproduce material dependence. Indeed, the wire temperature is rising fast and is identically rapid erasing resistivity differences. The evolution of the wire temperature and related circuit resistance for Cu are shown in the bottom graph of Figure 9.3.

One can note that the calculated wire temperature of $\approx 40\,\text{eV}$ for the case $k = 2$, at peak magnetic field ($t = 2\,\text{ns}$), would induce a thermal expansion velocity of $\approx 28\,\mu\text{m/ns}$, more than twice the velocity measured experimentally. However, we have to take into account the very high poloidal field around the coil's wire which induces a magnetic pressure ($p_B = B^2/2\mu_0$) and hinders the thermal expansion. Taking $B = \mu_0 I_{coil}/(2\pi b) = 2.72\,\text{kT}$ around the wire, which corresponds to 800 T at the coil center [see Figure 8.7)-a)], the magnetic pressure $p_B = B^2/(2\mu_0) \approx 29.5\,\text{Mbar}$ is comparable with the thermal pressure $p_{th} = n_e k_B T \approx 36\,\text{Mbar}$. Calculating the velocity from Bernoulli relation while taking into account the density drop from wire expansion, we have $u = \sqrt{2(p_{th} - p_B)/\rho} \approx 17\,\mu\text{m/ns}$, which is slightly higher than the measured velocity of $11\,\mu\text{m/ns}$. An estimation with the pressure gradient can also be obtained from Euler equation $\rho\frac{du}{dt} = -\nabla(p)$. At a time of 2 ns and with a pressure gradient length of $l_p = b/2 = 25\,\mu\text{m}$, one obtains a velocity of $\approx 12\,\mu\text{m/ns}$, still considering the density drop due to wire expansion. In both cases, these are rough estimations: a proper MHD simulation of the plasma dynamic with magnetic field would be necessary.

In another note, the model does not consider that the already escaped electrons reduces the number of hot electrons being able to escape at a given time. The modeling of the source by a capacitor suggests that the charging current is entirely circulating from one plate of the capacitor to another, meaning that all the escaped hot electrons reach the front plate. Consequently, one may expect that

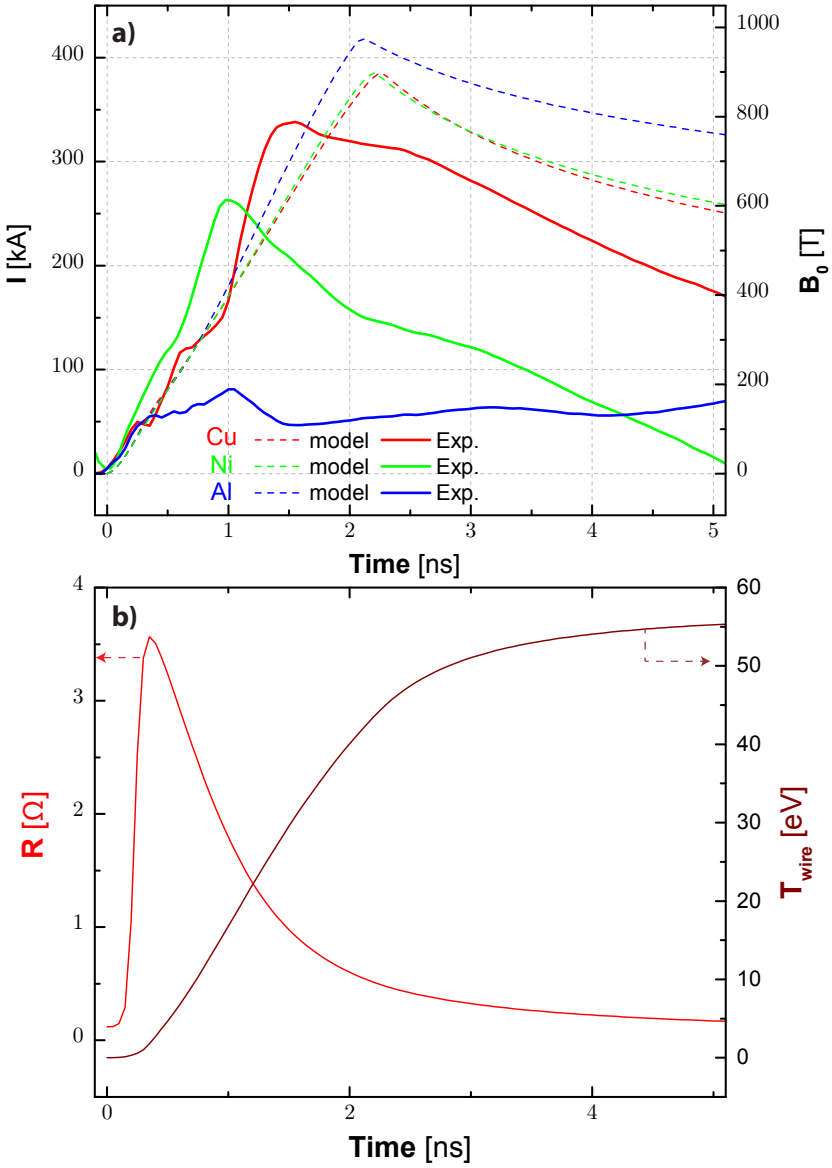

Figure 9.3 – Top: Calculated magnetic field evolution for Cu (red), Ni (green) and Al (blue). The experimental curves from B-dot measurements are shown in solid lines with the same color code. **Bottom:** Evolution of the circuit resistance $R(t)$ (in red, left ordinates) and wire temperature $T_{wire}(t)$ (in brown, right ordinates) for the case of Cu

this model will globally overestimate the current. Besides, coming back to the main assumption of Eq. 9.6 (or Eq. 9.7), we can calculate that the ratio eV_0/k_BT_h is ≈ 6. We have then $eV_0 > k_BT_h$, yet in a proportion that may question the fact that we neglected k_BT_h.

More importantly, the question raise by this model is the voltage source formulation (Eq. 9.2) where $I_h \neq I$. We will now discuss the issues related to this formulation.

Issues related to a voltage-source model

It is crucial to remember that this model decouples the charging (C) and discharging (RL) parts of the circuit. Indeed, the source term V_0 is calculated independently of the discharge current I, under the assumption of an isolated charging capacitor. As a matter of fact, due to a small capacitance, a small current I_h can produce a large tension. We have then an problem with the current conservation:

$$\text{charge:} \qquad I_h = C\frac{dV_0}{dt} \sim 10^{-13}\,\text{F} \times 10^{6}\,\text{V}/10^{-9}\,\text{s} \sim 100\,\text{A} \tag{9.17}$$

$$\text{discharge:} \qquad I \sim 100\,\text{kA} \tag{9.18}$$

It is obvious that we have $I_h \neq I$ and in particular $I_h \ll I$ by a factor ~ 1000: the energy of the charge is then approximately 1000 times lower than the energy of the discharge. Therefore, this model does not physically describe the charging mechanism and the voltage-source decoupling appears to not be a satisfying hypothesis. With such a low capacitance, the quasi-stationary regime implies instead $I_h \approx I$ and we need to define an equivalent circuit with a current source. The retroaction of the gap potential on the source still have to be included. The accurate current source having those characteristics is well-defined by a diode element. This diode is driven by the current ejection issuing from laser interaction: this is the reason why we call this alternative model *laser-pumped diode model*. We will detail it in the next section.

9.3 Current-source approach : laser-pumped diode model

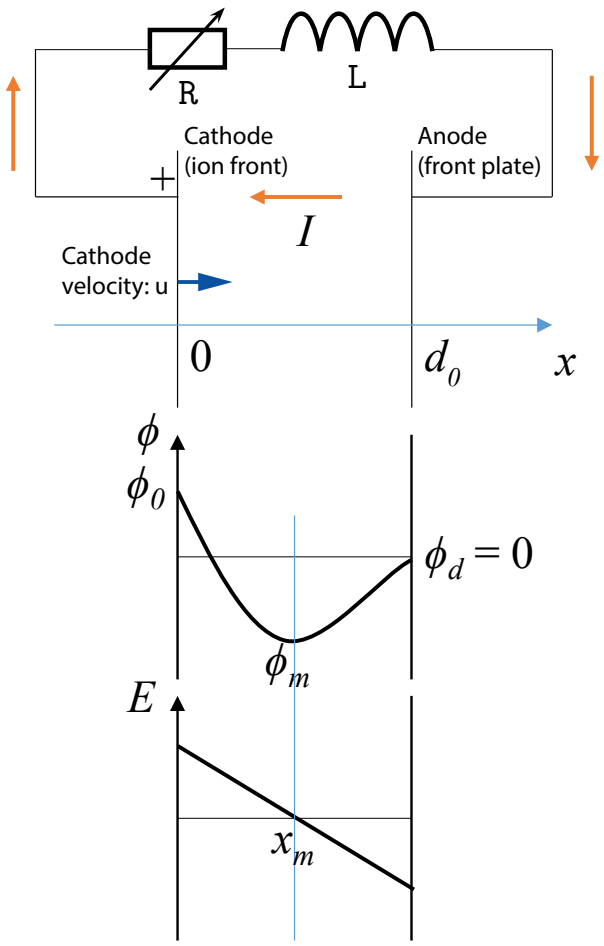

Figure 9.4 – Scheme of the parameters for the laser-pumped diode model. The 1D description between the two plates separated by the distance d exhibits the variables: ϕ for the total electric potential and E the electric field norm. The current I is recirculating through a wire of resistance R and inductance L.

We present here a new, alternative, model to describe the evolution of the discharge current based on a current-source (where $I_l = I$) instead of a voltage-source (where $I_l \ll I$). It describes the charging process as a laser-pumped diode between the two target plates. As before, the connected coil-shaped wire is described by an external circuit composed of an inductance L and a time-evolving resistance $R(t)$ in series. The circuit is schematized in Figure 9.4.

9.3.1 Potential description (1D model)

The population of transported electrons between the two plates, of velocity distribution $f(v)$, is described under the stationary approximation of the Vlasov equation with one dimension of space (x-axis):

$$v\frac{df}{dx} + \frac{e}{m_e}\frac{\partial\phi}{\partial x}\frac{\partial f}{\partial v} = 0 \tag{9.19}$$

At the irradiated plate position ($x = 0$), the electron distribution is given by the Maxwell-Boltzmann function:

$$f(v, x = 0) = \frac{n_0}{\sqrt{2\pi}v_T} e^{\frac{-v^2 + 2e/m(\phi_0 - \phi_m)}{2v_T^2}} \tag{9.20}$$

$v_T = \sqrt{k_B T_h / m_e}$ is the electron thermal velocity, characterized by the hot temperature T_h. ϕ_0 and ϕ_m are respectively potentials at the points $x = 0$ and $x = x_m$. The space-derivative of the potential at $x = x_m$ is $\phi'(x_m) = 0$: x_m is thus the position of a "virtual" cathode located ahead of the interaction zone. For $x < x_m$, electrons accelerated from the interaction surface stream ahead and are either ejected beyond x_m or reflected back. For $x > x_m$, the population is only constituted of transmitted electrons which escaped the potential barrier ϕ_m. One can write the current density of ejected electrons as:

$$j_0 = e \int_0^{+\infty} v f(v) dv = \frac{e n_0 v_T}{\sqrt{2\pi}} e^{-\frac{e}{k_B T_h}(\phi_0 - \phi_m)} \tag{9.21}$$

For the two zones of potential (upper signs for $x < x_m$ and lower signs for $x > x_m$), the electron density writes:

$$n(x) = \frac{j_0 \sqrt{\pi}}{\sqrt{2} e v_T} e^{\frac{e(\phi(x) - \phi_m)}{k_B T_h}} \left[1 \pm \operatorname{erf}\left(\frac{e(\phi(x) - \phi_m)}{k_B T_h} \right) \right] \tag{9.22}$$

The Poisson equation emerging from this density formulation gives, after integration:

$$\lambda_D \frac{d\phi(x)}{dx} = \sqrt{2} \sqrt{\pm e^{\frac{1}{4}} \left[\operatorname{erf}\left(\frac{1}{2} - (\phi(x) - \phi_m) \right) - \operatorname{erf}\left(\frac{1}{2} \right) \right] e^{\phi(x) - \phi_m} \left(1 \pm \operatorname{erf}\left(\phi(x) - \phi_m \right) \right) - 1} \tag{9.23}$$

The interaction surface will obviously move due to the expansion into vacuum of the laser-produced plasma plume, as described in Sec. 4.2. A formulation of the ion dynamics will be given in continuation. The electric field - or equivalently the electric potentials - in the diode gap are both affect the diode current and the ion dynamics. Using the dimensionless variable $\psi = \left| \frac{e\phi}{k_B T_h} \right|$, the potential continuity imposes:

$$\frac{d}{\lambda_D} = \int_0^{\psi_0 + \psi_m} \frac{d\xi}{\mathcal{L}(\xi)} + \int_0^{\psi_m} \frac{d\xi}{\mathcal{R}(\xi)} \tag{9.24}$$

where $d = d(t)$ is the time-decreasing effective gap-width of the diode. The function noted $\mathcal{L}$ for $x < x_m$ writes:

$$\mathcal{L}(x) = \sqrt{2} \sqrt{e^{\frac{1}{4}} \left[\operatorname{erf}\left(\frac{1}{2} - x \right) - \operatorname{erf}\left(\frac{1}{2} \right) \right] e^x \left(1 + \operatorname{erf} x \right) - 1} \tag{9.25}$$

and the function $\mathcal{R}$ for $x > x_m$ writes:

$$\mathcal{R}(x) = \sqrt{2} \sqrt{-e^{\frac{1}{4}} \left[\operatorname{erf}\left(\frac{1}{2} - x \right) - \operatorname{erf}\left(\frac{1}{2} \right) \right] e^x \left(1 - \operatorname{erf} x \right) - 1} \tag{9.26}$$

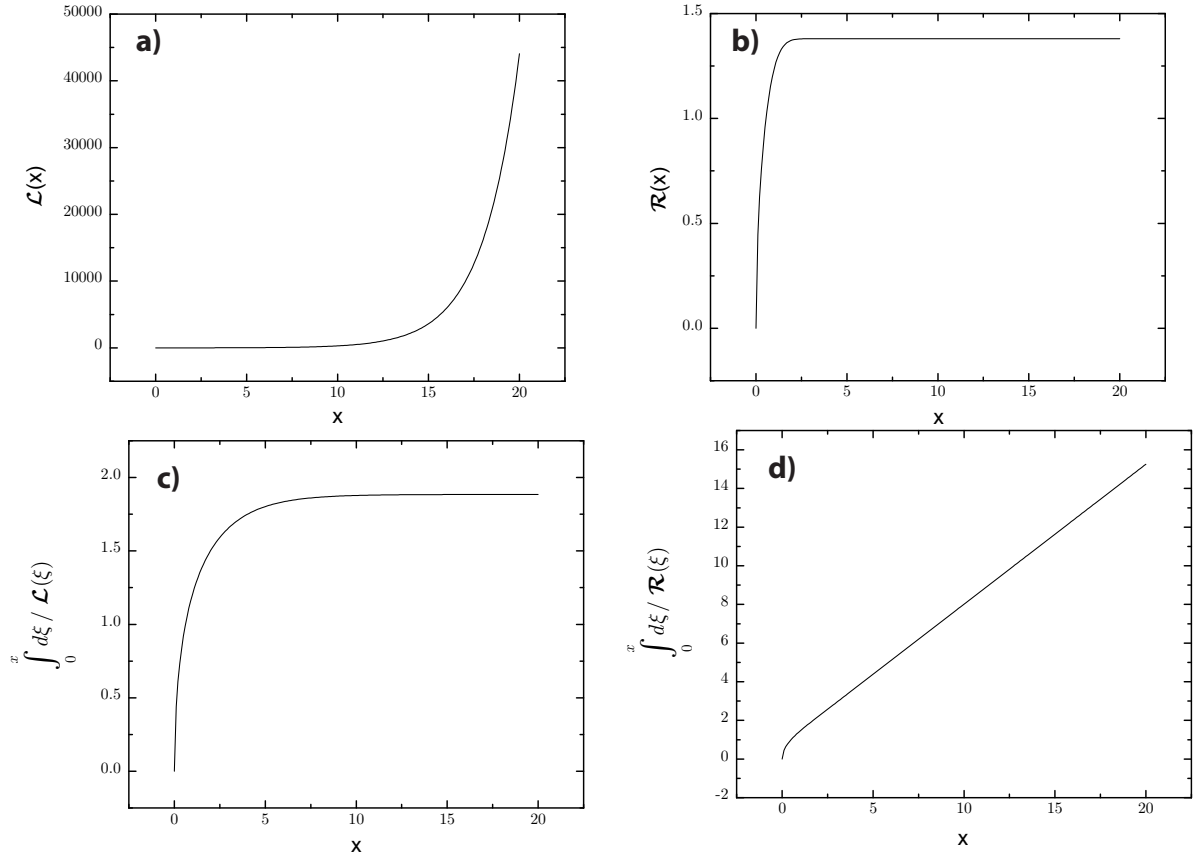

Figure 9.5 – Plot of the functions $\mathcal{L}$ (**a**) and $\mathcal{R}$ (**b**) with the integral functions $\int \mathcal{L}^{-1}$ (**c**) and $\int \mathcal{R}^{-1}$ (**d**). The integral functions are used to determine ψ_m in Eq. 9.24 and $\mathcal{L}$ is used in the calculation of the electric field in Eq. 9.27.

9.3.2 A 3D description of the potential and related issues of the 1D description

Electron-cloud radius

The hot electron cloud characteristics are described in Sec. 6.2 and more information can be found in [215]. The electron cloud is created in a process of transient charging described in Figure 6.1, whose characteristic time is $\sim 10\,\text{ps}$. As we describe here the interaction with a ns-duration laser driver, the hot electron cloud radius is considered to be sustained all along the irradiation. In other words, we place ourselves in conditions of a steady-state regime where the electron cloud temperature and size are maintained by the laser. We take then the converged value of the electron radius R_h as given by the dynamic model of Poyé *et al.* and it yields for the three target materials:

Mat.	R_h
Cu	88 µm
Ni	105 µm
Al	289 µm

Table 9.2 – Electron-cloud radius for the three target materials Cu, Ni and Al.

Ion dynamic from the 1D description

The ion dynamics originates from the force exerted by the electric field on ions. The electric field writes:

$$E = \frac{T_b}{x_m}\mathcal{L}(\psi_m + \psi_0), \tag{9.27}$$

where T_b is the plasma bulk temperature ($T_b \approx 1200\,\text{eV}$ in our experiments, determined by X-ray spectrometry measurement, see Sec. 22.2) and x_m is given by:

$$\frac{x_m}{\chi} = \int_0^{\psi_0+\psi_m} \frac{d\xi}{\mathcal{L}(\xi)} \tag{9.28}$$

The variables d, x_m , ψ_0 and ψ_m are all functions of time and especially the gap distance d is governed by the ion motion, driven by the electric field:

$$d(t) = d_0 - \int_0^t u(t)dt \tag{9.29}$$

$$u(t) = \int_0^t \frac{eZ^*}{m_i}E(t)dt \tag{9.30}$$

Issues related to the 1D description

This potential formulation for ψ_m is only valid for $d \sim \lambda_D$. It strongly overestimates the potential if $d \gg \lambda_D$. Four our 1D description, $d \to \infty$ would mean $\psi_m \to \infty$, which is not physical. To overcome the 1D issue, Poyé *et al.* computed in 3D the potential barrier and $\psi_m \approx 0.8$ for our conditions (see Figure 9.6 for $R_h/\lambda_D \approx 40$).

Matching $\psi_m = 0.8$ with the 1D description (Eq. 9.24) leads to $\lambda_D \approx d_0/2.4 \approx 333\,\mu\text{m}$.

In order to keep the dependence of ψ_m with the ion dynamics between the plates, one can assume a 3D parameter $\chi = d_0/2.4$ in place of the previous 1D parameter λ_D, and Eq. 9.24) rewrites:

$$\frac{d}{\chi} = \int_0^{\psi_0+\psi_m} \frac{d\xi}{L(\xi)} + \int_0^{\psi_m} \frac{d\xi}{R(\xi)}. \tag{9.31}$$

In this context, to correctly describe the case $d > \chi$, we take ψ_m as the minimum between the constant 3D potential and the varying potential from Eq. 9.31:

$$\psi_m = \min\left(\underbrace{\psi_{m,1}}_{\text{Eq. 9.31}}, \underbrace{\psi_{m,2}}_{[215]}\right) \tag{9.32}$$

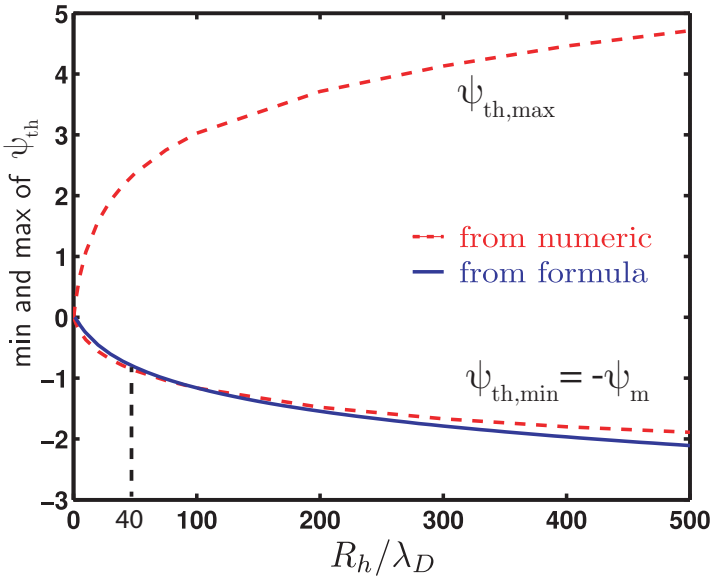

Figure 9.6 – Comparison of the minimum and the maximum of the thermal potential. Data from the analytical calculation or from the numerical reconstruction. *Figure taken from [215].*

Expression of the diode current

The diode current originates from the total number of hot electrons accelerated by the laser N_{tot}. It writes:

$$N_{tot}(t) = \frac{\eta_{abs} E_{las}(t)}{\varepsilon_m} \tag{9.33}$$

The absorption coefficient η_{abs} is fixed to 40 %, similarly to the previous voltage-source model. The total number of hot electrons follows continuous deposition of energy by the laser, namely $E_{las}(t)$. If E_{tot} is the total deposited laser energy and $\tilde{P}_{las}$ is the time-integral of the laser intensity profile, normalized to unity, one has:

$$E_{las}(t) = E_{tot} \int_0^t \tilde{P}_{las}(t) dt \tag{9.34}$$

The equation ruling the evolution of the amount of hot electrons reamaining available in the cloud at a given instant t is calculated as:

$$N_h(t) = \eta_{life} N_{tot}(t) - N_{ej}(t) \tag{9.35}$$

where $N_{ej}(t) = \int_0^t (I_h(t)/e) dt$ is the number of electrons who succeeded to escape the potential barrier, quit the cloud, and thus form the current looping in the target. η_{life} defines the proportion of hot electrons being available in the cloud at the instant t taking into account their cooling $\eta_{life} = t_{life}/t_{laser}$, as calculated under the steady-state regime introduced in Sec. 6.2.

An important modification for t_{life}, the mean cooling time of the laser-accelerated electrons, in respect to the model by Poyé *et al.*, need to be operated in order to consider the stopping power in warm dense matter conditions. Indeed, the laser pulse is energetic and long enough so that the cooling of hot electrons at the ion front ($0 < x < x_m$) processes in a corona at bulk temperature T_b and at nearly critical density. We recall that t_{life} is defined as the time needed for an electron of an energy $\varepsilon_h \sim T_h$ to be thermalized at the bulk temperature T_b:

$$t_{life} = \int_{T_h}^{T_b} \frac{dE}{-S_e(E)v(E)} \quad \left(= \int_{T_b}^{T_h} \frac{dE}{S_e(E)v(E)} \right) \tag{9.36}$$

using here the stopping power as calculated by Eq. 3.69, introduced in Sec. 3.3.1. It yields $\eta_{life} \approx 30\,\%$ for our conditions.

The expression for the ejection current is given with the ejection surface $S = \pi R_h^2$ and the hot electron density in the cloud n_h:

$$I_h(t) = j_h S = \frac{S e n_h v_T e^{-(\psi_m + \psi_0)}}{\sqrt{2\pi}}. \tag{9.37}$$

As seen before, the small capacity leads to a current balance where $I_h \approx I$. The current recirculation through the wire resistance and inductance also imposes:

$$R(t) I_h(t) + L \frac{dI_h(t)}{dt} = (1 + f)\phi_0(t) \tag{9.38}$$

One can note here the added factor f that is the fraction of ejected electrons being captured by the target's front disk. From now on, we shall use the variable $k = 1 + f$.

The description of the resistance evolution with wire temperature and the heat equation are described here using the same differential equations as in the previous model (Sec. 9.2).

Although, the volume of the electron cloud is chosen here to be hemispheric and the electron cloud volume is defined as $V = \frac{2}{3}\pi R_h^3$. We have then $n_h = N_h / V$.

9.3.3 Estimation of the maximum current of the diode in series with a resistance

According to Eq. 9.37, an expression of the current that can be delivered by the diode in series with only a resistance R (the inductance is neglected) is derived for $E_{las}(t) = E_L$ and assuming $N_{tot} \gg N_{ej}$ (*i.e.* $N_h \approx \eta_{life} N_{tot}$):

$$I_h^{\max} \approx \underbrace{\frac{e\eta_{life} N_{tot} v_T}{\sqrt{2\pi}\frac{2}{3}R_h}}_{i_0} e^{-(\psi_{m,1}+\psi_0)} \quad \propto \frac{\eta_{life} E_L \sqrt{T_h}}{R_h} e^{-(\psi_{m,1}+\psi_0)} \tag{9.39}$$

$$\underbrace{(1+f)}_{k}\phi_0 \approx \frac{eRI_h^{\max}}{k_B T_h} \tag{9.40}$$

These two equations determine the diode current and the diode voltage. The resolution of the system of these two equations is non-trivial because the diode law is nonlinear and the obtained equation is transcendental. Nonetheless, an explicit formula for I_h can be obtained applying the Lambert W-function (also called the Omega function, which is the inverse function of $f(w) = we^w$) to Eq. 9.40:

$$I_h \approx \frac{k_B T_h k}{eR} W\left(\frac{eR}{k_B T_h k} i_0 e^{-(\psi_{m,1})}\right) \tag{9.41}$$

The evaluation of the maximum diode current (for Cu) according to Eq. 9.41 is shown in Figure 9.7 for a pulse duration of 1 ns, and coil resistance of 3 Ω using either $k = 1$ (left panel) or $k = 2$ (right panel). The stars identify laser parameters from experiments providing measurements of B-fields driven by ≈ 1 ns-duration lasers (see figure's table and legend):

- ◇ the grey star corresponds to the best laser conditions of our experiment [238], yielding a maximum diode current of respectively 255 kA and 455 kA for $k = 1$ and $k = 2$. The maximum measured current was $I = 340$ kA, within the above estimated range.
- ◇ the orange star corresponds to the experiment by Daido *et al.* [58] using a laser of ≈ 100 J energy at an intensity of $\approx 2 \times 10^{14}$ W/cm^2 at $\lambda = 10.6$ µm. Yet, the laser irradiance $I\lambda^2$, which is the key parameter, amounts to $\approx 2 \times 10^{16}$ Wcm^{-2}µm^2. The current obtained in a single coil of 2 mm-diameter is ≈ 60 kA. At a temperature of ∼ 3 eV (consistent with this level of current), the coil resistance is $R \approx 5\,\Omega$. The maximum diode current yields ≈ 46 kA for $k = 1$ and ≈ 80 kA for $k = 2$, which is a fine agreement.
- ◇ the blue star correponds to the laser conditions of the experiment carried out by Courtois *et al.* and published in [53]. The laser energy was of ≈ 300 J and laser intensity of $\approx 4 \times 10^{16}$ W/cm^2 at $\lambda = 1$ µm. The current flowing through each of the two U-turn loops of 2.5 mm-diameter composing the Helmholtz coil target was ≈ 30 kA. The coil wire length of each loop is sensibly larger than in our experiments by ≈ 6×, yielding a resistance of ≈ 15 Ω at ∼ 3 eV. The maximum current in each loop (half the maximum diode current) is calculated to be of ≈ 17 kA for $k = 1$ and of ≈ 31 kA for $k = 2$, which is as well in fair agreement with the data.
- ◇ the green star corresponds to the best laser conditions of the experiment by Fujioka *et al.* [87], characterized by a laser energy of 1 kJ, and an intensity of $\approx 4.3 \times 10^{16}$ W/cm^2 at $\lambda = 1$ µm. The coil's wire length is comparable to our case and the resistance of 3 Ω at ∼ 10 eV remains valid. It yields a maximum diode current of respectively 132 kA for $k = 1$ and 235 kA for $k = 2$.

Experiment	*Laser parameters*	*Laser Irradiance*	*Coil resistance*	*Expected I_{max}*	*Measured I*
☆ *Our expriment* [239]	500 J, 10^{17} W/cm^2 λ = 1 µm	10^{17} W cm^{-2}µm^2	3 Ω (~10 eV)	255 kA (k=1) 455 kA (k=2)	340 kA
★ *Daido et al.* [58]	100 J, 2×10^{14} W/cm^2 λ = 10.6 µm	2×10^{16} W cm^{-2}µm^2	5 Ω (~3 eV)	46 kA (k=1) 80 kA (k=2)	60 kA
★ *Courtois et al.* [53]	300 J, 4×10^{16} W/cm^2 λ = 1 µm	4×10^{16} W cm^{-2}µm^2	15 Ω (~3 eV)	17 kA (k=1) 31 kA (k=2)	30 kA
★ Fujioka et al. [87]	1 kJ, 4×10^{16} W/cm^2 λ = 1 µm	4×10^{16} W cm^{-2}µm^2	3 Ω (~10 eV)	132 kA (k=1) 235 kA (k=2)	> 1 MA
★ Law et al. [157]	600 J, 3×10^{16} W/cm^2 λ = 1 µm	3×10^{16} W cm^{-2}µm^2	3 Ω (~10 eV)	120 kA (k=1) 213 kA (k=2)	340 kA
★ *Gao et al.* [89]	2.5 kJ, 3×10^{16} W/cm^2 λ = 0.351 µm	3×10^{15} W cm^{-2}µm^2	8 Ω (~3 eV)	16 kA (k=1) 28 kA (k=2)	20 kA

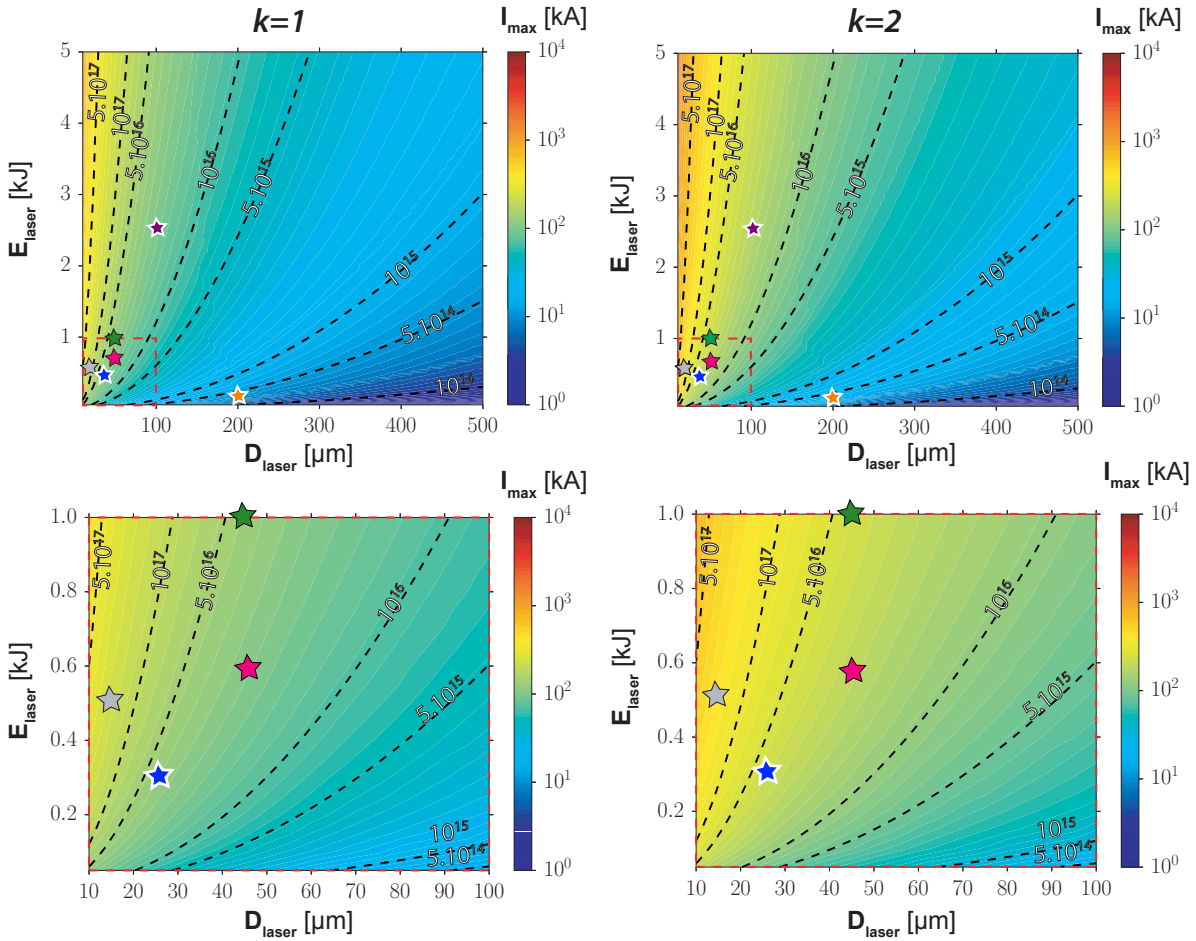

Figure 9.7 – Map representation for $k = 1$ (left panel) and $k = 2$ (right panel) of the maximum diode current I_{max}, as calculated by Eq. 9.40 for Cu, $\tau_L = 1$ ns, $\lambda = 1$ µm and $R = 3\,\Omega$. The dashed lines corresponds to intensity iso-contours identified by the labels in units of W/cm^2. The grey star identify the point with our laser parameters and yield a value of I_{max} ranging from 255 kA to 455 kA respectively for $k = 1$ and $k = 2$. The other star colors respectively stands for the laser conditions of the experiments: [58] (orange), [53] (blue), [87] (green), [157] (magenta) and [89] (purple). It is worth recalling that the values under the stars correspond to a laser wavelength of 1 µm and a fixed coil resistance of $R = 3\,\Omega$. To get the true estimation, resistance and wavelength have to be corrected for the given experiment. The reader should then refer to the above table and to the text for [58, 89, 53] (stars with white edges).

It does not agree with the $\sim$ MA currents measured in this experiment. As already discussed in Sec. 0.3, the Faraday rotation results would correspond to $\approx 15\,\mathrm{kT}$ extrapolated at the center of the 500 µm-diameter U-shaped coil, that would be both inconsistent with the latter estimation and with invested laser energy.

- ◇ the magenta star for the best laser conditions of our collaboration experiment with Law *et al.* [157], characterized by a laser energy of $\approx$ 600 J and a maximum intensity of $\sim 3 \times 10^{16}\,\mathrm{W/cm^2}$. The measured B-field of $\approx$ 610 T corresponds to a current of $\approx$ 250 kA. The coil length being similar to our experiment, the resistance $R = 3\,\Omega$ remains valid. We obtain a maximum diode current of $\approx 120\,\mathrm{kA}$ for $k = 1$ and $\approx 213\,\mathrm{kA}$ for $k = 2$. Although it is under the maximum current observed in experiment, it is quite close to it for $k = 2$.
- ◇ the purple star corresponds to the laser conditions of the experiment by Gao *et al.* [89], characterized by an energy of 2.5 kJ and a maximum intensity of $\sim 3 \times 10^{16}\,\mathrm{W/cm^2}$, with $\lambda = 0.351$ µm ($I\lambda^2 = 0.3 \times 10^{16}\,\mathrm{Wcm^{-2}\mu m^2}$). The 600 µm-diameter U-shaped coil of longer wire length used in this experiment correspond to a resistance value at $\sim 3\,\mathrm{eV}$ of $R \approx 8\,\Omega$. It yields a maximum diode current of respectively 16 kA for $k = 1$ and 28 kA for $k = 2$. These values are in the good order of magnitudes of the measured B-field in this experiment of $\sim 40 - 50\,\mathrm{T}$ ($I \approx 22kA$). It is worth noting that the short laser wavelength leads to a rather low laser irradiance $I\lambda^2$ in respect to previous experiments for equivalent laser intensity. It is the main reason of the low conversion efficiency of 0.01 % from laser pulse energy to magnetic field energy reported in the published results [89].

The maximum diode current calculated by our model is thus able to correctly estimate the order of magnitude of laser-driven B-fields measured in various experimental conditions. It is seen to depend strongly on T_h and therefore on the laser irradiance $I\lambda^2$. Moreover, the maximum current is noticeably influenced by the coil length (R): shorter length coils exhibit higher currents, other parameters being fixed. The latter variation was also noticed in our experiments when using bigger coil-targets.

9.3.4 Model results

In continuation, we will present the temporal evolution of the current in the coil, calculated with this model. First, the calculation will be made under the following assumptions, identified by the label "**(1)**":

- ◇ A constant potential $\psi_m = \psi_{m,1}$ taken from the model of Poyé *et al.*
- ◇ A constant ion velocity between the two plates $u(t) = \sqrt{3}c_s$ with c_s the ion acoustic speed.

The results obtained under these assumptions are presented in Figure 9.8-**(1)**. It is first notable that the maximum B-field in that approach is reached before the short-circuit time $t_{cc} = d_0/(\sqrt{3}c_s)$, as it can be also seen in the bottom-right graph of Figure 9.8 showing the time-evolution of the gap size $d(t)$. Indeed, the maximum current can be reached before short-circuit when the number of ejected electrons N_{ej} reaches a maximum such as that $N_h = \eta_{life}N_{tot} - N_{ej} = 0$. In both cases, the potential ϕ_0 then drop to 0 and afterwards the RL circuit discharges within a time-scale of R/L.

As 2^{nd} approach **(2)**, we used the ion velocity formulation in Eq. 9.30 and kept a constant potential $\psi_m = \psi_{m,1}$. The results are shown in Figure 9.8-**(2)**. The ion velocity rises due to the additional contribution of the gap potential and the peak B-field is reached at a lower time, of ≈ 1.3 ns. In the case of $k = 1$, the potential ψ_0 drops faster to zero and results in a B-field peaking time of ≈ 1 ns.

As a 3^{rd} approach **(3)**, we include the effect of the ion dynamics on the potential ψ_m and the equation Eq. 9.32 is used. The results are shown in Figure 9.8-**(3)** and one can see that the potential decrease occurring when $d(t) \lesssim d_0/2.4$ is boosting the current extraction. It yields stronger B-field magnitudes which are increasing by ≈ 100 T in respect to the approach **(2)**.

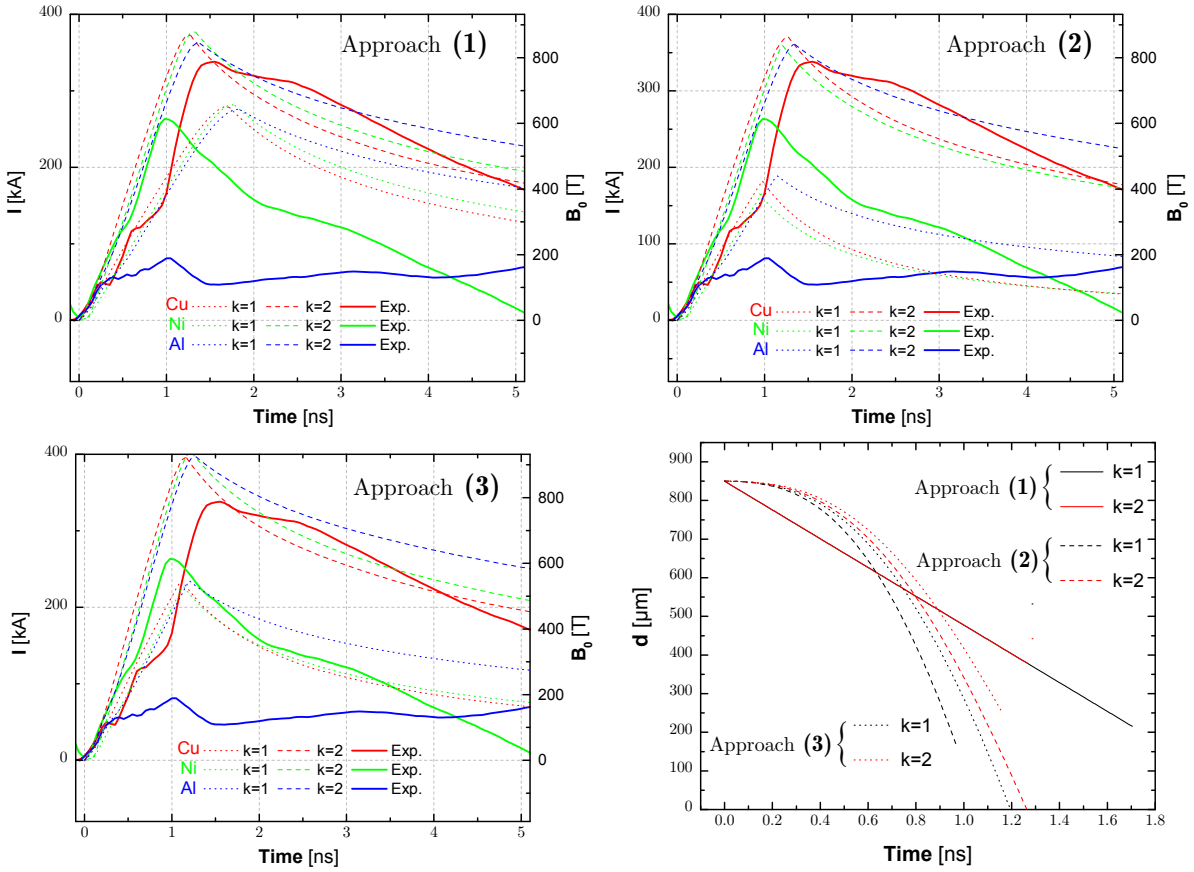

Figure 9.8 – Model results for the three materials: **(1)** Using a constant thermal potential $\psi_m = \psi_{m,1}$ and a constant ion velocity $u(t) = \sqrt{3}c_s$; **(2)** Still using a constant thermal potential but including the ion velocity dependence on gap potential, from Eq. 9.30; **(3)** Including finally the evolution of the thermal potential, as given by Eq. 9.31 and Eq. 9.32. In the bottom-right corner, a graph of the evolution of the gap distance $d(t)$ for the three latter cases is shown. The lines are intentionally set to terminate when the peak B-field is reached.

The results of the three approaches are seen to be very similar for $k = 2$, where the diode is extracting almost its maximum available current and deplete the hot electron cloud. The comparison with the case $k = 1$, where differences arises from the different formulations of the potential's evolution, will permit to characterize the different approaches.

In the simpler 1^{st} approach, the charging time is also limited by the maximum current for $k = 1$. Globally, the charging time is decreased in respect to the previous voltage-source model, yet, it is still slightly overestimated. For the 2^{nd} approach, the charging time is well reproduced. However, the potential ψ_0 for $k = 1$ drops fast to zero and blocks prematurely the diode. It is due to the inconsistency of the mixed approach using a potential-dependant ion velocity while keeping constant the minimum diode potential ψ_m. The 3^{rd} approach does contain both ion velocity and potential time-evolutions consistently coupled and it reproduces fairly well the charging duration. Moreover, the lower current is not blocking the diode anymore: in this approach, for $k = 1$, the charging time is logically limited by

the short-circuit occuring when $d \to 0$. Nevertheless, the potential drop when the cathode gets close to the anode leads to an overestimated B-field strength. A full 3D model of the potential evolution appears to be necessary. Work in progress on this fuller description is currently ongoing.

Optimization on initial gap length d_0

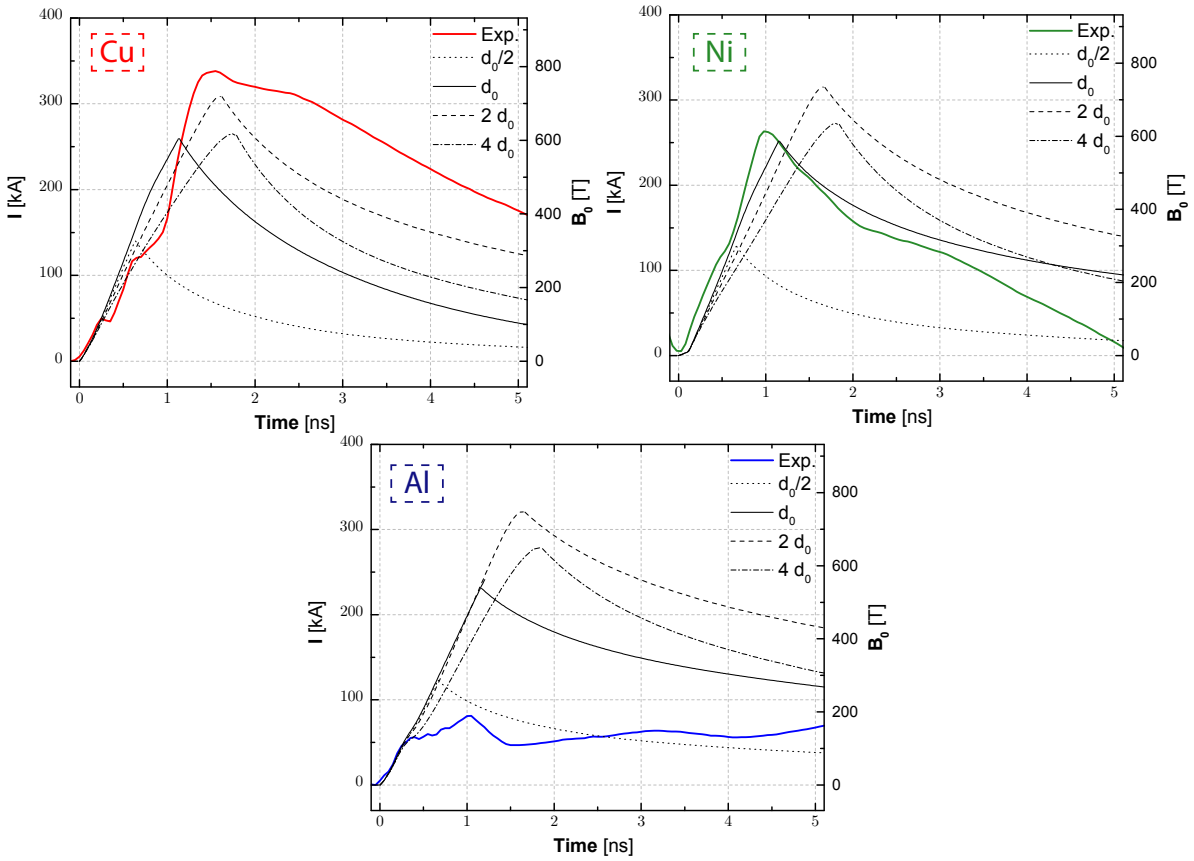

Figure 9.9 – Influence of the initial gap distance using 0.5× (dotted lines), 1× (full line), 2× (dashed lines) and 4× (dashed-dotted lines) the initial gap distance of our targets $d0 = 850\,\mu m$. An optimum is found for the three materials using an initial gap distance of $2 \times d_0$.

Based on the 3^{rd} approach formulation **(3)**, to correctly infer the influence of the initial gap distance d_0 on the B-field strengths, the fraction of hot electrons which are captured by the front disk includes here an additional geometrical factor. A proposition is made assuming that electrons are captured on the fraction of the front disk in a section $[\pi(r_e^2 - r_i^2)]$ delimited by its inner hole radius r_i and its outer radius r_e. The solid angle of the hot electron ejection at the moving ion front is evaluated from the backscattering angle β modeled in [128], and β is given by:

$$\beta = \arctan\left(\frac{2.2g(1+g)}{1+2g-0.21g^2}\right) \tag{9.42}$$

with the factor $g = 0.187Z^{2/3}$ which accounts for the electron ion collision ratio in different materials. The fraction of captured hot electrons f is then reevaluated as follows:

$$f = \frac{\left(\min\left(\tan\beta d(t), r_e\right) - \min\left(\tan\beta d(t), r_i\right)\right)^2}{\left(\tan\beta d(t)\right)^2} \tag{9.43}$$

Results are given in Figure 9.8 using an initial gap distance of either 0.5× (dotted lines), 1× (full line), 2× (dashed lines) and 4× (dashed-dotted lines) the initial gap distance of our targets $d_0 = 850\,\mu m$. The value of f for $t = 0$, with inner and outer radius of 875 µm and 1750 µm, are respectively 34.3 %, 71.6 % and 70.7 % for Al, Ni and Cu.

One can note in Figure 9.9 that the B-field maximum is higher, independently of the considered material, for the case of an initial gap distance of $2 \times d_0 = 1700\,\mu m$. This result may be overestimated since no $\vec{E} \wedge \vec{B}$ drift on electrons is considered here. Still, it would be worth testing to see if the model prediction of this optimum can also be found experimentally.

9.4 Conclusions on the modeling

In conclusion, the two presented models give a correct estimation of the B-field order of magnitude, similar to what is measured experimentally. However we pointed out that the formulation of the first model of Courtois *et al.*, even with the added improvements of a time-evolving resistance and wire expansion, does suffer of an inaccurate modeling of the voltage-source which is imposed independently of the discharge.

A more complex approach was pursued in the *laser-pump diode model* using a current source description instead of a voltage source, while considering the discharge current retroaction on the current source. It yields lower B-field magnitudes, resulting in a closer matching with the measurements. Besides, the estimation of the maximum current made in Sec. 9.3.3 does also match with experiments found in litterature and in particular conveys the strong dependance of the maximum current with the laser irradiance $I\lambda^2$.

However, none of these models was able to reproduce the strong material dependence observed in the experiment. The material's model dependence on the source is low and we already saw that resistivity differences are erased rapidly while increasing the wire temperature. The ion dynamics with the added contribution of the gap electric potential was the last candidate to explain the material differences increasing the ion velocity of lighter materials and then causing a bigger dispersion on the short-circuit time. Nevertheless, the material dependent ratio Z^*/m_i in the expression of the ion velocity (Eq. 9.30) being sensibly equal for Al, Ni and Cu, the electric field does not play such a role. The material dependence remains then unclear at this stage of the modeling (as it remains also unclear the reproducibility of the experimental shots for Cu and Al used only during few shots of the 1^{st} experiment).

9.5 Energetic qualifications

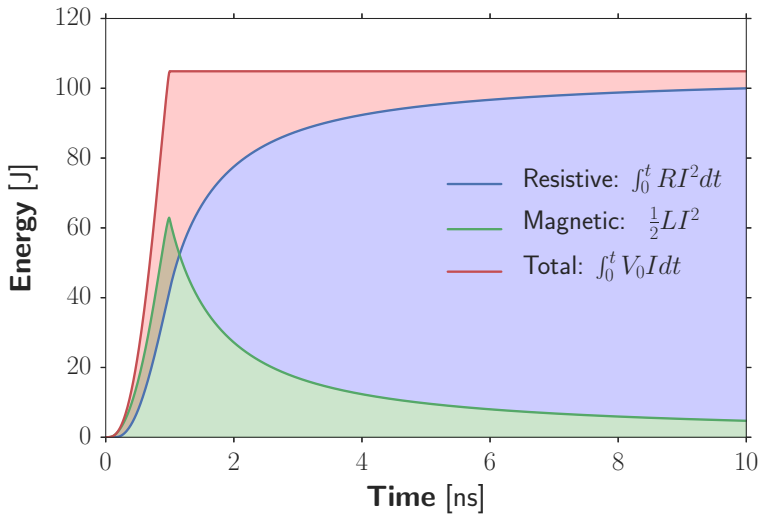

Figure 9.10 – Energy balance of the RL circuit corresponding to the measured B-field trace of the Ni target peaking at $\approx 600\,\mathrm{T}$ at $\approx 1\,\mathrm{ns}$.

Under the light of the modeling, and in particular regarding energetic considerations, a qualification of the obtained B-fields magnitudes will be drawn here.

First, from the RL circuit equation, one can calculate an energetic balance that would correspond to a current trace matching the experimental curve of Ni (fairly reproduced on several shots). The total RL circuit energy is given by $\int_0^t V_0 I dt$ split into magnetic energy $\frac{1}{2}LI^2$ and resitive energy (Joule effect) $\int_0^t RI^2 dt$. The result is presented in Figure 9.10.

The total integrated circuit energy corresponds to $\approx$ 20 % of the laser energy. It is worth mentioning that it would lead to a questionable strong laser-to-hot-electrons efficiency. For the measured B-field magnitude of Cu, it would be an even stronger conversion efficiency ($\approx$ 40 %). Instead, a maximum conversion efficiency of 10 % at $\approx 1.4 \times 10^{17}\,\mathrm{W/cm^2}$ would mean a maximum current of $\approx 150\,\mathrm{kA}$ (or $\approx 350\,\mathrm{T}$ at coil center).

Both presented models are semi-analytical models and therefore needed some assumptions. Unfortunately, it results in a break of the energy consistency throughout the models. Notably, the input of an *ad-hoc* hot electron distribution, characterized by an estimated temperature T_h did play a big role in the resulting conversion efficiency. For instance, using in place of Beg's or Gibbon's scaling fits (see Sec. 3.2.2) a moderate hot-electron temperature T_h of 45 keV - which is the temperature of the lower part of the spectrum inferred from Hard X-ray measurements (see Sec. 8.2.4) - both models give more adequate results in terms of energy conversion, but the magnetic field strengths are lower than those measured:

- ◇ from the improved voltage-source model (Sec. 9.2), one obtains a maximum current in the coil of $\approx 160\,\mathrm{kA}$.
- ◇ from the laser-pumped diode model (Sec. 9.3), one obtains a maximum current in the coil of $\approx 150\,\mathrm{kA}$ (for $k = 2$)

Similarly, using a moderate hot-electron temperature of $T_h = 10\,\mathrm{keV}$ for the experiment of Gao *et al.* instead of Beg's or Gibbon's scaling fits (yielding respectively $T_h = 29.5\,\mathrm{keV}$ and $T_h = 21.3\,\mathrm{keV}$), one obtains from the laser-pumped diode model a maximum current of $\approx 6.5\,\mathrm{kA}$ (for $k = 2$), which also would underestimate their measurements by more than a factor 2.

At this point, it is worth recalling that an experimental error of a factor 2 on the B-dot extrapolation cannot be envisaged from a B-dot position error of only $\sim \pm 1\,\mathrm{mm}$, or from an error on the 3D modeling of the target, or even from a combination of both. Indeed, an error on the B-dot position of $\sim 1\,\mathrm{mm}$ would correspond roughly to a relative error on coil center B-field of at most

$\approx 3 \times 1\,\mathrm{mm}/3\,\mathrm{cm} \approx 10\,\%$, 3 cm being the minimal B-dot distance used in the experiments. Moreover, one would need an error such as an open angle of the coil equals to twice the measured one to amount to a factor 2 inaccuracy in the extrapolation. The manufacturing reproducibility of the coil was good enough to discard the possibility of such strong errors on the target geometry modeling.

In conclusion, the measurements of the B-field performed during this thesis work do suppose very high conversion to hot electrons. The physical origin of such high conversion is nonetheless not fully understood and a direct experimental measure is missing at present day. Yet, the consistency of other diagnostics, and in particular the similar magnitude obtained in [157] with proton probing at B-field peak amplitude, qualify the hypothesis of a B-dot measurement proned to such large errors.

To answer this open-ended question, a possibility for next experiments would be to characterize *in situ*, by a dedicated measurement, the ejected hot electron current between the disks, or equivalently, their energy distribution with known conversion efficiency. In addition, it should be repeated the shielded proton probing setup in combination with B-dot measurement varying laser parameters and eventually the distance between the plates. The use of different materials have also to be repeated to get increased statistics on the material dependence.

Part III

Application of imposed external B-field to guide charged particle beams in dense matter or in vacuum

Summary

10 Fast-Electron guiding by laser-driven strong external magnetic field in dense matter 166

10.1 Existing techniques to guide fast electron beams . . . 166
10.2 Experimental setup description . . . 167
10.3 Simulations of the magnetic-field diffusion over the transport targets . . . 169
10.4 Experimental results . . . 170
10.5 Fast electron transport simulations with external magnetic field in Particle In Cell (PIC) Hybrid - Code . . . 171
10.6 Calculation of CTR emission (post-processor) . . . 172
10.7 Simulations results and discussion . . . 172
10.8 Complementary information . . . 180
10.9 Conclusions . . . 182

11 High discharge current and application to proton beam tailoring in high laser intensity regime (picosecond interaction) 183

11.1 Experimental setup description . . . 183
11.1.1 Time-resolving proton radiography . . . 184
11.2 Previous results of electromagnetic lenses . . . 184
11.3 Experimental Results . . . 186
11.3.1 TNSA proton source characterization by Thompson Parabola . . . 186
11.3.2 Time-resolving proton radiography results . . . 187
11.4 Static simulations results . . . 191
11.4.1 Influence of an Electric Field only . . . 191
11.4.2 Influence of a combined Electric and Magnetic Field . . . 192
11.5 Dynamic simulation results . . . 193
11.6 2D PIC simulation results . . . 195
11.7 Conclusions . . . 197

10 Fast-Electron guiding by laser-driven strong external magnetic field in dense matter

We already saw that upon the interaction of intense laser-pulses with dense targets, high-current relativistic electron beam (REB) are accelerated and can transport a significant fraction of the laser energy deep into the target [289, 195, 288].

The REB flux degrades rapidly against the penetration depth due to resistive and collisional energy losses [212, 275, 241, 280] and mostly to its intrinsically large divergence [239, 263, 96]. One of the main bottleneck issue related to the fast ignition scheme is thus the control of the REB divergence before and over its propagation to the D-T core.

Besides that, the production of high-energy-density (HED) flows through solid-density or denser matter is a major challenge for improving laser-driven sources of energetic particles and radiation [158, 262], or for optimizing the isochoric heating of dense matter. A part from ICF, this is also of major relevance in the study of stellar opacities [108] or of warm dense matter states [207].

External magnetic field is a potentially promising candidate to guide the fast electron beam. For instance, it has been shown numerically that imposed axial magnetic-fields in the $1-10\,\mathrm{kT}$ range should be able to guide GA currents of MeV electrons over 100 µm distances from the laser-absorption region up to the dense core of nuclear fuel [268, 285]. This would enhance the electrons kinetic energy coupling to the core potentially leading to high-gain fusion energy release while reducing the needed ignitor laser-energy. More details on those perspectives will be given in the *Conclusions and perspectives* of this thesis work, Sec. 13.1.

In continuation, we will present existing techniques to guide fast electron beams and present afterwards an alternative by applying for the first time an external B-field enough strong to guide MeV-electrons aligned with the REB propagation axis in solid targets.

10.1 Existing techniques to guide fast electron beams

We saw in Sec. 3.3.2 that the propagation of a fast electron beam in matter induces a return current. This return current is responsible of self-generated field which could be sufficient to collimate the fast electron beam. However, the self-collimation of the beam is not strong enough when considering, for instance, the expected divergence in a fast ignition target being in excess of 50 ° [64, 136].

An extended approach of self-generated fields (resistive B-fields) in order to radially-confine the REB has been experimentally reported by using specific laser irradiation [231] and/or target structures [134, 221, 40, 206, 249]. The common principle is that collimating B-fields are induced by REB intense currents in resistive media, due either by the beam inhomogeneity or by radially-converging gradients of resistivity along the REB propagation axis [19, 230]. In a fast ignition target, two conditions are mandatory to obtain an efficient guiding. First, the resistive fields need to persist during the entire ignitor laser pulse. Second, the high resistivity path must survive the compression of the spherical shell.

A first advanced/integrated concept has been proposed by Solodov *et al.* in 2010 [257], using wire-like structures of mid-Z materials (such as copper) connecting the cone tip to a region close to the D-T core. In that case, fast electrons are guided by the collimating magnetic field created at the interface between the wire-structure and the D-T background plasma. Another approach is to structure the cone tip itself (in [245] the authors proposed an ellipsoidal structure), which produces an azimuthal magnetic field deflecting the electrons specularly at the interface and thus reducing the electron initial angular spray. Numerical simulations have shown an improvement by a factor $2-3$ in the coupling efficiency with the core, compared to the unguided case [229]. A design using two concentric cones separated by a vacuum gap was also proposed by Campbell *et al.* [41] and the idea was extended to also cover the cone tip [121]. Numerical simulations showed that this last method could enhance the core heating by a factor 4.

These encouraging enhancements are nonetheless nuanced since many electrons are not magnetically-trapped, maintain their initial divergence and are scattered through collisions. For

above-mentioned techniques, the number of guided electrons remains under 50 %. Moreover, proposed improvements involve sophisticated target structures, which could hardly be tested in the harsh conditions of an ICF target.

In the next section, we will present the first experimental evidence of the guiding of relativistic electron beams in dense matter by longitudinally imposed strong magnetic fields, supported by transport simulations.

10.2 Experimental setup description

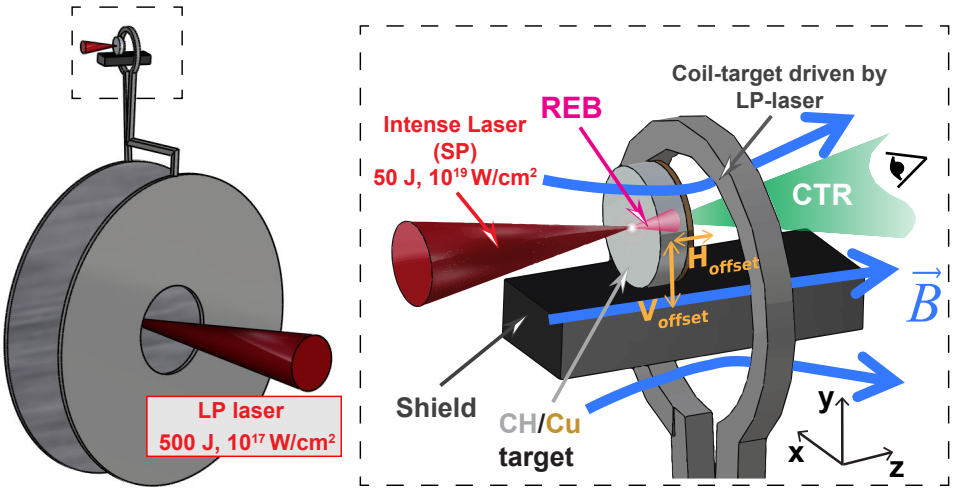

Figure 10.1 – Sketch of the experimental setup for the study of REB-transport with imposed B-field. The REB is generated by the intense SP laser, focused parallel to the coil axis and at normal incidence onto the center of the front surface of a neighboring solid 50 µm-CH / 10 µm-Cu thick target of 200 µm diameter. The Ni coil-target (coil radius of 250 µm) is previously driven by the ns LP laser. REB-patterns were investigated by imaging the CTR emitted from the transport targets' rear surface.

A 600 T B-field was produced by our all-optical platform using laser-driven coil targets (see Part II). This technique has shown to create a quasi-static magnetic field that is of sufficiently long duration to fully magnetize a transport target prior to REB generation. The guiding experiments were conducted at the LULI pico 2000 laser facility simultaneously to the characterization of the produced B-fields. We used a dual laser beam configuration sketch in Figure 10.1. It consists of i) a high energy long-pulse beam [LP: 1 ns, 500 ± 30 J, $(1.4 \pm 0.6) \times 10^{17}$ W/cm^2] focused into Ni coil-targets to produce a B-field of several hundreds Tesla and duration of a few ns; ii) at different delays Δt with respect to the LP, a high-intensity short-pulse beam [SP: 1 ps, $47 - 49$ J, $(1.5 - 3) \times 10^{19}$ W/cm^2] focused at normal incidence to generate a REB in solid plastic targets, located at the coil vicinity. The setup at the coil vicinity is sketched on the right part of Figure 10.1.

The REB transport targets were 200 µm-diameter and 50 µm-thick plastic (CH) cylinders with a 10 µm-thick Cu-coating on the rear side. The cylinder's axis was invariably parallel to the coil axis, and for the two experimental runs, we explored successively positioning the target i) shifted from the coil plane (with horizontal and vertical offsets of the target center with respect to the coil center of $H_{\text{offset}} = -70$ µm, $V_{\text{offset}} = 120$ µm) and ii) at the coil plane ($H_{\text{offset}} = 0$ µm, $V_{\text{offset}} = 50$ µm). This enabled us to explore two different 3D spatial distributions for the B-field imposed to the transport targets, as seen in Figure 10.2-a) and b) for configuration i) and Figure 10.2-c) and d) for configuration ii). For each of the two configurations, the choice of Δt controlled the time allowed for B-field diffusion in the transport targets prior to REB injection, testing REB-transport in different conditions of target magnetization.

The REB transverse pattern after crossing the target thickness was investigated by imaging the Coherent Transition Radiation (CTR) emission from the rear surface at twice the SP-laser frequency,

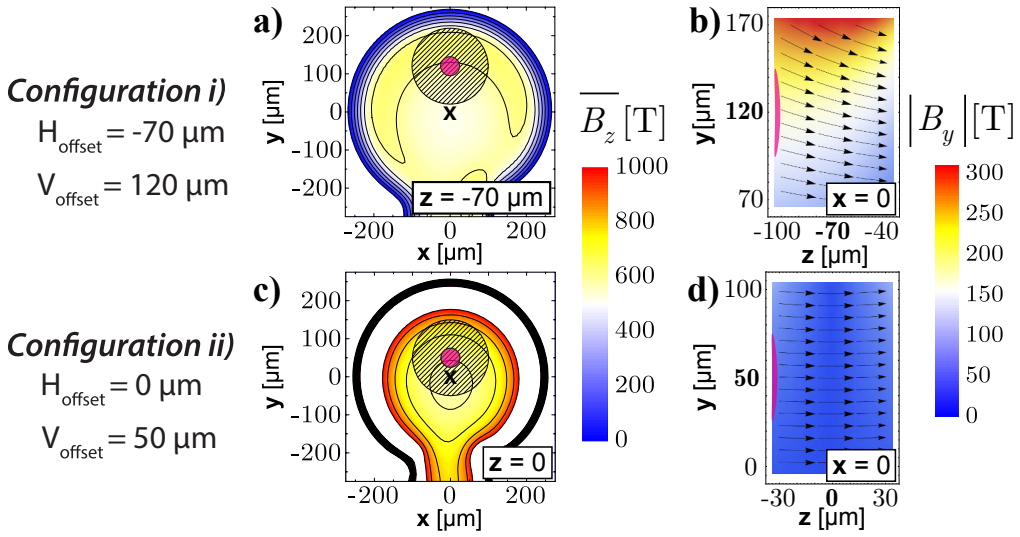

Figure 10.2 – Experimental B-field distributions, in vacuum, at peak value, 1 ns after LP-laser driving (origin of the spatial coordinates at the coil center). **a)**, **c)** Amplitude of the B-field longitudinal component averaged over the 60 µm target thickness, $\overline{B_z}$, at the two explored positions of the transport target. The dashed circles represent the position of the transport target in the perpendicular plane: the coil axis and the SP laser axis are respectively represented by the cross-signs and the center of the pink circles, which radius corresponds to the REB initial radius, r_0, in the REB-transport simulations. **b)**, **d)** Absolute value of the B-field vertical component $|B_y|$ (color scale) and arrow representation of the B-field lines over the target $x = 0$ -slice, for the two target positions. The plots correspond also to the B-field embedded into the targets as initial conditions for the REB-transport simulations in magnetized conditions, in agreement with predictions of the B-field resistive diffusion.

$2\omega_0$. CTR is produced by the REB crossing the target-vacuum boundary (see [12, 214] and *Appendix*, Sec. 23). Its time-scale, of the order of a few ps, follows that of the fast electron flux envelope. Yet, the pulsed character of relativistic laser-acceleration mechanisms modulates longitudinally the REB-current as a comb of periodic micro-bunches. The coherent interference of the transition radiation produced by the electron-com crossing the rear surface yields peak emissions at the spectral harmonics of the bunch frequency.

In the present experiment, the CTR imaging system of the transport targets's rear surface was composed by two doublet-lenses with an optical aperture of $f/9$ and was aligned on the equator plane looking at the target rear Cu-surface with a 22.5 °-angle with respect to its normal. The optical system produced images with a magnification of ≈ 20 with a spatial resolution of $\approx 7\,\mu$m full-width-at-half-maximum (FWHM). The streak camera was used with an open slit ($\approx 5\,$mm) and the faster sweep speed of 0.5 ns/screen synchronized to the SP laser beam interaction, allowing to freeze the 2D pattern of the prompt CTR emission from the target surface, acting as a fast gated 2D frame grabber [239]. $2\omega_0$-light was selected by a 10 nm FWHM-bandwidth interferometric filter centered at 532 nm. As an extra precaution for reducing the noise level due to any spurious light from the coil-target, only the central region of the imaged field, corresponding to the REB-transport target surface, was selected after the first lens. For more information about transition radiation and CTR, a dedicated section has been added to the *Appendix*, Sec. 23.

10.3 Simulations of the magnetic-field diffusion over the transport targets

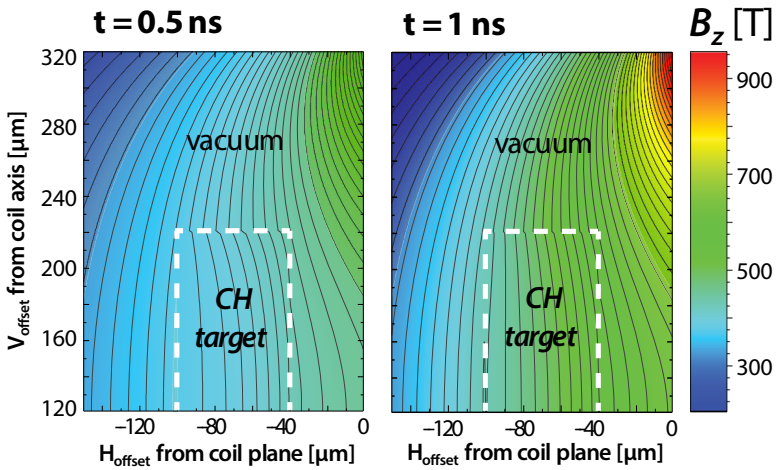

Figure 10.3 – Axis-symmetric simulations of the B-field resistive diffusion over the transport targets. The B-field spatial distribution is given at $\Delta\tau = 0.5\,$ns (left panel) and at $\Delta\tau = 1\,$ns (right panel) for the target positioning configuration with $H_{\text{offset}} = 70\,\mu$m and $V_{\text{offset}} = 120\,\mu$m. From the breaking on the contour lines at the target-vacuum interface, we conclude that there is a discontinuity of the B-field for $\Delta\tau = 0.5\,$ns and that discontinuity practically disappears at $\Delta\tau = 1\,$ns, assumed as the time of full target magnetization.

The evolution of the transport-target magnetization has been predicted by simulations of the B-field resistive diffusion inside the target [112] as the B-field rises up to its peak-value (rise time of $\approx 1\,$ns, consistent with the duration of the LP-laser driver). The model describes the penetration of external B-fields in the target material, according to the diffusion equation:

$$\frac{\partial \vec{B}}{\partial t} = \frac{1}{\mu_0}\eta\nabla^2 B \tag{10.1}$$

which is valid for small magnetic Reynolds number. At each time iteration, Ampère's law calculates the induced current density from which Ohmic heating is then computed for the temperature map of the target along with a new resistivity map. Figure 10.3 presents sample results for the target position configuration i) at $t = 0.5\,$ns (left panel) and $t = 1\,$ns (right panel). At $t \approx 1\,$ns we consider the target

to be fully magnetized, as the B-field spatial distribution inside the target becomes comparable to what is simulated in vacuum at the same position. Further, the B-field gradients discontinuities practically disappear at the target edges.

This magnetization time agrees with a simple linear estimation of the B-field diffusion time:

$$\tau_{\text{diff}} \approx \frac{\mu_0 L^2}{\eta} \sim 1\,\text{ns} \tag{10.2}$$

over the length $L = 50\,\mu\text{m}$ of the target CH-layer assuming a constant resistivity of $\eta = 10^{-6}\,\Omega\text{m}$ (expected for CH at 1 eV).

10.4 Experimental results

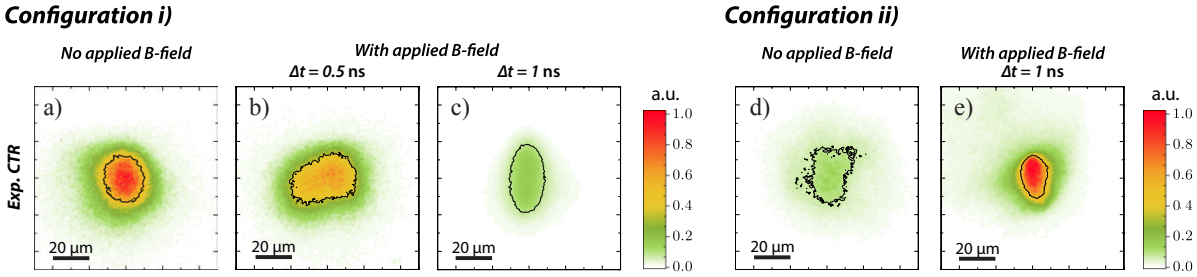

Figure 10.4 – Results of the experimental CTR imaging, for the two configurations i) target out of the coil plane and ii) target at the coil plane (see Figure 10.2), without imposed B-field and with imposed B-field (for the two delays $\Delta t = 0.5\,\text{ns}$ and $\Delta t = 1\,\text{ns}$), as labeled. The contour lines correspond to the half-height of the signals.

Sample results of the CTR signals are shown in Figure 10.4, for target position configurations i) on the left, and ii) on the right, with or without imposing an external B-field, as labeled. The aspect ratio of the signals has been corrected from the observation angle. For the two data sets, the average SP laser energy and intensity were respectively i) $47 \pm 6\,\text{J}$ and $3 \pm 0.8 \times 10^{19}\,\text{W/cm}^2$, ii) $49 \pm 1\,\text{J}$ and $1.5 \pm 0.4 \times 10^{19}\,\text{W/cm}^2$. The difference in laser intensity is mainly due to different focal spots in the two independent experimental runs.

Without externally imposed B-field [Figure 10.4-a) and d)], we obtained rather large ($\approx 14 \pm 2\,\mu\text{m}$ half-width-half-maximum, HWHM) and fairly-symmetric CTR patterns. When imposing the longitudinal B-field for the target position i) and varying the delay of REB-injection, at $\Delta t = 0.5\,\text{ns}$ [Figure 10.4-b)] the CTR yield is slightly weaker and its pattern looks twisted, yet the average size is comparable to the case without B-field. As mentioned before, the target should not be yet fully magnetized.

At $\Delta t = 1\,\text{ns}$, we have obtained CTR patterns significantly different than the case without B-field, for both target positions i) and ii) [respectively Figure 10.4-c) and e)]. The CTR-patterns are clearly narrower horizontally. Vertically, the signal is also narrower for configuration ii), while it is elongated for configuration i). These correspond to half-height areas of equivalent radius $\approx 13\,\mu\text{m}$ for configuration i) and $\approx 9\,\mu\text{m}$ for configuration ii). The CTR yield decreased for configuration i) and increased for configuration ii) relative to the corresponding signals without B-field. As discussed above, the delay $\Delta t = 1\,\text{ns}$ corresponds to REB transport in magnetized targets. The differences in the patterns shape and yield between Figure 10.4-c) and e) are then related to the different B-field distributions inside the targets, as represented in Figure 10.2-c) and e). One can estimate the field strength that is needed to confine a fast electron of radius r_B and velocity $\vec{v}$:

$$B > \frac{m_e c}{e r_B} \gamma\beta(1 - \cos\theta) \tag{10.3}$$

where θ is the angle between $\vec{v}$ and the injection axis. An equivalent formulation of this criterion can be given by comparing the electron Larmor radius (see Sec. 2) with the fast electron beam radius :

an efficient guiding is obtained when $r_L \leq r_B$. beam electrons are *trapped* and follow B-field lines if their Larmor radius becomes comparable or smaller than the beam radius. A 600 T field [see values of $\overline{B_z}$ around the REB axis in Figure 10.2-b) and d)] is strong enough to *confine* MeV-electrons which are then *trapped* along B-field lines. It is worth noting that the B_y-component in config. i) [Figure 10.2-c)] deviates downwards the REB propagation axis. The consequent inclined REB path in the transport target results in an observed yield drop on the detected CTR. This behavior of the CTR is reproduced and will be further explained in the following part, by means of REB transport simulations. In comparison, for config. ii) with optimum imposed B-field symmetry, the narrowing of the signal e) compared to d) is significant and is a signature of a radially-pinched REB. Here the REB axis is not deviated. As a result, an increase in the REB density occurs and is directly observed as an enhancement of the CTR yield by a factor 6.

10.5 Fast electron transport simulations with external magnetic field in Particle In Cell (PIC) Hybrid - Code

Details of the REB propagation and energy transport were unfolded by simulations using a 3D PIC-hybrid code for the electron transport [111], accounting for fast electron collisions with the background material and REB self-generated fields. PIC-hybrid simulations allow to describe fast electron beam transport in dense matter, where the injected beam current is modeled kinetically by a particle-in-cell (PIC) method and the neutralizing return current of background thermal electrons is described by the generalized Ohm's law as an inertialess fluid [62, 98, 111]. Indeed, the hybrid method for simulating REB-transport neglects high frequency effects, hence enabling a simplification of Maxwell equations by neglecting the Poisson equation and the displacement current in the Maxwell-Ampere equation. Both collisional and ionization processes are taken into account for computing the evolution of the background resistivity, according to the Eidmann-Chimier model [73, 49].

Our simulation box corresponded to the transport-target dimensions, reproducing its CH-Cu structure in terms of background density and resisitivity behavior, as a function of the evolving background electron temperature due to the REB-deposited energy. The background electron temperature is initiated at 0.1 eV and 1 eV, respectively for the cases without and with B-field. The higher initial temperature in the latter case accounts for the target pre-heating by intense X-rays issuing from the LP-laser interaction and the coil driven by the intense discharge current.

Given the ps-time scale of the REB-transport, very fast if compared to the ns-scale evolution of the B-field strength or of is diffusion in the target, we assumed that the B-field distribution is constant over each transport simulation run-time. In our case, the total simulation time is set to 3.6 ps with temporal and spatial resolutions of 3 fs and 1 µm, respectively.

We simulated REB transport both with and without imposed B-fields. For the former case, we assumed full target magnetization (corresponding to the experimental $\Delta t = 1$ ns) imposing as initial conditions the 3D B-field distributions illustrated in Figure 10.2-b)-e). The B-field spatial distribution inside the target is calculated as in vacuum by the 3D magnetostatic code Radia, consistently with the experimental characterization of the B-field space-time evolution obtained with laser-driven coil-targets (Part II and [238]). The initial REB total kinetic energy was set to 30 % of the on target SP-laser energy, and injected at the front surface over a region of HWHM radius $r_0 \approx 24$ µm for configuration i) and $r_0 \approx 27$ µm for configuration ii), corresponding to empiric factors 4 or 3 of the SP-laser focal spot size HWHM, respectively for config. i) or ii).
This empiric factor, noted f_{res} depends mostly on the laser intensity, and similarly to the REB divergence, it tends to increase with higher laser intensities. Its value range between 3 and 4 agrees with PIC simulations at a similar intensity regime [64]. The REB-source injected to the simulations at the target front surface were characterized by kinetic energy spectra given by power laws for the low energy part $\propto (E_k)^{-1.6}$ and exponential laws for the high energy part $\propto \exp\left(-\frac{E_k}{T_h}\right)$ with $T_h^{i)} = 2.0$ MeV and $T_h^{ii)} = 1.3$ MeV, as predicted by the ponderomotive potential for the corresponding laser parameters of the two configurations $T_h = m_e c^2 \left(\sqrt{1+a_0^2} - 1\right)$, where a_0 is the normalized laser intensity (Sec. 3, [290]).

The injection angular distribution was approximated by the form defined in [63]:

$$f_h(\theta, r) \propto \exp\left[-\frac{(\theta-\theta_r)^2}{\Delta\theta_0^2}\right] \tag{10.4}$$

with a dispersion angle $\Delta\theta_0 = 55\,^\circ$ and $\theta_r = \arctan\left(tan(\Theta)r/r_0\right)$, where $\Theta = 30\,^\circ$ is the mean divergence angle. All the above geometric and energy REB source parameters are consistent with our previous characterization in the same laser facility using equivalent laser parameters, which were supported by benchmarked simulations [282, 281].

10.6 Calculation of CTR emission (post-processor)

For a direct comparison between the results of the electron transport simulations and the experiment, we developed a synthetic CTR-emission post-processor, applied to the transport code output. As the hybrid transport code continuously injects particles during the laser pulse duration without any longitudinal(or temporal) modulations, assumptions are needed to replicate the coherent addition of the transition radiation fields from periodic electron micro-bunches. In particular, it is assumed that the electron bunches produced throughout the duration of the laser-plasma interaction are identical, so that the spectrum and angular distribution of the REB injected in the hybrid code are representative of each individual electron bunch. In this scenario the total CTR emission at one given wavelength can be obtained in arbitrary units directly from the CTR emission of a single electron bunch [239], and the CTR spatial pattern and angular distribution are not dependent on the number of bunches. In other words, the problem reduces to calculating the CTR for a single electron bunch.

In general, the coherence of the radiation can be decomposed into a temporal and a spatial component [20]. For the temporal coherence, the phase difference, $\Phi_i - \Phi_j$ of the transition radiation fields emitted at the target rear side is calculated after considering the time of flight (TOF) of each individual macro-particle, *i.e.* we record the time difference between injection and time of arrival at the target rear side:

$$\Phi_i - \Phi_j = \frac{2\pi c}{\lambda}\,\mathrm{TOF} \tag{10.5}$$

with $\lambda = 523\,\mathrm{nm}$ (corresponding to the observed radiation frequency $2\omega_0$). For the spatial coherence, we assume no phase shift between macro-particles belonging to the same cell at the target rear side. This is justified by noting that the cell size in the simulation, of $1\,\mu\mathrm{m} \times 1\,\mu\mathrm{m}$, is comparable to the observed wavelength and smaller than the spatial resolution of the experimental imaging system. The finite spatial resolution is taken into account by convoluting the CTR out of the simulation with a $3\,\mu\mathrm{m}$ standard deviation Gaussian function.

The intensity resulting from the coherent addition of the fields $\vec{E}_i$ emitted by each macro-particles is given by:

$$I_{\mathrm{TR}} \propto \sum_i |\vec{E}_i|^2 + \sum_i \sum_{j,j\neq i} |\vec{E}_i||\vec{E}_j| \exp\left(i(\Phi_i - \Phi_j)\right). \tag{10.6}$$

where the first and second terms correspond to the incoherent and coherent parts of the emission, respectively. More details are given in *Appendix*, Sec. 23.1.

10.7 Simulations results and discussion

Synthetic CTR-signals are presented in Figure 10.5-f), g), h) and i), reproducing fairly well the experimental CTR patterns as well as the relative signal yield change when imposing the B-field. In more details, the simulations reproduce with $15 \pm 2\,\%$ relative errors the ratio of CTR-yield (with B-field / without B-field) for both target positions. Regarding the patterns, the synthetic CTR in the magnetized conditions is, in fair agreement with the experimental data, radially-pinched for configuration ii) [Figure 10.5-i)] and vertically-elongated for configuration i) [Figure 10.5-g)]. The experimental patterns' radius (azimuthally averaged), with or without B-field, is reproduced with $15 \pm 5\,\%$ relative errors, except for the magnetized case of configuration i), where the elliptic shape of the experimental signal is not exactly the same and the relative error amounts to $\approx 33\,\%$.

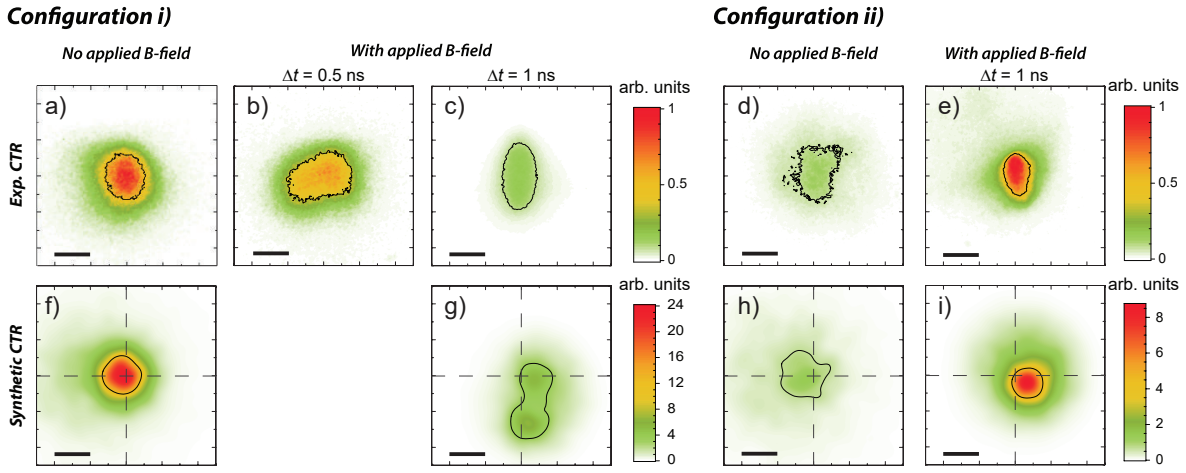

Figure 10.5 – Results of the experimental CTR imaging (first row) and of the synthetic CTR calculated from 3D-PIC hybrid simulations of fast electron transport (second row), for the two configurations i) target out of the coil plane and ii) target at the coil plane (see Figure 10.2), with and without imposed B-field. The contour lines correspond to the half-height of the signals. The crossed dashed lines indicate the position of REB-injection at the targets' front surface.

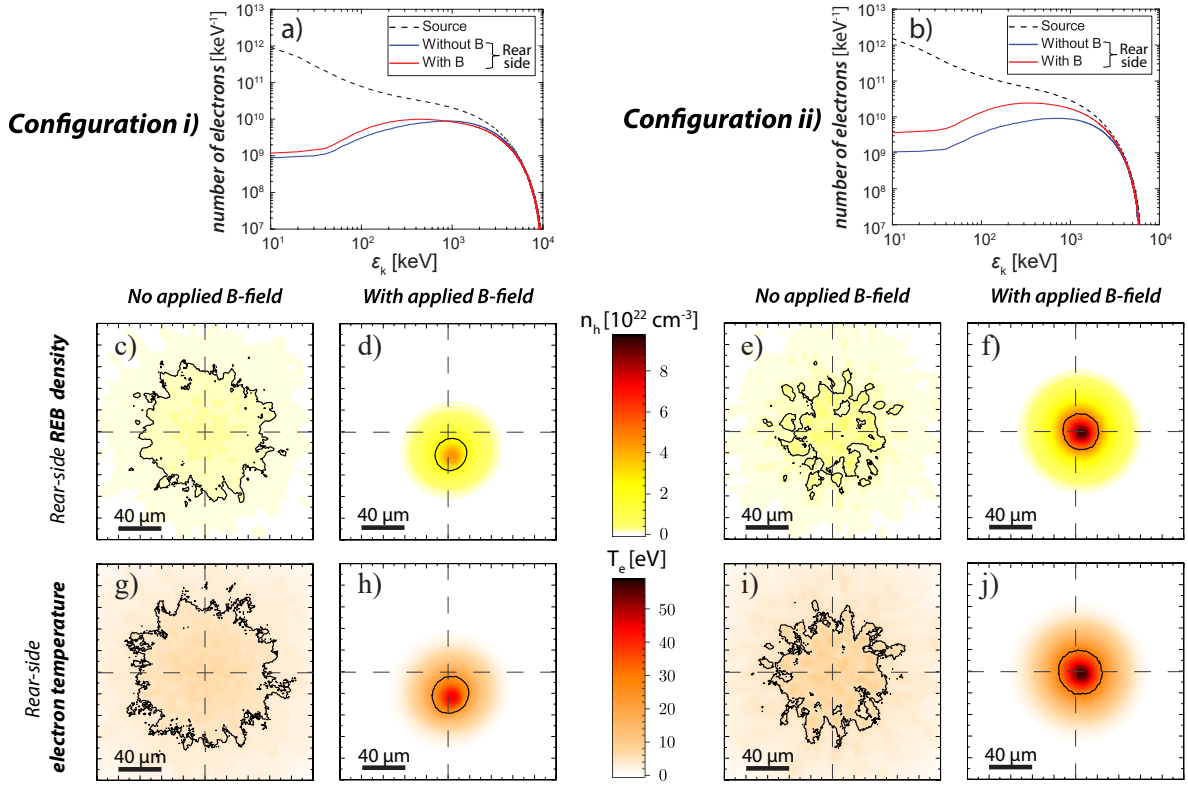

Figure 10.6 – REB energy spectra (first row), rear-side REB density (second row) and background electron-temperature (third row) unfolded from 3D PIC-hybrid transport simulations. The results are plotted for target-position configurations i) on the left and ii) on the right, without and with B-field. **a), b)** REB energy spectra at the targets' front-side (source, dashed lines) and rear-side (full lines). **c) - f)** REB density at the target rear surface (time-integrated). **g) - j)** Final background electron-temperature at the target rear surface. In **c) - j)** the contour lines correspond to the half-height of the signals and the crossed dashed lines indicate the position of REB-injection at the targets' front surface.

As for the REB-features and energy transport, Figure 10.6 shows the corresponding simulation results at the 60 µm-thick targets rear side surface. Panels a) and b) show the time-integrated electron energy spectra ε_k for simulations with (red) and without (blue) external B-field, compared to the spectrum at the front surface (dashed black).

A significant number of electrons with energies $\varepsilon_k < 100$ keV are absorbed or scattered out of the simulation box before crossing the target, as expected from the direct collisions with the background material and by electric-field stopping linked to the resistive neutralizing current of thermal electrons [282, 281]. A calculation of the integrated hot stopping power (see Eq. 3.69 in Sec. 3.3.1) for electrons of kinetic energy $\varepsilon = 100$ keV in a plasma at 10 eV temperature and at solid density gives a range of ≈ 25 µm which is effectively lower than the target thickness of 60 µm. These losses are slightly mitigated with the symmetric B-field, configuration ii).

The time integrated REB-density patterns [panels c)-f)] clearly show radial pinching due to the imposed B-fields, increasing the peak density by factors ≈ 15 and ≈ 20 and decreasing the beam mean radius by factor ≈ 3 and ≈ 2, respectively for configurations i) and ii). An other encouraging outcome is that the imposed B-field smooths the REB-filaments compared to simulations without B-field, for both target positions. The substantially smoother, narrower and denser beams in panels d) and f) correspond to unprecedented efficient guiding and improved energy-density flux. The impact is clearly seen in the reached peak background electron temperature [panels g)-j)], which is higher with B-field by a factor ≈ 5.9 for both target positions.

Yet, it is noticeable in simulations that the B-field asymmetry in configuration i) deviates vertically the REB from its injection axis, exiting the target with a vertical shift of ≈ 23 µm and an angle of $\approx 20°$ with respect to it. This deviation increases and broadens the electrons' transport time and momentum-angle distribution at the target rear side, contributing to roughly half of the CTR-yield drop [Figure 10.5-c),g)] compared to the unmagnetized transport case [Figure 10.5-a),f)]. The vertical deviation also directs the REB away from the CTR collecting lens. Calculations on how the CTR yield would depend on the collecting lens position are given in *Appendix* - Sec. 23.3 and lead to conclude that the setup lens position accounts for the other half of the total CTR signal drop.

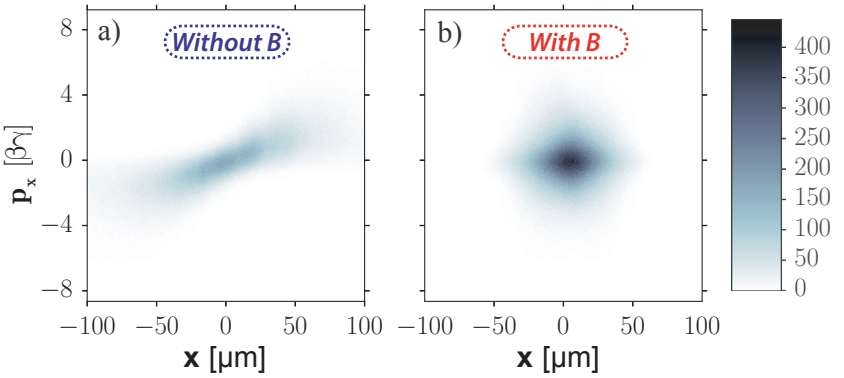

Figure 10.7 – REB transverse phase-space (x, p_x) at the target's rear surface, for the case without B-field a) and with B-field b).

The efficient magnetic guiding of the REB is further evidenced by analyzing the phase-space maps of the electrons reaching the targets' rear surface. For configuration ii), the transverse horizontal coordinates phase-space (x,p_x) is plotted in Figure 10.7: in a) without B-field, the inclined shape of high ellipticity is characteristic of symmetric correlated transverse momentum and position of a regularly diverging beam; in b) with B-field, the phase-space map is significantly narrower than in a) but only for the spatial-coordinates. The induced cyclotron effect de-correlates positions and momenta and their radial spread is limited as they are trapped and flow along (rotating around) the B-field lines. This is expected as the 10 µm-Larmor radius, calculated for the REB-source mean kinetic energy $\approx$ 1MeV and a 600 T B-field, is smaller than the REB-source radius $r_0 \approx 25$ µm.
Yet, the B-field does not really affect the electrons intrinsic divergence as the width of the transverse momenta distribution is maintained.

Figure 10.8 summarizes the evolution with target depth of the REB normalized root-mean-square (RMS) emittance in both horizontal (ε_x) and vertical (ε_y) transverse coordinates. Emittance is a

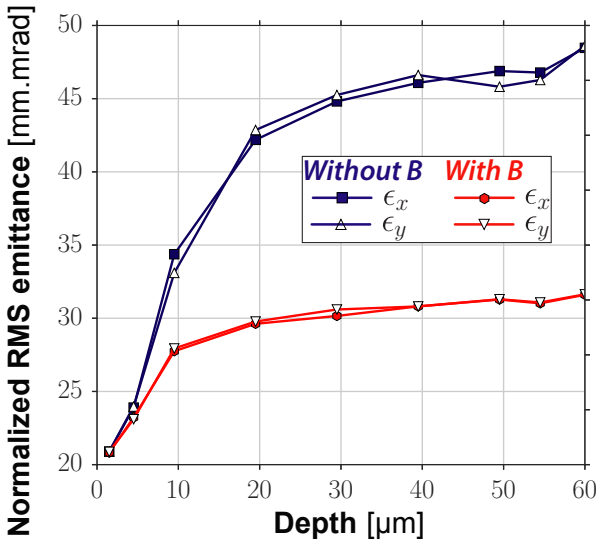

Figure 10.8 – Evolution along propagation depth of the REB normalized RMS emittance in horizontal ϵ_x, and vertical ϵ_y, transverse directions, for configuration ii) with transport targets at the coil plane and cases with (red) or without (blue) imposed B-field.

quantity of area or volume in phase-space of particles. It is usually used as a property to describe a beam along its propagation when the motion of particles in transverse and longitudinal planes are weakly coupled. As in conventional accelerators, fast electron beams accelerated by high intensity lasers have momentum mostly directed in the longitudinal direction. On the canonical phase-space, a statistical definition of the RMS emittance in the (x,p_x) plane is given by:

$$\varepsilon_{x,n,RMS} = \sqrt{\langle x^2 \rangle \langle {p_x}^2 \rangle - \langle x\, p_x \rangle^2} \tag{10.7}$$

It is convenient to use momenta in dimensionless units of $\beta\gamma$ (relativistic parameters). $\langle x^2 \rangle$ defines the second central moment of the particle distribution x. For macroparticules distributions extracted from PIC simulations, the weights w_i of each macroparticle have to be taken into account:

$$\left\langle x^2 \right\rangle = \frac{\sum_i \left(w_i (x_i - \bar{x})^2 \right)}{\sum_i w_i} \tag{10.8}$$

and

$$\langle x\, p_x \rangle = \frac{\sum_i \left(w_i (x_i - \bar{x})(p_{x_i} - \bar{p}_x) \right)}{\sum_i w_i} \tag{10.9}$$

where $\bar{x}$ and $\bar{p}_x$ are respectively the weighted-average of x and p_x:

$$\bar{x} = \sum_i (w_i x_i) \,/\, \sum_i w_i \quad \text{and} \quad \bar{p}_x = \sum_i (w_i p_{x_i}) \,/\, \sum_i w_i. \tag{10.10}$$

The plot of Figure 10.8 clearly shows the effect of the imposed B-field: without B-field the electron beam emittance rises considerably due to the collisions (full blue lines), an effect significantly mitigated in case of REB magnetic guiding (full red lines). The emittance evolution over the first $\sim 10\,\mu$m is particularly steep for the unmagnetized case, this is related to the high diffusivity of lower-energy electrons in the REB. For larger depths, the two slopes are less steep, as the low energy electrons are previously lost due to collisions and Ohmic heating [282, 281, 280].

To complete the above description, a focus on the REB radial size and energy balance along the transport in the dense target will be now given. We present in Figure 10.9 the evolution of the REB density along the target's depth for configuration ii). The REB radial size is seen to decrease when applying the external B-field (second row), a behavior encouragingly different from the usual strong filamentation and strong increase of the radial spread experienced by the REB in solid dieletric targets when any external B-field is applied (first row).

The plot in Figure 10.10 shows the evolution of the REB radial size over the transport in the dense target for the two cases with external B-field or not, confirming the emittance (or phase-space) evolution commented before.

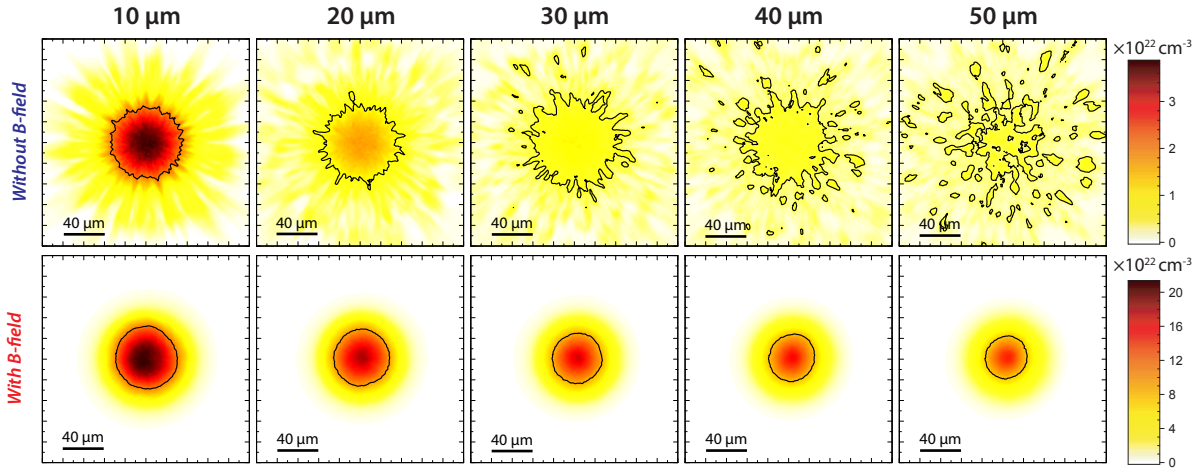

Figure 10.9 – Evolution of the REB density along the target's depth for configuration ii). The first and second row are obtained respectively with and without applying the external B-field. The related evolution of the REB radial size is presented in Figure 10.10. Note the different color scale.

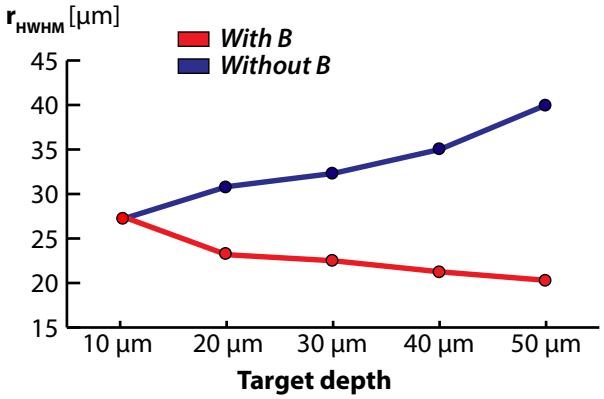

Figure 10.10 – Evolution of the REB radial size (HWHM) along the target's depth for configuration ii) in the cases: without external B-field (blue curve) and with external B-field (red curve).

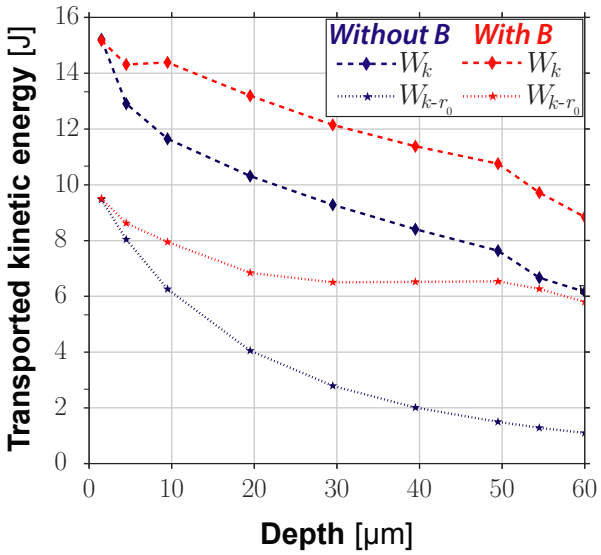

Figure 10.11 – Evolution along propagation depth of the REB kinetic energy, where W_k and W_{k-r_0} are respectively the total transported kinetic energy (diamonds) and its fraction within the initial REB radius r_0 centered in target axis (stars). It corresponds also for simulations in configuration ii) with transport targets at the coil plane and cases with (red) or without (blue) imposed B-field.

To further understand the energy transport, we plot in Figure 10.11 the evolution of the time-integrated REB total energy (W_k, diamonds connected by dashed lines) and REB energy encircled over the surface corresponding to the initial REB-source, πr_0^2 (r_0 is the initial REB radius) kept centered with the injection axis (W_{k,r_0}, stars connected by dotted lines). The loss rate of W_k against target depth is comparable for the two cases without (blue) and with (red) B-field, except for the first $\sim 10\,\mu$m where the B-field efficiently confines electrons and also smooths the REB filaments. About 45 % more energy is transported to the target rear in the magnetized case due to the magnetic confinement mitigating the high diffusivity of low-energy particles. Much more importantly, the r_0-encircled energy around the injection axis at the target rear in the magnetized case contains $\approx$ 66 % of the total transported energy against only $\approx$ 18 % for the unmagnetized case. As consequence, the REB energy-density flux after crossing the target thickness increases by $\approx 5.3\times$ when applying the B-field.

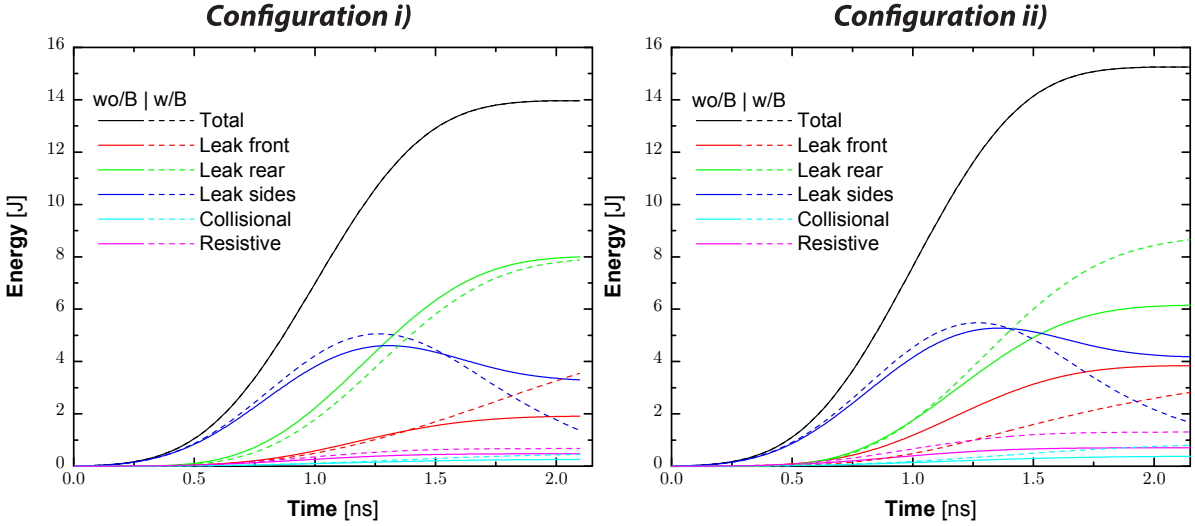

Figure 10.12 – REB energy balance for configuration i) (left graph) and configuration ii) (right graph) either without imposed B-field (in full lines) and with imposed B-field (in dashed lines).

The REB energy balance presented in Figure 10.12 is giving a deeper insight on the REB transport losses throughout its transport in the dense target. It results that the ohmic (resistive) and coulomb

scattering (collisional) losses are very low and energy losses are rather due to leaks at the target borders. We will now detail the recorded features for the different leaks' locations.

It is clear first that for both configurations the guiding of the REB significantly decreases the losses in the radial direction (blue lines). One can note also the already discussed higher total electron energy at the rear-side by applying the external B-field for configuration ii).

On another note, the B-field of configuration ii) is seen to reduce the electron losses at the injection surface - front surface - (red lines), while it is seen to reversely increase them for configuration i). The latter can be explained by the mirror effect arisen for electron propagating in the B-field of configuration i) with an higher injected current. The B-field of configuration ii) does not trigger such mirror effect and reversely helps the injection of the REB at the front surface. For both configurations, the collisional and resistive losses increase when applying the external B-field, as a result of an higher current-density. The effect is bigger for the latter as they are $\propto j_h^2$ while the former are $\propto j_h$. Logically, this effect is more pronounced for configuration ii), due to the more effective guiding of the REB in this case.

Influence of the imposed B-field strength

To study the influence on the CTR synthetic patterns of the imposed B-field strength, we ran academic transport simulations applying a dividing factor on the B-field map values of 2, 4 and 6 respectively shown in the successive columns of Figure 10.13, as labeled. The related rear-side REB density patterns are shown in the second row. It is worth noting that the CTR synthetic imprint for B_0 between 100 T and 300 T exhibits a yield of $\approx 50\,\%$ of the yield obtained for $B_0 = 600$ T together with a bigger pattern size ($\approx 2\times$ bigger). Besides, the yield and size is fairly similar to what was obtained experimentally at $\Delta t = 0.5$ ns [Figure 10.5-b)]: the diffusion of the growing B-field till ≈ 300 T at 0.5 ns would correspond, as a matter of fact, to this order of B-field strength. The CTR yield without applied B-field ($B_0 = 0$ T) drops to $\approx 16\,\%$ of the yield value at peak B-field ($B_0 = 600$ T), as commented before (see Figure 10.5).

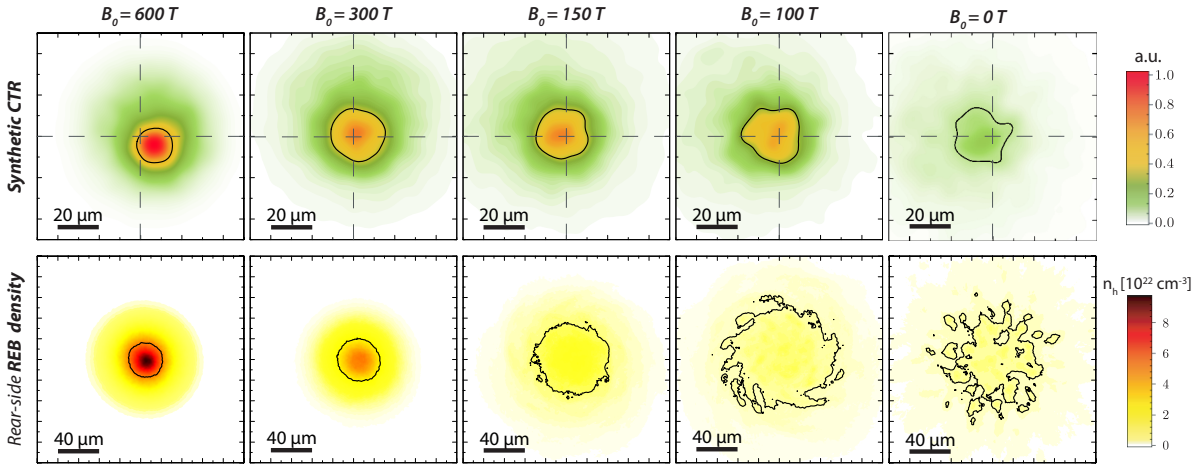

Figure 10.13 – Influence of the applied B-field strength on the guiding efficiency, as obtained by the transport simulations. The synthetic CTR imprints and related rear-side REB density are shown in the first and second row, respectively.

The guiding effect is seen to be particularly effective for B_0 above 300 T and this confirms the guiding criterion introduced in Eq. 10.3. Applying the latter formula for 1 MeV-electrons and a beam radius of 25 µm, the needed B-field strength to confine efficiently the REB is $B_0 > 200$ T (it is $B_0 > 330$ T for 2 MeV-electrons). Yet, it is observed that a field of $B_0 = 100$ T is enough strong to almost entirely smooth the REB filaments its density pattern.

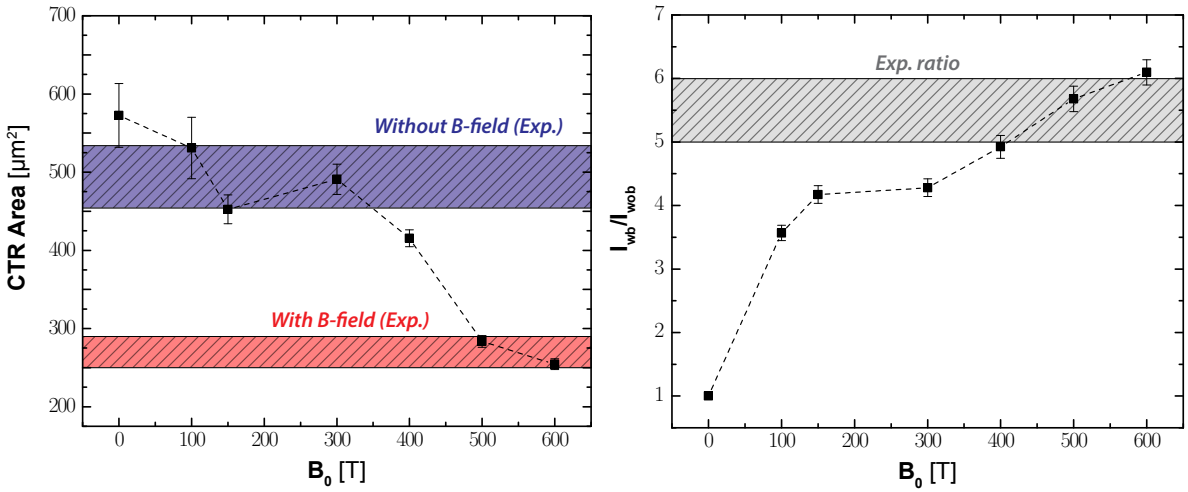

Figure 10.14 – Left: Synthetic CTR pattern surface (at FWHM) size evolution with B_0. The blue and red bands identify the experimental CTR pattern sizes respectively for the cases without and with applied B-field, accounting for experimental uncertainties. **Right:** Ratio of synthetic CTR yield *with/without* applied B-field. The gray band identify the experimental ratio, accounting for experimental uncertainties.

Finally, in Figure 10.14, we present the evolution as a function of the B-field at coil center (B_0) of the two key CTR simulation parameters (black symbols):

Left: Synthetic CTR pattern size at FWHM, where the blue and red horizontal bands denote the experimental CTR pattern sizes respectively without and with applied B-field. The error bars account for uncertainties inherent to the shape of the CTR pattern.

Right: Ratio of synthetic CTR yield *with/without* applied B-field. Here the uncertainties account for the background noise level (for experimental values) and an optical resolution variation of ± 1 µm (for synthetic values).

These graphs show clearly that the simulation with a B-field strength of $B_0 = 600$ T, as experimentally characterized in parallel measurements (dedicated shots) [238], is particularly accurate to reproduce the two key parameters matching experiment and simulations. A B-field slightly smaller by $\approx 50 - 100$ T would also accurately reproduce the experiment CTR pattern characteristics. This variation is relatively small in relation with the complex simulations and post-processing assumptions leading to the synthetic CTR results. Furthermore, it is in the range of actual predictability of B-field strength variation with laser parameters and target geometry uncertainties.

Interestingly, the REB guiding efficiency as a function of B_0 is particularly well highlighted by the CTR yield depicted in the right graph of Figure 10.14: for B_0 up to 200 T, the mitigation of Weibel instabilities is evidenced by a strong increase of the CTR yield, then it reaches a plateau, and for $B_0 >$ 300 T a second increase occurs and corresponds to an efficient guiding of the REB which is radially confined (further seen by the drop of CTR pattern size area on the left graph), thereby confirming the accuracy of the previously introduced guiding criterion (330 T for 2 MeV electrons).

10.8 Complementary information

Complementary data obtained with Al targets

In Figure 10.15, we present results of experimental CTR imaging in configuration ii) involving Al targets. First, the measured CTR yield without applied B-field is seen to be $\approx 17\,\%$ of the one measured for CH targets and shown in Figure 10.5. Indeed, even though the CTR yield is measured in arbitrary units, it was obtained under the same conditions of configuration ii) and can thus be compared in relative values. This drop in CTR yield is a mark of higher REB losses in the denser Al targets.

More interesting, the magnetization diffusion time in the Al is expected to be longer than for CH due to its lower resistivity for temperatures $\lesssim 1\,\text{eV}$ (see Eq. 10.2). For the same delay of $\Delta t = 1\,\text{ns}$ [Figure 10.15-b)], the CTR pattern variation in respect to the case without B-field [a)] looks similar to what was obtained for CH target at $\Delta t = 0.5\,\text{ns}$[Figure 10.5-b)]. The conclusion is thus identical and is the sign of a not fully magnetized target. A longer delay of $\Delta t = 1.5\,\text{ns}$ may have been enough to magnetize the Al targets but unfortunately the target rear surface does not survive on such longer times and the CTR signal resulted to be very faint.

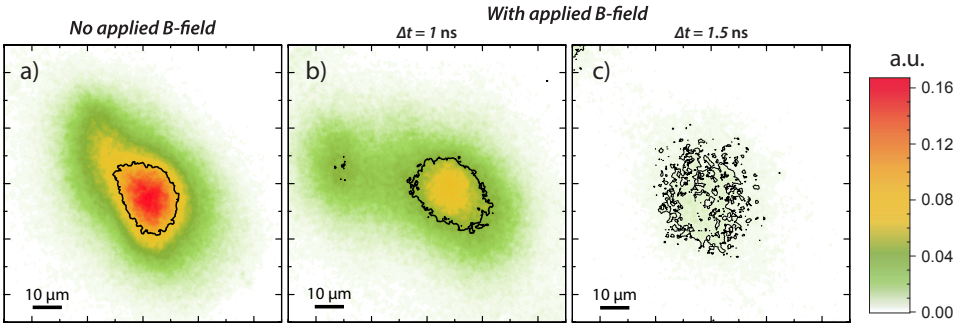

Figure 10.15 – Results of experimental CTR imaging for Al transport targets in configuration ii) without (1^{st} column) and with (2^{nd} and 3^{rd} column) imposed B-field. Applying the B-field, two delays were investigated: $\Delta t = 1\,\text{ns}$, at peak B-field (2^{nd}-column) and $\Delta t = 1.5\,\text{ns}$ (3^{rd}-column). The color bar shown here in arbitrary units can be compared to the color bar for the same configuration ii) in Figure 10.5.

Secondary target location

As a complementary information for discussion, three additional simulations were performed using a secondary target made of a CH cylinder of unchanged diameter but with 100 µm-thickness. In the three cases, the B-field configuration was different, using an horizontal offset of the center plane of the target in respect to coil plane of $H_{\text{offset}} = -50\,\mu\text{m}$, $H_{\text{offset}} = 0\,\mu\text{m}$ and $H_{\text{offset}} = +50\,\mu\text{m}$, respectively shown in the three columns of Figure 10.16. In this figure, one can note that the converging B-field configuration in the first case ($H_{\text{offset}} = -50\,\mu\text{m}$) contributes to reduce the radial size of the REB at the rear target surface. The effect is decreasing while increasing the horizontal offset (*i.e.* moving the target to the right).

For the three cases presented in Figure 10.16, the REB radial size is respectively reduced by 36 %, 24 % and 13 % over the transport in the dense target, compared to the case of 100 µm-thick CH targets without applied B-field.

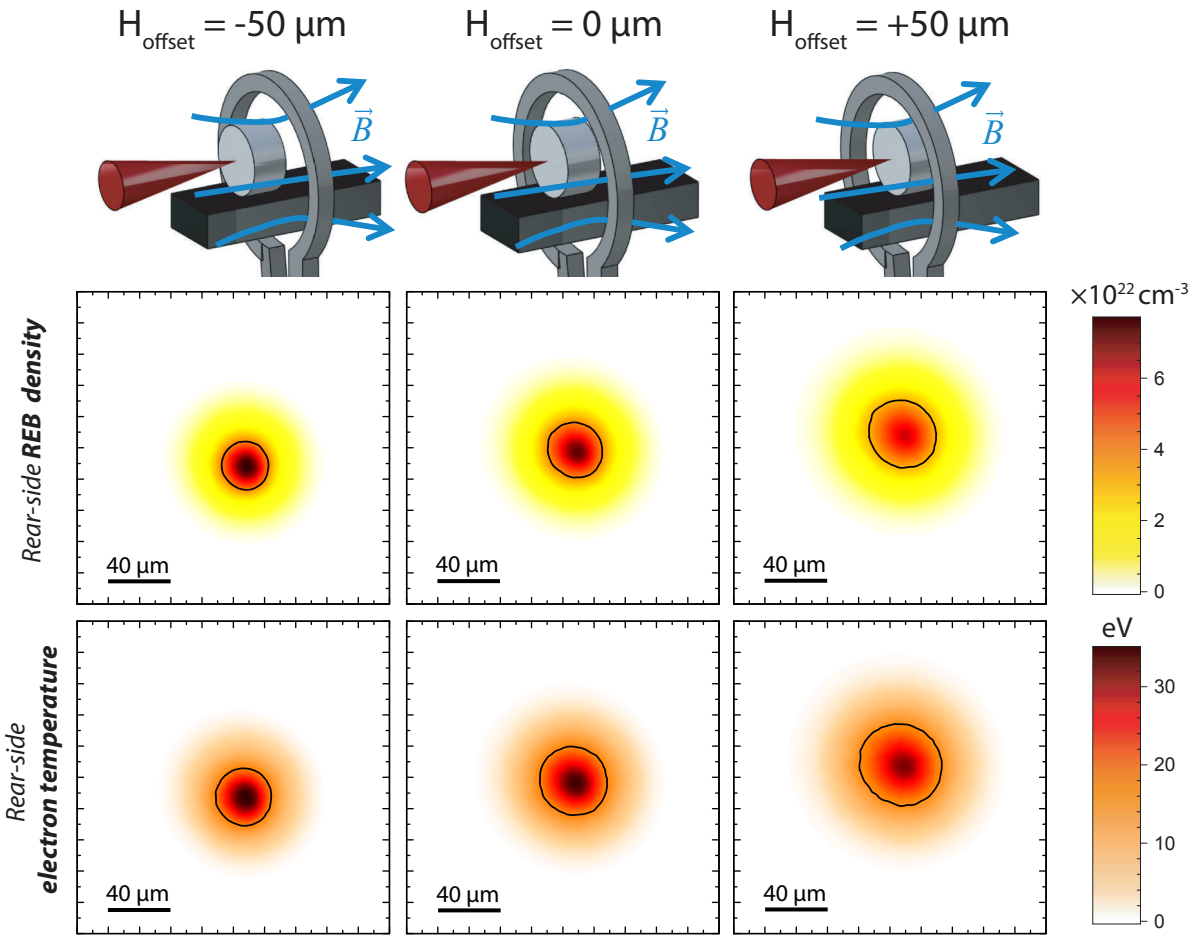

Figure 10.16 – Rear-side REB density (first row) and background electron temperature (second row) for three external B-field configurations: with the target center plane shifted from coil plane by $H_{\text{offset}} = -50\,\mu\text{m}$ (first column), $H_{\text{offset}} = 0\,\mu\text{m}$ (second column) and $H_{\text{offset}} = +50\,\mu\text{m}$ (third column). In all cases the target is made of a CH cylinder of 100 µm-height with its axis shifted by $V_{\text{offset}} = 50\,\mu\text{m}$ up in respect to coil axis, to let enter the Ta shield in the coil (see the sketches illustrating the configuration of each column).

10.9 Conclusions

In conclusion, we succeeded to efficiently guide a laser-accelerated MeV electron beam through solid-density matter by imposing a 600 T B-field parallel to the electron beam propagation axis. The B-field was generated by a coil-target driven by a high-energy ns laser interaction, as previously characterized in Part II. This B-field was driven 1 ns before the REB acceleration, providing a sufficient time for the magnetization of the CH 60 µm-thick transport targets. In our best setup configuration, we found at the targets' rear surface that the energy density transported by the fast electrons and the peak background electron temperature increase respectively by factors of ≈ 5.3 and ≈ 5.9 compared to the case without imposed B-field.

This enhancement in energy-density transport through dense matter is notable when compared to experiments based on the REB-guiding by self-generated resistive B-fields (see Sec. 10.1). Our experimental all-optical platform for strong B-field production is thus setting the ground for laboratory studies in new regimes of matter opacities and equations of state at extreme temperatures, and in dense matter magnetized conditions. In the particular context of laser-fusion research, relevant experiments with target compression in magnetized conditions and magnetically-guided REB should potentially optimize energy coupling to high density cores of nuclear fuel [232, 285, 122, 112, 180, 9]). A further insight on the prospects of ICF assisted by external magnetic fields will be given in the perspectives of this thesis, Sec. 13.1.

11 High discharge current and application to proton beam tailoring in high laser intensity regime (picosecond interaction)

11.1 Experimental setup description

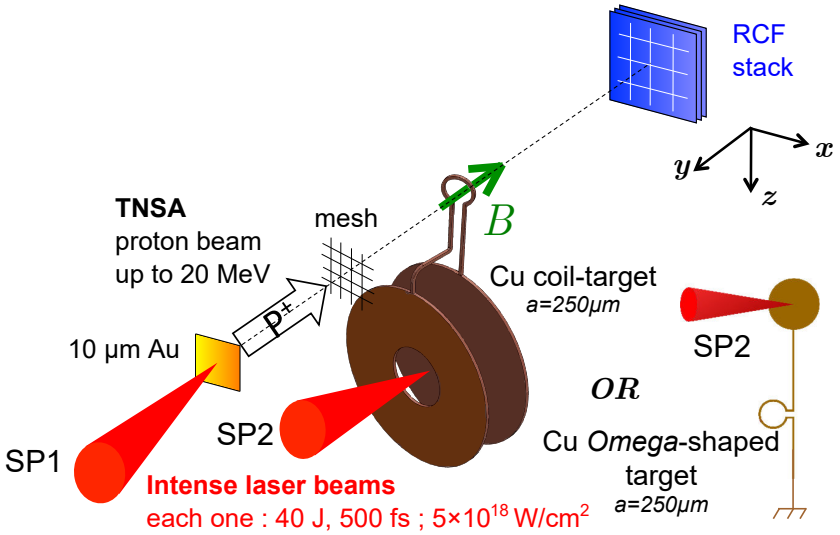

Figure 11.1 – Sketch of the experimental setup.

This experiment was carried out in January 2016 at the *Petawatt High Energy Laser for Heavy Ion Experiments* (PHELIX) located at the GSI facility in Darmstadt, Germany. The laser beam, of 80 J-energy and 0.5 ps pulse-duration, was split in two (SP1 and SP2) and focused independently – with an optically-controlled delay – on the proton beam generation foil (SP1) and on the coil target (SP2), with intensities $\approx 5 \times 10^{18}\,\mathrm{W/cm^2}$. In this experiment, a different setup geometry was used: the TNSA probe beam is propagating along the coil axis. Both targets are driven independently and the controlled delay between the two laser pulses allows particle-field interaction at different times. This setup, sketched in Figure 11.1, was designed to realize proton beam tailoring and focusing by the induced electromagnetic fields developing in the coil.

The 10 µm-thick Au foil is located either at a distance $d = 2\,\mathrm{mm}$ or $d = 5\,\mathrm{mm}$ away from coil plane. The RCF stack is located behind the coil plane at a distance $D = 65\,\mathrm{mm}$ (see general sketch in Figure 7.1, Sec. 7.2.2). Up to 17 RCF layers are used (HD+MD+EBT), protected by a 11 µm-thick Al filter. In addition, either 25 or 50 µm-thick Cu filter is used to block lowest proton energies and guarantee a readable signal in the first HD layer of the stack. In some shots with $d = 5\,\mathrm{mm}$, proton deflections were quantified using a 42 µm-pitch mesh inserted between the Au foil and the coil targets. In such shots, the grid is positioned 3 mm before the coil targets.

The coil targets are made of copper in this experiment and in addition to the already used coil-shaped capacitor-coil design with $a = 250\,\mu\mathrm{m}$ (see Figure 8.2), a simplified coil geometry was tested. This alternative target does not need any folding, which is the most time-consuming step of fabrication. Besides, they have no capacitor part and the interaction of the laser-driver is made on a small single disk of 1 mm-diameter. The coil part, with radius $a = 250\,\mu\mathrm{m}$, is connected to a vertical wire extending on one side to the interaction disk and on the other side to the ground. The electrical connection to the ground is ensured by using a metal needle supporting the target. As a result of target cutting, the axes of symmetry of coil and disc part are parallel but horizontally deviated by 350 µm. The coil's center is located vertically 3 mm below the laser-plasma interaction point on the disc while it was located 3 mm above the laser-plasma interaction point for capacitor-coil targets. Consequently, the SP2 laser was either located 3 mm above or below SP1 focal point. In continuation, this alternative coil target will be denoted *Omega-shaped coil*.

11.1.1 Time-resolving proton radiography

As presented in Sec. 5.2.3, laser-driven protons exhibit a very short bunch duration allowing to obtain high temporal resolution in respect to beams produced by conventional accelerators. At the same time, low emittance provides high intrinsic spatial resolution. Moreover, the broadband spectrum of laser-accelerated proton beams permits to employ them in a time-of-flight arrangement consenting to temporally resolve the interaction region, that is particularly suitable for fast transient phenomena. More importantly, typical TNSA beam (Sec. 5.2.1) are composed of charged particles and thus can be used to probe ultrafast, transient electromagnetic fields generated during laser-solid interaction. The data presented for this experiment in Sec. 11.3.2 were collected using the proton radiography technique, arranged with radiochromic film detectors (RCF) in a time-resolving configuration.

Time-of-flight (TOF) techniques are based on the very simple fact that particles with different velocities cross a fixed point in space at different times. A proton with energy ε_p will therefore diagnose a point located at distance d from the proton source at the probing time:

$$t_{p,0} = t_0 + d\sqrt{\frac{m_p}{2\varepsilon_p}} \tag{11.1}$$

with t_0 the time at which the proton is produced at the metal foil.

Yet, the proton beam have a certain divergence angle depending on its position on the RCF surface: the time-of-flight calculation have to be corrected to take into account the oblique distance traveled by protons, depending on their radial shift r on the RCF surface. Considering that the magnification of the proton radiography setup is M, then the correct time of flight of protons of energy ϵ is:

$$t_{p,r}(r,\epsilon) = t_{p,0} + \frac{d}{v_p}\left(\sqrt{1+\frac{(r/M)^2}{d^2}} - 1\right) \tag{11.2}$$

where v_p is the proton velocity.

Hence, when dealing with different proton velocities, characteristic of the broadband spectrum of TNSA accelerated protons, time-resolved information about the probed phenomenon in the interaction region can be acquired. Of course, there is the need to have a detector capable of energy spectral resolution. Usually TOF techniques employ scintillating plates coupled to photo multipliers, Faraday Cups or semiconductor detectors. But in this case, not only these detectors have a limited early-time response so that they cannot resolve very high energetic particles, but also they do not provide spatial information on the proton beams. Multiple RCFs arranged in a stack configuration [219] permit to associate an accurate energy value, *i.e.* a fixed probing time, to each layer of the RCF stack, ensured by the unique characteristics of proton energy deposition in matter (see Sec. 18.1).

Several examples of the effectiveness of the time-of-flight resolving arrangement can be found in literature [31, 233, 132, 218, 219, 242].

11.2 Previous results of electromagnetic lenses

In [277], by charging an hollow microcylinder (3 mm-height, 700 µm-diameter) irradiating its outer wall (of 50 µm-thickness) with an intense subpicosecond laser pulse (3×10^{18} W/cm^2), they observed focusing and energy selection of a high-current, MeV-energy proton beam. The electromagnetic lens feature is attributed to transient radial electric fields of 10^7 to 10^{10} V/m developing on the cylinder inner wall's surface. It is associated, according to authors, to the hot-electron sheath that extends over a Debye length ahead of the plasma expanding toward the cylinder's axis.

The proton characteristics was measured by a magnetic spectrometer which evidenced the energy selection of $6-7$ MeV protons, with an increase in their energy density observed in RCF imprints by a factor up to ~ 10. The proton spectrum was reproduced simulating the proton propagation through the space- and time-dependent fields obtained from PIC code simulation.

In a smilar experiment [133], two different micro-lens geometries were employed: either rectangular-shape or cylindrical-shape (see Figure 11.2), with the proton generating foil directly

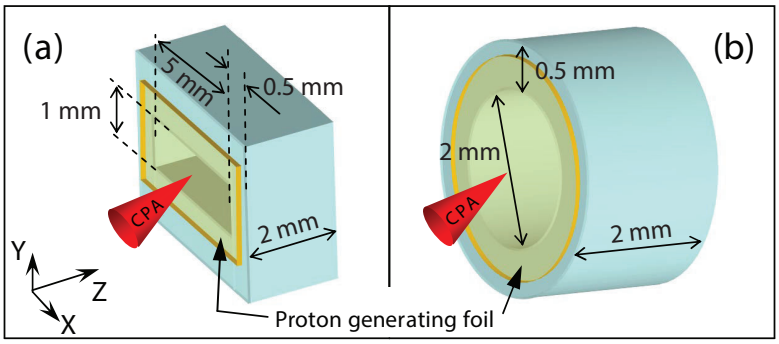

Figure 11.2 – Schematic of (a) rectangular and (b) cylindrical lens targets used in [133]. *Figure from [133].*

attached to the lens target. Therefore, only one intense laser pulse was used (energy of $\sim$ 300 J, 500 $-$ 600 fs-duration and intensity of $\sim$ 10^{21} W/cm^2). When compared to the performance of freestanding proton generating foils, a reduction in the proton beam divergence of up to a factor 2 was observed with the lens target. Besides, for the rectangular lens target, an elleptical profile is observed. Therefore, the effect is unambiguously related to the target geometry. The emittance of the proton beam with lens target was also measured to be a factor $\approx$ 1.4 smaller than in straight foil target.

The target discharges through the target-holder was limited by the use of insulating stalks. Still, the discharge time-scale is also function of the lens material and Aluminium lens was seen to discharge in a time constant of roughly $\sim$ 7.5 ps while it was $\sim$ 15 ps for a Plastic one. The discharge can then be tuned to build an achromatic lens system, playing on target geometry and material.

Based on the wave propagation evidenced with the proton imaging of laser-driven discharges in wire targets (see Sec. 6.3.2), an experiment carried out by Kar *et al.* on ARCTURUS laser facility (Düsseldorf, Germany), showed for the first time a post-acceleration of laser-driven protons with dynamic beam collimation and energy selection. The discharge wave propagates on a helical coil-shaped wire directly attached to the proton generating foil and its axis is coincident with the normal direction of the foil. The coil pitch/diameter ratio determines the longitudinal velocity of the wave along proton propagation axis and can thus be synchronized with a given energy of protons.

To illustrate this, we calculated which proton energy would correspond to the longitudinal velocity of a speed-of-light wave propagating in an helical coil with a given ratio pitch/radius. The curve is shown in Figure 11.3.

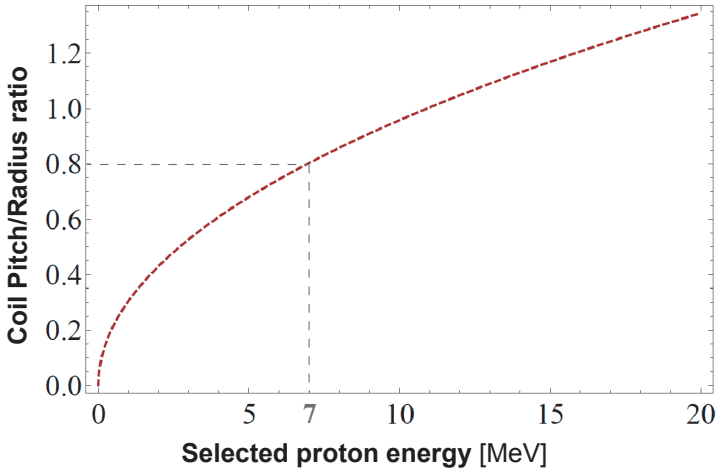

Figure 11.3 – Curve of the proton energy matching the longitudinal speed of a speed-of-light wave propagating in an helical coil, given its pitch/radius ratio.

In [131], the helical coil target was made of 100 µm aluminium wire and had internal diameter, pitch and length of 0.7, $\sim$ 0.28 and 8.7 mm. Therefore, the coil pitch/radius was of $\sim$ 0.8 and

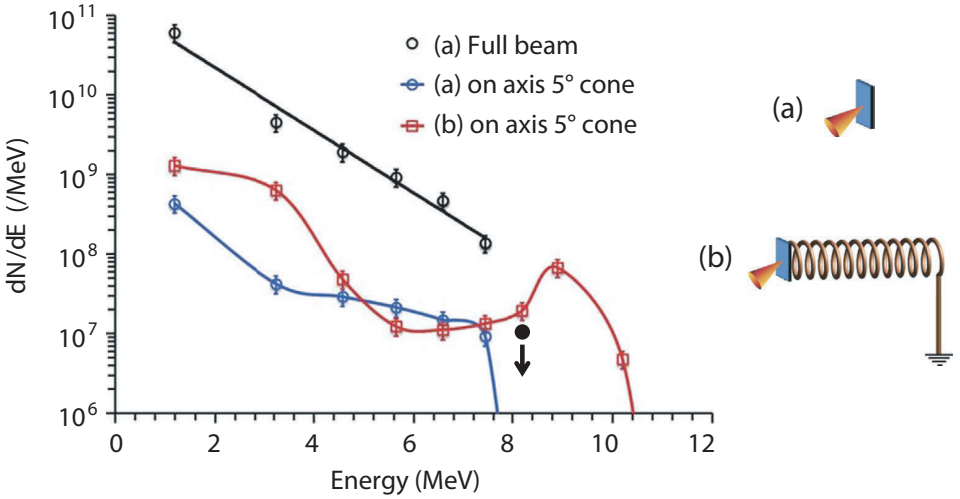

Figure 11.4 – Comparison between proton spectra from the reference flat-foil target (a) and the helical coil target (b) obtained by spectral deconvolution of the RCF signals. The error bars were estimated from the possible error in dose conversion and uncertainties in background substraction. Since the flat-foil proton signal at $\sim$ 8 MeV was below the detection threshold, the solid black circle shows the upper bound for proton signal calculated by considering the detection threshold of the RCF ($\sim 10^5$ protons per MeVmm^{-2}) and an overly generous beam size (10 mm diameter on the RCF, which is similar to the beam size at 6.6 MeV for the flat-foil target (a), at that energy. *Figure and caption from [131].*

correspond to the energy selection of protons with kinetic energy of $\sim$ 7 MeV.

In Figure 11.4, we show a comparison between spectrum from the reference flat-foil target and the helical coil target. It can be easily seen that the coil target accelerated protons from $\sim$ 7 MeV up to $\sim$ 10 MeV. Yet, it is also clear that all proton with lower energies were not synchronized with the pulse and a big part of them were expeled outside the coil. An overall collection efficiency of 7 % was calculated in [131]. Yet, the synchronous protons collected within the 5 ° solid angle cone of coil's exit ring, amount to three times that would be captured for an undeflected beam. The helical coil target is then accurately focusing and accelerating a narrow band of energy of $\pm$1 MeV.

11.3 Experimental Results

The experiment we made at PHELIX was conducted before the publication of this latter paper by Kar *et al.* [131], and we made indepedently a proof-of-principle study using discharging pulses over coil-shaped wires. Besides, our system has a quite different design and characteristics.

We will see, in particular, that the energy-selection band of our device is broader and the total collection efficiency is significantly larger. However, no significant acceleration is expected to occur (very short length for longitudinal E-field to accelerate particles).

An acceleration of some protons to higher energies is predicted by simulations. However, no experimental evidence on that was recorded during this first experiment. It should be looked more carefully for the next experiment by measuring the proton spectrum in shots with driven coil.

Last but not least, our coil target was driven by a separate laser pulse appropriately timed in respect to the laser pulse driving protons: the energy selection can then be made adjusting the timing delay between two pulses to match the proton time-of-flight from the generating foil to the coil.

11.3.1 TNSA proton source characterization by Thompson Parabola

In this introductive section of PHELIX results, we will present first the proton distribution of the TNSA generating foil, as infered from a Thompson Parabola (TP) located at $\sim$ 30 cm from TCC in the proton

axis direction. For more information about this diagnostic and how data is analyzed, the reader can refer to *Appendix*, Sec. 21.

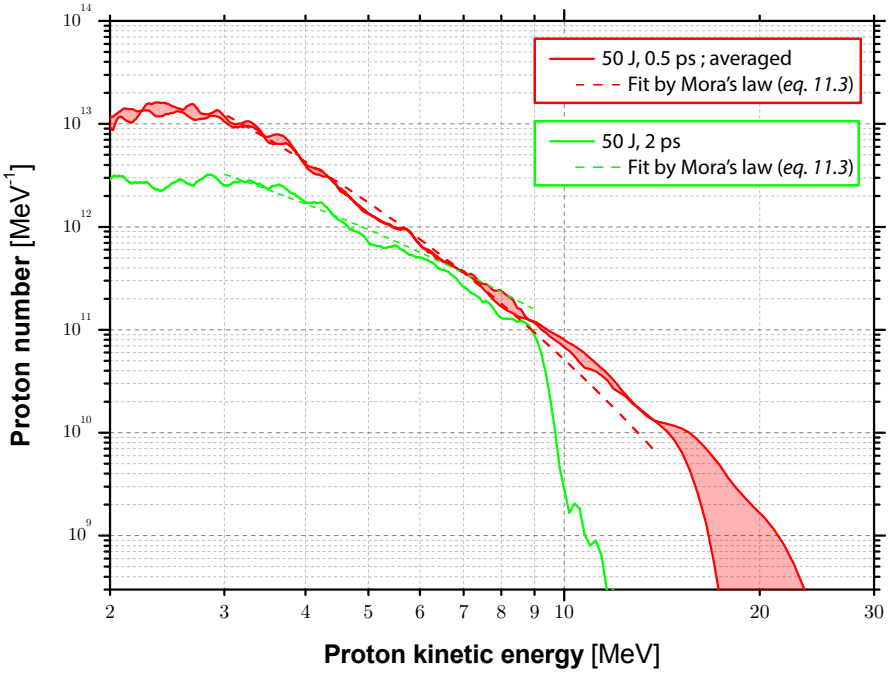

Figure 11.5 – Proton distribution obtained from TP and averaged over a few shots with a laser-duration of 0.5 ps (solid red), and for a shot with a laser duration of 2 ps (solid green). The laser energy was invariably ≈ 40 J on target. The associated dashed curves are fitted function of the experimental data with the distribution law introduced by Mora in [185].

In Figure 11.5, we present the final proton distribution, averaged over a few shots with laser-durations of 0.5 ps (solid red curve) and a complentary measure for a shot with a laser-duration of 2 ps (solid green curve). In both cases the energy on target was 40 J. The TNSA proton distribution was fitted to the law introduced by Mora in [185]:

$$\frac{dN}{d\varepsilon} = \frac{A}{\sqrt{2\varepsilon\varepsilon_0}} e^{-\sqrt{2\varepsilon/\varepsilon_0}} \tag{11.3}$$

where $A[\mathrm{m}^{-1}]$ and $\varepsilon_0[\mathrm{eV}]$ are two constants. It results in a fair agreement with the experimental distribution. The law was fitted over the range extending from the lower bound of 3 MeV (limit of proton collisions with TP electrodes using a 10 kV gap voltage) up to the energy cutoff.

11.3.2 Time-resolving proton radiography results

In Figure 11.6 we present a time-resolved measurement of the fields building up in the coil target, using the technique presented in the last subsection. The coil was situated at a distance of $d = 5$ mm from the proton generating foil. First of all, we can notice on the first RCF imprint - at probing time $t = -9 \pm 20$ ps after SP2 interaction - a field propagation along the wire connected to the laser-irradiated disk. The observed deflection corresponds to a positive charge inducing an electric field which expels protons radially outwards. The uncertainty ± 20 ps is due to the synchronization accuracy between SP1 and SP2 laser pulses. It has to be considered mathematically as a modulo of [20 ps] on the reported probing times and it does not reflect the much lower resolution on the TOF between two timing of ~ 2 ps.

On the second RCF of Figure 11.6, the deflection is clearly visible and has progressed over the coil. Moreover, the electric field spreading in the coil is also seen to slowly decrease in magnitude over the wire. The third RCF - probing the coil 30 ps after first RCF - shows an uniform deviation of protons all over the coil. In addition to the outer halo, a nearly circular bright inner spot of protons appears in

the coil's center : it is the sign of a collimation of the protons which entered inside the coil. Later on, the following RCF imprints evidence that the positive charge remains during almost 40 ps, with clear focusing effect. It is equivalent to say that the discharge pulse traveling in the coil wire has a duration of ≈ 40 ps.

The last RCF imprint shows heavy perturbations with filamentation probably due to plasma effects and subsequent electromagnetic instabilities. Nonetheless, the bright inner proton spot is still present and the focusing capability is not yet affected.

For the case of the simpler Omega-shaped target, the RCF stack imprints are shown in Figure 11.7. We obtain similar deflections than for the previous case.
For instance, one can compare the deflections at the same probing time of 13.5 ps and it comes out that the outer halo size is ≈ 82 % the one for capacitor-coil target and the inner spot is of the same size while slightly deformed. This focusing effect is then stable for ≈ 40 ps and then fades at later times, when effects of plasma expansion from the coil in the form of filamentary field structures appear evident.

The energy-band width of selected protons for $d = 5$ mm amounts to ≈ 5 MeV, which is more than twice the energy-band selection width for the helical coil target of the experiment by Kar *et al.* , previously presented in Sec. 11.2. Although our design results to be less efficient in selecting a monoenergetic beam out of the TNSA distribution, the total collection efficiency within coil solid angle (> 50 %) is higher by almost one order of magnitude. The current density of a quasi-monoenergetic proton beam being proportional to W/Δ_0, with W the total kinetic energy and Δ_0 the energy spread (see Eq. 5.18 in Sec. 5.2.2), our design is expected to yield ≈ 50 % more current density from the selected energy range.

It is worth noting that this energy-band width increases (less dispersion on time-of-flights) together with the amount of collected protons in the coil, while decreasing the distance d from proton generating foil to coil target.

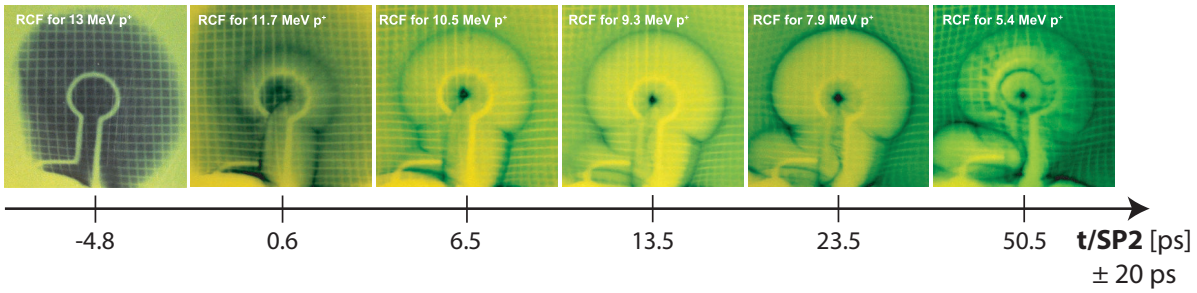

Figure 11.6 – Time-resolved build-up of the charge propagation and fields in the target's coil part as imaged by the RCF stack arrangement. $t = 0$ refers to the beginning of the SP1 interaction with the coil-target. The distance from Au foil to coil target is $d = 5$ mm. The absolute uncertainty on the delay of ± 20 ps is due to the synchronization accuracy between SP1 and SP2 laser pulses.

Given the two different target designs and distinct electrical connections to the ground, the similarity between the two data images conveys that the charge pulse does not depend on the ground connection present in the second case.

To check the influence of the electron neutralizing current, we drove a capacitor-coil target whose holed front disk was cutout by laser. A comparison is made with the usual capacitor-coil target in Figure 11.8 for RCF imprints of ~ 8 MeV probing the coil-part of both target at the same probing time of $t \sim 25$ ps. As the results are again fairly similar, the discharge mechanisms is consequently not related neither to the electron current neutralization from the front disk.

A measurement of the discharge propagation speed (see Box. 11.1) yields $0.95 \pm 0.01c$ which is much faster that the transport velocity of relativistic electrons issuing from the laser interaction, expected to be of $\sim 0.7c$ to $0.8c$. Therefore, the target discharge and consequent coil's focusing effect can unambiguously be attributed to the sheath-like electric fields normal to the wire rod surface, propagating along the wire as an EMP directly driven from the interaction region, as previously described in Sec. 11.2.

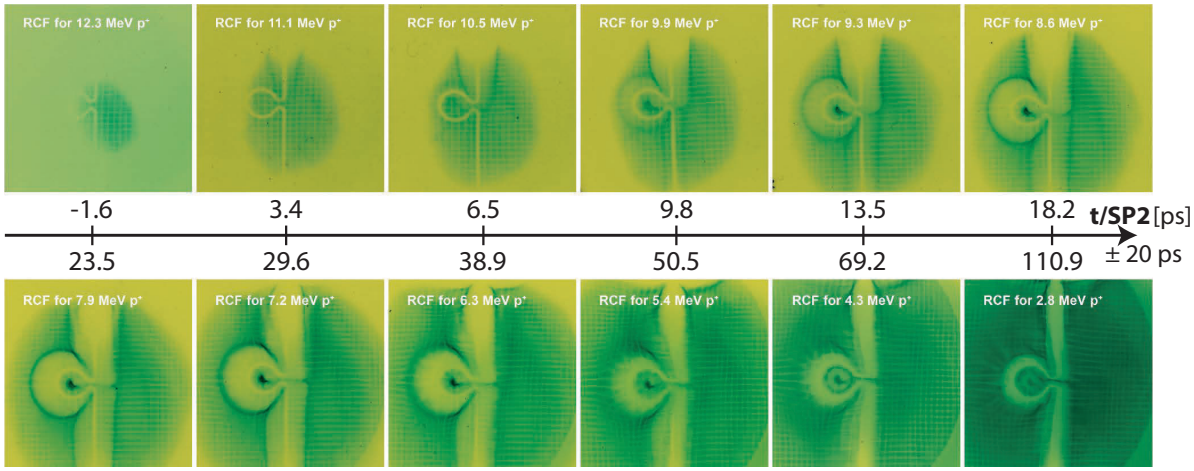

Figure 11.7 – Same as Figure 11.6 for the Omega-shaped coil target identically located at a distance $d = 5\,\text{mm}$ from the Au foil.

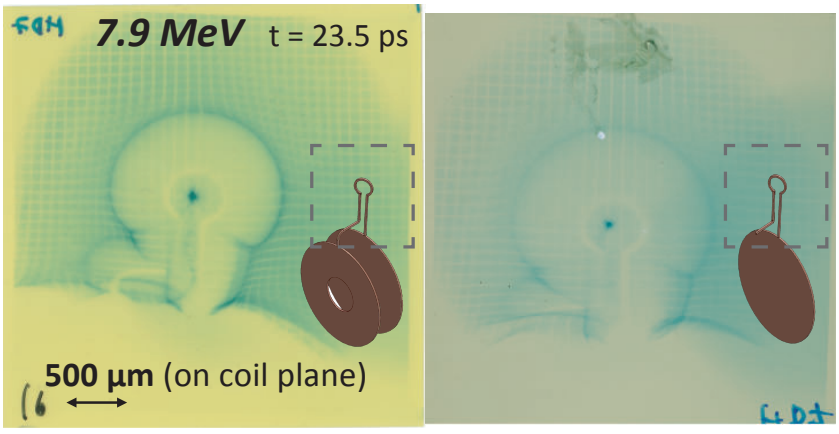

Figure 11.8 – In comparison with an RCF imprint obtained with the usual capacitor coil target (a), an RCF imprint is shown in (b) with a capacitor-coil target whose front holed disk was cutout.

Box. 11.1: Propagation speed

Between RCF imprints at probing time of respectively $t_1 = 3.4\,\text{ps}$ and $t_2 = 6.5\,\text{ps}$ after SP2 interaction for the Omega-shaped target (Figure 11.7), we measure a propagation length of $l = 640 \pm 10\,\mu\text{m}$. It yields a propagation velocity of $(2.89 \pm 0.1) \times 10^8\,\text{m/s}$, accounting for the divergence angle correction on protons time-of-flights (Eq. 11.2).

Equivalently, we measure a propagation length of $l = 930 \pm 10\,\mu\text{m}$ between RCF imprints probing at $t_1 = 6.5\,\text{ps}$ and $t_2 = 9.8\,\text{ps}$ after SP2 interaction. It yields a propagation velocity of $(2.83 \pm 0.05) \times 10^8\,\text{m/s}$. The uncertainty is here reduced by looking at deflections of protons with very low divergence angle.

Finally, by combining the two previous results, we find a pulse propagation velocity of:

$$(2.84 \pm 0.04)\,\text{m/s} \approx (0.95 \pm 0.01)c$$

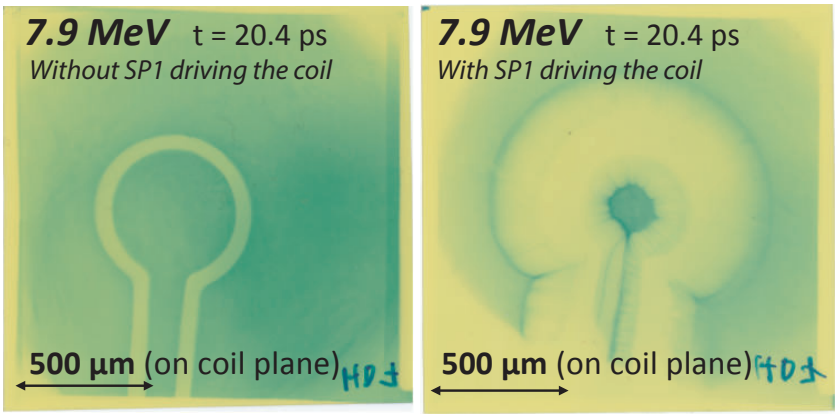

Figure 11.9 – RCF imprints with a distance between proton generating foil and capacitor-coil target of 2 mm. Protons of 7.9 MeV are probing the undriven coil (without SP1 interaction) (a) and the driven coil (with SP1 interaction) (b) at the same time $t = 20.4\,\text{ps}$ after SP2 interaction on the proton generating foil. The emittance of protons passing through the coil is estimated to be divided by a factor 3 from (a) to (b).

In the previous results with a distance between proton generating foil and coil of 5 mm, a significant amount of the total proton beam size was not collected inside the coil. To better determine the signature of focusing protons, we moved the proton generating foil closer to the coil at a distance of 2 mm. RCF imprints with this configuration are shown in Figure 11.9 for proton of 7.9 MeV probing either an undriven capacitor-coil target (a) and a driven capacitor-coil target (b) at the same probing time of 20.4 ps.

An emittance was calculated in both cases, based on a source divergence estimation from results with the two positions of the proton generating foil. It resulted that the emittance of protons collected inside the coil for the distance of 2 mm is divided by a factor 3 due to the focusing effect of the driven capacitor-coil target.

11.4 Static simulations results

11.4.1 Influence of an Electric Field only

Box. 11.2: Estimation of charge density

An estimation of the electric field which causes proton deviation can be easily made by looking at the outer deflection around wires of coil's target.
The electric field of an infinite charged wire is:

$$\vec{E} = \frac{\rho}{2\pi r \epsilon_0} \cdot \vec{e}_r \tag{11.4}$$

We measure that the deflection for protons of 9.3 MeV is of $\approx$ 468 µm and $\approx$ 382 µm at coil plane respectively for the capacitor-coil target (Figure 11.6) and Omega-shaped coil target (Figure 11.7).
Using the estimate made in Box. 8.4 (Sec. 8.1.4), one find that it would be coherent for a charge linear density ($\lambda_+ = Q/\Delta_x$) of respectively 12.3 nC/mm and 8.2 nC/mm. It corresponds to a radial electric field around the wire rods of $\sim 10^{10}$ V/m.

As a preliminary study, we aim here to reconstruct the observed deflections in RCF images by assuming a static and constant charge density filling the coil part. The coil part is charged with approximately the same charge density value as calculated in Box. 11.2. It leads to some tens of nC for the total positive charge on the coil part. Ballistic simulations were performed by Michael Ehret in the framework of his Master diploma internship. He injected 9.3 MeV protons, imposing an *ad-hoc* amount of positive charge in the coil part (Q_c) of either 30 nC or 60 nC: the results are respectively shown in Figure 11.10-a) and b). On both figures, the simulation are overlapped with an RCF imprint with the source located at $d = 2$ mm from the coil and corresponding also to protons of 9.3 MeV.

For $Q_c = 30$ nC, we can see a good agreement of the outer halo size while the inner spot is significantly bigger in the simulation. For $Q_C = 60$ nC instead, the outer halo size is strongly overestimated while the inner spot size is getting closer to the experimental one. It is not surprising because an electrostatic consideration of an uniformly charged coil would lead to an almost zero electric field inside the coil (by mutual cancellation of the electric field of two opposite wires). It was thus unexpected to see a strong collimation of protons inside the coil with only a static electric field.

Besides, the needed charge density in the coil part for $Q_c = 30$ nC, yielding $\lambda_+ \approx 7$ nC/mm, is seen to be effectively lower than what was estimated in Box. 11.2. The reason is that protons approaching the positively charged coil decelerate, interacting for a longer time with the charged coil's electric field, and then accelerate back to their original velocity after the coil. For instance, for a charge of 30 nC in the coil, protons can loose up to 2 MeV of kinetic energy in the coil's vicinity. This leads to an overall increased effect of the fields' action on protons.

This study leads to the conclusion that a static electric-field cannot accurately reproduce both the outer halo and the inner spot sizes. There is some evidence at this point in assuming a combined effect of electric and magnetic field. The magnetic field is induced by a current that is inevitably present due to charge conservation ($\partial_t \rho + \vec{\nabla} \cdot \vec{j} = 0$). One can estimate a current of a few kA from this later equation: $\lambda_+ 0.95c \approx 3.4$ kA.

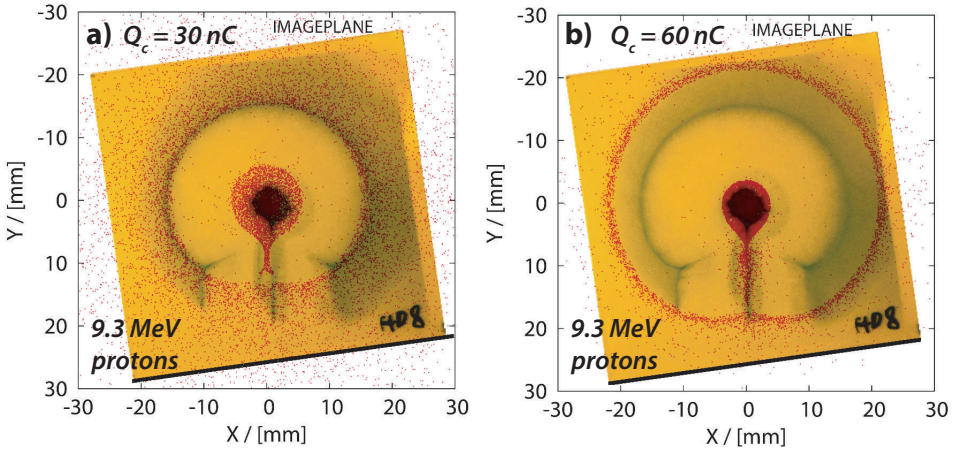

Figure 11.10 – Overlapped ballistic simulations and experimental results of 9.3 MeV protons imaging the coil 13.4 ps after SP2 interaction (for the capacitor-coil target). The coil is respectively charged uniformly with a) $Q_c = 30$ nC and b) $Q_c = 60$ nC. The source-to-coil distance is $d = 2$ mm.

11.4.2 Influence of a combined Electric and Magnetic Field

Michael Ehret also imposed independently a given amount of charge in the coil with a constant static current flowing through it.

To both reproduce the outer halo size (more sensitive to E-field) and the inner spot size (more sensitive to B-field), a given pair of values for charge and current can be found. The data from ballistic simulations was collected and two fitted functions F and G were built, referring respectively to the inner spot and outer halo sizes on detector plane (at $D = 60$ mm).

They write:

$$\begin{aligned} F(E_k, Q, I) = &\left(l_{cc} + l_{clb}Q + l_{cla}I + l_{mqc}QI + l_{cqa}I^2\right) E_k \\ &+ \left(q_{cc} + q_{clb}Q + q_{cla}I + q_{mqc}QI + q_{cqa}I^2\right) E_k^2 \\ &+ \left(c_{cc} + c_{clb}Q + c_{cla}I + c_{mqc}QI + c_{cqa}I^2\right) E_k^3 \end{aligned} \tag{11.5}$$

$$\begin{aligned} G(E_k, Q, I) = &\left(l_{cc} + l_{clb}Q + l_{cla}I + l_{mqc}QI + l_{cqb}Q^2 + l_{cqa}I^2\right) E_k \\ &+ \left(q_{cc} + q_{clb}Q + q_{cla}I + q_{mqc}QI + q_{cqb}Q^2\right) E_k^2 \\ &+ \left(c_{cc} + c_{clb}Q + c_{cla}I + c_{mqc}QI\right) E_k^3 \end{aligned} \tag{11.6}$$

Polynom coefficients are given in Sec. 19.4 (*Appendix*). Q and I denote the total charge in the coil and the current flowing through it. The variance of function F and G is respectively of $\sigma_S = 0.3$ mm and $\sigma_S = 0.4$ mm.

An example of analysis is depicted in Figure 11.11. A total charge and current of $Q_c = 23$ nC and $I = 234$ kA leads to a fair comparison with the experimental image for the same proton energy of 9.3 MeV. However, in the same figure, one can see that the tail of protons located below the inner spot is not correctly reproduced. In the simulation, the static magnetic field created by the constant current flowing through the coil causes a rotation of protons around the coil's axis. Moreover, the needed static current which was needed to reproduce the inner spot size is surprisingly high.

The static approach used until now gave us a coherent estimation of the charge in the coil. Yet, this approach is not able to correctly infer the transient nature of the charged pulse propagating in the coil wires.

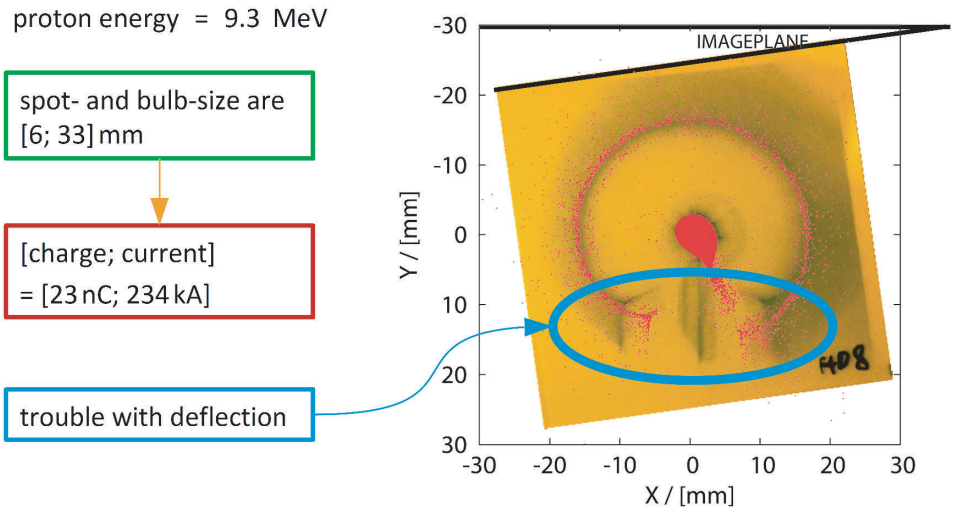

Figure 11.11 – Overlapped ballistic simulation and experimental RCF imprint of 9.3 MeV protons imaging the coil 13.4 ps after SP2 interaction (for the capacitor-coil target). The coil is charged with $Q_c = 23$ nC and a constant current of $I = 234$ kA is flowing through it. The source-to-coil distance is $d = 2$ mm.

11.5 Dynamic simulation results

In this section, we present preliminary results of ballistic simulations treating heuristically the transient propagation of an electromagnetic wave in coil-targets.

An electromagnetic wave results of the charge propagation ($\partial_t \rho$) and its related displacement current (j_D). The fields and currents are ruled by the local Maxwell-Ampere and charge conservation equations:

$$\vec{\nabla} \wedge \vec{B} = \mu_0 \vec{j} + \mu_0 \epsilon_0 \frac{\partial \vec{E}}{\partial t} = \mu_0 (\vec{j} + \vec{j_D}) \tag{11.7}$$

$$\vec{\nabla} \cdot \vec{j} + \frac{\partial \rho}{\partial t} = 0 \tag{11.8}$$

with ρ the charge density.

To treat correctly the transient nature of the charging pulse, ballistic simulations implementing the latter equations needed to be performed.

More precisely, an assumption is made here that there are neither electric nor magnetic field components along the direction of propagation: it is the definition of a Transverse Electromagnetic Mode (TEM) propagation. For instance, the electric field is radial and the magnetic field is poloidal.

The profile of the positive charge pulse traveling along the wire is presented in Figure 11.12-(a). The profile was inferred from the evolution of proton deflections at a fixed point of the wire at different probing times. It was then approximated by a reduced *Crystal Ball* function which consists of a Gaussian core portion and an exponential low-end tail below a certain threshold. The conversion of probing time to linear length is made considering the pulse velocity of $0.95c$ (see Box. 11.1). The current of the pulse is calculated using Eq. 11.8, and shown in Figure 11.12-(b).

In the simulation, an uniform distribution of protons covering the RCF imprint energy range is launched prior to the pulse, with a delay of 112 ps between each initialization (the delay measured in experiment was 105 ± 20 ps). The ballistic simulation compute the proton trajectories in the time-evolving field, which are then projected till the RCF detector plane. In Figure 11.13, the proton positions in the detector plane for each RCF energy range, as recorded in simulations, are plotted next to the experimental RCF imprints of Figure 11.7.

The deflected positions of protons on synthetic imprints are seen to fairly well match the experimental images. It is particularly true for protons of energies > 8.6 MeV corresponding to the instants before the rising edge of the pulse density reaches the bottom edge of the RCF imprint. Then, for

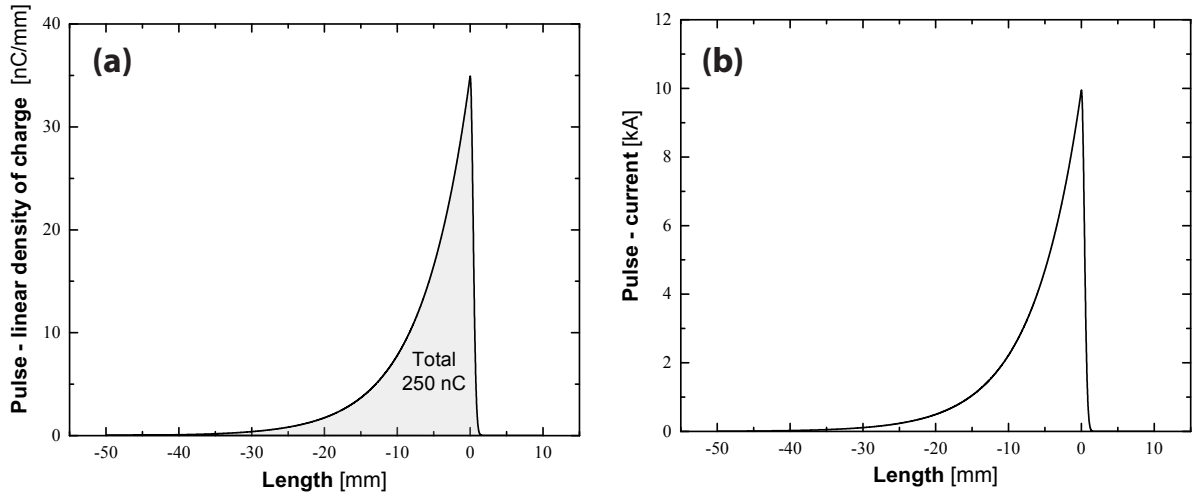

Figure 11.12 – (a) Linear charge distribution of the positive charge pulse travelling along the wire of coil-targets. **(b)** Associated current, as calculated from Eq. 11.8.

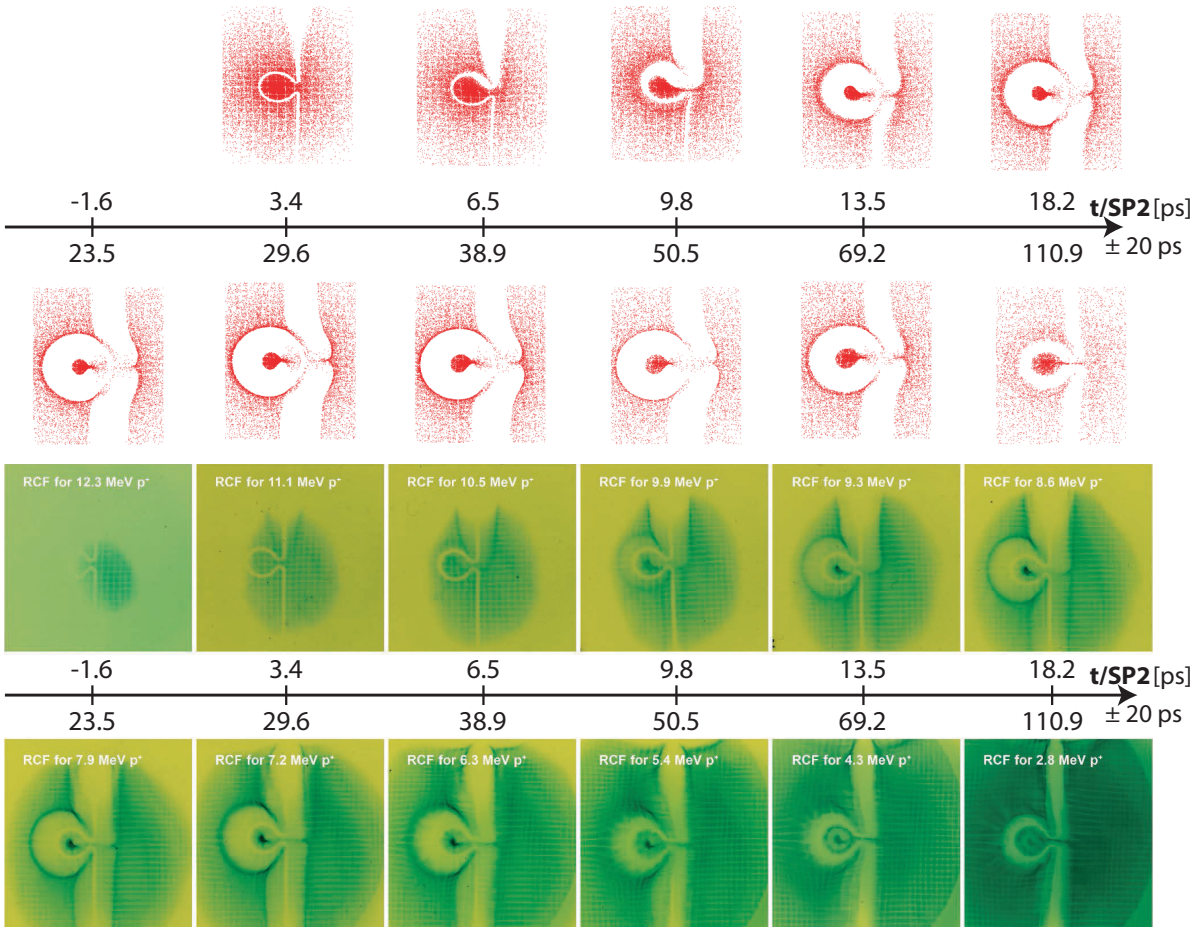

Figure 11.13 – Synthetic and experimental RCF imprints for the Omega-shaped coil target. Synthetic imprints are obtained with a ballistic simulation of a positive charge pulse propagation at 0.95*c* in the target, determined by its linear charge density and current spatial distributions (Figure 11.12).

the proton energy of 2.8 MeV probing the fields $\approx$ 93 ps later, we have again a nice consistency. Consequently, the accuracy of the decay part of the input charge density may be the source of the problem and should thus be improved. It is worth mentioning that the analysis of the density charge evolution from RCF imprints was "loosely" done in this preliminary study and a deeper analysis still need to be done. Nonetheless, these results are very encouraging and the E-field contribution to the halo around wires is correctly simulated and understood. Still, the inner size of focused protons inside the coil is not very well reproduced with this current distribution. Again, some current contribution is missing, as noted earlier for static simulations. This work will then be pursued to better reproduce the behavior of focused protons.

Nonetheless, we can take a look at the energy and angular distributions for initial proton energies of 8 ± 0.3 MeV forming the imprints of the RCF labeled with the Bragg peak energies 8.6 MeV and 7.9 MeV in Figure 11.13. The results are shown in Figure 11.14.

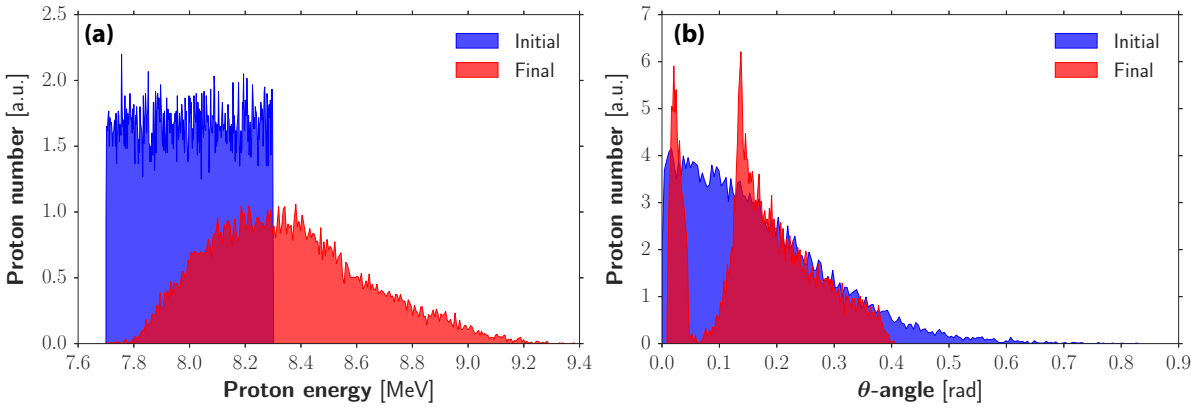

Figure 11.14 – Initial and final energy **(a)** and angular **(b)** distributions of protons stopped in the RCF imprints identified by the Bragg peak energies 8.6 MeV and 7.9 MeV.

We denote also in Figure 11.14-**(a)** that the initial proton distribution is shifted toward higher energies: the coil electric field seems thus to accelerate protons. In addition, some protons inside the coil (for this energy range of interest) are also seen to be *focused* and their divergence angle θ converge to $\approx$ 20 mrad [Figure 11.14-**(b)**]. The second peak in the angular distribution corresponds to protons piling up in a caustic which forms the outer halo seen on RCF imprints.

11.6 2D PIC simulation results

Preliminary 2D PIC simulation with 10$\times$ downscaled Omega-shaped coil target was carried out by A. Morace (ILE, Osaka, Japan) with the PIC code named EPOCH. Figure 11.15-(a) shows the initial plasma density in the simulation box and permits to identify the landmark of the Omega-shaped wire initialized at nearly solid density. It is worth noting that in contrast to the Omega-loop, the two vertical wires lengths and interaction disks are not proportionally scaled and the laser interaction point would be actually located $\approx$ 155 µm upper in the scaled down target. In the panel (b) and (c) of the same figure, the fast electron density and transverse electric field are respectively shown at the same time t_{sim} after laser interaction. In the real scale of the target, accounting for the not properly scaled wires and interaction disk, this time corresponds to $t_{\text{real}} \approx 11.8$ ps. The fast electron and EMP E-field position are identified by horizontal red dashed lines which leads to propagation velocities of respectively $0.75 \pm 0.02c$ and $\approx 0.94 \pm 0.02c$. Therefore, it also confirms that the EMP is traveling ahead of fast electrons as observed in [276].

In addition to that, both EMP and fast electrons are not "jumping" through the Omega-coil's open-angle gap. Fast electrons are instead *surfing* on the wire surface and they follow the coil geometry. Indeed, the very strong electric field inside the Debye length ($T_h/\lambda_D \sim 10^5/10^{-6} = 10^{11}$ V/m) is higher than the electric field in the Omega-coil's open-angle gap: fast electrons are confined in the wire sheath. For the EMP, the reason is different, it comes from the fact that the EMP wavelength for frequencies of $\sim$ 0.1 THz (3 mm) is far larger than the variations of bending radius along the wire geometry.

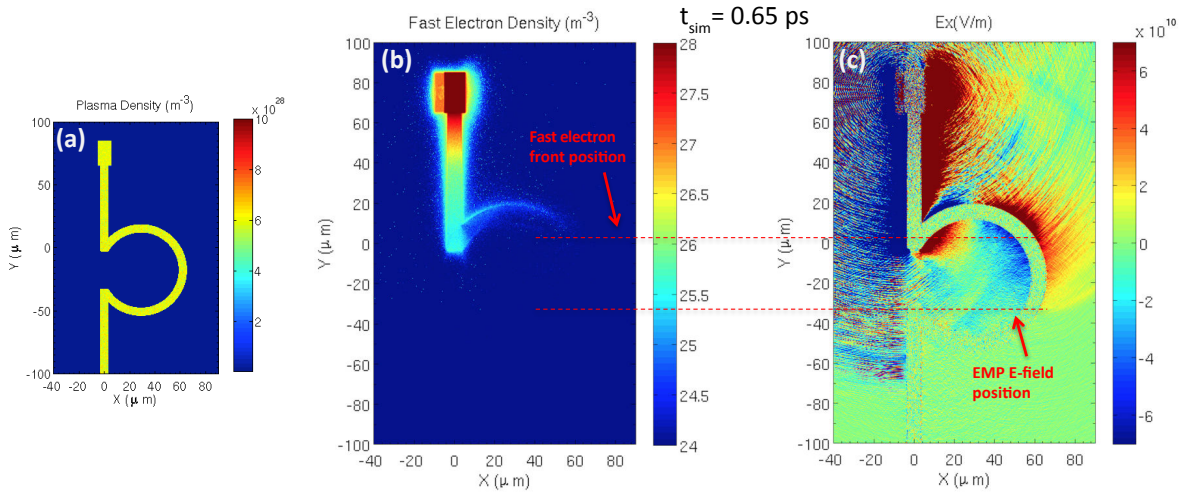

Figure 11.15 – 2D PIC simulations with a $10\times$ downscaled Omega-shaped coil target. **(a)** Initial plasma density of the simulation evidencing the coil shape. The plasma is initialized at nearly solid density. **(b)** Fast electron density and **(c)** Transverse electric field, at $t_{\mathrm{sim}} = 0.65\,\mathrm{ps}$ after laser interaction. The front positions for fast electron and electromagnetic wave are displayed by the two horizontal red dashed lines.

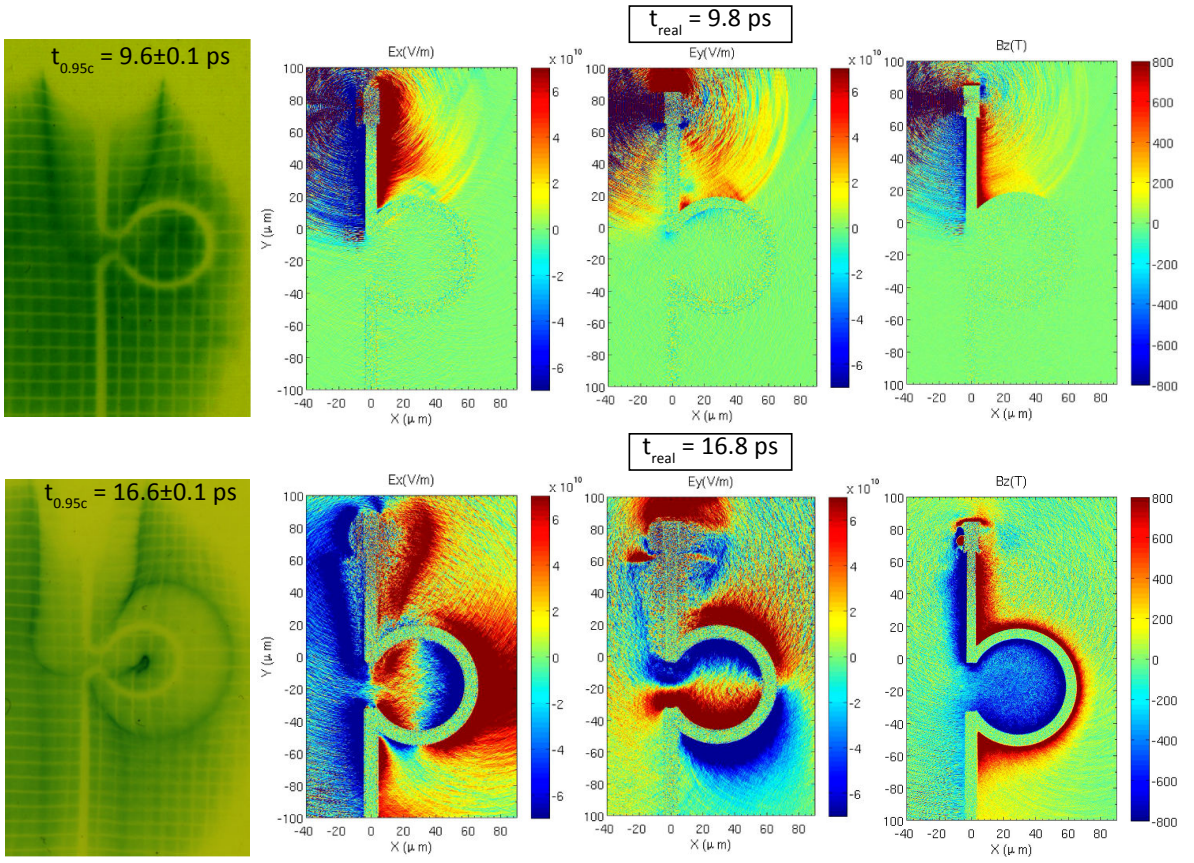

Figure 11.16 – Comparison of the RCF imprints with the two E-field transverse components and the longitudinal B-field component in 2D PIC simulations, at the real time after interaction of respectively $t_{\mathrm{real}} = 9.8\,\mathrm{ps}$ (up) and $t_{\mathrm{real}} = 16.8\,\mathrm{ps}$ (down). Note that the E-field magnitudes are $\sim 5 \times 10^{10}\,\mathrm{V/m}$. The time $t_{0.95\mathrm{c}}$ in RCF imprints corresponds to the delay after SP2 interaction, considering an EMP propagation velocity of $0.95 \pm 0.01c$.

In Figure 11.16, we present 2D PIC simulations results (electric fields and magnetic field) at a time t_{real}, chosen to match the probing time of protons in the RCF imprint shown on the left side of the figure. Taking the EMP wave velocity equals to $0.95 \pm 0.01c$, the probing time (after SP2 interaction) is evaluated to be $t_{0.95c} = 9.6 \pm 0.1$ ps for the first row of the figure and $t_{0.95c} = 16.6 \pm 0.1$ ps for the second row. The zones of high E-field correspond fairly well to the outer halo's shape and size on the RCF imprint. Besides that, both the converging E-field structure and the fairly uniform B-field of $\sim 30 - 60$ T inside the coil (scaled to the real coil size) conveys to a significant collimation effect of protons passing through the coil. The small asymmetry denoted in each coil quadrants for E-field can be an indication to explain the not so symmetric inner spot of protons seen in RCF imprints.

11.7 Conclusions

In this experiment we studied the production of strong electromagnetic discharge fields in coil-shaped targets driven by high-intensity sub-ps pulse lasers. We pointed out their potential to tailor laser-accelerated ion beams improving their energy-density within a tunable energy-range. In the presented design, the energy-selection band can reach up to 5 MeV-width ($\approx$ 40 ps discharge duration) and is easily adjusted by varying the delay between laser pulses, driving separately the proton generating foil target and the coil-shaped target. Moreover, the total collection efficiency within the coil solid angle is > 50 % and the coil-discharges are seen to efficiently focus protons with energy up to 10 MeV over $\approx$ 10 cm distances. In this context, the design is particularly robust considering in addition that the coil-targets can be very simply cut by laser from a 2D metal sheet, without need of additional folding.

The discharges observed by proton imaging in our experiments using a 100 TW laser, was seen to correspond to a positively charged pulse streaming at a velocity close to the speed of light which can be described as a propagating TEM (Transverse Electromagnetic Mode).

Static ballistic simulations permitted to estimate the positive charge in the coil matching the deflections observed in experimental RCF imprints. A linear charge density of $\approx$ 10 nC/mm was found to reproduce the caustic size of protons expelled by the induced E-field of $\sim$ 10 GV/m. However the size of the protons focused in the coil (bright spot seen on RCF) was not correctly reproduced with the same charge, unless imposing a very high current in the coil to magnetically enforce the focusing effect.

To further characterize the dynamic of the transient E-field developing in the coil-target, as observed by the time-resolved proton imaging, we modeled the discharge by imposing a distribution of positive charge and its associated current, both propagating in the coil at close to the speed of light. This heuristic approach is sufficiently accurate to match with experimental images and nicely resolve the transient E-field evolution in the coil-target. A margin of improvement for this approach can still be performed characterizing better the charge and current distributions profiles. Again, the focused protons spot size in the coil was not perfectly reproduced: this could be regarded as an incomplete description of the current in the coil. Besides that, this preliminary approach evidenced that protons are slightly accelerated by the coil E-field. Further investigations on the exhibited features introduced here are currently ongoing.

Preliminary 2D PIC simulations of a downscaled omega-shaped coil target confirmed the order of magnitudes of the induced fields and the velocity of the EMP wave. It permitted also to access to the fast electrons' propagation characteristics which are seen to follow downstream of the EMP, at lower propagation velocity along the wire. Here also, the continuation of this work will permit to further understand the EMP features and complete the description of experimental images and related phenomena.

Part IV

Conclusions and perspectives

Summary

12 Highlights of the obtained results **200**

13 Discussion and perspectives **202**

13.1 Perspectives of ICF assisted by external magnetic fields 202

13.2 Applying external B-field reduces the non-locality of electron heat fluxes . . . 205

13.3 Applications related to the control of laser-driven ion beams 206

13.4 Highly magnetized plasmas 207

13.5 Atomic physics under strong B-field 207

12 Highlights of the obtained results

In Part II, the described experimental campaign was devoted to produce and characterize strong quasi-static B-fields generated by ns-duration laser pulses of $\approx$ 500 J focused to intensities in the range of 10^{17} W/cm^2. Using three independent diagnostics, we successfully measured B-fields in the excess of 0.6 kT - corresponding to discharge currents above 250 kA - over ns-time scales in targets with 250 µm-radius coils. The time-evolution of the B-field strength at the coil center was extrapolated from measurements of high-frequency-bandwidth B-dot pickup probes located at a few cm from the target-coil. The early time measurements were confirmed by using the Faraday rotation effect on the polarization of a probe optical laser beam and by the deflections of a multi-MeV proton-beam recorded on radiochromic films. For times $>$ 0.35 ns, the B-field measurements by Faraday rotation and by proton-deflectometry were disturbed by strong radiation and electrostatic effects due to plasma-electrons magnetization. Yet, the proton deflection maps confirmed the dipole-like spatial distribution of the B-field around the coil over a characteristic volume of 1 mm^3, as expected for the given size of the coils. The spatial-integrated magnetic energy of the coil at peak-time corresponds to 8 % and to 4.5 % of the driver laser energy, respectively for the Cu and Ni coil-targets. In a subsequent experiment, carried out at the Gekko-LFEX laser facility (ILE - Univ. Osaka, Japan), peak B-fields of $\approx$ 600 T were consistently measured by a B-dot probe and by proton-deflectometry by mechanically shielding the coils from the interaction region between the disks. Given the open geometry and the relatively small expansion velocity of the coil's rod, $\approx$ 10 µm/ns - evaluated from optical shadowgraphy - the system gives access to the magnetization of secondary samples over several ns. Consequently, the system for B-field production is as simple as a laser-target with a specific coil-design and can be readily used in any laser-facility that offers the possibility of driving both coil and secondary sample, without the need for engineering other source of power discharge besides laser power.

A model of quasi-stationary magnetic fields generation with capacitor-coil target was also presented. It relies on the description of the target charging, resulting from the high-power ns laser interaction with the rear disk, of the blow-off plasma creation and subsequent ejection into vacuum of supra-thermal electrons. The source of current flowing between the disks and simultaneously through the coil-shaped wire - reacting like an RL circuit - was derived from a steady-state description of a diode-like potential structure building up across the disks and determining the maximum electron ejection current. The actual model description correctly predicts the maximum current for different laser-interaction conditions and phenomenological parameters of the looping circuit (RL) and was successfully compared with other experiments. A time-resolved description is also proposed and reproduces fairly well the charging and discharging durations. Nonetheless, the material dependence observed in our experiments was not yet understood, as well as the inferred high conversion efficiency from laser energy to hot electrons for which we have not yet a direct experimental evidence. Yet, the time-varying potential building up between the disks is a difficult picture to describe and will necessitate the use of a complete 3D modeling which is currently ongoing.

As a first proof-of-principle application experiment, our laser-generated B-field platform was promptly applied to radially confine the propagation of relativistic electron beams (REB) in solid-density targets. In the experiment detailed in Sec. 10, the REB was generated by focusing an intense laser pulse ($>$ 10^{19} W/cm^2) along the coil axis onto a solid, 50 µm-thick plastic (CH) sample with a 10 µm-thick Cu coating on the rear surface, positioned at the coil plane. We used Ni-coil targets driven by the above described ns-laser pulse to generate the B-field externally applied to the REB transport target. Different magnetization conditions were explored by changing the transport-target position relative to the coil and, for each position, the delay between the ns-laser driving the coil and the ps-laser generating the electron beam. The REB transverse patterns after crossing the target thickness were investigated by imaging the Coherent Transition Radiation (CTR) emitted from the rear surface. By comparing reference REB-transport shots without imposed B-field, with shots in presence of a driven coil, we obtained a clear narrowing and yield enhancement of the CTR pattern in the latter case of magnetized-transport, when allowing sufficient time for the full target magnetization, $\sim$ 1 ns. Benchmarked PIC-hybrid simulations of REB-transport coupled with a CTR post-processor permitted to unfold the corresponding REB transport features: the imposed B-field is able to guide a 30 MA electron current of 2 MeV average energy over the 60 µm-thick CH/Cu target. The REB density transverse profile is significantly smoothed and narrowed and correspond to both energy-density flux and peak background electron temperature improved by factors $\approx$ 5 compared to the reference shots

without imposed B-field. The energy transported to the rear target surface within the REB injection radius amounts to 70 % of the total energy transported to the rear surface. It represents a collimation efficiency quite notable with respect to experiments based on the REB-guided transport by only self-generated resistive B-fields. Our results are the first experimental demonstration that it is possible to efficiently guide through dense matter electron beams of MeV-average kinetic energy and of currents of 10s of MA. Incidentally, the CTR pattern sizes with external B-field are consistent with a magnetic field at coil center of (550 ± 50) T for Ni targets and thus confirm the measurements of B-field carried out on previous experiments. Magnetic-guiding effects for higher REB currents is currently being studied, and we expect to demonstrate a guided propagation over thicker targets. Thereupon we could test magnetic-guiding effects for REB generated by the 10 ps-long PW Petal Laser at LMJ facility and further propose magnetically-assisted FI-scaled experiments.

In the second part of Part III, we also studied the production of strong electromagnetic-discharge fields in coil-shaped targets driven by high-intensity sub-ps laser pulses, and their potential use to tailor laser-accelerated ion beams (improvement of the energy-density flux and/or energy selection). The discharges observed in our experiments using a 100 TW laser correspond to a neutralizing pulse streaming close to the speed of light that can be described as a propagating TEM mode. More heuristically, the discharge is also consistent with a propagating positive charge-density distribution of several hundred nC total charge, inducing fields of the order of 10 GV/m. The related current induced by this positive charge-density distribution peaks at $\sim$ 10 kA. Preliminary 2D PIC simulations of a downscaled target confirmed these order of magnitudes and the velocity of the EMP wave. It also permitted to characterize the fast electrons behavior which are seen to follow the EMP at a lower speed of $\sim 0.7c$. From time-resolving proton imaging, we saw that the coil-discharges are efficient in focusing protons with energy up to 10 MeV over $\approx$ 10 cm distances. The selected energy-band width amounts to $\approx$ 5 MeV. Besides, the relatively short duration of the discharge, $\approx$ 40 ps allows to select the energy of the focused protons by controlling the lasers timing. Our preliminary study also shows that the total collection efficiency within coil solid angle remains high ($>$ 50 %). The preliminary results presented in this thesis work will be pursued and further analyses are currently ongoing.

13 Discussion and perspectives

13.1 Perspectives of ICF assisted by external magnetic fields

The potentiality of external B-fields is related here with the issues encountered by fast ignition sources. The intrinsic divergence of the beams is a bottleneck issue for FI feasibility, especially when using fast electrons as the ignitor beam. For instance, by considering the expected divergence angle for fast electrons close to 50 ° [96, 199], ignoring even the scattering of fast electrons with the background plasma, one estimates that about 90 % of the fast electrons generated by the ignition laser will not reach the compressed DT core. A major challenge is therefore to ensure a guided FEB propagation within the FI integrated target design. Ignition scale calculations [21] were performed on Particle-In-Cell (PIC) simulations and their conclusions were that there is an absolute necessity to reduce the FEB divergence before its propagation into the fast ignition target, and over its propagation before it reaches the D-T core.

Among other techniques that have been presented in Sec. 10.1 for controlling fast electron transport, the use of imposed magnetic field arose from its already known success in accelerator physics. It consists on imposing an external magnetic field in order to confine and guide electrons within a small radius along their transport into the capsule depth, increasing their energy-density flux into the DT core. One has to distinguish confinement (or guiding), which consists on limiting the fast electrons from spreading in space, from collimation (or focusing) which consists also in reducing their velocity-space divergence. A confining magnetic field generally will not collimate the beam and fast electrons would quit ideally the confining magnetic field with their original divergence.

A set of numerical simulations of fast ignition cone target implosions, with artificially imposed axial magnetic field were performed by Strozzi *et al.* [268]. It has been shown that a 5 kT axial magnetic field resulted in a fast electron ignition energy reduced from $\sim$ 1 MJ to $\sim$ 130 kJ. A more potentially attainable initial axial seed field of $20-100$ T was imposed on spherical implosions of ignition-scale cyrogenic capsules and showed a compression of the magnetic field up to 40 kT, thereby relaxing hotspot areal densities and pressures required for ignition and propagating burn by $\sim$ 50 % [209]. The magnetic compression relies on its advection with the compressing plasma ($\int BdA$ is conserved), consequently the implosion of the capsule results in an increase of the seed magnetic field. Experimentally, the compression of a seed magnetic field of $\leq$ 10 T by imploding spherical capsules on Omega laser facility, showed that the B-field can reach up to $2-4$ kT [95, 142, 45, 109]. However, more recent results [122] showed that the compressed field is weaker around the fast electron generation point, that is the low-density relativistic laser-plasma interaction region, and then it is intensified towards the dense core region. According to simulations in these more realistic conditions, such converging B-field structure triggers the so-called *magnetic mirror* effect which is causing backward reflection of particles. Yet, in [122], the authors also demonstrated that a kilotesla-class external magnetic field in the case of moderate mirror ratio ($\leq$ 10) is giving an efficient guiding over the collisional dense plasma (see Figure 13.1). The mirror ratio is the ratio between the maximum B-field strength along an electron trajectory line and the B-field strength at critical density point, where the fast electron is generated.

However, such low mirror ratio is not easily obtained with the classic shell design because the core is considerably deformed by the magnetic fields (a cigar-like shape is observed on simulations) which reduces significantly the transverse size of the dense core and the fraction of electrons depositing energy into it. To overcome this issue, the idea to use a solid spherical target to increase the areal density core plasma was studied [192] and showed that the compression of the solid ball under strong external magnetic field is stable and magnetic mirror ratio remains under 4, yielding favorable core-heating properties for the fast ignition scheme, as seen in Figure 13.2. Interestingly, in [180], the author claimed that a seed B-field of 100 T is sufficient and is amplified to 10 kT at the cone-tip by the implosion. For an hot electron energy of less than 5 MeV, it is seen that the mitigation of the Weibel instabilities by the external B-field contributes to collimate the hot electron beam to the core.

The reader can also refer to refs. [285, 112] for alternative magnetically-assisted ICF schemes, still relying on the capability of generating ns-duration B-fields of several hundreds of Teslas. Briefly, for the fast ignition scheme assisted by external B-field, the three major challenges are:

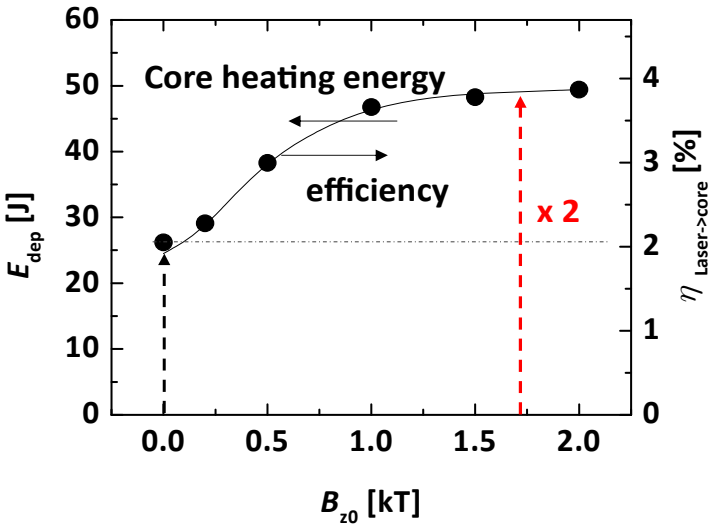

Figure 13.1 – Core heating energy by REB as a function of magnetic field strength at the injection point B_{z0}. The right-hand-side ordinate axis indicates the energy coupling efficiency from the heating laser to the fuel core, where an experimentally measured energy conversion ratio from the laser to REB, 31 %, is assumed. Figure taken from [123].

- ◇ to dispose of an external B-field with the good features (duration, volume and strength),
- ◇ to deal with the field compression to avoid magnetic mirror effects,
- ◇ to be able to magnetize as uniformly as possible the capsules prior to the ignitor beam propagation.

Fast-ignition demonstration would still require significant development in laser technology in order to achieve a 100 kJ, 10 ps, 10^{19} W/cm^2 laser source, delivered into a facility also providing $\sim$ 300 kJ ns-lasers in spherical irradiation for the cone-in-spherical target compression. Given the recent results of REB guiding, we consider that efforts for fast-ignition should be persued, with an accent into integrated experiments in magnetized conditions. This should go along with integrated simulations covering the time-scales of the various mechanisms, in order to optimize the target design and to provide a reliable predictability to full-scale fast-ignition conditions. A milestone for the next few years would be the demonstration of 20 % energy coupling between the igniting source and the dense compressed core.

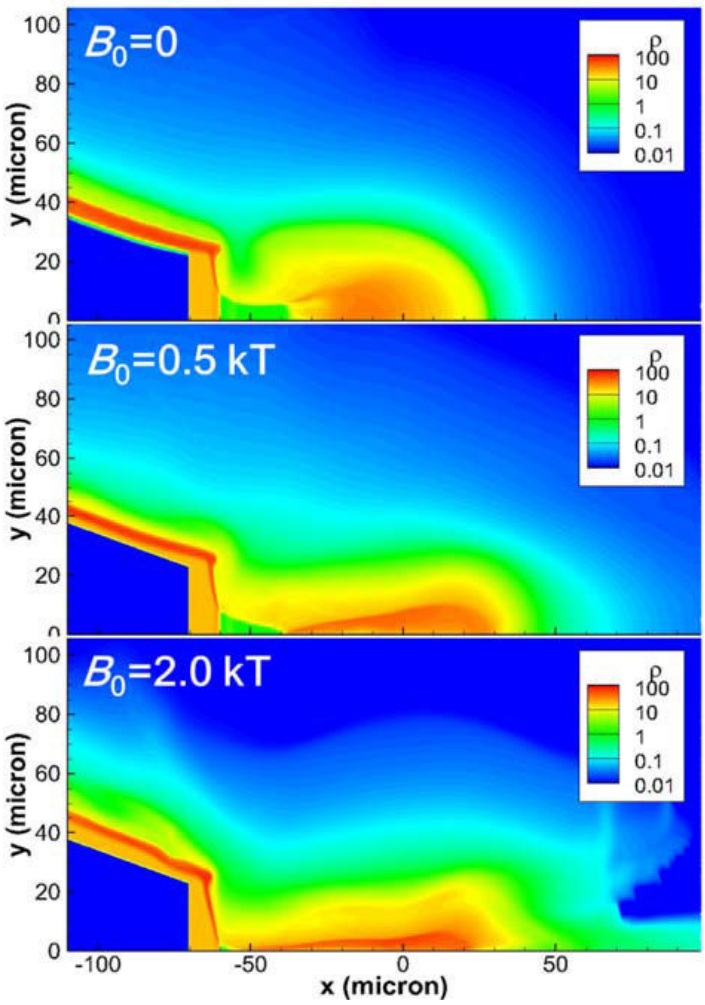

Figure 13.2 – Mass density contours at the maximum compression time of a solid ball target, for initial axial B-field strength (B_0) of $0, 0.5, 2$ kT. Figure taken from [192]

.

On the other hand, the effects of an imposed B-field were also studied in Hohlraum plasmas in order to improve laser-coupling efficiency. In the papers [267] and [183] they demonstrated both numerically and experimentally that external B-field aligned along the holhraum axis result in up to 50 % increase in plasma temperature (measured in [183] by Thomson scattering for a moderate magnetic field strength of 7.5 T and using a low-Z gas filled hohlraum target). A higher B-field strength of 70 T was studied in NIF conditions by means of simulations and showed that the imposed external magnetic field can enhance hohlraum performance reducing electron-heat and alpha-particle loss from the hotspot and improve inner-beam propagation by reducing Raman scattering during peak laser power.

These exciting numerical results pave the way to pulsed-power field generator for NIF and integrated hohlraum experiments are undergoing for the next few years (a conceptual sketch design is shown in Figure 13.3). A NIF Discovery Science project is currently dedicated to these studies and proposals with an inserted-cone design for fast ignition under assistance of laser-driven external B-field are also planned on at Omega-EP and were proposed to NIF.

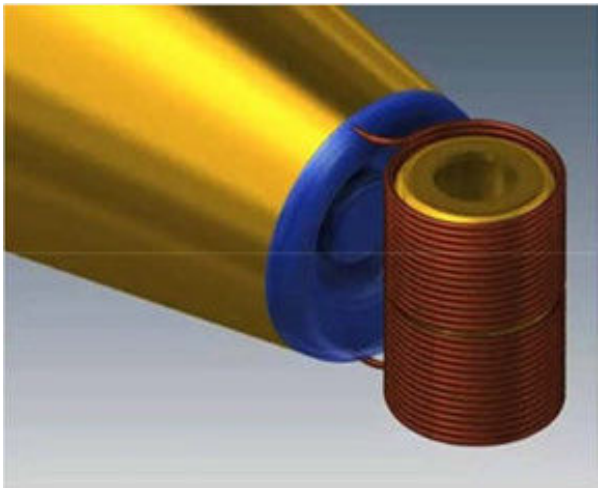

Figure 13.3 – Sketch of a pulsed-power coil concept design to impose axial magnetic field on NIF hohlraum.

Finally, the magnetization of the ignited target could also benefit to the alternative ICF scheme of *shock-ignition*. This scheme, which was not detailed in the thesis, was proposed by Betti *et al.* in 2007 [25] and like fast-ignition it relies on lower implosion velocities. Here, laser-driven converging shock waves are launched at stagnation to compensate the lower hot spot pressure/temperature and trigger the ignition. To avoid pre-heating of the fuel by hot electrons which deteriorates the core compression efficiency, they have to be stopped in the outer layer of the imploding target where they can in turn additionally contribute to the ablation shock pressure [227]. Hence, the use of an external magnetic field could help to localize the hot electrons and force them to be confined in the target's outer layer enhancing concurrently the shock pressure. First and foremost, integrated simulations are needed to confirm this scenario.

13.2 Applying external B-field reduces the non-locality of electron heat fluxes

We saw in Sec. 4.1.2 that the localization of the hot electrons by strong magnetic fields can reduce the non-local electronic heat fluxes and make the hydro simulations valid again with the Spitzer-Harm transport theory. This consideration is only valid if the magnetic field is high enough in all the studied plasma. The only way to do this is by applying an external magnetic field to magnetize the entire target. In [82] it has been shown with temporally resolved Thomson Scattering measurements that large externally applied magnetic field > 10 T induced extremely strong local heating and an agreement with hydrodyamic modeling (with Spitzer-Harm transport coefficients) when including a magnetic field model. This result was tempered by an experiment showing a significant degree of cavitation (> 40 %) of the magnetic field in the laser-heated region [228]. This cavitation was attributed

to the Nernst effect and leads to the reemergence of nonlocality even if the initial value of the applied magnetic field strength was sufficient to localize the transport (12 T).

A recent article in 2015 about Nernst effect in Magnetized Hohlraums using a full kinetic code [120] showed that the Nernst cavitation is even stronger ($\sim 2\times$) than the previously expected values for magnetic fields strengths between 10 and 100 T. An important result then is that the cavitation does not occur with externally imposed B-field with amplitude above 100 T: the magnetic field at the Hohlraum axis decreases as applied field strength is increased because the Nernst effect is mitigated at higher magnetic field strengths, preventing the magnetic field from accumulating near the Hohlraum axis. The localization of the electrons and local heating flow is then occurring again. This result is of great interest when envisaging the magnetization of an Hohlraum (see Sec. 13.1) by applying laser-driven B-fields. Indeed, the regime of > 100 T external B-field, suitable for a laser fusion facility, is only possible at the present day with laser-driven B-fields such as presented in this thesis work.

13.3 Applications related to the control of laser-driven ion beams

The properties of laser-driven ion beams are appealing for many applications, especially those requiring a highly localized energy deposition in matter, where laser-driven ion sources are competitive. Laser-driven ion beams possesses high-energy flux over ps temporal duration, making them particularly suitable for isochoric matter heating to produce warm dense matter [205], where the density is 1 to 10 times the solid density and temperatures which amounts to up to 100 eV. This range of densities and temperatures for plasma is relevant to geophysical and planetary science. Especially, scientists look for equation-of-state and opacity measurements at those extremes state of matter. In order to achieve those measurements, a sufficiently large volume of uniformly heated matter has to be produced and diagnosed before hydrodynamic expansion occurs. To ensure a better isochoring heating, one would require some degree of energy selection in the ion beam spectrum, such as to have less spread over Bragg peak deposition of the ions. The perspectives of energy selection presented in Sec. 11 is a path of interest to both guide/focus and energy-select the ions with laser-driven electromagnetic fields.

Moreover, laser-driven ion beams in the Fast Ignition (FI) concept for Inertial Confinement Fusion (ICF) (see *Introduction* - Sec. 0.2) has been proposed [235] upon promising development of sources of multi-MeV proton beams in PW-laser experiments with highly localized energy deposition profile and low beam emittance ($< 10^{-3}\pi$ mm mrad). Nevertheless, ion beam transport towards an ICF target raises several complications. In particular, those unexplored issues might rise the need to focus the ion beam. This feature can be illustrated by a fit formula estimating the needed ignition energy ϵ_{ig} for proton temperature of 5 MeV as a function of fuel density ρ and distance d between proton source and fuel core [7, 271]:

$$\epsilon_{ig}[\mathrm{kJ}] \approx 90(d[\mathrm{mm}])^{0.7}(\rho[\mathrm{g\,cm^{-3}}]/100)^{-1.3} \tag{13.1}$$

Considering a conversion efficiency from laser to protons of 10 % (not achieved yet for a mono-energetic laser-driven proton beam of several MeV), a 100 kJ laser-driver, and a compressed pellet at $\rho = 300\,\mathrm{g\,cm^{-3}}$, the minimal distance to get ignition would be $d \approx 333\,\mu$m. This distance is small and the integration of a foil inside the cone of conically-guided ICF targets - already designed for electron FI - has been proposed. However, it raised the issue of shielding the foil from pre-heating caused for example by external radiation, preventing from an efficient production of protons. In order to nearly suppress this distance dependence and avoid shielding issues of ion production near the pellet, one would need a collimated or focused ion beam. This could be achieved only by the means of focusing techniques to transport the ion beam from a far distance till the dense core. Since protons are heavy particles, only laser-driven fields are nowadays viable candidates to provide the needed strength while avoiding the use of cumbersome accelerator techniques.
The reader can refer to [79] in order to get a detailed summary on the current status of the ion fast ignition scheme.

Last but not least, recent developments of ion acceleration, particularly with new acceleration mechanisms such as BOA [106, 125, 124, 103], put a landmark on the path toward laser-driven accelerators for medical (oncology) purposes. Conventional accelerators actually lead the topic with typical acceleration gradients of 1 MeV/m and ion energy of 100 MeV/nucleon. However, the space and cost are rather big for practical applications, especially for medical ones. Based on

the present situation, it arose a research direction for the implementation of a compact laser-driven proton/ion accelerator. The needed energies required for cancer therapy are $> 200\,\mathrm{MeV}$ for protons and $\sim 400\,\mathrm{MeV/nucleon}$ for carbon ions (meaning energies in range of $4 - 5\,\mathrm{GeV}$) with a particle number of $\approx 10^9$. The energy reached with BOA (see Sec. 5.2.1) is getting close to the requirements. However, in spite of the tremendous development made so far in laser-driven proton and heavy ion sources, there is still a lot of long-term efforts which are required for the real implementation of laser-driven medical accelerators. Among main difficulties, one can mention for instance: i) the needed repetition rate needed of $\geq 10\,\mathrm{Hz}$ for both laser and target supply system, ii) small shot-to-shot variations, strongly constraining the control of the beam characteristics, iii) ion beam divergence and spectral bandwidth should be reduced and iv) other high-energy particles such as electrons and hard X-rays resulting from the laser-interaction should be minimized. For the point iii), the development of compact laser-driven electromagnetic lenses explored in this thesis work and by other research groups (Part III) are in this context of great interest. The point iv) can also be enhanced using laser-driven electromagnetic lenses which focus the proton beam over 10s of cm and thus allow an increased separation distance from source to patient.

13.4 Highly magnetized plasmas

The few laser-driven plasma experiments performed to date on externally magnetized samples have relied on capacitor-bank pulsed discharges in solenoids, with B-field strengths up to 70 T. Using this method, B-fields strengths that could be generated in any laser facility reach a cap, in order to keep a relative easy deployment and an easy access to multiple angle diagnostics probing the magnetized plasma. In our experiment of relativistic electron beam guiding, we succeeded to magnetize a secondary sample of plastic to a high B-field strength of $\approx 600\,\mathrm{T}$. The reached strengths of our platform which is in addition all-optical and permits wide access to the magnetized sample could bring *de facto* new solutions and perspectives.

In particular, it would be of interest for laboratory astrophysics studies, where this unprecedented magnetization level can permit to experimentally scale astrophysical processes such as collisionless shock formation and acceleration of high-energy particles in colliding magnetized plasmas. While some of these processes have started being studied in laser facilities [54, 4, 80, 243], our B-field platform would be able to extend the studies to higher magnetization levels and with easier diagnostic access. We can also think of using bigger coils or Helmholtz-like geometries in order for the laser-driven B-fields to be rather uniform and of bigger volume, at the cost of lower B-field strengths (yet higher or comparable to conventional generator techniques).

Higher magnetization levels means also other astrophysical phenomena to observe and to understand. Processes such as turbulence growth in highly magnetized plasma and the origin of cosmic rays in the high-energy astrophysical settings of supernova remnants might be experimentally scaled.

For instance, blast waves developing upon strong laser-driven hot electron energy deposition can be strengthened by localizing electrons in a highly magnetized plasma and this could be a way to mimic the Sedov-Taylor blast wave structure of such supernova remnants.

Finally, the access to high level of magnetization would be an occasion to check theories relevant to non-local transport (like Braginski transport coefficients under strong B-fields, just to name one).

Highly magnetized plasmas phenomena are numerous and field of possible investigations is thus very broad. The reader can refer to [225] for an exhaustive description of astrophysics phenomena potentially scalable to laser and Z-pinch experiments.

13.5 Atomic physics under strong B-field

There is also motivation for studying light atoms submitted to strong magnetic fields in order to better understand the magnetized atomic physics processes expected in the crusts of compact stars such as white dwarfs stars and neutron stars. The B-field strength expected in white dwarfs ranges from 10 T up to 10 kT (see *Magnetic fields in Nature* in *Introduction*) that is already partially accessible with

our B-field platform. The story is different for neutron stars where B-fields are generally in excess of 100 kT.

The total energy of an atom in a magnetized plasma can be described in quantum mechanics by the total Hamiltonian H which can be decomposed as follows:

$$H = H_0 + H_{mag} \tag{13.2}$$

where H_0 is the unperturbed Hamiltonian and H_{mag} is the Hamiltonian resulting from the interaction with the magnetic field.

If this interaction term H_{mag} is small (less than the fine structure), it can be treated as a perturbation: this is the so-called *Zeeman effect*. For higher H_{mag} (*i.e.* higher magnetic fields) - but still small compared to H_0 - the so-called *Paschen-Back* effect appears and atomic splitting occurs. For even higher magnetic fields $H_{mag} > H_0$ the atomic levels are replaced by the Landau levels. There are, of course, intermediate cases which are more complex than these limit cases. Moreover, even if Landau levels regime appears in Hydrogen for B-fields strengths of $10^3 - 10^4$ T, in magnetized plasma there is a strong competition between plasma effects and magnetic effects and it would be hardly perceptible in line emissions.

A former colleague of our group in CELIA, O. Peyrusse, made some estimations with his atomic code and concluded that for B-field strengths of $1 - 2$ kT and beyond, the spectral profile of Lyman-α lines of Carbon or Fluorine would be noticeably modified (see Figure 13.4 for Carbon results).

We leave now the exciting field of astrophysical studies to enter in an other exciting field: solid-state physics, where laser-driven strong B-fields may eventually be applied to study atomic physics in solid-state matter submitted to a strong B-field. In solid state, Landau-level splitting for molecules/crystals appear in more modest B-field strengths of > 10 T [301, 42]. Experimental campaigns on this field use pulsed magnets to study the solid matter submitted to high magnetic fields. If we manage to protect the sample from being sensibly ionized (*e.g.* with mechanical shielding or using less energetic short-pulse irradiations) keeping its crystal structure, our applied B-fields would be then able to reach new Landau levels and would extend experimental studies in this area.

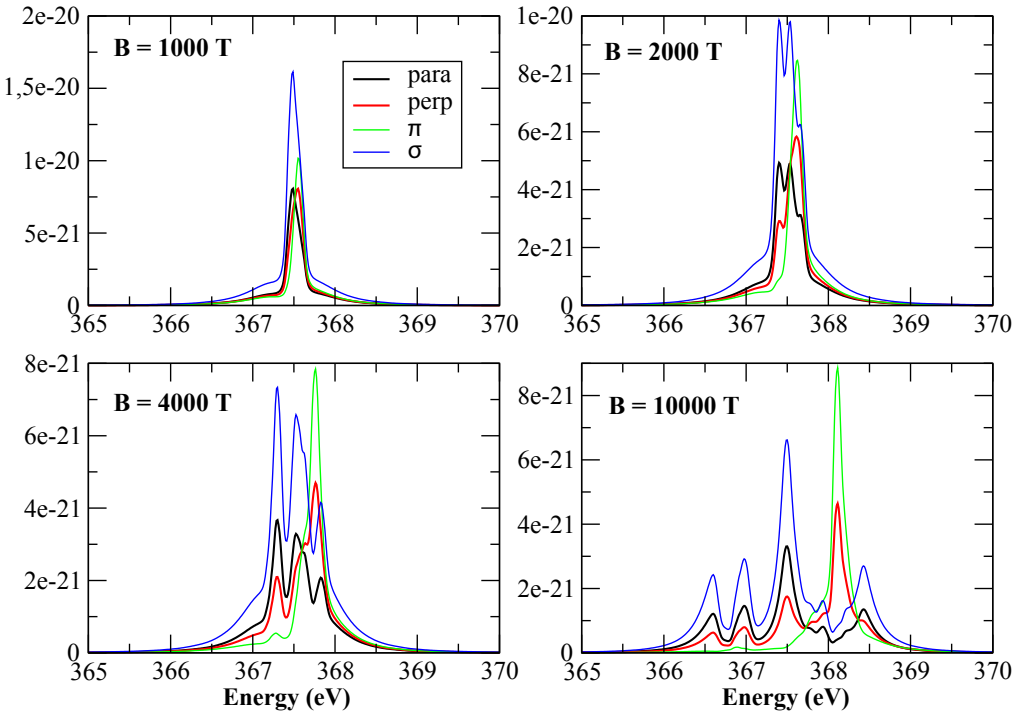

Figure 13.4 – Carbon Lyman-α line emissions (with fine structure) in a surrounding plasma with $n_e = 3.9 \times 10^{21}$ cm^{-3} and $T_e = 200$ eV. The different curve's colors identify the polarization components of the emission. *Results and graphs courtesy of O. Peyrusse.*

PUNCHLINE

To conclude, we obviously do not pretend to provide a breakthrough in all the domains presented so far, since complications may naturally arise under a pragmatic approach for experimental demonstrations. The given insights should be also prioritized and strategic choices have thus to be made, considering in addition that we reasonably cannot enter in all of them.

As mentioned before, the future work on an experimental demonstration for FI-scaled fast electron guiding with assistance of external B-field remains our priority. Obviously, there will be also, in parallel, spin-off projects on some other applications introduced in the above perspectives.

The viability of our B-field platform for fast electron guiding should be first demonstrated on OMEGA-EP and GekkoXII-LFEX facilities in integrated experiments.
This should go along with integrated simulations covering the time-scales of the various mechanisms, in order to optimize target design and to provide a reliable predictability to full-scale FI conditions. It could be then pursed experimentally in NIF-ARC or LMJ-Petal facilities.

Part V

Appendix

Summary

14 Intense laser beams as laboratory tools **212**
14.1 LULI 2000 Laser Chain . . . 215

15 Coil-target manufacturing **216**

16 B-dot probes **216**
16.1 Single strand loops . . . 216
16.2 Cylindrical loops . . . 218
16.3 Bandwidth of a B-dot probe . . . 220
16.4 Rise time and frequency limits . . . 220
16.5 Commercial B-dot probe Prodyn RB-230 . . . 220
16.6 Measurement system . . . 221
16.7 Calibration of B-dot probes . . . 222
16.7.1 Experimental setup description . . . 222
16.7.2 Experimental results compared to magnetostatic simulations . . . 224
16.8 Time synchronization of B-dot signals . . . 229

17 Magnetostatic code ©Radia **231**

18 Radiochromic Films (RCF) **233**
18.1 Stopping power determination . . . 233
18.2 Dose calibration . . . 235
18.3 Proton dose to spectrum . . . 240

19 Proton deflectometry analisis **241**
19.1 Analysis of grid deflections from the RCF imprint . . . 241
19.2 Particle ray-tracing simulations . . . 243
19.3 Simulation with one-step trajectory . . . 244
19.4 Parameter of the fits functions F and G . . . 246

20 Imaging Plate (IP) detectors **247**

21 Thompson Parabola **248**

22 X-ray diagnostics **251**
22.1 K-α emission . . . 251
22.2 X-ray spectrometry . . . 251
22.3 X-ray K-α imager . . . 253
22.4 Hard X-ray spectrometry - "Bremsstrahlung Canons" . . . 255

23 Coherent Transition Radiation (CTR) **257**
23.1 Focus on the CTR post-processor developed in this thesis work . . . 258
23.2 Benchmarked simulations . . . 259
23.3 Influence of the observation angle . . . 261

14 Intense laser beams as laboratory tools

Lasers (acronym of **l**ight **a**mplification by **s**timulated **e**mission of **r**adiation) are devices that generate or amplify electromagnetic radiation. It comes from the fact that an atom in an excited level could decay to lower energetic level by emitting spontaneously photons or by stimulated emission. Einstein who was at the origin of this hypothesis in 1917, in order to prove this statement, studied a system of atoms at a temperature T in thermal equilibrium with electromagnetic radiation [74]. Giving n_1 and n_2 the number of atoms per unit of volume respectively of the excited state and the lower energetic state, having energies E_1 and E_2, an atom can emit or absorb a photon with a energy $h\nu$ equals to the difference of energy $E_2 - E_1$ (h is the Planck constant). The spectral distribution of the photons in thermal equilibrium is given by black body radiation as suggested by Planck's law :

$$U_p(\omega) = \frac{\hbar\,\omega^3}{\pi^2 c^3}\left[\exp\left(\frac{\hbar\,\omega}{k_B T}\right) - 1\right]^{-1} \tag{14.1}$$

with $\hbar = h/2\pi$, c the speed of light, k_B the Boltzmann's constant and $U_p(\omega)\mathrm{d}\omega$ the radiation energy per unit of volume within the frequency interval $[\omega, \omega + \mathrm{d}\omega]$ in $\mathrm{J\,s/m^3}$. The population of the level 1 and 2 can be calculated by following rate equations :

$$\begin{cases} \dfrac{\mathrm{d}n_2}{\mathrm{d}t} = -An_2 - B_{21}U_p(\omega)n_2 + B_{12}U_p(\omega)n_1 = 0 \\ \dfrac{\mathrm{d}n_1}{\mathrm{d}t} = +An_2 + B_{21}U_p(\omega)n_2 - B_{12}U_p(\omega)n_1 = 0 \end{cases} \tag{14.2}$$

The parameters A, B_{12} and B_{21} are known as Einstein coefficients, and in thermal equilibrium the populations are constant. An_2 is the rate of spontaneous emission of photons from the upper level 2, $B_{21}U_p(\omega)n_2$ is the rate of stimulated emission from the upper level 2 to the lower level 1 and $B_{12}U_p(\omega)n_1$ is the rate of stimulated absorption from the lower level 1 to the upper level 2. In thermal equilibrium the levels 1 and 2 are related by the Boltzmann distribution :

$$\frac{n_2}{n_1} = \frac{g_2}{g_1}\exp\left(-\frac{\hbar(E_2 - E_1)}{k_B T}\right) \tag{14.3}$$

where g_1 and g_2 are the degeneracy of the atomic levels 1 and 2 and we have :

$$B_{12}\left(\frac{g_1}{g_2}\right) = B_{21} \equiv B, \qquad \frac{A}{B} = \frac{\hbar\,\omega^3}{\pi^2 c^3}, \qquad \frac{A}{B\,U_p(\omega)} = \exp\left(\frac{\hbar\,\omega}{k_B T}\right) - 1 \tag{14.4}$$

One can see that for $\hbar\omega \ll k_B T$, the number of stimulated emissions is much larger than the number of spontaneous emissions. In the above analisis, only one laser frequency was considered (resonant frequency given by $E_2 - E_1$). In general, the atom transition from the excited level to the lower level can be induced by radiation over a range of frequencies around the resonant frequency. The probability of the interaction is a function of frequency. Therefore, a laser beam is not a delta function in frequency (*i.e.* one single frequency) but a function $g(\omega)$ known as the line shape function normalized by 1. It is a Lorentzian profile where there is homogeneous broadening of spectral lines with a natural full width at half maximum of $g(\omega)$ given by $(\Delta\omega)_{\mathrm{FWHM}} = A = 1/\tau_{\mathrm{sp}}$ (τ_{sp} is the natural lifetime of the excited state). In practice, Doppler effect and inhomogeneities in a laser medium (for example in the solid crystal lattice) produce random inhomogeneous broadening and the associated laser line shape function is Gaussian.

If we consider the propagation in one dimension (x), of a monochromatic electromagnetic beam in medium, a good approximation is given by the following equation for the energy flux $I(\omega)$ (energy per surface area and per second) :

$$\frac{dI(\omega)}{dx} = (G - \kappa)I(\omega), \qquad G = \frac{\pi^2 c^2 \tilde{n}(n_2 - n_1)g(\omega)}{\omega^2 \tau_{sp}} \tag{14.5}$$

$\tilde{n}$ is the refractive index of the medium so that $c/\tilde{n}$ is the phase velocity of the electromagnetic field in the medium. G is the gain for a system with population inversion satisfying $n_2 > n_1$ and

κ are losses due mainly to collisions. In order to achieve the population inversion, it is required to "pump energy" into the laser medium, violating the thermodynamic equilibrium and thus allow the population inversion. There are various ways to provide energy into the laser medium. For example, a solid state laser can be pumped with flash lamps or with other laser devices such as laser diodes. A gas laser can receive its energy from various electrical discharges and also from different particle beams. One of the important issues for a large laser system is the quality and the uniformity of the energy input. Assuming that $n_1 - n_2$ is independent of $I(\omega)$, the solution of Eq. 14.5 is:

$$I(\omega, x) = I(\omega, 0)e^{(G-\kappa)x} \tag{14.6}$$

We can see that the population inversion yielding $n_2 > n_1$ and $G > \kappa$, produces light amplification and the intensity of the radiation increases exponentially. In the oscillator of a laser, the medium is place between two mirrors and the reflectivity of those two mirrors R_1 and R_2 with a given length of medium L needs to satisfy $R_1 R_2 e^{2L(G-\kappa)} \geq 1$. In comparison with other radiation sources, the laser is characterized by the following properties :

◇ The laser **wavelength** as it is nearly monochromatic because the amplification is done for frequencies very close to the resonant frequency and the two mirrors forming the resonant cavity cause the natural line-width (of the spontaneous transition from 2 to 1) to be narrowed by many orders of magnitude.

◇ The **spatial coherence**, defined by the phase change of the electric and magnetic field of two points in space, is constant in time. The maximum distance L satisfying this coherency is denoted by L_{coh}, that is the laser coherent length.

◇ The **temporal coherence** is defined by the phase change of the electric and magnetic field in time at a given point in space. If the phase of this point is conserved between t and $t + \tau$ for all t, we say that this point is coherent during a time τ. The maximum value of τ is denoted as τ_{coh}, that is the temporal coherence of the laser.

◇ The **divergence** of the laser beam, due to the fact that there is diffraction from the finite aperture of the cavity. For a perfect spatial coherent wave, with a wavelength λ and a beam diameter D, the diffraction limited divergence is $\theta_d = \dfrac{\beta\lambda}{D}$. β is a numerical factor of order 1 ($\beta = 1.22$ for a plane wave beam with a constant intensity over its circular section).

◇ The **brightness** of the beam, defined as the power emitted per unit of surface area per unit of solid angle, is usually many orders of magnitude brighter for lasers than any conventional sources.

Moreover, there are two classes of high power lasers, solid state lasers and gas lasers. The term solid state laser is usually used for lasers having an insulating medium made of crystal or a glass. These lasers use impurity ions as their active medium. The neodymium doped glass (Nd:glass) lasers are the most popular type of solid state lasers. Neodymium lasers can oscillate on several lines, the strongest and therefore the most commonly used have a wavelength of $\lambda = 1.06\,\mu\text{m}$. At present there are four other media which are of interest of high power laser interactions, the CO_2 with $\lambda = 10.6\,\mu\text{m}$, the iodine ($I_2$) with $\lambda = 1.3\,\mu\text{m}$, the KrF with $\lambda = 0.249\,\mu\text{m}$ and the titanium sapphire with $\lambda = 0.8\,\mu\text{m}$.

The first laser was demonstrated in 1960 by Maiman with a lasing medium made of ruby crystal, pumped by xenon flash discharge, and the pulse duration was between 1 ms and 1 µs [170]. One year later, Hellwarth invented the concept of *Q-switching* and tried it with a ruby laser by using a Kerr cell shutter. He achieved a pulse duration of about 10 ns [105]. Some years later, in 1964, Hargrove *et al.* achieved the first *active mode locking* for a helium-neon laser and a pulse duration of about 1 ns. The mode locking was obtained by modulating the index of refraction acoustically with one round trip of the light in the cavity [100]. Using as saturable absorber, the idea of *passive mode locking* was suggested [182] and in 1966 a neodymium glass laser pulse shorter than a nanosecond was first obtained [66]. Nowadays, using this technique, pulses of the order of 10 ps duration are common in many laboratories around the world. With Ti-sapphire laser pulses of 10 fs were achieved [305]. A technique called *chirped pulse amplification* used in microwave devices for many years was first suggested for the lasers in 1985 to amplify short laser pulses [266]. To do so, the femtosecond laser pulse is first stretched in time (chirped in frequency) then amplified and finally re-compressed. For more details about the development of laser pulses, the reader can refer to [28].

The laser-to-target system consists of oscillator, amplifiers, propagation an oscillator devices, a target system and diagnostics. The purpose of this system is to deposit energy in an appropriate time interval. The laser input to the target must be well controlled, repeatable and predictable, in order to study the laser-target interaction physics or to operate laser-induced plasma devices. To investigate the laser-target interaction, physical quantities of the target such as plasma density and temperature, x-ray production, nuclear reaction yields, particle acceleration, shock waves, heat waves, etc. are usually measured. The components of a laser system are :

- ◇ The **oscillator** that creates the laser pulse with output energy of about $10^{-3} - 10^{-1}$ J. The output energy of the oscillator is kept small in order to control laser pulses.
- ◇ The **beam expander** (telescope) system magnifies the laser beam radius emerging from the oscillator and direct it into the amplifiers.
- ◇ The **amplifiers** amplify the oscillator pulse to energies in the domain of $10 - 10^5$ J. Thus, the amplifier gains are in the range $10^4 - 10^8$. In order to obtain the maximum energy, one requires about 10 amplifiers in series. The diameter of amplifiers increases from about 1 cm to about 50 cm, in order to avoid glass damage, while increasing the energy in the beam. Megajoules lasers are now operating in France (LMJ) and USA (NIF).
- ◇ The **isolating elements** prevent target specular reflections returning and damaging the oscillator. These oscillators prevent also the amplifiers from self-oscillating making resonances between target and one of the optical surfaces. With a high amplification gain as seen before, the smallest reflection from the target through the amplifiers can totally damage the oscillator and many other small optical components at the beginning of the laser line.
- ◇ **Frequency conversion** (optional).
- ◇ **Mirrors and final focusing optic** (lens or parabola), directs the light along the line and focus it into the target.
- ◇ **The target** that can be a solid, a gas jet, a plasma, etc...
- ◇ The **diagnostics** which analyze the laser beam and measure the parameters of the interaction of laser light with the target.

In strongly ionized plasmas ($\Xi < 1$, or *kinetic* plasmas) is the usual domain of laser plasma interaction studied in this manuscript. It is worth noting however that deeply inside the target, denser and colder, degeneracy effects can play an important role. Indeed, at high density, when the distance between atoms and ions is less or comparable to Bohr radius, the Saha equation (Sec. 1 - Eq. 1.16) is not anymore valid due to degeneracy of electrons. The degeneracy can be characterized by the Fermi temperature T_F given by:

$$T_F = \frac{1}{8}\left(\frac{3}{\pi}\right)^{2/3} \frac{h^2}{k_B m_e} {n_e}^{2/3} \simeq 36.5 \left[\frac{n_e}{10^{24}\,\mathrm{cm}^{-3}}\right]^{2/3} \tag{14.7}$$

If $T \gg T_F$, electrons are "classical" while for $T \preceq T_F$, degeneracy effects of electrons have to be taken into account.

Concepts of laser interaction with overdense matter have been presented in the first chapter of the manuscript.

14.1 LULI 2000 Laser Chain

The LULI2000 facility is composed of two Nd:glass laser chains, called North and South, delivering up to 1 kJ pulses at $\lambda_L = 1.053\,\mu m$ in a flat-top spatial profile.

The North chain uses a square temporal pulse profile whose duration can be adjusted from 0.5 to 5 ns, with a rising front of ~ 150 ps.

The South chain have a CPA option and can generate ultra-intense laser pulses of the order of $\sim 10^{19}\,W/cm^2$ with 1 ps duration. The duration can be extended up to 30 ps. The energy is limited to ~ 100 J to avoid any damage in optics and on compressor gratings. The South chain is composed of a Ti:Sa oscillator generating an initial pulse of 250 mW, 100 fs-duration, which is stretched up to a few ns through an Offner stretcher. The output laser pulse, is then sent in a Nd:glass regenerative-amplifier and is amplified by a factor $\sim 10^7$, making about 55 passes through the amplifying medium. The amplifier output is controlled by a combination of a Pockels cell and a polarizer. The preamplified impulsion of 2 nm bandwidth, carrying an energy of 7 mJ, is then amplified again in the main amplifier, made of a combination of rods and disks, to an energy up to ~ 150 J. This high-energy pulse is then compressed by a combination of two multi-layer dielectric (MLD) gratings. The output pulse is then transported and focused at the target chamber center using an $f/4$, $f = 800$ mm off-axis parabola. A set of laser diagnostics, either set-up on every shot or on request, allows to precisely characterize the laser pulse (spectrum, energy at TCC, duration, ...).

The delay between the two laser pulses can be adjusted with a delay line. The repetition rate is limited to 1 shot every 90 minutes because of the required amplifier cooling, mandatory to avoid strong wavefront aberrations. A 10 Hz laser pulse is available for alignment operations. The laser pulses can also be frequency doubled on request. Several other chains, of a moderate energy and intensity, are also available for diagnostic purposes. The so-called blue chain for example delivers ns laser pulses of 80 J of energy.

15 Coil-target manufacturing

The capacitor-coil targets are manufactured from one piece, to avoid unwanted fields at material boundaries. After the laser cutting from 50 µm thin metal films, the obtained planar geometry is then folded by hand - under the microscope - by means of two ordinary painting brushes. The folding is similar to an *Origami* game. Still, the fabrication process allows to fulfill geometric specifications with a precision of ± 10 µm. The dimensions of each target is carefully logged.

All targets are glued on glass needle tips which are themselves fixed in aluminum posts. The final mounting in the target chamber is made by fitting aluminum posts in holed mechanical parts which are assembled to magnetic bases attached to a set of manual stages allowing 3D translation and rotation in any direction. This mechanical design allows a fast shot-to-shot change of targets.

16 B-dot probes

16.1 Single strand loops

Magnetic field probes known as B-dot probes or pick-up coils are composed of a loop of conductive material. The name "B-dot" came from the mathematical dot notation for the time derivative of B : $\dot{B} = \frac{dB}{dt}$. B is the induction of the magnetic field (or magnetic field density) in units of T, which is linked to the magnetic field H in units of A/m by the magnetic permeability μ_0 ($B = \mu_0 H$). The loops considered here are small respect to the measured wavelength (less than one tenth). When a plane electromagnetic wave is incident on a loop (see Figure 16.1), an open circuit voltage V_0 develops across the loop terminals, denoted 1 and 2 in Figure 16.1.

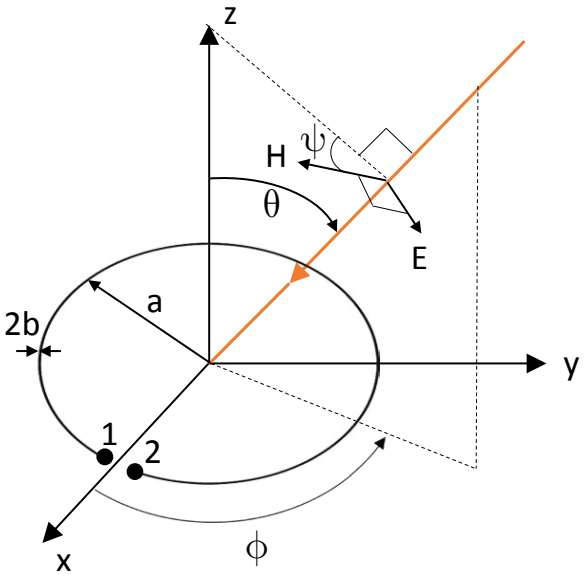

Figure 16.1 – Plane electromagnetic wave incident on a loop.

The induced voltage is proportional to the encircled area and to the time derivative of the magnetic field according to :

$$V_0(t) = \vec{A}_{\text{eq}} \cdot \mu_0 \frac{d\vec{H}(t)}{dt} = \vec{A}_{\text{eq}} \cdot \frac{d\vec{B}(t)}{dt} \tag{16.1}$$

Assuming a circular loop of radius a, Eq. 16.1 rewrites :

$$V_0(t) = \pi a^2 \cdot \frac{dB(t)}{dt} \cos\psi \sin\theta \tag{16.2}$$

A circuit containing a loop to detect the magnetic field must be terminated by a load over which the voltage can be measured by an oscilloscope or corresponding equipment. Figure 16.2 shows an

equivalent circuit where Z_{in} is the input impedance of the loop and Z_{load} is the load impedance.

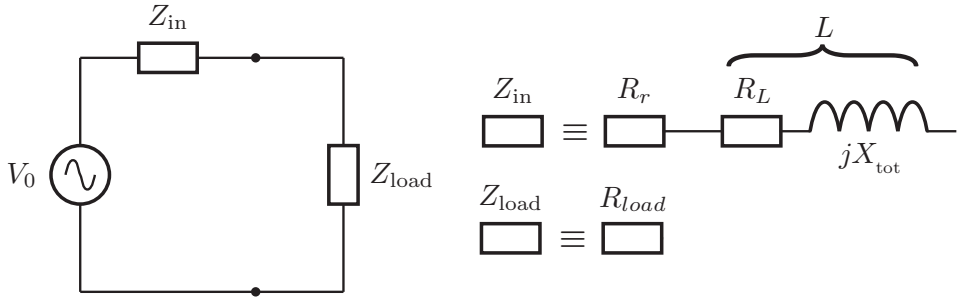

Figure 16.2 – Equivalent circuit of B-dot probe.

The voltage across the load is given by voltage division of the open-circuit voltage according to :

$$V_{\text{load}}(f) = V_0(f)\frac{Z_{\text{load}}(f)}{Z_{\text{in}} + Z_{\text{load}}} \tag{16.3}$$

The input impedance Z_{in} is the sum of the loop resistance and the loop reactance. The loop resistance itself is the sum of the radiation resistance R_r and the loss resistance R_L, while the reactive losses is the total inductive reactance of the loop X_{tot}. Eq. 16.3 can be thus rewrites as :

$$V_{\text{load}}(f) = V_0(f)\frac{Z_{\text{load}}(f)}{R_r + R_L + Z_{\text{load}}(f) + jX_{\text{tot}}(f)} \tag{16.4}$$

For a B-dot loop sensor of a size much smaller than the measured wavelength and terminated by a 50 Ω impedance, the main loss can be shown to be inductive. This is exemplified by Figure 16.3 which shows the ratio V_{load}/V_0 for different total loop inductances ignoring resistive losses in the sensor and having a purely resistive 50 Ω termination. In the case the frequency of the field measured is enough

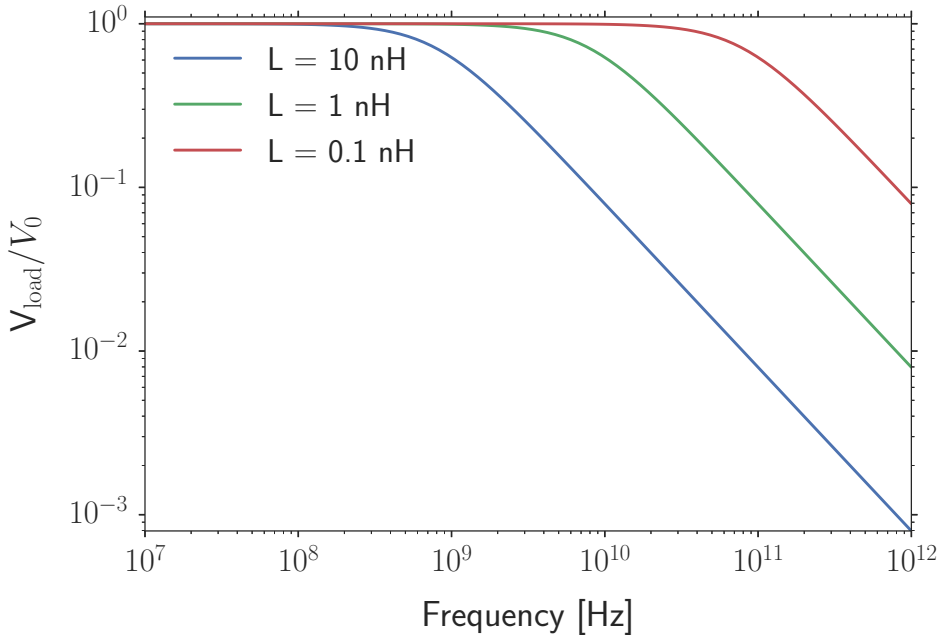

Figure 16.3 – Reactive losses for different inductances.

low that the inductive losses can be ignored ($X_{\text{tot}}/R_{\text{load}} \ll 1$), the load voltage is equal to the open circuit voltage. It is called the differentiating mode of the sensor where the Eq. 16.1 is valid. The magnetic field component normal to the loop is then obtained by integration of the load voltage signal :

$$B(t) = \frac{\int V_{\text{load}}(t)dt}{A_{\text{eq}}} \tag{16.5}$$

In a case of a purely sinusoidal voltage at frequency f_0 the previous equation writes :

$$B(t) = \frac{V_{\text{load}}(t)dt}{2\pi f_0 A_{\text{eq}}} \tag{16.6}$$

At higher frequencies ($X_{\text{tot}}/R_{\text{load}} \gg 1$), the sensor operates in its self integrating mode. The magnetic field is then proportional to the voltage signal:

$$B(t) = \frac{V_{\text{load}}(t)}{A_{\text{eq}}} \frac{L_{\text{tot}}}{R_{\text{load}}} \tag{16.7}$$

Between these pure modes, the sensor operates in its transitional mode ($X_{\text{tot}}/R_{\text{load}} \sim 1$) and the magnetic field is obtained by:

$$B(t) = \frac{V_{\text{load}}(t)}{2\pi f_0 A_{\text{eq}}} \sqrt{\left(\frac{2\pi f_0 L_{\text{tot}}}{R_{\text{tot}}}\right) + 1} \tag{16.8}$$

16.2 Cylindrical loops

To avoid having a large inductive signal loss in loop sensor, the inductance can be reduced by extending the loop in its axial direction and form a cylinder [13, 14]. The inductance of a very long cylinder, considered as a solenoid with a small thickness is given by [13]:

$$L_{\text{cyl}} = \mu_0 \frac{\pi a^2}{h} \tag{16.9}$$

where h is the length of the cylinder and a is its radius. For shorter coils or coils of non negligible thickness, Eq. 16.9 has to be multiplied by a correction factor K_L [143]. The correction factor is a function of the length to diameter ratio of the outer/inner ratio. In Figure 16.4, we plot the correction factor K_L for a short-coil with outer/inner radius ratio equals to 1. In that case, the correction factor writes :

$$K_L = \frac{4}{3\pi} \frac{1}{\kappa'} \left[\frac{\kappa'^2}{\kappa} \left(K(\kappa^2) - E(\kappa^2) \right) + E(\kappa) - \kappa \right] \tag{16.10}$$

with $\kappa = \dfrac{1}{\sqrt{1 + (h/2a)^2}}$, $\kappa' = \sqrt{1 - \kappa^2}$ and K and E are respectively the complete elliptic integral of first and second kind. For the influence of the outer/inner ratio over the correction factor, see [143] for reference.

By requiring the cylindrical sensor to have time constant τ, or an upper 3 dB frequency $f_{3\,\text{dB}}$, a condition for the induction is obtained:

$$L_{\text{cyl}} = R_{\text{load}} \tau = R_{\text{load}} \frac{1}{2\pi f_{3\,\text{dB}}} \tag{16.11}$$

Introducing the correction factor into Eq. 16.9, and combining with Eq. 16.11, we obtain:

$$\mu_0 \frac{\pi a^2}{l} K_L = R_{\text{load}} \tau = R_{\text{load}} \frac{1}{2\pi f_{3\,\text{dB}}} \tag{16.12}$$

The response of the loop itself is limited by the rise time, given by:

$$t_r = \frac{2\pi a}{c} \tag{16.13}$$

and represents the time it takes for an electromagnetic wave to travel around the loop. This means that the loop itself has a maximum frequency response given by Eq. 16.22. An optimum situation would be if the maximum frequency of the loop based on the transit time and the frequency limitation of the inductance and termination were equal. Combining Eq. 16.12 and Eq. 16.22, the expression found is:

$$\mu_0 \frac{\pi a^2}{l} K_L = R_{\text{load}} \tau = R_{\text{load}} \frac{1}{2\pi \dfrac{\sqrt{2}}{4t_r}} = R_{\text{load}} \frac{4a}{\sqrt{2}c} \tag{16.14}$$

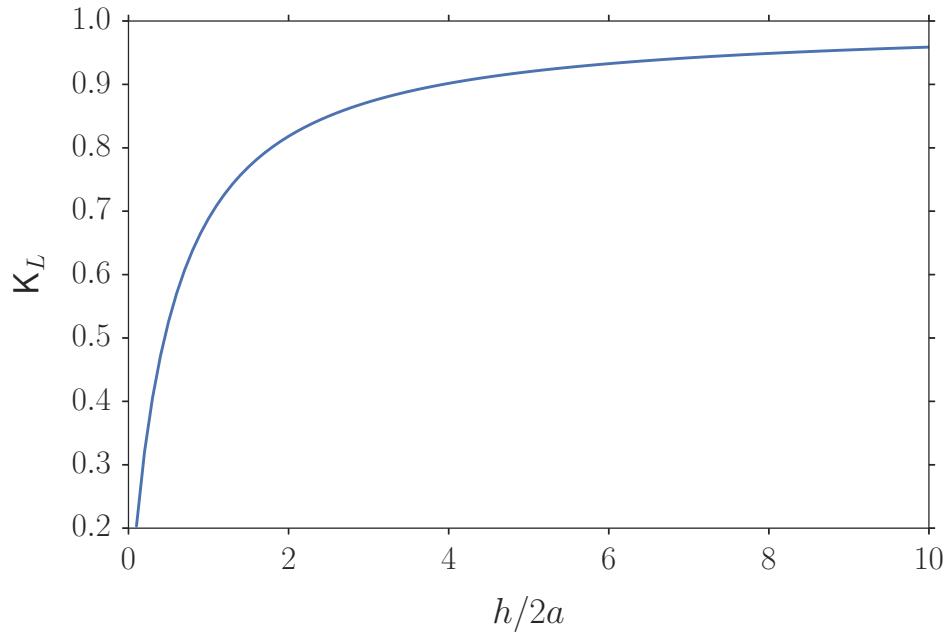

Figure 16.4 – Inductance correction factor K_L for a short coil.

The Eq. 16.14 can be put in the form:

$$\frac{l}{a} = \frac{K_L \mu_0 c \pi \sqrt{2}}{4 R_{\text{load}}} \tag{16.15}$$

A 50 Ω transmission line matching the load impedance ($R_{\text{load}} = 50\,\Omega$) and a correction factor $K_L = 0.9$ gives a ratio $l/a \approx 7.5$, assuming a negligible thickness of the solenoid.

The time response given by Eq. 16.13 assumes that the signal is introduced at the center of the cylinder axis. This means that the transit time for a signal is longer if introduced at the farthest point of the cylinder, *i.e.* at one end of the cylinder. The transit time for that signal would be:

$$t_r = \frac{2}{c}\sqrt{(\pi a)^2 + \left(\frac{l}{2}\right)^2} \tag{16.16}$$

which for $l = 0$ is the same relation as Eq. 16.13. The high frequency limit would depend on the cylinder radius and length by:

$$f_{\text{max}} = \frac{\sqrt{2}}{4 t_r} = \frac{\sqrt{2}}{4\frac{2}{c}\sqrt{(\pi a)^2 + \left(\frac{l}{2}\right)^2}} \tag{16.17}$$

Combining Eq. 16.12 and Eq. 16.16 gives a more accurate condition for the size of the sensor given either radius or length:

$$\mu_0 \frac{\pi a^2}{l} K_L = R_{\text{load}} \frac{\frac{2}{c}\sqrt{(\pi a)^2 + \left(\frac{l}{2}\right)^2}}{\pi \sqrt{2} c} \tag{16.18}$$

Solving for the ratio l/a gives:

$$\frac{l}{a} = \sqrt{2}\pi \sqrt{\sqrt{1 + \frac{\mu_0^2 c^2 K_L^2}{8 R_{\text{load}}^2}} - 1} \tag{16.19}$$

The l/a ratio is 6.038 for a 50 Ω load when the transit time for a cylinder is taken from one end of the cylinder.

16.3 Bandwidth of a B-dot probe

The bandwidth of a probe is defined as the frequency at which the measured voltage has dropped 3 dB compared to the open circuit voltage. Using the differentiating mode or self integrating mode expressions (Eq. 16.5 or Eq. 16.7), the error would be 29.3% at this frequency. For the B-dot probe, the 3 dB limit is obtained when:

$$f_{3\,\mathrm{dB}} = \frac{R_{\mathrm{load}}}{2\pi L_{\mathrm{tot}}} \tag{16.20}$$

where R_{load} is the terminating resistance and L_{tot} is the total loop inductance. Eq. 16.20 corresponds to a time constant τ of the sensor given by:

$$\tau = \frac{L_{\mathrm{tot}}}{R_{\mathrm{load}}} = \frac{1}{2\pi f_{3\,\mathrm{dB}}} \tag{16.21}$$

16.4 Rise time and frequency limits

The equivalent frequency of a signal corresponds is given by the rise time of the signal [71, 72]. For a continuous wave the frequency f_{CW}, the time period T and the rise time t_r relate according to:

$$f_{CW} = \frac{1}{T} = \frac{1}{4t_r} \tag{16.22}$$

A sensor that required to have a given fastest rise time t_r needs a 3 dB frequency limit estimated by [71, 72]:

$$f_{3\,\mathrm{dB}} = \frac{\sqrt{2}}{4t_r} \approx \frac{0.35}{t_r} \tag{16.23}$$

16.5 Commercial B-dot probe Prodyn RB-230

The PRODYN B-dot sensors have a half cylinder loop that measures the time rate-of-change of a magnetic field. The sensor design consists of a half cylinder, with a gap structure located in the middle of each of it's two quadrants. The voltage developed across the gap is combined on a parallel-series wiring structure which averages the signal over the loop structure.

In particular, the RB-230 sensor is a cylindrical loop with differential output. The sensing cylinder consists of two half cylinders both connected to a 50 Ω transmission line, yielding opposite signs on the output signals. The sensor is then connected to a *balun* taking the difference of the two signals, increasing the signal and reducing the noise. The sensor is used with a Prodyn Balun BIB100G. The sensor head is encapsulated in a resin that provide breakdown resistance and hardened radiation protection.

The 3 dB frequency limit of the Prodyn RB-230 is 10 GHz corresponding to a rise time of 35 ps using Eq. 16.23. The 3 dB corresponds to a time constant

$$\frac{L}{R} = \frac{1}{\omega_{3\,\mathrm{dB}}} = \frac{1}{2\pi f_{3\,\mathrm{dB}}} = \frac{1}{2\pi 8.5 \times 10^9} \approx 16\,\mathrm{ps} \tag{16.24}$$

The sensing loop head has a diameter of 9.46 mm and a height of 11.7 mm.

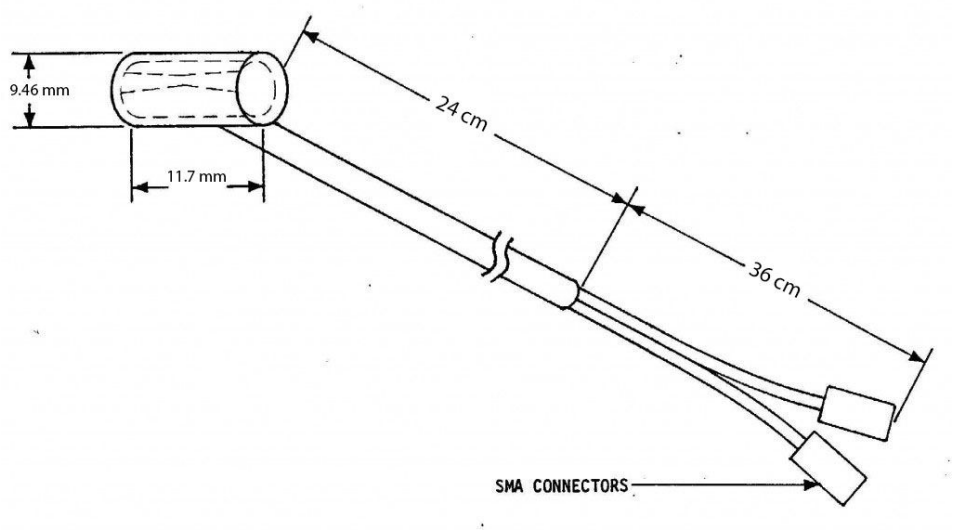

Figure 16.5 – RB-230 free-field radiation-hardened B-dot sensor

16.6 Measurement system

The magnetic field measurement system consist of the B-dot RB-230 sensor, the Prodyn balun BIB-100G, coaxial SMA cables connected to a high bandwidth scope.

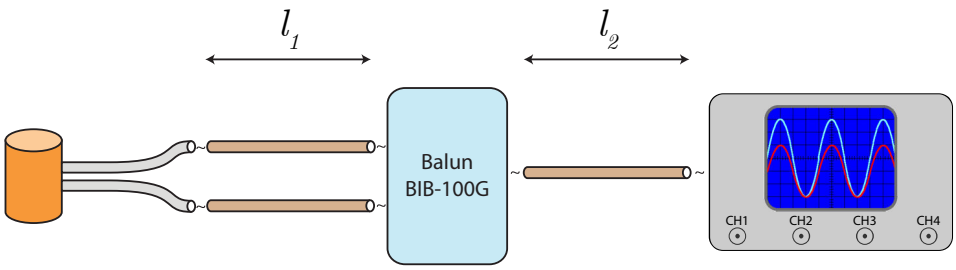

Figure 16.6 – Magnetic field measurement system.

Balun

The balun used together with the B-dot probe is a Prodyn BIB-100G, which accepts the two signals from the sensor and outputs the unbalanced difference signal. The BIB-100G has an attenuation of 8 dB and a 3 dB bandwidth of 250 kHz − 10 GHz.

Coaxial cables

The signal attenuation in the connecting coaxial cables is usually frequency dependent, and must be accounted for in the evaluation of the measurement results. The cables used in our experiments will be detailed on each respective setups. The attenuation in voltage amplitude is given by:

$$G_{\mathrm{dB}} = 10^{-\alpha l/20} \tag{16.25}$$

where α is the attenuation in dB/m and l is the total cable length in m. In Figure 16.6, we identified $l = l_1 + l_2$. It is important that the two cables from the sensor to the balun are of equal length!

Data extraction

Assuming that the B-dot is acting in differentiating mode, the component of the B-field normal to the loop plane $B_\perp(t)$ writes:

$$B_\perp(t) = \frac{\int V_{\text{osc}}}{A_{\text{eq}} 10^{-\frac{8}{20}} 10^{-\frac{\alpha l}{20}}} \tag{16.26}$$

$V_{\text{osc}}(t)$ is the voltage signal as recorded on the oscilloscope. The spectral sensitivity of the measurement is determined by the shortest range of frequencies available for sensor, cables and balun. All of these components can be regarded as filters, each one with its own transfer function. Recorded data are then reduced to field amplitudes applying the inverse transfer functions.

16.7 Calibration of B-dot probes

In this preparation campaign, the goal was to determine a calibration technique for the B-dot probe Prodyn® RB-230. An equivalent area is given by the constructor for this B-dot sensor model. The calibration will confirm this equivalent area.

16.7.1 Experimental setup description

The setup consists of a pulse generator with a known voltage input and a given geometry path for the current. A simplified connection scheme is given in Figure 16.7.

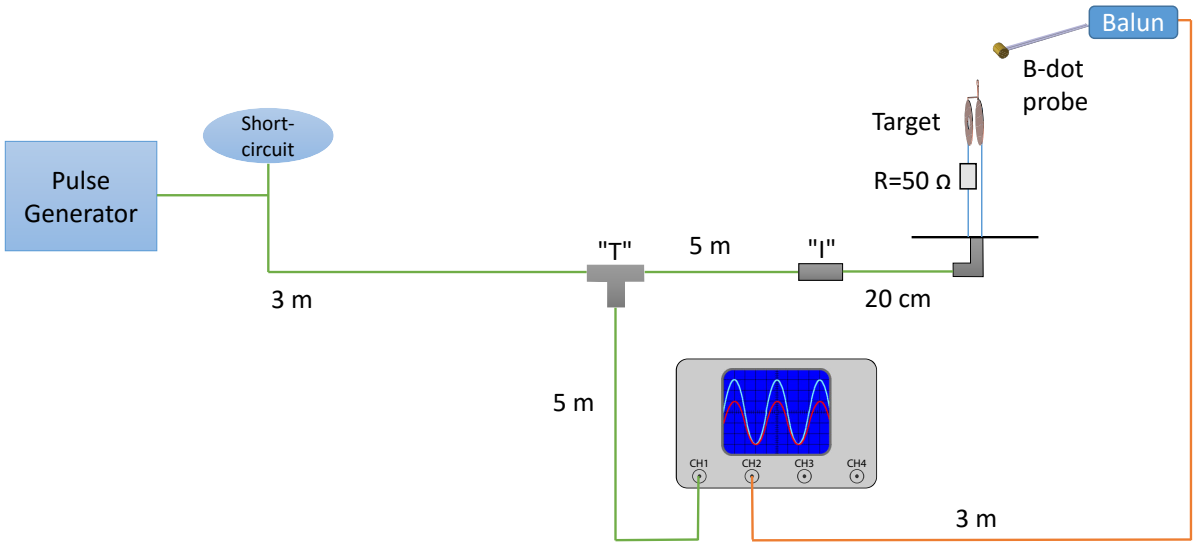

Figure 16.7 – Simplified setup scheme of the preliminary campaign for B-dot calibration at CEA-Cesta

The target was composed by a rectangular ground plate of 15 cm edges from which a bifilar line of 30 cm-height with wires of 500 µm-radius separated by a distance of 1200 µm were connected directly to a capacitor-coil target. The capacitor-coil target specification are extensively described in Sec. 15.

The first step was to correctly characterize the pulse generation and the posterior reflections measured on the time line of the oscilloscope channel. First we made tests without the "short-circuit" on the pulse generator and the target was disconnected from the ground plate's connection. The results in Figure 16.8 show a first reflection which is consistent with the reflection on the generator. The expected value for the signal speed is 2/3 of speed of light. The additional cable length for the reflection on the generator is $\approx 2 \times 3\,\text{m} = 6\,\text{m}$. The time offset is then calculated for the first reflection to be 30 ns, which is in good agreement with the 33 ns measured. For the second reflection, the additional cable length is $\approx 2 \times (5\,\text{m} + 20\,\text{cm}) = 10.4\,\text{m}$. The calculated time offset for this second reflection is 52 ns also in good agreement with the 48 ns measured. The measurements with

the short circuit connected on the generator are shown in the right panel of Figure 16.8. The short-circuit obviously does not change the speed of signals and time offsets are similar : 31 ns for the first reflection and 48 ns for the second reflection. The role of the short-circuit is to have shorter pulses with Gaussian-like shape. In conclusion, the referenced speed of signal in this type of coaxial SMA cable is consistent with the measurements.

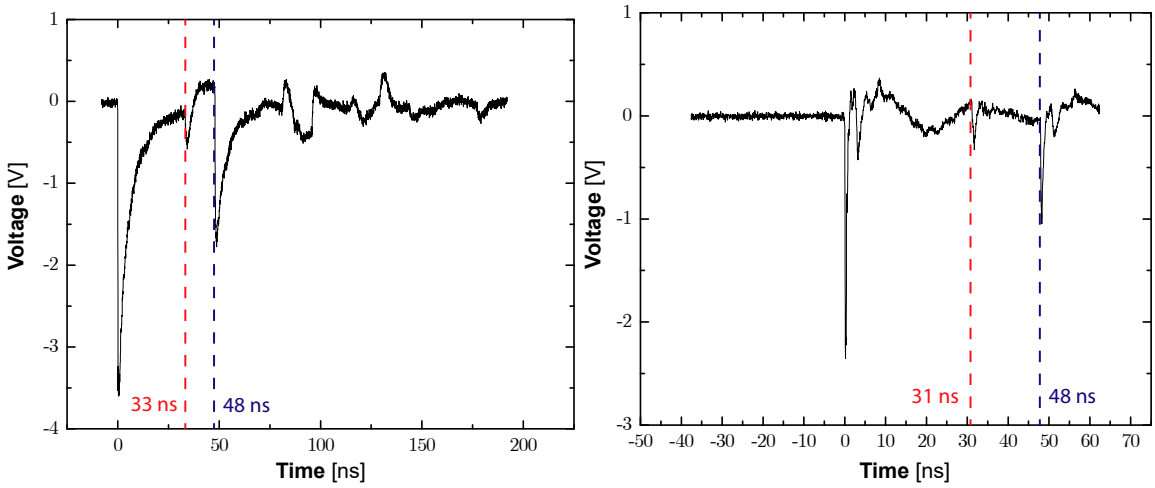

Figure 16.8 – Reflections on the line without short-circuit (left panel) and with short-circuit (right panel) on generator, the target was not connected. The first reflection (red) is consistent with a reflection on the generator and the second reflection (blue) is the reflection after the free 5 m of SMA cable.

In order to know the current input, we needed to put a calibrated resistance in the circuit. A resistance of 50 Ω was placed in the left wire of the bifilar line, below the capacitor-coil target. The total target resistance was measured with a multimeter and at the beginning we found 85 Ω. It was not consistent with the 50 Ω resistance placed in the target circuit. The guess was that the conductive glue - attaching the coil-target to the vertical wires - needed to be submitted once to an high voltage to create a conductive path in the glue. After executing this test, we measured again the total resistance of the target and we found $\approx 50\,\Omega$. This was a first clue that the current was effectively flowing through the capacitor-coil target. A second indication was to measure the reflection of the signal at the target, as shown in the red curve of Figure 16.9. The reflection which occurs at $\sim$ 51 ns is consistent with $\approx 2 \times 30$ cm of additional length from ground plate to target ($\Delta\tau \approx 3$ ns) and result to be far smaller than the reflection of the black curve at ≈ 48 ns. It indicates that almost all the input current emerging at the ground plate efficiently flows through the target.

Pulsed current

One can evaluate the current which is flowing through the target dividing the input voltage by its resistance, measured to be 50 Ω. The input voltage pulse from the generator has a duration of ≈ 400 ps-FWHM and an amplitude of ≈ 5 kV after the short-circuit. For information, the source without short-circuit is 10 kV amplitude and is characterized by an exponential decay time of $\approx$ 5.5 ns. One can see the shape of the source in Figure 16.8 for both situations (with and without short-circuit). For all further measurements, the short-circuit was maintained. It is worth noting that the amplitude is divided approximately by 2 after the "T" connection and the scope channel was attenuated by 60 dB, it means by a factor 1000. Identically, the voltage of the pulse going to the target is also half of the signal amplitude before the "T" connection, in practice we measured an amplitude of 2.3 kV in Figure 16.8. Taking finally into account the reflection of 2×160 V observed at the target connection, we obtained an effective input signal amplitude of ≈ 2 kV. The effective input current is then evaluated to ≈ 40 A.

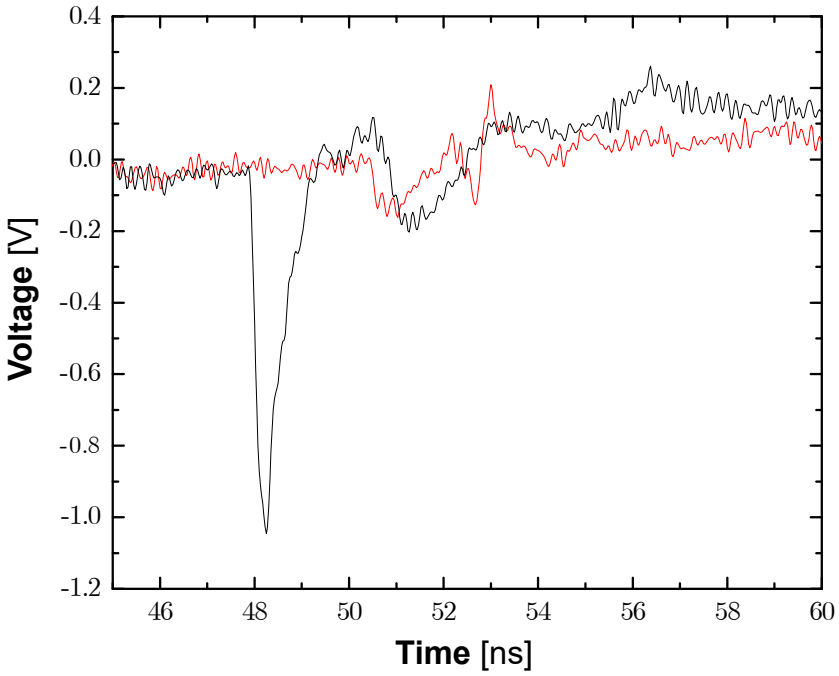

Figure 16.9 – Reflection at the target : the black curve is obtained with target disconnected at ground plate while the red curve is obtained connecting the target. No significant reflections are observed with the target connected, meaning that almost all the current is flowing through the target.

16.7.2 Experimental results compared to magnetostatic simulations

The first series of measurements is made with the B-dot placed at half-height of the two-wires line connecting the ground plate to the capacitor-coil. The line will transmit the total pulsed current from ground plate to target: each wire will then carry half of the current. The B-field due to two infinite wires separated by a gap $2d$ and driving the current I can be derived analytically and writes in the axis between the two wires at a distance r of the wires plane :

$$B = \frac{\mu_0 I d}{\pi(d^2 + r^2)} \tag{16.27}$$

The curves obtained for the B-field are presented in Figure 16.10. The procedure to obtain the B-field from the measured signal on the oscilloscope is extensively described in *Appendix*, Sec. 16. The comparison of the measured B-field by the B-dot probe and the estimation made in Radia is shown in Figure 16.11. The estimation by Radia is made by three different methods of calculation. The blue symbols are obtained estimating the B-field at the center position of the cylinder head of the B-dot. In purple, the B-field is averaged over the height of the cylinder head, and in green, over its total volume. We see that the different methods gives similar results. We can notice that the estimation is better in all cases when the B-dot is probing at a distance from the coil center from 20 cm to 50 cm (mid-field). In near-field, the estimation yields important error bars when calculating the deviation over the volume of the B-dot. Nevertheless, the averaged value is close to the B-field measured by the B-dot probe. A measure at $r = 48$ mm with the B-dot pivoted by 180 ° along its axis give the same result of B, reversed in polarity (see red dashed curve in Figure 16.10).

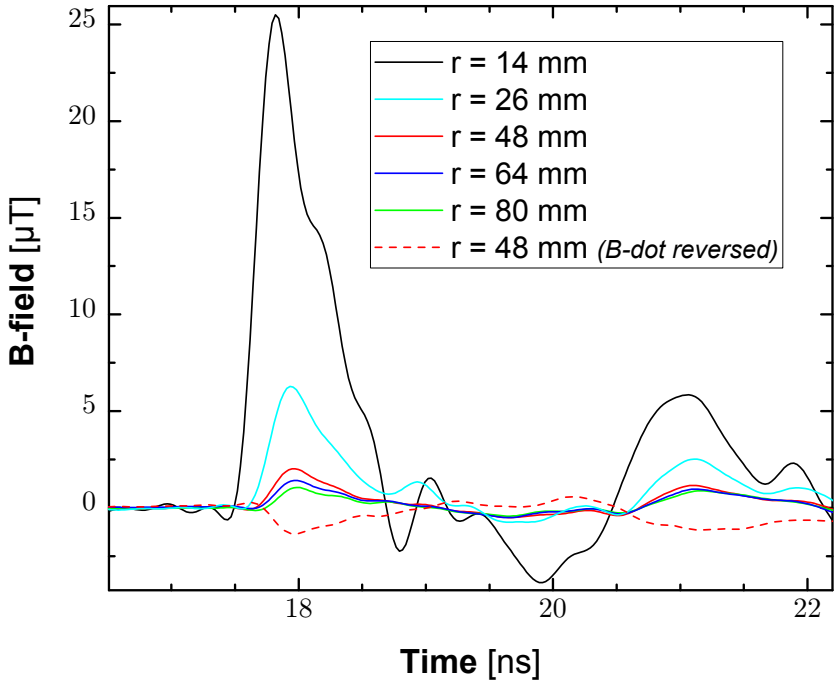

Figure 16.10 – Series of measurements made with the B-dot placed at half height of the two-wires line connecting the ground plate to the capacitor-coil, for labeled distances of the B-dot from the two-wires plane.

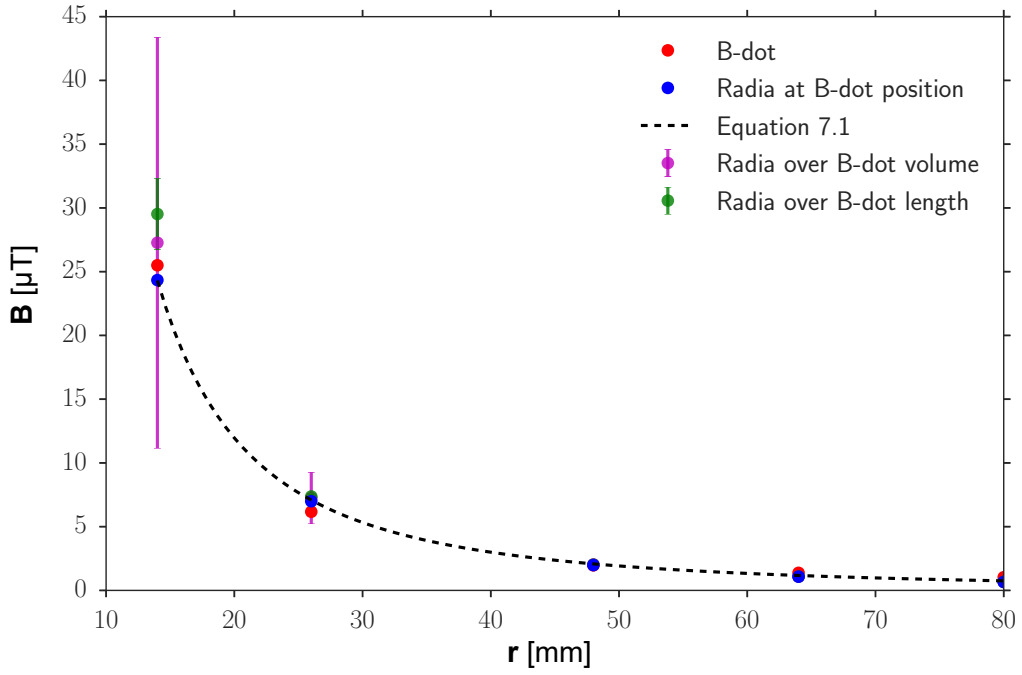

Figure 16.11 – Measurements of the peak B-field by the B-dot for the distances labeled in Figure 16.10 (red circles). It is compared with estimations by Radia for three different methods of calculation, detailed in the text. The dashed line correspond to values calculated from Eq. 16.27.

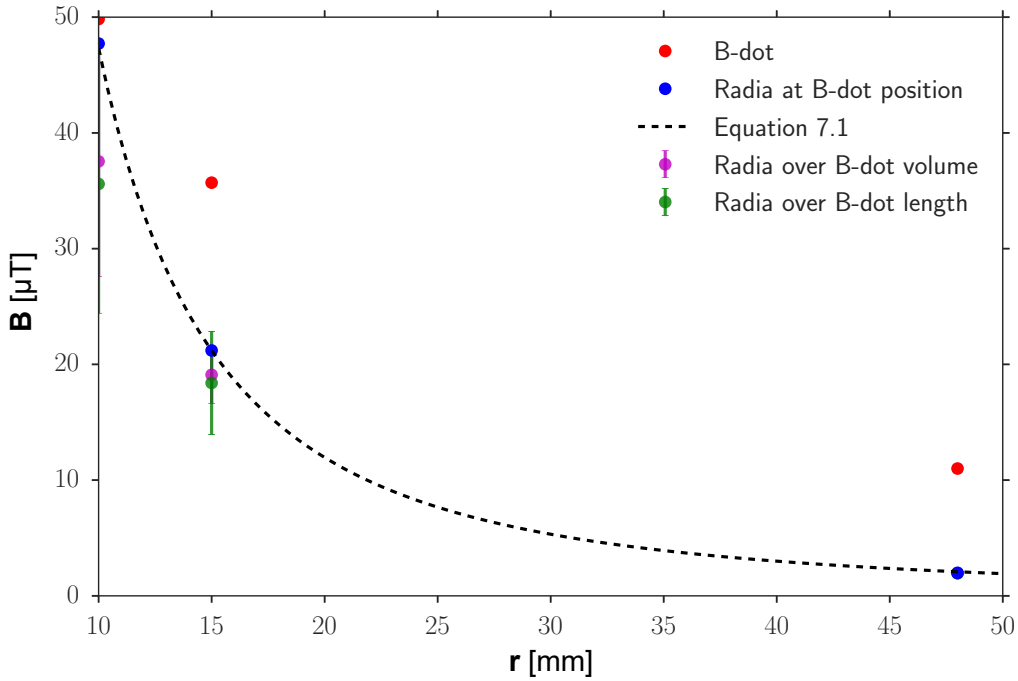

Figure 16.12 – Measurements of the peak B-field by the B-dot along the same axis as in Figure 16.11 but with the B-dot orientated perpendicularly. The comparison with Radia and Eq. 16.27 gives here important errors. The B-dot orientation reveals to be very important.

The second series of measurement is made along the same axis but with the B-dot orientated perpendicularly. The component of the B-field along B-dot axis is very low and we suspect that the measured B-field will be given by the predominant component of the B-field at the B-dot position. The results are shown in Figure 16.12. One can note that the B-dot measurement in that case is in the same order of magnitude with the calculated value by Radia, but the discrepancies are very high. It is then important to orientate the B-dot along the major component of the B-field. Indeed, the equivalent area given by the B-dot constructor is given for the B-field normal to cylinder section. The resulting equivalent area and transfer function of the B-dot when it probes a B-field with a major component not anymore normal to the B-dot section is unknown.

An equivalent measure was made with the B-dot oriented vertically at $r = 48\,\text{mm}$ and yields a B-field value of $1.5\,\mu\text{T}$. This value is surprisingly closer to the measured $B = 2\,\mu\text{T}$. To conclude the B-dot should be oriented preferentially as resumed in Figure 16.13.

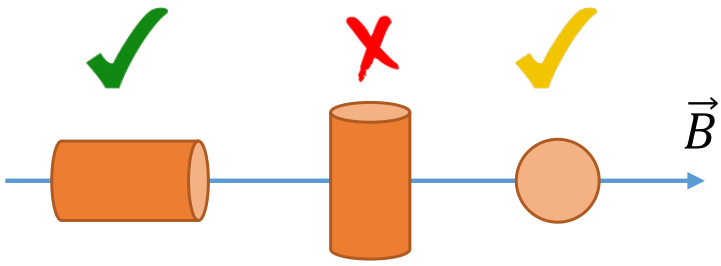

Figure 16.13 – Summary of the orientations of the B-dot giving consistent results with Radia calculations. In experiments, one has to care about orientating the B-dot axis along the major component of the B-field.

The last series of measurements is made at the height of the loop of the coil target, as it will be done in the laser-driven experiments. We will scan the distance from the loop in the plane of the two wires line, forming thus an angle of 22.5 ° respect to the loop plane. In this region of space, the B-field contribution of the two wires line is smaller than from the capacitor-coil target. The contribution ratio of the two wires line in respect with coil target is shown in Figure 16.14.

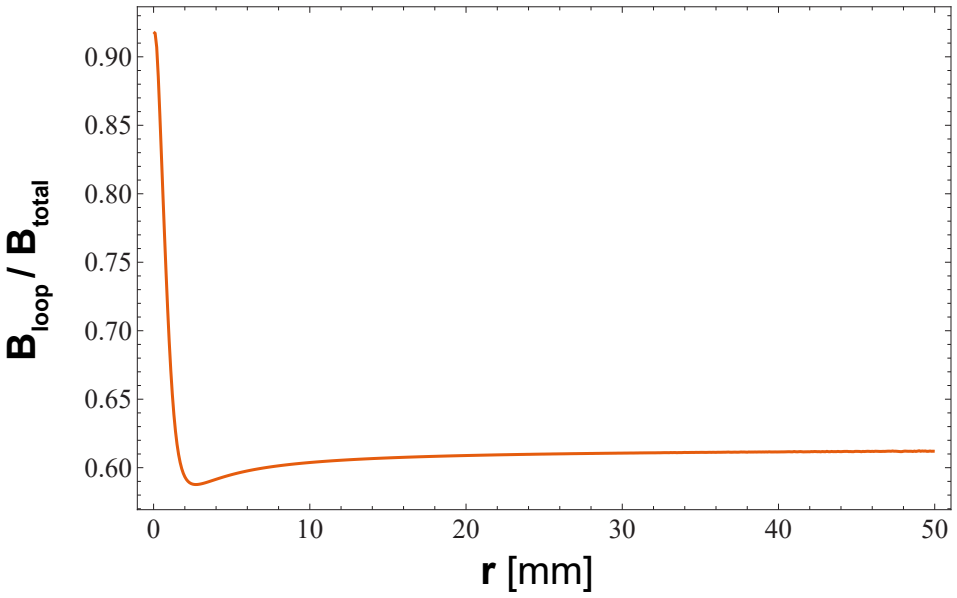

Figure 16.14 – Magnetic field contribution of the loop divided by total magnetic field calculated along a line of 22.5 ° above loop's equator. The contribution of the loop is predominant at close distances and then drops to $\approx 62\,\%$.

The results of the Radia calculation compared with B-dot measurements are shown in Figure 16.15. Again, the calculation over B-dot volume is yielding important error bars in the near-field. As the calculation over B-dot length give consistent results for near-field and mid-field, with reasonable error bars, we will privilege this method for reference.

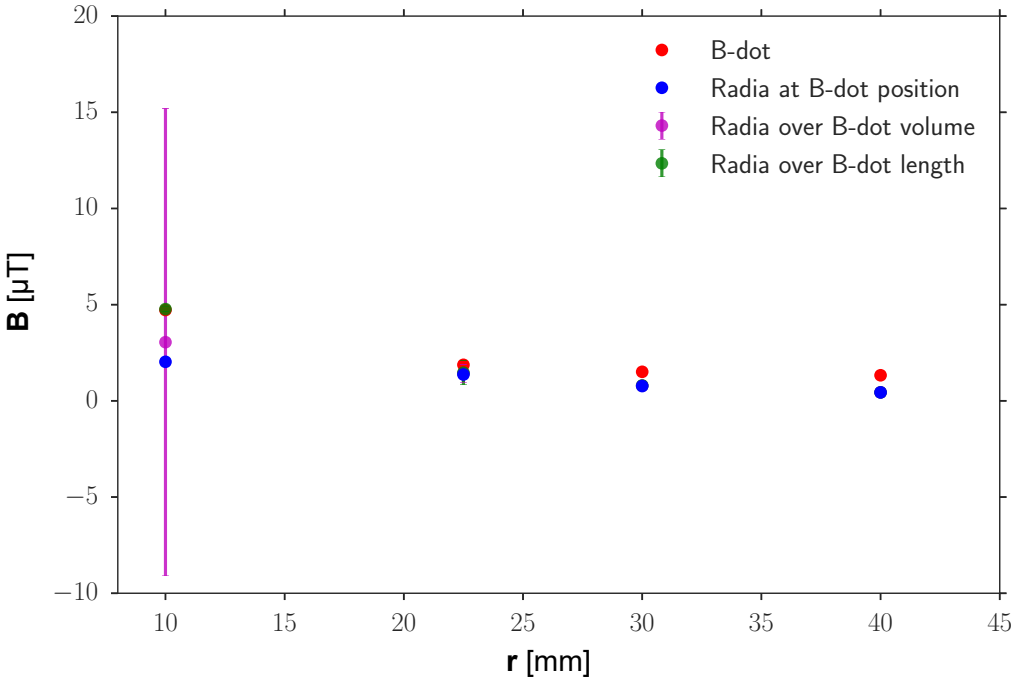

Figure 16.15 – Measurements of the peak B-field by the B-dot along a line of 22.5° above loop's equator. Calculating the B-field from Radia over B-dot length yields consistent values for distances $\leq 30\,\text{mm}$. The errors found at bigger distances, in addition to complexity added by the two-wires line contribution, may also emerge from some imprecision in positioning the B-dot, since angle errors increases with distance.

16.8 Time synchronization of B-dot signals

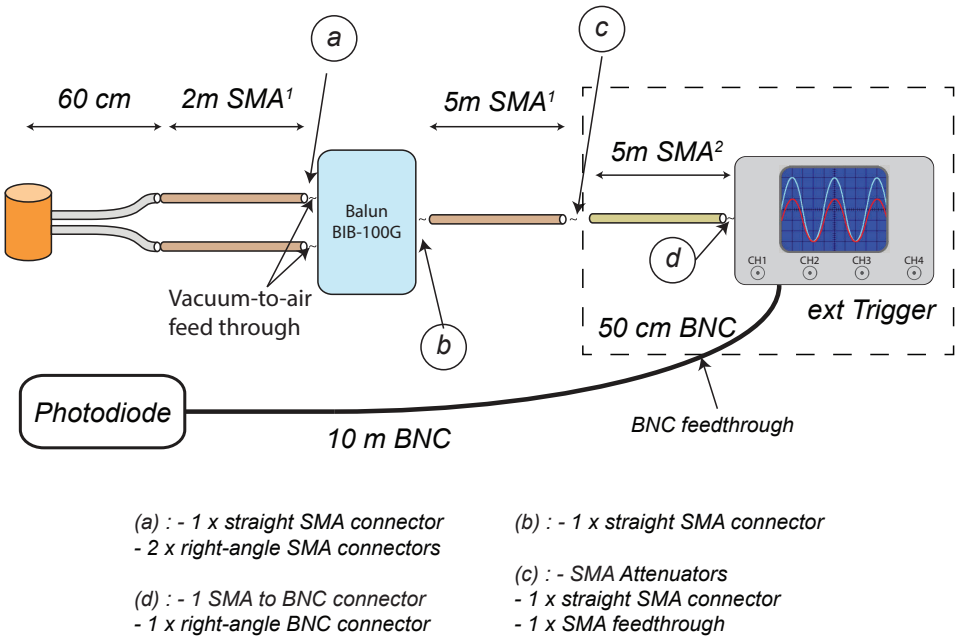

Figure 16.16 – Detailed B-dot measurement system for the 2^{nd} experiment.

B-field production initial instant has been consistently measured as synchronized with the beginning of the laser irradiation. In this purpose, a photodiode was put at a window of the interaction chamber and connected to the oscilloscope. To know exactly the delay imposed by cables, a small setup was made in the 2^{nd} experiment to calculate the propagation time through cables and connectors for an impulsion of 1.2 ns FWHM duration, generated by a pulse generator at a frequency that is thus close to B-dot signals ($\sim$ 1 GHz). Each component of the measurement system (see Figure 16.16) was characterized by this method, as summarized in Tab. 16.1. There was two types of SMA cables (different kind of shielding and cable section). The type called [1] has a typical signal propagation velocity of 70 % of the speed of light and a resulting delay of 4.8 ns/m. For the type [2], the signal propagation velocity is 83 % the speed of light and a resulting delay of 4 ns/m. The B-dot itself is a SMA propagation medium (similar to type [1] and one can expect an attenuation over 60 cm of B-dot length equals to approximately 1 % and an additional delay of $\approx$ 2.4 ns. A measurement of a back and forth signal propagation through the measurement system till the B-dot input is shown in Figure 16.17. The total propagation over this distance divided by two yields a delay of 54.4 ns and an attenuation of 69.4 %. A comparison with the sum of individual parts of this system excluding small connectors and B-dot (Tab. 16.1) shows that the connectors induce a delay of $\approx$ 200 ps and an attenuation of $\approx$ 5 %, that is a negligible contribution in respect to other parts. Finally, for the calibration of the measurement system attenuation of the 2^{nd} experiment, one has to consequently take into account an additional $\approx$ 2.5 dB.

With all this collected data (Tab. 16.1), one can estimate the instant time for the B-field production in the time-frame of the oscilloscope and compare it with the B-dot signal growing instant. Here in the 2^{nd} experiment, the B-dot is placed at 7 cm far from interaction point (the time for the EM signal to reach the B-dot is $\approx$ 200 ps). Besides, the photodiode is placed at a window which is 1.5 m distant from interaction point. There is a time-of-flight difference of 4.8 ns at the speed of light between the two positions. Finally, the estimated instant for the growing B-field on B-dot channel is then estimated to be visible 1 ± 0.2 ns before the photodiode triggers on oscilloscope time-frame. This estimation is successfully compared with the experimental delay on signals of 0.98 ± 0.1 ns. All the B-dot results shown in Figure 8.8 (Part II) are then corrected from instant time shift to get $t = 0$ as the interaction instant.

Item	Att.	Delay [ns]
2 m SMA[1]	4 %	9.6 ns
5 m SMA[1]	10 %	23.9 ns
5 m SMA[2]	6.5 %	20.1 ns
Balun	60.2 %(8 dB)	0.6 ns
Estimated TOTAL (without connectors and B-dot)	67.8 %	54.2 ns
Measured TOTAL (without B-dot)	69.4 %	54.4 ns
B-dot	1 %	2.4 ns
7 cm at c		0.2 ns
TOTAL B-dot chain (all)	70.4 %	57 ± 0.1 ns
10 m BNC	23 %	50.5 ns
50 cm BNC	1.2 %	2.5 ns
1.5 ± 0.03 m at c		5 ± 0.1 ns
TOTAL photodiode chain		58 ± 0.1 ns
Delay B-dot/Photodiode		1 ± 0.2 ns

Table 16.1 – List of attenuations (1-X_{dB}) and delays for the elements of the measurement system.

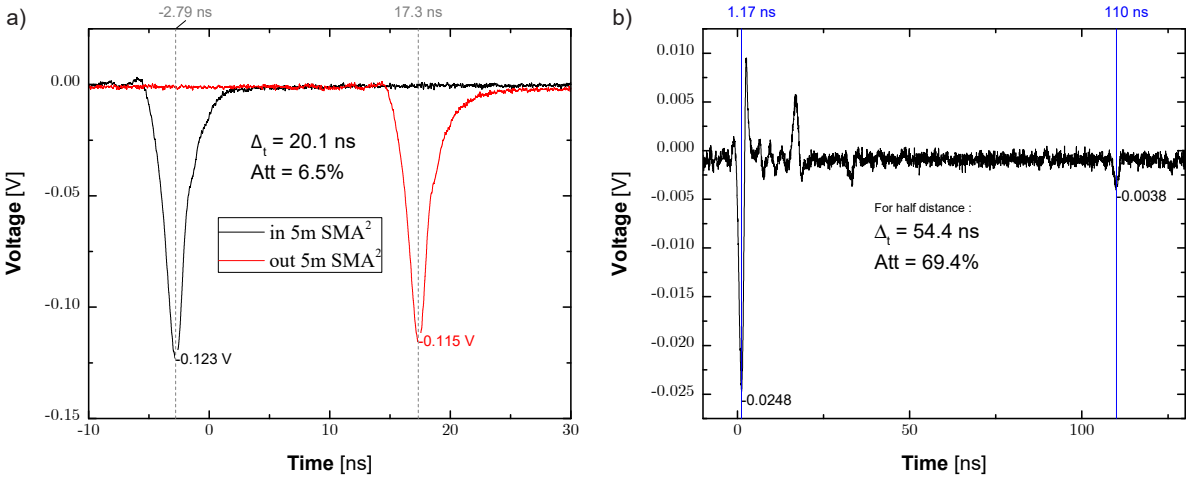

Figure 16.17 – a) Measure example for 5m SMA[2] cable: the red curve is obtained after one propagation of the input signal (black curve) through the cable. Equivalent measure has been done for the different items of the measurement system. **b)** Back and forth propagation over the measurement system till B-dot probe input (the B-dot probe itself is thus excluded): the delay and attenuation are given considering half distance, *i.e.* for one single propagation.

17 Magnetostatic code ©Radia

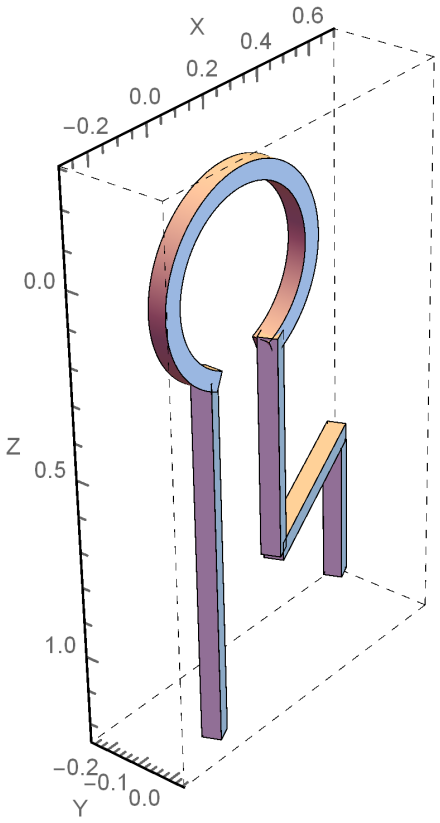

Figure 17.1 – 3D Geometry of the coil part (top-part) of a typical capacitor-coil target (so-called *B-loop*), as coded in Radia and displayed in Mathematica. Scale units are in mm.

The Radia software is a package of ©Mathematica programming environment. It was designed for solving physical and technical problems one encounters during the development of Insertion Devices for Synchrotron Light Sources. In particular, it was developed by O. Chubar, P. Elleaume and J. Chavanne [50] for the European Synchrotron facility (ESRF) in Grenoble, France. However, it can also be used in different branches of physics, where efficient solutions of 3D boundary problems of Magnetostatics are needed, as it is the case for current carrying generation of magnetic fields in solid targets.

The Radia package is essentially a 3D magnetostatics computer code optimized for Undulators and Wigglers. In Radia, a special attention is paid to the accurate and fast computation of the magnetic field and the field integrals along a line. For this reason, the code is also specially optimized in our case for integrating the trajectory of charged particles in a B-field distribution created by current carrying elements.

Besides, Radia can solve a variety of problems with linear and nonlinear, isotropic and anisotropic magnetic materials (such as iron and permanent magnets, respectively). For the work presented here, the use was limited to the capability of solving B-field from current-carrying elements of different shapes.

The code has been extensively benchmarked with respeect to a commercial finite element code. All ESRF Insertion Devices built since 1992 have been designed using this code or its earlier versions. Many predictions made by Radia concerning the magnetic field and field integrals were verified on real insertion devices after manufacture.

Computation Method

The method used in Radia belongs to the category of boundary Integral Methods (BIM) and differs strongly from the Finite Element Methods (FEM). Volume objects are created, material properties are applied to these objects. Each object can be subdivided into a number of smaller objects for which one tries to solve for the general problem in terms of magnetization. The solution is performed by building a large matrix in memory which represents mutual interactions between the objects, the so-called Interaction Matrix. The final magnetization in each small object is obtained iteratively, by a sequence of multiplications of the Interaction Matrix by instant magnetization vectors, taking into account the material properties. This is called the Relaxation procedure in the program. Concerning the computation of the field due to the conductors, the computation is using the Biot-Savart law. In this approach, one applies some kind of segmentation to the field producing objects (typically iron). For current carrying objects only, no relaxation procedure is needed and material properties are useless. In any case, contrary to FEM approach, one does not need to mesh the vacuum. This has a number of important consequences:

- ◇ Geometries opened to infinity are more easily simulated
- ◇ The number of elements required for a given precision is reduced, and consequently the CPU time required.
- ◇ Once the Relaxation is done (or directly after object declaration in the case without relaxation), the magnetic field and field integrals can be computed anywhere in space whatever the distance to the field-producing objects.
- ◇ Field integrals can be computed using analytic formulas. This might be one of the most significant advantages of the Radia code over a FEM code.
- ◇ In the case of field producing objects by magnetization, such as iron, accurate predictions of the magnetic field integrals are possible with Radia (even-through it may require a large segmentation of the iron), which are practically impossible with FEM codes.
- ◇ Accurate geometry creation (respect to accurate meshing for FEM) and solving criteria are much simpler. In fact, a hybrid undulator can be created and solved using no more than 20 lines of Mathematica code. However, the versatility of shapes that can be created are intrinsically limited compared to the universality of FEM approach. This is the main drawback when dealing with Radia for coding the geometry of laser-driven targets.
- ◇ The essential drawback of Radia compared to a FEM code is the fast divergence of memory required for a given number of elements. In the present version of Radia, the memory scales proportionally to the square of the number of elements. For example, one roughly needs 50 MB of memory to solve a geometry made of 1000 elements (which roughly corresponds to 20000 elements in a FEM code for a similar precision on the field). This drawback is seriously not an issue with actual computer memory availability, unless the number of elements is huge.
- ◇ Another drawback of Radia is an "artificial" discontinuity in computation of magnetic field inside subdivided iron objects or between geometrically connected current-carrying objects, occurring on the boundary between any adjacent sub-objects.

Implementation Features

The core part of Radia is written in object-oriented C++. The application is interfaced to Mathematica via the MathLink module. Pre and post processing of the field data is done in the Mathematica language. 1D and 2D field plots for example can be directly preformed using the Graphics buit-in features of Mathematica. Geometries can be exported into 3D Mathematica objects for display and rendering in the Mathematica Front-End.

The software is available on the following link web-hosted by the ESRF group :
http://www.esrf.eu/Accelerators/Groups/InsertionDevices/Software/Radia

18 Radiochromic Films (RCF)

Radiochromic films (RCF) are detectors made of plastic-based material which are capable of making dosimetry measurements of the deposited ionization by energetic particles and radiation (electrons, protons, X-rays, etc...). Depending on the required range of measurement for the dose, several types of RCF are available with different chemical composition of the sensitive layer and different thicknesses. Here is the list of ©Gafchromic films one can buy with their dynamic range:

- ◇ HD-V2: $10 - 1000\,\mathrm{Gy}$
- ◇ MD-V3: $1 - 100\,\mathrm{Gy}$
- ◇ EBT-3: $0.1 - 20\,\mathrm{Gy}$

The upper limits defines the saturation doses inherent to the above enumerated types of films. The main advantage of those detectors is the high reliability of the active medium polymerization process and the very high spatial resolution (the manufacter claims 10^4 ppi, which is 2.5 µm resolution [29]). The RCF response has low energy dependence: in [140], they measured it as totally independent for protons energy above $\sim 7\,\mathrm{MeV}$. Other advantage is the very fast scanning procedure and the direct observation by eye which permits to glance instantaneously if the result looks like or not with what was expected. Hereinafter, a table of the atomic composition of the films used in our experiments is provided.

Material	**Thickness**	**Density**	**Composition (Atom%)**									
	µm	g/cm^3	H	C	O	N	Li	Cl	Na	S	Br	Al
HD-v2												
Active layer	8	1.2	58.4	27.9	11.7	0.1	0.6	0.6	0.5			0.3
Polyester film	97	1.35	36.4	45.5	18.2							
MD-v3												
Polyester film	120	1.35	36.4	45.5	18.2							
Active layer	15	1.08	56.8	29.14	7.12	6.94						
Polyester film	120	1.35	36.4	45.5	18.2							
EBT-3												
Polyester film	125	1.35	36.4	45.5	18.2							
Active layer	30	1.2	58.33	29.61	10.79	0.06	0.82	0.19	0.11	0.03	0.06	
Polyester film	125	1.35	36.4	45.5	18.2							

Table 18.1 – Composition data for GafCrhomic film used in this thesis. This table was compiled from different sources: [140, 250]

18.1 Stopping power determination

The way protons and other particles lose their energy when passing through a material is described by the linear stopping power (or linear transfer energy function, LTE).

Proton energy is mainly deposited at the end of the propagation range, in the so-called Bragg peak. This special behavior is explained by the fact that protons lose energy mainly because of Coulomb collisions, whose cross section is proportional to ϵ_p^{-2}, being ϵ_p the proton energy. One can then judiciously associate, in first approximation, an RCF layer in a stack to protons whose Bragg peaks is located at the depth of the considered layer, as shown in Figure 18.1. More the Bragg peak is located deeper in the stack, more its height decreases: it is due to the proton energy lost when traversing the previous layers. Moreover, its width increases because the spreading of proton induce

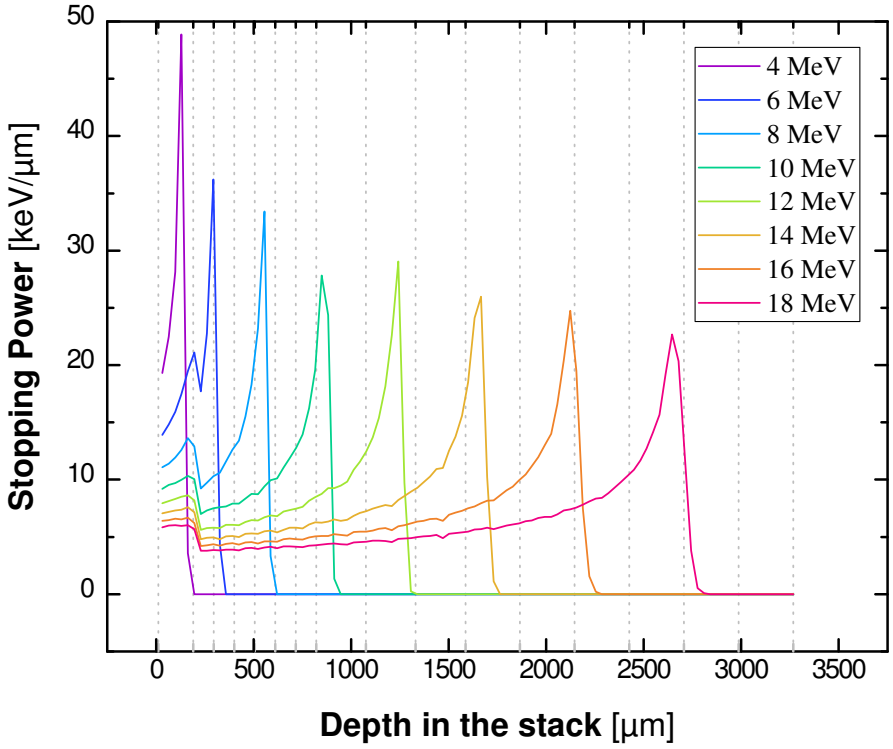

Figure 18.1 – Ionization curves in a typical RCF stack composed of 6×HD/3×MD/6×EBT and a $11 + 180\,\mu$m-thick Al filter in front. The highly localized Bragg peak allows to assign to each RCF layer a well-defined proton energy and probing time. Proton stopping power curves were simulated for different initial proton energies (in legend) using SRIM.

scattering and the trajectories inside the material and the Bragg peak is broadened at slightly different depths [140].

At fist glance, calibrating the RCF stack corresponds to associate to each layer of the stack a proton energy ϵ_p whose Bragg peak is situated in the layer. Different stopping power curves are obtained using SRIM, by modeling the RCF stack used in the experiment and using the atomic composition found in Tab. 18.1.

An accurate RCF stack calibration must take into account that protons deposit a non-negligible amount of energy also in the layers located at lower depth than the one in which they stop at the Bragg peak. Although the energy lost at the Bragg peak is about 4 times the energy deposited in the Bragg peak, the sum of all these contributions actually affects the dose absorbed by each RCF. To calculate the total amount of energy deposited in the i^{th} layer of the RCF stack, the RCF layer response function must be convolved with the proton energy spectrum, which will consider all the energies available in the proton beam [200].
The RCF response function $\epsilon_{loss}(\epsilon_{p,0})$ is simply the energy deposited in the RCF per proton, as a function of the initial proton energy: it can be found by integrating all the stopping power curves over the i^{th} active layer thickness. Accordingly, the total deposited energy on the i^{th} layer, ϵ^i_{dep} is expressed as:

$$\epsilon^i_{dep} = \int_{\text{spectrum}} \frac{dN(\epsilon)}{d\epsilon}\epsilon^i_{loss}(\epsilon)d\epsilon = \int_0^{\epsilon_{\text{cut-off}}} \frac{dN(\epsilon)}{d\epsilon}\int_{x^i-dx/2}^{x^i+dx/2}\frac{d\epsilon^i_{loss}(\epsilon)}{dx}dxd\epsilon \tag{18.1}$$

An example of the RCF response, calculated for the first layer of the stack (*HD1*), corresponding to $\approx 5\,$MeV protons, is shown in Figure 18.2.

It is clear that the major amount of energy is deposited by protons whose Bragg peak is expected to occur in the considered layer. However, more energetic protons also show a non negligible contribution. Lower energetic protons, instead, do not reach the layer because their Bragg peak is located ahead in the stack depth. The deposited energy calculation also demonstrates that a single value of initial proton energy or equivalent probing time cannot be directly associated to the RCF layer. There

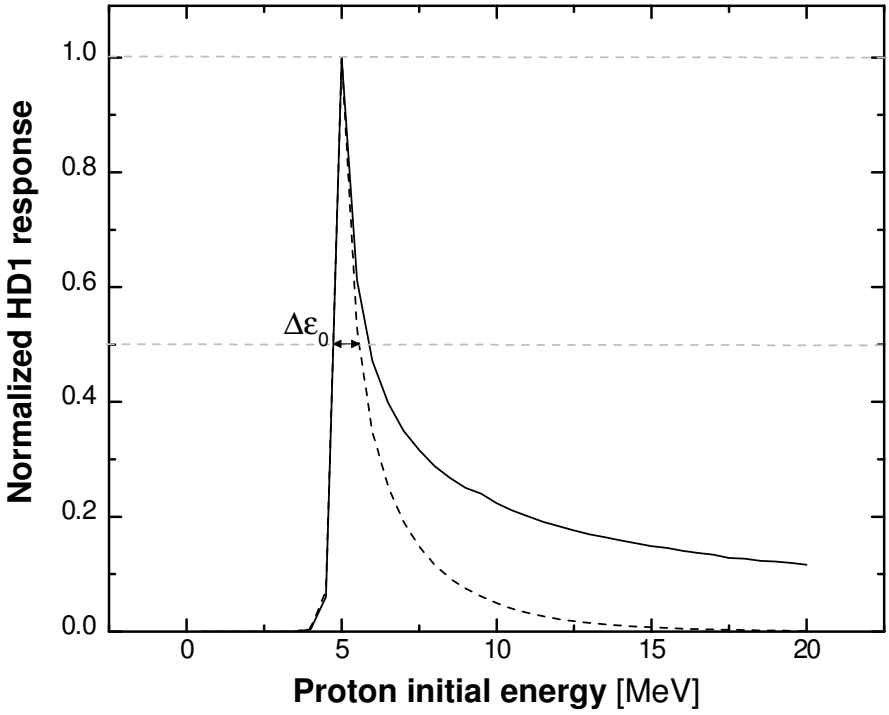

Figure 18.2 – Normalized deposited energy in the first layer *HD1* of a the RCF stack presented in Figure 18.1, as a function of initial proton energy. The solid curve is obtained assuming a flat spectrum and the dashed line for an exponential spectrum with $T_p = 3.3\,\text{MeV}$. For the exponential spectrum, the energy uncertainty $\Delta\epsilon_0$ is reduced.

is an energy determination $\Delta\epsilon_0$ that is assumed to be equal to the FWHM of the RCF response curve. This uncertainty is reduced by considering an exponential spectrum (like the one predicted by the TNSA model) since higher protons contribute less to the energy deposition. As an example, for the curve in Figure 18.2, the associated energy to *HD1* is $5.2 \pm 0.4\,\text{MeV}$ for the exponential spectrum and $5.3 \pm 0.6\,\text{MeV}$ for a flat spectrum. The exponential temperature T_p used for the exponential spectrum has been chosen to fit with PIC simulation (LSP code) of the LULI-Pico2000 (SP) interaction with a 10 µm gold foil, reported in Sec. 5.2.2-Figure 5.3.

18.2 Dose calibration

As seen before, the optical density is mainly related to the absorbed dose. On this basis, one can relate the optical density (OD) measured for one specific scanning wavelength to a certain amount of radiation I_0 and the transmitted part of this radiation, noted I:

$$OD = \log \frac{I_0}{I} \tag{18.2}$$

The calibration of the dose depends on the types of RCF used and on the scanning procedure adopted, so there is no universal calibration curve. The optical density values on RCF imprints are here digitized with an Epson 11000XL Pro flatbed scanner with a transparency acquisition. No software-dependent image correction filters were applied for our scans. The scan is made in our case with mutli-exposure option enabled. The response of the scanner is seen to be perfectly flat along the long-side direction. Along the short side, the scanner answer can vary a bit and decreases slightly on the borders, as seen for the three color channels in Figure 18.3.

This feature can causes an overestimation of film-darkening for measurements made on the borders. It is then important to favor dosimetry scans along the so-called *sweet axis*, where the scanner response is flat.

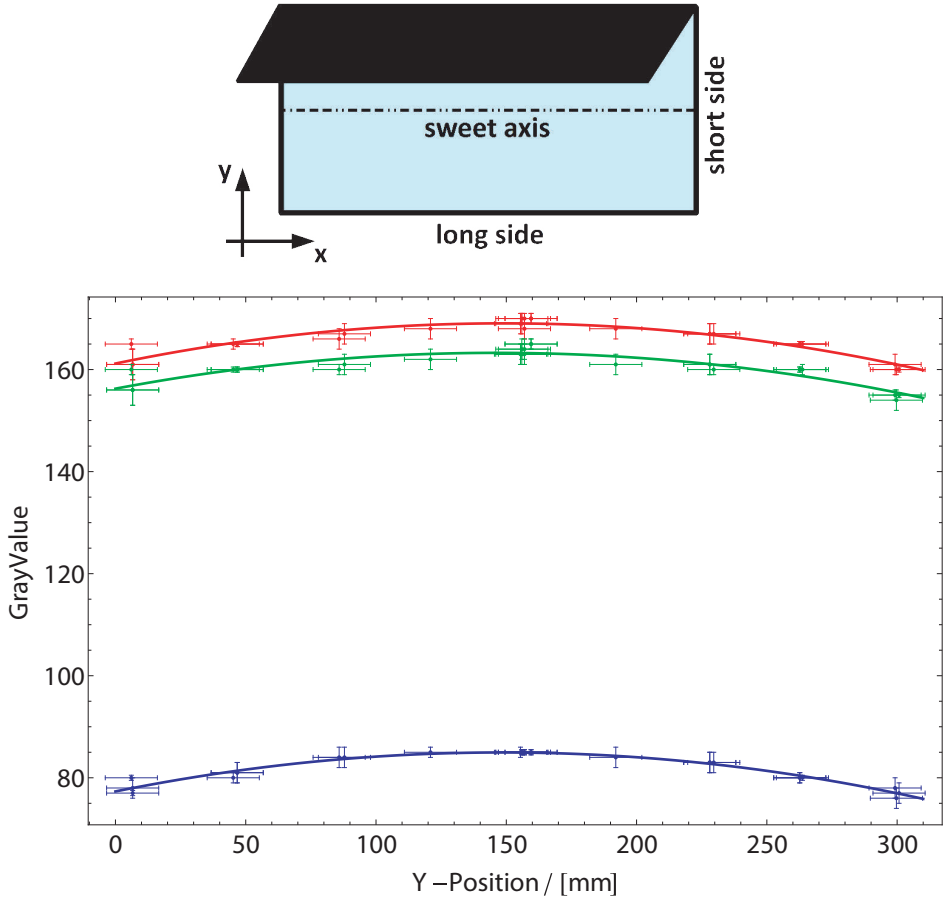

Figure 18.3 – Variation of the scanner answer along the short side of the scanner, with corresponding fit.

Thereafter, it will be presented the calibration curves obtained for the two main types of RCF used in our experiments: *HD-v2* and *EBT-3*. The dose deposition was handled using the medical accelerator of the Bergonie hospital in Bordeaux. Electrons or photons with different energies can be used to deposit the dose in RCF. We compared with one specific dose (10 Gy) between electrons and photons: as expected the film show no evident differences in their answer to either photons or electrons. For the results presented here, electrons with an initial energy of 9 MeV were used. Films are irradiated uniformly using various doses. The uniform irradiation of a flat-top square beam is shaped by a 15 cm $\times$ 15 cm aperture for electrons and a 10 cm $\times$ 10 cm aperture for photons before arriving on the film. The centering of the films relative to the beam is ensured by a cross-hair in every shot, thus the 3 cm $\times$ 3 cm cut films are fully and uniformly irradiated with the specified dose.

As the on-surface active layer of HD-v2 films is directly exposed to the surrounding environment, a measurement in a dry environment using RW3 slab phantoms for pre-stopping was used, instead of water. To keep the same methodology, the other types of films (potentially not affected by water) were also irradiated using the same phantom.

In Figure 18.4 and Figure 18.5 are shown calibration curves obtained respectively for *HD-v2* and *EBT-3* RCF films. The color -channel dependent function $d(g_{\text{channel}})$ links the scanned gray-value g_{channel} to a dose. The function, as proposed by the RCF manufacturer GAFCRHOMIC is of the form:

$$d(g_{\text{channel}}) = c + \frac{b}{g_{\text{channel}} - a} \tag{18.3}$$

The values for c, b and a stay constant for a given film-type scanned under same circumstances. From dose measurements, the inverse function is fitted to data points:

$$g_{\text{channel}} = a + \frac{b}{d - c} \tag{18.4}$$

For calibration, a whole film corresponding to one dose is scanned. This scan delivers a matrix with a gray-value for each color in each pixel. The color channels are processed separately. To obtain a center gray value with an error for each dose, a gaussian peak is fitted to the gray value distribution of one film. Result is a color-channel dependent gray-value for a given dose which corresponds to one data point for the fit.

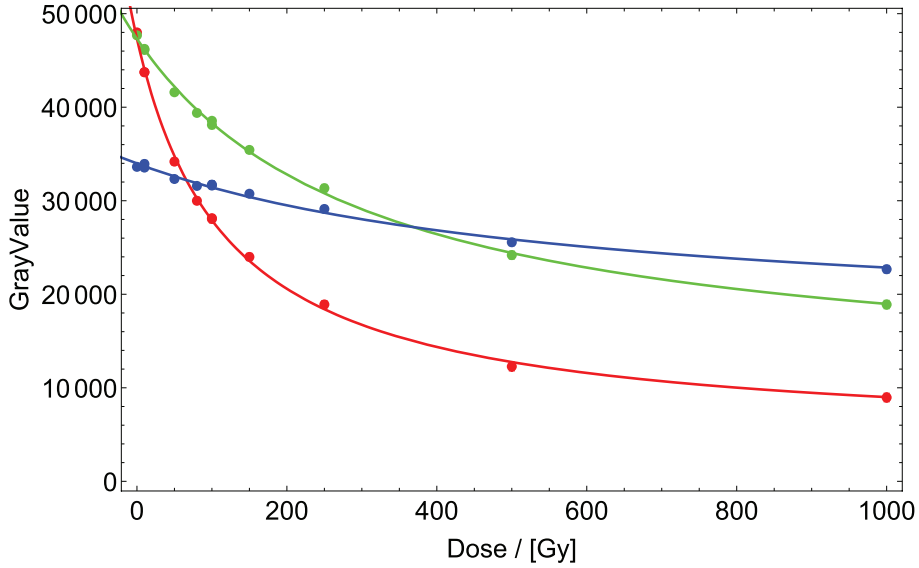

HD Angle: 0 Deg | Channel: 1
Function: $a + \frac{b}{-c+d}$ Red

	Estimate	Standard Error	t-Statistic	P-Value
a	4353.01	561.133	7.75755	0.00005446
b	5.21722×10^6	267 130.	19.5306	4.90944×10^{-8}
c	−121.439	5.31647	−22.842	1.43069×10^{-8}

HD Angle: 0 Deg | Channel: 2
Function: $a + \frac{b}{-c+d}$ Green

	Estimate	Standard Error	t-Statistic	P-Value
a	10 130.7	801.032	12.6471	1.43538×10^{-6}
b	1.15932×10^7	840 131.	13.7993	7.34516×10^{-7}
c	−311.695	17.4572	−17.8548	9.91798×10^{-8}

HD Angle: 0 Deg | Channel: 3
Function: $a + \frac{b}{-c+d}$ Blue

	Estimate	Standard Error	t-Statistic	P-Value
a	16 276.	1384.56	11.7554	2.5078×10^{-6}
b	1.04689×10^7	2.46294×10^6	4.25056	0.00279701
c	−591.52	98.2805	−6.01869	0.000316734

Figure 18.4 – Calibration curves of *HD-v2* RCF, with corresponding fits. Fits parameters are summarized in tables for the three RBG channels, on the bottom part.

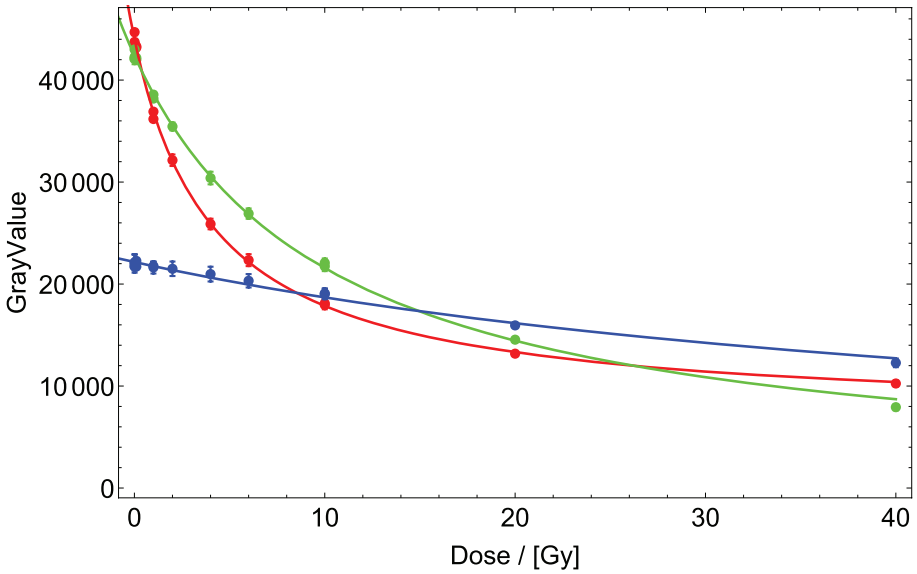

EBT Angle: 0 Deg | Channel: 1
Function: $a + \frac{b}{-c+d}$ Red

	Estimate	Standard Error	t-Statistic	P-Value
a	6859.97	393.929	17.4142	2.34704×10^{-9}
b	156 257.	6905.95	22.6264	1.41709×10^{-10}
c	−4.205	0.154237	−27.2632	1.88495×10^{-11}

EBT Angle: 0 Deg | Channel: 2
Function: $a + \frac{b}{-c+d}$ Green

	Estimate	Standard Error	t-Statistic	P-Value
a	3.43357×10^{-8}	752.471	4.56306×10^{-11}	1
b	438 421.	26 456.1	16.5717	3.97568×10^{-9}
c	−10.3405	0.469607	−22.0195	1.89975×10^{-10}

EBT Angle: 0 Deg | Channel: 3
Function: $a + \frac{b}{-c+d}$ Blue

	Estimate	Standard Error	t-Statistic	P-Value
a	0.	3656.83	0.	1.
b	1.19472×10^{6}	496 056.	2.40844	0.0347102
c	−53.9134	13.7114	−3.93201	0.00234395

Figure 18.5 – Calibration curves of *EBT-3* RCF, with corresponding fits. Fits parameters are summarized in tables for the three RGB channels, on the bottom part.

18.3 Proton dose to spectrum

By calculating the deposition in SRIM with an input flat spectrum characterized by an energy range and an energy bin, a matrix M_{ij} of the deposition can be built and represents the ionization for each energy bin of index i over the successive active layers of index j of the RCF stack. The size of the matrix is $b \times l$ with b the number of energy bins and l the number of active layers in the stack where ionization is integrated. One has the relation:

$$\begin{pmatrix} M_{1,1} & \dots & M_{1,j} & \dots & M_{1,l} \\ \vdots & \vdots & \vdots & \vdots & \vdots \\ M_{i,1} & \dots & M_{i,j} & \dots & M_{i,l} \\ \vdots & \vdots & \vdots & \vdots & \vdots \\ M_{b,1} & \dots & M_{b,j} & \dots & M_{b,l} \end{pmatrix} \begin{pmatrix} N_1 & N_2 & \dots & N_i & \dots & N_b \end{pmatrix} = \begin{pmatrix} E_1 \\ E_2 \\ \vdots \\ E_j \\ \vdots \\ E_l \end{pmatrix} \tag{18.5}$$

By finding the inverse of the matrix M, one can then relate the dose deposition measured on RCF (vector $\vec{E_j}$) to the number of protons per energy bin (vector $\vec{N_i}$), by doing simply $\vec{N_i} = M^{-1}\vec{E_j}$. The true inverse could not be found as generally the matrix M is not squared (or it will imply to only work with a number of energy bins equals to the number of RCF in the stack), and even it was, the determinant would be of zero. This issue can be overcome by using instead a pseudo-inverse matrix calculated by singular value decomposition method (not detailed here).

An other method is not to inverse the matrix but instead to iteratively solve the system by imposing the form of the solution, as given by an analytic distribution. This analytic distribution is not chosen randomly and for proton accelerated beam by TNSA, the formula given in the paper of Mora [185] is particularly reliable. This latter method avoid outliers issues related to the matrix inversion.

19 Proton deflectometry analisis

19.1 Analysis of grid deflections from the RCF imprint

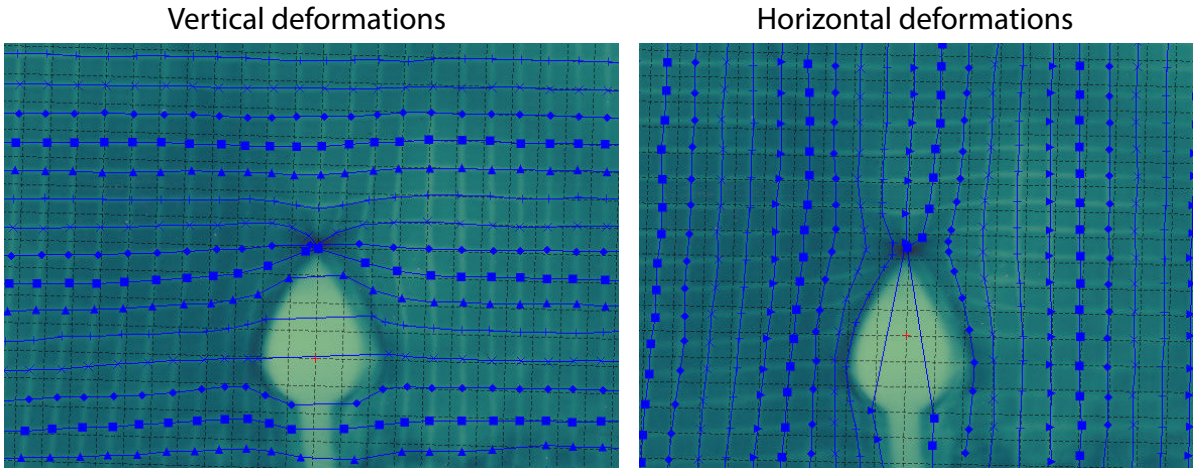

Figure 19.1 – Vertical and horizontal grid deformations of a RCF imprint.

The grid deformed positions are first obtained by digitizing the vertical and horizontal deformed mesh lines (see Figure 19.1). The unperturbed mesh is built based on the pitch size on the coil plane ($2.5\times$ the real pitch $= 105\,\mu m$). The frame is adequately rotated to correspond to the unperturbed mesh orientation. Respectively for vertical and horizontal lines, the line points are interpolated on the unperturbed horizontal and vertical grid points. Together, they form an uniformly-spaced 2D grid of the mesh positions in the reference frame.

Then, in order to get the deflections, the vertical/horizontal positions of the unperturbed grid are subtracted to the vertical/horizontal positions of the deformed mesh:

$$\Delta x' = x'_{\text{deformed}} - x'_{\text{unperturbed}} \tag{19.1}$$

$$\Delta y' = y'_{\text{deformed}} - y'_{\text{unperturbed}} \tag{19.2}$$

It is worth noting that here the operations are made in a rotated frame of angle θ, one need to correct from the rotation by applying the following relation:

$$\begin{pmatrix} \Delta_x \\ \Delta_y \end{pmatrix} = \begin{pmatrix} \cos\theta & \sin\theta \\ -\sin\theta & \cos\theta \end{pmatrix} \cdot \begin{pmatrix} \Delta'_x \\ \Delta'_y \end{pmatrix} \tag{19.3}$$

This procedure permits to construct a 2D map of the deflections around the coil. The relation between deflections and magnetic field is not direct and will be discussed in the following.

From deflections to magnetic field

Here we will detail the procedure used to infer the distribution of the B-field around the coil from the proton deflectometry measurements. It is worth mentioning that the 2D grid deflections obtained in the RCF imprint are related to transverse deflections of protons summed up along all their trajectory path. At this point, two strategies can be used to deconvoluate the grid deflections to obtain the B-field distribution in which protons have passing through. The faster strategy is to assume that the field is weak enough to allow the use of a perturbation technique associated with the integration of the transverse force exerted on protons along an unperturbed straight trajectory [152]. If the direction of the unperturbed trajectory is z, being x and y the transverse coordinates, one has:

$$\vec{F}_\perp = e\vec{v} \wedge \vec{B} \tag{19.4}$$

so that:

$$\Delta\vec{p}_\perp = e\int_{-\infty}^{+\infty}(\vec{v}\wedge\vec{B})dt \tag{19.5}$$

where the integration is made along the unperturbed trajectory. Introducing the vector potential $\vec{A}$ of the magnetic field, one end up after some calculations that the deflections angles are given on the unperturbed trajectory point (x_0,y_0,z_0) by:

$$\alpha_x = \frac{e}{\sqrt{2m_pE_p}}\frac{\partial}{\partial x_0}\int_{-\infty}^{+\infty}A_z(x_0,y_0,z_0)dz_0 \tag{19.6}$$

$$\alpha_y = \frac{e}{\sqrt{2m_pE_p}}\frac{\partial}{\partial y_0}\int_{-\infty}^{+\infty}A_z(x_0,y_0,z_0)dz_0 \tag{19.7}$$

Or equivalently, within the paraxial approximations:

$$\alpha_x \approx \frac{-e}{\sqrt{2m_pE_p}}\int_{-\infty}^{+\infty}B_y dz \tag{19.8}$$

$$\alpha_y \approx \frac{e}{\sqrt{2m_pE_p}}\int_{-\infty}^{+\infty}B_x dz \tag{19.9}$$

The latter expressions can be even simplified to make an estimation of the B-field magnitude, assuming that A_z is constant over a characteristic B-field effective length l_B and is equal to zero outside. Under this assumption, the deflections Δ_x and Δ_y at one grid point yields average B-field values given by:

$$\overline{B_x} = \frac{\int_{-\infty}^{+\infty}B_x dl}{l_B} \approx \frac{\sqrt{2E_pm_p}\sin\alpha_y}{l_Be} \tag{19.10}$$

$$\overline{B_y} = \frac{\int_{-\infty}^{+\infty}B_y dl}{l_B} \approx \frac{\sqrt{2E_pm_p}\sin\alpha_x}{l_Be} \tag{19.11}$$

The B-field integral can be more exactly calculated by the mean of magnetostatic calculations (see Sec. 17) and one can estimate that the B-field effective length $l_B \approx 2a$ with a the coil radius. This estimation is only valid for proton trajectories passing near the inside part of the coil, the parameter l_B is obviously decreasing for trajectories passing further. The method given by Kugland *et al.* gives accurate results but with moderate B-fields values only.

It is interesting to note at this point that electric field and magnetic field induced deflections exhibit a different energy scaling. The deflection angle indeed scales as $1/\epsilon_p$ for electric field only and as $1/\sqrt{\epsilon_p}$ for magnetic field only. Of course, these scaling are obtained under very strong assumptions and are therefore very difficult to be tested experimentally.

The synthetic detector image reconstruction by the method of Kugland *et al.* can also be used to estimate the proton density at the detector plane $n_p(x,y)$ calculated from proton density before the interaction region $n_{p,0}$ by the simple relation:

$$n_p(x,y) = \frac{dN_p}{dS} = \frac{dN_p}{|J|dS_0} = \frac{n_{p,0}}{|J|} \tag{19.12}$$

with $|J| = \left|\frac{\partial(x,y)}{\partial(x_0,y_0)}\right|$ the Jacobian determinant. By noting the deflection $\xi \approx \alpha L$, where L is the distance from source to detector, the relation for positions from object $((x_0,y_0))$ to image plane $((x,y))$ is given by the equations:

$$x = Mx_0 \pm \xi_x(x_0,y_0); \qquad y = Mx_0 \pm \xi_y(x_0,y_0) \tag{19.13}$$

and M is the magnification factor. For usual diverging beam, the sign $+$ has to be used. The Jacobian can be calculated based on these latter mapping equations and writes:

$$|J| = \begin{vmatrix} M+\frac{\partial\xi_x}{\partial x_0} & \frac{\partial\xi_x}{\partial y_0} \\ \frac{\partial\xi_y}{\partial x_0} & M+\frac{\partial\xi_y}{\partial y_0} \end{vmatrix} = M^2 + M\left(\frac{\partial\xi_x}{\partial x_0}+\frac{\partial\xi_y}{\partial y_0}\right) = M^2\left(1+\frac{1}{M}\vec{\nabla}_{\perp,0}\cdot\vec{\xi}_\perp\right) \tag{19.14}$$

The proton density at the detector results then from the object proton density with the relation:

$$n_p(x,y) = \frac{n_{p,0}}{M^2}\left(1 + \frac{1}{M}\vec{\nabla}_{\perp,0}\cdot\vec{\xi}_\perp\right)^{-1} \approx \frac{n_{p,0}}{M^2}\left(1 - \frac{1}{M}\vec{\nabla}_{\perp,0}\cdot\vec{\xi}_\perp\right) = n_{unp} + \delta n_p(x,y) \tag{19.15}$$

where n_{unp} is the unperturbed density at the detector plane ($n_{p,0}/M^2$) which was isolated from the modulations due to the field (δn_p). Under the hypothesis of this model, the average electromagnetic field gradients can be estimated from the proton density modifications at the detector plane. It is however difficult to use it for experimental RCF imprints of TNSA accelerated proton beam where the unperturbed profile of the beam yields inherent inhomogenities which are difficult to predict. Although, the previous equations remains only valid when the laminarity of the proton beam is conserved: if proton trajectories cross each other, caustics are expected to form and the previous equations become invalid.

Small angle and paraxial approximations also affects the estimation accuracy that one can make from the equations introduced in this subsection. In the next subsection, we will introduce a method which is a lot more accurate and which can be directly linked with a magnetostatic code. This approach both permits to deal with a more precise field distribution and avoid the simplification of the perturbed proton trajectory.

19.2 Particle ray-tracing simulations

The other strategy to estimate even more accurately the deflections is to perform a Monte-Carlo like propagation of protons in the magnetostatic 3D B-field distribution. The protons are propagating ballistically in the field and at each time step of the integration scheme, the Lorentz force exerted on protons is calculated. It is the strategy adopted for building synthetic proton imprints in this thesis work. The results are shown in Sec. 8.1.4. The code developed for this purpose will be detailed in the following.

The ballistic code uses a relativistic form of the Lorentz force to be able to deal also with the propagation of relativistic electrons and the resulting acceleration is calculated in the general case of a constant electromagnetic field. The relation between the Lorentz force and resulting acceleration writes:

$$\vec{F} = \gamma m\vec{a} + \gamma^3 m\frac{\vec{v}\cdot\vec{a}}{c^2}\vec{v} \tag{19.16}$$

In Cartesian coordinates, one obtains the acceleration $\vec{a}$ as:

$$\vec{a} = \frac{1}{\gamma\, m\,(c^2+\gamma^2 v^2)}\begin{pmatrix} c^2F_x + \gamma^2\left[-F_y v_x v_y - F_z v_x v_z + F_x({v_y}^2 + {v_z}^2)\right] \\ c^2F_y + \gamma^2\left[-v_y\left(F_x v_x + F_z v_z\right) + F_y\left({v_x}^2 + {v_z}^2\right)\right] \\ c^2F_z + \gamma^2\left[F_z\left({v_x}^2 + {v_y}^2\right) - \left(F_x v_x + F_y v_y\right)v_z\right] \end{pmatrix} \tag{19.17}$$

Obviously, if only a magnetic contribution is calculated, the particle energy is conserved and the accelerations reduces simply to:

$$\vec{a} = \frac{\vec{F}}{\gamma m} \tag{19.18}$$

The particle pusher uses an integration scheme based on the Verlet velocity algorithm that has been changed to use a modified evaluation for the acceleration at time $t + \Delta t$, Δt being the time step. Indeed, it would necessitate the more complex computation of a predictor-corrector scheme since the acceleration depends itself on the velocity and position. The used scheme has been benchmarked with a Runge-Kutta scheme of order 4 and it results that the precision is similar, while having a great gain on computation time. The scheme is resumed in the following set of equations (we define as $\vec{r}$ the Cartesian position vector):

$$\vec{r}(t+\Delta t) = \vec{r} + \Delta t\vec{v}(t) + 0.5\Delta t^2\vec{a}(t) \tag{19.19}$$

$$\vec{v}(t+\Delta t) = \vec{v}(t) + 0.5\Delta t\vec{a}^*(t+\Delta t) + 0.5\Delta t\vec{a}(t) \tag{19.20}$$

$$\vec{a}^*(t+\Delta t) = \underbrace{\vec{a}[\vec{r}(t+\Delta t), \vec{v} + \Delta t\vec{a}(t)]}_{Eq.\ 19.17} \tag{19.21}$$

The particles properties initiated at a source point are determined by random estimators, following defined probability density functions. The particles are exiting the point source at $t = 0$ inside a cone directed along propagation axis $\vec{z}$, we have the initial velocity vector:

$$\vec{v_0} = \begin{pmatrix} V|\cos\theta| \\ V\sqrt{1-\cos^2\theta}\cos\phi \\ V\sqrt{1-\cos^2\theta}\sin\phi \end{pmatrix} \tag{19.22}$$

Where V is the velocity norm ($V = c\sqrt{(\gamma^2-1)/\gamma^2}$). The $\cos\theta$ variable is distributed over an Half Normal distribution defined by its FWHM angle ($\sim 20\,°$), called also *half-cone divergence angle*. The variable ϕ is distributed uniformly in the interval $[-\pi, \pi]$. As an extra feature, the code can also use a divergence angle which depends on the kinetic energy of the particle (to better mimic TNSA beam properties). The kinetic energy of the launched particles can also be determined by a statistical distribution. Usually, when dealing with magnetic deflections only, an uniform distribution has been used in the interval of energies given by stopping power calculations (see Sec. 18.1) to make the synthetic imprint of one layer of the RCF stack. For both electric and magnetic deflections, the interval is broadened and the imprint is made only with particles whose final kinetic energy is in the good range. This first trial permits to identify the accurate input energy range forming the imprint. The simulation can be run again with an higher particle number in this input energy range.

To get an image of the deformed grid in the detector of the simulation, the code is generating a mesh at the experimental mesh position and particles whose trajectories cross one of the mesh wires is stopped. The propagation distance for the particles is of $\approx 50\,\text{mm}$: a constant time step would lead either to big inaccuracy or huge computation time. That is the reason why the time step is refined near the coil ($\sim 10a$ on each side) and pre-/post- trajectory are calculated projecting the trajectories in a straight line.

In Sec. 8.1.4, we gave the synthetic proton imprints emerging from this approach. The use of laws describing the width evolution of the void zone observed in RCF imprints, as a function of the electric current and proton kinetic energy, are the privileged method to infer the magnetic field produced by our targets.

19.3 Simulation with one-step trajectory

In this approach, the particle's deviation angle is calculated from analytical expressions. The approximations hold for small deviation angles and the integration of the magnetic field for the complex 3D geometry is realized by a Monte-Carlo integration of the fields. We have here only one spatial step ane the particle trajectory along z is built as a result of the calculated deviation angles α_x and α_y. To do so, the fields zone of influence has to be way smaller than the distance between the field source and the particle source. This justifies the paraxial limit.

The mapping relation for a point in the object plane to a point in the image plane follows:

$$\begin{pmatrix} x_1 \\ y_1 \end{pmatrix} = \begin{pmatrix} 1+M & 0 \\ 0 & 1+M \end{pmatrix} \cdot \begin{pmatrix} x_0 \\ y_0 \end{pmatrix} + \begin{pmatrix} \alpha_x \\ \alpha_y \end{pmatrix} \cdot L \tag{19.23}$$

being M the magnification of the system and L the distance from object plane to image plane. A one step transport from source to image plane is then possible by calculating the small deflection angle in the paraxial limit $\alpha_{x,y} \approx v_{x,y}/v_z$. The problem will be regarded relativistically to include the effects on relativistic electrons and under the previous assumption:

$$\alpha_{x,y} = \frac{1}{\gamma m v_z^2} \int_{-\infty}^{\infty} \vec{F}_L \cdot \vec{e}_{y,x} dz \tag{19.24}$$

Besides, the size of the object (field source) has to be small with respect to the distance from the particle source to the object l. Otherwise, one cannot anymore assume that the proton kinetic energy results only of its momentum along z.

An intensity map on the image plane can be synthetically constructed for a given proton energy source by using the determinant of the problem's Jacobian [152]. This is only valid for analytically-given fields. For a specific particle source (including the divergence of the beam) and for complex

numerical description of the fields in 3D, this treatment is not sufficient. A code was developed by Micha Ehret during his master thesis, under supervision of Joao Santos and me. The code takes every particle's initial propagation direction and speed to construct its deviation angle. Electric and magnetic field are treated independently. Merging the two fields was simply adding up their effects. In the following, we will introduce the methodology adopted to calculate the deviation angles from a given 3D map of magnetic field and electric field.

For electric field

The electrostatic force can be determined by a known field or a known electric potential Φ.

$$\alpha_{x,y} = -\frac{q}{\gamma m v_z^2} \partial_{x_0,y_0} \int_{-\infty}^{\infty} \Phi dz \tag{19.25}$$

For magnetic field

The magnetostatic force can be determined by a known field source by calculating the vector potential $\vec{A}$.

$$\begin{aligned}
\alpha_{x,y} &= -\frac{q}{\gamma m v_z^2} \int_{-\infty}^{\infty} \left[\vec{v} \wedge \left(\vec{\nabla} \wedge \vec{A} \right) \right]_{x,y} dz \\
&= -\frac{q}{\gamma m v_z^2} \int_{-\infty}^{\infty} \left[\partial_{x,y} \left(\vec{v} \cdot \vec{A} \right) - \left(\vec{v} \cdot \vec{\nabla} \right) A_{x,y} \right] dz \\
&= \frac{q}{p_z} \left(\int_{-\infty}^{\infty} \partial_{x,y} A_z dz - \int_{-\infty}^{\infty} \partial_{x,y} A_{x,y} dz \right) = \frac{q}{p_z} \left(\partial_{x,y} \int_{-\infty}^{\infty} A_z dz - [A_{x,y}]_{-\infty}^{\infty} \right) \\
&= \frac{q}{p_z} \partial_{x,y} \int_{-\infty}^{\infty} A_z dz
\end{aligned} \tag{19.26}$$

The vector potential is integrated numerically by a Monte-Carlo integration and its derivative is calculated under a first order approximation for parallel trajectories. Monte-Carlo integration is iteratively performed until the Monte-Carlo precision is reached: the Monte-Carlo iteration is aborted if the relation of the absolute value for the integral's difference from one to another step related to the actual value of the integral is smaller than a given precision m.

The same methodology can be used to perform the integral of an electrostatic potential if such potential is not analytically-given.

Actually one can point out that the field integrals could have been calculated in Radia, which uses its one method of computation (see Sec. 17). Here the code developed by Michael Ehret is independent of Mathematica software and Radia package. Another version of the code also performs the ballistic approach, similarly as presented in Sec. 19.2. The main advantage to dissociate from Radia and Mathematica is the computation speed that has been optimized in Fortran.

19.4 Parameter of the fits functions F and G

The fits function F and G were introduced in Sec. 11.4.2 and they respectively approximate the inner spot and the outer bulb sizes of protons on RCF imprints, as observed during the experiment at PHELIX (Sec. 11).

	Estimate	Standard Error	t-Statistic	P-Value
lcla	−13.0776	1.81702	−7.19729	4.87836×10^{-11}
lclb	−110.222	3.05432	−36.0873	2.75719×10^{-68}
lcqa	−0.0268139	0.00594797	−4.50807	0.0000147668
lmqc	0.219883	0.0311737	7.05346	1.02675×10^{-10}
lcc	5700.53	116.831	48.7931	1.09908×10^{-83}
qcla	1.84925	0.327458	5.64728	1.029×10^{-7}
qclb	15.4403	0.531634	29.0431	1.12568×10^{-57}
qcqa	0.00308646	0.00106406	2.90064	0.00439581
qmqc	−0.0324799	0.00532091	−6.1042	1.18197×10^{-8}
qcc	−633.57	21.5243	−29.4351	2.57837×10^{-58}
ccla	−0.067926	0.014022	−4.84423	3.65903×10^{-6}
cclb	−0.562948	0.0221511	−25.4139	1.9817×10^{-51}
ccqa	−0.000101362	0.0000453248	−2.23634	0.0270888
cmqc	0.00121395	0.00021772	5.57576	1.43218×10^{-7}
ccc	21.3067	0.937674	22.7229	2.148×10^{-46}

(a) F for 2 mm source to coil distance.

	Estimate	Standard Error	t-Statistic	P-Value
lcla	−14.9558	1.78465	−8.38026	1.22988×10^{-12}
lclb	−69.1678	4.16332	−16.6136	5.69087×10^{-28}
lcqa	0.030962	0.00788285	3.92776	0.000177911
lmqc	0.245732	0.054681	4.49392	0.000022727
lcc	2423.98	87.8989	27.5769	3.04552×10^{-43}
qcla	2.22385	0.324539	6.85231	1.23876×10^{-9}
qclb	9.7029	0.709704	13.6718	7.45567×10^{-23}
qcqa	−0.00620349	0.00142859	−4.34239	0.0000400124
qmqc	−0.0373654	0.00927095	−4.03037	0.000123961
qcc	−271.104	16.1144	−16.8237	2.55866×10^{-28}
ccla	−0.083937	0.0139633	−6.01128	4.88271×10^{-8}
cclb	−0.355229	0.0289907	−12.2532	3.20693×10^{-20}
ccqa	0.000264606	0.0000612481	4.32024	0.0000434237
cmqc	0.00141868	0.000376805	3.76503	0.000312015
ccc	9.17969	0.698605	13.14	7.04061×10^{-22}

(b) F for 5 mm source to coil distance.

	Estimate	Standard Error	t-Statistic	P-Value
lcla	12.3813	0.760066	16.2897	8.4151×10^{-33}
lclb	325.907	3.33288	97.7853	1.10754×10^{-120}
lcqa	0.00204683	0.000352564	5.80555	4.91129×10^{-8}
lcqb	−0.18696	0.017501	−10.6828	2.31616×10^{-19}
lmqc	−0.225233	0.0311438	−7.23204	4.07217×10^{-11}
lcc	7040.17	109.713	64.1689	4.29642×10^{-98}
qcla	−1.65996	0.139591	−11.8915	2.49788×10^{-22}
qclb	−43.579	0.587319	−74.1998	7.74889×10^{-106}
qcqb	0.0114187	0.0012746	8.95867	3.68284×10^{-15}
qmqc	0.0321571	0.00533446	6.02818	1.70439×10^{-8}
qcc	−799.422	20.6969	−38.6252	1.06534×10^{-71}
ccla	0.0582494	0.00609842	9.55155	1.35471×10^{-16}
cclb	1.54338	0.0257925	59.8384	2.16735×10^{-94}
cmqc	−0.00118352	0.000219169	−5.40002	3.19489×10^{-7}
ccc	27.3337	0.920021	29.7098	9.25627×10^{-59}

(c) G for 2 mm source to coil distance.

	Estimate	Standard Error	t-Statistic	P-Value
lcla	7.04259	1.40644	5.00739	3.10978×10^{-6}
lclb	263.396	8.73486	30.1546	3.83684×10^{-46}
lcqa	0.00119605	0.000714224	1.67462	0.0978189
lcqb	−0.433	0.0519177	−8.34012	1.47777×10^{-12}
lmqc	−0.142583	0.107555	−1.32568	0.188627
lcc	3131.43	164.208	19.0699	6.97936×10^{-32}
qcla	−0.839999	0.257765	−3.25877	0.00162959
qclb	−33.7883	1.56739	−21.5571	1.57197×10^{-35}
qcqb	0.0259964	0.00354512	7.333	1.43977×10^{-10}
qmqc	0.0155314	0.0182922	0.849071	0.398314
qcc	−366.792	30.9359	−11.8565	1.82036×10^{-19}
ccla	0.0266321	0.0112281	2.37191	0.0200395
cclb	1.16049	0.0681737	17.0225	1.20692×10^{-28}
cmqc	−0.000431731	0.000746351	−0.578456	0.564542
ccc	12.8343	1.36949	9.37159	1.31318×10^{-14}

(d) G for 5 mm source to coil distance.

Figure 19.2 – Parameter tables with error estimation for fit functions F and G

20 Imaging Plate (IP) detectors

The detector used for X-ray diagnostics presented so far are called "Imaging Plates", frequently shortened for the acronym IP. They are composed of a metallic magnetic frame covered by a layer of $BaFBr$ doped with photo-stimulable europium. The tiny grains (5 µm) composing the active layer are inserted over a polymer layer of C_2H_2O and sometime also covered by a protective layer of the same polymer.

The exposition of a grain under X-irradiation (or any ionizing radiation) will excite the $BaFBr$ in a meta-stable state lasting several hours [Meadowcroft 2008]. The reading of the IP is done by a laser light in the red color, causing the desexcitation of the $BaFBr$. This latter is consequently emitting a luminescence blue light which is detected back by the scanner arm. The scanned image is resolved spatially and the intensity collected is linked to the number of electron/hole pairs created by the ionizing radiation. The IP can be fully erased after an exposition to white light and then be reusable. For this reason, one has then to keep the IP in dark before the scanning procedure to not loose the signal.

In our experiments, we used IP from the brand Fuji©, in particular the so-called MS type. Each type of IP (Fuji produced three types: MS, SR and TR) has different layer's chemical composition, number and thickness.

The time shift between the irradiation and the scanning of the IP have to be measured in order to quantify the signal loss induced by the fading phenomenon. The term fading is used to describe the spontaneous recombination of the electron/hole pairs overt time and its evolution (the fading function) have to be known in order to correct from the signal losses.

The scanner we used in experiments is the model FLA-7000 from Fuji. The scanner outputs an image containing a numerical value per pixel which is coded over 2 octets and is named *Quantum Level (QL)*. The scanner response, being logarithmic, the values of QL have to be converted in *Photo Stimulated Luminescence (PSL)* level by the function:

$$PSL = \left(\frac{Res}{100}\right)^2 \frac{4000}{S} 10^{L\left(\frac{Q_L}{2^D-1}-\frac{1}{2}\right)} \tag{20.1}$$

with:

- PSL: Number of luminescence photons red in a pixel;
- Res: Size of the pixels in µm (resolution);
- S: Sensitivity of the scanner;
- L: Latitude;
- D: Reading dynamic (8 bits or 16 bits);
- Q_L: Numerical value of a pixel (ranging between 0 and $2^D - 1$).

In our case, the scanner was configured to use a resolution of 50 µm, a sensitivity of 4000, a latitude of 5 and a coding over 16 bits. With those values, the image saturation inherent to the scanner is 31000 PSL/mm^2.

21 Thompson Parabola

A Thomson parabola (TP) disperses the ions in parallel electric and magnetic fields due to their charge-to-mass (q/m) ratio. For each q/m value a separate ion trace in the shape of a parabola is detectable behind the fields. With the knowledge of the deflecting fields the dispersion relation is accessible: the traces can be connected to specific ions (q/m values) and a relation between ion energy and position on the parabolic trace is obtained (so-called *dispersion relation*). For protons with $q/m = 1$ a unique trace identification is possible. For other ions this is not always the case, as for example C^{6+} and O^{8+} ions which have the same q/m value and thus overlapping traces on the detector. Still, much information is obtained about different ion species and charge states within the beam.

A more important drawback of the method is the necessity of a very small (sub-mm) entrance pinhole to the dispersing EM fields to provide an acceptable energy resolution within the trace. As a consequence, a TP covers only a very small solid angle of the initial beam. Positioning of several TPs at different angles to the beam helps for characterizing the angular distribution, but still results in losing a lot of information.

Assuming a non-relativistic ion and constant fields ($\vec{B} = B\vec{e}_y$, $\vec{E} = E\vec{e}_y$) orientated normally to the ion propagation (along $\vec{z}$). If d_M is the extent of the magnets, one has for $0 < z < d_M$:

$$\begin{cases} m\dfrac{d^2x}{dt^2} &= -e\dfrac{dz}{dt}B \\ m\dfrac{d^2z}{dt^2} &= -e\dfrac{dx}{dt}B \end{cases} \tag{21.1}$$

Taking the initial conditions $\vec{v}_0 = v_0\vec{e}_z$ and $x_0 = y_0 = z_0 = 0$, one gets:

$$\begin{cases} v_x &= -v_0 \sin(\omega_c t) \\ v_z &= v_0 \cos(\omega_c t) \end{cases} \quad \text{and} \quad \begin{cases} x &= \dfrac{v_0}{\omega_c}(\cos(\omega_c t) - 1) \\ z &= \dfrac{v_0}{\omega_c}\sin(\omega_c t) \end{cases} \tag{21.2}$$

with $\omega_c = eB/m$. At the end of the propagation along the magnets, the ions position is given by $(x(t_M), z(t_M))$ with $t_M = \dfrac{1}{\omega_c}\arcsin\left(\dfrac{\omega_c d_M}{v_0}\right)$. The deflection of ions along $\vec{x}$ is not occurring anymore after the magnets and one can calculate the position x_D on detector after the total distance along $\vec{z}$ from source to detector z_D:

$$x_D = x(t_M) + \frac{v_x(t_M)}{v_z(t_M)}\Delta_{z,M}. \tag{21.3}$$

with $\Delta_{z,M}$ the distance along $\vec{z}$ from the end of the magnets till z_D.

Assuming that the electrodes extent along $\vec{z}$ equals to d_E, the deviation in the y-axis along the electrodes is given by:

$$v_y = \frac{eE}{m}t \quad \text{and} \quad y = \frac{eE}{2m}t^2 \tag{21.4}$$

One can consider in first approximation that the time taken by the ion to travel along the electrodes is $t_E = d_E/v_0$, and the position y_D of the ion on the detector at $z = z_D$ is:

$$y_D = y(t_E) + \frac{v_y(t_E)}{v_z(t_M)}\Delta_{z,E} \tag{21.5}$$

with $\Delta_{z,E}$ the distance along $\vec{z}$ from the end of the electrodes till z_D.

Finally, by considering that $\omega_c t_M \ll 1$ (when the deviations are small), a Taylor expansion gives the equation of a parabola (we now see the origin of the denomination "Thomson Parabola"):

$$y_D = \frac{Em}{eB^2}\frac{d_E}{d_M^2}\frac{1 + d_E/2}{(z_D - d_M/2)^2}x_D^2 \tag{21.6}$$

The parabola we used in experiment is sketched in Figure 21.1 with a simulation of proton trajectories with kinetic energies from 300 eV to 30 meV (from blue to red in the colorscale). In this design

[43], the electrodes are forming an angle to one another in order to reduce the collisions of low energy particles on electrodes. Yet, for the level of gap voltage applied during our experiment ($\sim$ 10 kV), this lower limit was limited to $\approx$ 3 MeV. Although, the electrodes are acting simultaneously with the magnets along magnet length, the latter being embodied in an iron cast.

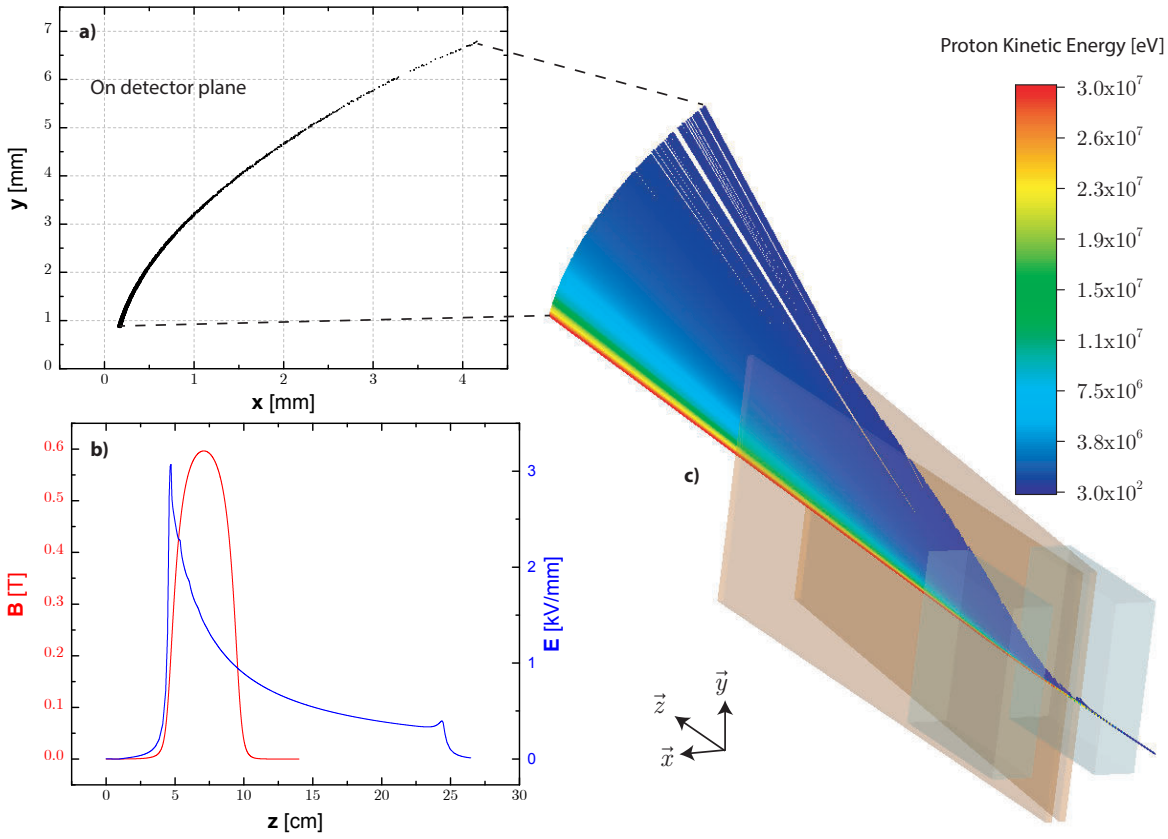

Figure 21.1 – a) Trace of protons on detector for the kinetic energy range from 300 eV to 30 MeV. **b)** Electric and magnetic field along the z-axis. This line would correspond to an unperturbed trajectory. It is clear that the approximation of a constant magnetic field along magnets extent in z is a rough approximation and in this particular design of electrodes, the electric field is far from being constant along the electrodes extent. **c)** Simulation of the trajectories of protons in the TP. This simulation and curves on the left were computed on CST©, and the source file is a courtesy of O. Deppert from GSI, Darmstadt. In this parabola system, the magnets have a magnetization of 1.153 T along $\vec{x}$, and a gap voltage of 7 kV was applied on electrodes.

Analysis of PHELIX TP results

A first analysis using the dispersion relation corresponding to a perfectly aligned parabola yielded inconsistent results for the proton energy cutoff in respect to RCF. Therefore, we performed new simulations in CST introducing a small tilt angle of $\approx$ 3 mrad, in order to reproduce the position of zero order point on IP for an undeflected beam.

In Figure 21.2, an example of analysis is shown for a typical shot of the experiment, with the resulting proton spectrum in PSL/MeV. The conversion from PSL/MeV to number of protons/MeV was made afterwards, based on the IP fading (time shift between irradiation and scanning) and on the number of successive scans (done often several times to desaturate the IP). For that, we used the model of Bonnet *et al.* described in [30].

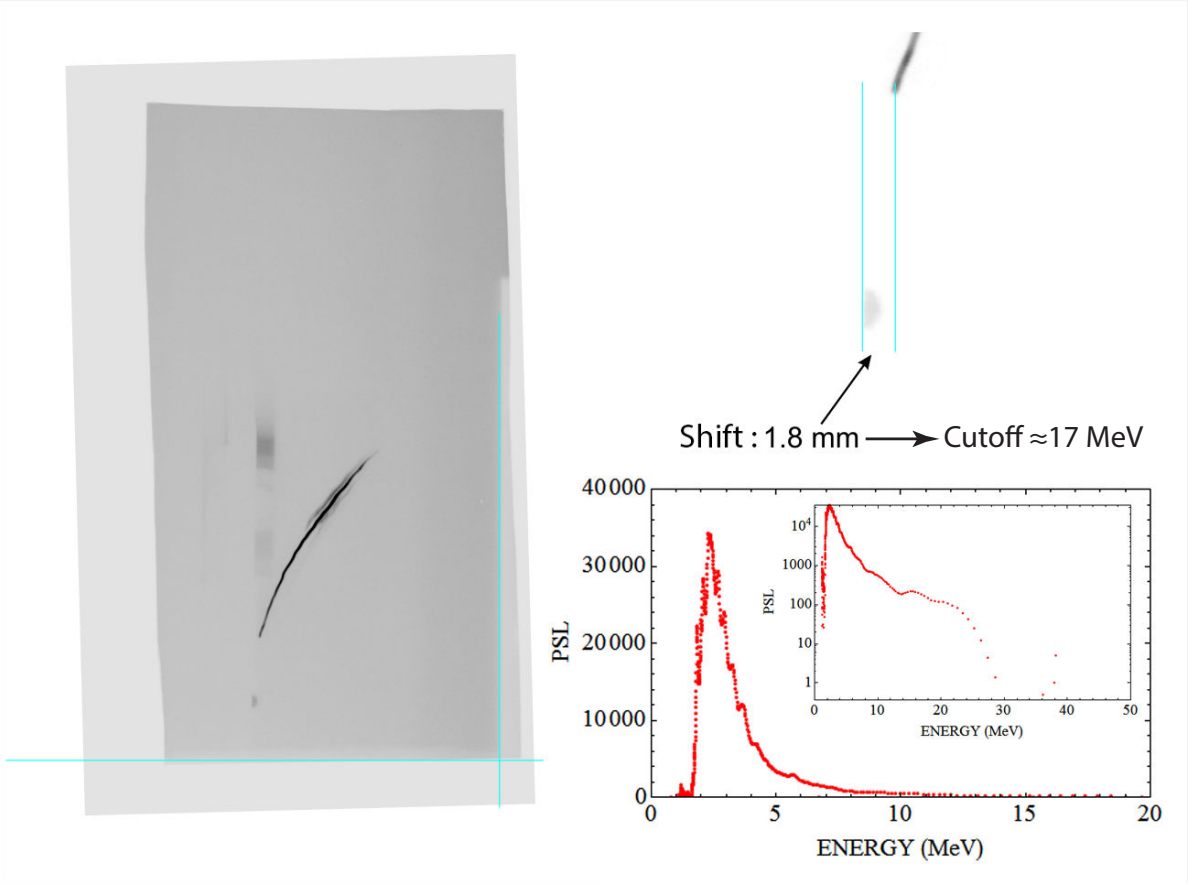

Figure 21.2 – Example of a TP result: IP image, zoom at cutoff zone and processed spectrum in PSL/MeV.

The TP only collect protons passing through the pinhole (of 15 µm-diameter), which represent a tiny fraction of the overall proton beam. Indeed, knowing that the TP was located at 31.8 cm from TCC, one calculate a solid angle of 1.75×10^{-9} sr. Assuming a proton divergence angle of 20 °, the collected number of protons by the TP represents a factor $\approx 4.6 \times 10^{-9}$ of the total beam. More accurately, the energy-dependence of the divergence angle have to be taken into account, to not overestimate the fraction of high energy protons which propagates at lower divergence and go more in proportion trhough the pinhole. To estimate this energy-dependent divergence angle, we took the law extracted from measurements by P. Antici *et al.* at similar laser conditions. These results were published in his Ph.D. thesis (Ecole Polytechnique, 2007).

We obtain finally the proton distribution of the TNSA proton beam, as inferred from TP. The result, averaged over a few shots in PHELIX, is presented in the results section of this experiment (Sec. 11.3.1).

22 X-ray diagnostics

22.1 K-α emission

When an hot electron collide with an ion, the acquired energy can be sufficient to ionize the ion and release it, even from the most inner shell of the atom, characterized by the quantum number $n = 1$, also called K-shell or $1s$ orbital. In this ionization process, the excited ion can decay down to a more stable state and filling-in the inner shell gap let by the excited electron with an outer shell one. The transition energy is either transmitted to an other electron (Auger electron) or emit a photon of the corresponding energy (radiative transition). It is this latter that is detected and measured in X-ray spectroscopy techniques, presented in the two next sections. There are a lot of different transitions for a given atom and each one concerns different transition states. The transition from the orbital $2p$ to $1s$ (L-shell to K-shell) is called K_α emission. It is called K_β for the $3p$ to $1s$ transition (M-shell to K-shell). K_α transition are in fact allowed from two possible orbitals of the L-shell and when it occurs from $2p_{1/2}$ orbital, it is called $K_{\alpha,1}$ and from $2p_{3/2}$ orbital, it is called $K_{\alpha,2}$. In usual range of temperatures and materials used in our experiments, the probability of K_β emission is much lower than the probability of the two K_α emissions, being $K_{\alpha,1}$ the more probable of the two. Figure 22.1 represents the energy levels and inner-shell radiative transitions for an atom of copper.

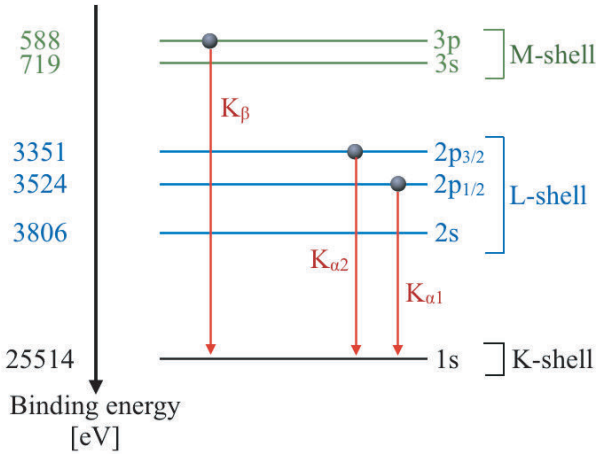

Figure 22.1 – Energy levels in copper atoms. The radiative transitions after inner-shell ionization of the atom are represented with red arrows.

A rough estimation for the K_α energy transition is given by the Moseley's empirical law as a function of the atomic number ($3 < Z < 60$):

$$E_{K-\alpha}[\text{eV}] \approx 10.206(Z-1)^2 \tag{22.1}$$

22.2 X-ray spectrometry

Most of the diagnostics in laser-plasma community used to detect line emissions, as it is also the case for the K_α-emission which will be detailed in the next section, rely on the use of crystals of different shapes. The detection by those crystals is base on the Bragg's diffraction law that we will explain here. The Bragg's relation should be valid in order for a certain reflected light of wavelength λ to interfere constructively for a given grazing angle θ on a crystal. The law writes:

$$n\lambda = 2d\sin\theta \tag{22.2}$$

with n simply a positive natural integer (called diffraction order) and d is the spacing length between two crystal planes. The crystal spacing $2d$ and the incidence angle θ will give the photon wavelength and energy $E_\nu = hc/\lambda$ that can be reflected by the crystal. The different diffraction orders n of photon energies will also be reflected, but with less efficiency. The reflected signal also decrease strongly for increasing incidence angle. One is generally limited to $n \leq 5$ and $\theta > 10\,°$.

The accessible photo energy range detectable by crystals can extend from a few keV to ~ 100 keV. Flat crystals are crystals which permits to have a high detectable bandwidth and high photon collection, but the spectral resolution is limited to $\sim$ 50 eV and does not permit for example to distinguish between $K_{\alpha,1}$ and $K_{\alpha,2}$ of Cu. Other geometries using Cylindrical crystal permit to have a much better spectral resolution: *e.g.* the *Von Hámos* configuration (named from the pioneer work by Von Hámos in 30s) or Conical crystal (proposed by Hall in 1984). The emission lines presented in Sec. 8.2.3 were obtained with a conical-shape crystal spectrometer made of potassium-acid-phtalate (called KAP crystal). The parameters of this crystal are given in Tab. 22.1 and was developed by Martinolli *et al.* [174].

Crystal type	n	$2d$	α	**Dimensions**	L
KAP	5	26.632 Å	17.35 °	$5 \times 4\,\mathrm{cm}^2$	32.65 cm

Table 22.1 – Parameters of the KAP crystal used in our experiments, α is the cone half-angle. This configuration suited to resolve Cu-K_α and Al-K_α at the diffraction orders $n = 5$ and $n = 1$.

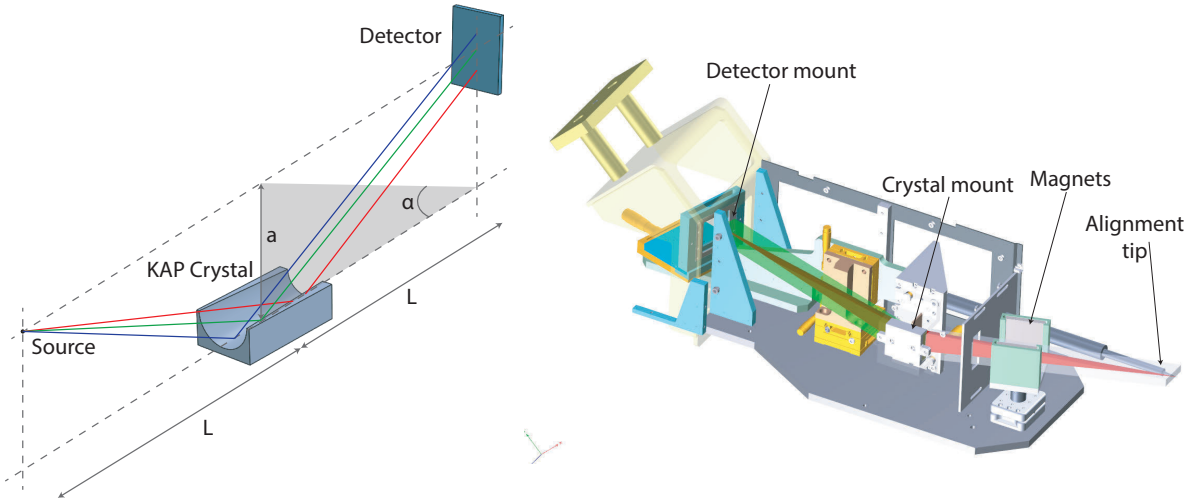

Figure 22.2 – Sketch of the tronconic spectrometer. The setup parameters annotated on the left are summarized in Tab. 22.1.

One can consider that the conical crystal is acting as a cylindrical mirror and obey to equation:

$$\frac{1}{p} + \frac{1}{q} = \frac{2\sin\theta_c}{R} \tag{22.3}$$

R is the radius of curvature of the conical crystal and is a function of the crystal position coordinate:

$$R(x_c) = -2\frac{y_c}{L}(L - x_c) \tag{22.4}$$

with x_c and y_c the coordinates where the incoming ray intersects with the crystal. Time image position on the focus line y_i is then given by:

$$y_i = \frac{y_c}{x_c}(L - 2x_c) \tag{22.5}$$

The Bragg's law is introduced here to obtain the dispersion relation between the image position and the incoming wavelength:

$$\frac{dy_i}{d\lambda} = \frac{L}{2d}\left[1 + \left(\frac{y_i + 2y_c}{L}\right)^2\right]^{3/2}. \tag{22.6}$$

This geometric dispersion relation does not take into account the real curvature radius R assuming it is equal to the crystal radius r. Moreover, the oblique incidence of X-rays also propagating in the z axis direction is not considered. Those rays, reflecting at different x_c positions on the crystal are focused on the image plan at different positions. The assumptions taken here lead to an spectral resolution given by:

$$\frac{dE_\nu}{E_\nu} = \frac{\cos^2\theta}{2}\frac{dz}{a} \tag{22.7}$$

a being the distance along z between the crystal center and the reflected position of the crystal center line onto detector (in our case $a = 102\,\text{mm}$). One obtains a spectral resolution of $\sim 1\,\text{eV}$ in our conditions. In reality one can find that it is limited to $\sim 2eV$ due to the geometrical effects described above.

Box. 22.1: Filtering

The image plate is covered with filters in order to get an appropriate transmission in the energy range of interest and prevent the saturation of the IP. The emission line obtained in the image plate needs to be further corrected from the transmission of the filters. The transmission of the filters varies with the photon energy and tables can be found in `http://henke.lbl.gov/optical_constants/`. In our experiments we used either a single filter of 15 µm-thick Be filter (see Figure 22.3), either a combination of the latter with a 10 µm-thick Cu filter.

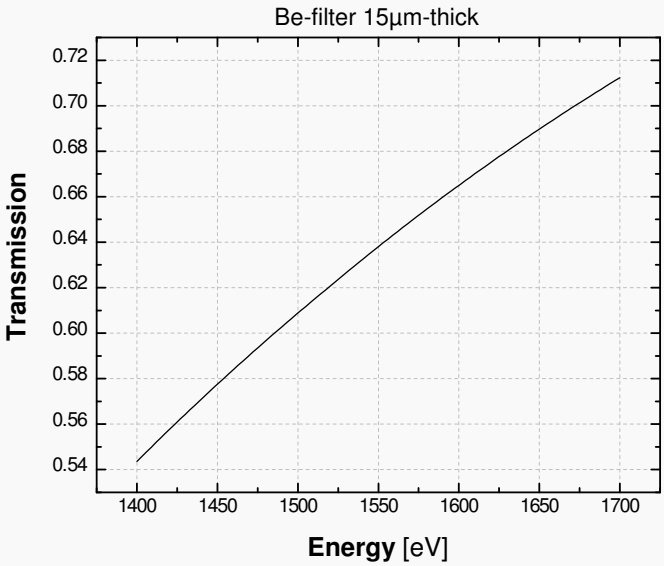

Figure 22.3 – Transmission of a 15 µm-thick Be filter from CXRO database (URL above).

22.3 X-ray K-α imager

The X-ray imager is used to make 2D images, integrated over time, at a given wavelength, of the K_α emission, by the mean of a spherical bent Bragg crystal [187, 5]. It is particularly useful to estimate the spatial pattern of an electron beam crossing the layer generating this emission (a layer of Cu in our case). A sketch of principle is presented in Figure 22.4.

In order to get a good spatial resolution, the Bragg angle should be very close to 90 ° to merge the two perpendicular sagittal and tangential image planes (their definition are given hereinafter). The spatial resolution σ is limited by the astigmatism in vertical direction (sagittal plane) [254]:

$$\sigma = (M+1)(1-\sin^2\theta_{\text{Bragg}})\frac{D}{M} \tag{22.8}$$

where M is the optical system magnification and θ_{Bragg} the Bragg angle of the crystal and D the

aperture diameter of the pinhole placed before the crystal. The symmetry break induced by an object located away from mirror axis leads to the creation of two perpendicular image planes called tangential and sagittal planes. The tangential planes contain the mirror axis and is perpendicular to the sagittal plane. Both contain the ray emerging from source and going through the crystal center.

Concerning the spectral resolution, spherical crystals have a $\Delta\lambda/\lambda \sim 10^{-3} - 10^{-4}$ [254].

If P is the distance from source to crystal center and Q from crystal center to detector, one has the optical relation :

$$\frac{1}{P} + \frac{1}{Q} = \frac{2}{R_c} \tag{22.9}$$

with R_c the radius of curvature of the crystal, and the theoretical magnification is given by:

$$M = \frac{Q}{P} \tag{22.10}$$

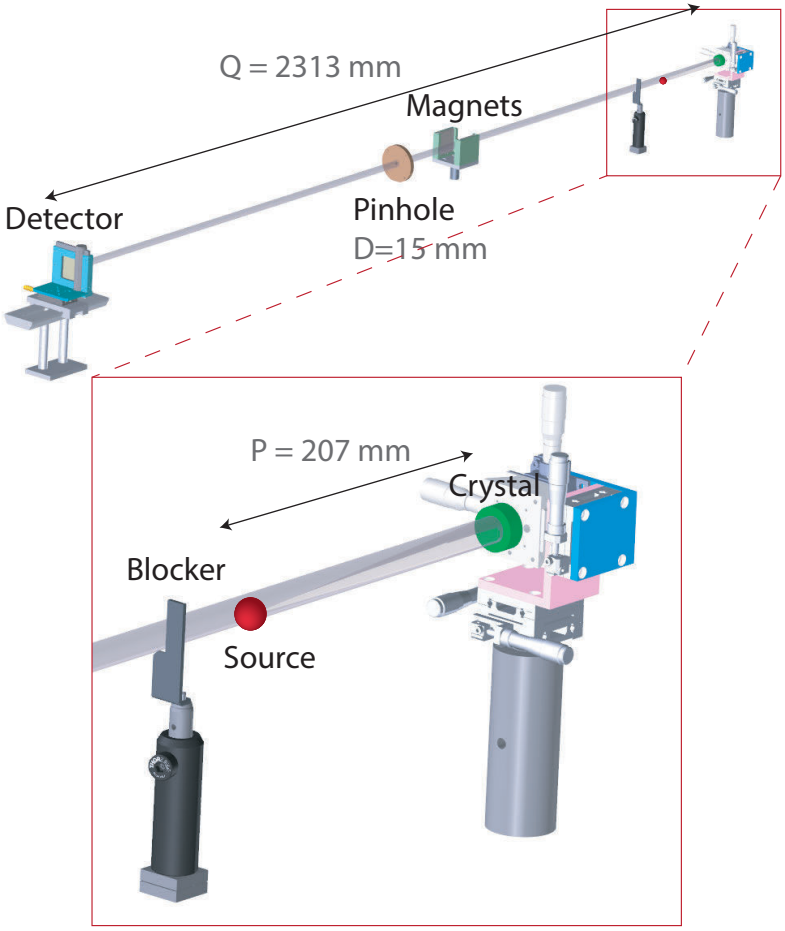

Figure 22.4 – Setup of the K_α imager as used in our experiments.

In an experimental setup, in order to protect the detector from the direct radiation of the source and from its emission of particles, a block of lead is placed on the direct line of sight between source and detector and a pair of magnets is used to deviate the charged particles away, without hiding the reflected signal. It is important to work well on the suppression of unwanted emissions since it affects strongly the ability to have a good enough signal-to-noise ratio.

Although, the paraxial conditions to preserve the good spatial resolution constrains the choice of the crystal in order to get an intense enough emission line to observe. The Cu-K_α fluorescence is bright enough at low diffraction orders and is energetic enough to avoid its attenuation along propagation. Tab. 22.2 presents the parameters of the spherical crystal used in our experiments. The sketch in Figure 22.4 also gives annotated distances of the setup.

The reflectivity of the Bragg's crystal depends on the plasma temperature [207] and one has to take care that a significant increase of the temperature does not shift the line emissions of interest out of the limited bandwidth of the crystal $\sim 10\,\mathrm{eV}$.

Crystal type (Miller's indices)	n	$2d$	R_c	$\theta_{\mathbf{Bragg}}$	**Emission line**
Quartz (2131)	2	3.082 Å	380 mm	88.7 °	Cu-$K_{\alpha,1}$@8047.78 eV

Table 22.2 – Parameters of the spherical crystal used in our experiments.

22.4 Hard X-ray spectrometry - "Bremsstrahlung Canons"

Fast electrons generate an intense and continuous emission of hard X-rays throughout their propagation. The broad spectrum emitted by fast electrons has an intensity-dependence with the kinetic energy of electrons who produce it and therefore one can relate the emitted photon spectrum with the fast electron distribution.

In our experiments we used a technique consisting of the use of a stack of successive layers of material of different composition and thickness to characterize the bremsstrahlung emission. This technique is based on differential filtering and the spectrometer is called *bremsstrahlung cannon* and was first developed by [46]. This spectrometer is composed of fifteen $1 \times 1\,\mathrm{in}^2$ filters with increasing atomic number, ranging from aluminium to lead with different thicknesses (see Tab. 22.3). Between each layer a MS-type imaging plate (see Sec. 20) is inserted and yields thus fifteen energy bins which have to be deconvoluated to infer the electron distribution at the origin of the hard x-ray emission.

The stack of filters and IPs is enclosed into a plastic-made cartridge which avoid any deleterious exposure of IPs to ambient light. Both the cartridge and 250 µm-tick mylar foils surrounding each filter allow to minimize the contribution to the measured signal of secondary electrons that could be created in the stack. The cartridge is itself contained in a 1.8 cm thick lead box shielding against fast electrons up to 2 MeV. A 12.5 cm long lead collimator with a $\frac{1}{2}$ inch diameter centered hole is located in front of the cannon in order to suppress the fluorescence from the target, the chamber walls or all the other diagnostics. A sketch of the cannon design used in our experiments is shown in Figure 22.5.

Material	**Thickness** [mm]	**Density** [$\mathrm{g/cm^3}$]
Al	10	2.2
Ti	10	2.7
Fe	10	4.54
Cu	10	8.96
Mo	10	10.22
Ag	15	10.5
Sn	50	7.31
Ta	50	16.65
Au	15.6	19.3
Pb	10	11.35
Pb	20	11.35
Pb	30	11.35
Pb	40	11.35
Pb	63.5	11.35
Pb	63.5	11.35

Table 22.3 – Characteristics of the filters composing the bremsstrahlung cannon used in our experiments.

The deconvolution of electron spectrum from measured bremsstrahlung is not direct and rely on complex Monte-Carlo numerical simulations. An electron spectrum is injected as source and collisions with the target ions are computed by the Monte-Carlo code. An iterative solver is used to match the

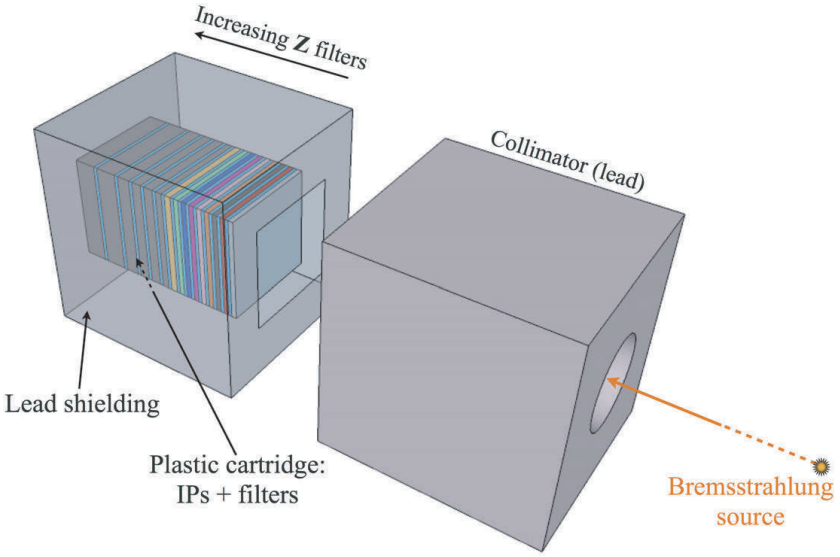

Figure 22.5 – Bremsstrahlung cannon design as used in our experiments. Fifteen IPs are used to measure the bremsstrahlung signal. Each IP is surrounded by different materials of different thicknesses, as detailed in Tab. 22.3.

energy deposition within the active layer of each IP with the experimental PSL signals. The electron source parameters need to be somehow constrained since the limited number of detectors used in bremsstrahlung cannon does not imply an unique electron spectrum. For this reason, several cannons inside the chamber at different angles can be used to increase the accuracy of the deconvolution procedure.

For a given angle and position of the cannon, an interaction matrix can be built from the Monte-Carlo code and finding the spectrum then rely on a linear system of equations similar to what we have for RCFs (see Sec. 18.3). As for RCFs, a direct solve of the system can also be substituted by an iterative solver since the true inverse of the interaction matrix cannot be calculated.

23 Coherent Transition Radiation (CTR)

The transition radiation (TR) can be described by classical electrodynamics and corresponds to the passage of an electron through an interface that separates two media with different dielectric responses. The Maxwell's equations of the problem reduce to:

$$\vec{\nabla} \wedge \vec{H} = \frac{\partial \vec{D}}{\partial t} + e\vec{v}\delta(\vec{r} - \vec{v}t) \tag{23.1}$$

$$\vec{\nabla} \wedge \vec{E} = -\frac{\partial \vec{B}}{\partial t} \tag{23.2}$$

$$\vec{\nabla} \cdot \vec{B} = 0 \tag{23.3}$$

$$\vec{\nabla} \cdot \vec{D} = e\delta(\vec{r} - \vec{v}t) \tag{23.4}$$

where δ is the Dirac distribution and $\vec{r} = \vec{v}t$ defines the electron's trajectory. The solution of the system of equation Eq. 23.4 is obtained for the case of a semi-infinite plasma ([302, 303, 247, 20]). The energy W emitted per unit angular frequency and solid angle in the forward direction, for a particle traversing normal to an interface separating plasma and vacuum is:

$$\left.\frac{d^2W}{d\omega d\Omega}\right|_{\parallel} = \frac{e^2}{\pi^2 c}\frac{\beta^2 \sin^2\theta}{(1-\beta^2\cos^2\theta)^2} \tag{23.5}$$

where the subscript $\parallel$ is used to denote that the transition radiation field is radially polarized for a particle normally incident to the interface (due to the radial symmetry of the dipole response of the material) and θ is the angle between the direction of the particle and the direction of the observation. Eq. 23.5 shows that the radiation is peaked at $\theta \approx 1/\gamma$ (γ is the Lorentz relativistic factor) and exhibits a zero of emission along the axis, due to the symmetry of the problem. The radiation is thus emitted in a cone of half-angle $\sim 1/\gamma$ and the total emitted radiation is roughly proportional to the particle's energy (or identically to γ).

We introduce the particle momentum vector $\vec{p} = |p|(\sin\psi\cos\phi, \sin\psi\sin\phi, \cos\psi)$ and the observation vector $\vec{k} = \omega/c(\sin\theta\cos\alpha, \sin\theta\sin\alpha, \cos\theta)$. Geometrical parameters are shown in Figure 23.1.

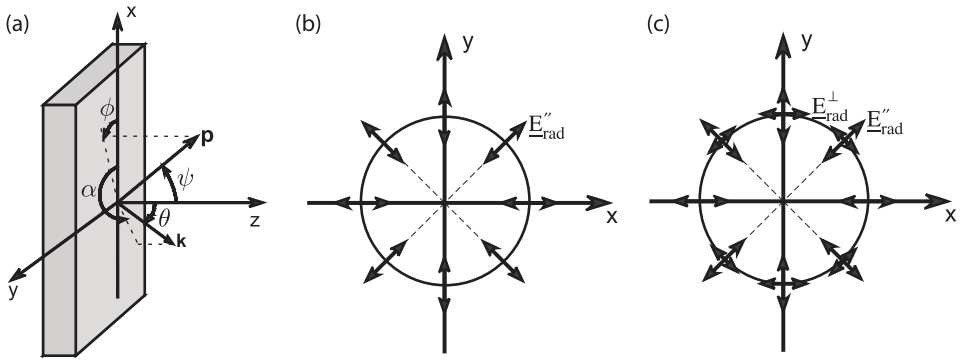

Figure 23.1 – (a) Geometrical parameters involved in the calculations of TR. $\boldsymbol{p}$ is the particle's direction, $\boldsymbol{k}$ is the wave (observation) vector and z is the normal to the target rear surface. (b) For a charge crossing normal to the interface, the radiation is radially polarized. The magnetic field (not shown) is azimuthal. (c) In general, there is a component of the electric field parallel and normal to the radiation plane, withe the magnitude dependent on the angle of observation (this figure is relevant to an electron moving in the $x-z$ plane). *Figure and legend taken from [20].*

The total emitted TR per unit angular frequency and unit solid angle can be written as:

$$\frac{d^2W}{d\omega d\Omega} = \frac{e^2N}{\pi^2 c}\left[\int d^3\vec{p}\,(\epsilon_{\parallel}^2 + \epsilon_{\perp}^2) + (N-1)\left(\left|\int d^3\vec{p}\,g(\vec{p})\epsilon_{\parallel}F\right|^2 + \left|\int d^3\vec{p}\,g(\vec{p})\epsilon_{\perp}F\right|^2\right)\right]. \tag{23.6}$$

$g(\vec{p})$ is the momentum distribution function, $\epsilon_{\parallel}$ and $\epsilon_{\perp}$ are the Fourier-transforms of the electric fields in the plane parallel and perpendicular to the radiation plane and F is a coherence function that takes into account the exact time and position at which electrons reach the interface:

$$F = \frac{1}{g(\vec{p})} \int d^2\vec{r}_{\perp} e^{-i\vec{k}_{\perp}\cdot\vec{r}_{\perp}} \int_{-\infty}^{+\infty} dz\, e^{-iz(\omega t - \vec{k}_{\perp}\cdot\vec{v}_{\perp})/v_z}\, h(\vec{r},\vec{p}). \tag{23.7}$$

and we note the phase term:

$$\Phi = \vec{k}_{\perp}\cdot\vec{r}_{\perp} - \omega t \tag{23.8}$$

The coherent component of the radiation is given by the second line in Eq. 23.6. The phase term is the sum of a spatial term Φ_s and a temporal term Φ_t. $|\vec{k}_{\perp}| = \omega/c \sin\theta$ is the component of the wave vector in the plane $x-y$ and the space shift associated to the planes waves emitted at positions A_1 and A_2 reaching the observer after having respectively traveled a distance L_1 and L_2, writes:

$$\Delta\Phi_s = 2\pi\frac{L_1 - L_2}{\lambda} = \vec{k_{\perp}}\cdot(\vec{r}_{\perp 2} - \vec{r}_{\perp 1}), \tag{23.9}$$

while the temporal component is:

$$\Delta\Phi_t = \omega(t_2 - t_1) \tag{23.10}$$

The parameters used in the previous equation are schematized in Figure 23.2.

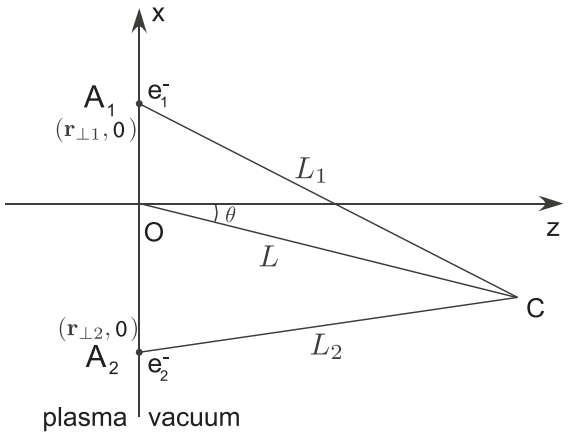

Figure 23.2 – Parameters used for the evaluation of the phase term for a single electron. *Figure and legend taken from [20].*

The discrete version of Eq. 23.6 writes:

$$I_{TR} \sim \underbrace{\sum_i |\vec{E}_i|^2}_{\text{incoherent}} + \underbrace{\sum_i \sum_{j,j\neq i} |\vec{E}_i||\vec{E}_j| \exp\left[i(\Phi_j - \Phi_i)\right]}_{\text{coherent}} \tag{23.11}$$

Where the electric field $\vec{E} = \vec{E}_{\parallel} + \vec{E}_{\perp}$ and "$\exp\left[i(\Phi_j - \Phi_i)\right]$" is the phase term.

In the case of relativistic laser-plasma interactions, which generate a huge amount of fast electrons, coherent radiation can be emitted for wavelengths $\lambda > c\tau_b$, where τ_b is the duration of the fast electron population crossing the radiating interface. Typically, these are wavelengths much bigger than the usually observed visible spectrum. Yet, due to modulations in the electron current, coherent emission appears from the interference of emission produced by multiple consecutive micro-bunches of fast electrons [12, 214].

23.1 Focus on the CTR post-processor developed in this thesis work

Here, we will further detail the equations used under the asumptions adopted for the CTR post-processor, as presented in Sec. 10.6.

We remind that only the temporal phase term is considered and the CTR emission is calculated in arbitrary units. The phase term thus writes:

$$\Phi_j - \Phi_i = \omega\, TOF \tag{23.12}$$

with the observation angular frequency $\omega = 2\pi c/\lambda$ and TOF the time-of-flight of the considered electron over the target's depth.

The expression of the parallel and perpendicular electric field used in Eq. 23.11 can be obtained integrating Eq. 23.6, with the equivalent formulation presented in [20] - (Equation 28):

$$E_{\parallel} = \frac{u\cos\psi\left(u\cos(\alpha-\phi)\sin\psi - \sqrt{1+u^2}\sin\theta\right)}{\left(\sqrt{1+u^2} - u\cos(\alpha-\phi)\sin\psi\sin\theta\right)^2 - u^2\cos^2\psi\cos^2\theta} \tag{23.13}$$

$$E_{\perp} = \frac{u^2\cos\psi\cos\theta\sin(\alpha-\phi)\sin\psi}{\left(\sqrt{1+u^2} - u\cos(\alpha-\phi)\sin\psi\sin\theta\right)^2 - u^2\cos^2\psi\cos^2\theta} \tag{23.14}$$

with $u = |\vec{u}|$ the norm of the electron velocity at the target rear side.

23.2 Benchmarked simulations

In order to benchmark the CTR post-processor, simulations were performed in the conditions of the experiment held by Santos *et al.* and described in the article [239]. The experiment was performed at the LULI 100 TW laser facility using a 350 fs, 1.057 µm laser pulse with an energy of 10 J on target, yielding intensities of $\approx 1 \times 10^{19}\,\mathrm{W/cm^2}$. In this paper, the authors report rear-side optical self-emission results from ultra-intense laser pulse interactions with Al solid targets of varying thicknesses. The prompt self-emission is mostly due to CTR at $2\omega_0$, as seen in similar conditions by spectral measurements made by Popescu *et al.* in [214]. For this reason, we can reasonably compare the results of CTR emission size at the rear-side of varying length simulation boxes with the emission measured in [239].

The results obtained in that latter paper are shown in Figure 23.3.

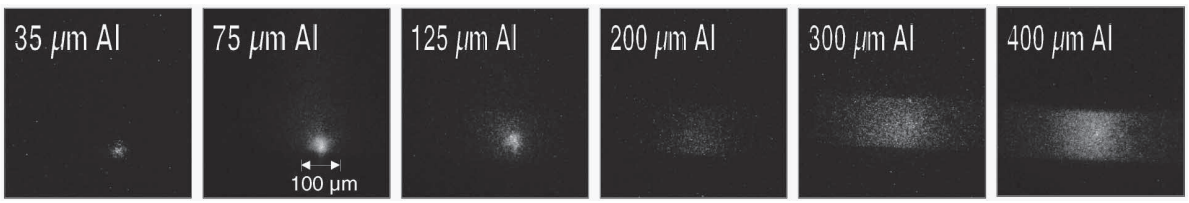

Figure 23.3 – Time-resolved snapshots of the self-emission from the rear side of Al targets with thicknesses ranging from 35 up to 400 µm. The laser energy on target was 10 J and laser intensity of $\sim 10^{19}\,\mathrm{W/cm^2}$. Used neutral densities were, from left to right, ND = 3.5, 1, 1, 1, 0.5, 0. *Images from [239].*

The source parameters used in the simulations are:

- ◇ 30 % of conversion efficiency from $E_L = 10$ J to hot electrons.
- ◇ An initial REB radius $r_0 \approx 24$ µm, using an empiric factor $f_{res} = 3$ between focal spot radius and initial REB radius.
- ◇ A mean divergence angle of 25 °, consistent with a lower laser intensity than in our experiments (see [96]). The dispersion angle is fixed to 55 °.
- ◇ An energy distribution similar to that described above for our experiments, with here $T_h = 1$ MeV.
- ◇ An initial electron background temperature of 0.1 eV, as used in simulations without external B-field.

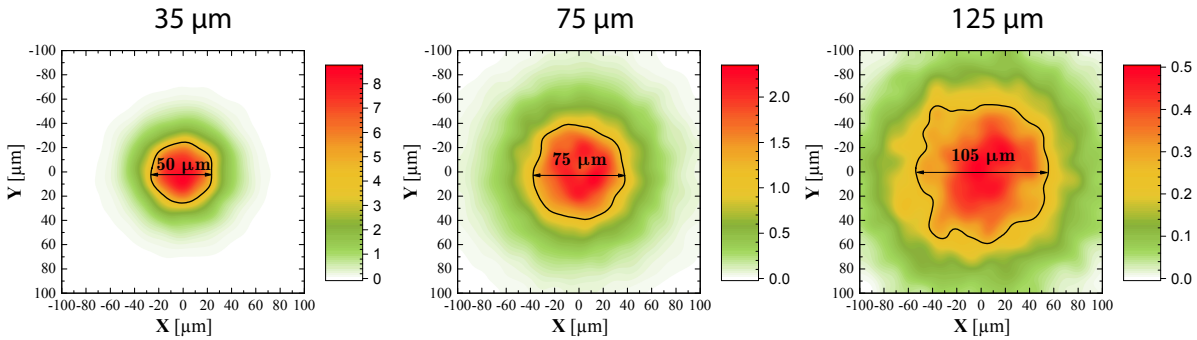

Figure 23.4 – Synthetic CTR emission at target rear side of Al targets of varying thicknesses, from left to right : 35 µm, 75 µm and 125 µm. The FWHM of the obtained emission patterns are given in each image. The emission yields (color scales) are given in arbitrary units.

Simulation results are given in Figure 23.4 for three simulated thicknesses of Al sample of 35 µm, 75 µm and 125 µm. We obtained respectively FWHM of the CTR patterns at target rear side of 50 µm, 75 µm and 125 µm. These simulation results are compared in Figure 23.5 with the direct measurements of the rear side emission in the reported experiment.
The simulation process with PIC Hybrid code and CTR post-processing is seen to fairly reproduce the size of the CTR pattern measured experimentally, using REB source parameters consistent with the characteristics of laser irradiation in the regime of intensity of $\sim 10^{19}\,\mathrm{W/cm^2}$.

It is worth mentioning here that the lens was located in the equatorial plane of the target with a normal angle of observation (0 °). The final synthetic images take into account the imaging system solid angle, angle of observation and magnification factor, and we finally compared to the experimental CTR data.

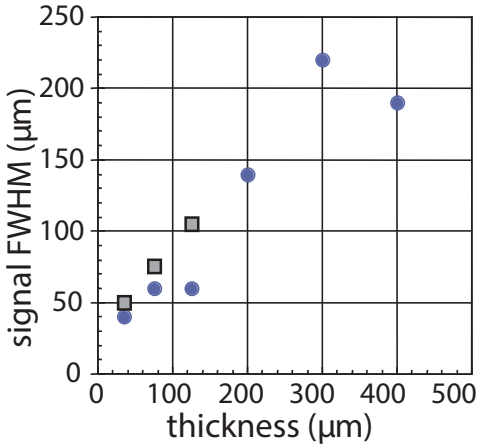

Figure 23.5 – Evolution of the rear-side self-emission with different Al target thicknesses, from experiments (in blue dots) compared with the results of PIC hybrid + CTR post-processor (grey squares). *Original graph from [239].*

23.3 Influence of the observation angle

Here we study the influence of the lens observation angle, as computed by the CTR post-processor. The simulations have been made with the source parameters of our experimental configurations analyzed in this thesis work in Sec. 10.5.

Figure 23.6 shows results for the synthetic CTR for the experimental conditions: with and without B-field, with in config. i) the transport target outside the coil plane and in config. ii) the transport target at the coil plane, as already presented in Figure 10.2. The time and space integrated CTR yields are plotted as a function of the imaging diagnostic orientation with respect to the target normal, by varying both latitude (dashed lines) and longitude (full lines). The figure also shows sample synthetic CTR images, corresponding to the lens coordinates indicated in the graphs. The four images corresponding to the experimental setup (longitude 22.5 °, latitude 0 °) are identified by the thicker box frames and by the dots on the graphs. The size of the dots are representative of the solid angle of the collecting lens in the experiment. The CTR yield calculation obtained either by considering the full solid angle of the lens or its center point differs by less than 1 %, justifying the point-like lens approximation made in calculations of Sec. 10.7.

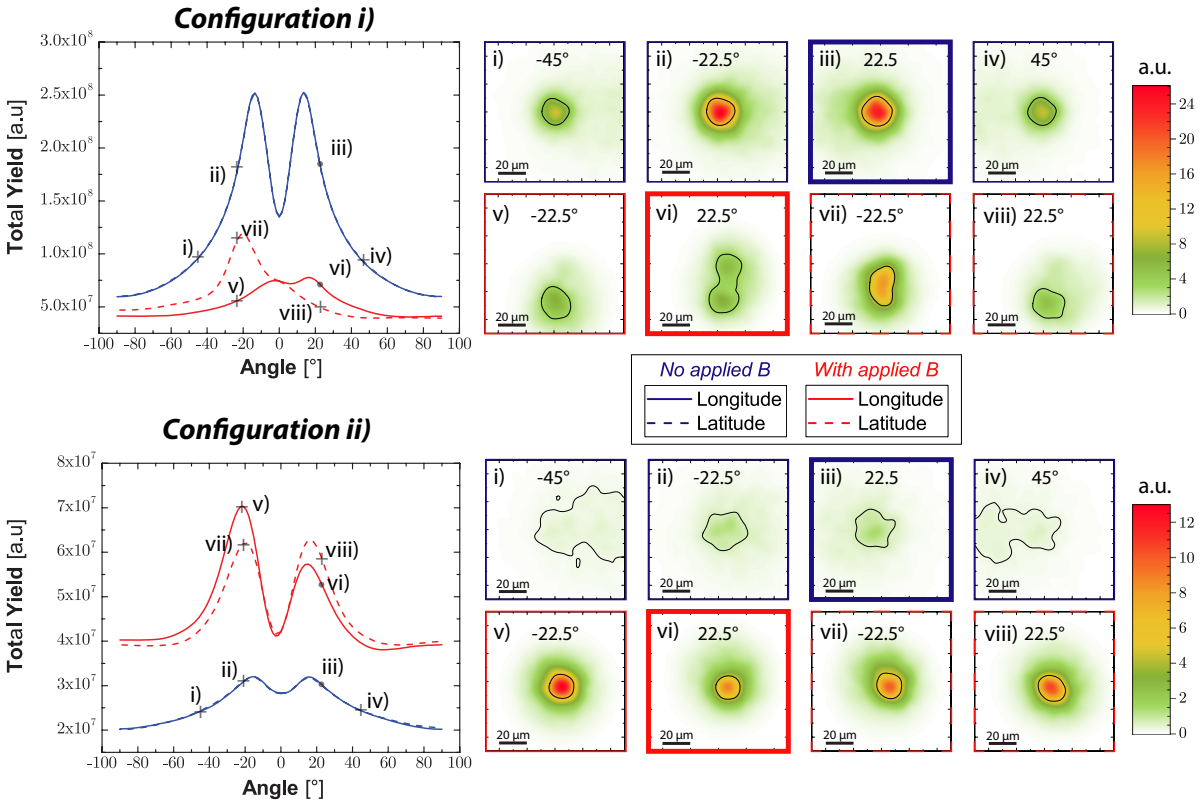

Figure 23.6 – Synthetic CTR calculated from the benchmarked simulations of REB transport in the experimental conditions. The graphs on the left plot the total CTR yield as a function of the lens position, in terms of varying longitude (full lines) or varying latitude (dashed lines). The symbols identify the coordinates corresponding to the sample synthetic CTR images on the right. Blue curves and boxes correspond to REB transport without B-field, red curves and boxes to REB transport with imposed B-field. The four experimental configurations analyzed in text are identified by the thicker frames and by the dot-symbols in the graphs.

In the case without applied B-field (blue curves/frames), the diverging REB propagation is symmetric around the injection axis. The result is a symmetric CTR emission pattern. As expected [20], peak emission in the CTR image occurs at an angle close to $1/\gamma$, where γ is the relativistic factor corresponding to the mean energy of the REB. With B-field (red curves/frames), the REB propagation is confined to a small radius and revolves at the cyclotron frequency around its symmetry axis.

In configuration i), the REB axis deviates downwards due to the inclination in B-field lines, explaining the asymmetric angular dependence of the CTR emission. The peak emission in latitude corresponds to the direction angle of the REB exiting at the target rear. In configuration ii) the angular distribution is closer to that of a beam symmetric to the target normal, yet due to the cyclotron movement, the exiting position and angle are related to the target thickness.

To conclude, the yield, spatial and angular distributions of CTR are non-linearly dependent on the density of fast electrons crossing the target-vacuum boundary, on their momentum distribution (norm and angle relative to the target normal) and on the observation angle relative to the symmetry axis of the momentum distribution.

List of publications and communications

First author

[A1] M. Bailly-Grandvaux, J. J. Santos, C. Bellei, P. Forestier-Colleoni, S. Fujioka, L. Giuffrida, J. J. Honrubia, D. Batani, R. Bouillaud, M. Chevrot, J. E. Cross, R. Crowston, S. Dorard, J.-L. Dubois, M. Ehret, G. Gregori, S. Hulin, S. Kojima, E. Loyez, J.-R. Marques, A. Morace, P. Nicolai, M. Roth, S. Sakata, G. Schaumann, F. Serres, J. Servel, V. T. Tikhonchuk, N. Woolsey, and Z. Zhang, "Guiding of relativistic electron beams in dense matter by longitudinally imposed strong magnetic fields", Nature Communications (accepted) (2017).

Second author

[B1] K. F. F. Law, M. Bailly-Grandvaux, A. Morace, S. Sakata, K. Matsuo, S. Kojima, S. Lee, X. Vaisseau, Y. Arikawa, A. Yogo, K. Kondo, Z. Zhang, C. Bellei, J. J. Santos, S. Fujioka, and H. Azechi, "Direct measurement of kilo-tesla level magnetic field generated with laser-driven capacitor-coil target by proton deflectometry", Applied Physics Letters **108**, 091104 (2016).

[B2] J. J. Santos, M. Bailly-Grandvaux, L. Giuffrida, P. Forestier-Colleoni, S. Fujioka, Z. Zhang, P. Korneev, R. Bouillaud, S. Dorard, D. Batani, M. Chevrot, J. E. Cross, R. Crowston, J.-L. Dubois, J. Gazave, G. Gregori, E. d'Humières, S. Hulin, K. Ishihara, S. Kojima, E. Loyez, J.-R. Marquès, A. Morace, P. Nicolaï, O. Peyrusse, A. Poyé, D. Raffestin, J. Ribolzi, M. Roth, G. Schaumann, F. Serres, V. T. Tikhonchuk, P. Vacar, and N. Woolsey, "Laser-driven platform for generation and characterization of strong quasi-static magnetic fields", New Journal of Physics **17**, 083051 (2015).

Co-author

[C1] S. Fujioka, Y. Arikawa, S. Kojima, T. Johzaki, H. Nagatomo, H. Sawada, S. H. Lee, T. Shiroto, N. Ohnishi, A. Morace, X. Vaisseau, S. Sakata, Y. Abe, K. Matsuo, K. F. F. Law, S. Tosaki, A. Yogo, K. Shigemori, Y. Hironaka, Z. Zhang, A. Sunahara, T. Ozaki, H. Sakagami, K. Mima, Y. Fujimoto, K. Yamanoi, T. Norimatsu, S. Tokita, Y. Nakata, J. Kawanaka, T. Jitsuno, N. Miyanaga, M. Nakai, H. Nishimura, H. Shiraga, K. Kondo, M. Bailly-Grandvaux, C. Bellei, J. J. Santos, and H. Azechi, "Fast ignition realization experiment with high-contrast kilo-joule peta-watt lfex laser and strong external magnetic field", Physics of Plasmas **23**, 056308 (2016).

[C2] E. d'Humières, S. Chen, M. Lobet, M. Sciscio, P. Antici, M. Bailly-Grandvaux, T. Gangolf, G. Revet, J. Santos, A. Schroer, O. Willi, V. Tikhonchuk, H. Pépin, and J. Fuchs, "Longitudinal laser ion acceleration in low density targets: experimental optimization on the titan laser facility and numerical investigation of the ultra-high intensity limit", Proc. SPIE **9514**, 95140B (2015).

[C3] A. Poyé, J.-L. Dubois, F. Lubrano-Lavaderci, E. D'Humières, M. Bardon, S. Hulin, M. Bailly-Grandvaux, J. Ribolzi, D. Raffestin, J. J. Santos, P. Nicolaï, and V. Tikhonchuk, "Dynamic model of target charging by short laser pulse interactions", Phys. Rev. E **92**, 043107 (2015).

[C4] A. Poyé, S. Hulin, M. Bailly-Grandvaux, J.-L. Dubois, J. Ribolzi, D. Raffestin, M. Bardon, F. Lubrano-Lavaderci, E. D'Humières, J. J. Santos, P. Nicolaï, and V. Tikhonchuk, "Physics of giant electromagnetic pulse generation in short-pulse laser experiments", Phys. Rev. E **91**, 043106 (2015).

Oral communications

◇ M. Bailly-Grandvaux, L. Giuffrida, D. Batani, R. Bouillaud, M. Chevrot, J. Cross, R. Crowston, S. Dorard, J-L. Dubois, P. Forrestier-Colleoni, S. Fujioka, J. Gazave, G. Gregori, S. Hulin, E. d'Humières, K. Ishihara, S. Kojima, P. Korneev, E. Loyez, J-R. Marques, A. Morace, Ph. Nicolaï, H. Nishimura, A. Poyé, D. Raffestin, J. Ribolzi, M. Roth, G. Schaumann, F. Serres, V. Tikhonchuk, Ph. Vacar, N. Woolsey, Z. Zhang and J.J. Santos, "Multiple characterization of strong magnetic fields generated by ns-laser pulses", *13th International Workshop on the Fast Ignition of Fusion Targets*, September 14th-18th 2014, Oxford, UK

◇ M. Bailly-Grandvaux, L. Giuffrida, P. Forestier-Colleoni, S. Fujioka, Z. Zhang, R. Bouillaud, S. Dorard, D. Batani, M. Chevrot, J. Cross, R. Crowston, J.-L. Dubois, J. Gazave, G. Gregori, J.J. Honrubia, E. d'Humières, S. Hulin, K. Ishihara, S. Kojima, Ph. Korneev, E. Loyer, J.-R. Marqués, A. Morace, Ph. Nicolaï, O. Peyrusse, A. Poyé, D. Raffestin, J. Ribolzi, M. Roth, G. Schaumann, F. Serres, C. Spindloe, V.T. Tikhonchuk, Ph. Vacar, N. Woolsey and J. J. Santos, "Pulsed strong magnetic field generation by laser and application to guided electron beam transport", *PLS seminar in Livermore National Laboratory (LLNL)*, December 5th 2014, Livermore, USA

◇ M. Bailly-Grandvaux, L. Giuffrida, P. Forestier-Colleoni, S. Fujioka, Z. Zhang, R. Bouillaud, S. Dorard, D. Batani, M. Chevrot, J. Cross, R. Crowston, J.-L. Dubois, J. Gazave, G. Gregori, J.J. Honrubia, E. d'Humières, S. Hulin, K. Ishihara, S. Kojima, Ph. Korneev, E. Loyer, J.-R. Marqués, A. Morace, Ph. Nicolaï, O. Peyrusse, A. Poyé, D. Raffestin, J. Ribolzi, M. Roth, G. Schaumann, F. Serres, C. Spindloe, V.T. Tikhonchuk, Ph. Vacar, N. Woolsey and J.J. Santos, "Measurements of laser-driven strong magnetic fields", *1st EPS Conference on Plasma Diagnostics*, April 14th-17th 2015, Frascati, Italy

◇ M. Bailly-Grandvaux, D. Batani, C. Bellei, J.-L. Dubois, M. Ehret, P. Forestier-Colleoni, S. Fujioka, L. Giuffrida, J. Honrubia, S. Hulin, S. Kojima, P. Korneev, J.-R. Marquès, A. Morace, P. Nicolaï, O. Peyrusse, A. Poyé, M. Roth, S. Sakata, G. Schaumann, J. Servel, V.T. Tikhonchuk, Z. Zhang, and J.J. Santos, "Collimation of relativistic electron beams in dense matter by externally imposed magnetic Field", *14th International Workshop on the Fast Ignition and High-Fields with High-Power Lasers*, May 17th-20th 2016, Yokohama, Japan (invited talk)

◇ M. Bailly-Grandvaux, M. Ehret and J.J. Santos, "Laser-driven B-field platform for LIGHT?", *Light Collaboration Meeting 2016*, September 26-27 2016, Darmstadt, Germany

Contribution to poster sessions

◇ M. Bailly-Grandvaux, L. Giuffrida, D. Batani, J.-L. Dubois, P. Forestier-Colleoni, S. Fujioka, J. Gazave, S. Hulin, K. Ishiara, J.-R. Marquès, Ph. Nicolaï, H. Nishimura, D. Raffestin, J. Ribolzi, V. Tikhonchuck, X. Vaisseau, Z. Zhang and J.J. Santos, "kT magnetic field generated by laser: experimental results and modeling", *Forum Institut Lasers et Plasmas (ILP)*, February 2nd-7th 2014, Orcières, France

◇ M. Bailly-Grandvaux, L. Giuffrida, D. Batani, J.-L. Dubois, P. Forestier-Colleoni, S. Fujioka, J. Gazave, S. Hulin, K. Ishiara, J.-R. Marquès, Ph. Nicolaï, H. Nishimura, D. Raffestin, J. Ribolzi, V. Tikhonchuck, X. Vaisseau, Z. Zhang and J.J. Santos, "kT magnetic field generated by laser: experimental results and modeling", *LMJ-Petal - COST Workshop*, March 5th-7th 2014, Bordeaux, France

◇ M. Bailly-Grandvaux, L. Giuffrida, P. Forestier-Colleoni, S. Fujioka, Z. Zhang, R. Bouillaud, S. Dorard, D. Batani, M. Chevrot, J. Cross, R. Crowston, J.-L. Dubois, J. Gazave, G. Gregori, J.J. Honrubia, E. d'Humières, S. Hulin, K. Ishihara, S. Kojima, Ph. Korneev, E. Loyer, J.-R. Marqués, A. Morace, Ph. Nicolaï, O. Peyrusse, A. Poyé, D. Raffestin, J. Ribolzi, M. Roth, G. Schaumann, F. Serres, C. Spindloe, V.T. Tikhonchuk, Ph. Vacar, N. Woolsey and J.J. Santos, "External magnetic field pinching effect on a relativistic electron beam in dense matter", *42nd EPS Conference on Plasma Physics*, June 22nd-26th 2015, Lisbon, Portugal (Award: *1st prize of Student Poster Prize*)

References

[1] J. C. Adam, A. Héron, and G. Laval, "Dispersion and transport of energetic particles due to the interaction of intense laser pulses with overdense plasmas", Phys. Rev. Lett. **97**, 205006 (2006) (cit. on p. 79).

[2] H. Ahmed, S. Kar, G. Cantono, G. Nersisyan, S. Brauckmann, D. Doria, D. Gwynne, A. Macchi, K. Naughton, O. Willi, C. Lewis, and M. Borghesi, "Investigations of ultrafast charge dynamics in laser-irradiated targets by a self probing technique employing laser driven protons", Nuclear Instruments and Methods in Physics Research Section A: Accelerators, Spectrometers, Detectors and Associated Equipment **829**, 2nd European Advanced Accelerator Concepts Workshop - {EAAC} 2015, 172 (2016) (cit. on p. 94).

[3] B. Albertazzi, J. Béard, A. Ciardi, T. Vinci, J. Albrecht, J. Billette, T. Burris-Mog, S. N. Chen, D. Da Silva, S. Dittrich, T. Herrmannsdörfer, B. Hirardin, F. Kroll, M. Nakatsutsumi, S. Nitsche, C. Riconda, L. Romagnagni, H.-P. Schlenvoigt, S. Simond, E. Veuillot, T. E. Cowan, O. Portugall, H. Pépin, and J. Fuchs, "Production of large volume, strongly magnetized laser-produced plasmas by use of pulsed external magnetic fields", Review of Scientific Instruments **84**, 043505 (2013) (cit. on p. 28).

[4] B. Albertazzi, A. Ciardi, M. Nakatsutsumi, T. Vinci, J. Béard, R. Bonito, J. Billette, M. Borghesi, Z. Burkley, S. N. Chen, T. E. Cowan, T. Herrmannsdörfer, D. P. Higginson, F. Kroll, S. A. Pikuz, K. Naughton, L. Romagnani, C. Riconda, G. Revet, R. Riquier, H.-P. Schlenvoigt, I. Y. Skobelev, A. Y. Faenov, A. Soloviev, M. Huarte-Espinosa, A. Frank, O. Portugall, H. Pépin, and J. Fuchs, "Laboratory formation of a scaled protostellar jet by coaligned poloidal magnetic field", Science **346**, 325 (2014) (cit. on pp. 18, 28, 207).

[5] L. Antonelli, P. Forestier-Colleoni, G. Folpini, R. Bouillaud, A. Faenov, L. Fedeli, C. Fourment, L. Giuffrida, S. Hulin, S. Pikuz, J. J. Santos, L. Volpe, and D. Batani, "Measurement of reflectivity of spherically bent crystals using Kα signal from hot electrons produced by laser-matter interaction", Review of Scientific Instruments **86**, 073507, 073507 (2015) (cit. on p. 253).

[6] S. Atzeni, "Inertial fusion fast ignitor: Igniting pulse parameter window vs the penetration depth of the heating particles and the density of the precompressed fuel", Physics of Plasmas **6**, 3316 (1999) (cit. on p. 25).

[7] S. Atzeni, M. Temporal, and J. Honrubia, "A first analysis of fast ignition of precompressed icf fuel by laser-accelerated protons", Nuclear Fusion **42**, L1 (2002) (cit. on pp. 26, 206).

[8] S. Atzeni and J. Meyer-ter-Vehn, *The physics of inertial fusion: beam plasma interaction, hydrodynamics, hot dense matter*, International Series of Monographs on Physics (Oxford University Press, Oxford, 2004), 480 pp. (cit. on p. 128).

[9] H. Azechi and FIREX Project Team, "The status of Fast Ignition Realization Experiment (FIREX) and prospects for inertial fusion energy", Journal of Physics Conference Series **717**, 012006, 012006 (2016) (cit. on p. 182).

[10] S. A. Balbus, "Enhanced Angular Momentum Transport in Accretion Disks", Annu. Rev. Astron. Astrophys. **41**, 555 (2003) (cit. on p. 17).

[11] D. H. Barnak, P.-Y. Chang, G. Fiksel, R. Betti, and C. Taylor, "Increasing Magnetic-Field Capability of MIFEDS Using an Inductively Coupled Coil", in Aps meeting abstracts (Oct. 2013) (cit. on p. 28).

[12] S. D. Baton, J. J. Santos, F. Amiranoff, H. Popescu, L. Gremillet, M. Koenig, E. Martinolli, O. Guilbaud, C. Rousseaux, M. Rabec Le Gloahec, T. Hall, D. Batani, E. Perelli, F. Scianitti, and T. E. Cowan, "Evidence of Ultrashort Electron Bunches in Laser-Plasma Interactions at Relativistic Intensities", Physical Review Letters **91**, 105001, 105001 (2003) (cit. on pp. 169, 258).

[13] C. Baum, *Maximizing frequency response of a b-dot loop*, Sensor and Simulation Notes 8, Dec. 1964 (cit. on p. 218).

[14] C. Baum, *The single-gap cylindrical loop in non-conducting and conducting media*, Sensor and Simulation Notes 30, Jan. 1967 (cit. on p. 218).

[15] F. N. Beg, A. R. Bell, A. E. Dangor, C. N. Danson, A. P. Fews, M. E. Glinsky, B. A. Hammel, P. Lee, P. A. Norreys, and M. Tatarakis, "A study of picosecond laser–solid interactions up to 10^{19} Wcm^{-2}", Physics of Plasmas **4**, 447 (1997) (cit. on pp. 55, 73, 80).

[16] F. N. Beg, M. S. Wei, E. L. Clark, A. E. Dangor, R. G. Evans, P. Gibbon, A. Gopal, K. L. Lancaster, K. W. D. Ledingham, P. McKenna, P. A. Norreys, M. Tatarakis, M. Zepf, and K. Krushelnick, "Return current and proton emission from short pulse laser interactions with wire targets", Physics of Plasmas **11**, 2806 (2004) (cit. on p. 87).

[17] A. R. Bell, "Electron energy transport in ion waves and its relevance to laser-produced plasmas", Physics of Fluids **26**, 279 (1983) (cit. on p. 73).

[18] A. R. Bell, F. N. Beg, Z. Chang, A. E. Dangor, C. N. Danson, C. B. Edwards, A. P. Fews, M. H. R. Hutchinson, S. Luan, P. Lee, P. A. Norreys, R. A. Smith, P. F. Taday, and F. Zhou, "Observation of plasma confinement in picosecond laser-plasma interactions", Phys. Rev. E **48**, 2087 (1993) (cit. on p. 73).

[19] A. R. Bell and R. J. Kingham, "Resistive Collimation of Electron Beams in Laser-Produced Plasmas", Physical Review Letters **91**, 035003, 035003 (2003) (cit. on p. 166).

[20] C. Bellei, J. R. Davies, P. K. Chauhan, and Z. Najmudin, "Coherent transition radiation in relativistic laser-solid interactions", Plasma Physics and Controlled Fusion **54**, 035011, 035011 (2012) (cit. on pp. 172, 257–259, 262).

[21] C. Bellei, L. Divol, A. J. Kemp, M. H. Key, D. J. Larson, D. J. Strozzi, M. M. Marinak, M. Tabak, and P. K. Patel, "Fast ignition: dependence of the ignition energy on source and target parameters for particle-in-cell-modelled energy and angular distributions of the fast electrons", Physics of Plasmas **20**, 052704 (2013) 10.1063/1.4804277 (cit. on p. 202).

[22] R. F. Benjamin, G. H. McCall, and A. W. Ehler, "Measurement of return current in a laser-produced plasma", Physical Review Letters **42**, 890 (1979) (cit. on p. 143).

[23] M. J. Berger and S. M. Seltzer, "Tables of Energy Losses and Ranges of Electrons and Positrons", in Studies in penetration of charged particles in matter (1964), p. 205 (cit. on p. 61).

[24] H. Bethe, "Quantenmechanik der ein- und zwei-elektronenprobleme", in *Quantentheorie*, edited by H. Bethe, F. Hund, N. F. Mott, W. Pauli, A. Rubinowicz, G. Wentzel, and A. Smekal (Springer Berlin Heidelberg, Berlin, Heidelberg, 1933), pp. 273–560 (cit. on p. 59).

[25] R. Betti, C. D. Zhou, K. S. Anderson, L. J. Perkins, W. Theobald, and A. A. Solodov, "Shock Ignition of Thermonuclear Fuel with High Areal Density", Physical Review Letters **98**, 155001, 155001 (2007) (cit. on p. 205).

[26] S. Betti, F. Ceccherini, F. Cornolti, and F. Pegoraro, "Expansion of a finite-size plasma in vacuum", Plasma Physics and Controlled Fusion **47**, 521 (2005) (cit. on p. 76).

[27] B. Bezzerides, D. F. DuBois, and D. W. Forslund, "Magnetic field generation by resonance absorption of light", Phys. Rev. A **16**, 1678 (1977) (cit. on p. 78).

[28] N. Bloembergen, "From nanosecond to femtosecond science", Rev. Mod. Phys. **71**, S283 (1999) (cit. on p. 213).

[29] P. Bolton, M. Borghesi, C. Brenner, D. Carroll, C. De Martinis, F. Fiorini, A. Flacco, V. Floquet, J. Fuchs, P. Gallegos, D. Giove, J. Green, S. Green, B. Jones, D. Kirby, P. McKenna, D. Neely, F. Nuesslin, R. Prasad, S. Reinhardt, M. Roth, U. Schramm, G. Scott, S. Ter-Avetisyan, M. Tolley, G. Turchetti, and J. Wilkens, "Instrumentation for diagnostics and control of laser-accelerated proton (ion) beams", Physica Medica: European Journal of Medical Physics **30**, 255 (cit. on p. 233).

[30] T. Bonnet, M. Comet, D. Denis-Petit, F. Gobet, F. Hannachi, M. Tarisien, M. Versteegen, and M. M. Aleonard, "Response functions of Fuji imaging plates to monoenergetic protons in the energy range 0.6-3.2 MeV", Review of Scientific Instruments **84**, 013508 (2013) (cit. on p. 250).

[31] M. Borghesi, D. H. Campbell, A. Schiavi, M. G. Haines, O. Willi, A. J. MacKinnon, P. Patel, L. A. Gizzi, M. Galimberti, R. J. Clarke, F. Pegoraro, H. Ruhl, and S. Bulanov, "Electric field detection in laser-plasma interaction experiments via the proton imaging technique", Physics of Plasmas **9**, 2214 (2002) (cit. on pp. 86, 93, 184).

[32] M. Borghesi, A. J. Mackinnon, D. H. Campbell, D. G. Hicks, S. Kar, P. K. Patel, D. Price, L. Romagnani, A. Schiavi, and O. Willi, "Multi-mev proton source investigations in ultraintense laser-foil interactions", Phys. Rev. Lett. **92**, 055003 (2004) (cit. on pp. 86, 100).

[33] B. A. Boyko, A. I. Bykov, M. I. Dolotenko, N. P. Kolokol'Chikov, I. M. Markevtsev, O. M. Tatsenko, and A. M. Shuvalov, "More than 20 MG Magnetic Field Generation in the Cascade Magnetocumulative MC-1 Generator", in Megagauss magnetic field generation, its application to science and ultra-high pulsed-power technology, edited by H. J. Schneider-Muntau (Nov. 2004), pp. 61–66 (cit. on p. 27).

[34] S. I. Braginskii, "Transport Processes in a Plasma", Reviews of Plasma Physics **1**, 205 (1965) (cit. on p. 72).

[35] F. Brunel, "Not-so-resonant, resonant absorption", Physical Review Letters **59**, 52 (1987) (cit. on p. 50).

[36] S. Buffechoux, J. Psikal, M. Nakatsutsumi, L. Romagnani, A. Andreev, K. Zeil, M. Amin, P. Antici, T. Burris-Mog, A. Compant-La-Fontaine, E. d'Humières, S. Fourmaux, S. Gaillard, F. Gobet, F. Hannachi, S. Kraft, A. Mancic, C. Plaisir, G. Sarri, M. Tarisien, T. Toncian, U. Schramm, M. Tampo, P. Audebert, O. Willi, T. E. Cowan, H. Pépin, V. Tikhonchuk, M. Borghesi, and J. Fuchs, "Hot electrons transverse refluxing in ultraintense laser-solid interactions", Phys. Rev. Lett. **105**, 015005 (2010) (cit. on p. 81).

[37] O. Buneman, "Dissipation of currents in ionized media", Phys. Rev. **115**, 503 (1959) (cit. on p. 79).

[38] V. Y. Bychenkov, V. N. Novikov, D. Batani, V. T. Tikhonchuk, and S. G. Bochkarev, "Ion acceleration in expanding multispecies plasmas", Physics of Plasmas **11**, 3242 (2004) (cit. on p. 76).

[39] A. Bykov, M. Dolotenko, N. Kolokolchikov, V. Selemir, and O. Tatsenko, "{vniief} achievements on ultra-high magnetic fields generation", Physica B: Condensed Matter **294-295**, Proceedings of the Sixth International Symposium on Research in High Magnetic Fields, 574 (2001) (cit. on p. 27).

[40] H.-b. Cai, S.-p. Zhu, X. T. He, S.-z. Wu, M. Chen, C. Zhou, W. Yu, and H. Nagatomo, "Magnetic collimation of fast electrons in specially engineered targets irradiated by ultraintense laser pulses", Physics of Plasmas **18**, 023106 (2011) 10.1063/1.3553453 (cit. on p. 166).

[41] R. B. Campbell, J. S. DeGroot, T. A. Mehlhorn, D. R. Welch, and B. V. Oliver, "Collimation of petawatt laser-generated relativistic electron beams propagating through solid matter", Physics of Plasmas **10**, 4169 (2003) (cit. on p. 166).

[42] J. Cao, S. Liang, C. Zhang, Y. Liu, J. Huang, Z. Jin, Z.-G. Chen, Z. Wang, Q. Wang, J. Zhao, S. Li, X. Dai, J. Zou, Z. Xia, L. Li, and F. Xiu, "Landau level splitting in Cd_3As_2 under high magnetic fields", Nature Communications **6**, 7779, 7779 (2015) (cit. on p. 208).

[43] D. Carroll, P. Brummitt, D. Neely, F. Lindau, O. Lundh, C.-G. Wahlström, and P. McKenna, "A modified thomson parabola spectrometer for high resolution multi-mev ion measurements—application to laser-driven ion acceleration", Nuclear Instruments and Methods in Physics Research Section A: Accelerators, Spectrometers, Detectors and Associated Equipment **620**, {COULOMB09Ions} Acceleration with high Power Lasers: Physics and Applications, 23 (2010) (cit. on p. 249).

[44] P. J. Catto and R. M. More, "Sheath inverse bremsstrahlung in laser produced plasmas", Physics of Fluids **20**, 704 (1977) (cit. on p. 50).

[45] P. Y. Chang, G. Fiksel, M. Hohenberger, J. P. Knauer, R. Betti, F. J. Marshall, D. D. Meyerhofer, F. H. Séguin, and R. D. Petrasso, "Fusion Yield Enhancement in Magnetized Laser-Driven Implosions", Physical Review Letters **107**, 035006, 035006 (2011) (cit. on pp. 28, 202).

[46] C. D. Chen, J. A. King, M. H. Key, K. U. Akli, F. N. Beg, H. Chen, R. R. Freeman, A. Link, A. J. Mackinnon, A. G. MacPhee, P. K. Patel, M. Porkolab, R. B. Stephens, and L. D. V. Woerkom, "A bremsstrahlung spectrometer using k-edge and differential filters with image plate dosimeters", Review of Scientific Instruments **79**, 10E305 (2008) (cit. on p. 255).

[47] C. D. Chen, P. K. Patel, D. S. Hey, A. J. Mackinnon, M. H. Key, K. U. Akli, T. Bartal, F. N. Beg, S. Chawla, R. R. Chen H. Vand Freeman, D. P. Higginson, A. Link, T. Y. Ma, A. G. MacPhee, R. B. Stephens, L. D. Van Woerkom, B. Westover, and M. Porkolab, "Bremsstrahlung and K_α fluorescence measurements for inferring conversion efficiencies into fast ignition relevant hot electrons", Physics of Plasmas **16**, 082705 (2009) 10.1063/1.3183693 (cit. on p. 53).

[48] B. Chimier, V. T. Tikhonchuk, and L. Hallo, "Effect of pressure relaxation during the laser heating and electron ion relaxation stages", Applied Physics A: Materials Science & Processing **92**, 843 (2008) (cit. on pp. 65, 66).

[49] B. Chimier, V. T. Tikhonchuk, and L. Hallo, "Heating model for metals irradiated by a subpicosecond laser pulse", Phys. Rev. B **75**, 195124, 195124 (2007) (cit. on p. 171).

[50] O. Chubar, P. Elleaume, and J. Chavanne, "A three-dimensional magnetostatics computer code for insertion devices", Journal of Synchrotron Radiation **5**, 481 (1998) (cit. on pp. 114, 231).

[51] A. Ciardi, T. Vinci, J. Fuchs, B. Albertazzi, C. Riconda, H. Pépin, and O. Portugall, "Astrophysics of Magnetically Collimated Jets Generated from Laser-Produced Plasmas", Physical Review Letters **110**, 025002, 025002 (2013) (cit. on p. 18).

[52] E. L. Clark, K. Krushelnick, J. R. Davies, M. Zepf, M. Tatarakis, F. N. Beg, A. Machacek, P. A. Norreys, M. I. K. Santala, I. Watts, and A. E. Dangor, "Measurements of energetic proton transport through magnetized plasma from intense laser interactions with solids", Phys. Rev. Lett. **84**, 670 (2000) (cit. on p. 80).

[53] Courtois, C. and Ash, A. D. and Chambers, D. M. and Grundy, R. A. D. and Woolsey, N. C., "Creation of a uniform high magnetic-field strength environment for laser-driven experiments", Journal of Applied Physics **98**, 054913 (2005) (cit. on pp. 30, 96, 143, 144, 156, 157).

[54] C. Courtois, R. A. D. Grundy, A. D. Ash, D. M. Chambers, N. C. Woolsey, R. O. Dendy, and K. G. McClements, "Experiment on collisionless plasma interaction with applications to supernova remnant physics", Physics of Plasmas **11**, 3386 (2004) (cit. on p. 207).

[55] T. E. Cowan, J. Fuchs, H. Ruhl, A. Kemp, P. Audebert, M. Roth, R. Stephens, I. Barton, A. Blazevic, E. Brambrink, J. Cobble, J. Fernández, J.-C. Gauthier, M. Geissel, M. Hegelich, J. Kaae, S. Karsch, G. P. Le Sage, S. Letzring, M. Manclossi, S. Meyroneinc, A. Newkirk, H. Pépin, and N. Renard-LeGalloudec, "Ultralow emittance, multi-mev proton beams from a laser virtual-cathode plasma accelerator", Phys. Rev. Lett. **92**, 204801 (2004) (cit. on p. 85).

[56] T. Cowan, J. Fuchs, H. Ruhl, Y. Sentoku, A. Kemp, P. Audebert, M. Roth, R. Stephens, I. Barton, A. Blazevic, E. Brambrink, J. Cobble, J. Fernández, J.-C. Gauthier, M. Geissel, M. Hegelich, J. Kaae, S. Karsch, G. L. Sage, S. Letzring, M. Manclossi, S. Meyroneinc, A. Newkirk, H. Pépin, and N. Renard-LeGalloudec, "Ultra-low emittance, high current proton beams produced with a laser-virtual cathode sheath accelerator", Nuclear Instruments and Methods in Physics Research Section A: Accelerators, Spectrometers, Detectors and Associated Equipment **544**, Proceedings of the 15th International Symposium on Heavy Ion Inertial Fusion HIF 2004, 277 (2005) (cit. on p. 85).

[57] J. E. Crow, P. L. Auer, and J. E. Allen, "The expansion of a plasma into a vacuum", Journal of Plasma Physics **14**, 65 (1975) (cit. on p. 82).

[58] H. Daido, F. Miki, K. Mima, M. Fujita, K. Sawai, H. Fujita, Y. Kitagawa, S. Nakai, and C. Yamanaka, "Generation of a strong magnetic field by an intense CO_2 laser pulse", Phys. Rev. Lett. **56**, 846 (1986) (cit. on pp. 29, 96, 156, 157).

[59] F. David and R. Pellat, "Resonant absorption by a magnetic plasma at a rippled critical surface", The Physics of Fluids **23**, 1682 (1980) (cit. on p. 49).

[60] J. R. Davies, "Laser absorption by overdense plasmas in the relativistic regime", Plasma Physics and Controlled Fusion **51**, 014006 (2009) (cit. on p. 53).

[61] J. R. Davies, "Electric and magnetic field generation and target heating by laser-generated fast electrons", Phys. Rev. E **68**, 056404 (2003) (cit. on p. 69).

[62] J. R. Davies, A. R. Bell, M. G. Haines, and S. M. Guérin, "Short-pulse high-intensity laser-generated fast electron transport into thick solid targets", Phys. Rev. E **56**, 7193 (1997) (cit. on pp. 77, 78, 171).

[63] A. Debayle, L. Gremillet, J. J. Honrubia, and E. d'Humières, "Reduction of the fast electron angular dispersion by means of varying-resistivity structured targets", Physics of Plasmas **20**, 013109, 013109 (2013) (cit. on p. 172).

[64] A. Debayle, J. J. Honrubia, E. d'Humières, and V. T. Tikhonchuk, "Divergence of laser-driven relativistic electron beams", Phys. Rev. E **82**, 036405 (2010) (cit. on pp. 57, 59, 79, 166, 171).

[65] F. Debray and P. Frings, "State of the art and developments of high field magnets at the "Laboratoire National des Champs Magnétiques Intenses"", Comptes Rendus Physique **14**, 2 (2013) (cit. on pp. 26, 27).

[66] A. J. DeMaria, D. A. Stetser, and H. Heynau, "Self Mode-Locking of Lasers with Saturable Absorbers", Applied Physics Letters **8**, 174 (1966) (cit. on p. 213).

[67] V. Dervieux, B. Loupias, S. Baton, L. Lecherbourg, K. Glize, C. Rousseaux, C. Reverdin, L. Gremillet, C. Blancard, V. Silvert, J.-C. Pain, C. R. D. Brown, P. Allan, M. P. Hill, D. J. Hoarty, and P. Renaudin, "Characterization of near-LTE, high-temperature and high-density aluminum plasmas produced by ultra-high intensity lasers", High Energy Density Physics **16**, 12 (2015) (cit. on p. 17).

[68] T. Ditmire, J. W. G. Tisch, E. Springate, M. B. Mason, N. Hay, R. A. Smith, J. Marangos, and M. H. R. Hutchinson, "High-energy ions produced in explosions of superheated atomic clusters", Nature **386**, 54 (1997) (cit. on p. 80).

[69] Q.-L. Dong, S.-J. Wang, Q.-M. Lu, C. Huang, D.-W. Yuan, X. Liu, X.-X. Lin, Y.-T. Li, H.-G. Wei, J.-Y. Zhong, J.-R. Shi, S.-E. Jiang, Y.-K. Ding, B.-B. Jiang, K. Du, X.-T. He, M. Y. Yu, C. S. Liu, S. Wang, Y.-J. Tang, J.-Q. Zhu, G. Zhao, Z.-M. Sheng, and J. Zhang, "Plasmoid ejection and secondary current sheet generation from magnetic reconnection in laser-plasma interaction", Phys. Rev. Lett. **108**, 215001 (2012) (cit. on p. 18).

[70] J.-L. Dubois, F. Lubrano-Lavaderci, D. Raffestin, J. Ribolzi, J. Gazave, A. C. L. Fontaine, E. d'Humières, S. Hulin, P. Nicolaï, A. Poyé, and V. T. Tikhonchuk, "Target charging in short-pulse-laser-plasma experiments", Phys. Rev. E **89**, 013102 (2014) (cit. on pp. 88, 105, 106).

[71] W. R. Edgel, *Electric & magnetic field sensor application*, Prodyn Application Note 192 (cit. on p. 220).

[72] W. R. Edgel, *Primer on electromagnetic field measurements*, Prodyn Application Note 1195 (cit. on p. 220).

[73] K. Eidmann, J. Meyer-ter-Vehn, T. Schlegel, and S. Hüller, "Hydrodynamic simulation of subpicosecond laser interaction with solid-density matter", Phys. Rev. E **62**, 1202 (2000) (cit. on pp. 66, 171).

[74] A. Einstein, "Zur Quantentheorie der Strahlung", Physikalische Zeitschrift **18** (1917) (cit. on p. 212).

[75] D. Engel and G. Wunner, "Hartree-Fock-Roothaan calculations for many-electron atoms and ions in neutron-star magnetic fields", Phys. Rev. A **78**, 032515, 032515 (2008) (cit. on p. 17).

[76] K. Estabrook and W. L. Kruer, "Properties of resonantly heated electron distributions", Phys. Rev. Lett. **40**, 42 (1978) (cit. on p. 49).

[77] A. J. Estin, "The propagation of electromagnetic waves in plasmas. v. l. ginzburg. translated from the russian edition (moscow, 1960) by j. b. sykes and r. j. tayler. pergamon, london; addison-wesley, reading, mass., 1964.", Science **147**, 1563 (1965) (cit. on p. 49).

[78] E. Fermi, "The ionization loss of energy in gases and in condensed materials", Phys. Rev. **57**, 485 (1940) (cit. on p. 60).

[79] J. Fernández, B. Albright, F. Beg, M. Foord, B. Hegelich, J. Honrubia, M. Roth, R. Stephens, and L. Yin, "Fast ignition with laser-driven proton and ion beams", Nuclear Fusion **54**, 054006 (2014) (cit. on pp. 26, 206).

[80] G. Fiksel, W. Fox, A. Bhattacharjee, D. H. Barnak, P.-Y. Chang, K. Germaschewski, S. X. Hu, and P. M. Nilson, "Magnetic reconnection between colliding magnetized laser-produced plasma plumes", Phys. Rev. Lett. **113**, 105003 (2014) (cit. on pp. 28, 207).

[81] D. W. Forslund, J. M. Kindel, and K. Lee, "Theory of hot-electron spectra at high laser intensity", Phys. Rev. Lett. **39**, 284 (1977) (cit. on p. 49).

[82] D. H. Froula, J. S. Ross, B. B. Pollock, P. Davis, A. N. James, L. Divol, M. J. Edwards, A. A. Offenberger, D. Price, R. P. J. Town, G. R. Tynan, and S. H. Glenzer, "Quenching of the nonlocal electron heat transport by large external magnetic fields in a laser-produced plasma measured with imaging thomson scattering", Phys. Rev. Lett. **98**, 135001 (2007) (cit. on pp. 74, 96, 205).

[83] J. Fuchs, J. C. Adam, F. Amiranoff, S. D. Baton, N. Blanchot, P. Gallant, L. Gremillet, A. Héron, J. C. Kieffer, G. Laval, G. Malka, J. L. Miquel, P. Mora, H. Pépin, and C. Rousseaux, "Experimental study of laser penetration in overdense plasmas at relativistic intensities. I: Hole boring through preformed plasmas layers", Physics of Plasmas **6**, 2563 (1999) (cit. on p. 45).

[84] J. Fuchs, P. Antici, E. d'Humieres, E. Lefebvre, M. Borghesi, E. Brambrink, C. A. Cecchetti, M. Kaluza, V. Malka, M. Manclossi, S. Meyroneinc, P. Mora, J. Schreiber, T. Toncian, H. Pepin, and P. Audebert, "Laser-driven proton scaling laws and new paths towards energy increase", Nat Phys **2**, 48 (2006) (cit. on pp. 76, 85).

[85] J. Fuchs, T. E. Cowan, P. Audebert, H. Ruhl, L. Gremillet, A. Kemp, M. Allen, A. Blazevic, J.-C. Gauthier, M. Geissel, M. Hegelich, S. Karsch, P. Parks, M. Roth, Y. Sentoku, R. Stephens, and E. M. Campbell, "Spatial uniformity of laser-accelerated ultrahigh-current mev electron propagation in metals and insulators", Phys. Rev. Lett. **91**, 255002 (2003) (cit. on pp. 83, 85).

[86] J. Fuchs, Y. Sentoku, S. Karsch, J. Cobble, P. Audebert, A. Kemp, A. Nikroo, P. Antici, E. Brambrink, A. Blazevic, E. M. Campbell, J. C. Fernández, J.-C. Gauthier, M. Geissel, M. Hegelich, H. Pépin, H. Popescu, N. Renard-LeGalloudec, M. Roth, J. Schreiber, R. Stephens, and T. E. Cowan, "Comparison of laser ion acceleration from the front and rear surfaces of thin foils", Phys. Rev. Lett. **94**, 045004 (2005) (cit. on p. 85).

[87] S. Fujioka, Z. Zhang, K. Ishihara, K. Shigemori, Y. Hironaka, T. Johzaki, A. Sunahara, N. Yamamoto, H. Nakashima, T. Watanabe, H. Shiraga, H. Nishimura, and H. Azechi, "Kilotesla Magnetic Field due to a Capacitor-Coil Target Driven by High Power Laser", Scientific Reports **3**, 1170, 1170 (2013) (cit. on pp. 31, 96, 114, 156, 157).

[88] H. P. Furth, M. A. Levine, and R. W. Waniek, "Production and use of high transient magnetic fields. ii", Review of Scientific Instruments **28**, 949 (1957) (cit. on p. 27).

[89] L. Gao, H. Ji, G. Fiksel, W. Fox, M. Evans, and N. Alfonso, "Ultrafast proton radiography of the magnetic fields generated by a laser-driven coil current", Physics of Plasmas **23**, 043106, 043106 (2016) (cit. on pp. 120, 157, 158).

[90] P. Gibbon, *Short pulse laser interactions with matter* (World Scientific Publishing Company) (cit. on pp. 49, 50, 53, 55–57).

[91] P. Gibbon and A. R. Bell, "Collisionless absorption in sharp-edged plasmas", Phys. Rev. Lett. **68**, 1535 (1992) (cit. on p. 51).

[92] L. A. Gizzi, S. Betti, E. Förster, D. Giulietti, S. Höfer, P. Köster, L. Labate, R. Lötzsch, A. P. L. Robinson, and I. Uschmann, "Role of resistivity gradient in laser-driven ion acceleration", Phys. Rev. ST Accel. Beams **14**, 011301 (2011) (cit. on p. 85).

[93] W. Goldstein, "Science of Fusion Ignition on NIF", in Science of Fusion Ignition Workshop LLNL-TR-570412 (Lawrence Livermore National Laboratory, 2012) (cit. on p. 23).

[94] M. R. Gomez, S. A. Slutz, A. B. Sefkow, D. B. Sinars, K. D. Hahn, S. B. Hansen, E. C. Harding, P. F. Knapp, P. F. Schmit, C. A. Jennings, T. J. Awe, M. Geissel, D. C. Rovang, G. A. Chandler, G. W. Cooper, M. E. Cuneo, A. J. Harvey-Thompson, M. C. Herrmann, M. H. Hess, O. Johns, D. C. Lamppa, M. R. Martin, R. D. McBride, K. J. Peterson, J. L. Porter, G. K. Robertson, G. A. Rochau, C. L. Ruiz, M. E. Savage, I. C. Smith, W. A. Stygar, and R. A. Vesey, "Experimental Demonstration of Fusion-Relevant Conditions in Magnetized Liner Inertial Fusion", Physical Review Letters **113**, 155003, 155003 (2014) (cit. on p. 27).

[95] O. V. Gotchev, P. Y. Chang, J. P. Knauer, D. D. Meyerhofer, O. Polomarov, J. Frenje, C. K. Li, M. J.-E. Manuel, R. D. Petrasso, J. R. Rygg, F. H. Séguin, and R. Betti, "Laser-Driven Magnetic-Flux Compression in High-Energy-Density Plasmas", Physical Review Letters **103**, 215004, 215004 (2009) (cit. on pp. 28, 202).

[96] J. S. Green, V. M. Ovchinnikov, R. G. Evans, K. U. Akli, H. Azechi, F. N. Beg, C. Bellei, R. R. Freeman, H. Habara, R. Heathcote, M. H. Key, J. A. King, K. L. Lancaster, N. C. Lopes, T. Ma, A. J. MacKinnon, K. Markey, A. McPhee, Z. Najmudin, P. Nilson, R. Onofrei, R. Stephens, K. Takeda, K. A. Tanaka, W. Theobald, T. Tanimoto, J. Waugh, L. Van Woerkom, N. C. Woolsey, M. Zepf, J. R. Davies, and P. A. Norreys, "Effect of laser intensity on fast-electron-beam divergence in solid-density plasmas", Phys. Rev. Lett. **100**, 015003 (2008) (cit. on pp. 57, 166, 202, 259).

[97] L. Gremillet, "Theoretical and experimental study of fast electron transport in ultra-high-intensity laser-solid interaction", PhD thesis (Ecole polytechnique, Palaiseau, France, 2001) (cit. on pp. 68, 79).

[98] L. Gremillet, G. Bonnaud, and F. Amiranoff, "Filamented transport of laser-generated relativistic electrons penetrating a solid target", Physics of Plasmas **9**, 941 (2002) (cit. on p. 171).

[99] D. A. Hammer and N. Rostoker, "Propagation of High Current Relativistic Electron Beams", Physics of Fluids **13**, 1831 (1970) (cit. on p. 63).

[100] L. E. Hargrove, R. L. Fork, and M. A. Pollack, "Locking of He-Ne Laser Modes Induced by Synchronous Intracavity Modulation", Applied Physics Letters **5**, 4 (1964) (cit. on p. 213).

[101] S. P. Hatchett, C. G. Brown, T. E. Cowan, E. A. Henry, J. S. Johnson, M. H. Key, J. A. Koch, A. B. Langdon, B. F. Lasinski, R. W. Lee, A. J. Mackinnon, D. M. Pennington, M. D. Perry, T. W. Phillips, M. Roth, T. C. Sangster, M. S. Singh, R. A. Snavely, M. A. Stoyer, S. C. Wilks, and K. Yasuike, "Electron, photon, and ion beams from the relativistic interaction of petawatt laser pulses with solid targets", Physics of Plasmas **7**, 2076 (2000) (cit. on pp. 53, 80).

[102] B. M. Hegelich, B. Albright, P. Audebert, A. Blazevic, E. Brambrink, J. Cobble, T. Cowan, J. Fuchs, J. C. Gauthier, C. Gautier, M. Geissel, D. Habs, R. Johnson, S. Karsch, A. Kemp, S. Letzring, M. Roth, U. Schramm, J. Schreiber, K. J. Witte, and J. C. Fernández, "Spectral properties of laser-accelerated mid-zmev/u ion beams", Physics of Plasmas **12**, 056314 (2005) 10.1063/1.1915350 (cit. on p. 81).

[103] B. M. Hegelich, D. Jung, B. J. Albright, M. Cheung, B. Dromey, D. C. Gautier, C. Hamilton, S. Letzring, R. Munchhausen, S. Palaniyappan, R. Shah, H.-C. Wu, L. Yin, and J. C. Fernández, "160 MeV laser-accelerated protons from CH_2 nano-targets for proton cancer therapy", ArXiv e-prints (2013) (cit. on pp. 84, 206).

[104] M. Hegelich, S. Karsch, G. Pretzler, D. Habs, K. Witte, W. Guenther, M. Allen, A. Blazevic, J. Fuchs, J. C. Gauthier, M. Geissel, P. Audebert, T. Cowan, and M. Roth, "Mev ion jets from short-pulse-laser interaction with thin foils", Phys. Rev. Lett. **89**, 085002 (2002) (cit. on p. 81).

[105] R. W. Hellwarth, "Theory of the pulsation of fluorescent light from ruby", Phys. Rev. Lett. **6**, 9 (1961) (cit. on p. 213).

[106] A. Henig, D. Kiefer, K. Markey, D. C. Gautier, K. A. Flippo, S. Letzring, R. P. Johnson, T. Shimada, L. Yin, B. J. Albright, K. J. Bowers, J. C. Fernández, S. G. Rykovanov, H.-C. Wu, M. Zepf, D. Jung, V. K. Liechtenstein, J. Schreiber, D. Habs, and B. M. Hegelich, "Enhanced laser-driven ion acceleration in the relativistic transparency regime", Phys. Rev. Lett. **103**, 045002 (2009) (cit. on pp. 83, 206).

[107] A. Hewish, S. J. Bell, J. D. H. Pilkington, P. F. Scott, and R. A. Collins, "Observation of a Rapidly Pulsating Radio Source", Nature **217**, 709 (1968) (cit. on p. 17).

[108] D. J. Hoarty, P. Allan, S. F. James, C. R. D. Brown, L. M. R. Hobbs, M. P. Hill, J. W. O. Harris, J. Morton, M. G. Brookes, R. Shepherd, J. Dunn, H. Chen, E. Von Marley, P. Beiersdorfer, H. K. Chung, R. W. Lee, G. Brown, and J. Emig, "Observations of the Effect of Ionization-Potential Depression in Hot Dense Plasma", Physical Review Letters **110**, 265003, 265003 (2013) (cit. on pp. 17, 166).

[109] M. Hohenberger, P.-Y. Chang, G. Fiksel, J. P. Knauer, R. Betti, F. J. Marshall, D. D. Meyerhofer, F. H. Séguin, and R. D. Petrasso, "Inertial confinement fusion implosions with imposed magnetic field compression using the OMEGA Lasera)", Physics of Plasmas **19**, 056306, 056306 (2012) (cit. on pp. 28, 202).

[110] J. J. Honrubia, J. C. Fernández, M. Temporal, B. M. Hegelich, and J. Meyer-ter-Vehn, "Fast ignition of inertial fusion targets by laser-driven carbon beams", Physics of Plasmas **16**, 102701 (2009) 10.1063/1.3234248 (cit. on p. 85).

[111] J. J. Honrubia, M. Kaluza, J. Schreiber, G. D. Tsakiris, and J. Meyer-ter-Vehn, "Laser-driven fast-electron transport in preheated foil targets", Physics of Plasmas **12**, 052708, 052708 (2005) (cit. on p. 171).

[112] J. J. Honrubia, M. Murakami, K. Mima, T. Johzaki, A. Sunahara, H. Nagatomo, S. Fujioka, H. Shiraga, and H. Azechi, "Enhancement of fast electron energy deposition by external magnetic fields", Journal of Physics Conference Series **688**, 012033, 012033 (2016) (cit. on pp. 169, 182, 202).

[113] J. Honrubia and J. Meyer-ter-Vehn, "Three-dimensional fast electron transport for ignition-scale inertial fusion capsules", Nuclear Fusion **46**, L25 (2006) (cit. on p. 25).

[114] , in *Laser-plasma interactions*, Vol. 3, edited by M. B. Hooper (Camelot Press, South Hampton, U.K., 1986) (cit. on p. 60).

[115] W. B. Hubbard, "Studies in Stellar Evolution. V. Transport Coefficients of Degenerate Stellar Matter", ApJ **146**, 858 (1966) (cit. on p. 66).

[116] O. A. Hurricane, D. A. Callahan, D. T. Casey, P. M. Celliers, C. Cerjan, E. L. Dewald, T. R. Dittrich, T. Döppner, D. E. Hinkel, L. F. B. Hopkins, J. L. Kline, S. Le Pape, T. Ma, A. G. Macphee, J. L. Milovich, A. Pak, H.-S. Park, P. K. Patel, B. A. Remington, J. D. Salmonson, P. T. Springer, and R. Tommasini, "Fuel gain exceeding unity in an inertially confined fusion implosion", Nature **506**, 343 (2014) (cit. on p. 23).

[117] I. H. Hutchinson, *Principles of Plasma Diagnostics* (July 2005), p. 458 (cit. on p. 102).

[118] IAEA, *Key World Energy Statistics*, 2015 (cit. on pp. 18, 19).

[119] J. D. Huba, Naval Research Laboratory, Washington DC 20375, USA, *NRL Plasma Formulary*, 2013 (cit. on p. 21).

[120] A. S. Joglekar, A. G. R. Thomas, C. P. Ridgers, and R. J. Kingham, "Nernst Effect in Magnetized Plasmas", ArXiv e-prints (2015) (cit. on p. 206).

[121] T. Johzaki, H. Nagatomo, A. Sunahara, H.-B. Cai, H. Sakagami, Y. Nakao, and K. Mima, "Pre-plasma effects on core heating and enhancing heating efficiency by extended double cone for FIREX", Nuclear Fusion **51**, 073022, 073022 (2011) (cit. on p. 166).

[122] T. Johzaki, T. Taguchi, Y. Sentoku, A. Sunahara, H. Nagatomo, H. Sakagami, K. Mima, S. Fujioka, and H. Shiraga, "Control of an electron beam using strong magnetic field for efficient core heating in fast ignition", Nuclear Fusion **55**, 053022 (2015) (cit. on pp. 182, 202).

[123] T. Johzaki, Y. Sentoku, H. Nagatomo, A. Sunahara, H. Sakagami, S. Fujioka, H. Shiraga, T. Endo, and F. project group, "Electron beam guiding by external magnetic fields in imploded fuel plasma", Journal of Physics: Conference Series **717**, 012025 (2016) (cit. on p. 203).

[124] D. Jung, L. Yin, D. C. Gautier, H.-C. Wu, S. Letzring, B. Dromey, R. Shah, S. Palaniyappan, T. Shimada, R. P. Johnson, J. Schreiber, D. Habs, J. C. Fernández, B. M. Hegelich, and B. J. Albright, "Laser-driven 1 gev carbon ions from preheated diamond targets in the break-out afterburner regime", Physics of Plasmas **20**, 083103 (2013) 10.1063/1.4817287 (cit. on pp. 26, 84, 206).

[125] D. Jung, L. Yin, B. J. Albright, D. C. Gautier, S. Letzring, B. Dromey, M. Yeung, R. Hörlein, R. Shah, S. Palaniyappan, K. Allinger, J. Schreiber, K. J. Bowers, H.-C. Wu, J. C. Fernández, D. Habs, and B. M. Hegelich, "Efficient carbon ion beam generation from laser-driven volume acceleration", New Journal of Physics **15**, 023007 (2013) (cit. on pp. 26, 84, 206).

[126] M. P. Kalashnikov, P. V. Nickles, T. Schlegel, M. Schnuerer, F. Billhardt, I. Will, W. Sandner, and N. N. Demchenko, "Dynamics of laser-plasma interaction at 10^{18} W/cm^2", Physical Review Letters **73**, 260 (1994) (cit. on p. 51).

[127] M. Kaluza, J. Schreiber, M. I. K. Santala, G. D. Tsakiris, K. Eidmann, J. Meyer-ter-Vehn, and K. J. Witte, "Influence of the laser prepulse on proton acceleration in thin-foil experiments", Phys. Rev. Lett. **93**, 045003 (2004) (cit. on pp. 83, 85).

[128] K. Kanaya and S. Okayama, "Penetration and energy-loss theory of electrons in solid targets", Journal of Physics D Applied Physics **5**, 43 (1972) (cit. on p. 160).

[129] P. Kapitza, "Further developments of the method of obtaining strong magnetic fields", Proceedings of the Royal Society of London. Series A, Containing Papers of a Mathematical and Physical Character **115**, 658 (1927) (cit. on p. 26).

[130] P. L. Kapitza, "A method of producing strong magnetic fields", Proceedings of the Royal Society of London A: Mathematical, Physical and Engineering Sciences **105**, 691 (1924) (cit. on p. 26).

[131] S. Kar, H. Ahmed, R. Prasad, M. Cerchez, S. Brauckmann, B. Aurand, G. Cantono, P. Hadjisolomou, C. L. S. Lewis, A. Macchi, G. Nersisyan, A. P. L. Robinson, A. M. Schroer, M. Swantusch, M. Zepf, O. Willi, and M. Borghesi, "Guided post-acceleration of laser-driven ions by a miniature modular structure", Nature Communications **7**, 10792, 10792 (2016) (cit. on pp. 185, 186).

[132] S. Kar, M. Borghesi, C. A. Cecchetti, L. Romagnani, F. Ceccherini, T. V. Liseykina, A. Macchi, R. Jung, J. Osterholz, O. Willi, L. A. Gizzi, A. Schiavi, M. Galimberti, and R. Heathcote, "Dynamics of charge-displacement channeling in intense laser plasma interactions", New Journal of Physics **9**, 402 (2007) (cit. on p. 184).

[133] S. Kar, K. Markey, P. T. Simpson, C. Bellei, J. S. Green, S. R. Nagel, S. Kneip, D. C. Carroll, B. Dromey, L. Willingale, E. L. Clark, P. McKenna, Z. Najmudin, K. Krushelnick, P. Norreys, R. J. Clarke, D. Neely, M. Borghesi, and M. Zepf, "Dynamic Control of Laser-Produced Proton Beams", Physical Review Letters **100**, 105004, 105004 (2008) (cit. on pp. 184, 185).

[134] S. Kar, A. P. L. Robinson, D. C. Carroll, O. Lundh, K. Markey, P. McKenna, P. Norreys, and M. Zepf, "Guiding of Relativistic Electron Beams in Solid Targets by Resistively Controlled Magnetic Fields", Physical Review Letters **102**, 055001, 055001 (2009) (cit. on p. 166).

[135] S. B. Kemic, "Hydrogen and helium features in magnetic white dwarfs", ApJ **193**, 213 (1974) (cit. on p. 17).

[136] A. J. Kemp and L. Divol, "Interaction Physics of Multipicosecond Petawatt Laser Pulses with Overdense Plasma", Physical Review Letters **109**, 195005, 195005 (2012) (cit. on p. 166).

[137] J. C. Kemp, J. B. Swedlund, J. D. Landstreet, and J. R. P. Angel, "Discovery of Circularly Polarized Light from a White Dwarf", ApJ **161**, L77 (1970) (cit. on p. 17).

[138] M. H. Key, M. D. Cable, T. E. Cowan, K. G. Estabrook, B. A. Hammel, S. P. Hatchett, E. A. Henry, D. E. Hinkel, J. D. Kilkenny, J. A. Koch, W. L. Kruer, A. B. Langdon, B. F. Lasinski, R. W. Lee, B. J. MacGowan, A. MacKinnon, J. D. Moody, M. J. Moran, A. A. Offenberger, D. M. Pennington, M. D. Perry, T. J. Phillips, T. C. Sangster, M. S. Singh, M. A. Stoyer, M. Tabak, G. L. Tietbohl, M. Tsukamoto, K. Wharton, and S. C. Wilks, "Hot electron production and heating by hot electrons in fast ignitor research", Physics of Plasmas **5**, 1966 (1998) (cit. on p. 53).

[139] N. King, E. Ables, K. Adams, K. Alrick, J. Amann, S. Balzar, P. B. Jr, M. Crow, S. Cushing, J. Eddleman, T. Fife, P. Flores, D. Fujino, R. Gallegos, N. Gray, E. Hartouni, G. Hogan, V. Holmes, S. Jaramillo, J. Knudsson, R. London, R. Lopez, T. McDonald, J. McClelland, F. Merrill, K. Morley, C. Morris, F. Naivar, E. Parker, H. Park, P. Pazuchanics, C. Pillai, C. Riedel, J. Sarracino, F. S. Jr, H. Stacy, B. Takala, R. Thompson, H. Tucker, G. Yates, H.-J. Ziock, and J. Zumbro, "An 800-mev proton radiography facility for dynamic experiments", Nuclear Instruments and Methods in Physics Research Section A: Accelerators, Spectrometers, Detectors and Associated Equipment **424**, 84 (1999) (cit. on p. 86).

[140] D. J. Kirby, "Radiation dosimetry of conventional and laser-driven particle beams", PhD thesis (University of Birmingham, UK, 2011) (cit. on pp. 233, 234).

[141] T. Kluge, T. Cowan, A. Debus, U. Schramm, K. Zeil, and M. Bussmann, "Electron temperature scaling in laser interaction with solids", Phys. Rev. Lett. **107**, 205003 (2011) (cit. on p. 55).

[142] J. P. Knauer, O. V. Gotchev, P. Y. Chang, D. D. Meyerhofer, O. Polomarov, R. Betti, J. A. Frenje, C. K. Li, M. J.-E. Manuel, R. D. Petrasso, J. R. Rygg, and F. H. Séguin, "Compressing magnetic fields with high-energy lasersa)", Physics of Plasmas **17**, 056318, 056318 (2010) (cit. on pp. 28, 202).

[143] H. Knoepfel, *Pulsed high magnetic fields* (John Wiley & Sons Canada, Limited, 1997) (cit. on p. 218).

[144] R. Kodama, P. A. Norreys, K. Mima, A. E. Dangor, R. G. Evans, H. Fujita, Y. Kitagawa, K. Krushelnick, T. Miyakoshi, N. Miyanaga, T. Norimatsu, S. J. Rose, T. Shozaki, K. Shigemori, A. Sunahara, M. Tampo, K. A. Tanaka, Y. Toyama, T. Yamanaka, and M. Zepf, "Fast heating of ultrahigh-density plasma as a step towards laser fusion ignition", Nature **412**, 798 (2001) (cit. on p. 25).

[145] A. M. Koehler, "Proton radiography", Science **160**, 303 (1968) (cit. on p. 86).

[146] P. Korneev, E. d'Humières, and V. Tikhonchuk, "Gigagauss-scale quasistatic magnetic field generation in a snail-shaped target", Phys. Rev. E **91**, 043107 (2015) (cit. on p. 96).

[147] V. V. Korobkin and S. L. Motylev, "Laser method for producing strong magnetic fields", Pisma v Zhurnal Tekhnischeskoi Fiziki **5**, 1135 (1979) (cit. on pp. 29, 96).

[148] S. I. Krivosheev, V. V. Titkov, and G. A. Shneerson, "Two-dimensional field diffusion and magnetohydrodynamic flow in an electric explosion of a miniature single-turn solenoid in a megagauss magnetic field", Technical Physics **42**, 352 (1997) (cit. on p. 27).

[149] W. L. Kruer and K. Estabrook, "J × B heating by very intense laser light", Physics of Fluids **28**, 430 (1985) (cit. on p. 51).

[150] W. Kruer, *The physics of laser plasma interactions* (Reading, MA (US); Addison-Wesley Publishing Co., Jan. 1988) (cit. on p. 47).

[151] K. Krushelnick, E. L. Clark, Z. Najmudin, M. Salvati, M. I. K. Santala, M. Tatarakis, A. E. Dangor, V. Malka, D. Neely, R. Allott, and C. Danson, "Multi-mev ion production from high-intensity laser interactions with underdense plasmas", Phys. Rev. Lett. **83**, 737 (1999) (cit. on p. 80).

[152] N. L. Kugland, D. D. Ryutov, C. Plechaty, J. S. Ross, and H.-S. Park, "Invited Article: Relation between electric and magnetic field structures and their proton-beam images", Review of Scientific Instruments **83**, 101301 (2012) (cit. on pp. 120, 241, 244).

[153] W. Kunz, "First measurement of poloidal-field-induced Faraday rotation in a tokamak plasma", Nuclear Fusion **18**, 1729 (1978) (cit. on p. 102).

[154] C. Labaune, "Laser-driven fusion: Incoherent light on the road to ignition", Nature Physics **3**, 680 (2007) (cit. on p. 24).

[155] D. Lai, "Matter in strong magnetic fields", Reviews of Modern Physics **73** (2001) 10.1103/RevModPhys.73.629 (cit. on p. 17).

[156] A. B. Langdon, "Nonlinear inverse bremsstrahlung and heated-electron distributions", Phys. Rev. Lett. **44**, 575 (1980) (cit. on p. 47).

[157] K. F. F. Law, M. Bailly-Grandvaux, A. Morace, S. Sakata, K. Matsuo, S. Kojima, S. Lee, X. Vaisseau, Y. Arikawa, A. Yogo, K. Kondo, Z. Zhang, C. Bellei, J. J. Santos, S. Fujioka, and H. Azechi, "Direct measurement of kilo-tesla level magnetic field generated with laser-driven capacitor-coil target by proton deflectometry", Applied Physics Letters **108**, 091104 (2016) (cit. on pp. 157, 158, 163).

[158] K. W. D. Ledingham and W. Galster, "Laser-driven particle and photon beams and some applications", New Journal of Physics **12**, 045005, 045005 (2010) (cit. on p. 166).

[159] Y. T. Lee and R. M. More, "An electron conductivity model for dense plasmas", Physics of Fluids **27**, 1273 (1984) (cit. on p. 66).

[160] W. P. Leemans, B. Nagler, A. J. Gonsalves, C. Tóth, K. Nakamura, C. G. R. Geddes, E. Esarey, C. B. Schroeder, and S. M. Hooker, "GeV electron beams from a centimetre-scale accelerator", Nature Physics **2**, 696 (2006) (cit. on p. 45).

[161] C. K. Li, F. H. Séguin, J. A. Frenje, J. R. Rygg, R. D. Petrasso, R. P. J. Town, O. L. Landen, J. P. Knauer, and V. A. Smalyuk, "Observation of megagauss-field topology changes due to magnetic reconnection in laser-produced plasmas", Phys. Rev. Lett. **99**, 055001 (2007) (cit. on p. 18).

[162] Z. Lin, L. V. Zhigilei, and V. Celli, "Electron-phonon coupling and electron heat capacity of metals under conditions of strong electron-phonon nonequilibrium", Phys. Rev. B **77**, 075133 (2008) (cit. on pp. 68, 69).

[163] J. Lindl, "Development of the indirect-drive approach to inertial confinement fusion and the target physics basis for ignition and gain", Physics of Plasmas **2**, 3933 (1995) (cit. on p. 25).

[164] M. Lontano and M. Passoni, "Electrostatic field distribution at the sharp interface between high density matter and vacuum", Physics of Plasmas **13**, 042102 (2006) 10.1063/1.2184067 (cit. on pp. 82, 83).

[165] R. V. Lovelace and R. N. Sudan, "Plasma heating by high-current relativistic electron beams", Phys. Rev. Lett. **27**, 1256 (1971) (cit. on p. 68).

[166] A. Macchi, F. Cattani, T. V. Liseykina, and F. Cornolti, "Laser Acceleration of Ion Bunches at the Front Surface of Overdense Plasmas", Physical Review Letters **94**, 165003, 165003 (2005) (cit. on p. 45).

[167] A. J. Mackinnon, M. Borghesi, S. Hatchett, M. H. Key, P. K. Patel, H. Campbell, A. Schiavi, R. Snavely, S. C. Wilks, and O. Willi, "Effect of plasma scale length on multi-mev proton production by intense laser pulses", Phys. Rev. Lett. **86**, 1769 (2001) (cit. on p. 81).

[168] A. J. Mackinnon, P. K. Patel, M. Borghesi, R. C. Clarke, R. R. Freeman, H. Habara, S. P. Hatchett, D. Hey, D. G. Hicks, S. Kar, M. H. Key, J. A. King, K. Lancaster, D. Neely, A. Nikkro, P. A. Norreys, M. M. Notley, T. W. Phillips, L. Romagnani, R. A. Snavely, R. B. Stephens, and R. P. J. Town, "Proton radiography of a laser-driven implosion", Phys. Rev. Lett. **97**, 045001 (2006) (cit. on pp. 86, 101).

[169] A. J. Mackinnon, P. K. Patel, R. P. Town, M. J. Edwards, T. Phillips, S. C. Lerner, D. W. Price, D. Hicks, M. H. Key, S. Hatchett, S. C. Wilks, M. Borghesi, L. Romagnani, S. Kar, T. Toncian, G. Pretzler, O. Willi, M. Koenig, E. Martinolli, S. Lepape, A. Benuzzi-Mounaix, P. Audebert, J. C. Gauthier, J. King, R. Snavely, R. R. Freeman, and T. Boehlly, "Proton radiography as an electromagnetic field and density perturbation diagnostic (invited)", Review of Scientific Instruments **75**, 3531 (2004) (cit. on p. 86).

[170] T. H. Maiman, "Stimulated Optical Radiation in Ruby", Nature **187**, 493 (1960) (cit. on p. 213).

[171] A. Maksimchuk, S. Gu, K. Flippo, D. Umstadter, and V. Y. Bychenkov, "Forward ion acceleration in thin films driven by a high-intensity laser", Phys. Rev. Lett. **84**, 4108 (2000) (cit. on p. 80).

[172] R. C. Malone, R. L. McCrory, and R. L. Morse, "Indications of strongly flux-limited electron thermal conduction in laser-target experiments", Phys. Rev. Lett. **34**, 721 (1975) (cit. on p. 73).

[173] M. J.-E. Manuel, A. M. Rasmus, C. C. Kurnaz, S. R. Klein, J. S. Davis, R. P. Drake, D. S. Montgomery, S. C. Hsu, C. S. Adams, and B. B. Pollock, "Results from colliding magnetized plasma jet experiments executed at the Trident laser facility", in Aps meeting abstracts (Nov. 2015) (cit. on p. 28).

[174] E. Martinolli, M. Koenig, J. M. Boudenne, E. Perelli, D. Batani, and T. A. Hall, "Conical crystal spectrograph for high brightness x-ray kα spectroscopy in subpicosecond laser–solid interaction", Review of Scientific Instruments **75**, 2024 (2004) (cit. on p. 252).

[175] Y. Matsumoto, T. Amano, T. N. Kato, and M. Hoshino, "Stochastic electron acceleration during spontaneous turbulent reconnection in a strong shock wave", Science **347**, 974 (2015) (cit. on p. 17).

[176] P. McKenna, D. C. Carroll, R. J. Clarke, R. G. Evans, K. W. D. Ledingham, F. Lindau, O. Lundh, T. McCanny, D. Neely, A. P. L. Robinson, L. Robson, P. T. Simpson, C.-G. Wahlström, and M. Zepf, "Lateral electron transport in high-intensity laser-irradiated foils diagnosed by ion emission", Phys. Rev. Lett. **98**, 145001 (2007) (cit. on p. 87).

[177] P. McKenna, A. P. L. Robinson, D. Neely, M. P. Desjarlais, D. C. Carroll, M. N. Quinn, X. H. Yuan, C. M. Brenner, M. Burza, M. Coury, P. Gallegos, R. J. Gray, K. L. Lancaster, Y. T. Li, X. X. Lin, O. Tresca, and C.-G. Wahlström, "Effect of lattice structure on energetic electron transport in solids irradiated by ultraintense laser pulses", Phys. Rev. Lett. **106**, 185004 (2011) (cit. on p. 85).

[178] P. McKenna, F. Lindau, O. Lundh, D. C. Carroll, R. J. Clarke, K. W. D. Ledingham, T. McCanny, D. Neely, A. P. L. Robinson, L. Robson, P. T. Simpson, C.-G. Wahlström, and M. Zepf, "Low- and medium-mass ion acceleration driven by petawatt laser plasma interactions", Plasma Physics and Controlled Fusion **49**, B223 (2007) (cit. on p. 81).

[179] S. Micheau, A. Debayle, E. d'Humières, J. J. Honrubia, B. Qiao, M. Zepf, M. Borghesi, and M. Geissler, "Generation and optimization of electron currents along the walls of a conical target for fast ignition", Physics of Plasmas **17**, 122703, 122703 (2010) (cit. on p. 55).

[180] K. Mima, T. Johzaki, J. Honrubia, H. Nagatomo, T. Taguchi, A. Sunahara, H. Sakagami, S. Fujioka, and G. Logan, "Magnetized Fast ignition (MFI) and Laser Plasma Interactions in Strong Magnetic Field", Journal of Physics Conference Series **688**, 012066, 012066 (2016) (cit. on pp. 182, 202).

[181] N. Miura, T. Osada, and S. Takeyama, "Research in super-high pulsed magnetic fields at the megagauss laboratory of the university of tokyo", Journal of Low Temperature Physics **133**, 139 (2003) (cit. on p. 27).

[182] H. W. Mocker and R. J. Collins, "Mode Competition and Self-Locking Effects in a Q-Switched Ruby Laser", Applied Physics Letters **7**, 270 (1965) (cit. on p. 213).

[183] D. S. Montgomery, B. J. Albright, D. H. Barnak, P. Y. Chang, J. R. Davies, G. Fiksel, D. H. Froula, J. L. Kline, M. J. MacDonald, A. B. Sefkow, L. Yin, and R. Betti, "Use of external magnetic fields in hohlraum plasmas to improve laser-coupling", Physics of Plasmas **22**, 010703 (2015) 10.1063/1.4906055 (cit. on p. 205).

[184] P. Mora, "Plasma expansion into a vacuum", Phys. Rev. Lett. **90**, 185002 (2003) (cit. on pp. 74, 75, 144).

[185] P. Mora, "Thin-foil expansion into a vacuum", Phys. Rev. E **72**, 056401 (2005) (cit. on pp. 76, 187, 240).

[186] P. Mora, "Theoretical model of absorption of laser light by a plasma", Physics of Fluids **25**, 1051 (1982) (cit. on pp. 47, 48).

[187] A. Morace and D. Batani, "Spherically bent crystal for X-ray imaging of laser produced plasmas", Nuclear Instruments and Methods in Physics Research A **623**, 797 (2010) (cit. on p. 253).

[188] R. More, in , Vol. 21, edited by D. Bates and B. Bederson, Advances in Atomic and Molecular Physics (Academic Press, 1985), pp. 305–356 (cit. on pp. 59, 64).

[189] G. A. Mourou, T. Tajima, and S. V. Bulanov, "Optics in the relativistic regime", Reviews of Modern Physics **78**, 309 (2006) (cit. on p. 44).

[190] H.-U. Müller, H. Scholz, N. Puhlmann, O. Portugall, M. Barczewski, I. Stolpe, and M. von Ortenberg, "High sensitivity data acquisition during strong transient electromagnetic fields", Physica B: Condensed Matter **246-247**, 356 (1998) (cit. on p. 98).

[191] P. Mulser and D. Bauer, "High Power Laser-Matter Interaction", Springer Tracts in Modern Physics **238** (2010) (cit. on p. 44).

[192] H. Nagatomo, T. Johzaki, T. Asahina, K. Matsuo, A. Sunahara, H. Sakagami, T. Sano, K. Mima, A. Morace, Z. Zhang, S. Fujioka, K. Shigemori, H. Shiraga, and F. project group, "An optimum design of implosion with external magnetic field for electron beam guiding in fast ignition", Journal of Physics: Conference Series **717**, 012041 (2016) (cit. on pp. 202, 204).

[193] P. Nicolaï, J.-L. Feugeas, C. Regan, M. Olazabal-Loumé, J. Breil, B. Dubroca, J.-P. Morreeuw, and V. Tikhonchuk, "Effect of the plasma-generated magnetic field on relativistic electron transport", Phys. Rev. E **84**, 016402, 016402 (2011) (cit. on p. 73).

[194] B. P. Nigam, M. K. Sundaresan, and T.-Y. Wu, "Theory of Multiple Scattering: Second Born Approximation and Corrections to Molière's Work", Physical Review **115**, 491 (1959) (cit. on p. 58).

[195] P. M. Nilson, A. A. Solodov, J. F. Myatt, W. Theobald, P. A. Jaanimagi, L. Gao, C. Stoeckl, R. S. Craxton, J. A. Delettrez, B. Yaakobi, J. D. Zuegel, B. E. Kruschwitz, C. Dorrer, J. H. Kelly, K. U. Akli, P. K. Patel, A. J. MacKinnon, R. Betti, T. C. Sangster, and D. D. Meyerhofer, "Scaling Hot-Electron Generation to High-Power, Kilojoule-Class Laser-Solid Interactions", Physical Review Letters **105**, 235001, 235001 (2010) (cit. on pp. 53, 166).

[196] P. M. Nilson, W. Theobald, J. Myatt, C. Stoeckl, M. Storm, O. V. Gotchev, J. D. Zuegel, R. Betti, D. D. Meyerhofer, and T. C. Sangster, "High-intensity laser-plasma interactions in the refluxing limit", Physics of Plasmas **15**, 056308, 056308 (2008) (cit. on p. 53).

[197] P. M. Nilson, L. Willingale, M. C. Kaluza, C. Kamperidis, S. Minardi, M. S. Wei, P. Fernandes, M. Notley, S. Bandyopadhyay, M. Sherlock, R. J. Kingham, M. Tatarakis, Z. Najmudin, W. Rozmus, R. G. Evans, M. G. Haines, A. E. Dangor, and K. Krushelnick, "Magnetic reconnection and plasma dynamics in two-beam laser-solid interactions", Phys. Rev. Lett. **97**, 255001 (2006) (cit. on p. 18).

[198] M. Nishiuchi, H. Daido, A. Yogo, S. Orimo, K. Ogura, J. Ma, A. Sagisaka, M. Mori, A. S. Pirozhkov, H. Kiriyama, S. V. Bulanov, T. Z. Esirkepov, I. W. Choi, C. M. Kim, T. M. Jeong, T. J. Yu, J. H. Sung, S. K. Lee, N. Hafz, K. H. Pae, Y.-C. Noh, D.-K. Ko, J. Lee, Y. Oishi, K. Nemoto, H. Nagatomo, K. Nagai, and H. Azuma, "Efficient production of a collimated mev proton beam from a polyimide target driven by an intense femtosecond laser pulse", Physics of Plasmas **15**, 053104 (2008) 10.1063/1.2928161 (cit. on p. 85).

[199] P. Norreys, D. Batani, S. Baton, F. N. Beg, R. Kodama, P. Nilson, P. Patel, F. Pérez, J. Santos, R. Scott, V. Tikhonchuk, M. Wei, and J. Zhang, "Fast electron energy transport in solid density and compressed plasma", Nuclear Fusion **54**, 054004 (2014) (cit. on pp. 25, 202).

[200] F. Nürnberg, M. Schollmeier, E. Brambrink, A. Blažević, D. C. Carroll, K. Flippo, D. C. Gautier, M. Geißel, K. Harres, B. M. Hegelich, O. Lundh, K. Markey, P. McKenna, D. Neely, J. Schreiber, and M. Roth, "Radiochromic film imaging spectroscopy of laser-accelerated proton beams", Review of Scientific Instruments **80**, 033301 (2009) (cit. on pp. 85, 100, 234).

[201] R. Nuter, L. Gremillet, P. Combis, M. Drouin, E. Lefebvre, A. Flacco, and V. Malka, "Influence of a preplasma on electron heating and proton acceleration in ultraintense laser-foil interaction", Journal of Applied Physics **104**, 103307 (2008) (cit. on p. 55).

[202] F. Pacini, "Energy Emission from a Neutron Star", Nature **216**, 567 (1967) (cit. on p. 17).

[203] M. Passoni and M. Lontano, "One-dimensional model of the electrostatic ion acceleration in the ultraintense laser–solid interaction", Laser and Particle Beams **22**, 163 (2004) (cit. on p. 83).

[204] M. Passoni and M. Lontano, "Theory of light-ion acceleration driven by a strong charge separation", Phys. Rev. Lett. **101**, 115001 (2008) (cit. on p. 82).

[205] P. K. Patel, A. J. Mackinnon, M. H. Key, T. E. Cowan, M. E. Foord, M. Allen, D. F. Price, H. Ruhl, P. T. Springer, and R. Stephens, "Isochoric heating of solid-density matter with an ultrafast proton beam", Phys. Rev. Lett. **91**, 125004 (2003) (cit. on p. 206).

[206] F. Pérez, A. Debayle, J. Honrubia, M. Koenig, D. Batani, S. D. Baton, F. N. Beg, C. Benedetti, E. Brambrink, S. Chawla, F. Dorchies, C. Fourment, M. Galimberti, L. A. Gizzi, L. Gremillet, R. Heathcote, D. P. Higginson, S. Hulin, R. Jafer, P. Koester, L. Labate, K. L. Lancaster, A. J. MacKinnon, A. G. Macphee, W. Nazarov, P. Nicolai, J. Pasley, R. Ramis, M. Richetta, J. J. Santos, A. Sgattoni, C. Spindloe, B. Vauzour, T. Vinci, and L. Volpe, "Magnetically Guided Fast Electrons in Cylindrically Compressed Matter", Physical Review Letters **107**, 065004, 065004 (2011) (cit. on p. 166).

[207] F. Pérez, L. Gremillet, M. Koenig, S. D. Baton, P. Audebert, M. Chahid, C. Rousseaux, M. Drouin, E. Lefebvre, T. Vinci, J. Rassuchine, T. Cowan, S. A. Gaillard, K. A. Flippo, and R. Shepherd, "Enhanced Isochoric Heating from Fast Electrons Produced by High-Contrast, Relativistic-Intensity Laser Pulses", Physical Review Letters **104**, 085001, 085001 (2010) (cit. on pp. 166, 255).

[208] F. Pérez, A. J. Kemp, L. Divol, C. D. Chen, and P. K. Patel, "Deflection of mev electrons by self-generated magnetic fields in intense laser-solid interactions", Phys. Rev. Lett. **111**, 245001 (2013) (cit. on p. 96).

[209] L. J. Perkins, B. G. Logan, G. B. Zimmerman, and C. J. Werner, "Two-dimensional simulations of thermonuclear burn in ignition-scale inertial confinement fusion targets under compressed axial magnetic fields", Physics of Plasmas **20**, 072708, 072708 (2013) (cit. on p. 202).

[210] G. J. Pert, "The analytic theory of linear resonant absorption", Plasma Physics **20**, 175 (1978) (cit. on p. 49).

[211] D. Pines and D. Bohm, "A Collective Description of Electron Interactions: II. Collective vs Individual Particle Aspects of the Interactions", Physical Review **85**, 338 (1952) (cit. on p. 61).

[212] F. Pisani, A. Bernardinello, D. Batani, A. Antonicci, E. Martinolli, M. Koenig, L. Gremillet, F. Amiranoff, S. Baton, J. Davies, T. Hall, D. Scott, P. Norreys, A. Djaoui, C. Rousseaux, P. Fews, H. Bandulet, and H. Pepin, "Experimental evidence of electric inhibition in fast electron penetration and of electric-field-limited fast electron transport in dense matter", Phys. Rev. E **62**, R5927 (2000) (cit. on p. 166).

[213] B. B. Pollock, D. H. Froula, P. F. Davis, J. S. Ross, S. Fulkerson, J. Bower, J. Satariano, D. Price, K. Krushelnick, and S. H. Glenzer, "High magnetic field generation for laser-plasma experiments", Review of Scientific Instruments **77**, 114703 (2006) (cit. on pp. 28, 96).

[214] H. Popescu, S. D. Baton, F. Amiranoff, C. Rousseaux, M. R. Le Gloahec, J. J. Santos, L. Gremillet, M. Koenig, E. Martinolli, T. Hall, J. C. Adam, A. Heron, and D. Batani, "Subfemtosecond, coherent, relativistic, and ballistic electron bunches generated at ω_0 and $2\omega_0$ in high intensity laser-matter interaction", Physics of Plasmas **12**, 063106, 063106 (2005) (cit. on pp. 169, 258, 259).

[215] A. Poyé, J.-L. Dubois, F. Lubrano-Lavaderci, E. D'Humières, M. Bardon, S. Hulin, M. Bailly-Grandvaux, J. Ribolzi, D. Raffestin, J. J. Santos, P. Nicolaï, and V. Tikhonchuk, "Dynamic model of target charging by short laser pulse interactions", Phys. Rev. E **92**, 043107 (2015) (cit. on pp. 88, 89, 153, 154).

[216] A. Poyé, S. Hulin, M. Bailly-Grandvaux, J.-L. Dubois, J. Ribolzi, D. Raffestin, M. Bardon, F. Lubrano-Lavaderci, E. D'Humières, J. J. Santos, P. Nicolaï, and V. Tikhonchuk, "Physics of giant electromagnetic pulse generation in short-pulse laser experiments", Phys. Rev. E **91**, 043106 (2015) (cit. on pp. 88, 90–92, 105, 106).

[217] W. Priedhorsky, D. Lier, R. Day, and D. Gerke, "Hard-X-Ray Measurements of 10.6-μm Laser-Irradiated Targets", Physical Review Letters **47**, 1661 (1981) (cit. on p. 57).

[218] K. Quinn, P. A. Wilson, C. A. Cecchetti, B. Ramakrishna, L. Romagnani, G. Sarri, L. Lancia, J. Fuchs, A. Pipahl, T. Toncian, O. Willi, R. J. Clarke, D. Neely, M. Notley, P. Gallegos, D. C. Carroll, M. N. Quinn, X. H. Yuan, P. McKenna, T. V. Liseykina, A. Macchi, and M. Borghesi, "Laser-driven ultrafast field propagation on solid surfaces", Phys. Rev. Lett. **102**, 194801 (2009) (cit. on pp. 93, 101, 184).

[219] K. Quinn, P. A. Wilson, B. Ramakrishna, L. Romagnani, G. Sarri, C. A. Cecchetti, L. Lancia, J. Fuchs, A. Pipahl, T. Toncian, O. Willi, R. J. Clarke, D. Neely, M. Notley, P. Gallegos, D. C. Carroll, M. N. Quinn, X. H. Yuan, P. McKenna, and M. Borghesi, "Modified proton radiography arrangement for the detection of ultrafast field fronts", Review of Scientific Instruments **80**, 113506 (2009) 10.1063/1.3262630 (cit. on pp. 93, 101, 184).

[220] K. E. Quinn, "Plasma dynamics following ultraintense laser-solid interactions", PhD thesis (Queen's University Belfast, Belfast, UK, 2010) (cit. on pp. 93, 94).

[221] B. Ramakrishna, S. Kar, A. P. L. Robinson, D. J. Adams, K. Markey, M. N. Quinn, X. H. Yuan, P. McKenna, K. L. Lancaster, J. S. Green, R. H. H. Scott, P. A. Norreys, J. Schreiber, and M. Zepf, "Laser-Driven Fast Electron Collimation in Targets with Resistivity Boundary", Physical Review Letters **105**, 135001, 135001 (2010) (cit. on p. 166).

[222] A. Ramani and G. Laval, "Heat flux reduction by electromagnetic instabilities", Physics of Fluids **21**, 980 (1978) (cit. on p. 79).

[223] A. Ravasio, L. Romagnani, S. Le Pape, A. Benuzzi-Mounaix, C. Cecchetti, D. Batani, T. Boehly, M. Borghesi, R. Dezulian, L. Gremillet, E. Henry, D. Hicks, B. Loupias, A. MacKinnon, N. Ozaki, H. S. Park, P. Patel, A. Schiavi, T. Vinci, R. Clarke, M. Notley, S. Bandyopadhyay, and M. Koenig, "Proton radiography of a shock-compressed target", Phys. Rev. E **82**, 016407 (2010) (cit. on p. 86).

[224] A. Raven, O. Willi, and P. T. Rumsby, "Megagauss magnetic field profiles in laser-produced plasmas", Phys. Rev. Lett. **41**, 554 (1978) (cit. on p. 73).

[225] B. A. Remington, R. P. Drake, and D. D. Ryutov, "Experimental astrophysics with high power lasers and Z pinches", Reviews of Modern Physics **78**, 755 (2006) (cit. on pp. 18, 207).

[226] C. Ren, M. Tzoufras, F. S. Tsung, W. B. Mori, S. Amorini, R. A. Fonseca, L. O. Silva, J. C. Adam, and A. Heron, "Global simulation for laser-driven mev electrons in fast ignition", Phys. Rev. Lett. **93**, 185004 (2004) (cit. on p. 55).

[227] X. Ribeyre, S. Gus'kov, J.-L. Feugeas, P. Nicolaï, and V. T. Tikhonchuk, "Dense plasma heating and Gbar shock formation by a high intensity flux of energetic electrons", Physics of Plasmas **20**, 062705, 062705 (2013) (cit. on p. 205).

[228] C. P. Ridgers, R. J. Kingham, and A. G. R. Thomas, "Magnetic cavitation and the reemergence of nonlocal transport in laser plasmas", Phys. Rev. Lett. **100**, 075003 (2008) (cit. on pp. 74, 205).

[229] A. P. L. Robinson and H. Schmitz, "Elliptical magnetic mirror generated via resistivity gradients for fast ignition inertial confinement fusion", Physics of Plasmas **20**, 062704 (2013) 10.1063/1.4812193 (cit. on p. 166).

[230] A. P. L. Robinson and M. Sherlock, "Magnetic collimation of fast electrons produced by ultraintense laser irradiation by structuring the target composition", Physics of Plasmas **14**, 083105, 083105 (2007) (cit. on p. 166).

[231] A. P. L. Robinson, M. Sherlock, and P. A. Norreys, "Artificial collimation of fast-electron beams with two laser pulses", Phys. Rev. Lett. **100**, 025002 (2008) (cit. on p. 166).

[232] A. Robinson, D. Strozzi, J. Davies, L. Gremillet, J. Honrubia, T. Johzaki, R. Kingham, M. Sherlock, and A. Solodov, "Theory of fast electron transport for fast ignition", Nuclear Fusion **54**, 054003 (2014) (cit. on pp. 25, 182).

[233] L. Romagnani, J. Fuchs, M. Borghesi, P. Antici, P. Audebert, F. Ceccherini, T. Cowan, T. Grismayer, S. Kar, A. Macchi, P. Mora, G. Pretzler, A. Schiavi, T. Toncian, and O. Willi, "Dynamics of Electric Fields Driving the Laser Acceleration of Multi-MeV Protons", Physical Review Letters **95**, 195001, 195001 (2005) (cit. on p. 184).

[234] M. Roth, A. Blazevic, M. Geissel, T. Schlegel, T. E. Cowan, M. Allen, J.-C. Gauthier, P. Audebert, J. Fuchs, J. Meyer-ter-Vehn, M. Hegelich, S. Karsch, and A. Pukhov, "Energetic ions generated by laser pulses: a detailed study on target properties", Phys. Rev. ST Accel. Beams **5**, 061301 (2002) (cit. on p. 85).

[235] M. Roth, T. E. Cowan, M. H. Key, S. P. Hatchett, C. Brown, W. Fountain, J. Johnson, D. M. Pennington, R. A. Snavely, S. C. Wilks, K. Yasuike, H. Ruhl, F. Pegoraro, S. V. Bulanov, E. M. Campbell, M. D. Perry, and H. Powell, "Fast ignition by intense laser-accelerated proton beams", Phys. Rev. Lett. **86**, 436 (2001) (cit. on pp. 26, 206).

[236] M. Roth, E. Brambrink, P. Audebert, M. Basko, A. Blazevic, R. Clarke, J. Cobble, T. E. Cowan, J. Fernández, J. Fuchs, M. Hegelich, K. Ledingham, B. G. Logan, D. Neely, H. Ruhl, and M. Schollmeier, "Laser accelerated ions in icf research prospects and experiments", Plasma Physics and Controlled Fusion **47**, B841 (2005) (cit. on pp. 85, 101).

[237] W. Rozmus, V. T. Tikhonchuk, and R. Cauble, "A model of ultrashort laser pulse absorption in solid targets", Physics of Plasmas **3**, 360 (1996) (cit. on p. 48).

[238] J. J. Santos, M. Bailly-Grandvaux, L. Giuffrida, P. Forestier-Colleoni, S. Fujioka, Z. Zhang, P. Korneev, R. Bouillaud, S. Dorard, D. Batani, M. Chevrot, J. E. Cross, R. Crowston, J.-L. Dubois, J. Gazave, G. Gregori, E. d'Humières, S. Hulin, K. Ishihara, S. Kojima, E. Loyez, J.-R. Marquès, A. Morace, P. Nicolaï, O. Peyrusse, A. Poyé, D. Raffestin, J. Ribolzi, M. Roth, G. Schaumann, F. Serres, V. T. Tikhonchuk, P. Vacar, and N. Woolsey, "Laser-driven platform for generation and characterization of strong quasi-static magnetic fields", New Journal of Physics **17**, 083051 (2015) (cit. on pp. 156, 171, 179).

[239] J. J. Santos, F. Amiranoff, S. D. Baton, L. Gremillet, M. Koenig, E. Martinolli, M. Rabec Le Gloahec, C. Rousseaux, D. Batani, A. Bernardinello, G. Greison, and T. Hall, "Fast electron transport in ultraintense laser pulse interaction with solid targets by rear-side self-radiation diagnostics", Phys. Rev. Lett. **89**, 025001 (2002) (cit. on pp. 83, 166, 169, 172, 259, 260).

[240] J. J. Santos, D. Batani, S. D. Baton, F. N. Beg, T. Ceccotti, A. Debayle, F. Dorchies, J.-L. Feugeas, C. Fourment, L. Gremillet, J. J. Honrubia, S. Hulin, A. Morace, P. Nicolaï, F. Pérez, H. Sawada, H.-P. Schlenvoigt, V. T. Tikhonchuk, X. Vaisseau, B. Vauzour, M. Wei, and Wei, "Supra-thermal electron beam stopping power and guiding in dense plasmas", Journal of Plasma Physics **79**, 429 (2013) (cit. on p. 53).

[241] J. J. Santos, A. Debayle, P. Nicolaï, V. Tikhonchuk, M. Manclossi, D. Batani, A. Guemnie-Tafo, J. Faure, V. Malka, and J. J. Honrubia, "Fast-electron transport and induced heating in aluminum foils", Physics of Plasmas **14**, 103107, 103107 (2007) (cit. on p. 166).

[242] G. Sarri, A. Macchi, C. A. Cecchetti, S. Kar, T. V. Liseykina, X. H. Yang, M. E. Dieckmann, J. Fuchs, M. Galimberti, L. A. Gizzi, R. Jung, I. Kourakis, J. Osterholz, F. Pegoraro, A. P. L. Robinson, L. Romagnani, O. Willi, and M. Borghesi, "Dynamics of Self-Generated, Large Amplitude Magnetic Fields Following High-Intensity Laser Matter Interaction", Physical Review Letters **109**, 205002, 205002 (2012) (cit. on pp. 78, 184).

[243] D. B. Schaeffer, E. T. Everson, A. S. Bondarenko, S. E. Clark, C. G. Constantin, D. Winske, W. Gekelman, and C. Niemann, "Experimental study of subcritical laboratory magnetized collisionless shocks using a laser-driven magnetic piston", Physics of Plasmas **22**, 113101, 113101 (2015) (cit. on pp. 18, 207).

[244] P. F. Schmit, P. F. Knapp, S. B. Hansen, M. R. Gomez, K. D. Hahn, D. B. Sinars, K. J. Peterson, S. A. Slutz, A. B. Sefkow, T. J. Awe, E. Harding, C. A. Jennings, G. A. Chandler, G. W. Cooper, M. E. Cuneo, M. Geissel, A. J. Harvey-Thompson, M. C. Herrmann, M. H. Hess, O. Johns, D. C. Lamppa, M. R. Martin, R. D. McBride, J. L. Porter, G. K. Robertson, G. A. Rochau, D. C. Rovang, C. L. Ruiz, M. E. Savage, I. C. Smith, W. A. Stygar, and R. A. Vesey, "Understanding Fuel Magnetization and Mix Using Secondary Nuclear Reactions in Magneto-Inertial Fusion", Physical Review Letters **113**, 155004, 155004 (2014) (cit. on p. 27).

[245] H. Schmitz, R. Lloyd, and R. G. Evans, "Collisional particle-in-cell modelling of the generation and control of relativistic electron beams produced by ultra-intense laser pulses", Plasma Physics and Controlled Fusion **54**, 085016 (2012) (cit. on p. 166).

[246] J. Schreiber, F. Bell, F. Grüner, U. Schramm, M. Geissler, M. Schnürer, S. Ter-Avetisyan, B. M. Hegelich, J. Cobble, E. Brambrink, J. Fuchs, P. Audebert, and D. Habs, "Analytical model for ion acceleration by high-intensity laser pulses", Phys. Rev. Lett. **97**, 045005 (2006) (cit. on p. 83).

[247] C. B. Schroeder, E. Esarey, J. van Tilborg, and W. P. Leemans, "Theory of coherent transition radiation generated at a plasma-vacuum interface", Phys. Rev. E **69**, 016501, 016501 (2004) (cit. on p. 257).

[248] G. P. Schurtz, P. D. Nicolaï, and M. Busquet, "A nonlocal electron conduction model for multidimensional radiation hydrodynamics codes", Physics of Plasmas **7**, 4238 (2000) (cit. on p. 74).

[249] R. H. H. Scott, C. Beaucourt, H.-P. Schlenvoigt, K. Markey, K. L. Lancaster, C. P. Ridgers, C. M. Brenner, J. Pasley, R. J. Gray, I. O. Musgrave, A. P. L. Robinson, K. Li, M. M. Notley, J. R. Davies, S. D. Baton, J. J. Santos, J.-L. Feugeas, P. Nicolaï, G. Malka, V. T. Tikhonchuk, P. McKenna, D. Neely, S. J. Rose, and P. A. Norreys, "Controlling Fast-Electron-Beam Divergence Using Two Laser Pulses", Physical Review Letters **109**, 015001, 015001 (2012) (cit. on p. 166).

[250] M. Seimetz, P. Bellido, A. Soriano, J. G. López, M. C. Jiménez-Ramos, B. Fernández, P. Conde, E. Crespo, A. J. González, L. Hernández, A. Iborra, L. Moliner, J. P. Rigla, M. J. Rodríguez-Álvarez, F. Sánchez, S. Sánchez, L. F. Vidal, and J. M. Benlloch, "Calibration and performance tests of detectors for laser-accelerated protons", IEEE Transactions on Nuclear Science **62**, 3216 (2015) (cit. on p. 233).

[251] Y. Sentoku, T. E. Cowan, A. Kemp, and H. Ruhl, "High energy proton acceleration in interaction of short laser pulse with dense plasma target", Physics of Plasmas **10**, 2009 (2003) (cit. on p. 81).

[252] H. D. Shay, P. Amendt, D. Clark, D. Ho, M. Key, J. Koning, M. Marinak, D. Strozzi, and M. Tabak, "Implosion and burn of fast ignition capsules–Calculations with HYDRA", Physics of Plasmas **19**, 092706, 092706 (2012) (cit. on p. 26).

[253] J. W. Shearer, "Interaction of capacitor-bank-produced megagauss magnetic field with small single-turn coil", Journal of Applied Physics **40**, 4490 (1969) (cit. on p. 27).

[254] D. B. Sinars, G. R. Bennett, D. F. Wenger, M. E. Cuneo, and J. L. Porter, "Evaluation of bent-crystal x-ray backlighting and microscopy techniques for the sandia z machine", Appl. Opt. **42**, 4059 (2003) (cit. on pp. 253, 254).

[255] R. A. Snavely, M. H. Key, S. P. Hatchett, T. E. Cowan, M. Roth, T. W. Phillips, M. A. Stoyer, E. A. Henry, T. C. Sangster, M. S. Singh, S. C. Wilks, A. MacKinnon, A. Offenberger, D. M. Pennington, K. Yasuike, A. B. Langdon, B. F. Lasinski, J. Johnson, M. D. Perry, and E. M. Campbell, "Intense high-energy proton beams from petawatt-laser irradiation of solids", Phys. Rev. Lett. **85**, 2945 (2000) (cit. on pp. 80, 85).

[256] A. A. Solodov and R. Betti, "Stopping power and range of energetic electrons in dense plasmas of fast-ignition fusion targets", Physics of Plasmas **15**, 042707, 042707 (2008) (cit. on p. 59).

[257] A. A. Solodov, R. Betti, K. S. Anderson, J. F. Myatt, W. Theobald, and C. Stoeckl, "Controlling the Divergence of Laser-Generated Fast Electrons Through Resistivity Gradients in Fast-Ignition Targets", in Aps meeting abstracts (Nov. 2010) (cit. on p. 166).

[258] A. Spitkovsky, "Particle Acceleration in Relativistic Collisionless Shocks: Fermi Process at Last?", ApJ **682**, L5, L5 (2008) (cit. on p. 17).

[259] L. Spitzer, *Physics of Fully Ionized Gases* (1956) (cit. on p. 65).

[260] L. Spitzer and R. Härm, "Transport phenomena in a completely ionized gas", Phys. Rev. **89**, 977 (1953) (cit. on p. 73).

[261] J. A. Stamper, K. Papadopoulos, R. N. Sudan, S. O. Dean, E. A. McLean, and J. M. Dawson, "Spontaneous magnetic fields in laser-produced plasmas", Phys. Rev. Lett. **26**, 1012 (1971) (cit. on p. 72).

[262] D. J. Stark, T. Toncian, and A. V. Arefiev, "Enhanced multi-mev photon emission by a laser-driven electron beam in a self-generated magnetic field", Phys. Rev. Lett. **116**, 185003 (2016) (cit. on p. 166).

[263] R. B. Stephens, R. A. Snavely, Y. Aglitskiy, F. Amiranoff, C. Andersen, D. Batani, S. D. Baton, T. Cowan, R. R. Freeman, T. Hall, S. P. Hatchett, J. M. Hill, M. H. Key, J. A. King, J. A. Koch, M. Koenig, A. J. MacKinnon, K. L. Lancaster, E. Martinolli, P. Norreys, E. Perelli-Cippo, M. Rabec Le Gloahec, C. Rousseaux, J. J. Santos, and F. Scianitti, "K_α fluorescence measurement of relativistic electron transport in the context of fast ignition", Phys. Rev. E **69**, 066414, 066414 (2004) (cit. on p. 166).

[264] R. M. Sternheimer, "Shielding and antishielding effects for various ions and atomic systems", Phys. Rev. **146**, 140 (1966) (cit. on p. 60).

[265] R. M. Sternheimer, S. M. Seltzer, and M. J. Berger, "Density effect for the ionization loss of charged particles in various substances", Phys. Rev. B **26**, 6067 (1982) (cit. on p. 60).

[266] D. Strickland and G. Mourou, "Compression of amplified chirped optical pulses", Optics Communications **56**, 219 (1985) (cit. on pp. 44, 213).

[267] D. J. Strozzi, L. J. Perkins, M. M. Marinak, D. J. Larson, J. M. Koning, and B. G. Logan, "Imposed magnetic field and hot electron propagation in inertial fusion hohlraums", Journal of Plasma Physics **81**, 475810603, 475810603 (2015) (cit. on p. 205).

[268] D. J. Strozzi, M. Tabak, D. J. Larson, L. Divol, A. J. Kemp, C. Bellei, M. M. Marinak, and M. H. Key, "Fast-ignition transport studies: realistic electron source, integrated particle-in-cell and hydrodynamic modeling, imposed magnetic fields", Physics of Plasmas **19**, 072711 (2012) 10.1063/1.4739294 (cit. on pp. 166, 202).

[269] R. N. Sudan, "Mechanism for the generation of 10^9 G magnetic fields in the interaction of ultraintense short laser pulse with an overdense plasma target", Phys. Rev. Lett. **70**, 3075 (1993) (cit. on p. 78).

[270] M. Tabak, J. Hammer, M. E. Glinsky, W. L. Kruer, S. C. Wilks, J. Woodworth, E. M. Campbell, M. D. Perry, and R. J. Mason, "Ignition and high gain with ultrapowerful lasers", Physics of Plasmas **1**, 1626 (1994) (cit. on p. 25).

[271] M. Temporal, J. J. Honrubia, and S. Atzeni, "Numerical study of fast ignition of ablatively imploded deuterium-tritium fusion capsules by ultra-intense proton beams", Physics of Plasmas **9**, 3098 (2002) (cit. on p. 206).

[272] W. Theobald, K. Akli, R. Clarke, J. A. Delettrez, R. R. Freeman, S. Glenzer, J. Green, G. Gregori, R. Heathcote, N. Izumi, J. A. King, J. A. Koch, J. Kuba, K. Lancaster, A. J. MacKinnon, M. Key, C. Mileham, J. Myatt, D. Neely, P. A. Norreys, H.-S. Park, J. Pasley, P. Patel, S. P. Regan, H. Sawada, R. Shepherd, R. Snavely, R. B. Stephens, C. Stoeckl, M. Storm, B. Zhang, and T. C. Sangster, "Hot surface ionic line emission and cold K-inner shell emission from petawatt-laser-irradiated Cu foil targets", Physics of Plasmas **13**, 043102, 043102 (2006) (cit. on p. 53).

[273] J. J. Thomson, C. E. Max, and K. Estabrook, "Magnetic fields due to resonance absorption of laser light", Phys. Rev. Lett. **35**, 663 (1975) (cit. on p. 78).

[274] D. A. Tidman and R. A. Shanny, "Field-generating thermal instability in laser-heated plasmas", Physics of Fluids **17**, 1207 (1974) (cit. on p. 73).

[275] V. T. Tikhonchuk, "Interaction of a beam of fast electrons with solids", Physics of Plasmas **9**, 1416 (2002) (cit. on pp. 87, 166).

[276] S. Tokita, S. Sakabe, T. Nagashima, M. Hashida, and S. Inoue, "Strong sub-terahertz surface waves generated on a metal wire by high-intensity laser pulses", Scientific Reports **5**, 8268, 8268 (2015) (cit. on pp. 94, 195).

[277] T. Toncian, M. Borghesi, J. Fuchs, E. d'Humières, P. Antici, P. Audebert, E. Brambrink, C. A. Cecchetti, A. Pipahl, L. Romagnani, and O. Willi, "Ultrafast Laser-Driven Microlens to Focus and Energy-Select Mega-Electron Volt Protons", Science **312**, 410 (2006) (cit. on p. 184).

[278] E. H. Turner and R. H. Stolen, "Fiber Faraday circulator or isolator", Optics Letters **6**, 322 (1981) (cit. on p. 102).

[279] U.S. Energy Information Administration (EIA), *International Energy Outlook*, 2016 (cit. on p. 18).

[280] X. Vaisseau, A. Debayle, J. J. Honrubia, S. Hulin, A. Morace, P. Nicolaï, H. Sawada, B. Vauzour, D. Batani, F. N. Beg, J. R. Davies, R. Fedosejevs, R. J. Gray, G. E. Kemp, S. Kerr, K. Li, A. Link, P. McKenna, H. S. McLean, M. Mo, P. K. Patel, J. Park, J. Peebles, Y. J. Rhee, A. Sorokovikova, V. T. Tikhonchuk, L. Volpe, M. Wei, and J. J. Santos, "Enhanced Relativistic-Electron-Beam Energy Loss in Warm Dense Aluminum", Physical Review Letters **114**, 095004, 095004 (2015) (cit. on pp. 166, 175).

[281] B. Vauzour, A. Debayle, X. Vaisseau, S. Hulin, H.-P. Schlenvoigt, D. Batani, S. D. Baton, J. J. Honrubia, P. Nicolaï, F. N. Beg, R. Benocci, S. Chawla, M. Coury, F. Dorchies, C. Fourment, E. d'Humières, L. C. Jarrot, P. McKenna, Y. J. Rhee, V. T. Tikhonchuk, L. Volpe, V. Yahia, and J. J. Santos, "Unraveling resistive versus collisional contributions to relativistic electron beam stopping power in cold-solid and in warm-dense plasmas", Physics of Plasmas **21**, 033101, 033101 (2014) (cit. on pp. 55, 68, 172, 174, 175).

[282] B. Vauzour, J. J. Santos, A. Debayle, S. Hulin, H.-P. Schlenvoigt, X. Vaisseau, D. Batani, S. D. Baton, J. J. Honrubia, P. Nicolaï, F. N. Beg, R. Benocci, S. Chawla, M. Coury, F. Dorchies, C. Fourment, E. d'Humières, L. C. Jarrot, P. McKenna, Y. J. Rhee, V. T. Tikhonchuk, L. Volpe, and V. Yahia, "Relativistic High-Current Electron-Beam Stopping-Power Characterization in Solids and Plasmas: Collisional Versus Resistive Effects", Physical Review Letters **109**, 255002, 255002 (2012) (cit. on pp. 53, 55, 172, 174, 175).

[283] L. Volpe, R. Jafer, B. Vauzour, P. Nicolai, J. J. Santos, F. Dorchies, C. Fourment, S. Hulin, C. Regan, F. Perez, S. Baton, K. Lancaster, M. Galimberti, R. Heathcote, M. Tolley, C. Spindloe, W. Nazarov, P. Koester, L. Labate, L. A. Gizzi, C. Benedetti, A. Sgattoni, M. Richetta, J. Pasley, F. N. Beg, S. Chawla, D. P. Higginson, A. G. MacPhee, and D. Batani, "Proton radiography of cylindrical laser-driven implosions", Plasma Physics and Controlled Fusion **53**, 032003 (2011) (cit. on p. 86).

[284] T. F. Wall, "The generation of very intense magnetic fields", Electrical Engineers, Journal of the Institution of **64**, 745 (1926) (cit. on p. 26).

[285] W.-M. Wang, P. Gibbon, Z.-M. Sheng, and Y.-T. Li, "Magnetically Assisted Fast Ignition", Physical Review Letters **114**, 015001, 015001 (2015) (cit. on pp. 166, 182, 202).

[286] E. S. Weibel, "Anomalous Skin Effect in a Plasma", Physics of Fluids **10**, 741 (1967) (cit. on p. 49).

[287] E. S. Weibel, "Spontaneously growing transverse waves in a plasma due to an anisotropic velocity distribution", Phys. Rev. Lett. **2**, 83 (1959) (cit. on p. 79).

[288] B. Westover, C. D. Chen, P. K. Patel, H. McLean, and F. N. Beg, "Characterization of the fast electrons distribution produced in a high intensity laser target interaction", Physics of Plasmas **21**, 031212, 031212 (2014) (cit. on p. 166).

[289] K. B. Wharton, S. P. Hatchett, S. C. Wilks, M. H. Key, J. D. Moody, V. Yanovsky, A. A. Offenberger, B. A. Hammel, M. D. Perry, and C. Joshi, "Experimental measurements of hot electrons generated by ultraintense ($> 10^{19}$ W/cm^2) laser-plasma interactions on solid-density targets", Phys. Rev. Lett. **81**, 822 (1998) (cit. on pp. 53, 166).

[290] S. C. Wilks, W. L. Kruer, M. Tabak, and A. B. Langdon, "Absorption of ultra-intense laser pulses", Phys. Rev. Lett. **69**, 1383 (1992) (cit. on pp. 45, 51, 55, 171).

[291] S. C. Wilks, A. B. Langdon, T. E. Cowan, M. Roth, M. Singh, S. Hatchett, M. H. Key, D. Pennington, A. MacKinnon, and R. A. Snavely, "Energetic proton generation in ultra-intense laser–solid interactions", Physics of Plasmas **8**, 542 (2001) (cit. on p. 80).

[292] L. Willingale, P. M. Nilson, M. C. Kaluza, A. E. Dangor, R. G. Evans, P. Fernandes, M. G. Haines, C. Kamperidis, R. J. Kingham, C. P. Ridgers, M. Sherlock, A. G. R. Thomas, M. S. Wei, Z. Najmudin, K. Krushelnick, S. Bandyopadhyay, M. Notley, S. Minardi, M. Tatarakis, and W. Rozmus, "Proton deflectometry of a magnetic reconnection geometry", Physics of Plasmas **17**, 043104, 043104 (2010) (cit. on p. 18).

[293] L. Willingale, A. G. R. Thomas, P. M. Nilson, M. C. Kaluza, S. Bandyopadhyay, A. E. Dangor, R. G. Evans, P. Fernández, M. G. Haines, C. Kamperidis, R. J. Kingham, S. Minardi, M. Notley, C. P. Ridgers, W. Rozmus, M. Sherlock, M. Tatarakis, M. S. Wei, Z. Najmudin, and K. Krushelnick, "Fast advection of magnetic fields by hot electrons", Phys. Rev. Lett. **105**, 095001 (2010) (cit. on p. 72).

[294] D. G. Yakovlev and V. A. Urpin, "Thermal and Electrical Conductivity in White Dwarfs and Neutron Stars", Soviet Astronomy **24**, 303 (1980) (cit. on p. 65).

[295] T. Y. B. Yang, W. L. Kruer, R. M. More, and A. B. Langdon, "Absorption of laser light in overdense plasmas by sheath inverse bremsstrahlung", Physics of Plasmas **2**, 3146 (1995) (cit. on p. 50).

[296] K. Yasuike, M. H. Key, S. P. Hatchett, R. A. Snavely, and K. B. Wharton, "Hot electron diagnostic in a solid laser target by k-shell lines measurement from ultraintense laser–plasma interactions ($310^20\,\mathrm{W/cm^2}$, $\leqslant 400\,\mathrm{J}$)", Review of Scientific Instruments **72**, 1236 (2001) (cit. on p. 53).

[297] Q. Z. Yu, Y. T. Li, S. M. Weng, Q. L. Dong, F. Liu, Z. Zhang, J. Zhao, X. Lu, C. Danson, D. Pepler, X. H. Jiang, Y. G. Liu, L. Z. Huang, S. Y. Liu, Y. K. Ding, Z. B. Wang, Y. Gu, X. T. He, Z. M. Sheng, and J. Zhang, "Nonlocal heat transport in laser-produced aluminum plasmas", Physics of Plasmas **17**, 043106 (2010) 10.1063/1.3372109 (cit. on pp. 73, 74).

[298] X. H. Yuan, A. P. L. Robinson, M. N. Quinn, D. C. Carroll, M. Borghesi, R. J. Clarke, R. G. Evans, J. Fuchs, P. Gallegos, L. Lancia, D. Neely, K. Quinn, L. Romagnani, G. Sarri, P. A. Wilson, and P. McKenna, "Effect of self-generated magnetic fields on fast-electron beam divergence in solid targets", New Journal of Physics **12**, 063018 (2010) (cit. on p. 85).

[299] R. T. Zavala and G. B. Taylor, "Faraday Rotation Measure Gradients from a Helical Magnetic Field in 3C 273", ApJ **626**, L73 (2005) (cit. on p. 102).

[300] K. Zeil, S. D. Kraft, S. Bock, M. Bussmann, T. E. Cowan, T. Kluge, J. Metzkes, T. Richter, R. Sauerbrey, and U. Schramm, "The scaling of proton energies in ultrashort pulse laser plasma acceleration", New Journal of Physics **12**, 045015 (2010) (cit. on p. 85).

[301] Y. Zhang, Z. Jiang, J. P. Small, M. S. Purewal, Y.-W. Tan, M. Fazlollahi, J. D. Chudow, J. A. Jaszczak, H. L. Stormer, and P. Kim, "Landau-Level Splitting in Graphene in High Magnetic Fields", Physical Review Letters **96**, 136806, 136806 (2006) (cit. on p. 208).

[302] J. Zheng, K. A. Tanaka, T. Miyakoshi, Y. Kitagawa, R. Kodama, T. Kurahashi, and T. Yamanaka, "Spectrum of transition radiation from hot electrons generated in ultra-intense laser plasma interaction", Physics of Plasmas **9**, 3610 (2002) (cit. on p. 257).

[303] J. Zheng, K. A. Tanaka, T. Miyakoshi, Y. Kitagawa, R. Kodama, T. Kurahashi, and T. Yamanaka, "Theoretical study of transition radiation from hot electrons generated in the laser-solid interaction", Physics of Plasmas **10**, 2994 (2003) (cit. on p. 257).

[304] J. Zhong, Y. Li, X. Wang, J. Wang, Q. Dong, C. Xiao, S. Wang, X. Liu, L. Zhang, L. An, F. Wang, J. Zhu, Y. Gu, X. He, G. Zhao, and J. Zhang, "Modelling loop-top X-ray source and reconnection outflows in solar flares with intense lasers", Nature Physics **6**, 984 (2010) (cit. on p. 18).

[305] J. Zhou, G. Taft, C.-P. Huang, M. M. Murnane, H. C. Kapteyn, and I. P. Christov, "Pulse evolution in a broad-bandwidth Ti:sapphire laser", Optics Letters **19**, 1149 (1994) (cit. on p. 213).